

Francesco Chiadini
Vincenzo Fiumara *Editors*

More Adventures in Contemporary Electromagnetic Theory

 Springer

More Adventures in Contemporary Electromagnetic Theory


Francesco Chiadini • Vincenzo Fiumara
Editors

More Adventures in Contemporary Electromagnetic Theory

 Springer

Editors

Francesco Chiadini 
University of Salerno
Fisciano, Italy

Vincenzo Fiumara 
University of Basilicata
Potenza, Italy

ISBN 978-3-031-83130-0 ISBN 978-3-031-83131-7 (eBook)
<https://doi.org/10.1007/978-3-031-83131-7>

© The Editor(s) (if applicable) and The Author(s), under exclusive license to Springer Nature Switzerland AG 2025

This work is subject to copyright. All rights are solely and exclusively licensed by the Publisher, whether the whole or part of the material is concerned, specifically the rights of translation, reprinting, reuse of illustrations, recitation, broadcasting, reproduction on microfilms or in any other physical way, and transmission or information storage and retrieval, electronic adaptation, computer software, or by similar or dissimilar methodology now known or hereafter developed.

The use of general descriptive names, registered names, trademarks, service marks, etc. in this publication does not imply, even in the absence of a specific statement, that such names are exempt from the relevant protective laws and regulations and therefore free for general use.

The publisher, the authors and the editors are safe to assume that the advice and information in this book are believed to be true and accurate at the date of publication. Neither the publisher nor the authors or the editors give a warranty, expressed or implied, with respect to the material contained herein or for any errors or omissions that may have been made. The publisher remains neutral with regard to jurisdictional claims in published maps and institutional affiliations.

This Springer imprint is published by the registered company Springer Nature Switzerland AG
The registered company address is: Gewerbestrasse 11, 6330 Cham, Switzerland

If disposing of this product, please recycle the paper.

Introduction

This book is based on talks delivered at the 2nd Weiglhofer Symposium on Electromagnetic Theory. The symposium was dedicated to the memory of Werner Siegfried Weiglhofer, formerly Professor of Applied Mathematics at the University of Glasgow, who died in January 2003 in a mountaineering accident in Norway (Fig. 1).

The 1st Weiglhofer Symposium on Electromagnetic Theory was held in July 2022 in Edinburgh, Scotland. A book comprising talks delivered at that symposium was published the following year [1].

The 2nd Weiglhofer Symposium, held in Cetara, Italy, was coordinated by the two of us. Francesco is Professor of Optics, Department of Industrial Engineering, University of Salerno, and Vincenzo is Professor of Electromagnetics, Department of Engineering, University of Basilicata. Although not having worked directly with Prof. Weiglhofer, both of us have deeply appreciated and capitalized on his pioneering work on theoretical electromagnetics of complex materials.

Twenty-two papers on cutting-edge topics of electromagnetic theory and applications were presented at the 2nd Weiglhofer Symposium by researchers from 13 different countries (Fig. 2).

This book consists of 16 chapters showcasing significant recent progress in theoretical electromagnetics ranging from engineering science to nanotechnology. The topics covered are diverse, ranging from foundational concepts to practical applications, and include both analytical and numerical approaches.

The book also includes a chapter that is an English translation from German of a seminal paper published by Eduard Reusch in 1869. The last chapter in the book is a report on a round-table discussion held in the closing session of the symposium, on the critical role of Electromagnetism—particularly in the fields of Optics and Photonics—addressing some of today’s most pressing societal challenges, including Energy, Climate, and Health.

Fig. 1 Werner Siegfried Weiglhofer (25 Aug 1982–12 Jan 2003)



Fig. 2 Speakers at the 2nd Weiglhofer Symposium on Electromagnetic Theory, photographed by the co-organizer Roberta De Simone at the Hotel Cetus, Cetara (SA), Italy

Department of Industrial Engineering, University
of Salerno, Fisciano SA, Italy,
e-mail: fchiadini@unisa.it
Department of Engineering, University of
Basilicata, Potenza, Italy,
e-mail: vincenzo.fiumara@unibas.it

Francesco Chiadini

Vincenzo Fiumara

Reference

1. T.G. Mackay, A. Lakhtakia (eds.), *Adventures in Contemporary Electromagnetic Theory* (Springer, Cham, 2023)

Contents

Optical Investigations on Periodic Multilayers of Mica	1
Eduard Reusch and Akhlesh Lakhtakia	
Unidirectional Waves in Discrete Plasmonic Waveguides	17
Vadim A. Markel	
Survey and Perspectives on Line-Wave Electromagnetics	43
Massimo Moccia, Marino Coppolaro, Giuseppe Castaldi, and Vincenzo Galdi	
Oddly Shaped Inclusions: Depolarization Dyadics and Homogenization	63
Tom G. Mackay and Akhlesh Lakhtakia	
Photonic Metamaterials for Light Modulation, Energy Saving, and Sensing Applications	87
Majd Abu Aisheh, Amaljith CK, Anand M. Shrivastav, and Ibrahim Abdulhalim	
The Role of Maxwell's Equations in Design of Metamaterials and in 3D Imaging	133
Partha P. Banerjee, Austin M. Scott, and Guo Chen	
Nanophotonics Applications of Gradient Surface Electromagnetic Waves	151
Igor I. Smolyaninov and Vera N. Smolyaninova	
The Circular Bragg Phenomenon Updated	173
Akhlesh Lakhtakia	
Computational Plasmonics: Boundary Integral Equation Methods in Scattering Problems	195
Christos Mystilidis, Guy Vandenbosch, and Xuezhong Zheng	

On a List of Problems for Research in Generalized Lorenz-Mie Theories, More Generally T-Matrix Approach for Structured Beams: The State-of-the-Art	223
G�rard Gouesbet	
Sum Rules and Physical Bounds for a Particulate Slab	253
Gerhard Kristensson	
Optics with Tightly Interlaced Matched Ambidextrous Bilayers	281
Francesco Chiadini, Roberta De Simone, Vincenzo Fiumara, and Akhlesh Lakhtakia	
Analysis of Multiple Scattering by Cylindrical Arrays and Applications to Electromagnetic Shielding	307
Grigorios P. Zouros, Minas Kouroublakis, and Nikolaos L. Tsitsas	
Static Bragg-Less and Dynamic Bragg-Like Resonances	329
Martin W. McCall and Stefanos Fr. Koufidis	
Geometric Phase and Nanoscale Architected Morphology of Reusch Piles	361
Akhlesh Lakhtakia	
UWVF: A Trefftz Numerical Method for Maxwell's Equations	393
Timo L�hivaara, William F. Hall, Matti Malinen, Dale Ota, Vijaya Shankar, and Peter Monk	
Weiglhofer Symposium Panel Discussion: Future Developments	421
Ibrahim Abdulhalim, G�rard Gouesbet, Gerhard Kristensson, Guy Vandenbosch, and Theo Rasing	
Index	423

Optical Investigations on Periodic Multilayers of Mica



Eduard Reusch and Akhlesh Lakhtakia 

Annalen der Physik und Chemie (Leipzig) **138**, 628–638 (1869)

Untersuchung über Glimmercombinationen; von E. Reusch.

(Aus d. Monatsberichten d. Akad. Juli 1869.)

1. Wenn man eine gerade Anzahl dünner Plättchen zweiachsigem Glimmers in der Art über einander legt, daß die Hauptschnitte (Supplementarlinien) der Plättchen sich unter 90° abwechselnd kreuzen, so erhält man schon bei einer mäßigen Zahl von Kreuzungen ein Präparat, das sich nahe wie ein einaxiger Krystall verhält. Fallen die Glimmerhauptschnitte mit den gekreuzten Polarisationssebenen zusammen, so ist die Imitation vollständig; dreht man aber das Präparat in seiner Ebene, so bleiben zwar die Farbenringe, aber die Arme des schwarzen Kreuzes hellen sich auf und nach einer Drehung um 45° bleibt nur im innersten Ring ein kurzarmiges Kreuz übrig. Nörremberg, von dem dieser Versuch stammt, wurde dazu durch die bekannten Arbeiten Senarmont's über Glimmer und Seignettesalz veranlaßt. Quenstedt's Mineralogie (2. Auflage, S. 239) ist meines Wissens die einzige Schrift, in der dieser Versuch erwähnt wird. Uebrigens liefert Hr. Steeg in Homburg (No. 77 seines Katalogs von 1867) diese Präparate in ausgezeichnete Schönheit.
2. In letzter Zeit habe ich neue Glimmercombinationen versucht, durch welche die Wirkung rechts oder links drehender einaxiger Krystalle nachgeahmt werden sollte. Mit Hülfe der untenstehenden Figuren will ich vorerst eine Vorstellung von diesen Combinationen geben.

E. Reusch

Eberhard Karls Universität Tübingen, Baden-Württemberg, Germany

A. Lakhtakia (✉)

The Pennsylvania State University, University Park, PA, USA

e-mail: akhlesh@psu.edu

Fig. 1

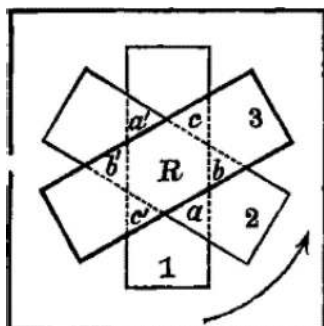
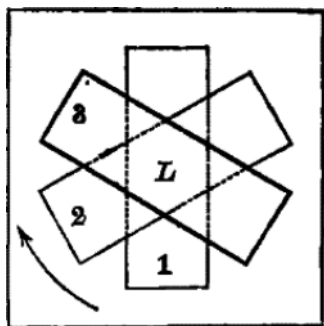


Fig. 2



Auf zwei Glasplatten wurden Cartons geklebt, welche vorher je drei unter 60° sich schneidende rechtwinklige Ausschnitte zum Einlegen der länglichen Glimmerlamellen erhalten hatten. Die Lamellen selber stammten von einem zweiachsigem Glimmer von über 70° Axenwinkel; sie waren möglichst dünn und gleich dick, und in allen fiel die Supplementarlinie (der Hauptschnitt) mit der längeren Dimension zusammen. Angenommen man habe 48 Lamellen; die eine Hälfte wird nun verwendet um nach Fig. 1 die Lamellen in der Ordnung 1, 2, 3 zu einer von links nach rechts ansteigenden Treppe zu schichten; die andere Hälfte wird nach Fig. 2 zu einer von rechts nach links aufsteigenden Treppe geschichtet. Vor dem Auflegen einer neuen Lamelle wird auf die liegende ein Tropfen von dickflüssigem Kopalfirnifs gegeben und die neu aufgelegte Lamelle leicht angedrückt. Man erhält so zwei Präparate, deren Lamellen in dem mit *R* bezeichneten Stück (Fig. 1), für einen Beobachter, der die Treppe von der Seite ansieht, nach Rechts, in *L* (Fig. 2) nach Links ansteigen. Der Botaniker, welcher zur Bestimmung der Windungsrichtung einer Schraube sich in deren Axe stellt, wird allerdings und vielleicht mit größerer Consequenz das Stück *R* ein linksgewundenes, und das Stück *L* ein rechtsgewundenes nennen; im Folgenden werde ich aber an dem in der Technik und im gewöhnlichen Leben gebräuchlichen Begriff der rechten und linken Schraube festhalten.

Die Präparate *R* und *L* verhalten sich nun in der centralen regulär sechseckigen Ueberdeckung sehr nahe wie ein rechts oder linksdrehender Bergkrystall. Schon bei vier bis sechs Umgängen aus nicht übermäßig dünnem Glimmer

läßt sich beim Drehen des oberen Nicols die Drehrichtung bestimmen; im Nörremberg'schen Instrument mit großem Sehfeld sieht man das Ringsystem mit dem bläulichen Mittelkreuz und beim Ueberdecken beider Präparate sehr befriedigende Andeutungen der Airy'schen Spiralen.

Ganz dieselben Wirkungen erhält man mit zwei Präparaten, in welchen vier Lamellensysteme unter 45° zu einer rechten und linken Treppe geschichtet sind.

Die von mir zuerst hergestellten Präparate bestanden theils aus nicht sehr dünnen und nicht vollkommen gleich dicken Lamellen, theils war die Zahl der Umgänge eine kleine (3 bis 6); ich wandte mich daher an Hrn. Steeg und erhielt von demselben nach kurzer Zeit zwei Paare 60grädiger Präparate von überraschender Größe und außerordentlicher Schönheit, welche namentlich den Farbenwechsel bei Drehung des oberen Nicols in brillanter Weise zeigen. Das eine Paar besteht aus je 30 Lamellen von $1/8 \lambda$, das andere gar aus je 36 Lamellen von noch geringerer Dicke. Das erste Paar giebt für rothes Licht eine Drehung von 150° , was einer Quarzdicke von etwa 8^{mm} entspricht.

Zum Beweis für die große Sicherheit und Kunstfertigkeit, mit welcher Hr. Steeg den Glimmer zu behandeln weiß, führe ich an, daß die 72 Lamellen des zweiten Paares, 12^{mm} breit und 30^{mm} lang, aus derselben Tafel herausgeschnitten worden sind. Aus einer dünnen Tafel ($1/8 \lambda$), die ich der besonderen Güte des Hrn. Steeg verdanke, habe ich später Präparate mit vier Lamellensystemen unter 45° hergestellt, welche die Airy'schen Spiralen gaben, während meine ersten Präparate zwar den Farbenwechsel beim Drehen des Nicols, beim Ueberdecken aber ein confuses Bild der Ringe zeigten.

Wenn im convergirenden Licht bei gekreuzten Polarisationssebenen eine solche Glimmer combination in ihrer Ebene gedreht wird, so bleiben wohl die Ringe, aber die Arme des schwarzen Kreuzes erfahren Aenderungen; namentlich sieht man, wie an den Enden der in die Polarisationssebenen fallenden Durchmesser des innersten Rings abwechselnd schwarze Flecken ein- und austreten. Ebenso erfährt bei parallelem Licht die Färbung kleine Wechsel beim Drehen des Nicols, jedoch mehr in der Intensität, als im Farbton.

Ich habe gefunden, daß man einem Quarze diese Eigenschaften einer Glimmercombination dadurch ertheilen kann, daß man über und unter demselben je eine Achtelundulationsglimmerplatte mit rechtwinklich gekreuzten Hauptschnitten einschaltet. Die Glimmercombinationen sind daher aufzufassen als elliptisch rechts und links polarisirende Medien, welche sich dem Quarz wohl um so mehr nähern, je dünner die Lamellen und je größer die Zahl der Umgänge.

Ebenso lassen sich die unter (1) besprochenen Modificationen des schwarzen Kreuzes der Nörremberg'schen Combination dadurch an einer zur Axe senkrecht geschnittenen Kalkspathplatte hervorbringen, daß man dieselbe in der angegebenen Weise mit den Achtelundulationsplatten verbindet und das Ganze in seiner Ebene dreht; man hat daher in der Glimmercombination die Erscheinung, wie wenn ein einaxiger nicht drehender Krystall elliptisch polarisirt und analysirt würde.

3. Beim Schichten der Lamellen unter 60° ergeben sich gleichseitige Dreiecke auf den Seiten des centralen Sechsecks, in welchen nur zwei Lamellensysteme sich

Fig. 3

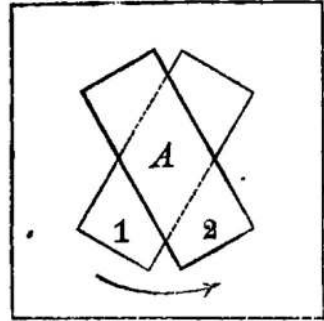
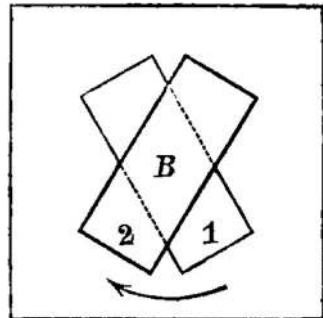


Fig. 4



abwechselnd unter 60° kreuzen. Man überzeugt sich leicht, daß es sich bei diesen Dreiecken, je nach ihrer Lage, um elliptische Rechts- oder Linksdrehung handelt. Dief's hat mich veranlaßt, zunächst die Combination zweier Platten von beliebiger Dicke, deren Hauptschnitte einen von 90° verschiedenen Winkel bilden, zu untersuchen. Eine solche Combination giebt im Allgemeinen rechts oder links elliptisch polarisirtes Licht, d. h. es gelingt beim Drehen des oberen Nicols eine Drehrichtung zu bestimmen, aber beim Drehen der Combination in ihrer Ebene ändert sich die Intensität und wohl auch die Nüance der Farbe. Der Versuch gelingt sowohl mit zwei beliebigen Glimmer als Gypsplatten, oder bei Combinirung von Glimmer mit Gyps, wenn nur deren Farben keiner zu hohen Ordnung angehören.

Im Folgenden beschäftige ich mich blos mit *Glimmertarfe'n von gleicher Dicke*. Zwei solche Tafeln, in welchen wie früher die längere Dimension dem Hauptschnitt entspreche, können nun entweder zu einer *rechten Stufe A* (Fig. 3) oder zu einer *linken Stufe B* (Fig. 4) zusammengelegt werden. Zwei solche Stufen haben jedenfalls entgegengesetzte optische Drehung, aber der Sinn der Drehung ist durch die Dicke der Platten mit bestimmt. Zeigen z. B. die Platten ein Grün zweiter Ordnung, so giebt die rechte Stufe A auch Rechtsdrehung; bei Platten, welche ein Gelb erster Ordnung zeigen, ist es umgekehrt. Der Winkel der Hauptschnitte ist ohne Einfluß auf die Drehrichtung, nur muß er von 0° und 90° gehörig abweichen. Legt man zwei z. B. 60° grädige Stufen A und B

mit parallelen Hauptschnitten über einander, so bleibt immer eine Drehung im Sinne der oben liegenden Stufe. Kreuzt man die Stufen rechtwinklich, so findet in der mittleren Ueberdeckung keinerlei Wirkung statt, was auch das Azimut der Stufenverbindung seyn mag: die zwei Arme des Sternkreuzes, welches aus der Ueberdeckung der Platten verschiedener Stufen entsteht, haben entgegengesetzte Drehung.

Von größerem Interesse ist aber der Fall, dafs viele gleiche Stufen aus sehr dünnen Glimmerlamellen zu einer *rechten* oder *linken Stufensäule* geschichtet sind: in diesem Fall dreht die rechte Stufensäule rechts, die linke links. Hiermit begreift man sofort z. B. bei der 60grädigen Combination Fig. 1 die Wirkungen der Dreiecke *a*, *b*, *c*; die zwei ersten gehören zu einer rechten Stufensäule, das letztere zu einer linken. Die Dreiecke *a'*, *b'*, *c'* wirken natürlich wie die gegenüberliegenden gleicharmigen. Mit derselben Regel bestimmen sich die Drehrichtungen in den äufseren Sternspitzen bei der 45grädigen Combination von vier Lamellensystemen.

Solche Stufensäulen zeigen noch eine andere Eigenthümlichkeit: im convergirenden Lichte sieht man durch die Ueberdeckung ein zweiaxiges Ringsystem, dessen Supplementarlinie den spitzigen Winkel der Hauptschnitte der Glimmerlamellen halbirt und dessen Axenwinkel kleiner ist als der des angewandten Glimmers. Die schwarzen Hyperbeln erscheinen jedoch nur, wenn die Supplementarlinie des Combinationsglimmers mit den Polarisations Ebenen 45° macht: fällt sie mit der einen oder andern zusammen, so enthalten die innersten Ringe nur schwarze Tupfen.

Die Wirkung einer Stufensäule läfst sich mit ziemlicher Annäherung an einer dicken Glimmerplatte dadurch nachahmen, dafs man sie zwischen zwei Achtelundulationsplatten mit rechtwinklig gekreuzten Hauptschnitten in der Art einschaltet, dafs der Hauptschnitt der Glimmerplatte 45° mit jenen macht; und zwar hat diese Combination im parallelen Licht verschiedene Drehrichtung, je nachdem der Hauptschnitt der Platte das eine oder andere Paar der Scheitelquadranten halbirt, welche durch die Hauptschnitte der Achtelundulationsplatten gebildet werden. Es erinnert diefs an eine von J. Müller (Lehrb. d. Physik, 7. Aufl., I, S. 906) beschriebene Anordnung, bei welcher durch eine analoge Verbindung einer Gypsplatte mit zwei Viertelundulationsglimmerplatten, wenigstens im parallelen Licht die Wirkung des Quarzes nachgeahmt wird.

4. Die optischen Wirkungen der bisher besprochenen Glimmercombination lassen eine mathematische Behandlung zu, welche für die Erscheinungen in parallelem Licht voraussichtlich mit viel geringerer Schwierigkeit, als für die im convergirenden Licht verbunden seyn wird. Vielleicht findet sich ein tüchtiger Rechner veranlaßt, diese wohl nicht ganz undankbare Aufgabe anzufassen.

Ob diese Combinationen dazu angethan sind, uns Aufschluß oder wenigstens Andeutungen über den Verband der mit Circularpolarisation begabten Moleküle zu geben, das wird die Zukunft lehren. Vor der Hand weifs ich in dieser Beziehung nur eine schwache Analogie und einige Vermuthungen beizubringen, die ich der Nachsicht der Fachmänner empfehlen möchte.

In einer früheren Mittheilung über die sogenannte Lamellarpolarisation des Alauns¹⁾ habe ich nachzuweisen versucht, daß es sich hier um eine schwache Doppelbrechung in Folge innerer Spannungen handle, die man sich in den Octaëderflächen in der Art wirksam zu denken habe, daß die optische Elasticität in diesen Flächen nach allen Richtungen gleich, aber kleiner als senkrecht sey. Ferner habe ich gezeigt, wie die Wirkung eines optisch activen Alaunoctaëders oder eines Präparats daraus nach zwei parallelen Würfelflächen, in den vier distincten Quadranten durch vier dünne Glimmerplättchen vollständig nachgeahmt werden kann. Bei diesem Glimmerpräparate kommen aber keine Ueberdeckrungen vor, während der Nerv der neuen Präparate eben in den Ueberdeckungen liegt. Es entsteht daher umgekehrt die Frage nach derjenigen Krystallstructur, welche einer Glimmercombination mit Ueberdeckungen entspricht.

Ein nahe liegender, Gedanke ist nun wohl folgender: im idealen activen Alaunoctaëder reichen die irgend einer Octaëderfläche parallelen Spannungsebenen nur bis an die drei rechtwinklichen Axenebenen heran; es ist aber auch denkbar, daß in einem Krystall die durch innere Spannungen und Contractionen herbeigeführte Störung der ursprünglichen Structur, sich auf eine oder mehrere von einander verschiedene, gegen die Richtung des durchgehenden Lichtes geneigte Spannungsebenen werde zurückführen lassen, welche den ganzen Krystall je in constanter Richtung durchsetzen. Nun wissen wir zwar sehr Weniges über die normale Krystallstructur und folglich noch viel weniger über die factisch vorhandenen Störungen derselben: will man daher die Sache überhaupt anfassen, so sieht man sich vor der Hand auf einige instinctmäßige Vermuthungen beschränkt.

Im regularen System ist der Fall einzelner nicht durchgehender Spannungsebenen in dem Octaëder des activen Alaunoctaëders verwirklicht. Die optischen Erscheinungen müssen verwicelter werden, wenn andere Flächen, z. B. die des Leucitoëders als einzelne Spannungsflächen auftreten (Leucit. Analcim?). Die von Marbach entdeckte Circularpolarisation des chlorsauren Natrons ist möglicherweise das Resultat von Spannungen nach den Dodekaëderflächen, verbunden mit secundären Spannungen nach den Flächen des rechten oder linken Tetraëders; die 45grädige Glimmercombination von vier Lamellensystemen giebt vielleicht, bei außerordentlich schwacher Wirkung der einzelnen Umgänge, ein Bild hieran.

Dieselbe Glimmercombination entspricht vielleicht auch dem Falle der Circularpolarisation im quadratischen System. Von den vier Lamellensystemen würden 1 und 3 die Structur des einaxigen nicht drehenden Krystalls einigermaßen versinnlichen; die Lamellensysteme 2 und 4 wären das Aequivalent von durchgehenden Spannungen nach den Flächen des rechten oder linken Hemioctaëdera. — Das Auftreten einer einzelnen gegen die Axe geneigten Spannungsebene, oder die ungleiche Intensität der einzelnen Spannungen müßte sich

¹ Ann. Bd. 132 (1867) S. 618.

durch zweiaxigen Habitus der optischen Erscheinungen kund thun (Dislocation des schwarzen Kreuzes im Beryll, gelben Blutlaugensalz usw.).

Die Circularpolarisation im rhomboëdrischen System ist wohl das Resultat von drei gegen die Axe gleich geneigten durchgehenden Spannungsebenen, welche vielleicht den Flächen des einen oder andern der zwei zusammengehörigen Halbskalenoëder folgen. Der Gedanke an die Möglichkeit solcher innerer Spannungen liegt wohl bei keiner Substanz so nahe, wie bei der Kieselerde. Sind die drei Spannungen vollkommen gleichwerthig, so hätte man die normale rechts oder links drehende Wirkung des Quarzes; fallen alle drei Spannungen fort, oder gleichen sich dieselben gegenseitig aus, so bliebe, wie man diefs an vielen Amethysten stellenweise beobachtet, die rein einaxige Wirkung ohne Rotation. Noch bleibt aber die Möglichkeit, dafs nach Umständen jene drei Spannungen von ungleicher Intensität sind, oder sich auf zwei reduciren, und dann hätte man die an manchen Quarzen so prägnant auftretende zweiaxige elliptische rechts oder links drehende Polarisation, wie man sie an den oben besprochenen Stufensäulen, oder an Präparaten beobachtet, an welchen absichtlich eins der drei Lamellensysteme aus etwas dickerem oder dünnerem Glimmer besteht.

In Betreff der mannigfaltigen Erscheinungen am Quarz und Amethyst erlaube ich mir auf die reichhaltigen und wohlgeordneten Beobachtungen von Dove in seiner Farbenlehre (S. 247–260) zu verweisen.

Zum Schlufs bemerke ich noch, dafs die Kenntnifs der Wirkungen der Glimmercombinationen auch von einigem Werth seyn dürfte für das Verständnifs gewisser Erscheinungen am Glimmer selber. Die Wandlungen des Ringsystems bei Zwillingen, so wie die oft sehr erheblichen Aenderungen im Winkel der optischen Axen an demselben Stücke begreifen sich einigermaafsen, wenn man regelmässige Verwachsungen und Durchdringungen verschiedener Individuen annimmt. Die Kenntnifs dieser Erscheinungen verdanke ich zum gröfsten Theil den Mittheilungen und vielfachen gütigen Glimmersendungen von G. Rose, und diese waren es auch, welche für mich ursprünglich die Veranlassung zur Herstellung der neuen Glimmercombinationen geworden sind.

Tübingen, den 29. Juni 1869.

Zusatz.

Aus zuverlässiger Quelle habe ich erfahren, dafs von einigen Physikern behauptet worden ist, der Nachweis der Drehung bei geschichteten Glimmerlamellen rühre von Nörremberg her. Ich erlaube mir nun zu erklären, dafs unter den Präparaten Nörremberg's, welche zu gleichen Theilen in die hiesige Sammlung und in die der polyt. Schule zu Stuttgart übergegangen sind, nur rechtwinkliche Combinationen vorkommen. Die durch 60grädige Combinationen bewirkte Rechts- und Linksdrehung habe ich in der Pfingstwoche dieses Jahres durch selbständige Versuche gefunden und sobald ich des Resultats ganz sicher war, Hrn. Steeg in Homburg um Herstellung derartiger Präparate gebeten; ein Wunsch, dem derselbe in der oben angegebenen ausgezeichneten Weise nachgekommen ist. — Zur Bekräftigung dieser meiner Behauptungen

mögen zwei Documente dienen, die Hr. Prof. Poggendorff etwaigen Zweiflern vorzuweisen die Güte haben wird.

Tübingen, 24. Oct. 1869.

E. Reusch.

Zusatz des Herausgebers.

Die beiden Documente, von denen hier die Rede ist sind: ein Attest des Hrn. Prof. Zech und ein Brief des Optikers Hrn. W. Steeg.

In dem ersteren heisst es schliesslich:

— Der Unterzeichnete ist sonach und dann noch insbesondere wegen seines häufigen Verkehrs mit Nörremberg von 1854 bis 1862 berechtigt und befähigt, auszusprechen, dafs Nörremberg nie andere Glimmercombinationen gemacht hat, als rechtwinklige. Im hiesigen physikalischen Kabinet befindet sich kein einziges Präparat von Nörremberg, bei welchem zwei Glimmerblättchen unter einem andern Winkel, als einem rechten, gekreuzt wären, insbesondere keines, das eine Drehung der Polarisationssebene zeigt.

Stuttgart, 20. Oct. 1869.

Prof. Dr. Zech.

Und der Brief des letzteren sagt:

— Hierzu erlaube ich mir zu bemerken, dafs ich bestimmt weifs, dafs Nörremberg derartige *circular polarisirende* Präparate *nie* dargestellt hat. Ich habe mit demselben viel verkehrt und seine ganze Sammlung gesehen.

Seine derartigen Glimmerpräparate waren nur in *rechten Winkeln* gekreuzt, um Sénarmont's Hypothese als richtig zu beweisen, dafs man aus dünnen Lamellen von zweiaxigem Glimmer einen einaxigen Körper etwa wie Kalkspath herstellen kann.

Die geniale Idee des Kreuzens der Glimmer-Lamellen in Winkeln von 60° , also im hexagonalen Sinne, ging aber zuerst und ganz allein von Prof. Reusch aus, wie aus dessen Briefe an mich vom 16. Mai ersichtlich ist.

Die Sache hat mich so interessirt, weil ich früher schon ähnliche Versuche gemacht hatte, welche mir aber nicht gelungen waren. Gerade die Kreuzung im Winkel von 60° hat das glückliche Resultat herbeigeführt. Dieses Verdienst gebührt Hrn. Prof Reusch und es ist Unrecht, wenn es ihm von anderer Seite streitig gemacht werden sollte.

Homburg v. d. Höhe den 21. Oct. 1869.

Wilhelm Steeg.

Annalen der Physik und Chemie (Leipzig) **138**, 628–638 (1869)

Investigation into mica combinations; by E. Reusch.

(From the monthly reports of the Academy, July 1869.)

1. If an even number of thin plates of biaxial mica are placed on top of each other in such a way that the main sections (supplementary lines) of the plates cross alternately at 90° , even with a moderate number of crossings, a preparation is obtained that behaves almost like a uniaxial crystal. If the main mica sections coincide with the crossed polarization planes, the imitation is complete; if,

however, the preparation is rotated in its plane, the color rings remain, but the arms of the black cross lighten, and after a rotation of 45° , only a short-armed cross remains in the innermost ring. Nörremberg, who carried out this experiment, was prompted to do it by the well-known work of Senarmont on mica and Rochelle salt. Quenstedt's Mineralogy (2nd edition, p. 239) is, to my knowledge, the only text in which this experiment is mentioned. Incidentally, Mr. Steeg in Homburg (No. 77 of his 1867 catalogue) supplies these preparations in excellent beauty.

2. Recently, I have tried new mica combinations by which the effect of right- or left-rotating uniaxial crystals could be imitated. With the help of the following figures, I will first give an idea of these combinations.

Cardboard boxes were glued to two glass plates, each of which had previously been provided with three rectangular cutouts intersecting at 60° for the insertion of the elongated mica lamellae. The lamellae themselves came from biaxial mica with an axis angle of over 70° ; they were as thin as possible and of the same thickness, and in all of them, the supplementary line (the main cut) coincided with the longer dimension. Suppose you have 48 lamellae; one half is now used to layer the lamellae in the order 1, 2, 3 *to form a staircase rising from left to right* as shown in Fig. 5; the other half is layered *to form a staircase rising from right to left* as shown in Fig. 6. Before placing a new lamella on top, a drop of thick copal varnish is placed on the one lying on top, and the newly placed lamella is

Fig. 5

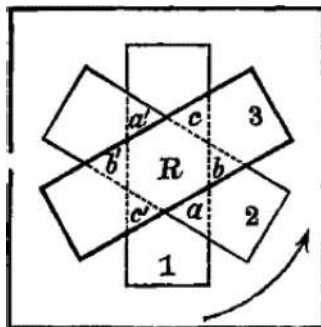
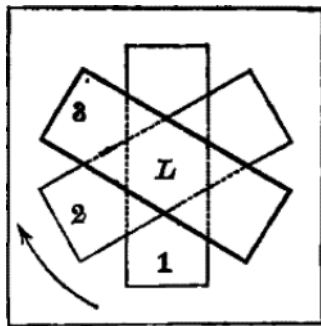


Fig. 6



lightly pressed down. In this way, two preparations are obtained, the lamellae of which rise to the right in the section marked *R* (Fig. 5) for an observer who looks at the staircase from the side and to the left in *L* (Fig. 6). The botanist who, in order to determine the direction of the winding of a screw, stands on its axis will, of course and perhaps with greater consistency, call the section *R* a left-handed one and the section *L* a right-handed one; in the following, however, I will stick to the concept of right and left screws, which is common in technology and in everyday life.

The preparations *R* and *L* now behave in the central regular hexagonal covering very similarly to a right- or left-turning rock crystal. After just four to six turns of the not excessively thin mica, the direction of rotation can be determined by turning the upper Nicol prism; in the Nörremberg instrument with a large field of view, one can see the ring system with the bluish central cross and, when both preparations are covered, very satisfactory results of the Airy spirals can be seen.

Exactly the same effects are obtained with two preparations in which four lamella systems are layered at 45° to form a right and a left staircase.

The preparations I first made consisted partly of lamellae that were not very thin and not of exactly the same thickness, and partly the number of turns was small (3 to 6). I therefore turned to Mr. Steeg and after a short time received from him two pairs of 60° preparations of surprising size and extraordinary beauty, which particularly show the color change brilliantly when the upper Nicol prism is rotated. One pair consists of 30 lamellae of $1/8 \lambda$ each, the other of 36 lamellae of even lesser thickness. The first pair gives a rotation of 150° for red light, which corresponds to a quartz thickness of about 8 mm.

As proof of the great certainty and skill with which Mr. Steeg knows how to handle the mica, I state that the 72 lamellae of the second pair, 12 mm wide and 30 mm long, were cut out of the same plate. From a thin plate ($1/8 \lambda$), for which I owe the special kindness of Mr. Steeg, I later made preparations with four systems of lamellae at 45° , which gave the Airy spirals, while my first preparations showed the color change when the Nicol prism was rotated, but a confused image of the rings when covered.

If such a mica combination is rotated in its plane in converging light with crossed polarization planes, the rings remain, but the arms of the black cross undergo changes; in particular, one can see how black spots alternately enter and exit the ends of the diameters of the innermost ring that fall into the polarization planes. Likewise, in parallel light, the coloring undergoes small changes when the Nicol prism is rotated, but more in intensity than in hue.

I have found that quartz can be given these properties of a mica combination by inserting an eighth-undulation mica plate with right-angled crossing cuts above and below it. The mica combinations can therefore be regarded as elliptically right- and left-polarizing media, which come closer to quartz the thinner the lamellae and the greater the number of turns.

Likewise, the modifications of the black cross of the Nörremberg combination discussed under (1) can be produced on a calcite plate cut perpendicular to the

axis by connecting it in the manner described with the eighth undulation plates and rotating the whole in its plane; one therefore has in the mica combination the appearance as if a uniaxial non-rotating crystal that is elliptically polarized and analyzed.

- When the lamellae are layered at 60° , equilateral triangles are formed on the sides of the central hexagon, in which only two systems of lamellae intersect each other alternately at 60° . It is easy to see that these triangles are elliptical, right or left-handed, depending on their position. This prompted me to first investigate the combination of two plates of any thickness, whose main sections form an angle other than 90° . Such a combination generally produces light that is elliptically polarized to the right or left, i.e., it is possible to determine the direction of rotation by rotating the upper Nicol prism, but when the combination is rotated in its plane, the intensity and probably also the nuance of the color change. The experiment is successful with any two mica or gypsum plates, or by combining mica with gypsum, provided that their colors do not belong to too high an order.

In the following, I will only deal with *mica plates of the same thickness*. Two such plates, in which, as before, the longer dimension corresponds to the main section, can now be put together to form either a *right step A* (Fig. 7) or a *left step B* (Fig. 8). Two such steps always have opposite optical rotations, but the direction of the rotation is determined by the thickness of the plates. If, for

Fig. 7

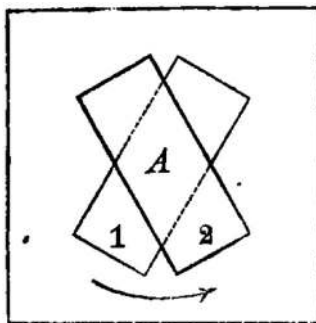
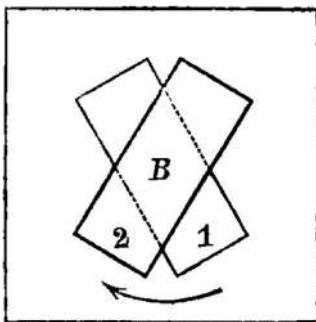


Fig. 8



example, the plates show a second-order green, the right-hand step *A* also gives a right-hand rotation; for plates that show a first-order yellow, it is the other way round. The angle of the main sections has no influence on the direction of rotation, only it must deviate considerably from 0° and 90° . If, for example, two 60-degree steps *A* and *B* with parallel main sections are placed on top of each other, there is always a rotation in the direction of the previous step. If the steps are crossed at right angles, no effect is found in the middle overlap, whatever the azimuth of the step connection: the two arms of the star cross, which is created by the overlap of the plates of different steps, have opposite rotation.

Of greater interest, however, is the case where many equal steps made of very thin mica lamellae are layered into a *right or left step column*: in this case, the right step column turns right, the left one left. This immediately makes it possible to understand, for example, the effects of triangles *a*, *b*, *c* in the 60-degree combination Fig. 5; the first two belong to a right step column, the last one to a left one. The triangles *a'*, *b'*, *c'* naturally work like the opposite equal-armed ones. The same rule determines the directions of rotation in the outer star points in the 45-degree combination of four lamella systems.

Such step columns show another peculiarity: in converging light, one can see through the overlap a two-axis ring system, the supplementary line of which bisects the acute angle of the main sections of the mica lamellae and whose axial angle is smaller than that of the applied mica. The black hyperbolas, however, only appear when the supplementary line of the combination mica makes 45° with the polarization planes: if it coincides with one or the other, the innermost rings contain only black dots.

The effect of a stepped column can be imitated with a fair approximation on a thick mica plate by inserting it between two eighth-undulation plates with main sections crossed at right angles in such a way that the main section of the mica plate makes 45° with the latter; this combination has a different direction of rotation in parallel light, depending on whether the main section of the plate bisects one or the other pair of vertex quadrants formed by the main sections of the eighth-undulation plates. This is reminiscent of an arrangement described by J. Müller (Lehrb. d. Physik, 7th ed., I, p. 906), in which the effect of quartz is imitated, at least in parallel light, by an analogous connection of a gypsum plate with two quarter-undulation mica plates.

4. The optical effects of the mica combination discussed so far allow for a mathematical treatment, which will probably be much less difficult for the phenomena in parallel light than for those in converging light. Perhaps a capable calculator will be prompted to take on this not entirely thankless task.

Whether these combinations are capable of giving us information or at least hints about the association of molecules endowed with circular polarization is something that only the future will tell. For the time being, I can only offer a weak analogy and a few conjectures in this regard, which I would like to recommend to the indulgence of experts.

In an earlier communication on the so-called lamellar polarization of alum²), I tried to prove that this is a weak double refraction as a result of internal tensions, which must be imagined to be effective in the octahedron surfaces in such a way that the optical elasticity in these surfaces is the same in all directions, but smaller than perpendicular. Furthermore, I showed how the effect of an optically active alum octahedron or a preparation made from it can be completely imitated in the four distinct quadrants by four thin mica plates on two parallel cube surfaces. However, this mica preparation does not have any overlap rings, whereas the nerve of the new preparations lies precisely in the overlaps. This raises the converse question of the crystal structure that corresponds to a mica combination with overlaps.

An obvious idea is the following: in the ideal active alum octahedron, the tension planes parallel to any octahedral surface only extend as far as the three right-angled axial planes; however, it is also conceivable that in a crystal, the disturbance of the original structure caused by internal tensions and contractions can be traced back to one or more different tension planes inclined against the direction of the light passing through, which pass through the entire crystal in a constant direction. Now, we know very little about the normal crystal structure and consequently even less about the disturbances that actually exist in it: if one wants to tackle the matter at all, one is limited for the time being to a few instinctive assumptions.

In the regular system, the case of individual non-continuous tension planes is realized in the octahedron of the active alum octahedron. The optical phenomena must become more complicated when other surfaces, e.g., that of the leucitohedron, appear as individual tension surfaces (leucite, analcime?). The circular polarization of sodium chloride discovered by Marbach is possibly the result of tensions along the dodecahedron surfaces, combined with secondary tensions along the surfaces of the right or left tetrahedron; the 45-degree mica combination of four lamella systems perhaps gives an example of this, given the extremely weak effect of the individual turns.

The same mica combination perhaps also corresponds to the case of circular polarization in the square system. Of the four lamellar systems, 1 and 3 would somewhat represent the structure of the uniaxial non-rotating crystal; lamellar systems 2 and 4 would be the equivalent of continuous tensions along the surfaces of the right or left hemioctahedron. The appearance of a single tension plane inclined against the axis, or the unequal intensity of the individual tensions, would have to be manifested by a biaxial attitude of the optical phenomena (dislocation of the black cross in beryl, yellow prussiate of blood, etc.).

The circular polarization in the rhombohedral system is probably the result of three continuous tension planes that are equally inclined to the axis and that perhaps follow the surfaces of one or the other of the two associated half-

² Reusch, E.: Ueber die sogenannte Lamellarpolarisation des Alauns. *Annalen der Physik und Chemie* (Leipzig) **132**, 618–622 (1867).

scalenohedrons. The idea of the possibility of such internal tensions is probably more obvious in silica than in any other substance. If the three tensions are completely equal, then one would have the normal right- or left-turning effect of quartz; if all three tensions disappear, or if they balance each other out, then the purely uniaxial effect without rotation would remain, as is observed in places on many amethysts. However, the possibility still remains that, depending on the circumstances, these three tensions are of unequal intensity, or are reduced to two, and then one would have the two-axis elliptical right- or left-turning polarization that occurs so prominently in some quartz, as observed in the step columns discussed earlier, or in preparations in which one of the three lamellar systems intentionally consists of somewhat denser or thinner mica.

With regard to the various phenomena on quartz and amethyst, I would like to refer to the extensive and well-organized observations by Dove in his theory of colors (pp. 247–260).

Finally, I would like to note that the condensation of the effects of mica combinations may also be of some value for understanding certain phenomena on mica itself. The changes in the ring system in twins, as well as the often very significant changes in the angle of the optical axes on the same piece, can be understood to some extent if one assumes regular intergrowths and penetrations of different individuals. I owe my knowledge of these phenomena largely to the information and many kind mica shipments from G. Rose, and it was these that originally gave me the impetus to produce the new mica combinations.

Tübingen, June 29, 1869.

Addition.

I have learned from a reliable source that some physicists have claimed that the proof of rotation in layered mica lamellae comes from Nörremberg. I now take the liberty of explaining that among Nörremberg's preparations, which have been transferred in equal parts to the local collection and to that of the polytechnic school in Stuttgart, only right-angled combinations occur. I discovered the right and left rotation caused by 60-degree combinations during the Whitsun week of this year through independent experiments, and as soon as I was completely sure of the result, I asked Mr. Steeg in Homburg to produce such preparations; a request that he fulfilled in the excellent manner described earlier. To confirm my claims, two documents may serve that Prof. Poggendorff will be kind enough to show to any doubters.

Tübingen, Oct. 24, 1869.

E. Reusch.

Editor's note.

The two documents we are talking about here are: a certificate from Prof. Zech and a letter from the optician Mr. W. Steeg.

The first one finally states:

The undersigned is therefore entitled and qualified, especially because of his frequent contact with Nörremberg from 1854 to 1862, to state that Nörremberg never made any other mica combinations than right-angled ones. In the physics

cabinet here there is not a single preparation by Nörremberg in which two mica sheets were crossed at an angle other than a right one, and in particular none that shows a rotation of the plane of polarization.

Stuttgart, Oct. 20, 1869.

Prof. Dr. Zech.

And the latter's letter says:

— I would like to point out that I know for certain that Nörremberg has never produced such *circularly polarizing* preparations. I have had a lot of contact with him and have seen his entire collection.

His preparations of such mica were only crossed at right angles in order to prove the correctness of Sénarmont's hypothesis that one can produce a uniaxial body, such as calcite, from thin lamellae of biaxial mica.

The ingenious idea of crossing the mica lamellae at angles of 60° , i.e., in a hexagonal sense, came first and solely from Prof. Reusch, as can be seen from his letter to me dated May 16th.

The matter interested me so much because I had already made similar attempts before, but had not succeeded. It was precisely the crossing at an angle of 60° that brought about the happy result. This credit goes to Prof. Reusch, and it would be unjust if anyone else were to dispute it.

Homburg v. d. Höhe Oct. 21, 1869.

Wilhelm Steeg.

Translator's Notes

1. An earlier version of Reusch's journal paper appeared in the Monthly Report of the Royal Prussian Academy of Sciences in Berlin for July 1869 [1].
2. An English-language translation of Ref. [1] was provided by W. G. Lettson in 1870 [2].
3. Reusch slightly revised Ref. [1] for publication in the December 1869 issue of *Annalen der Physik und Chemie*, and he also added a paragraph dated October 24, 1869. Furthermore, this paper [3] had an accompanying note from Johann Christian Poggendorff, the Editor of the journal, and the testimonies of Paul Heinrich Zech (Polytechnikum Stuttgart) and Wilhelm Steeg. This chapter provides an English-language translation of all of these items together.
4. A French-language commentary on the research of Reusch encompassing the 1869 paper was published in 1870 [4].

References

1. E. Reusch, Über Glimmercombinationen. Monatsberichte der Königlich Preussischen Akademie der Wissenschaften zu Berlin **69**, 530–538 (1869)
2. E. Reusch, On mica-combinations. Lond. Edinb. Dublin Philos. Mag. J. Sci. Series 4 **39**, 195–201 (1870)

3. E. Reusch, Untersuchung über Glimmercombinationen. *Annalen der Physik und Chemie* (Leipzig) **138**, 628–638 (1869)
4. M. Bertin, Sur les combinaisons de mica; par M. Reusch. *Annales de Chimie et de Physique* (Paris), Quatrième Série **20**, 207–214 (1870)



Eduard Reusch, also known as Friedrich Eduard Reusch and after 1871 as Friedrich Eduard von Reusch, was born on April 17, 1812 in Kirchheim, Württemberg. He was educated at the Latin school in Kirchheim and at seminaries at Urach and Tübingen. Thereafter, he spent a year and a half at École Polytechnique and Sorbonne in Paris. Returning from France, he became a high-school teacher of mathematics at Heilbronn in 1837. From 1840 to 1851, he was an instructor of mechanical engineering and physics at Polytechnikum Stuttgart, where he wrote a booklet on statics and dynamics as well as a monograph on the construction of pointed arches. On October 31, 1845, the philosophical faculty at the University of Tübingen awarded him a doctorate. In 1851, he became a professor of physics at the University of Tübingen, where he carried out research on crystal optics in addition to lecturing on mechanical engineering and technology from 1855 to 1871. He became the interim director of the university observatory in 1874 and regularly taught a course on popular astronomy. Retiring in 1884, he relocated to Stuttgart where he conducted research on geometry until his death on July 22, 1891.

The Catalogue of Scientific Papers (1800–1900) published by the Royal Society of London records at least 42 journal publications of Reusch. He also authored eight books. In 1873, Reusch was elected a member of the Imperial Leopold-Karol German Academy of Natural Sciences. In 1871, he received the Knight's Cross of Honor of the Order of the Württemberg Crown, followed by the addition of a crown to that cross in 1877. In 1884, he was made a Commander second Class of the Order of Frederick of Württemberg.

The salt print (photograph) of Reusch shown here was produced in 1860 by Friedrich Brandseph of Stuttgart.

Unidirectional Waves in Discrete Plasmonic Waveguides



Vadim A. Markel 

1 Introduction

Linear periodic chains of metal nanoparticles have attracted significant attention in the past 20 years or so with envisaged applications in spectroscopy and sensing [1–4] as well as in waveguiding and information transfer [5–8]. In our previous work, we investigated the electromagnetic properties of simple linear plasmonic chains using the point dipole approximation [9–12]. Theories accounting for higher-order multipole interactions have also been developed [13–15]. Topological properties of Bloch modes in chains with a more complicated geometry were studied in [16, 17]. Additional references can be found in the review articles [18, 19].

One aspect of plasmonic chains that received little attention so far is directionality. The radiation pattern of an electrically small antenna is symmetric with respect to the coordinate inversion $\mathbf{r} \rightarrow -\mathbf{r}$. If such an antenna illuminates a small central segment of a chain that is invariant under the same transformation, the electromagnetic excitation in the form of a surface plasmon polariton (SPP) will travel in both directions with the same amplitude. However, if we give the chain a sense of direction, the inversion symmetry of the system “antenna+chain” would be broken. In this case, it is possible to engineer the source antenna so that it would send the SPP in one direction only. The direction can be switched by tuning the phase relations of the elementary dipoles comprising the antenna. When placed in free space, the source antenna of this type would radiate as a single dipole (in the radiation zone). However, when placed in a close vicinity of a directional chain, it will send the SPP in only one of the two possible directions, depending on its internal phase relations. Intuition may suggest that such direction-selective coupling is possible only if non-reciprocal materials are used in the chain. However, we will

V. A. Markel (✉)

University of Pennsylvania, Philadelphia, PA, USA

e-mail: vmarkel@upenn.edu; vmarkel@penmedicine.upenn.edu

show that non-reciprocity is not required. This is so because the operator of dipole sum, which plays a fundamental role in the theory of discrete waveguides, is not generally symmetric, even if all the materials involved are reciprocal.

This chapter contains the general theory of directional discrete waveguides in the framework of the point dipole approximation and a numerical example demonstrating the feasibility of direction-selective coupling. While under some conditions the dipole approximation may not be accurate, the basic observation that the dipole sum in chains with a sense of direction is not symmetric is not expected to change if we account for the higher multipoles or use a more general method for solving the electromagnetic problem. In Sect. 2, we describe the geometry of a discrete structured chain. Section 3 introduces the coupled-dipole equation and the dipole sum. In Sect. 4, we derive the dispersion equation that is specific to metal particles with the Drude dielectric function. In Sect. 5, we discuss some algebraic properties of the dispersion equation, which will prove useful for understanding the direction-selective coupling. In Sect. 7, we provide a simple example of a directional chain and demonstrate that direction-selective coupling is possible. Section 8 contains a discussion and further examples.

Gaussian system of base dimensions and the corresponding form of electromagnetic equations are used throughout. We work in the frequency domain using the $\exp(-i\omega t)$ phasor convention.

2 Waveguide Geometry

Consider a linear discrete waveguide consisting of periodically arranged, electrically small particles of the same permittivity $\epsilon(\omega)$ embedded in a host medium with the constant dielectric permittivity $\epsilon_h \geq 1$ where $\epsilon_h = 1$ corresponds to vacuum and ω is the frequency. We work in the dipole approximation, so that the only relevant parameters of a particle are its location and the dipole polarizability tensor $\hat{\alpha}(\omega)$. We will use the model of metal ellipsoids to obtain physically accessible values of $\hat{\alpha}(\omega)$ while making sure that the dipole approximation is still valid. In this case, the location coincides with the ellipsoid center and $\hat{\alpha}(\omega)$ can be expressed analytically in terms of the ellipsoid semi-axes and $\epsilon(\omega)$. While the ellipsoids comprising the waveguide can have different shapes and orientations, we assume that the material from which the particles are made is the same; otherwise, theory becomes too complicated.

Geometry of a discrete waveguide is illustrated in Fig. 1. The system is periodic in the Z direction with the lattice step h , and we label the unit cells by $n = 0, \pm 1, \pm 2, \dots$. Each cell contains $p > 0$ particles labeled by $v = 1, 2, \dots, p$. We introduce the composite index (nv) to label the particles. The locations and dipole moments of all particles are denoted by $\mathbf{r}_{nv} = (x_v, y_v, z_{nv})$ and \mathbf{d}_{nv} . Here x_v and y_v are independent of n due to periodicity and

$$z_{n+1,v} = z_{nv} + h. \quad (1)$$

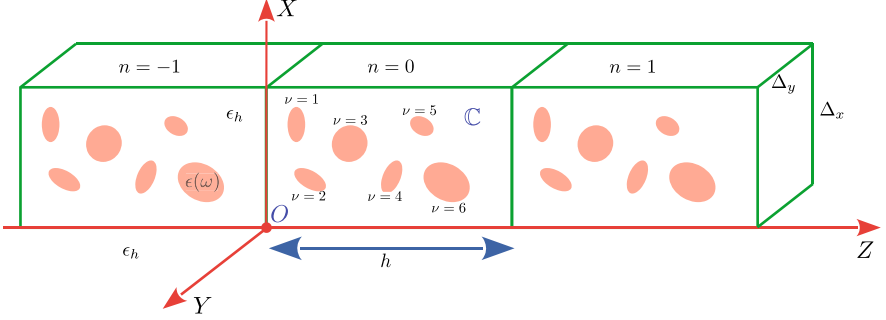


Fig. 1 Schematic illustration of a discrete waveguide with $p = 6$ particles per cell. Three unit cells are shown including the reference cell \mathbb{C} with the index $n = 0$

As the polarizabilities are also periodic, we write $\hat{\alpha}_\nu(\omega)$ for ν -th article in an arbitrary cell. The set of points $\mathbf{r}_{0\nu}$ together with the polarizabilities $\hat{\alpha}_\nu$ define the reference unit cell \mathbb{C} . Thus, the waveguide consists of three-dimensional rectangular cells periodically repeated in the Z -direction; however, there is no periodicity in X or Y . Note that the transverse dimensions of a unit cell Δ_x and Δ_y are ambiguous and do not enter any equations; we have introduced these quantities in the figure only for visual convenience.

3 Coupled Dipole Equation and the Dipole Sum

The frequency-domain coupled dipole equations in the discrete waveguide have the form

$$\hat{\chi}_\nu(\omega) \mathbf{d}_{n\nu} = \mathbf{e}_{n\nu} + \sum_{\substack{m\mu \\ (m\mu) \neq (n\nu)}} \hat{G}(\mathbf{r}_{n\nu}, \mathbf{r}_{m\mu}; \omega) \mathbf{d}_{m\mu}, \quad (2)$$

where

$$\hat{\chi}_\nu(\omega) = \hat{\alpha}_\nu^{-1}(\omega) \quad (3)$$

is the inverse polarizability tensor, $\mathbf{d}_{n\nu}$ are the dipole moments, $\mathbf{e}_{n\nu}$ are the external fields (e.g., generated by a source antenna), ω is the working frequency, and $\hat{G}(\mathbf{r}, \mathbf{r}'; \omega)$ is the free-space Green's tensor for the electric field. We have tacitly assumed that $\hat{\alpha}_\nu(\omega)$ are invertible, which is the case for ellipsoids with any realistic dielectric function $\epsilon(\omega) \neq \epsilon_h$. The condition $(n\nu) \neq (m\mu)$ ensures that the electric field at the particle $(n\nu)$ is the sum of the external field $\mathbf{e}_{n\nu}$ and the fields generated by all other particles excluding the particle $(n\nu)$ itself. Additional details pertaining to the form of the coupled dipole equation (2), alternative forms of this equation,

and accounting for the radiative correction to the quasi-static polarizability can be found in [20].

The expression for \hat{G} applicable to free space is given in the Appendix. What is important for us now is that the Green's tensor satisfies the following symmetry properties:

$$\hat{G}(\mathbf{r}, \mathbf{r}'; \omega) = \hat{G}^T(\mathbf{r}', \mathbf{r}; \omega) , \quad (4a)$$

$$\hat{G}(\mathbf{r}, \mathbf{r}'; \omega) = \hat{G}(\mathbf{r} + s\hat{\mathbf{z}}, \mathbf{r}' + s\hat{\mathbf{z}}; \omega) . \quad (4b)$$

Here the superscript T denotes matrix transposition, and s is an arbitrary real scalar (translation along the Z axis). The first equation aforementioned is Lorentz reciprocity, and the second is a consequence of the translational invariance of the waveguide. If the waveguide is embedded in an infinite homogeneous space, as we assume here, the Green's tensor possesses even stronger symmetries. We then have, additionally, $\hat{G}(\mathbf{r}, \mathbf{r}'; \omega) = \hat{G}^T(\mathbf{r}, \mathbf{r}'; \omega)$ and $\hat{G}(\mathbf{r}, \mathbf{r}'; \omega) = \hat{G}(\mathbf{r} + \mathbf{s}, \mathbf{r}' + \mathbf{s}; \omega)$, where \mathbf{s} is an arbitrary translation vector. However, if the waveguide is placed in an external cladding, the latter properties may be lost while the properties in (4) would survive. Therefore, the theoretical results presented further are generalizable to the case of an external cladding as they rely only on (4) and not on any of the stronger symmetries.

To find guided waves, we set external fields \mathbf{e}_{nv} to zero and seek Bloch-periodic solutions to (2) of the form

$$\mathbf{d}_{nv} = \mathbf{d}_v e^{i(qh)n} . \quad (5)$$

Upon substituting this ansatz into (2), we obtain the equation

$$\hat{\chi}_v(\omega) \mathbf{d}_v = \sum_{\substack{m\mu \\ (m\mu) \neq (nv)}} \hat{G}(\mathbf{r}_{nv}, \mathbf{r}_{m\mu}; \omega) e^{i(qh)(m-n)} \mathbf{d}_\mu . \quad (6)$$

Since summation in (6) is carried out over all integer m , the result does not depend on n , and we can set $n = 0$ in the right-hand side of (6). Using this observation, we can rewrite (6) as

$$\hat{\chi}_v(\omega) \mathbf{d}_v = \sum_{\mu=1}^p \hat{S}_{v\mu}(\omega, q) \mathbf{d}_\mu , \quad (7)$$

where

$$\hat{S}_{v\mu}(\omega, q) := \sum_{\substack{m=-\infty \\ (m\mu) \neq (0v)}}^{\infty} \hat{G}(\mathbf{r}_{0v}, \mathbf{r}_{m\mu}; \omega) e^{i(qh)m} \quad (8)$$

is known as the dipole sum. Here $1 \leq \nu, \mu \leq p$. Note also that $\mathbf{r}_{0\nu}$ are in the reference cell \mathbb{C} .

Most previous investigations of discrete plasmonic waveguides were restricted to simple periodic 1D chains or 2D lattices where all particles are equivalent [18], although more complicated geometries have also been considered [16, 17]. In the case of simple periodic 1D chains, the dipole sum is reduced to a 3×3 tensor $\hat{S}(\omega, q)$, which is diagonal in the reference frame of Fig. 1. It is straightforward to show that $\hat{S}(\omega, q) = \hat{S}^T(\omega, q)$ and $\hat{S}(\omega, -q) = \hat{S}(\omega, q)$. These symmetry relations are special cases of the more general relation

$$\hat{S}_{\nu\mu}(\omega, -q) = \hat{S}_{\mu\nu}^T(\omega, q), \quad (9)$$

which is applicable to structured chains. And while it is possible, under some additional conditions, to have $\hat{S}_{\nu\mu}(\omega, -q) = \hat{S}_{\nu\mu}(\omega, q)$, the latter relation does not always hold. This observation is the main difference between simple and structured chains, and it will be exploited further to find localized excitation schemes that excite only the SPPs propagating in a given direction along the chain. We refer to this phenomenon as to the direction-selective coupling and to the resulting SPPs as unidirectional.

We can prove (9) by starting from the definition (8) and following the chain of equalities

$$\begin{aligned} \hat{S}_{\nu\mu}(\omega, -q) &= \sum_{\substack{m=-\infty \\ (0\nu) \neq (m\mu)}}^{\infty} \hat{G}(\mathbf{r}_{0\nu}, \mathbf{r}_{m\mu}; \omega) e^{-i(qh)m} \\ &= \sum_{\substack{m=-\infty \\ (0\nu) \neq (-m\mu)}}^{\infty} \hat{G}(\mathbf{r}_{0\nu}, \mathbf{r}_{-m\mu}; \omega) e^{i(qh)m} \\ &= \sum_{\substack{m=-\infty \\ (0\nu) \neq (m\mu)}}^{\infty} \hat{G}(\mathbf{r}_{m\nu}, \mathbf{r}_{0\mu}; \omega) e^{i(qh)m} \\ &= \sum_{\substack{m=-\infty \\ (0\nu) \neq (m\mu)}}^{\infty} \hat{G}^T(\mathbf{r}_{0\mu}, \mathbf{r}_{m\nu}; \omega) e^{i(qh)m} \\ &= \hat{S}_{\mu\nu}^T(\omega, q). \end{aligned} \quad (10)$$

To derive the third expression aforementioned, we have used translational invariance of \hat{G} , Eq. (4b). In the fourth expression, we have used Lorentz reciprocity, Eq. (4a).

4 Inverse Polarizability and Dispersion Equation

Equation (6) is a set of linear homogeneous equations with a $3p \times 3p$ matrix $\mathbf{M}(\omega, q)$ (we denote $3p$ -dimensional quantities such as matrices and vectors by a straight typewriter-style letters like \mathbf{M} or \mathbf{F}). Correspondingly, the dispersion equation has the general form $\det[\mathbf{M}(\omega, q)] = 0$. The set of complex pairs (ω, q) that satisfy this equation is a rather complicated four-dimensional algebraic variety. To simplify the problem, we can apply various physically motivated restrictions. For example, we will consider further only real frequencies ω . We will also use a more specific expression for $\hat{\chi}_v(\omega)$, which will allow us to disentangle the material and geometric properties of the chain in the expression for $\mathbf{M}(\omega, q)$.

First, to ensure energy conservation and mathematical stability of numerical results, we account for the first nonvanishing radiative correction to the quasi-static polarizability of an ellipsoid [20] by writing

$$\hat{\chi}(\omega) = \hat{\alpha}_{\text{qs}}^{-1}(\omega) - i \frac{2k^3}{3} \hat{I}, \quad k = \sqrt{\epsilon_h} \frac{\omega}{c}. \quad (11)$$

Here $\hat{\alpha}_{\text{qs}}(\omega)$ is the quasi-static polarizability, \hat{I} is the identity tensor, and k is the wave number in the host medium. In the case of ellipsoids, $\hat{\alpha}_{\text{qs}}(\omega)$ can be conveniently written as

$$\hat{\alpha}_{\text{qs}}(\omega) = \frac{\epsilon_h v}{4\pi} \sum_{j=1}^3 \frac{\hat{\mathbf{u}}_j \otimes \hat{\mathbf{u}}_j}{\epsilon_h / [\epsilon(\omega) - \epsilon_h] + \kappa_j}, \quad (12)$$

where $\hat{\mathbf{u}}_j$ are three mutually orthogonal unit vectors, which define the principal axes of the ellipsoid, and κ_j are the corresponding depolarization factors ($\kappa_1 + \kappa_2 + \kappa_3 = 1$). The ellipsoid volume v is given in terms of the three semi-axes a_j by

$$v = \frac{4\pi}{3} a_1 a_2 a_3, \quad (13)$$

and the depolarization factors κ_j can be expressed as functions of the two independent ratios a_1/a_2 and a_1/a_3 . Now we can easily invert (12) and obtain for a generic ellipsoid

$$\hat{\chi}(\omega) = \frac{4\pi}{\epsilon_h v} \left[\frac{\epsilon_h}{\epsilon(\omega) - \epsilon_h} \hat{I} + \sum_{j=1}^3 \kappa_j \hat{\mathbf{u}}_j \otimes \hat{\mathbf{u}}_j \right] - i \frac{2k^3}{3} \hat{I}. \quad (14)$$

It is notable that the scalar factor

$$s(\omega) := \frac{\epsilon_h}{\epsilon(\omega) - \epsilon_h} \quad (15)$$

is independent of the ellipsoid shape while the tensor

$$\hat{K} := \sum_{j=1}^3 \kappa_j \hat{\mathbf{u}}_j \otimes \hat{\mathbf{u}}_j \quad (16)$$

is independent of the material properties. The function $s(\omega)$ defined in (15) is known in the theory of composites as the Bergman–Milton spectral parameter. Further, the radiative correction depends only on the frequency. We have therefore disentangled the geometric and material properties of an ellipsoid. Returning to the problem at hand, we can write for the ν -th ellipsoid

$$\hat{\chi}_\nu(\omega) = \frac{1}{\beta_\nu} \left[s(\omega) \hat{I} + \hat{K}_\nu \right] - i \frac{2k^3}{3} \hat{I}, \quad (17)$$

where

$$\beta_\nu := \frac{\epsilon_h v_\nu}{4\pi}. \quad (18)$$

Equation (17) is the expression we sought. Here only the geometric tensor \hat{K}_ν and the volume-related coefficient β_ν depend on the ellipsoid index. Note that all tensors \hat{K}_ν are symmetric, so that $\hat{K}_\nu = \hat{K}_\nu^T$.

Although equation (17) applies to any material of the ellipsoids, we will specialize further to the case when this material is a Drude metal with the permittivity

$$\epsilon(\omega) = \epsilon_0 - \frac{\omega_p^2}{\omega(\omega + i\gamma)}, \quad (19)$$

where ω_p is the plasma frequency, and γ is the relaxation constant. We then have

$$s(\omega) = \epsilon_h \frac{\omega(\omega + i\gamma)}{(\epsilon_0 - \epsilon_h)\omega(\omega + i\gamma) - \omega_p^2}. \quad (20)$$

This expression becomes particularly simple in the case $\epsilon_0 = \epsilon_h$.

We now return to (7) and use the functional form (17) of $\hat{\chi}_\nu(\omega)$. This results in the equation

$$s(\omega) \mathbf{d}_\nu = \beta_\nu \left[\sum_{\mu=1}^p \hat{S}_{\nu\mu}(\omega, q) \mathbf{d}_\mu + i \frac{2k^3}{3} \mathbf{d}_\nu \right] - \hat{K}_\nu \mathbf{d}_\nu. \quad (21)$$

We need to find points in the two-dimensional region

$$\mathbb{D} := \left\{ -\frac{\pi}{h} \leq q \leq \frac{\pi}{h}; \omega > 0 \right\} \quad (22)$$

of the (q, ω) -plane for which (21) has nontrivial solutions. Of course, this is possible only if $\gamma = 0$ in the Drude formula and then only for $q > k$ (above the light line). To find the dispersion curves numerically, we will set $\gamma = 0$ in the expression for $s(\omega)$ (20), so that

$$s(\omega) \xrightarrow{\gamma=0} s_0(\omega) := \frac{\epsilon_h \omega^2}{(\epsilon_0 - \epsilon_h)\omega^2 - \omega_p^2} . \quad (23)$$

However, when simulating propagation due to an external excitation (e.g., by an antenna), we will include finite losses in the model.

5 Algebraic Considerations

For each pair of indexes (ν, μ) , the tensor $\hat{S}_{\nu\mu}(\omega, q)$ is a 3×3 matrix. We can arrange these matrices into a $3p \times 3p$ matrix $S(\omega, q)$ as shown further:

$$S(\omega, q) = \begin{bmatrix} \hat{S}_{11}(\omega, q) & \hat{S}_{12}(\omega, q) & \dots & \hat{S}_{1p}(\omega, q) \\ \hat{S}_{21}(\omega, q) & \hat{S}_{22}(\omega, q) & \dots & \hat{S}_{2p}(\omega, q) \\ \dots & \dots & \dots & \dots \\ \dots & \dots & \dots & \dots \\ \hat{S}_{p1}(\omega, q) & \hat{S}_{p2}(\omega, q) & \dots & \hat{S}_{pp}(\omega, q) \end{bmatrix} . \quad (24)$$

We denote matrices of the size $3p \times 3p$ by straight, typewriter-style letters such as S . We can use (4) to show that

$$S(\omega, -q) = S^T(\omega, q) . \quad (25)$$

We also introduce two block-diagonal matrices

$$B = \begin{bmatrix} \beta_1 \hat{I} & 0 & \dots & 0 \\ 0 & \beta_2 \hat{I} & \dots & 0 \\ \dots & \dots & \dots & \dots \\ \dots & \dots & \dots & \dots \\ 0 & 0 & \dots & \beta_p \hat{I} \end{bmatrix} , \quad K = \begin{bmatrix} \hat{K}_1 & 0 & \dots & 0 \\ 0 & \hat{K}_2 & \dots & 0 \\ \dots & \dots & \dots & \dots \\ \dots & \dots & \dots & \dots \\ 0 & 0 & \dots & \hat{K}_p \end{bmatrix} . \quad (26)$$

Then Eq. (21) takes the following form:

$$s(\omega) \mathbf{d} = \mathbb{W}(\omega, q) \mathbf{d} , \quad (27)$$

where

$$\mathbb{W}(\omega, q) = B \left[S(\omega, q) + i \frac{2k^3}{3} \mathbf{I} \right] - K \quad (28)$$

and \mathbf{d} is a column-vector of dipole moments \mathbf{d}_v of the length $3p$:

$$\mathbf{d} = [\mathbf{d}_1 \ \mathbf{d}_2 \ \dots \ \mathbf{d}_p]^T. \quad (29)$$

Equation (27) has nontrivial solutions if and only if one of the eigenvalues of $\mathbb{W}(\omega, q)$ is equal to $s(\omega)$.

5.1 Ellipsoids of Equal Volume

Let us first analyze the relatively simple case when \mathbf{B} is proportional to the identity matrix, $\mathbf{B} = \beta \mathbf{I}$. This happens if all ellipsoids are of the same volume (but not necessarily of the same shape and orientation). Then the symmetry property (25) of $\mathbf{S}(\omega, q)$ is inherited by $\mathbb{W}(\omega, q)$. Indeed, we have in the special case considered

$$\mathbb{W}(\omega, q) = \beta \left[\mathbf{S}(\omega, q) + i \frac{2k^3}{3} \mathbf{I} \right] - \mathbf{K}. \quad (30)$$

Here \mathbf{I} is the $3p \times 3p$ identity matrix. Since \mathbf{K} is symmetric and independent of q , we have

$$\mathbb{W}(\omega, -q) = \mathbb{W}^T(\omega, q) \quad (\text{if } \beta_v = \beta = \text{const}). \quad (31)$$

It immediately follows that $\mathbb{W}(\omega, q)$ and $\mathbb{W}(\omega, -q)$ have the same eigenvalues. Therefore, if a point (ω, q) is on the dispersion curve, then $(\omega, -q)$ is also on the dispersion curve (because $s(\omega)$ is independent of q). We thus have proved the following theorem:

Theorem 1 (Eigenvalues of $\mathbb{W}(\omega, q)$ for ellipsoids of fixed volume) *For structured chains made of general ellipsoids of equal volume, the following statements are true:*

- (i) $\mathbb{W}(\omega, q)$ and $\mathbb{W}(\omega, -q)$ share the same set of eigenvalues $\lambda_i(\omega, q)$. Therefore, the eigenvalues are even functions of q , $\lambda_i(\omega, -q) = \lambda_i(\omega, q)$.
- (ii) The dispersion curves $q = q(\omega)$ are symmetric with respect to the line $q = 0$.

Moreover, it is clear that, if $\mathbf{f}(\omega, q)$ and $\mathbf{f}(\omega, -q)$ are the right eigenvectors of $\mathbb{W}(\omega, q)$ and $\mathbb{W}(\omega, -q)$, respectively, with the same eigenvalue $\lambda(\omega, q)$, then $\mathbf{f}(\omega, -q)$ is a left eigenvector of $\mathbb{W}(\omega, q)$, and $\mathbf{f}(\omega, q)$ is a left eigenvector of $\mathbb{W}(\omega, -q)$. Indeed, start from the definitions

$$\begin{aligned}\mathbb{W}(\omega, q) \mathbf{f}(\omega, q) &= \lambda(\omega, q) \mathbf{f}(\omega, q), \\ \mathbb{W}(\omega, -q) \mathbf{f}(\omega, -q) &= \lambda(\omega, q) \mathbf{f}(\omega, -q).\end{aligned}\quad (32a)$$

Transposing the above equations and using (31), we obtain

$$\begin{aligned}\mathbf{f}^T(\omega, q) \mathbb{W}(\omega, -q) &= \lambda(\omega, q) \mathbf{f}^T(\omega, q), \\ \mathbf{f}^T(\omega, -q) \mathbb{W}(\omega, q) &= \lambda(\omega, q) \mathbf{f}^T(\omega, -q),\end{aligned}\quad (32b)$$

which proves the aforementioned statement.

Theorem 2 (Eigenvectors of $\mathbb{W}(\omega, q)$ for ellipsoids of fixed volume)

Assume that $\mathbb{W}(\omega, q)$ has $3p$ distinct eigenvalues $\lambda_i(\omega, q)$ corresponding to the eigenvectors $\mathbf{f}_i(\omega, q)$, $i = 1, 2, \dots, 3p$. Then $\mathbb{W}(\omega, -q)$ has $3p$ eigenvectors $\mathbf{f}_i(\omega, -q)$ corresponding to the same distinct eigenvalues and the two sets of eigenvectors are mutually dual bases so that

$$\mathbf{f}_j^T(\omega, -q) \mathbf{f}_i(\omega, q) = Z_i(\omega, q) \delta_{ji}$$

with $Z_i(\omega, q) \neq 0$ and $Z_i(\omega, -q) = Z_i(\omega, q)$, where δ_{ij} is the Kronecker delta-symbol.

Note that there is no complex conjugation in the orthogonality relation of Theorem 2. We can still normalize the eigenvectors by the conventional condition

$$\mathbf{f}_i^\dagger(\omega, q) \mathbf{f}_i(\omega, q) = 1. \quad (33)$$

Here \dagger denotes Hermitian conjugation (transposition and entry-wise complex conjugation).

Proof The first statement of Theorem 2 is obvious. Eigenvectors of any non-degenerate matrix form a basis, and $\mathbb{W}(\omega, q)$ and $\mathbb{W}(\omega, -q)$ share the same set of distinct eigenvalues. To show that the two bases are dual, we can consider the matrix element

$$\mathbf{f}_j^T(\omega, -q) \mathbb{W}(\omega, q) \mathbf{f}_i(\omega, q) \quad (34)$$

and use the relations (32). Acting with $\mathbb{W}(\omega, q)$ to the left and to the right, we obtain the equality

$$\lambda_i(\omega, q) \mathbf{f}_j^T(\omega, -q) \mathbf{f}_i(\omega, q) = \lambda_j(\omega, q) \mathbf{f}_j^T(\omega, -q) \mathbf{f}_i(\omega, q). \quad (35)$$

If $j \neq i$, the aforementioned equality implies that $\mathbf{f}_j^T(\omega, -q) \mathbf{f}_i(\omega, q) = 0$. This proves mutual orthogonality of the bases. It remains to show that $Z_i(\omega, q) \neq 0$. Assume that $Z_i(\omega, q) = 0$ for some i . We know that $\mathbf{f}_j^T(\omega, -q) \mathbf{f}_i(\omega, q) = 0$ for all $j \neq i$. Therefore, the set of $\mathbf{f}_j(\omega, -q)$ with $j \neq i$ forms the orthogonal complement to $\mathbf{f}_i(\omega, q)$. If, in addition, $\mathbf{f}_i(\omega, -q)$ has zero projection onto $\mathbf{f}_i(\omega, q)$, the set of all vectors $\mathbf{f}_j(\omega, -q)$ is the same orthogonal complement and therefore does not form a complete basis in contradiction to the assumption that $\mathbb{W}(\omega, q)$ is non-degenerate. Therefore, $Z_i(\omega, q) = 0$ is not a possibility. \square

We can now write the following spectral expansion for $\mathbb{W}(\omega, q)$ (assuming it is not degenerate)

$$\mathbb{W}(\omega, q) = \sum_{i=1}^{3p} \frac{1}{Z_i(\omega, q)} \lambda_i(\omega, q) \mathbf{f}_i(\omega, q) \mathbf{f}_i^T(\omega, -q). \quad (36)$$

Remark 1 (Degeneracy of $\mathbb{W}(\omega, q)$) If $\mathbb{W}(\omega, q)$ is degenerate but not defective (this means that its eigenvectors still form a complete basis), we can always construct dual bases of eigenvectors of $\mathbb{W}(\omega, q)$ and $\mathbb{W}(\omega, -q)$ according to the standard procedure. This case does not pose any difficulties, and the statements of Theorem (2) remain true. However, $\mathbb{W}(\omega, q)$ is, in general, neither symmetric nor Hermitian, and proving non-defectiveness for matrices with no special symmetry is usually difficult. From the physical point of view, defectiveness occurs due to random degeneracy with a probability close to 0 and therefore almost never. In simulations, it is safe to ignore this possibility.

5.2 Ellipsoids of Varying Volume

It is clear on physical grounds that allowing the volume of ellipsoids to vary should not cause any new effects. In fact, the spectral properties of $\mathbb{W}(\omega, q)$ remain in this case almost the same (with a slight modification), but the proofs are more difficult because \mathbf{B} is no longer proportional to the identity matrix and the symmetry relation (31) does not hold.

We start from the definition (28) where \mathbf{B} is not necessarily proportional to the identity matrix and write it in the form

$$\mathbb{W}(\omega, q) = \mathbf{B} \mathbf{S}(\omega, q) + i \frac{2k^3}{3} \mathbf{B} - \mathbf{K}. \quad (37)$$

Next we change the sign of q in the previous formula. This yields

$$\mathbb{W}(\omega, -q) = \mathbf{B} \mathbf{S}(\omega, -q) + i \frac{2k^3}{3} \mathbf{B} - \mathbf{K}. \quad (38)$$

Using the symmetry property (25) of $S(\omega, q)$, we also have

$$\mathbb{W}(\omega, -q) = \left[S(\omega, q) \mathbf{B} + i \frac{2k^3}{3} \mathbf{B} - \mathbf{K} \right]^T, \quad (39)$$

where we accounted for the symmetry of \mathbf{B} and \mathbf{K} . Let us denote the matrix in the square brackets by $\mathbf{U}(\omega, q)$;

$$\mathbf{U}(\omega, q) := S(\omega, q) \mathbf{B} + i \frac{2k^3}{3} \mathbf{B} - \mathbf{K}. \quad (40)$$

We therefore have

$$\mathbb{W}(\omega, -q) = \mathbf{U}^T(\omega, q). \quad (41)$$

The matrices $S(\omega, q)$ and \mathbf{B} do not generally commute. For this reason, $\mathbf{U}(\omega, q) \neq \mathbb{W}(\omega, q)$. We will, however, prove that $\mathbf{U}(\omega, q)$ and $\mathbb{W}(\omega, q)$ share the same eigenvalues. To this end, we will use the special properties of \mathbf{B} and \mathbf{K} . It will then follow from (41) that $\mathbb{W}(\omega, q)$ and $\mathbb{W}(\omega, -q)$ share the same eigenvalues, even though these two matrices are not transposes of each other.

Theorem 3 (Eigenvalues of $\mathbb{W}(\omega, q)$ for ellipsoids of variable volume)
Conclusions of Theorem 1 carry over to the case when the ellipsoids have variable volume.

Proof We can prove Theorem 3 by noticing that \mathbf{B} is diagonal, and all its elements are positive and removed from zero (since the same is true for the volumes v_v). We can therefore take the square root of \mathbf{B} and, moreover, this operation is numerically stable. Let $\mathbf{B} = \mathbf{D} \mathbf{D}$. From the same arguments as earlier, \mathbf{D} is invertible. We can use these properties of \mathbf{B} to write

$$\begin{aligned} \mathbb{W}(\omega, q) &= \mathbf{D} \left[\mathbf{D} S(\omega, q) \mathbf{D} + i \frac{2k^3}{3} \mathbf{B} - \mathbf{D}^{-1} \mathbf{K} \mathbf{D} \right] \mathbf{D}^{-1}, \\ \mathbf{U}(\omega, q) &= \mathbf{D}^{-1} \left[\mathbf{D} S(\omega, q) \mathbf{D} + i \frac{2k^3}{3} \mathbf{B} - \mathbf{D} \mathbf{K} \mathbf{D}^{-1} \right] \mathbf{D}. \end{aligned} \quad (42)$$

The key observation that we need is that $\mathbf{D}^{-1} \mathbf{K} \mathbf{D} = \mathbf{D} \mathbf{K} \mathbf{D}^{-1} = \mathbf{K}$. This is easy to verify directly. Denoting

$$\mathbb{W}_s(\omega, q) := \mathbf{D} S(\omega, q) \mathbf{D} + i \frac{2k^3}{3} \mathbf{B} - \mathbf{K}, \quad (43)$$

we arrive at the result

$$\begin{aligned}\mathbb{W}(\omega, q) &= \mathbf{D} \quad \mathbb{W}_s(\omega, q) \mathbf{D}^{-1}, \\ \mathbf{U}(\omega, q) &= \mathbf{D}^{-1} \mathbb{W}_s(\omega, q) \mathbf{D} \quad .\end{aligned}\quad (44)$$

Here $\mathbb{W}_s(\omega, q)$ is the symmetrized form of $\mathbb{W}(\omega, q)$ (compare to Eq. 37). In the case when $\mathbf{B} = \beta \mathbf{I}$, the two matrices coincide. It is now easy to see that $\mathbb{W}_s(\omega, q)$, $\mathbb{W}(\omega, q)$, and $\mathbf{U}(\omega, q)$ share the same eigenvalues. This proves Theorem 3. \square

Theorem 4 (Eigenvectors of $\mathbb{W}(\omega, q)$ for ellipsoids of variable volume) *Let the symmetrized matrix $\mathbb{W}_s(\omega, q)$ have $3p$ distinct eigenvalues $\lambda_i(\omega, q)$, $i = 1, 2, \dots, 3p$ with the corresponding eigenvectors $\mathbf{f}_i(\omega, q)$. Then $\mathbf{D}\mathbf{f}_i(\omega, q)$ and $\mathbf{D}^{-1}\mathbf{f}_i(\omega, -q)$ are the right and left eigenvectors of $\mathbb{W}(\omega, q)$ with the same eigenvalues. These two sets of eigenvectors are mutually dual bases.*

The proof is obvious since $\mathbb{W}_s(\omega, q)$ satisfies the symmetry property (31), and all conclusions of Theorem 2 hold for it verbatim. In particular, (36) holds for $\mathbb{W}_s(\omega, q)$. We can therefore use (44) to write

$$\mathbb{W}(\omega, q) = \sum_{i=1}^{3p} \frac{1}{Z_i(\omega, q)} \lambda_i(\omega, q) \mathbf{D} \mathbf{f}_i(\omega, q) \mathbf{f}_i^T(\omega, -q) \mathbf{D}^{-1}. \quad (45)$$

The statements of Theorem 4 can be verified directly by using this formula.

Remark 2 (Normalization) We assume that the vectors $\mathbf{f}_i(\omega, q)$ (for positive and negative q) are normalized by the conventional condition

$$\mathbf{f}_i^\dagger(\omega, q) \mathbf{f}_i(\omega, q) = 1. \quad (46)$$

Then the left and right eigenvectors of $\mathbb{W}(\omega, q)$,

$$\mathbf{g}_i(\omega, q) := \mathbf{D}\mathbf{f}_i(\omega, q), \quad \mathbf{g}_i(\omega, -q) := \mathbf{D}^{-1}\mathbf{f}_i(\omega, -q)$$

are not normalized. However, the overlap coefficients appearing in (45) are the same for the normalized and not normalized bases, viz,

$$Z_i(\omega, q) = Z_i(\omega, -q) = \mathbf{f}_i^T(\omega, -q) \mathbf{f}_i(\omega, q) = \mathbf{g}_i^T(\omega, -q) \mathbf{g}_i(\omega, q). \quad (47)$$

6 Forced Oscillations

6.1 Response to External Field

We now consider the response to an external field, e.g., produced by a source antenna. To this end, we return to the coupled-dipole equation (2) and seek the solution in the form of a Fourier integral

$$\mathbf{d}_{nv} = \frac{1}{2\pi} \int_{-\pi/h}^{\pi/h} \tilde{\mathbf{d}}_v(\xi) e^{i\xi hn} d\xi, \quad v = 1, 2, \dots, p. \quad (48)$$

Here $\tilde{\mathbf{d}}_v(\xi)$ is the Fourier coefficient to be determined. A similar decomposition can be written for the incident field:

$$\mathbf{e}_{nv} = \frac{1}{2\pi} \int_{-\pi/h}^{\pi/h} \tilde{\mathbf{e}}_v(\xi) e^{i\xi hn} d\xi, \quad v = 1, 2, \dots, p. \quad (49)$$

Using the $3p$ -dimensional matrix notations introduced earlier and the expression (17) for $\hat{\chi}(\omega)$, the coupled-dipole equation (2) can be written as

$$[s(\omega) \mathbf{I} - \mathbf{W}(\omega, \xi)] \tilde{\mathbf{d}}(\xi) = \mathbf{B} \tilde{\mathbf{e}}(\xi), \quad (50)$$

with the obvious solution

$$\tilde{\mathbf{d}}(\xi) = [s(\omega) \mathbf{I} - \mathbf{W}(\omega, \xi)]^{-1} \mathbf{B} \tilde{\mathbf{e}}(\xi). \quad (51)$$

We then substitute this result back to the Fourier integral (48) and find the real-space solution

$$\mathbf{d}_n = \frac{1}{2\pi} \int_{-\pi/h}^{\pi/h} [s(\omega) \mathbf{I} - \mathbf{W}(\omega, \xi)]^{-1} \mathbf{B} \tilde{\mathbf{e}}(\xi) e^{i\xi hn} d\xi. \quad (52)$$

In this expression, \mathbf{d}_n is the $3p$ -dimensional vector of dipole moments in the n -th cell. The correspondence to the three-dimensional vectors \mathbf{d}_{nv} , that is,

$$\mathbf{d}_n = [\mathbf{d}_{n1} \ \mathbf{d}_{n2} \ \dots \ \mathbf{d}_{np}]^T. \quad (53)$$

Next, we use the spectral expansion (45) to write

$$[s(\omega) \mathbf{I} - \mathbf{W}(\omega, \xi)]^{-1} = \sum_{i=1}^{3p} Z_i(\omega, \xi) \frac{\mathbf{D} \mathbf{f}_i(\omega, \xi) \mathbf{f}_i^T(\omega, -\xi) \mathbf{D}^{-1}}{s(\omega) - \lambda_i(\omega, \xi)}. \quad (54)$$

Substituting this result into (52), we obtain the spectral solution to the forced oscillation problem:

$$\mathbf{d}_n = \frac{1}{2\pi} \int_{-\pi/h}^{\pi/h} d\xi e^{i\xi hn} \sum_{i=1}^{3p} Z_i(\omega, \xi) \frac{\mathbf{D} \mathbf{f}_i(\omega, \xi) \mathbf{f}_i^T(\omega, -\xi) \mathbf{D} \tilde{\mathbf{e}}(\xi)}{s(\omega) - \lambda_i(\omega, \xi)}. \quad (55)$$

In the special case when all ellipsoids are of the same volume v , this expression simplifies to

$$\mathbf{d}_n = \frac{\epsilon_h v}{8\pi^2} \int_{-\pi/h}^{\pi/h} d\xi e^{i\xi hn} \sum_{i=1}^{3p} Z_i(\omega, \xi) \frac{\mathbf{f}_i(\omega, \xi) \mathbf{f}_i^T(\omega, -\xi) \tilde{\mathbf{e}}(\xi)}{s(\omega) - \lambda_i(\omega, \xi)}. \quad (56)$$

6.2 Localized Excitation of a Surface Plasmon Polariton

Of special interest is excitation that is localized and, ideally, restricted to the reference cell. This means that

$$\mathbf{e}_{nv} = \mathbf{e}_v \delta_{n0}. \quad (57)$$

In this case,

$$\tilde{\mathbf{e}}_v(\xi) = h \mathbf{e}_v \quad (58)$$

is independent of ξ , as can be easily verified by substitution into (49). In practice, the source antenna will illuminate all particles in the chain. However, by using directional antennas or by placing them close to the reference cell, we can minimize such effects. Mathematically, however, the approximation (58) is convenient as it allows one to compute the response due to some elementary excitations, whereas more complex and realistic excitations can be considered by linear superposition.

Assuming (58) is true, we rewrite (55)

$$\mathbf{d}_n = \frac{h}{2\pi} \int_{-\pi/h}^{\pi/h} d\xi e^{i\xi hn} \sum_{i=1}^{3p} Z_i(\omega, \xi) \frac{\mathbf{D} \mathbf{f}_i(\omega, \xi) \mathbf{f}_i^T(\omega, -\xi) \mathbf{D} \mathbf{e}}{s(\omega) - \lambda_i(\omega, \xi)}, \quad (59)$$

where \mathbf{e} is the $3p$ -dimensional vector whose elements are the electric fields created by the source antenna at the particles of the reference cell,

$$\mathbf{e} = [\mathbf{e}_1 \ \mathbf{e}_2 \ \dots \ \mathbf{e}_p]^T. \quad (60)$$

Equation (59) seems to be a small modification of (55) (the dependence on ξ and the overhead tilde in $\tilde{\mathbf{e}}(\xi)$ are gone; note also the extra power of h in the overall coefficient), but it will allow us to make further analytical progress as described further.

For each ω , the dominant input to the integral (59) is given by the values of ξ such that the denominator $s(\omega) - \lambda_i(\omega, \xi)$ is small. If the denominator could turn to zero, the integral would be ill-defined. However, it cannot turn to zero if there is some absorption in the particle material. The approach therefore is to compute the dispersion curves by solving the equation $s(\omega) = \lambda_i(\omega, \xi)$ with zero absorption; then evaluate the integral (59) for some small but nonzero absorption. In quantum mechanics, similar approximate evaluation of integrals is known as the quasi-particle pole approximation. We write

$$s(\omega) = s_0(\omega) + i\sigma(\omega), \quad (61)$$

where $\sigma(\omega) > 0$ and $s_0(\omega) = \lim_{\gamma \rightarrow 0} s(\omega)$. A particular expression for $s_0(\omega)$, which can be used conveniently in numerical simulations, is given in (23). Then the dispersion curves are obtained by finding all real-valued solutions to

$$s_0(\omega) = \lambda_i(\omega, \xi) \quad (\text{dispersion equation for } i\text{-th mode}), \quad (62)$$

where $\omega > 0$ and $-\pi/h < \xi \leq \pi/h$.

Not all modes may have such solutions at a given frequency ω . Let us fix ω and assume for simplicity that real values of ξ that satisfy (62) exist only for $i = r$ (the resonant mode). If such solutions exist for several values of i , a generalization is easily obtained by summation over all resonant modes. Assuming for now that a solution exists only for $i = r$, we may keep only one term in the summation of (59), viz,

$$\mathbf{d}_n = \frac{h}{2\pi} \int_{-\pi/h}^{\pi/h} d\xi e^{i\xi hn} Z_r(\omega, \xi) \frac{\mathbf{D} \mathbf{f}_r(\omega, \xi) \mathbf{f}_r^T(\omega, -\xi) \mathbf{D} \mathbf{e}}{s(\omega) - \lambda_r(\omega, \xi)}. \quad (63)$$

Due to the symmetry of $\lambda_i(\omega, \xi)$, roots of (62) always come in pairs. Consider the simplest case when there are only two roots, $\xi = \pm q(\omega)$, where $q(\omega) > 0$ for definitiveness. The set of all points $(\omega, q(\omega))$ defines the dispersion relation of the chain. We can expand $\lambda_r(\omega, \xi)$ for ξ near the roots $\pm q(\omega)$ as

$$\lambda_r(\omega, \xi) \approx s_0(\omega) - \sigma(\omega) \ell(\omega) \times \begin{cases} q(\omega) - \xi, & \xi \approx q(\omega) \\ q(\omega) + \xi, & \xi \approx -q(\omega) \end{cases}. \quad (64)$$

Here the factor $\sigma(\omega)$ has been introduced for convenience and $\ell(\omega)$ is a new independent coefficient. It may be computed numerically as

$$\ell(\omega) := \frac{1}{\sigma(\omega)} \left. \frac{\partial \lambda_r(\omega, \xi)}{\partial \xi} \right|_{\xi=q(\omega)} . \quad (65)$$

Although we do not prove this statement here, $\lambda_i(\omega, \xi)$ are real-valued for $\xi > k$ (where the solutions to the dispersion equation exist), and therefore, $\ell(\omega)$ is also real. The physical interpretation is that, below the light line, the SPPs propagate without radiative losses. However, $\ell(\omega)$ can be positive or negative. We say that dispersion is positive at ω if $\ell(\omega) > 0$ and negative otherwise.

We can now use (64) to rewrite (63), approximately, as

$$\begin{aligned} d_n &= \frac{h Z_r(\omega, q(\omega))}{2\pi \sigma(\omega) \ell(\omega)} \\ &\times \int_{-\infty}^{\infty} \left[\frac{d_-(\omega)}{\xi + q(\omega) + i/\ell(\omega)} - \frac{d_+(\omega)}{\xi - q(\omega) - i/\ell(\omega)} \right] e^{i\xi hn} d\xi . \end{aligned} \quad (66)$$

In this expression,

$$d_+(\omega) := P_r(\omega) \mathbf{e} , \quad d_-(\omega) := P_r^T(\omega) \mathbf{e} , \quad (67a)$$

where

$$P_r(\omega) := \mathbf{D} \mathbf{f}_r(\omega, q(\omega)) \mathbf{f}_r^T(\omega, -q(\omega)) \mathbf{D} . \quad (67b)$$

Note that we have expanded the integration in (66) to the real axis. It remains therefore to compute the integrals in (66). Consider first the case of positive dispersion, $\ell(\omega) > 0$. Accounting for the general condition $\sigma(\omega) > 0$, we arrive at

$$d_n = \frac{h Z_r(\omega, q(\omega)) e^{[i q(\omega) - 1/\ell(\omega)] h |n|}}{i \sigma(\omega) \ell(\omega)} \begin{cases} d_+(\omega) , & n > 0 \\ \frac{1}{2} [d_+(\omega) + d_-(\omega)] , & n = 0 \\ d_-(\omega) , & n < 0 \end{cases} . \quad (68)$$

We thus see that, for a generic point $(\omega, q(\omega))$ on the dispersion curve, it propagates to the right and left of the excitation site with the wave numbers $+q(\omega)$ and $-q(\omega)$, respectively. The coefficient $\ell(\omega)$ is the characteristic propagation distance, which describes the exponential decay of the SPPs due to Ohmic losses. The amplitudes of propagation to the right and to the left are in general not the same and given by $d_+(\omega)$ and $d_-(\omega)$ for positive dispersion, and vice versa for negative dispersion.

7 Direction-Selective Coupling

Here we demonstrate direction-selective coupling of SPPs to local excitation (confined to the reference cell \mathbb{C}). The question we are asking is whether it is possible to achieve direction-selective coupling by illuminating only the dipoles in the smallest periodic element of the cell. The latter qualifier is important. There are other means to excite SPPs propagating in a given direction only, but they require a spatially extended source antenna with the length of many periods of the chain. For example, the smallest cell in a simple linear periodic chain consists of just one particle, and local direction-selective coupling in such chains is impossible. More generally, local direction-selective coupling is not possible in chains that are invariant under the reflection $Z \rightarrow -Z$. Indeed, if the chain has this property, the matrix $W(\omega, q)$, in addition to the fundamental relation (31), is also symmetric, so that $W(\omega, q) = W^T(\omega, q) = W(\omega, -q)$. It is easy to see from (43) that, in this case, $d_+ = d_-$.

However, in a chain without the reflection symmetry, $W(\omega, q)$ is not symmetric. We can exploit this property to achieve direction-selective coupling with a fairly good precision. Indeed, at a frequencies corresponding to positive dispersion, direction-selective coupling to SPPs propagating to the right of the reference cell (in the positive Z direction) occurs if $d_+ \neq 0$ but $d_- = 0$. It can be seen from (68) that, within the precision of the approximation made, the dipole moments in the cells with $n < 0$ are in this case zero. Similarly, the SPP would propagate to the left of the reference cell if $d_- \neq 0$ but $d_+ = 0$. For negative dispersion, the directions are reversed.

7.1 Directional Chain with Three Particles Per Cell

There are several simple geometries of the reference cell that we can investigate for the purpose of providing examples. Here we illustrate how the direction-selective coupling can be achieved using the simple geometry illustrated in Fig. 2. Assume that the polarization is out-of-plane (along the Y -axis) and the particles are identical prolate spheroids whose major axis is aligned with Y . Figure 2 can be regarded as the “top view” of the waveguide. Further, we provide some analytical results for this geometry and illustrate the accuracy of the approximation that was made in evaluating the integral (59).

Since the Cartesian components of the dipole moments along X and Z are zero in the considered geometry and only the Y -components enter the equations, the size of W is effectively 3×3 . The algebraic structure of $W(\omega, q)$ is (regardless of ω and q)

$$W = \begin{bmatrix} w_{11} & w_{12} & w_{13} \\ w_{21} & w_{22} & w_{23} \\ w_{31} & w_{32} & w_{33} \end{bmatrix} = \begin{bmatrix} a & b & c \\ d & a & d \\ c & b & a \end{bmatrix}. \quad (69)$$

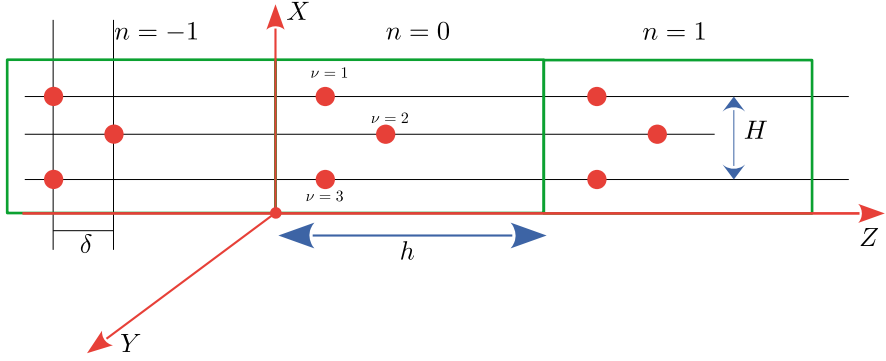


Fig. 2 Schematic illustration of the discrete waveguide for which direction-selective coupling is possible

Here we accounted for the symmetry relations

$$\begin{aligned}
 w_{11} &= w_{22} = w_{33} =: a, \\
 w_{12} &= w_{32} =: b, \\
 w_{13} &= w_{31} =: c, \\
 w_{21} &= w_{23} =: d,
 \end{aligned} \tag{70}$$

which are specific to the considered geometry. It is possible to prove that, for $q > k$, a and c are real while $d = b^*$. Therefore, \mathbb{W} is neither symmetric nor Hermitian. This fact will allow us to achieve direction-selective coupling. The matrix has three distinct eigenvalues

$$\lambda_1 = a - c, \quad \lambda_2 = a + \frac{c - \sqrt{c^2 + 8bd}}{2}, \quad \lambda_3 = a + \frac{c + \sqrt{c^2 + 8bd}}{2}. \tag{71}$$

It can be seen that for $q > k$ all eigenvalues are real. The dual bases of right and left eigenvectors, \mathbf{f}_i and \mathbf{g}_i , are

$$\begin{aligned}
 \mathbf{f}_1 &= [-1 \ 0 \ 1]^T, \quad \mathbf{f}_2 = \left[1 \ \frac{-\sqrt{c^2 + 8bd} - c}{2b} \ 1 \right]^T, \quad \mathbf{f}_3 = \left[1 \ \frac{\sqrt{c^2 + 8bd} - c}{2b} \ 1 \right]^T; \\
 \mathbf{g}_1 &= [-1 \ 0 \ 1]^T, \quad \mathbf{g}_2 = \left[1 \ \frac{-\sqrt{c^2 + 8bd} - c}{2d} \ 1 \right]^T, \quad \mathbf{g}_3 = \left[1 \ \frac{\sqrt{c^2 + 8bd} - c}{2d} \ 1 \right]^T.
 \end{aligned} \tag{72}$$

The orthogonality relations are, as expected, $\mathbf{f}_i^T \mathbf{g}_j = \delta_{ij}$ with

$$Z_1 = 2, \quad Z_2 = Z_3 = 4 + \frac{c(c + \sqrt{c^2 + 8bd})}{2bd}. \quad (73)$$

In addition, we have the following relations

$$\mathbf{f}_2^T \mathbf{f}_3 = 2(1 - d/b), \quad \mathbf{g}_2^T \mathbf{g}_3 = 2(1 - b/d). \quad (74)$$

We now have all the ingredients to build a source that couples only to the SPPs that propagate in a given direction. Assume that the pair (ω, q) is on the dispersion curve for the 2-nd mode, in other words, satisfy the equation $s_0(\omega) = \lambda_2(\omega, q)$. Then we can apply the theory of Sect. 6.2. In particular, we have

$$\mathbf{d}_+ = \mathbf{f}_2 \mathbf{g}_2^T \mathbf{e}, \quad \mathbf{d}_- = \mathbf{g}_2 \mathbf{f}_2^T \mathbf{e}, \quad (75)$$

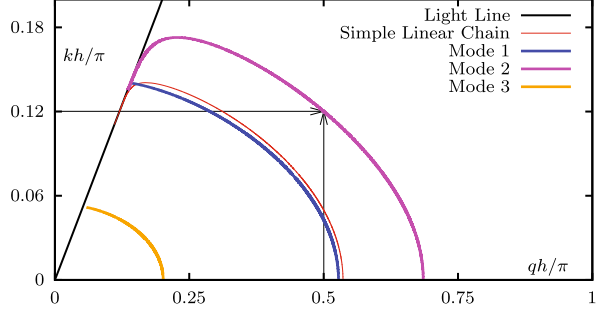
where all quantities should be evaluated at the selected dispersion point (ω, q) . If we choose $\mathbf{e} = \mathbf{f}_3$, we will have $\mathbf{d}_+ = 0$ and $\mathbf{d}_- = 2(1 - d/b)\mathbf{g}_2 \neq 0$. If we choose $\mathbf{e} = \mathbf{g}_3$, then $\mathbf{d}_- = 0$ and $\mathbf{d}_+ = 2(1 - b/d)\mathbf{f}_2 \neq 0$. Therefore, by using the right phase relations for the incident field, we can send the wave in either direction.

7.2 Numerical Example

To illustrate the effect numerically, we take the lattice period of the chain shown in Fig. 2 to be $h = 25.3$ nm and the spheroid semi-axes $a_x = a_z = 6.325$ nm and $a_y = 42.166 \dots$ nm, so that the proportions are $a_x = a_z = 0.25h = 0.15a_y$. The transverse width of the waveguide is $H = 2h = 50.6$ nm and the shift of the central dipole is $\delta = 0.25h = 6.325$ nm. Particles are made of a Drude metal with $\epsilon_0 = 5.0$ and the wavelength at the plasma frequency in vacuum $\lambda_p = 2\pi c/\omega_p = 136.1$ nm, which is characteristic of silver. The host medium is assumed to be a transparent dielectric with $\epsilon_h = 2.5$. These parameters and the geometry shown in Fig. 2 characterize the waveguide completely.

We have solved the dispersion equations $s_0(\omega) = \lambda_i(\omega, q)$ by the method of bisection. The dispersion curves for all three modes of the waveguide are shown in Fig. 3. The $i = 1$ mode does not involve the central dipole (which is identically zero for this mode), and therefore, it is not very different from the mode of a simple linear chain made of the same spheroids. The dispersion curve for the latter case is shown by a thin red line for comparison. As the eigenvectors $\mathbf{f}_1 = \mathbf{g}_1$ are orthogonal to all other eigenvectors, the $i = 1$ mode cannot be used for direction-selective coupling. However, we can use to this end the $i = 2$ and $i = 3$ modes. Without loss of generality, we choose $i = 2$. The point $(kh/\pi, qh/\pi) = (0.12, 0.5)$ belongs to the $i = 2$ dispersion curve as is shown by the arrows in Fig. 3. Note that, at

Fig. 3 Dispersion curves for the chain shown in Fig. 2 with the parameters described in the text. The thin red curve for a simple linear chain of the same spheroids and with the same period is shown for comparison



the normalized frequency $kh/\pi = 0.12$, there exist two solutions to the dispersion equation, one with $i = 1$ and another with $i = 2$. However, the $i = 1$ mode is antisymmetric and will not be excited. We can therefore focus on the $i = 2$ mode alone.

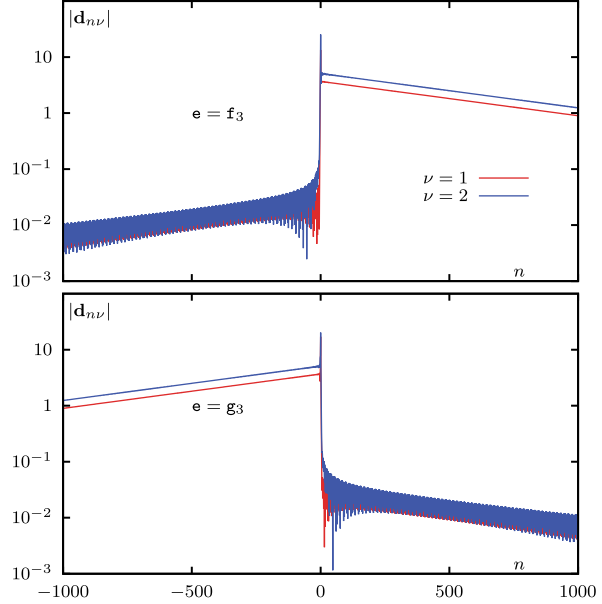
Having fixed a point on the dispersion curve $(kh/\pi, qh/\pi) = (0.12, 0.5)$, we have used numerical summation to compute the matrix elements $w_{11} = a$, $w_{12} = b$, $w_{13} = c$, and $w_{21} = d$. We then used (72) to find the eigenvectors. In this manner, we arrived at the numerical result

$$\begin{aligned} \mathbf{f}_3 &= [1 \quad -(1.37131 + 0.471286i) \quad 1]^T, \\ \mathbf{g}_3 &= [1 \quad -(1.37131 - 0.471286i) \quad 1]^T. \end{aligned} \quad (76)$$

The theory predicts that, if we use $\mathbf{e} = \mathbf{f}_3$ or $\mathbf{e} = \mathbf{g}_3$ at the normalized frequency $kh/\pi = 0.12$, the resulting SPPs will propagate only in one direction from the excitation site. We show that this is indeed the case by finding the solution to the coupled-dipole equation (2) directly. We have solved the equations in a chain consisting of 8,000 unit cells with the small relaxation constant $\gamma/\omega_p = 0.0005$ (smaller than in realistic metals). Only three dipoles in the central (reference) cell were illuminated, and the incident field amplitudes were given either by \mathbf{f}_3 or by \mathbf{g}_3 whose components are listed in (76).

The results are shown in Fig. 4. When interpreting Fig. 4, it should be kept in mind that dispersion at $kh/\pi = 0.12$ is negative. Therefore, when we take $\mathbf{e} = \mathbf{g}_3$, we have $d_- = 0$ and $d_+ \neq 0$, but the excitation propagates to the left (in the negative Z direction). In any event, we have demonstrated that, by changing the phase relations of the localized source, we can send the excitation either to the right or to the left, with a high efficiency. We note that the quantities shown in the figure are linear in dipole moments; the energy-related quantities are quadratic. Therefore, the ratio of energy propagating to the left and right in any of the two excitation schemes illustrated in the figure is of the order of 10^4 , which quantifies the directionality of excitation.

Fig. 4 Unidirectional propagation of SPPs in the chain shown in Fig. 2 at the dimensionless frequency $kh/\pi = 0.12$ and for the Drude relaxation constant $\gamma/\omega_p = 0.0005$. Only three dipoles in the reference cell $n = 0$ are illuminated either with the amplitudes $e = f_3$ or $e = g_3$, as labeled. Only the central part of the chain consisting of 8,000 cells is shown. Dipole moments for $\nu = 3$ are identical to those with $\nu = 1$ and are not shown

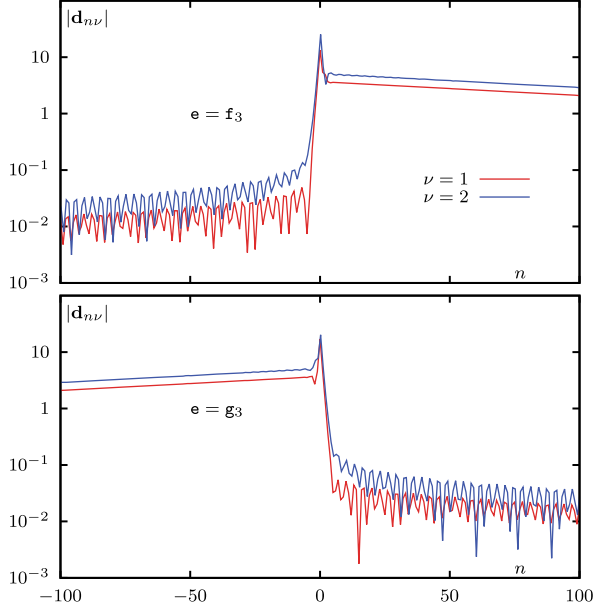


8 Discussion

Several aspects of the aforementioned numerical demonstration require additional discussion. First, we have used an unrealistically small value of the Drude relaxation constant, $\gamma/\omega_p = 0.0005$. This was done to demonstrate the accuracy of the approximation, which allowed us to evaluate the integral (59) analytically. In Fig. 5, we show the same computation with $\gamma/\omega_p = 0.002$, which is the characteristic value for silver. It can be seen that in this, more realistic case, the SPP can still propagate unidirectionally over 100 unit cells (about $2.5 \mu\text{m}$ for the parameters used in the simulation) without significant decay of the amplitude.

In the geometry considered earlier (discrete waveguide made of relatively small particles embedded in infinite free space or a transparent dielectric), the material of the waveguide must be metal. Otherwise, the dispersion relation $s_0(\omega) = \lambda_i(\omega, q)$ does not have real-valued solutions. If we relax the assumptions that the particles are small and the surrounding space is infinite and homogeneous, it may be possible to use other materials such as transparent dielectrics. Familiar examples include optical fibers and dielectric slab waveguides. In the conventional implementation, these waveguides are not directional and therefore do not allow direction-selective coupling. However, we can give the dielectric waveguides a sense of direction by corrugating them (i.e., by introducing voids) so that the inversion symmetry is lost. It is therefore possible to reproduce the effect described earlier in waveguides with

Fig. 5 Same as in Fig. 4 but for $\gamma/\omega_p = 0.002$



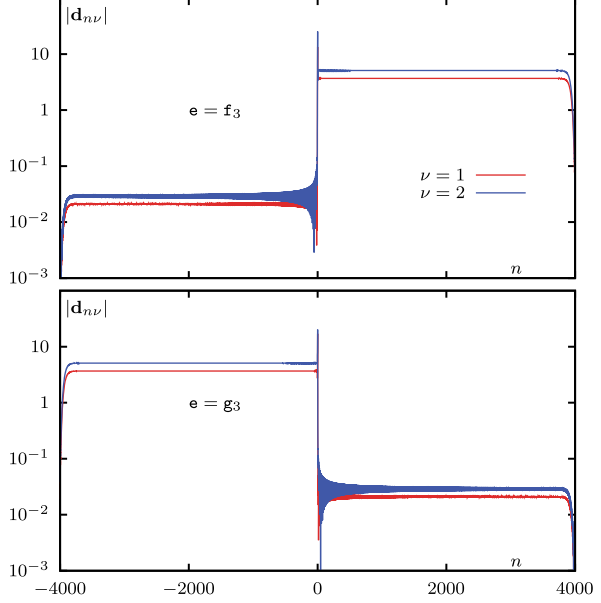
very low losses, although numerical demonstration of this possibility is much harder as the dipole approximation is no longer applicable to such waveguides.

In the metallic discrete waveguides described earlier, low losses may in fact be problematic. If the SPP reaches the physical end of the chain without significant decay, it may be reflected. Transient pulses can traverse the chain several times reflecting back and forth from the chain ends creating noise. In Fig. 6, we show that the problem can be ameliorated by introducing absorbing traps at the physical ends of the chain. One may think of these traps as detectors. The simulation of Fig. 6 was performed in a very long chain with zero absorption ($\gamma = 0$) everywhere except at the chain ends where it increases exponentially from 0 to $0.05\omega_p$ over the length of 100 cells. It can be seen that reflections in this case are completely suppressed.

Finally, it may seem that the excitation scheme used earlier where the source antenna illuminates only particles in the reference cell is artificial. A real antenna would illuminate all particles in the chain, albeit with a variable amplitude. The excitation scheme, however, is physical and in fact quite natural as we will now explain. Let us assume that the external fields $\mathbf{e}_{n\nu}$ in (2) are localized according to (57) and therefore are zero for all $n \neq 0$. We can iterate (2) once by writing

$$\mathbf{d}_{n\nu} = \alpha_\nu(\omega)\mathbf{e}_{n\nu} + \mathbf{d}'_{n\nu} . \quad (77)$$

Fig. 6 Unidirectional SPPs in a chain of 8,000 unit cells made mostly of nonabsorbing particles but with absorbing traps at both ends. The Drude relaxation constant increases exponentially near the chain ends as $\gamma_0 \exp(-\beta m)$ where $\gamma_0/\omega_p = 0.05$, $\beta = 0.01$ and m is the distance to the chain end in units of \hbar . The traps prevent SPP reflections that would occur otherwise



In the adopted excitation scheme, we have $\mathbf{d}_{nv} = \mathbf{d}'_{nv}$ for all $n \neq 0$, the difference being limited to the reference cell. By substituting (77) into (2), we find that the dipole moments \mathbf{d}'_{nv} satisfy

$$\hat{\chi}_v(\omega) \mathbf{d}'_{nv} = \mathbf{e}'_{nv} + \sum_{\substack{m\mu \\ (m\mu) \neq (nv)}} \hat{G}(\mathbf{r}_{nv}, \mathbf{r}_{m\mu}; \omega) \mathbf{d}'_{m\mu}, \quad (78)$$

where

$$\mathbf{e}'_{nv} = \sum_{\substack{\mu=1 \\ (0\mu) \neq (nv)}}^p \hat{G}(\mathbf{r}_{nv}, \mathbf{r}_{0\mu}; \omega) \hat{\alpha}_\mu(\omega) \mathbf{e}_\mu. \quad (79)$$

Equation (78) is similar to (2) but has a different source term, \mathbf{e}'_{nv} . This modified term is the field of an antenna consisting of the particles of the reference cell whose active (that is, externally controlled) dipole moments are $\mathbf{d}_v^{(\text{source})} = \hat{\alpha}_v(\omega) \mathbf{e}_v$. Thus, for all dipoles except those of the reference cell, the localized excitation scheme considered earlier is equivalent to the excitation scheme in which the particles of the reference cell are themselves an active source of radiation (the antenna). This alternative excitation scheme is illustrated in Fig. 7. We conclude that the direction-selective coupling can be achieved if the reference cell (located arbitrarily inside a chain) is an externally controlled active antenna.

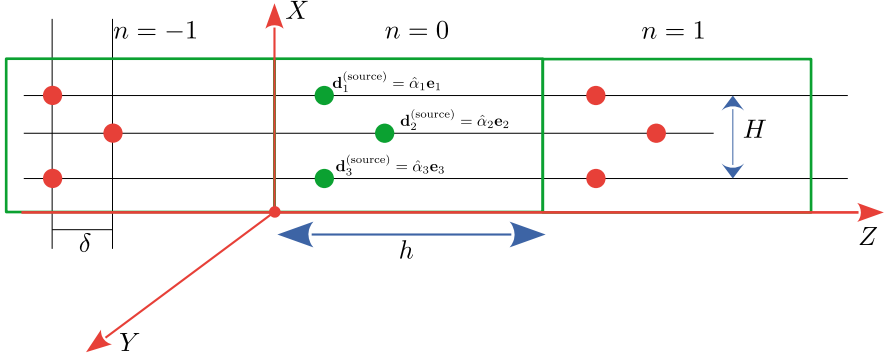


Fig. 7 Discrete waveguide similar to that of Fig. 2 but here the particles of the reference cell comprise an active antenna (the source of electromagnetic field) and have the externally controlled dipole moments $\mathbf{d}_v^{(\text{source})}$. This excitation scheme is equivalent to the localized excitation scheme considered elsewhere in this chapter for all cells with $n \neq 0$ provided that $\mathbf{d}_v^{(\text{source})} = \hat{\alpha}_v(\omega)\mathbf{e}_v$. The relation must hold at the working frequency for a monochromatic excitation or point-wise in Fourier domain for transient excitation

Appendix

The Green's tensor for Maxwell's equations is singular. The singular part appears implicitly in the definition of the polarizability tensor $\hat{\alpha}_v(\omega)$ but not in the coupled-dipole equation (2) or the definitions of the dipole sum (8). We therefore focus on the regular part of the Green's tensor, which gives the correct expression as long as $\mathbf{r} \neq \mathbf{r}'$. In terms of the scaled coordinates, the dimensionless Green's tensor appearing in (2) is given by

$$\hat{G}(\mathbf{r}, \mathbf{r}'; \omega) = \left[\left(\frac{\omega^2}{\rho} + \frac{i\omega}{\rho^2} - \frac{1}{\rho^3} \right) \hat{I} + \left(-\frac{\omega^2}{\rho} - \frac{3i\omega}{\rho^2} + \frac{3}{\rho^3} \right) \frac{\boldsymbol{\rho} \otimes \boldsymbol{\rho}}{\rho^2} \right] e^{i\omega\rho}, \quad (80)$$

where $\boldsymbol{\rho} = \mathbf{r} - \mathbf{r}'$ the symbol \otimes denotes tensor product, and \hat{I} is the identity tensor. Note that $\rho = |\boldsymbol{\rho}| = (\rho_x^2 + \rho_y^2 + \rho_z^2)^{1/2}$.

Let $\alpha, \beta = x, y, z$ label the Cartesian components of vectors in a rectangular frame. Then we can rewrite the aforementioned expression in components as

$$G_{\alpha\beta}(\mathbf{r}, \mathbf{r}'; \omega) = \left[\left(\frac{\omega^2}{\rho} + \frac{i\omega}{\rho^2} - \frac{1}{\rho^3} \right) \delta_{\alpha\beta} + \left(-\frac{\omega^2}{\rho} - \frac{3i\omega}{\rho^2} + \frac{3}{\rho^3} \right) \frac{\rho_\alpha \rho_\beta}{\rho^2} \right] e^{i\omega\rho}, \quad (81)$$

References

1. S. Zou, N. Janel, G.C. Schatz, J. Chem. Phys. **120**(23), 10871 (2004)
2. V.G. Kravets, F. Schedin, A.N. Grigorenko, Phys. Rev. Lett. **101**, 087403 (2008)
3. V.G. Kravets, F. Schedin, A.V. Kabashin, et al., Opt. Lett. **35**, 956 (2010)
4. B.D. Thackray, P.A. Thomas, G.H. Auton, F.J. Rodriguez, O.P. Marshall, V.G. Kravets, A.N. Grigorenko, Nano Lett. **15**, 3519 (2015)
5. M.L. Brongersma, J.W. Hartman, H.A. Atwater, Phys. Rev. B **62**(24), R16356 (2000)
6. D.S. Citrin, Opt. Lett. **31**(1), 98 (2006)
7. K.B. Crozier, E. Togan, E. Simsek, T. Yang, Opt. Expr. **15**(26), 17482 (2007)
8. P.J. Compaijen, V.A. Malyshev, J. Knoester, Opt. Expr. **23**(3), 2280 (2015)
9. V.A. Markel, J. Mod. Opt. **40**(11), 2281 (1993)
10. V.A. Markel, J. Phys. B **38**, L115 (2005)
11. V.A. Markel, A.K. Sarychev, Phys. Rev. B **75**, 085426 (2007)
12. A.A. Govyadinov, V.A. Markel, Phys. Rev. B **78**(3), 035403 (2008)
13. A.B. Evlyukhin, C. Reinhardt, U. Zywietz, B.N. Chichkov, Phys. Rev. B **85**, 245411 (2012)
14. S.D. Swiecicki, J.E. Sipe, Phys. Rev. B **95**, 195406 (2017)
15. V.E. Babicheva, A.B. Evlyukhin, Phys. Rev. B **99**, 1954444 (2019)
16. A. Poddubny, A. Miroshnichenko, A. Slobozhanyuk, Y. Kivshar, ACS Photon. **1**, 101 (2014)
17. Y.L. Zhang, R.P.H. Wu, A. Kumar, T. Si, K.H. Fung, Phys. Rev. B **97**, 144203 (2018)
18. V.G. Kravets, A.V. Kabashin, W.L. Barnes, A.N. Grigorenko, Chem. Rev. **118**, 5912 (2018)
19. A.D. Utyushev, V.I. Zakomirnyi, I.L. Rasskazov, Rev. Phys. **6**, 100051 (2021)
20. V.A. Markel, J. Quant. Spectrosc. Radiat. Transfer **236**, 106611 (2019)

Survey and Perspectives on Line-Wave Electromagnetics



Massimo Moccia , Marino Coppolaro , Giuseppe Castaldi ,
and Vincenzo Galdi

1 Introduction and Background

Electromagnetic waves, which generally extend in three dimensions, can exhibit an evanescent character when interacting with matter, resulting in their localization within a lower-dimensional space. A prominent example of this phenomenon is given by “surface waves” (SWs), which are tightly bound to a surface and propagate parallel to it [1] (see, e.g., Fig. 1a). These include surface plasmon polaritons, Bloch/Tamm waves, and Dyakonov waves, among others. The subwavelength confinement and field enhancement at the interface are crucial for various applications, such as chemical and biological sensing [2], nonlinear electromagnetics [3], and quantum electromagnetics [4].

This research area is experiencing renewed interest, spurred by the advent of artificial “metasurfaces” [5] and natural low-dimensional materials like graphene. These materials support SWs [6], whose propagation [7] and radiation [8] can be precisely controlled by locally tailoring surface properties. Additionally, they are easily integrable into planar microwave or photonic architectures.

Recent theoretical [9] and experimental [10] studies have demonstrated a new type of SW that propagates along an abrupt discontinuity between metasurfaces characterized by dual (capacitive–inductive) surface reactances. These waves, known as “line waves” (LWs), retain the out-of-plane localization typical of conventional SWs but also exhibit in-plane localization along the discontinuity (Fig. 1b). This unique feature allows them to transport energy along a one-dimensional (1D) track.

M. Moccia · M. Coppolaro · G. Castaldi · V. Galdi (✉)

Fields & Waves Lab, Department of Engineering, University of Sannio, Benevento, Italy
e-mail: massimo.moccia@unisannio.it; coppolaro@unisannio.it; castaldi@unisannio.it;
vgaldi@unisannio.it

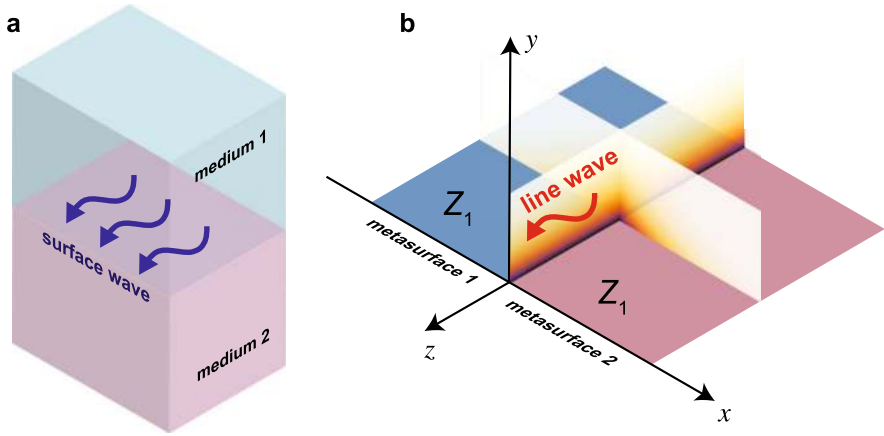


Fig. 1 (a) SWs at an interface between two media. (b) LW at a surface-impedance discontinuity

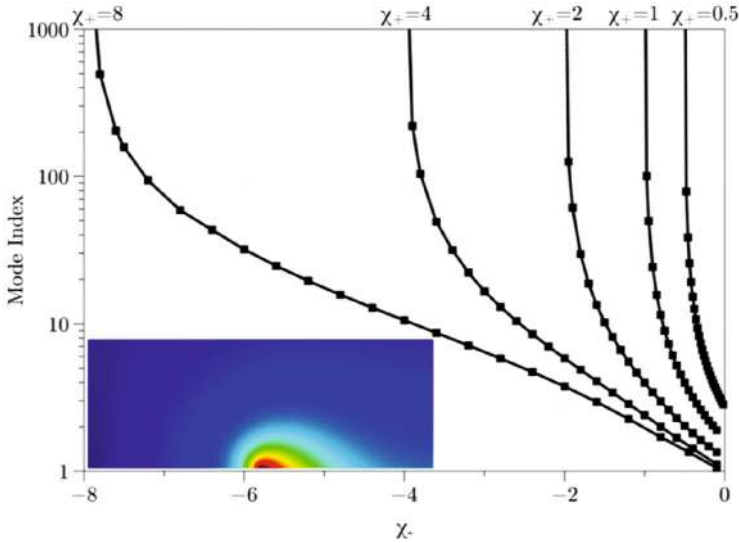


Fig. 2 Numerically computed modal effective index of an LW propagating at an interface between two reactive metasurfaces with normalized surface reactances χ_+ and χ_- , for various parameter combinations. The inset shows the field map of a typical mode. Reprinted from Ref. [9] under [CC BY 3.0](#)

LWs exhibit remarkable properties, including deeply subwavelength localization and field enhancement. As shown in Fig. 2, at a junction between two reactive impedance surfaces with opposite-signed reactances (capacitive–inductive), the effective mode index can approach infinity when the reactances are perfectly matched in magnitude but opposite in sign [9]. This singular behavior results

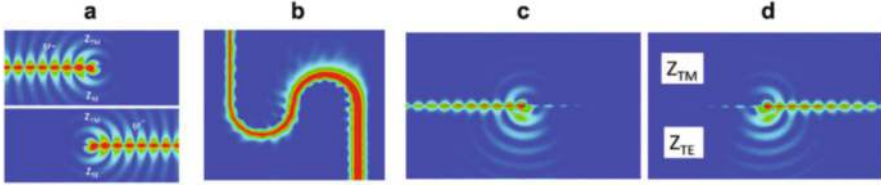


Fig. 3 (a) Numerically computed field maps of an LW propagating at an interface between dual (capacitive-inductive) metasurfaces, with direction-dependent polarization (pseudo-spin states) excited by electric and magnetic Hertzian dipoles in phase (above) or out of phase (below). (b) Field map illustrating the robustness with respect to bending effects. (c), (d) Illustration of chiral coupling effects induced by circularly polarized sources (left- and right-handed, respectively). Reprinted (adapted) with permission from Ref. [10]. Copyright ©2017 American Physical Society

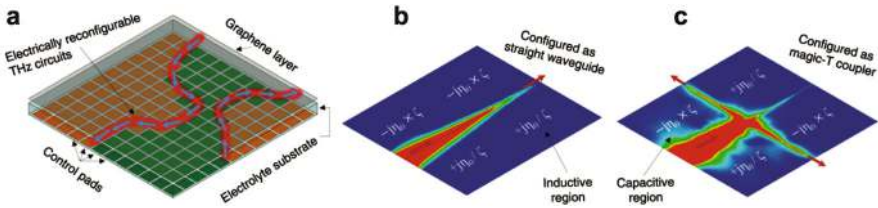


Fig. 4 Illustration of a graphene-based reconfigurable LW platform at THz frequencies. (a) Arbitrary-shaped pathways. (b) Delay lines with tunable phase-shift capabilities. (c) Magic-T coupler based on spin-filtered channels. Reprinted from Ref. [15] under CC BY-NC-ND 4.0

from the idealized assumption of a perfect discontinuity in surface impedance and vanishes with a more realistic, continuous yet sharp transition. Despite this, very high localization remains achievable. Additionally, LWs are characterized by wide bandwidth, propagation-dependent polarization, robustness, and potential reconfigurability [9, 10].

These characteristics make LWs highly promising for various applications, including integrated photonics, high-frequency communications, and optical sensing. Notably, LWs also exhibit topological-like robustness (see Fig. 3a, b) [10, 11], although there are some differences compared to topological photonics [12]. They also retain the spin-momentum locking properties typical of evanescent waves [13], which enable intriguing chiral-coupling effects (see Fig. 3c, d) that are of significant interest for quantum optics and valleytronics [14]. Furthermore, implementations at THz frequencies using gate-tunable graphene sheets have been proposed [15], suggesting exciting possibilities for dynamically reconfiguring wave pathways, confinement, and polarization states (see Fig. 4).

More recently, new classes of LWs have been demonstrated in settings with non-Hermitian (i.e., gain/loss) [16, 17] and anisotropic [18, 19] properties. However, due to the lack of simple analytical models, a clear and comprehensive phenomenological understanding is still missing, along with a thorough taxonomy of the classes of materials that can support LWs.

Experimentally, proof-of-concept demonstrations have been confined to the microwave range, where capacitive and inductive metasurfaces can be easily fabricated through suitable metallic texturing. Existing studies have primarily concentrated on waveguiding, field enhancement, topological properties, power routing/dividing, filtering, and coupling effects [10, 20–22]. However, no experimental results are available yet for reconfigurable effects or higher frequencies.

In this chapter, we offer a concise overview of the key developments in this emerging research area. Specifically, Sect. 2 addresses the modeling aspects from both analytical and numerical perspectives. Section 3 presents a selection of results, including potential material platforms, physical properties, and coupling effects. Finally, Sect. 4 provides concluding remarks, highlighting open challenges and suggesting potential research directions.

2 Modeling Aspects

2.1 Problem Formulation

Referring to the geometry illustrated in Fig. 1b, we consider a planar metasurface situated in vacuum on the $x - z$ plane. In the simplest scenario, this metasurface is characterized by an isotropic impedance boundary condition [23]:

$$\mathbf{E}_t = Z(x)\mathbf{u}_y \times \mathbf{H}|_{y=0}, \quad (1)$$

with the subscript “ t ” denoting the tangential component, and \mathbf{u}_y is a unit vector in the \mathbf{u}_y -direction. We henceforth assume a time-harmonic dependence of $\exp(-i\omega t)$ and a piecewise continuous impedance distribution with a jump at the $x = 0$ interface:

$$Z(x) = \begin{cases} Z_1, & x < 0, \\ Z_2, & x > 0. \end{cases} \quad (2)$$

Alternatively, surface properties can be described using different parameters. For instance, in the case of 2D materials such as graphene, the optical conductivity is commonly used. This conductivity is related to the surface impedance by [15]:

$$\sigma = \frac{2}{Z}, \quad (3)$$

where the factor of 2 accounts for the two-faced nature of a free-standing layer.

As is well known, purely reactive impedance surfaces (i.e., with purely imaginary $Z_{1,2}$) support SWs that exhibit either transverse-electric (TE) or transverse-magnetic (TM) polarization, depending on whether the surface is capacitive or inductive, respectively [23]. These SWs propagate without attenuation within the

$x - z$ plane and decay exponentially in the out-of-plane direction (i.e., along y). A surface-impedance discontinuity can induce additional in-plane localization, leading to field decay along the x -direction away from the interface. For instance, in a capacitive–inductive junction, this localization can be attributed to the TE/TM polarization mismatch occurring at the $x = 0$ interface [9, 10] (see also Fig. 2). However, this is not the only possible mechanism. Consequently, the resulting wave object is localized both in-plane and out-of-plane, concentrating around the line at $x = 0$, and is therefore referred to as an LW.

From a mathematical perspective, the problem involves finding the source-free solutions to the boundary-value problem defined by Eqs. (1) and (2). Specifically, it entails identifying the combinations of Z_1 and Z_2 that lead to LW behavior.

2.2 Analytical Approaches

While the aforementioned boundary-value problem described can be seen as a lower-dimensional analog of the SW problem (Fig. 1a), its analytical treatment is significantly more complex.

In [24], an exact analytical solution to the LW eigenproblem was derived by adapting a generalization of the Sommerfeld–Maliuzhinets method for scattering from impedance wedges [25, 26]. Alternatively, the Wiener–Hopf technique could also be applied [27]. These methods could, in principle, be extended to handle axially anisotropic impedances [28]. However, even in the simpler isotropic case, the resulting formulation is complex and lacks a clear physical parameterization.

Several analytical approximations have been proposed for this problem. In particular, approximations in the electrostatic limit [29] are generally inadequate for deriving the dispersion equation. More recently, in [19], a nonlocal integral equation formulation for general tensor impedances was introduced. In certain cases, this formulation can be reasonably approximated by a local differential equation, where LWs serve as 1D analogs of surface plasmons bound to nonlocal metals.

2.3 Numerical Approaches

For a rigorous and comprehensive treatment of the problem, full-wave numerical approaches are generally required.

In this context, general-purpose methods like finite element analysis [30] can naturally manage arbitrary (scalar and tensor) impedance combinations and multiple discontinuities. However, these methods still fall short in providing clear physical insights and are not well-suited for addressing critical aspects such as complex-valued eigenmodes and nonlocal effects.

In [31], a spectral method of moments was introduced for modeling LW waveguides. This approach not only offers computational efficiency and accuracy

but also accommodates general anisotropy and spatial dispersion. Additionally, it can naturally handle both proper and improper eigenmodes, providing a physically insightful framework for studying LWs.

The numerical studies presented here are conducted using the finite-element commercial software package COMSOL Multiphysics [30].

3 Selected Results

In the following sections, we review recent findings involving material combinations beyond the conventional capacitive–inductive case. These include non-Hermitian platforms with spatial modulations of gain and loss, as well as anisotropic materials. Additionally, we explore peculiar phenomena related to LW propagation, such as leakage and coupling effects, both in-plane and out-of-plane.

3.1 Non-Hermitian Junctions

In [16], a new type of LW was demonstrated at a planar surface-impedance discontinuity characterized by the same reactance but with oppositely signed resistance. Referring to the geometry in Fig. 1b, this configuration involves choosing:

$$Z_1 = -R + iX, \quad Z_2 = R + iX, \quad (4)$$

which represents a transition from gain to loss. The underlying localization mechanism relies on the parity-time (\mathcal{PT}) symmetry condition:

$$Z(x) = -Z^*(x). \quad (5)$$

Originally introduced in non-Hermitian quantum mechanics [32], this concept has been extended to optics [33] and other branches of wave physics [34]. In this context, the two halves of the metasurface individually support attenuated ($x > 0$) and amplified ($x < 0$) SWs, with TM ($X < 0$) or TE ($X > 0$) polarization. The resistance discontinuity creates an additional in-plane localization mechanism, resulting in an LW that propagates along the interface at $x = 0$ with a real-valued propagation constant k_z , experiencing neither attenuation nor amplification. This phenomenon can be seen as a 1D analog of the SWs supported at interfaces between \mathcal{PT} -symmetric metamaterial slabs [35, 36].

Unlike conventional LWs in capacitive–inductive metasurface junctions [9, 10], these non-Hermitian variants can also exhibit an out-of-plane “leaky” (radiative) regime for specific values of the complex surface impedance. As shown in Fig. 5a, the transition from the bound ($k_z > k$) to the leaky [$\text{Re}(k_z) < k$] regimes occurs at the unit-circle $|Z|/\eta = |\tilde{Z}| = 1$, where $k = \omega/c = 2\pi/\lambda$ represents the vacuum

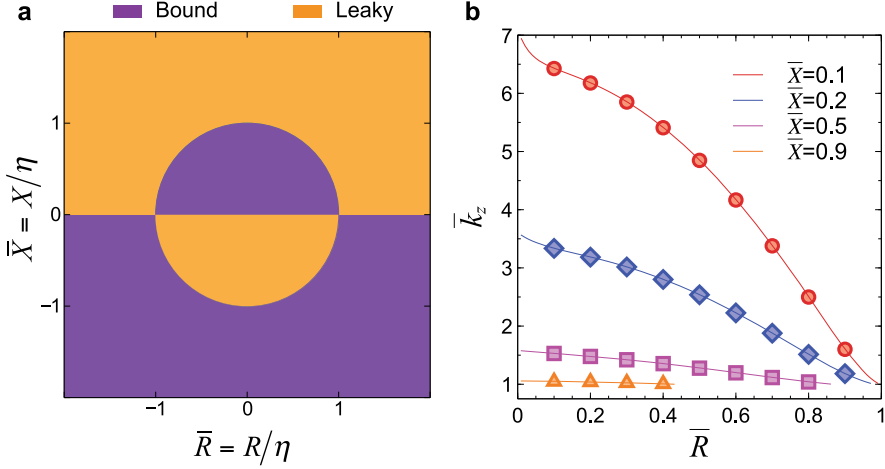


Fig. 5 Non-Hermitian LWs. **(a)** Partition of the \bar{Z} complex plane separating the bound (purple-shaded) and leaky (orange-shaded) modes. **(b)** Effective index k_z/k of bound modes, computed analytically (solid curves) and numerically (markers), as a function of the gain/loss parameter \bar{R} , for representative values of the normalized (capacitive) reactance \bar{X} . Reprinted (adapted) with permission from Ref. [16]. Copyright ©2020 American Chemical Society

wavenumber, and c , λ , and η denote the corresponding wavespeed, wavelength, and intrinsic impedance, respectively. Here and henceforth, the overbar denotes normalization with respect to the vacuum intrinsic impedance η .

For the bound regime, Fig. 5b illustrates the characteristic behaviors of the modal effective index as a function of the surface-impedance parameters, comparing the analytic predictions with full-wave (finite-element) computations [30]. The more realistic scenario of a smooth (though steep) surface-impedance profile was also numerically investigated [16]. Figure 6 illustrates representative modal-field distributions, revealing the hybrid character (with generally nonzero z -components) similar to conventional LWs [9, 10], but also highlighting some important differences. Notably, there is a transverse energy flow (Fig. 6c) that results in anomalous near-field forces [37], potentially useful for microfluidics and micro-optomechanical systems.

Figure 7 demonstrates the out-of-plane leakage effect. As illustrated in Fig. 7a, in this case, the out-of-plane confinement is lost, allowing the field to couple with the radiation continuum. As a result, Fig. 7b shows that propagation along the z -direction is attenuated as power progressively leaks out-of-plane. The far-field radiation pattern in Fig. 7c is consistent with leaky-wave radiation [38].

Similar to the conventional case, non-Hermitian LWs have demonstrated chiral-coupling properties with respect to circularly polarized sources [16]; however, spin-filtered waveguiding is generally not achievable.

Additionally, gain–loss imbalanced configurations have been explored [16] to achieve lasing (or coherent perfect absorption) and in-plane leakage effects (see also

Fig. 6 Non-Hermitian LWs.

(a), (b), (c) Numerically computed distributions (z-components as false-color maps, x and y components as vector plots) for electric and magnetic fields, and powerflux, respectively, for a bound mode ($\bar{R} = \bar{X} = 0.5$; $|\bar{Z}| < 1$). Reprinted (adapted) with permission from Ref. [16]. Copyright ©2020 American Chemical Society

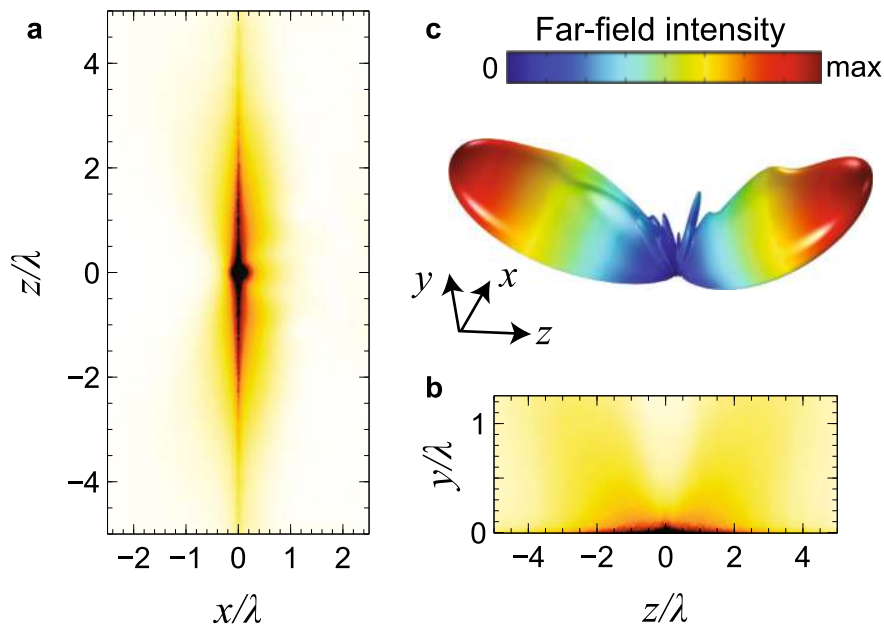
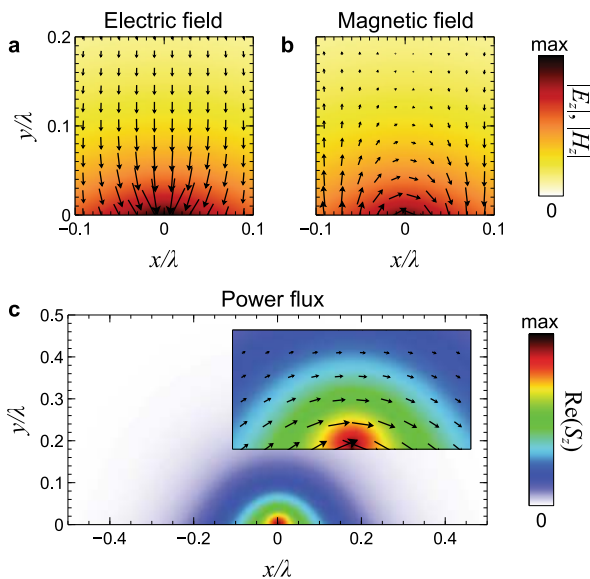


Fig. 7 Non-Hermitian LWs. (a), (b) Numerically computed in-plane ($y = 0.01\lambda$) and out-of-plane ($x = 0$) electric-field magnitude maps in false-color scale, respectively, with $\bar{R} = 1.1$ and $\bar{X} = 0.1$ ($|\bar{Z}| > 1$), showing the out-of-plane leakage effect. (c) Corresponding radiation pattern. The field is excited by a y -directed elementary electric dipole placed at $\mathbf{r} = \mathbf{z} = 0$ and $y = 0.02\lambda$. Reprinted (adapted) with permission from Ref. [16]. Copyright ©2020 American Chemical Society

Sect. 3.3). Potential THz implementations based on photoexcited graphene have also been proposed [16], with optical pumping offering an intriguing reconfigurability mechanism. At high frequencies, this mechanism could be more feasible than a capacitive–inductive transition.

The reader is also referred to [17] for additional results on non-Hermitian LWs.

3.2 Isotropic–Anisotropic Junctions

In [18], a junction between an isotropic metasurface and an anisotropic, reciprocal one was investigated, as schematically illustrated in Fig. 8. The isotropic half is characterized by a surface conductivity σ_i , while the anisotropic half is described by parallel and orthogonal surface conductivities σ_{\parallel} and σ_{\perp} , respectively. The optical axis of the anisotropic metasurface can be rotated by an angle ϕ . In the in-plane (x, z) reference system, this metasurface can be equivalently represented by a symmetric tensor $\underline{\underline{\sigma}}_a$ with components:

$$\sigma_{xx} = \sigma_{\perp} \cos^2 \phi + \sigma_{\parallel} \sin^2 \phi, \quad (6a)$$

$$\sigma_{zz} = \sigma_{\parallel} \cos^2 \phi + \sigma_{\perp} \sin^2 \phi, \quad (6b)$$

$$\sigma_{xz} = \sigma_{zx} = (\sigma_{\perp} - \sigma_{\parallel}) \cos \phi \sin \phi. \quad (6c)$$

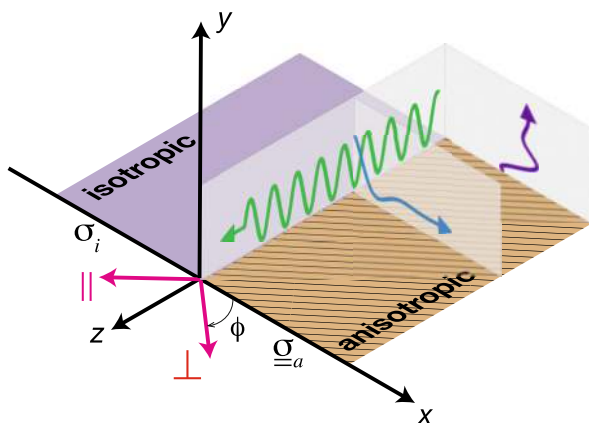
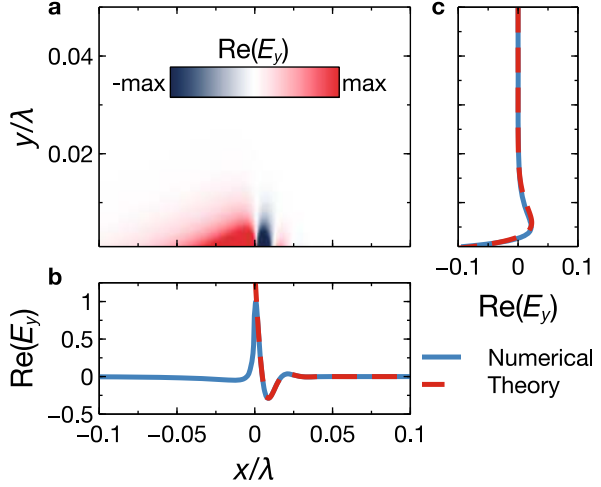


Fig. 8 Schematic of a planar junction between an isotropic metasurface and an anisotropic, reciprocal one with slanted optical axis. The wavy arrows depict a GLW that propagates unattenuated along the interface $x = 0$ and exhibits an oscillatory decay both in-plane and out-of-plane in the anisotropic halfplane $x > 0$. Reprinted with permission from Ref. [18]. Copyright ©2023 American Chemical Society

Fig. 9 Isotropic–anisotropic junction. **(a)** Numerically computed field-map of a GLW eigenmode for $\sigma_i = i0.055\eta^{-1}$, $\sigma_{\perp} = -i0.011\eta^{-1}$, $\sigma_{\parallel} = i0.041\eta^{-1}$, $\phi = 27^\circ$. **(b), (c)** Corresponding cuts (blue-solid) at $y = 0.001\lambda$ and $x = 0.0054\lambda$, respectively, compared with theoretical predictions (red-dashed) obtained from the study of the iso-frequency contours. Reprinted (adapted) with permission from Ref. [18]. Copyright ©2023 American Chemical Society

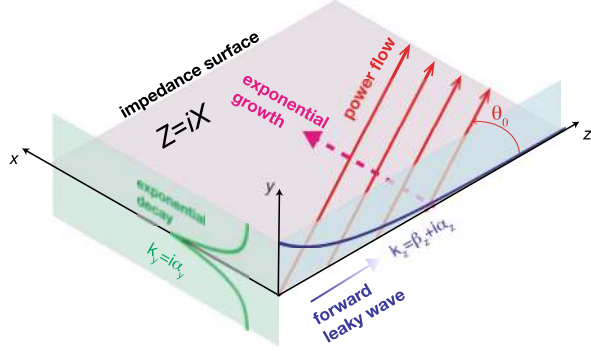


Unlike previous cases, no analytical solutions are currently available for this configuration, necessitating the use of full-wave numerical simulations [30]. However, useful physical insights can be gained by analytically studying the SWs supported by the anisotropic half, assuming that it extends infinitely. As detailed in [18], this configuration can support conventional LWs for either elliptic or hyperbolic anisotropy if the optical axis is aligned with the interface ($\phi = 0, \pi/2$). Conversely, for a slanted optical axis, a unique form of LW emerges, propagating without attenuation along the interface (i.e., z -direction), while decaying with an oscillatory behavior both in-plane (i.e., along x) and out-of-plane (i.e., along y). These modes can be viewed as the 1D equivalent of the “ghost waves” [39–41] and “ghost surface polaritons” [42] observed at interfaces between isotropic and biaxially anisotropic lossless media. These nonuniform waves exhibit complex-valued wavevectors (with nonzero real and imaginary parts) even in the absence of material losses, thus blending characteristics of both propagating and evanescent waves. This hybrid nature may have significant applications in various fields, such as nonlinear optics and sub-diffraction imaging.

Figure 9 illustrates a numerically computed ghost-LW (GLW) mode supported by a suitably designed inductive-hyperbolic junction, with anisotropic parameters compatible with those reported in the literature for a thin layer of α -MoO₃ [43]. This mode demonstrates deeply sub-wavelength localization and oscillatory decay within the anisotropic half. It has been shown that the spectral region admitting GLWs is critically dependent on the rotation angle of the optical axis [18].

For additional insights, the reader is referred to [19], which provides an approximate analytic approach to studying anisotropic junctions. Notably, the oscillatory decay associated with GLWs has been explained through an effective gauge field induced by the surface anisotropy.

Fig. 10 Schematic illustration of the flatland leaky-wave mechanism. Reprinted (adapted) from Ref. [44] under CC BY 4.0



3.3 Flatland Leakage

In [44], a novel LW radiation mechanism was explored, inspired by conventional leaky waves but restricted entirely to in-plane propagation. This differs from the mechanism discussed in Sect. 3.1 (see Fig. 7), which features instead a fast LW radiating out-of-plane.

Let us consider a purely reactive metasurface (in the x - z plane, embedded in vacuum), characterized by a surface impedance $Z = iX$ (Fig. 10). As previously noted, depending on the sign of X , this metasurface can support an SW with either TE or TM polarization and an in-plane propagation constant given by [23]:

$$k_t = \begin{cases} k \sqrt{1 + \left(\frac{X}{\eta}\right)^2}, & X < 0 \quad (\text{TM}), \\ k \sqrt{1 + \left(\frac{\eta}{X}\right)^2}, & X > 0 \quad (\text{TE}). \end{cases} \quad (7)$$

Additionally, let us assume a wave propagating along the z -direction with a complex-valued propagation constant $k_z = \beta_z + i\alpha_z$, where $\beta_z, \alpha_z > 0$ and $k < \beta_z < k_t$. In this scenario, the wave remains confined out-of-plane (exponentially decaying along the y -direction) and exhibits a complex-valued propagation constant along the x -direction, $k_x = \sqrt{k_t^2 - k_z^2} = \beta_x - i\alpha_x$, with $\alpha_x > 0$. This represents the “flatland” analog of conventional leaky-wave scenarios [38], where the radiation is entirely confined in the $x - z$ plane. Despite the seemingly unphysical exponential growth along the x -direction, this wavefield can effectively model in-plane radiation, with the parameters β_z and α_z controlling the radiation direction θ_0 (measured from the z -axis) and the beamwidth, respectively. Specifically, in the regime $\alpha_z \ll \beta_z$, the wave radiates a directive SW beam at an angle $\theta_0 \approx \arccos(\beta_z/k_t)$. This is formally analogous to observations in conventional leaky-wave scenarios [38], with the SW propagation constant replacing the vacuum one. This concept is also related to the recently observed phenomenon of 2D Cherenkov radiation [45].

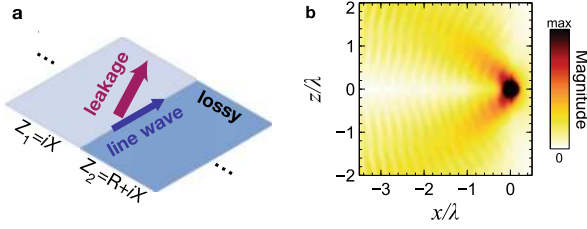


Fig. 11 (a) Schematic of non-Hermitian configuration supporting flat leaky waves. (b) Numerically computed in-plane field map (electric-field magnitude, at $y = 0.01\lambda$), for $\bar{R} = \bar{X} = 0.5$. The field is excited by a y -directed elementary electric dipole placed at $x = z = 0$, $y = 0.02\lambda$. The plot is restricted to the lossless region $x < 0$. Reprinted (adapted) with permission from Ref. [16]. Copyright ©2020 American Chemical Society

The question then arises: how can a wavefield with these characteristics be physically realized? A straightforward example was provided in [16] within a non-Hermitian LW scenario. As illustrated schematically in Fig. 11a, a planar junction between a lossy reactive metasurface and a lossless one can support an LW propagating along the interface, characterized by a complex-valued propagation constant with the desired properties. Figure 11b shows an example derived from the \mathcal{PT} -symmetric configuration in Fig. 6 by switching off the gain (i.e., $\bar{Z}_1 = i0.5$, $\bar{Z}_2 = 0.5 + i0.5$). As observed, two directive beams are obtained in the lossless region, with symmetry due to the bidirectional propagation induced by the dipolar excitation considered. However, relying on losses is suboptimal for efficiency. Thus, alternative configurations featuring purely reactive components can be conceived to achieve similar effects.

In an alternative configuration, illustrated in Fig. 12a, a planar junction between two semi-infinite dual (capacitive-inductive) metasurfaces with surface impedances Z_1 and Z_3 , respectively, separated by a strip of width d and surface impedance Z_2 (of same type as Z_3), can support this type of phenomenon. Referring to [44] for more details, the surface impedances Z_1 and Z_2 are selected such that the corresponding junction supports an LW that decays both in-plane and out-of-plane as $d \rightarrow \infty$. However, for finite values of d , the LW leaks power into the adjacent semi-infinite region of surface impedance Z_3 , radiating a directive beam. Remarkably, this mechanism enables the control and possible scanning of the beam direction via gate-tunable 2D materials such as graphene. Figure 12b–d show numerically computed results (near-field in-plane maps) for three representative configurations, achieved by varying the surface impedance Z_1 . These results exhibit the typical characteristics of leaky-wave radiation, with different beam directions observed for each configuration.

Alternative configurations supporting flat leaky waves, which do not necessarily rely on LWs, can also be conceived [44].

The reader is also referred to [46] for an experimental study at microwave frequencies.

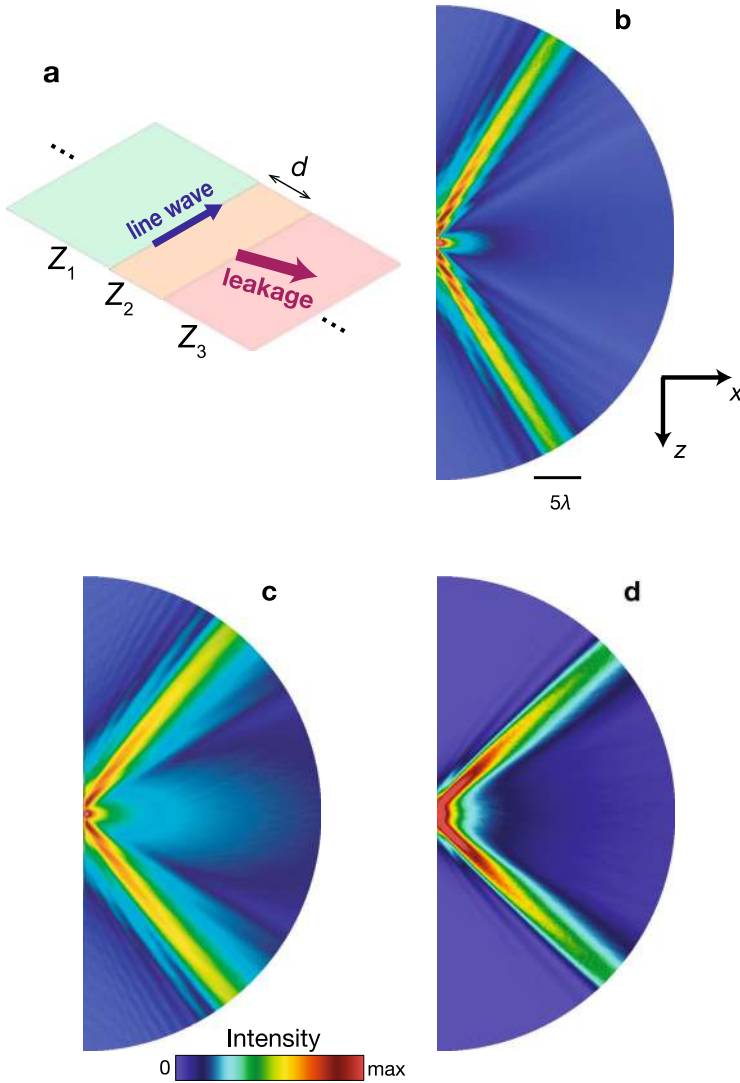


Fig. 12 (a) Schematic of fully reactive configuration supporting flat leaky waves. (b), (c), (d) Numerically computed field maps (electric-field intensity, at $y = 0.001\lambda$), for $d = 0.2\lambda$, $\bar{Z}_2 = -i0.067$, $\bar{Z}_3 = -i2$, and $\bar{Z}_1 = i4$, $i6.67$, and $i100$, respectively. The field is excited by a y -directed elementary electric dipole placed at $y = 0.1\lambda$ and the center of the semicircle shown. The plots are restricted to the region with surface impedance Z_3 . Reprinted (adapted) from Ref. [44] under CC BY 4.0

3.4 Coupling Effects

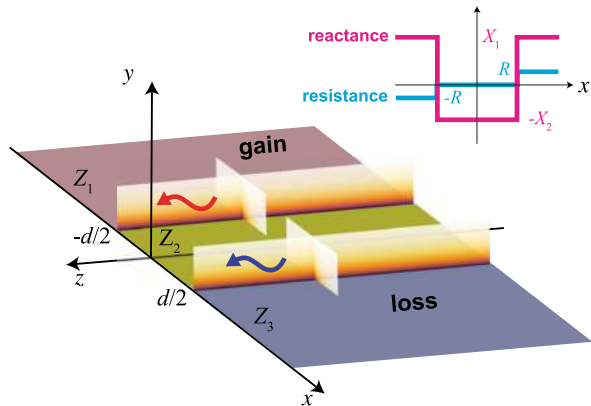
When two surface-impedance junctions supporting LWs are placed in proximity, intriguing coupling effects may arise, analogous to coupled surface plasmon polaritons [48]. Within this context, it is important to distinguish between in-plane and out-of-plane scenarios.

In-plane LW coupling effects have been explored in the context of non-Hermitian configurations with double planar, \mathcal{PT} -symmetric junctions [47], as illustrated in Fig. 13. Specifically, as schematized in the inset, the surface impedance profile is given by:

$$Z(x) = \begin{cases} Z_1 = -R + iX_1, & x < -d/2, \\ Z_2 = -iX_2, & -d/2 < x < d/2, \\ Z_3 = -Z_1^* = R + iX_1, & x > d/2. \end{cases} \quad (8)$$

Each capacitive–inductive junction supports an LW, either damped or amplified, and the coupling strength can be adjusted by varying the width d of the central lossless region. As shown in Fig. 14a,b, the modal indices exhibit a spontaneous symmetry breaking pattern typical of non-Hermitian systems [33]. This entails a transition between a “symmetric” regime, characterized by real-valued branches, and a “broken” regime, marked by complex-conjugate solutions. These regions are separated by an “exceptional point” (EP), at a critical distance d_{EP} , where two eigenstates coalesce, a phenomenon of significant interest for applications such as lasing and sensing [49]. As illustrated in Fig. 14c,d, the critical EP distance d_{EP} can be fine-tuned by adjusting the surface resistance and reactances, offering opportunities for dynamic modulation and the exploration of various paths in parameter space around the EP, especially using gate-tunable platforms like graphene. Notably, the surface-impedance parameters required for these configurations are achievable with models of photoexcited graphene metasurfaces at THz frequencies [47].

Fig. 13 Schematic of in-plane coupling in a \mathcal{PT} -symmetric configuration (see inset). Reprinted with permission from Ref. [47]. Copyright ©2021 American Physical Society



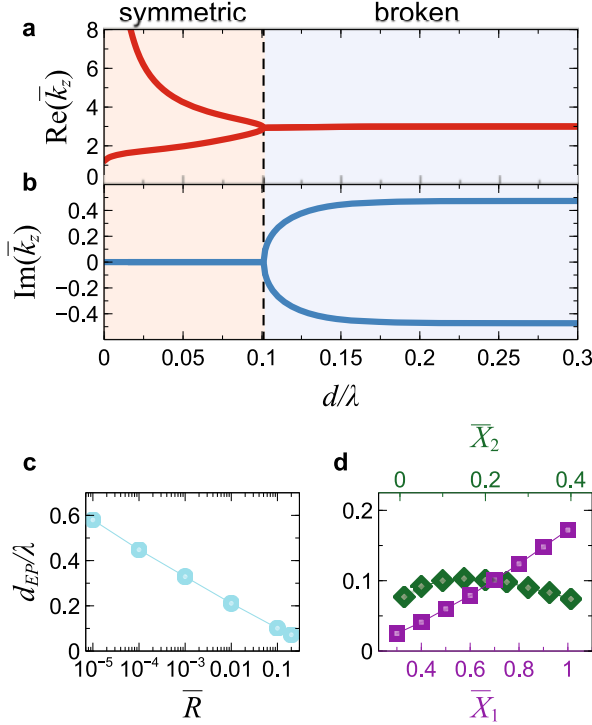


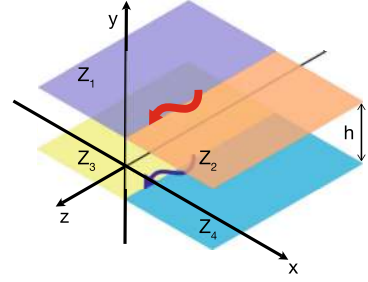
Fig. 14 In-plane coupling of LWs. (a), (b) Real and imaginary part, respectively, of numerically computed modal effective index $\bar{k}_z = k_z/k$, as a function of d/λ , for $\bar{X}_1 = 0.7$, $\bar{X}_2 = 0.2\eta$, $\bar{R} = 0.1\eta$; the symmetric and broken phases are highlighted with different color shades, and the dashed line identifies the EP. (c) Critical electrical separation between the metasurface interfaces to obtain an EP (d_{EP}/λ) as a function of the normalized gain or loss parameter \bar{R} , for $\bar{X}_1 = 0.7$ and $\bar{X}_2 = 0.2$. (d) Same as panel (c) (with $\bar{R} = 0.1$) but as a function of \bar{X}_1 (purple squares, bottom axis) for $\bar{X}_2 = 0.2$, and of \bar{X}_2 (green diamonds, top axis) for $\bar{X}_1 = 0.7$. Reprinted (adapted) with permission from Ref. [47]. Copyright ©2021 American Physical Society

In [50], the out-of-plane coupling of LWs was investigated within a general parallel-plate waveguide configuration. Specific examples of this type of coupling were also explored in [17, 22, 51].

The geometry of interest is illustrated in Fig. 15. We consider two planar metasurface junctions with surface impedances Z_1 and Z_2 , and Z_3 and Z_4 , respectively, arranged within a parallel-plate waveguide with spacing h in vacuum. Each junction supports an LW propagating along the impedance discontinuity (z -direction) while decaying both out-of-plane (along y) and in-plane (along x). Given the localized nature of these waves, they interact weakly when the spacing h is large relative to the wavelength. However, their interaction becomes significant when $h \ll \lambda$.

Interestingly, the configuration in Fig. 15 can also be viewed as a junction between two parallel-plate waveguides formed by pairs of metasurfaces (i.e., Z_1

Fig. 15 Schematic of out-of-plane coupling of LWs in a parallel-plate waveguide configuration. Reprinted with permission from Ref. [50]. Copyright ©2024 Materials Research Society



and Z_3 , and Z_3 and Z_4). These structures have been recently studied in isolation for both purely reactive and \mathcal{PT} -symmetric scenarios [52].

We first consider a purely reactive (capacitive-inductive) configuration that is symmetric along the y -direction, with $\bar{Z}_1 = \bar{Z}_3 = i$ and $\bar{Z}_2 = \bar{Z}_4 = -i0.1$. Figure 16a shows the numerically computed modal effective index k_z/k as a function of the electrical spacing h/λ . As shown, there are two real-valued modal branches, corresponding to modes with even and odd symmetry. For large values of h , the coupling effects are negligible, and the modal indices asymptotically approach $k_z/k \approx 1.89$, which corresponds to the values for the isolated LWs in each junction [10]. As h decreases, the interaction between the LWs intensifies, causing the two modal branches to diverge. In the limit $h \rightarrow 0$, one branch approaches a constant value of $k_z/k \approx 3.06$, corresponding to the modal index of an LW supported by a single junction formed by the combined metasurfaces, where the effective impedances are $Z_1 \parallel Z_3 = Z_1/2$ and $Z_2 \parallel Z_4 = Z_2/2$. The divergence of the upper modal branch represents an unphysical behavior, similar to what was observed in Sect. 3.1, and arises from the idealized assumption of discontinuous surface impedances. This artifact disappears when considering a smooth (albeit sharp) impedance transition. Despite this, the modal index for closely spaced junctions can still achieve significantly larger values compared to the isolated junctions, leading to highly localized modes with potential applications in nonlinear optics, subwavelength sensing, and near-field imaging.

Next, we examine a non-Hermitian configuration comprising two identical capacitive, \mathcal{PT} -symmetric impedance junctions, with parameters $\bar{Z}_1 = \bar{Z}_3 = (-0.5 + i0.5)$ (gain) and $\bar{Z}_2 = \bar{Z}_4 = (0.5 + i0.5)$ (loss), which are selected to satisfy the bound-mode condition (see Sect. 3.1) for the isolated junctions. A notable aspect of this non-Hermitian setup is its potential to exhibit EPs [49], similar to the in-plane coupling scenario discussed in Fig. 14. As illustrated in Fig. 16b,c, EPs can be induced by introducing asymmetry, i.e., displacing one of the junctions along the x -direction by an amount Δ while maintaining a fixed spacing h . This perturbation results in modal indices with complex values, which exhibit a spontaneous symmetry-breaking pattern, transitioning from a symmetric phase to a broken phase through an EP. Also in this configuration, the properties of the EP can be adjusted by varying the electrical thickness of the waveguide and by tuning the surface impedances, allowing for dynamic control.

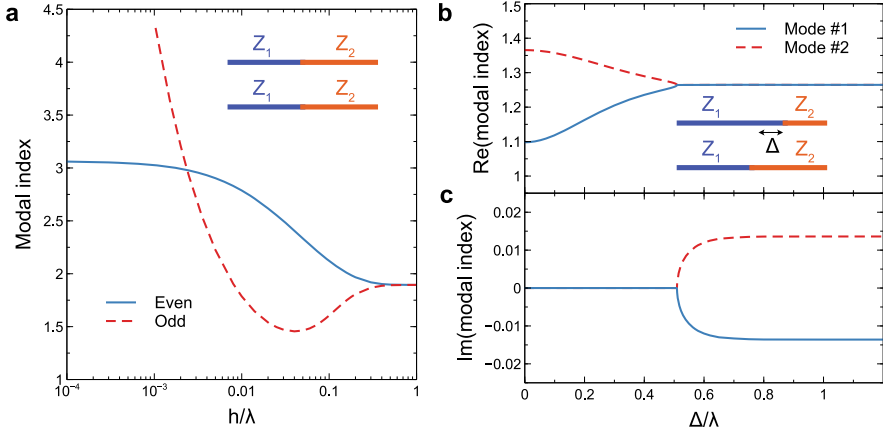


Fig. 16 Out-of-plane coupling of LWs. (a) Numerically computed modal indices kz/k as a function of electrical thickness h/λ for a symmetric configuration (see inset) with $\tilde{Z}_1 = \tilde{Z}_3 = i$ and $\tilde{Z}_2 = \tilde{Z}_4 = -i0.1$; note the semi-log scale. (b), (c) Numerically computed modal indices (real and imaginary part, respectively) as a function of electrical displacement Δ/λ for an \mathcal{PT} -symmetric configuration with $\tilde{Z}_1 = \tilde{Z}_3 = (-0.5 + i0.5)$, $\tilde{Z}_2 = \tilde{Z}_4 = (0.5 + i0.5)$, and $h = 0.31\lambda$. Reprinted (adapted) with permission from Ref. [50]. Copyright ©2024 Materials Research Society

4 Conclusions and Perspectives

In summary, this overview has highlighted recent advancements and emerging trends in the field of LW electromagnetics.

LWs represent a highly intriguing research domain with the potential to revolutionize various applications, ranging from sensing and communications to quantum computing. While LWs can be intuitively regarded as 1D analogs of SWs, their theoretical and experimental study presents significant complexities, necessitating the development of new analytical and numerical tools. Current analytical methods, which often rely on complex special functions, do not facilitate a straightforward physical interpretation of wave phenomena. Consequently, the material combinations that can support LWs and the extent to which their operational frequency can be advanced remain open questions.

Experimental studies to date are limited to microwave frequencies and underscore the need for carefully engineered coupling mechanisms. Theoretical and numerical investigations in the THz range offer preliminary insights, but extending these findings to optical frequencies remains uncertain.

In conclusion, despite the significant interest and potential of LWs, the field is still in its early stages, with many possibilities yet to be explored. This presents substantial opportunities for speculative research and emphasizes the need for experimental validation. Furthermore, translating these concepts to other areas of wave physics, such as mechanics, where SWs are well understood but a 1D counterpart remains elusive, could offer exciting new avenues for investigation.

Acknowledgments This work has been funded by the University of Sannio through the FRA 2023 program.

Competing Interests The authors have no conflicts of interest to declare that are relevant to the content of this chapter.

References

1. J. Polo, T.G. Mackay, A. Lakhtakia, *Electromagnetic Surface Waves: A Modern Perspective* (Newnes, Oxford, 2013)
2. J. Homola, Surface plasmon resonance sensors for detection of chemical and biological species. *Chem. Rev.* **108**(2), 462–493 (2008). <https://doi.org/10.1021/cr068107d>
3. M. Kauranen, A.V. Zayats, Nonlinear plasmonics. *Nat. Photon.* **6**(11), 737–748 (2012). <https://doi.org/10.1038/nphoton.2012.244>
4. M.S. Tame, K.R. McEnery, Ş.K. Özdemir, J. Lee, S.A. Maier, M.S. Kim, Quantum plasmonics. *Nat. Phys.* **9**(6), 329–340 (2013). <https://doi.org/10.1038/nphys2615>
5. C.L. Holloway, E.F. Kuester, J.A. Gordon, J. O'Hara, J. Booth, D.R. Smith, An overview of the theory and applications of metasurfaces: the two-dimensional equivalents of metamaterials. *IEEE Antennas Propag. Mag.* **54**(2), 10–35 (2012). <https://doi.org/10.1109/MAP.2012.6230714>
6. H. Bilow, Guided waves on a planar tensor impedance surface. *IEEE Trans. Antennas Propag.* **51**(10), 2788–2792 (2003). <https://doi.org/10.1109/TAP.2003.817568>
7. S. Maci, G. Minatti, M. Casaletti, M. Bosiljevac, Metasurfing: addressing waves on impenetrable metasurfaces. *IEEE Antennas Wirel. Propag. Lett.* **10**, 1499–1502 (2010). <https://doi.org/10.1109/LAWP.2012.2183631>
8. M. Faenzi, G. Minatti, D. González-Ovejero, F. Caminita, E. Martini, C. Della Giovampaola, S. Maci, Metasurface antennas: new models, applications and realizations. *Sci. Rep.* **9**, 10178 (2019). <https://doi.org/10.1038/s41598-019-46522-z>
9. S.A.R. Horsley, I.R. Hooper, One dimensional electromagnetic waves on flat surfaces. *J. Phys. D: Appl. Phys.* **47**(43), 435103 (2014). <https://doi.org/10.1088/0022-3727/47/43/435103>
10. D.J. Bisharat, D.F. Sievenpiper, Guiding waves along an infinitesimal line between impedance surfaces. *Phys. Rev. Lett.* **119**(10), 106802 (2017). <https://doi.org/10.1103/PhysRevLett.119.106802>
11. D.J. Bisharat, D.F. Sievenpiper, Electromagnetic-dual metasurfaces for topological states along a 1D interface. *Laser Photon. Rev.* **13**(10), 1900126 (2019). <https://doi.org/10.1002/lpor.201900126>
12. T. Ozawa, H.M. Price, A. Amo, N. Goldman, M. Hafezi, L. Lu, M.C. Rechtsman, D. Schuster, J. Simon, O. Zilberberg, I. Carusotto, Topological photonics. *Rev. Mod. Phys.* **91**(1), 015006 (2019). <https://doi.org/10.1103/RevModPhys.91.015006>
13. T.V. Mechelen, Z. Jacob, Universal spin-momentum locking of evanescent waves. *Optica* **3**(2), 118–126 (2016). <https://doi.org/10.1364/OPTICA.3.000118>
14. P. Lodahl, S. Mahmoodian, S. Stobbe, A. Rauschenbeutel, P. Schneeweiss, J. Volz, H. Pichler, P. Zoller, Chiral quantum optics. *Nature* **541**(7638), 473–480 (2017). <https://doi.org/10.1038/nature21037>
15. D.J. Bisharat, D.F. Sievenpiper, Manipulating line waves in flat graphene for agile terahertz applications. *Nanophotonics* **7**(5), 893–903 (2018). <https://doi.org/10.1515/nanoph-2017-0133>
16. M. Moccia, G. Castaldi, A. Alù, V. Galdi, Line waves in non-Hermitian metasurfaces. *ACS Photonics* **7**(8), 2064–2072 (2020). <https://doi.org/10.1021/acsp Photonics.0c00465>
17. H. Ahmadi, Z. Ahmadi, N. Razmjooei, M. Pasdari-Kia, A. Bagheri, H. Saghaei, K. Arik, H. Oraizi, Line-wave waveguide engineering using Hermitian and non-Hermitian metasurfaces. *Sci. Rep.* **14**(1), 5704 (2024). <https://doi.org/10.1038/s41598-024-56049-7>

18. M. Moccia, G. Castaldi, A. Alù, V. Galdi, Ghost line waves. *ACS Photonics* **10**(6), 1866–1872 (2023). <https://doi.org/10.1021/acsp Photonics.3c00262>
19. S.A.R. Horsley, A. Dwivedi, Theory of electromagnetic line waves. *Phys. Rev. B* **108**(15), 155437 (2023). <https://doi.org/10.1103/PhysRevB.108.155437>
20. K. Zafari, H. Oraizi, Surface waveguide and Y splitter enabled by complementary impedance surfaces. *Phys. Rev. Applied* **13**(6), 064025 (2020). <https://doi.org/10.1103/PhysRevApplied.13.064025>
21. Z. Xu, X. Yin, D.F. Sievenpiper, Adiabatic mode-matching techniques for coupling between conventional microwave transmission lines and one-dimensional impedance-interface waveguides. *Phys. Rev. Applied* **11**(4), 044071 (2019). <https://doi.org/10.1103/PhysRevApplied.11.044071>
22. Z. Xu, J. Chang, S. Fang, Q. Zhang, R.J. Davis, D. Sievenpiper, T.J. Cui, Line waves existing at junctions of dual-impedance metasurfaces. *ACS Photonics* **8**(8), 2285–2293 (2021). <https://doi.org/10.1021/acsp Photonics.1c00344>
23. F. Yang, Y. Rahmat-Samii, *Surface Electromagnetics* (Cambridge University, Cambridge, 2019)
24. X. Kong, D.J. Bisharat, G. Xiao, D.F. Sievenpiper, Analytic theory of an edge mode between impedance surfaces. *Phys. Rev. A* **99**(3), 033842 (2019). <https://doi.org/10.1103/PhysRevA.99.033842>
25. G.D. Maliuzhinets, Excitation, reflection and emission of surface waves from a wedge with given face impedances. *Sov. Phys. Doklady* **3**, 752 (1958)
26. V.G. Vaccaro, The generalized reflection method in electromagnetism. *Arch. Elektron. Uebertrag.* **34**, 493–500 (1980)
27. A. Kay, Scattering of a surface wave by a discontinuity in reactance. *IRE Trans. Antennas Propag.* **7**(1), 22–31 (1959). <https://doi.org/10.1109/TAP.1959.1144635>
28. A. Vallecchi, Oblique incidence diffraction by edges in anisotropic impedance surfaces: a collection of exact solutions for specific non-axial tensor boundary conditions. *Electromagnetics* **33**(2), 73–98 (2013). <https://doi.org/10.1080/02726343.2013.756272>
29. A.A. Sokolik, O.V. Kotov, Y.E. Lozovik, Plasmonic modes at inclined edges of anisotropic two-dimensional materials. *Phys. Rev. B* **103**, 155402 (2021). <https://doi.org/10.1103/PhysRevB.103.155402>
30. C. AB, COMSOL Multiphysics® v. 5.1
31. G. Lovat, W. Fuscaldo, M. Moccia, G. Castaldi, V. Galdi, P. Burghignoli, Spectral-domain method of moments for the modal analysis of line waveguides. *IEEE Trans. Antennas Propagat.* **71**(8), 6717–6727 (2023). <https://doi.org/10.1109/TAP.2023.3284377>
32. C.M. Bender, S. Boettcher, Real spectra in non-Hermitian Hamiltonians having PT symmetry. *Phys. Rev. Lett.* **80**(24), 5243–5246 (1998). <https://doi.org/10.1103/PhysRevLett.80.5243>
33. L. Feng, R. El-Ganainy, L. Ge, Non-Hermitian photonics based on parity–time symmetry. *Nat. Photon.* **11**(12), 752–762 (2017)
34. R. El-Ganainy, K.G. Makris, M. Khajavikhan, Z.H. Musslimani, S. Rotter, D.N. Christodoulides, Non-Hermitian physics and PT symmetry. *Nature Phys.* **14**(1), 11–19 (2018). <https://doi.org/10.1038/nphys4323>
35. S. Savoia, G. Castaldi, V. Galdi, A. Alù, N. Engheta, Tunneling of obliquely incident waves through PT -symmetric epsilon-near-zero bilayers. *Phys. Rev. B* **89**(8), 085105 (2014). <https://doi.org/10.1103/PhysRevB.89.085105>
36. S. Savoia, G. Castaldi, V. Galdi, A. Alù, N. Engheta, PT -symmetry-induced wave confinement and guiding in ϵ -near-zero metamaterials. *Phys. Rev. B* **91**(11), 115,114–10 (2015). <https://doi.org/10.1103/PhysRevB.91.115114>
37. M.A. Miri, M. Cotrufo, A. Alù, Anomalous optical forces in PT -symmetric waveguides. *Opt. Lett.* **44**(14), 3558–3561 (2019). <https://doi.org/10.1364/OL.44.003558>
38. F. Monticone, A. Alù, Leaky-wave theory, techniques, and applications: from microwaves to visible frequencies. *Proc. IEEE* **103**(5), 793–821 (2015). <https://doi.org/10.1109/JPROC.2015.2399419>

39. E.E. Narimanov, Ghost resonance in anisotropic materials: negative refractive index and evanescent field enhancement in lossless media. *Adv. Photon.* **1**(4), 046003 (2019) <https://doi.org/10.1117/1.AP.1.4.046003>
40. T.G. Mackay, A. Lakhtakia, Exorcizing ghost waves. *Optik* **192**, 162926 (2019). <https://doi.org/10.1016/j.ijleo.2019.06.026>
41. W.I. Waseer, Q.A. Naqvi, M.J. Mughal, Non-uniform plane waves (ghost waves) in general anisotropic medium. *Opt. Commun.* **453**, 124334 (2019). <https://doi.org/10.1016/j.optcom.2019.124334>
42. W. Ma, G. Hu, D. Hu, R. Chen, T. Sun, X. Zhang, Q. Dai, Y. Zeng, A. Alù, C.W. Qiu, P. Li, Ghost hyperbolic surface polaritons in bulk anisotropic crystals. *Nature* **596**(7872), 362–366 (2021). <https://doi.org/10.1038/s41586-021-03755-1>
43. W. Ma, P. Alonso-González, S. Li, A.Y. Nikitin, J. Yuan, J. Martín-Sánchez, J. Taboada-Gutiérrez, I. Amenabar, P. Li, S. Vélez, C. Tollan, Z. Dai, Y. Zhang, S. Sriram, K. Kalantar-Zadeh, S.T. Lee, R. Hillenbrand, Q. Bao, In-plane anisotropic and ultra-low-loss polaritons in a natural van der Waals crystal. *Nature* **562**(7728), 557–562 (2018). <https://doi.org/10.1038/s41586-018-0618-9>
44. M. Moccia, G. Castaldi, A. Alù, V. Galdi, Leaky waves in flatland. *Adv. Opt. Mater.* **12**(6), 2203121 (2024). <https://doi.org/10.1002/adom.202203121>
45. Y. Adiv, H. Hu, S. Tseskes, R. Dahan, K. Wang, Y. Kurman, A. Gorlach, H. Chen, X. Lin, G. Bartal, I. Kaminer, Observation of 2D Cherenkov radiation. *Phys. Rev. X* **13**(1), 011002 (2023). <https://doi.org/10.1103/PhysRevX.13.011002>
46. Z. Xu, S. Bao, J. Liu, J. Chang, X. Kong, V. Galdi, T.J. Cui, Observation of analog flatland Cherenkov radiations on metasurfaces. *Laser Photon. Rev.* **18**(2), 2300763 (2024). <https://doi.org/10.1002/lpor.202300763>
47. M. Moccia, G. Castaldi, F. Monticone, V. Galdi, Exceptional points in flat optics: A non-Hermitian line-wave scenario. *Phys. Rev. Applied* **15**(6), 064067 (2021). <https://doi.org/10.1103/PhysRevApplied.15.064067>
48. S.A. Maier, *Plasmonics: Fundamentals and Applications* (Springer US, Boston, 2007)
49. M.a. Miri, A. Alù, Exceptional points in optics and photonics. *Science* **363**(6422), eaar7709 (2019). <https://doi.org/10.1126/science.aar7709>
50. A. Di Paola, M. Moccia, G. Castaldi, V. Galdi, Coupled line waves in parallel-plate metasurface waveguides, in *MRS Communications* (2024). <https://doi.org/10.1557/s43579-024-00519-6>
51. E. Martini, M.G. Silveirinha, S. Maci, Exact solution for the protected TEM edge mode in a PTD-symmetric parallel-plate waveguide. *IEEE Trans. Antennas Propagat.* **67**(2), 1035–1044 (2019). <https://doi.org/10.1109/TAP.2018.2880091>
52. X. Ma, M.S. Mirmoosa, S.A. Tretyakov, Parallel-plate waveguides formed by penetrable metasurfaces. *IEEE Trans. Antennas Propagat.* **68**(3), 1773–1785 (2020). <https://doi.org/10.1109/TAP.2019.2934580>

Oddly Shaped Inclusions: Depolarization Dyadics and Homogenization



Tom G. Mackay and Akhlesh Lakhtakia 

1 Introduction

This chapter concerns the theory of a homogenized composite medium (HCM) comprising a host medium impregnated with randomly dispersed particulate inclusions. Crucially, the inclusions must be sufficiently small relative to the wavelengths involved so that the composite medium effectively behaves as a homogeneous medium [1–4]. HCMs are of considerable technological importance, especially with nanocomposite materials being increasingly developed for optical applications [5]. Notably, by means of judicious design, HCMs may exhibit properties not exhibited by their component mediums [6]. A straightforward example is furnished by anisotropic HCMs, which can arise from isotropic component mediums provided that the inclusions are shaped appropriately [7]. More generally, the notion of homogenization is of fundamental importance in electromagnetics as it underpins the transition from microscopic to macroscopic viewpoints [8, 9]

The constitutive parameters of HCMs are estimated using homogenization formalisms. A wide variety of these formalisms have been developed over many years [1, 4]. One of the most widely used formalisms is the Maxwell Garnett formalism [10]. The popularity of this formalism may be attributed, in part at least, to its computational simplicity and to its intimate connection with the Hashin–Shtrikman bounds [11]. In common with most other homogenization formalisms, this formalism adopts *depolarization dyadics* to represent the scattering responses of the inclusions [4]. As described in detail in Sect. 2.1, the depolarization dyadic

T. G. Mackay (✉) · A. Lakhtakia

School of Mathematics and Maxwell Institute for Mathematical Sciences, University of Edinburgh, Edinburgh, UK

NanoMM—Nanoengineered Metamaterials Group, Department of Engineering Science and Mechanics, Pennsylvania State University, University Park, PA, USA

e-mail: T.Mackay@ed.ac.uk; akhlesh@psu.edu

is the integrated singularity of the dyadic Green function for the host medium [12, 13]. Until very recently, closed-form expressions for depolarization dyadics were available only for a rather restrictive range of inclusion shapes [14–20], for examples, spherical, spheroidal, ellipsoidal, cubic, and cylindrical. More complex inclusion shapes could be accommodated only using numerical integration methods [21, 22]. Consequently, homogenization formalisms generally have been investigated for inclusions with simple shapes.

Within the past year, the range of inclusion shapes that can be readily catered for in homogenization formalisms was broadened by the derivation of closed-form expressions for depolarization dyadics for truncated spheres and truncated spheroids, and this methodology was extended to truncated ellipsoids [23]. Also, these depolarization dyadics were adopted in an implementation of the Maxwell Garnett formalism to estimate the relative permittivity parameters of HCMs comprising truncated spheres and spheroids as inclusions [24]. This implementation was extended to inclusions with truncated ellipsoidal shapes, with the corresponding depolarization dyadics being evaluated numerically. In this chapter, an overview of these recent developments to accommodate oddly shaped inclusions is provided.

In Sect. 2, a summary of the theoretical underpinnings of depolarization dyadics, polarizability density dyadics, and the Maxwell Garnett homogenization formalism is provided. No novelty is claimed for this background theory—it is presented for completeness for the reader’s convenience. Then, in Sect. 3, recently derived closed-form expressions for depolarization dyadics for truncated spheres and spheroids are presented and illustrated; the extension of the methodology to truncated ellipsoidal inclusions is also presented. In addition, the Maxwell Garnett formalism is presented for HCMs based on inclusions shaped as truncated spheres, spheroids, and ellipsoids. Finally, in Sect. 3, numerical results are presented to illuminate the relationship between the anisotropy of the HCM and inclusion shape. A brief discussion is provided in the closing Sect. 4.

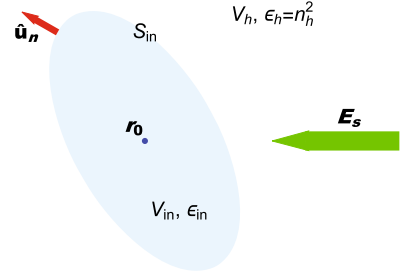
In the notation adopted, vectors are boldface; dyadics [4, 13] are double underlined; ε_0 and μ_0 are the free-space permittivity and permeability, respectively; and $\underline{\underline{I}} = \hat{\mathbf{u}}_x\hat{\mathbf{u}}_x + \hat{\mathbf{u}}_y\hat{\mathbf{u}}_y + \hat{\mathbf{u}}_z\hat{\mathbf{u}}_z$ is the identity dyadic with $\hat{\mathbf{u}}_x$, $\hat{\mathbf{u}}_y$, and $\hat{\mathbf{u}}_z$ being the unit vectors aligned with the coordinate axes of the Cartesian coordinate system (x, y, z). Angular frequency is denoted by ω , $k_0 = \omega\sqrt{\varepsilon_0\mu_0}$ denotes the free-space wavenumber, and an $\exp(-i\omega t)$ dependence on time t is implicit.

2 Background Theory

2.1 Depolarization Dyadics and Polarizability Density Dyadics

Suppose that a closed surface S_{in} encloses the electrically small region V_{in} and separates it from the unbounded region V_{h} , as shown in Fig. 1. The unit outward normal $\hat{\mathbf{u}}_{\text{n}}(\mathbf{r})$ is unambiguously identified at every point $\mathbf{r} \in S_{\text{in}}$; if present, wedges and vertexes on S_{in} can be rounded off slightly to hew to this restriction.

Fig. 1 Schematic of a finite region V_{in} separated from the external region V_h by the surface S_{in}



A homogeneous dielectric medium of relative permittivity $\varepsilon_{\text{in}}(\omega)$ fills V_{in} , while a homogeneous dielectric medium of relative permittivity $\varepsilon_h(\omega) = n_h^2(\omega)$ fills V_h .

The region V_{in} is irradiated by a monochromatic electromagnetic field phasor $\mathbf{E}_s(\mathbf{r}, \omega)$. The source of this field source is confined to the bounded region $V_s \subset V_h$ far from V_{in} . Accordingly, at any location $\mathbf{r} \notin V_s$ the electric field phasor is given exactly by Lakhtakia [25], Chew [26], and Sancer et al. [27] as

$$\mathbf{E}(\mathbf{r}, \omega) = \mathbf{E}_s(\mathbf{r}, \omega) + k_0^2 [\varepsilon_{\text{in}}(\omega) - \varepsilon_h(\omega)] \iiint_{V_{\text{in}}} [\underline{\underline{G}}_h(\mathbf{r}, \mathbf{r}'; \omega) \cdot \mathbf{E}(\mathbf{r}', \omega)] d^3 \mathbf{r}', \quad \mathbf{r} \notin V_s, \quad (1)$$

with

$$\underline{\underline{G}}_h(\mathbf{r}, \mathbf{r}'; \omega) = \left[\underline{\underline{I}} + \frac{\nabla \nabla}{k_0^2 \varepsilon_h(\omega)} \right] \frac{\exp[ik_0 n_h(\omega) |\mathbf{r} - \mathbf{r}'|]}{4\pi |\mathbf{r} - \mathbf{r}'|} \quad (2)$$

being the dyadic Green function for the medium that fills V_h . In particular, the electric field phasor at $\mathbf{r} = \mathbf{r}_0 \in V_{\text{in}}$ is given by Eq. (1) as

$$\mathbf{E}(\mathbf{r}_0, \omega) = \mathbf{E}_s(\mathbf{r}_0, \omega) + k_0^2 [\varepsilon_{\text{in}}(\omega) - \varepsilon_h(\omega)] \iiint_{V_{\text{in}}} [\underline{\underline{G}}_h(\mathbf{r}_0, \mathbf{r}'; \omega) \cdot \mathbf{E}(\mathbf{r}', \omega)] d^3 \mathbf{r}', \quad \mathbf{r}_0 \in V_{\text{in}}, \quad (3)$$

provided that $\mathbf{r}_0 \notin S_{\text{in}}$.

The integral on the right side of Eq. (3) needs to be treated carefully owing to the term $|\mathbf{r}_0 - \mathbf{r}'|^{-3}$ in its integrand [28]. Adding the term $\underline{\underline{G}}_P(\mathbf{r}_0, \mathbf{r}'; \omega) \cdot \mathbf{E}(\mathbf{r}_0, \omega)$ to the integrand and subtracting the same term from the integrand yields [29, 30]

$$\begin{aligned} \mathbf{E}(\mathbf{r}_0, \omega) &= \mathbf{E}_s(\mathbf{r}_0, \omega) + k_0^2 [\varepsilon_{\text{in}}(\omega) - \varepsilon_h(\omega)] \\ &\quad \times \iiint_{V_{\text{in}}} [\underline{\underline{G}}_h(\mathbf{r}_0, \mathbf{r}'; \omega) \cdot \mathbf{E}(\mathbf{r}', \omega) - \underline{\underline{G}}_P(\mathbf{r}_0, \mathbf{r}'; \omega) \cdot \mathbf{E}(\mathbf{r}_0, \omega)] d^3 \mathbf{r}' \\ &\quad + k_0^2 [\varepsilon_{\text{in}}(\omega) - \varepsilon_h(\omega)] \left[\iiint_{V_{\text{in}}} \underline{\underline{G}}_P(\mathbf{r}_0, \mathbf{r}'; \omega) d^3 \mathbf{r}' \right] \cdot \mathbf{E}(\mathbf{r}_0, \omega), \quad \mathbf{r}_0 \in V_{\text{in}}, \end{aligned} \quad (4)$$

with

$$\underline{\underline{G}}_P(\mathbf{r}, \mathbf{r}'; \omega) = \frac{1}{k_0^2 \varepsilon_h(\omega)} \nabla \nabla \frac{1}{4\pi |\mathbf{r} - \mathbf{r}'|}. \quad (5)$$

By means of the identity $\nabla \nabla (|\mathbf{r} - \mathbf{r}'|^{-1}) = -\nabla \nabla' (|\mathbf{r} - \mathbf{r}'|^{-1})$ together with the Gauss theorem, the second integral on the right side of Eq. (4) simplifies, allowing the electric field phasor to be recast as [25, 29]

$$\begin{aligned} \mathbf{E}(\mathbf{r}_0, \omega) &= \mathbf{E}_s(\mathbf{r}_0, \omega) + k_0^2 \\ &\times [\varepsilon_{in}(\omega) - \varepsilon_h(\omega)] \left[\mathbf{M}(\mathbf{r}_0, \omega) - \frac{1}{k_0^2 \varepsilon_h(\omega)} \underline{\underline{L}}(\mathbf{r}_0) \cdot \mathbf{E}(\mathbf{r}_0, \omega) \right], \quad \mathbf{r}_0 \in V_{in}, \end{aligned} \quad (6)$$

wherein the vector

$$\mathbf{M}(\mathbf{r}_0, \omega) = \iiint_{V_{in}} \left[\underline{\underline{G}}_h(\mathbf{r}_0, \mathbf{r}'; \omega) \cdot \mathbf{E}(\mathbf{r}', \omega) - \underline{\underline{G}}_P(\mathbf{r}_0, \mathbf{r}'; \omega) \cdot \mathbf{E}(\mathbf{r}_0, \omega) \right] d^3 \mathbf{r}', \quad (7)$$

and the depolarization dyadic

$$\underline{\underline{L}}(\mathbf{r}_0) = \frac{1}{4\pi} \iint_{S_{in}} \hat{\mathbf{u}}_n(\mathbf{r}') \frac{\mathbf{r}' - \mathbf{r}_0}{|\mathbf{r}' - \mathbf{r}_0|^3} d^2 \mathbf{r}' \quad (8)$$

emerge [31, 32].

Next we focus on the volume integral $\mathbf{M}(\mathbf{r}_0, \omega)$ defined on the right side of Eq. (7). The singularities of $\underline{\underline{G}}_h(\mathbf{r}_0, \mathbf{r}'; \omega)$ and $\underline{\underline{G}}_P(\mathbf{r}_0, \mathbf{r}'; \omega)$ that arise in the limit $\mathbf{r}' \rightarrow \mathbf{r}_0$ balance each other in such a way that the integrand is integrable provided that real constants $a_1 > 0$ and $a_2 > 0$ exist such that

$$|\hat{\mathbf{u}}_j \cdot [\mathbf{E}(\mathbf{r}, \omega) - \mathbf{E}(\mathbf{r}_0, \omega)]| \leq a_1 |\mathbf{r} - \mathbf{r}_0|^{a_2} \quad (9)$$

for all $\mathbf{r} \in V_{in}$ and $j \in \{x, y, z\}$ [29, 30]. This is the Hölder continuity condition.

It is common practice [25, 29, 30] to make the approximation $\mathbf{E}(\mathbf{r}', \omega) \simeq \mathbf{E}(\mathbf{r}_0, \omega)$ for all $\mathbf{r}' \in V_{in}$, which is reasonable as long as V_{in} is sufficiently small in relation to the wavelengths in both V_{in} and V_h . This step has been computationally justified [29] and follows the work of Maxwell [33]. Consequently, $\mathbf{M}(\mathbf{r}_0, \omega)$ can be expressed as $\underline{\underline{M}}(\mathbf{r}_0, \omega) \cdot \mathbf{E}(\mathbf{r}_0, \omega)$ and Eq. (6) reduces to

$$\begin{aligned} \mathbf{E}(\mathbf{r}_0, \omega) &\simeq \mathbf{E}_s(\mathbf{r}_0, \omega) + k_0^2 [\varepsilon_{in}(\omega) - \varepsilon_h(\omega)] \\ &\times \left[\underline{\underline{M}}(\mathbf{r}_0, \omega) - \frac{1}{k_0^2 \varepsilon_h(\omega)} \underline{\underline{L}}(\mathbf{r}_0) \right] \cdot \mathbf{E}(\mathbf{r}_0, \omega), \quad \mathbf{r}_0 \in V_{in}. \end{aligned} \quad (10)$$

The notion of $\underline{\underline{M}}(\mathbf{r}_0, \omega)$ is attributable to Lorenz [34, 35].

If V_{in} is sufficiently small [25, 36], it is also reasonable to assume that the volume integral represented by $\underline{\underline{M}}(\mathbf{r}_o, \omega)$ is negligible compared to $\underline{\underline{L}}(\mathbf{r}_o)/k_0^2 \varepsilon_h$ [25, 31, 37]. Hence, the electric field phasor is taken to be

$$\mathbf{E}(\mathbf{r}_o, \omega) \simeq \left[\underline{\underline{I}} + \frac{\varepsilon_{\text{in}}(\omega) - \varepsilon_h(\omega)}{\varepsilon_h(\omega)} \underline{\underline{L}}(\mathbf{r}_o) \right]^{-1} \cdot \mathbf{E}_s(\mathbf{r}_o, \omega), \quad \mathbf{r}_o \in V_{\text{in}}. \quad (11)$$

Electromagnetically, the small region V_{in} may be represented by as an electric dipole moment [25]

$$\mathbf{p}(\omega) = v_{\text{in}} \varepsilon_0 [\varepsilon_{\text{in}}(\omega) - \varepsilon_h(\omega)] \mathbf{E}(\mathbf{r}_o, \omega) \quad (12)$$

located at \mathbf{r}_o , with v_{in} being the volume of V_{in} . This electric dipole moment is regarded as the source of the field scattered into the external region V_h . By combining Eqs. (11) and (12), the electric dipole moment may be expressed as

$$\mathbf{p}(\omega) = v_{\text{in}} \underline{\underline{a}}(\omega) \cdot \mathbf{E}_s(\mathbf{r}_o, \omega), \quad (13)$$

wherein the polarizability density dyadic

$$\underline{\underline{a}}(\omega) \simeq \varepsilon_0 [\varepsilon_{\text{in}}(\omega) - \varepsilon_h(\omega)] \left[\underline{\underline{I}} + \frac{\varepsilon_{\text{in}}(\omega) - \varepsilon_h(\omega)}{\varepsilon_h(\omega)} \underline{\underline{L}}(\mathbf{r}_o) \right]^{-1} \quad (14)$$

is introduced.

It should be emphasized that Eq. (14) delivers an *approximation* of the polarizability density dyadic, for the following reasons. Firstly, in deriving Eq. (11), $\underline{\underline{M}}(\mathbf{r}_o, \omega)$ is taken to be negligible in relation to $\underline{\underline{L}}(\mathbf{r}_o)/k_0^2 \varepsilon_h$, but that is true *strictu sensu* when V_{in} is vanishingly small, regardless of the shape of V_{in} . Secondly, the Hölder continuity condition applies best within the largest ellipsoid contained in V_{in} that is centered at \mathbf{r}_o [33]. If the shape of V_{in} is not ellipsoidal, then the electric field phasor within V_{in} that is outside the largest inscribed ellipsoid is only approximately accounted for. This means that \mathbf{r}_o needs to be judiciously selected [23]. Notwithstanding this second source of approximation, Eq. (14) has been widely implemented for non-ellipsoidal inclusion shapes such cubes [38, 39], rectangular parallelepipeds [40], and circular cylinders of finite height [31].

2.2 Maxwell Garnett Formalism

In Sect. 2.1, a single inclusion embedded in a host medium was considered. Now we turn to a composite medium consisting of a collection of inclusions randomly distributed in a host medium. All inclusions have the same shape and orientation, and all are electrically small. The composite medium fills all space V_{all} . The volume

fraction of the composite medium filled by the inclusions is denoted by f_{in} , while N_{in} is the number density of inclusions. Thus, each inclusion's volume is $f_{\text{in}}/N_{\text{in}}$. As in Sect. 2.1, the inclusion medium has relative permittivity scalar $\varepsilon_{\text{in}}(\omega)$, and the host medium $\varepsilon_{\text{h}}(\omega)$.

In compliance with the Maxwell curl postulates, the electric field phasor in V_{all} satisfies

$$\nabla \times [\nabla \times \mathbf{E}(\mathbf{r}, \omega)] - k_0^2 \varepsilon_{\text{h}}(\omega) \mathbf{E}(\mathbf{r}, \omega) = i\omega\mu_0 \mathbf{J}(\mathbf{r}, \omega), \quad \mathbf{r} \in V_{\text{all}}. \quad (15)$$

If \mathbf{r} lies inside an inclusion, then the electric current density phasor $\mathbf{J}(\mathbf{r}, \omega) \neq \mathbf{0}$, otherwise $\mathbf{J}(\mathbf{r}, \omega) = \mathbf{0}$ [25, 41]. Suppose now that we assume the inclusions are sufficiently small in relation to wavelength that the composite medium may be regarded as being effectively homogeneous with relative permittivity dyadic $\underline{\underline{\varepsilon}}^{\text{eff}}(\omega)$. The constitutive relation

$$\mathbf{D}(\mathbf{r}, \omega) = \varepsilon_0 \varepsilon_{\text{h}}(\omega) \mathbf{E}(\mathbf{r}, \omega) + \mathbf{P}_{\text{xs}}(\mathbf{r}, \omega) = \varepsilon_0 \underline{\underline{\varepsilon}}^{\text{eff}}(\omega) \cdot \mathbf{E}(\mathbf{r}, \omega), \quad (16)$$

characterizes the homogenized composite medium (HCM). Herein $\mathbf{D}(\mathbf{r}, \omega)$ is the electric displacement phasor and $\mathbf{P}_{\text{xs}}(\mathbf{r}, \omega)$ is the excess polarization representing the homogenized distribution of the inclusion medium inside the HCM.

In the Maxwell Garnett formalism, the equivalent source term $\mathbf{J}(\mathbf{r}, \omega)$ in Eq. (15) becomes in the homogenized regime

$$\mathbf{J}_{\text{avg}}(\mathbf{r}, \omega) = -i\omega \mathbf{P}_{\text{xs}}(\mathbf{r}, \omega), \quad (17)$$

which represents the spatial average of $\mathbf{J}(\mathbf{r}, \omega)$ in an electrically small neighborhood of \mathbf{r} called the Lorentzian cavity [42]. Consequently, the electric field phasor in the HCM is given by the integral equation

$$\mathbf{E}(\mathbf{r}, \omega) = \mathbf{E}_{\text{cf}}(\mathbf{r}, \omega) + \omega^2 \mu_0 \iiint_{V_{\text{all}}} \underline{\underline{G}}_{\text{h}}(\mathbf{r}, \mathbf{r}'; \omega) \cdot \mathbf{P}_{\text{xs}}(\mathbf{r}', \omega) d^3 \mathbf{r}', \quad \mathbf{r} \in V_{\text{all}}, \quad (18)$$

where $\mathbf{E}_{\text{cf}}(\mathbf{r}, \omega)$ is the corresponding complementary function, which need not be explicitly specified.

Suppose that the region V_{ℓ} centered at \mathbf{r} is the Lorentzian cavity. By convention, V_{ℓ} is taken to be spherical. The local electric field phasor

$$\mathbf{E}_{\text{loc}}(\mathbf{r}, \omega) = \mathbf{E}_{\text{cf}}(\mathbf{r}, \omega) + \omega^2 \mu_0 \iiint_{V_{\text{all}} - V_{\ell}} \underline{\underline{G}}_{\text{h}}(\mathbf{r}, \mathbf{r}'; \omega) \cdot \mathbf{P}_{\text{xs}}(\mathbf{r}', \omega) d^3 \mathbf{r}' \quad (19)$$

is introduced to represent the electric field phasor present at \mathbf{r} provided that the excess polarization is null valued in V_{ℓ} . Equations (18) and (19) collectively deliver

$$\mathbf{E}(\mathbf{r}, \omega) = \mathbf{E}_{\text{loc}}(\mathbf{r}, \omega) + \omega^2 \mu_0 \iiint_{V_{\ell}} \underline{\underline{G}}_{\text{h}}(\mathbf{r}, \mathbf{r}'; \omega) \cdot \mathbf{P}_{\text{xs}}(\mathbf{r}', \omega) d^3 \mathbf{r}'. \quad (20)$$

In order to proceed, the standard practice is to assume that the excess polarization is spatially uniform inside the Lorentzian cavity [42]. Consequently, Eq. (20) reduces to

$$\mathbf{E}(\mathbf{r}, \omega) \simeq \mathbf{E}_{\text{loc}}(\mathbf{r}, \omega) - \frac{1}{3\varepsilon_0\varepsilon_h(\omega)} \mathbf{P}_{\text{xs}}(\mathbf{r}, \omega). \quad (21)$$

A key step in the Maxwell Garnett formalism is to take $\mathbf{P}_{\text{xs}} = N_{\text{in}}\mathbf{p}$ and allow $\mathbf{E}_s(\mathbf{r}, \omega)$ to play the part of $\mathbf{E}_{\text{loc}}(\mathbf{r}, \omega)$. Thus, Eq. (13) yields

$$\mathbf{P}_{\text{xs}}(\mathbf{r}, \omega) = f_{\text{in}} \underline{\underline{a}}(\omega) \cdot \mathbf{E}_{\text{loc}}(\mathbf{r}, \omega). \quad (22)$$

Now $\mathbf{E}_{\text{loc}}(\mathbf{r}, \omega)$ can be eliminated from Eq. (22) by means of Eq. (21), which leads to

$$\mathbf{P}_{\text{xs}}(\mathbf{r}, \omega) \simeq f_{\text{in}} \underline{\underline{a}}(\omega) \cdot \left[\underline{\underline{I}} - \frac{1}{3\varepsilon_0\varepsilon_h(\omega)} f_{\text{in}} \underline{\underline{a}}(\omega) \right]^{-1} \cdot \mathbf{E}(\mathbf{r}, \omega). \quad (23)$$

Finally, the Maxwell Garnett estimate

$$\underline{\underline{\varepsilon}}^{MG}(\omega) = \varepsilon_h(\omega) \underline{\underline{I}} + \frac{f_{\text{in}}}{\varepsilon_0} \underline{\underline{a}}(\omega) \cdot \left[\underline{\underline{I}} - \frac{1}{3\varepsilon_0\varepsilon_h(\omega)} f_{\text{in}} \underline{\underline{a}}(\omega) \right]^{-1} \quad (24)$$

of the relative permittivity dyadic $\underline{\underline{\varepsilon}}^{eff}(\omega)$ emerges, courtesy of Eqs. (16) and (23).

A couple of comments on Eq. (24) are in order here. Firstly, a particular choice of $\underline{\underline{a}}(\omega)$ is not really essential for the Maxwell Garnett formalism. The Mossotti–Clausius expression [35] for the polarizability scalar of an electrically small, isotropic, dielectric sphere was adopted by Maxwell Garnett himself [10] and others [43]; but even for that simple inclusion, other expressions may be implemented [34, 35, 44, 45]. Secondly, generalizations of Eq. (24) for $\underline{\underline{\varepsilon}}^{MG}$ have been developed for inclusions of more than one type as well as for anisotropic (and bianisotropic) inclusion and host mediums [4, 46].

3 Numerical Results

In this section, some recent developments pertaining to depolarization dyadics for truncated spheres, spheroids, and ellipsoids, and the implementation of the corresponding Maxwell Garnett homogenization formalism, are described and illustrated with numerical calculations.

3.1 Preliminaries

It follows from

$$\text{trace} \left\{ \underline{\underline{L}}(\mathbf{r}_o) \right\} = \frac{1}{4\pi} \iint_{S_{\text{in}}} \hat{\mathbf{u}}_n(\mathbf{r}') \cdot \left(\frac{\mathbf{r}' - \mathbf{r}_o}{|\mathbf{r}' - \mathbf{r}_o|^3} \right) d^2\mathbf{r}' \quad (25)$$

that

$$\text{trace} \left\{ \underline{\underline{L}}(\mathbf{r}_o) \right\} = 1, \quad (26)$$

which is useful to verify numerical treatments for truncated ellipsoids.

An outstanding matter is the following: Where inside the inclusion region V_{in} should \mathbf{r}_o be taken for the integration that delivers the depolarization dyadic in Eq. (8)? For a spherical inclusion region, $\underline{\underline{L}}(\mathbf{r}_o) = (1/3)\underline{\underline{I}}$ for any $\mathbf{r}_o \in V_{\text{in}}$ [32]. But for less symmetric inclusion shapes, $\underline{\underline{L}}(\mathbf{r}_o)$ is sensitive to the choice of $\mathbf{r}_o \in V_{\text{in}}$ [31, 43]. In order that the Hölder continuity condition (9) holds over the largest portion of V_{in} , \mathbf{r}_o must be taken as the center of the largest sphere that can be inscribed inside V_{in} . With this understanding, henceforth we write $\underline{\underline{L}}$ in lieu of $\underline{\underline{L}}(\mathbf{r}_o)$.

In the following, all truncation planes are taken to be parallel to the xy plane, without loss of generality. Consequently, $\underline{\underline{L}}$ and $\underline{\underline{\varepsilon}}^{MG}$ acquire the diagonal forms

$$\left. \begin{aligned} \underline{\underline{L}} &= L_x \hat{\mathbf{u}}_x \hat{\mathbf{u}}_x + L_y \hat{\mathbf{u}}_y \hat{\mathbf{u}}_y + L_z \hat{\mathbf{u}}_z \hat{\mathbf{u}}_z \\ \underline{\underline{\varepsilon}}^{MG} &= \varepsilon_x^{MG} \hat{\mathbf{u}}_x \hat{\mathbf{u}}_x + \varepsilon_y^{MG} \hat{\mathbf{u}}_y \hat{\mathbf{u}}_y + \varepsilon_z^{MG} \hat{\mathbf{u}}_z \hat{\mathbf{u}}_z \end{aligned} \right\}. \quad (27)$$

When the inclusions are truncated spheres and truncated spheroids, $L_x = L_y \equiv L_t$ and $\varepsilon_x^{MG} = \varepsilon_y^{MG} \equiv \varepsilon_t^{MG}$. Therefore, closed-form expressions for L_z need not be explicitly stated because $L_z = 1 - 2L_t$ for truncated spheres and spheroids, and $L_z = 1 - L_x - L_y$ for truncated ellipsoids, courtesy of Eq. (26).

In order to illustrate the estimates generated by the Maxwell Garnett homogenization formalism, the following representative values were chosen: $\varepsilon_h = 2 + 0.5i$, $\varepsilon_{\text{in}} = 3.5 + 0.9i$, and $f_{\text{in}} = 0.3$. Note that $f_{\text{in}} \gtrsim 0.3$ is inconsistent with the Maxwell Garnett formalism [1, 4].

3.2 Spherical Inclusion Geometry

The inclusion shape is based on truncations of the unit sphere, centered at the coordinate origin.

3.2.1 Double-Truncated Sphere

The inclusion shape is the middle part of the sphere that is truncated below by the plane $z = -\eta$ and truncated above by the plane $z = \eta$, where $0 < \eta < 1$. The

Fig. 2 Schematic of a double-truncated sphere

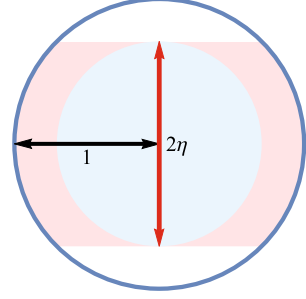
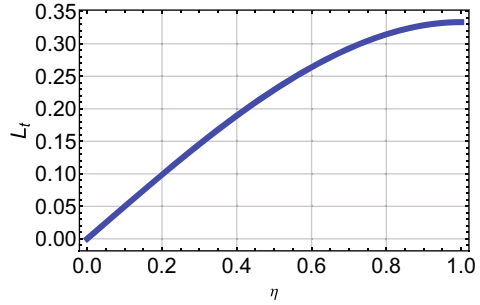


Fig. 3 Plot of L_t versus $\eta \in (0, 1)$ for the double-truncated spherical inclusion



largest sphere that can be inscribed inside the double-truncated sphere has radius η . A schematic representation is provided in Fig. 2.

The integration in Eq. (8) yields

$$L_t = \frac{(3 - \eta^2) \eta}{6}. \quad (28)$$

The depolarization factor L_t is plotted against η in Fig. 3. In keeping with standard results for a spherical inclusion [32], $L_t \rightarrow 0$ in the limit $\eta \rightarrow 0$, while $L_t \rightarrow 1/3$ in the limit $\eta \rightarrow 1$.

The real and imaginary parts of the relative permittivity parameters ε_t^{MG} and ε_z^{MG} of the HCM are plotted against η in Fig. 4. The HCM exhibits a monotonically decreasing degree of anisotropy as η increases and becomes isotropic in the limit $\eta \rightarrow 1$.

3.2.2 Truncated Sphere

The inclusion shape is the upper part of the sphere that is truncated below by the plane $z = 1 - 2\eta$, where $0 < \eta < 1$. The largest sphere that can be inscribed inside the truncated sphere has radius η . A schematic representation is provided in Fig. 5.

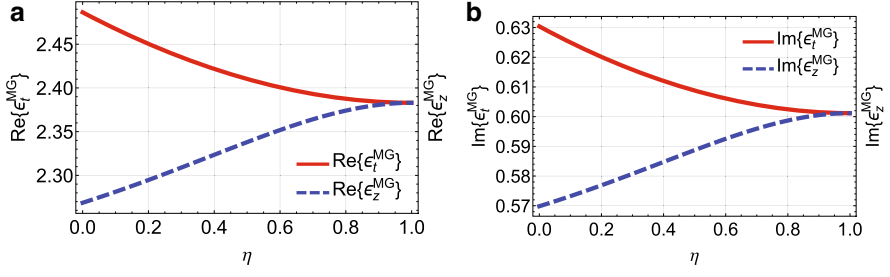


Fig. 4 Plots of real and imaginary parts of ε_t^{MG} and ε_z^{MG} versus $\eta \in (0, 1)$ for double-truncated spherical inclusion

Fig. 5 Schematic of a truncated sphere

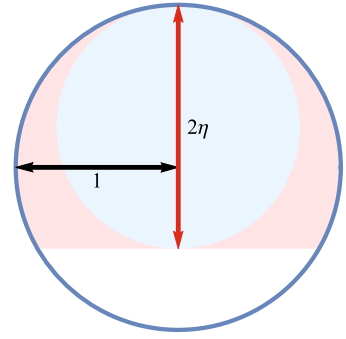
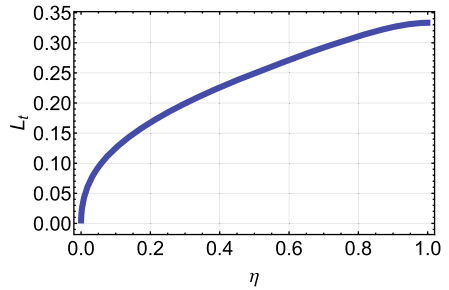


Fig. 6 Plot of L_t versus $\eta \in (0, 1)$ for the truncated spherical inclusion



The integration in Eq. (8) yields

$$L_t = \frac{\eta}{6(1-\eta)^3 \sqrt{(4-3\eta)\eta}} \left\{ 6 - \left(3 - 3\eta + \eta^2 \right) \sqrt{(4-3\eta)\eta} - \eta [11 - 3\eta(3-\eta)] \right\}. \quad (29)$$

This expression of L_t is plotted against η in Fig. 6. The plot in Fig. 6 is similar to that in Fig. 3. In particular, as in Fig. 3, $L_t \rightarrow 0$ in the limit $\eta \rightarrow 0$, while $L_t \rightarrow 1/3$ in the limit $\eta \rightarrow 1$.

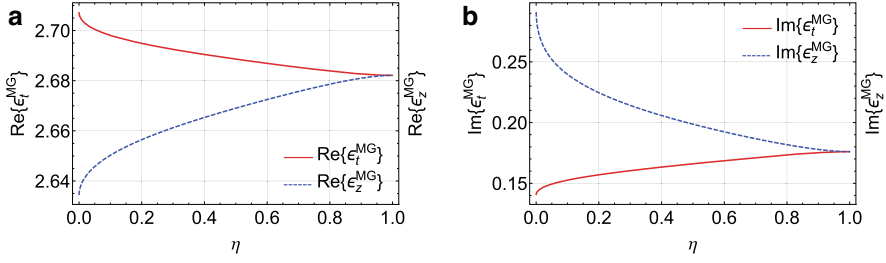


Fig. 7 Plots of real and imaginary parts of ϵ_t^{MG} and ϵ_z^{MG} versus $\eta \in (0, 1)$ for truncated spherical inclusion

The real and imaginary parts of the relative permittivity parameters ϵ_t^{MG} and ϵ_z^{MG} of the HCM are plotted against η in Fig. 7. The plots in Fig. 7 are similar to those in Fig. 4. In particular, the degree of anisotropy exhibited by the HCM decreases monotonically as η increases and in the limit $\eta \rightarrow 1$ the HCM becomes isotropic.

3.3 Spheroidal Inclusion Geometry

The inclusion shape is based on truncations of the spheroid

$$\frac{x^2 + y^2}{\alpha^2} + z^2 \leq 1, \quad (30)$$

centered at the coordinate origin with equatorial radius $\alpha > 0$.

3.3.1 Double-Truncated Spheroid

The inclusion shape is the middle part of the spheroid that is truncated below by the plane $z = -\eta$ and truncated above by the plane $z = \eta$, where $0 < \eta < 1$. The largest sphere that can be inscribed inside the double-truncated spheroid has radius α for $\eta > \alpha$ and radius η for $\eta < \alpha$. A schematic representation is provided in Fig. 8.

The integration in Eq. (8) yields

$$L_t = \frac{-\eta \sqrt{\frac{\alpha^2 - 1}{\alpha^2 - \eta^2(\alpha^2 - 1)}} + \alpha^2 \tan^{-1} \left[\eta \sqrt{\frac{\alpha^2 - 1}{\alpha^2 - \eta^2(\alpha^2 - 1)}} \right]}{2(\alpha^2 - 1)^{3/2}}. \quad (31)$$

Fig. 8 Schematic of a double-truncated spheroid with $\eta > \alpha$ (left) and $\eta < \alpha$ (right)

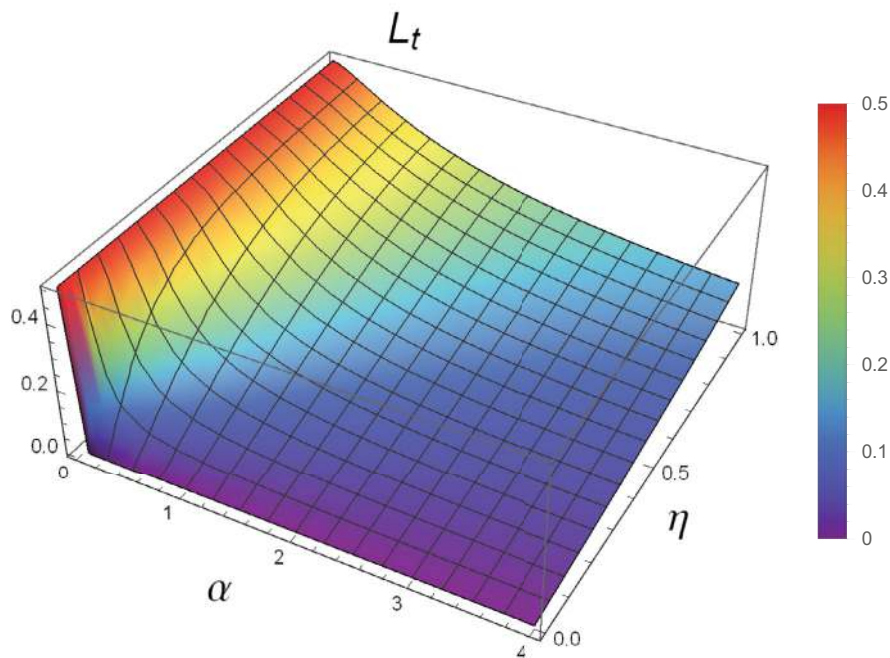
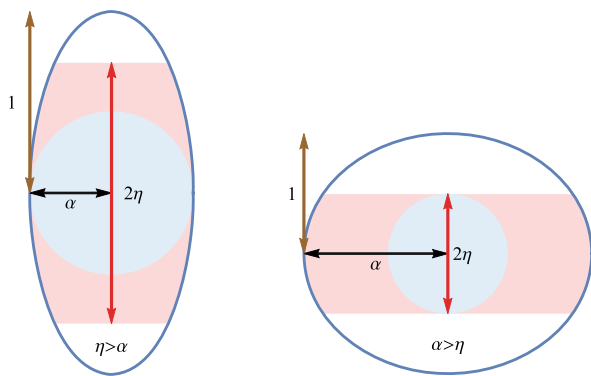


Fig. 9 Plot of L_t versus $\alpha \in (0, 4]$ and $\eta \in (0, 1)$ for the double-truncated spheroidal inclusion

Figure 9 presents a plot of L_t against α and η . For all values of η , L_t decreases monotonically as α increases. On the other hand, for all values of α , L_t increases monotonically as η increases. As $\eta \rightarrow 0$, the limiting value $L_t = 0$ is attained. As $\eta \rightarrow 1$, the limiting value

$$L_t = \frac{1}{2} \left(\frac{1}{1 - \alpha^2} + \alpha^2 \frac{\tan^{-1} \sqrt{\alpha^2 - 1}}{(\alpha^2 - 1)^{3/2}} \right), \quad (32)$$

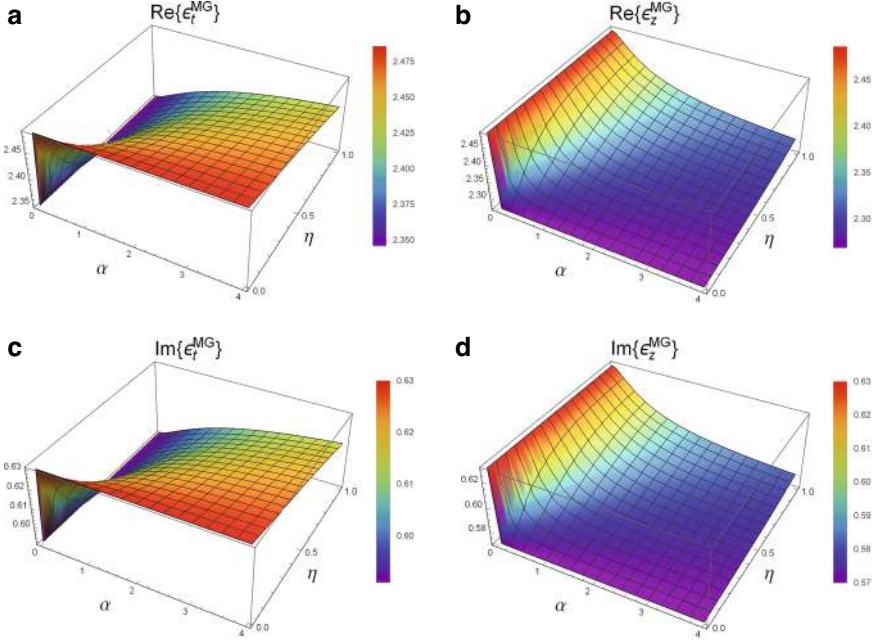


Fig. 10 Plots of real and imaginary parts of ϵ_t^{MG} and ϵ_z^{MG} versus $\alpha \in (0, 4]$ and $\eta \in (0, 1)$ for double-truncated spheroidal inclusions

is attained, which is a known result for spheroidal inclusions [15]. The limiting value $L_t = 1/2$ is attained as $\alpha \rightarrow 0$; and the limiting value $L_t = 0$ is attained in the limit $\alpha \rightarrow \infty$.

The real and imaginary parts of the relative permittivity parameters ϵ_t^{MG} and ϵ_z^{MG} of the HCM are plotted against α and η in Fig. 10. As α increases, $\text{Re}\{\epsilon_t^{MG}\}$ increases monotonically, and $\text{Re}\{\epsilon_z^{MG}\}$ decreases monotonically, for all values of η . As κ increases, $\text{Re}\{\epsilon_t^{MG}\}$ decreases monotonically, and $\text{Re}\{\epsilon_z^{MG}\}$ increases monotonically, for all values of α . The plots for $\text{Im}\{\epsilon_t^{MG}\}$ and $\text{Im}\{\epsilon_z^{MG}\}$ are qualitatively similar to those for $\text{Re}\{\epsilon_t^{MG}\}$ and $\text{Re}\{\epsilon_z^{MG}\}$, respectively. Apart from at the very smallest values of α , the values of ϵ_t^{MG} and ϵ_z^{MG} are insensitive to α in the limit $\eta \rightarrow 0$.

3.3.2 Hemispheroid

The inclusion shape is the upper half of the spheroid, lying between the plane $z = 0$ and the plane $z = 1$. The largest sphere that can be inscribed inside the hemispheroid has radius η , with $\eta = \alpha\sqrt{1 - \alpha^2} \in (0, 1/2)$ for $\alpha < 1/\sqrt{2}$ while $\eta = 1/2$ for $\alpha > 1/\sqrt{2}$. A schematic representation is provided in Fig. 11.

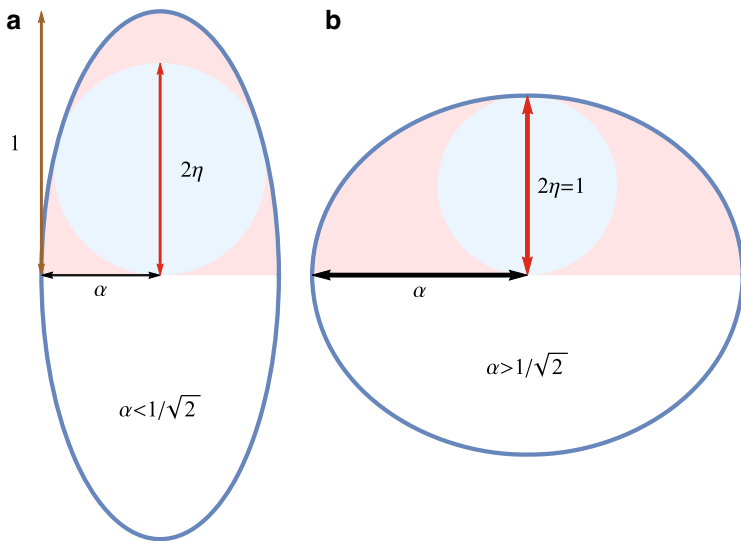


Fig. 11 Schematic of a hemispheroid with $\alpha < 1/\sqrt{2}$ (left) and $\alpha > 1/\sqrt{2}$ (right)

The integration in Eq. (8) yields

$$L_t = \frac{1}{4v\gamma^4} \left\{ 1 + v + \alpha^2 \left[\alpha \left(\alpha + \sqrt{2 - \alpha^2} \right) - v - 3 \right] - (\alpha\gamma)^2 \sqrt{2 - \alpha^2} \log \frac{(1 - \alpha^2 + \gamma)(1 - \alpha)}{\alpha(v - \gamma)} \right\} \quad (33)$$

for $\alpha < 1/\sqrt{2}$ and

$$L_t = \frac{3 \left(1 + \sqrt{1 + 4\alpha^2} \right) + \alpha^2 \left(10 - 8\sqrt{1 + 4\alpha^2} \right) - 8\alpha^4}{4\gamma^2 (3 + 8\alpha^2 - 16\alpha^4)} + \frac{\alpha^2 \log \frac{1 - 2\alpha^2 + \gamma}{\sqrt{1 + 3\alpha^2 - 4\alpha^4} - 1}}{4\gamma^3} \quad (34)$$

for $\alpha > 1/\sqrt{2}$, wherein

$$\begin{aligned} v &= \sqrt{2 - 3\alpha^2 + \alpha^4} \\ \gamma &= \sqrt{1 - \alpha^2} \end{aligned} \quad (35)$$

Fig. 12 Plot of L_t versus $\alpha \in (0, 5]$ for the hemispheroidal inclusion

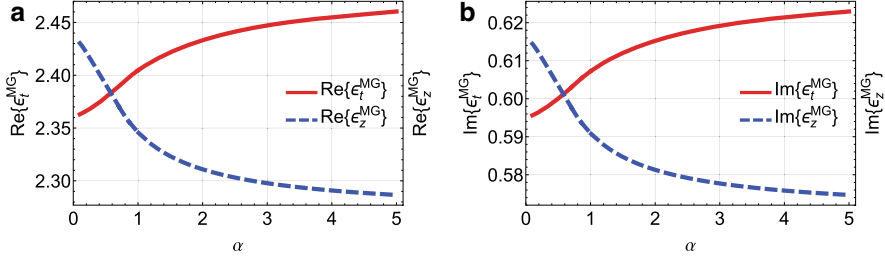
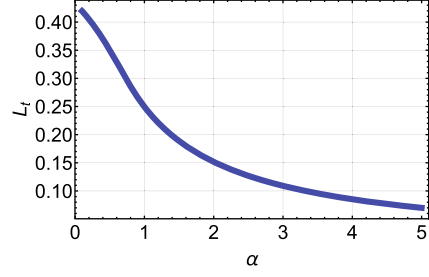


Fig. 13 Plots of real and imaginary parts of ε_t^{MG} and ε_z^{MG} versus $\alpha \in (0, 5)$ for hemispheroidal inclusions

In Fig. 12, the depolarization factor L_t is plotted against α . The value of L_t decreases monotonically as α increases. The limiting value $L_t = (2 + \sqrt{2})/8$ is attained as $\alpha \rightarrow 0$. The limiting value $L_t = 0$ is attained as $\alpha \rightarrow \infty$. The value of L_t coincides with that of L_z at $\alpha = 0.5818$. The results for the hemisphere are recovered at $\alpha = 1$.

The real and imaginary parts of the relative permittivity parameters ε_t^{MG} and ε_z^{MG} of the HCM are plotted against α in Fig. 13. The value of $\text{Re}\{\varepsilon_z^{MG}\}$ decreases monotonically and the value of $\text{Re}\{\varepsilon_t^{MG}\}$ increases monotonically as α increases. The graphs of $\text{Im}\{\varepsilon_t^{MG}\}$ and $\text{Im}\{\varepsilon_z^{MG}\}$ are qualitatively similar to those of $\text{Re}\{\varepsilon_t^{MG}\}$ and $\text{Re}\{\varepsilon_z^{MG}\}$. At $\alpha = 0.5818$, $\varepsilon_t^{MG} = \varepsilon_z^{MG}$; i.e., the HCM is isotropic. The more α increases or decreases from 0.5818, the greater is the degree of anisotropy that the HCM exhibits. At $\alpha = 1$, the results for hemispherical inclusions are recovered.

3.4 Ellipsoidal Inclusion Geometry

The inclusion shape is based on truncations of the ellipsoid

$$\frac{x^2}{\alpha^2} + \frac{y^2}{\beta^2} + z^2 \leq 1, \quad (36)$$

centered at the coordinate origin with semi-axis lengths $\alpha > 0$ and $\beta > 0$.

3.4.1 Double-Truncated Ellipsoid

The inclusion shape is the middle part of the ellipsoid that is truncated below by the plane $z = -\eta$ and truncated above by the plane $z = \eta$, where $0 < \eta < 1$. Numerical integration techniques are needed to evaluate \underline{L} per Eq. (8).

Plots of L_x and L_y against α and β are displayed in Fig. 14 for $\eta \in \{0.2, 0.4, 0.8\}$. The depolarization factors L_x and L_y vary smoothly as α and β increase from 0 to 3; L_x is most sensitive to α at small values of α while L_y is most sensitive to β at small values of β . In general, the values of the depolarization factors L_x and L_y are much less sensitive to variations in η than they are to variations in either α or β .

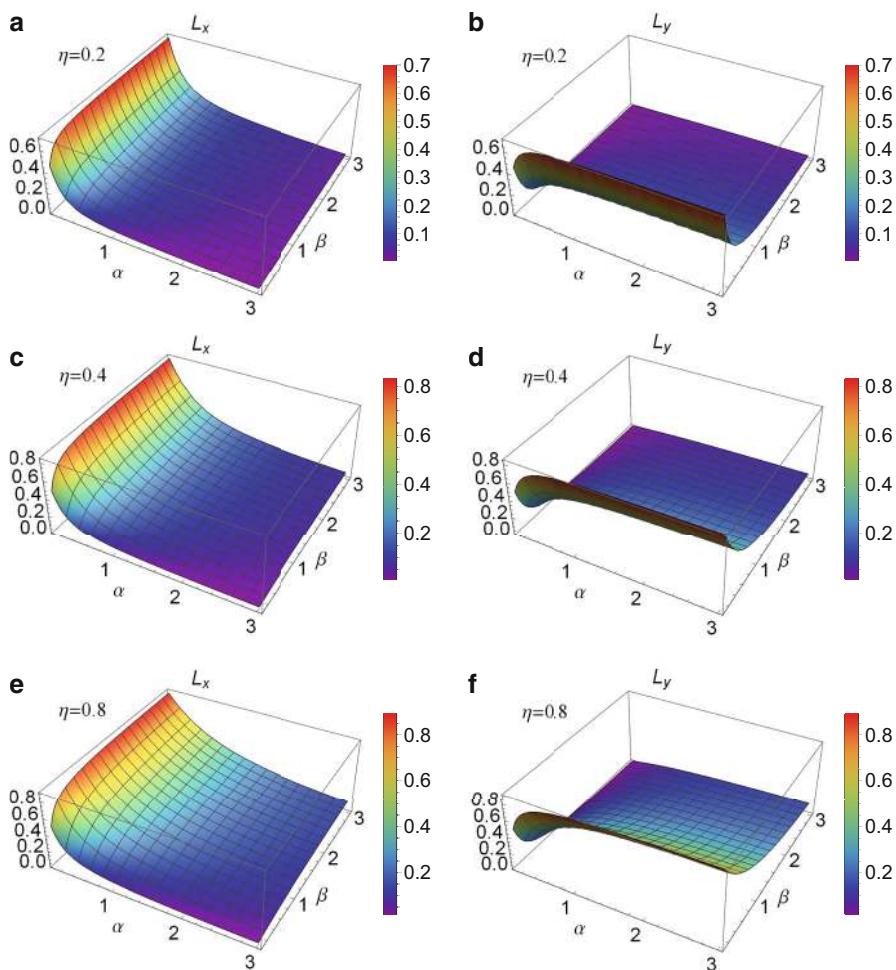


Fig. 14 Plots of L_x and L_y versus $\alpha \in (0, 3]$ and $\beta \in (0, 3]$ for the double-truncated ellipsoidal inclusion with $\eta \in \{0.2, 0.4, 0.8\}$

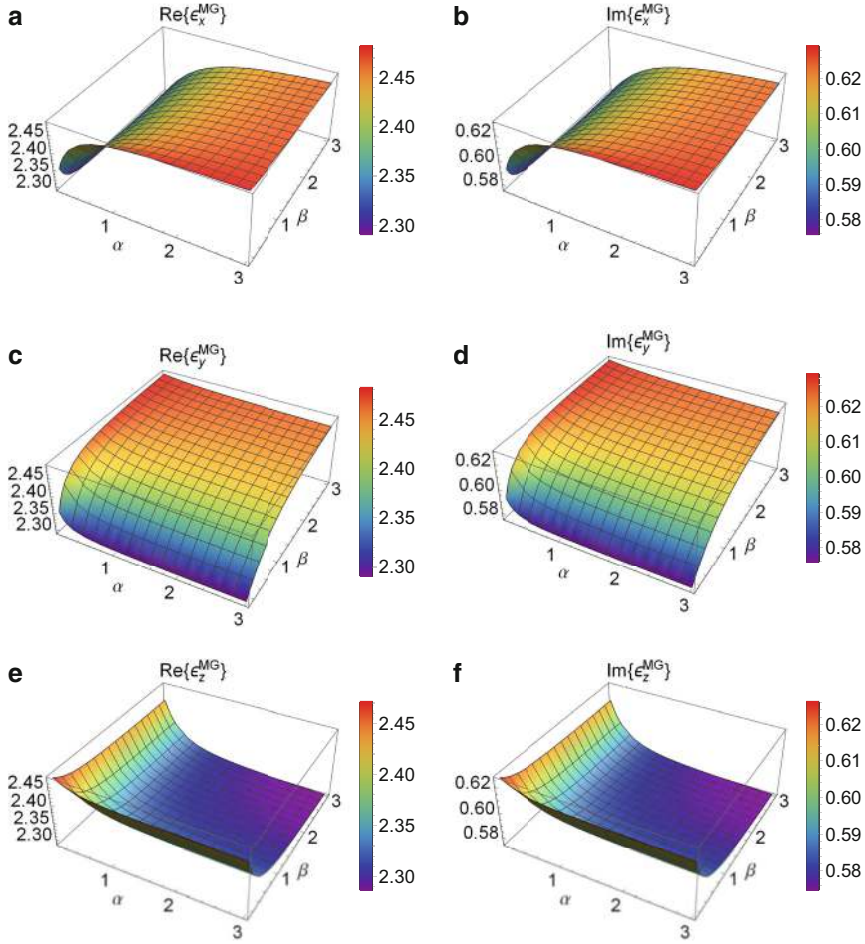


Fig. 15 Plots of real and imaginary parts of ϵ_x^{MG} , ϵ_y^{MG} , and ϵ_z^{MG} versus $\alpha \in (0, 3]$ and $\beta \in (0, 3)$ for double-truncated ellipsoidal inclusions with $\eta = 0.4$

The real and imaginary parts of the relative permittivity parameters ϵ_x^{MG} , ϵ_y^{MG} , and ϵ_z^{MG} of the HCM are plotted against α and β in Fig. 15 for $\eta = 0.4$. Both $\text{Re}\{\epsilon_x^{MG}\}$ and $\text{Im}\{\epsilon_x^{MG}\}$ are especially sensitive to variations in α at low values of α ; both $\text{Re}\{\epsilon_y^{MG}\}$ and $\text{Im}\{\epsilon_y^{MG}\}$ are especially sensitive to variations in β at low values of β ; and both $\text{Re}\{\epsilon_z^{MG}\}$ and $\text{Im}\{\epsilon_z^{MG}\}$ are especially sensitive to variations in α and β at low values of α and β . Additional numerical studies (not shown graphically here) revealed that ϵ_x^{MG} , ϵ_y^{MG} , and ϵ_z^{MG} are generally relatively insensitive to variations in $\eta \in (0, 1)$.

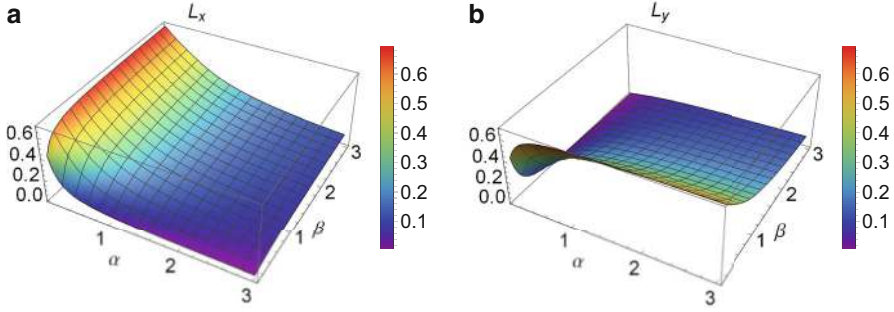


Fig. 16 Plots of L_x and L_y versus $\alpha \in (0, 3]$ and $\beta \in (0, 3]$ for the hemi-ellipsoidal inclusion

3.4.2 Hemi-Ellipsoid

The inclusion shape is the upper half of the ellipsoid that lies between the plane $z = 0$ and the plane $z = 1$. The radius of the largest sphere inscribed inside the hemi-ellipsoid is given as

$$\eta = \begin{cases} 1/2, & \text{for } \alpha > 1/\sqrt{2}, \quad \beta > 1/\sqrt{2} \\ \alpha\sqrt{1-\alpha^2} & \text{for } \alpha \leq 1/\sqrt{2}, \quad \alpha < \beta \\ \beta\sqrt{1-\beta^2} & \text{for } \beta \leq 1/\sqrt{2}, \quad \beta < \alpha \end{cases} \quad (37)$$

Numerical integration techniques are needed to evaluate \underline{L} per Eq. (8).

Plots of L_x and L_y against α and β are displayed in Fig. 16. The depolarization factors L_x and L_y vary smoothly as α and β increase from 0 to 3; specifically, L_x decreases markedly as α increases, and L_y decreases markedly as β increases.

The real and imaginary parts of the relative permittivity parameters ε_x^{MG} , ε_y^{MG} , and ε_z^{MG} of the HCM are plotted against α and β in Fig. 17. As both α and β vary, there are smooth variations in the real and imaginary parts of each of ε_x^{MG} , ε_y^{MG} , and ε_z^{MG} . Specifically, $\text{Re}\{\varepsilon_x^{MG}\}$ is particularly sensitive to variations in α at small values of α , $\text{Re}\{\varepsilon_y^{MG}\}$ is particularly sensitive to variations in β at small values of β , and $\text{Re}\{\varepsilon_z^{MG}\}$ is particularly sensitive to variations in both α and β at small values of α and β . The plots for $\text{Im}\{\varepsilon_x^{MG}\}$, $\text{Im}\{\varepsilon_y^{MG}\}$, and $\text{Im}\{\varepsilon_z^{MG}\}$ are qualitatively similar to those plots for $\text{Re}\{\varepsilon_x^{MG}\}$, $\text{Re}\{\varepsilon_y^{MG}\}$, and $\text{Re}\{\varepsilon_z^{MG}\}$, respectively.

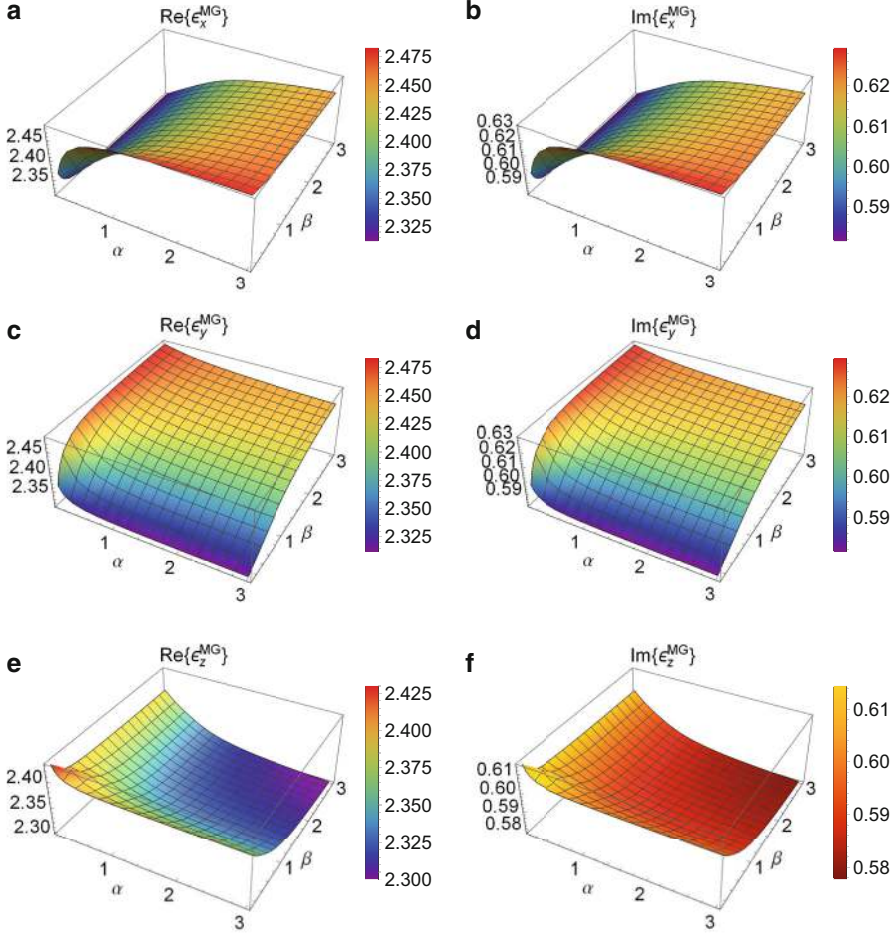


Fig. 17 Plots of real and imaginary parts of ϵ_x^{MG} , ϵ_y^{MG} , and ϵ_z^{MG} versus $\alpha \in (0, 3]$ and $\beta \in (0, 3]$ for hemi-ellipsoidal inclusions

4 Discussion

Depolarization dyadics are fundamental to theories of homogenization and scattering from electrically small particles. Hitherto, closed-form expressions for depolarization dyadics had been developed only for relatively simple inclusion shapes such as ellipsoids and cubes, but now the range of inclusion shapes has been broadened to include truncated spheres and truncated spheroids [23]. Furthermore, the formalism has been extended to truncated ellipsoidal inclusions, but in this case, numerical methods are needed to evaluate the depolarization dyadics.

These newly developed depolarization dyadics for truncated spheres, spheroids, and ellipsoids [23] have been incorporated [24] into the Maxwell Garnett formalism to represent inclusions embedded in an isotropic dielectric host medium. The applicability of this homogenization formalism has thus been substantially extended to HCMs comprising inclusions of more realistic shapes.

Through numerical investigations based on physically realistic constitutive parameter values, the anisotropy of the resulting HCM has been related to the geometry of the inclusions. To be specific, the degree of anisotropy exhibited by the HCM became greater as the shape of the inclusions deviated more from spherical.

Lastly, the Maxwell Garnett formalism has been well-established for many years for HCMs arising from inclusions shaped as spheres, spheroids, and ellipsoids [1]. An important foundation for this formalism is the assumption that the inclusions are sufficiently small that the electromagnetic field is spatially uniform within each inclusion [42]. This assumption is also taken to hold for the oddly shaped inclusions described herein. Physically, this assumption is reasonable provided that the inclusions are sufficiently small and provided that their shapes do not deviate too much from those of non-truncated spheres, spheroids, and ellipsoids. However, as with all homogenization formalisms, only through comparison with experimentally measured data can the usefulness of this recently developed implementation of the Maxwell Garnett formalism be truly assessed.

Acknowledgments TGM's work was supported in part by EPSRC (grant no. EP/V046322/1). AL thanks the Charles Godfrey Binder Endowment at The Pennsylvania State University for supporting his research endeavors from 2006 to 2024.

References

1. A. Lakhtakia (ed.), *Selected Papers on Linear Optical Composite Materials* (SPIE Optical Engineering Press, Bellingham, WA, USA, 1996)
2. P.S. Neelakanta, *Handbook of Electromagnetic Materials: Monolithic and Composite Versions and Their Applications* (CRC, New York, 1995)
3. T.C. Choy, *Effective Medium Theory: Principles and Applications*, 2nd edn. (Oxford University, Oxford, 2016)
4. T.G. Mackay, A. Lakhtakia, *Modern Analytical Electromagnetic Homogenization with Mathematica®*, 2nd edn. (IOP Publishing, Bristol, UK, 2020)
5. M.P. Mengüç, M. Francoeur (eds.), *Light, Plasmonics and Particles* (Elsevier, Amsterdam, 2023)
6. A. Lakhtakia, T.G. Mackay, Meet the metamaterials. *Opt. Photon. News* **6**(1), 32–39 (2007)
7. T.G. Mackay, W.S. Weiglhofer, Homogenization of biaxial composite materials: bianisotropic properties. *J. Opt. A: Pure Appl. Opt.* **3**, 45–52 (2001)
8. J.Z. Buchwald, *From Maxwell to Microphysics: Aspects of Electromagnetic Theory in the Last Quarter of the Nineteenth Century* (University of Chicago Press, Chicago, 1985)
9. J. Van Kranendonk, J.E. Sipe, Foundations of the macroscopic electromagnetic theory of dielectric media. *Prog. Optics* **15**, 245–350 (1977)
10. J.C. Maxwell Garnett, Colours in metal glasses and thin films. *Philos. Trans. R. Soc. Lond. A* **203**, 385–420 (1904) (Reproduced in Ref. 1)

11. Z. Hashin, S. Shtrikman, A variational approach to the theory of the effective magnetic permeability of multiphase materials. *J. Appl. Phys.* **33**, 3125–3131 (1962)
12. C.-T. Tai, *Dyadic Green Functions in Electromagnetic Theory*, 2nd edn. (IEEE, Piscataway, 1994)
13. M. Faryad, A. Lakhtakia, *Infinite-Space Dyadic Green Functions in Electromagnetism* (Morgan & Claypool, San Rafael, 2018)
14. B. Michel, A Fourier space approach to the pointwise singularity of an anisotropic dielectric medium. *Int. J. Appl. Electromagn. Mech.* **8**, 219–227 (1997)
15. A. Moroz, Depolarization field of spheroidal particles. *J. Opt. Soc. Am. B* **26**, 517–527 (2009)
16. J.A. Osborn, Demagnetizing factors of the general ellipsoid. *Phys. Rev.* **67**, 351–357 (1945)
17. E.C. Stoner, The demagnetizing factors for ellipsoids. *Phil. Mag.* **36**, 803–821 (1945)
18. B. Michel, W.S. Weiglhofer, Pointwise singularity of dyadic Green function in a general bianisotropic medium. *Arch. Elektron. Übertrag.* **51**, 219–223 (1997). Corrections: **52**, 310 (1998)
19. W.S. Weiglhofer, Electromagnetic depolarization dyadics and elliptic integrals. *J. Phys. A: Math. Gen.* **31**, 7191–7196 (1998)
20. W.S. Weiglhofer, T.G. Mackay, Needles and pillboxes in anisotropic mediums. *IEEE Trans. Antennas Propagat.* **50**, 85–86 (2002)
21. S.-W. Lee, J. Boersma, C.-L. Law, G.A. Deschamps, Singularity in Green's function and its numerical evaluation. *IEEE Trans. Antennas Propagat.* **28**, 311–317 (1980)
22. A. Lakhtakia, N.S. Lakhtakia, A procedure for evaluating depolarization dyadics of polyhedra. *Optik* **109**, 140–142 (1998)
23. T.G. Mackay, A. Lakhtakia, Depolarization dyadics for truncated spheres, spheroids, and ellipsoids. *IEEE Trans. Antennas Propagat.* **72**, 5420–5425 (2024); Erratum **72**, 6168 (2024)
24. T.G. Mackay, A. Lakhtakia, Anisotropic homogenized composite mediums arising from truncated spheres, spheroids, and ellipsoids. *Waves Random Complex Media*. <https://doi.org/10.1080/17455030.2024.2392792>
25. A. Lakhtakia, On two numerical techniques for light scattering by dielectric agglomerated structures. *J. Res. Nat. Inst. Stand. Technol.* **98**, 699–716 (1993)
26. W.C. Chew, *Waves and Fields in Inhomogeneous Media* (IEEE, Piscataway, 1995). Sec. 8.9.2
27. M. Sancer, K. Sertel, J. Volakis, P. Alstine, On volume integral equations. *IEEE Trans. Antennas Propagat.* **54**, 1488–1495 (2006)
28. O.D. Kellogg, *Foundations of Potential Theory* (Springer, Berlin, 1967). Sec. VI.2
29. J.J.H. Wang, A unified and consistent view of the singularities of the electric dyadic Green's function in the source region. *IEEE Trans. Antennas Propagat.* **30**, 463–468 (1982)
30. J.G. Fikioris, Electromagnetic field inside a current carrying region. *J. Math. Phys.* **6**, 1617–1620 (1965)
31. A.D. Yaghjian, Electric dyadic Green's function in the source region. *Proc. IEEE* **68**, 248–263 (1980)
32. J. Van Bladel, *Singular Electromagnetic Fields and Sources*. (Oxford University, Oxford, 1991)
33. J.C. Maxwell, *A Treatise on Electricity and Magnetism*, 3rd edn. (Clarendon, Oxford, 1904). Arts. 437 and 438
34. L.V. Lorenz, Experimentale og theoretiske Undersøgelser over Legemernes Brydningsforhold, II. K. Dan. Vidensk. Selsk. Forh. **10**, 485–518 (1875)
35. M.T. Prinkey, A. Lakhtakia, B. Shanker, On the extended Maxwell-Garnett and the extended Bruggeman approaches for dielectric-in-dielectric composites. *Optik* **96**, 25–30 (1994)
36. R.C. Robertson, Computation of the electric field within a region of uniform current density. *Int. J. Electron.* **69**, 707–716 (1990)
37. J. Van Bladel, Some remarks on Green's dyadic for infinite space. *IRE Trans. Antennas Propagat.* **9**, 563–566 (1961)
38. D.E. Livesay, K.-M. Chen, Electromagnetic field induced inside arbitrarily shaped biological bodies. *IEEE Trans. Microwave Theory Tech.* **22**, 1273–1280 (1974)

39. J. Avelin, A.N. Arslan, J. Brännback, M. Flykt, C. Icheln, J. Juntunen, K. Kärkkäinen, T. Niemi, O. Nieminen, T. Tares, C. Toma, T. Uusitupa, A. Sihvola, Electric fields in the source region: the depolarization dyadic for a cubic cavity. *Elec. Eng.* **81**, 199–202 (1998)
40. M. Cauterman, P. Degauque, B. Demoulin, R. Gabillard, Remote sensing of buried resistive inhomogeneities by electromagnetic transmission measurements between the ground surface and a borehole—Theory and experiment. *Radio Sci.* **13**, 371–378 (1978)
41. R.F. Harrington, *Time-Harmonic Electromagnetic Fields* (IEEE, Piscataway, 2001). Sec. 3–11
42. D.E. Aspnes, Local-field effects and effective-medium theory: a microscopic perspective. *Am. J. Phys.* **50**, 704–709 (1982). (Reproduced in Ref. 1)
43. A. Sihvola, *Electromagnetic Mixing Formulas and Applications* (Peter Peregrinus, London, 1999)
44. C.E. Dungey, C.F. Bohren, Light scattering by nonspherical particles: a refinement to the coupled-dipole method. *J. Opt. Soc. Am. A* **8**, 81–87 (1991)
45. P. Mallet, C.A. Guérin, A. Sentenac, Maxwell-Garnett mixing rule in the presence of multiple scattering: Derivation and accuracy. *Phys. Rev. B* **72**, 014205 (2005)
46. A. Lakhtakia, Frequency-dependent continuum electromagnetic properties of a gas of scattering centers. *Adv. Chem. Phys.* **85**(2), 311–359 (1993)



Tom G. Mackay is Professor of Applied Electromagnetic Theory in the School of Mathematics at the University of Edinburgh and an adjunct professor in the Department of Engineering Science and Mechanics at Pennsylvania State University. He graduated from the Universities of Edinburgh, Glasgow, and Strathclyde. His research has been supported by awards from the Carnegie Trust for The Universities of Scotland, Engineering and Physical Sciences Research Council, Nuffield Foundation, Royal Academy of Engineering/Leverhulme Trust, and Royal Society of Edinburgh/Scottish Executive. He is a fellow of the Institute of Physics (UK), Optica (formerly Optical Society of America), and SPIE—The International Society for Optics and Photonics. His current research interests include homogenization, complex materials, and surface waves.



Akhlesh Lakhtakia received his B.Tech. (1979) and D.Sc. (2006) degrees from the Banaras Hindu University and his M.S. (1981) and Ph.D. (1983) degrees from the University of Utah. He joined the Department of Engineering Science and Mechanics at The Pennsylvania State University in 1983, where now he is Evan Pugh University Professor of Engineering Science and Mechanics. He is also a Visiting Professor of Mathematics at the University of Edinburgh.

Dr. Lakhtakia has been elected a fellow of Optical Society of America, SPIE, Institute of Physics (UK), American Association for the Advancement of Science, American Physical Society, Institute of Electrical and Electronics Engineers, Royal Society of Chemistry, Royal Society of Arts, and Sigma Xi. He has been designated a Distinguished Alumnus of both of his *almae matres* at the highest level. Awards at Penn State include: Outstanding Research Award, Outstanding Advising Award, Premier Research Award, Outstanding Teaching Award, and the Faculty

Scholar Medal in Engineering. He received the 2010 SPIE Technical Achievement Award, the 2016 Walston Chubb Award for Innovation, the 2022 Smart Structures and Materials Lifetime Achievement Award, the 2022 IEEE Antennas and Propagation Society Distinguished Achievement Award, the 2022 Radio Club of America Lifetime Achievement Award, and the 2024 SPIE Gold Medal. He has served as a Sigma Xi Distinguished Lecturer (2022–24) and a Jefferson Science Fellow at the US State Department (2022–23). His current research interests include electromagnetic scattering, surface multiplasmonics, photovoltaic solar cells, sculptured thin films, mimics, engineered biomimicry, and forensic science.

Photonic Metamaterials for Light Modulation, Energy Saving, and Sensing Applications



Majd Abu Aisheh, Amaljith CK, Anand M. Shrivastav,
and Ibrahim Abdulhalim

1 Introduction

Light manipulation devices require materials that respond to an applied external stimulus such as electric, magnetic, thermal, mechanical, or optical fields. The speed, modulation range, depth, high light throughput, cost, and energy saving of photonic devices are competing parameters that can lead to bottlenecks in numerous critical applications, such as acquiring images at many wavelengths or polarization states during the heartbeat cycle or from the eye retina before eye movement or blinking, or for improving the yield of production in the nanoelectronics industry, or again in experimental cosmology where fast surveying of galaxies is required to search for extra-terrestrial life. One prominent emerging field combining nanotechnology with photonics is the field of photonic metamaterials; however, fast tunable devices exhibiting broadband, large modulation depth, high light throughput at a low cost, ease of scaling, and compact manner are still lacking. Since these are competing parameters, the existing solutions usually customize the device to a very limited application.

M. Abu Aisheh · Amaljith CK

Department of Electrooptics and Photonics Engineering, Ilse Katz Institute for Nanoscale Science and Technology, School of Electrical and Computer Engineering, Ben Gurion University, Beer Sheva, Israel

A. M. Shrivastav (✉)

Department of Physics and Nanotechnology, College of Engineering and Technology, SRM Institute of Science and Technology, Chennai, Tamil Nadu, India
e-mail: anandmos@srmist.edu.in

I. Abdulhalim (✉)

Ben Gurion University, Beër Sjeva, Israel
e-mail: abdulhim@bgu.ac.il

Photonic metamaterials (PMMs) offer many possibilities to resolve such problems [1, 2]. They are defined as artificial optical materials composed of subwavelength metallic or dielectric building blocks with properties determined mainly by their subwavelength nature rather than their chemical composition. These building blocks or “photonic atoms” (PAs) are structural elements densely packed into an effective material such that the operating wavelength is ideally much larger (typically an order of magnitude or more) than the diameter of the PAs. Highly unusual material properties become accessible, e.g., a negative refraction index that has recently acquired operation wavelengths in the infrared and visible ranges. Tunability of the properties of PMMs broadens their usability for fast light modulation, such as tunable filters, tunable focus flat lenses, spatial light modulators, and frequency reconfigurable antennae. Liquid crystals (LCs) possess strong electro-optic effects and can penetrate nanogaps, thus they can be ideal for tunable PMMs. Some preliminary works have demonstrated applications of PMMs using LCs infiltrating the PMM or as a layer adjacent to the PMM. Others have used thermotropic phase change materials, thermochromic materials, semiconductors, electromechanical, magneto-optic, and electro-optic materials. However, until now the majority of the demonstrated tunable PMM device concepts are limited either in their size, switching speed, tunability range, and spectral bandwidth, and usually, they require complex fabrication techniques, thus their practicality is limited.

Active control of the wavelength, polarization, or phase, of light—either temporally, spatially, or spatiotemporally—over a wide spectral range, wide field of view, in an achromatic manner, that is fast, has a high light throughput and small form factor, as well as low cost is always in demand for many important applications. These range from spectral imaging to optical communications, from quantum and optical computing to tunable lasers, from augmented reality devices to autonomous cars, and many other emerging applications [3–5]. Progress is ongoing in light manipulation methods and devices due to their utmost importance in many fields. Nonetheless, the existing solutions, often suffer either from low speed, narrow dynamic range, wide uncontrolled bandwidth, or low light throughput, and the majority are bulky and expensive to manufacture. Narrow resonances of micro- and nanostructures tuning can allow fast response and high sensitivity; however, the dynamic range is usually small [6–8]. A device combining all these quality parameters does not yet exist. Here, our main objective is to review recent advances in photonic metamaterial (PMM) structures for light modulation, sensing, and energy saving devices. The chapter is divided into three main sections, Sect. 2 is on PMMs for light modulation, Sect. 3 is on PMMs for energy saving, while Sect. 4 is on PMMs for sensing applications.

2 PMMs for Light Modulation

Photonic metamaterials (PMMs) show great potential for such light manipulation devices [9–13]. When the PMM is a 2D surface, in what is called a metasurface,

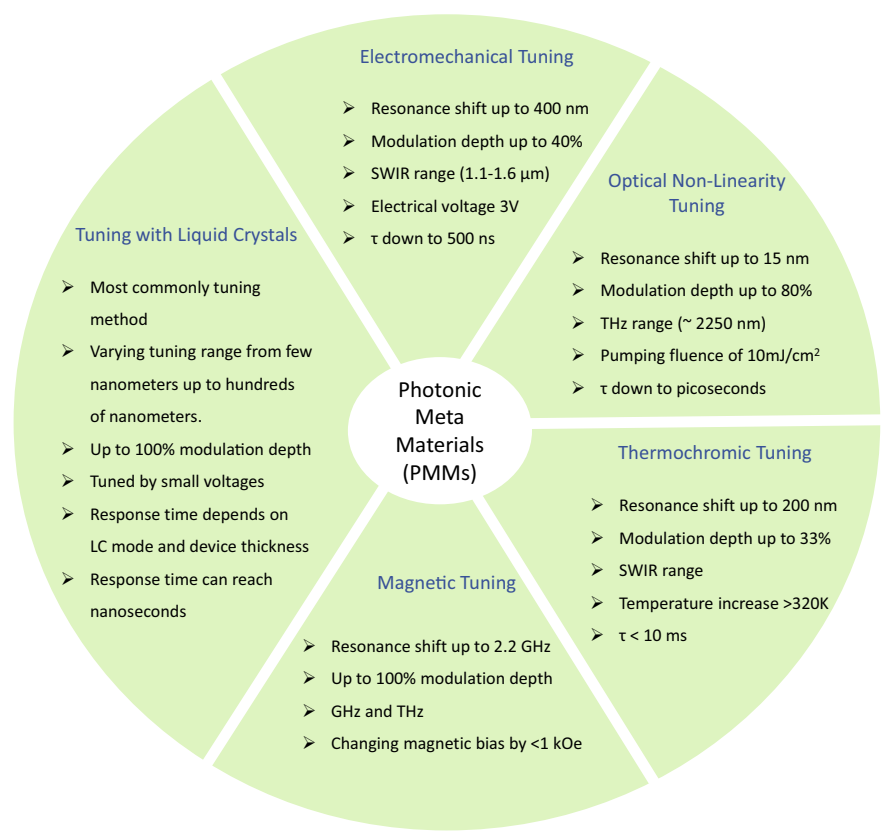


Fig. 1 PMMs tuning methods and their main characteristics

it can be prepared easily with well-established lithography fabrication processes as compared to the 3D PMM. By making the PMM, or part of it, from responsive material such as electrooptic, magneto-optic, thermoscopic, photosensitive, elastomeric, acousto-optic, electromechanical, or nonlinear optical material (see Fig. 1), it is possible to tune the properties of the PMM as exemplified by many works over the last decade [14–18]. In what follows, we present an overview of works done on tunable photonic metamaterials with an emphasis on tunability with liquid crystals.

2.1 Overview of Tunable PMMs

Electromechanical (EMC) EMC-driven metasurface operating in the Short-wave infrared (SWIR) was demonstrated by Ou et al. [19]. It was fabricated by focused

ion beam milling on a 50-nm-thick Si_3N_4 membrane. Under ~ 3 V, the transmittance becomes modulated, however, the depth was only 5%. Tunable plasmonic lattice grating patterned on a flexible and stretchable PDMS substrate was shown by Chen et.al [20]. It showed a response under external strain varying between 0% and 10%, giving almost a 40% modulation depth in reflectivity by external strain change from 1.6% to 3.5%. The surface plasmon resonance shifted approximately 80 nm in the visible at ~ 780 nm under the same strain variation. A focal-length tunable lens was demonstrated by Arbabi et al. [21], using a pair of metalenses based on the high-contrast dielectric arrays. One metalens is on a fixed glass substrate, whereas the other on a movable Si_3N_4 membrane. The doublet shifted the focal length up to 80 μm . Foland et al. presented a 2D deformable GMR strain sensor by embedding TiO_2 of 210 nm radius in PDMS [22]. The height of the pillars was 200 nm, and they were arranged in arrays of 480 nm period in the x-axis, and 560 nm in the y-axis. Two resonance peaks were obtained, one of wavelength around 775 nm for the short-period axis and the second of around 850 nm for the long-period axis. The resonant wavelength shifted along the long-period axis with a 4.8 nm/% ϵ sensitivity over a range of 5% strain.

Optical Nonlinearity Using the optical nonlinear Kerr effect of ITO, Zhu et.al [23], demonstrated tunable transparency plasmonic metasurface of gold on ITO. An optical transparency window shift to the short-wavelength direction in the SWIR range was observed. Optically tunable metasurface was demonstrated by Kim et.al [24], based on the structure Ag- Al_2O_3 -Ag, called metal-insulator-metal (MIM) nanocavity with a 70 nm-thick Ga: ZnO layer as an active layer. It showed fast switching in the sub-picosecond range with 80% depth at laser pumping fluence of 10 mJ/cm². The cavity resonance red-shifted by 15 nm in the SWIR range near the Epsilon-near-zero (ENZ) wavelength. At the ENZ condition, the field becomes drastically enhanced, and this is used to enhance optical nonlinear effects. A polarization switch was demonstrated using plasmonic metasurface and isomeric ethyl-red polymer [25] based on a 100-nm-thick gold periodic array of L-shaped slots on a 500- μm -thick fused quartz substrate and ~ 300 nm ethyl-red polymer top layer. By irradiating green laser (532 nm) the isomeric state of ethyl-red changed from *trans* to *cis* state, which caused the refractive index to decrease. This induced coupling between the resonant plasmonic modes and the isomeric state, and the resulting polarization change revealed 80% modulation depth at 6 Hz. Visible light fifth harmonic generation was observed [26] from the heterostructure of the Indium-doped CdO layer on gold coated with MgO top layer due to the field enhancement at the interface with MgO, although the ENZ condition occurs at the wavelength of 2250 nm.

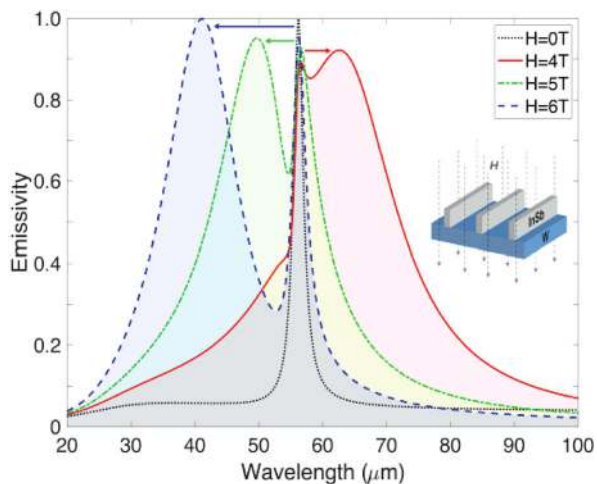
Thermochromic Thermal tuning of metamaterials was done using thermochromic phase change materials, such as germanium-antimony-tellurium (GST) or VO_2 . All-optical bidirectional metasurface based on the GST was demonstrated [27] using a 15 nm-thick GST layer sandwiched between SiO_2 and ZnS/SiO_2 layers. Also, the same group [28] demonstrated 10% reflectivity modulation depth in the UV and visible using patterned GST heterostructure with ZnS/SiO_2 . Plasmonic 50-nm-

thick Au trenches support plasmonic resonance and enhanced photo-absorption for a temperature change of GST. As the phase of the GST layer changes from the crystalline to the amorphous phase, the transmission at SWIR spectra rose from 20% to 40%. Electrically controllable VO₂ metasurface was demonstrated [29] with the VO₂ laterally sandwiched by structured gold electrodes and the voltage pulse train changes the phase of VO₂ between amorphous and crystalline phases. A modulation depth of 33% at the SWIR spectrum was observed with a response time < 10 msec. Thermal tuning of VO₂-TiO₂ multilayer metamaterial was demonstrated [30] due to the dispersion relation change from the elliptic form to the hyperbolic form as the temperature increases over the critical temperature of VO₂ around 325 K. Two types of VO₂ metasurfaces were produced by us showing operation as smart windows with improved performance, one by femtosecond pulsed laser [31] and the other by oblique angle deposition technique [32].

Magnetic Tuning MTM properties with the magnetic field has been done in many works, particularly in the GHz and sub-THz regimes, since in these ranges the metamaterial structure may be considered as a combination of electrical components, such as varactor diodes, capacitors, and inductors with a magnetic response, for instance, the split ring resonator structure [33]. Shifts of SRR resonances were reported [34–36]. Caratenuto et al. [37] demonstrated, theoretically and analytically, the magnetic field-induced spectral radiative properties of a metamaterial composed of Indium Antimonide (InSb) line-gratings on Tungsten (W) film in terahertz. They showed that the InSb grating has single narrowband emissivity of unity in terahertz, and by applying magnetic field, the light matter interactions are modified by broadening the resonant wavelength by 25 μm while still maintaining the near-unity resonance as shown in Fig. 2.

Tuning MTMs with Liquid Crystals Some materials change their refractive index when an electric field is applied to them. Some are nonlinear materials following the

Fig. 2 InSb-W grating structure under external magnetic fields of varying magnitudes. Field-induced curves are color filled to highlight the broadband red or blue emissivity shifts brought on by the magnetic field. Arrows denote the direction of the dominant resonance shift from the original narrowband peak to longer (red) or shorter (blue) wavelengths. The figure was reproduced from [37] with permission from OPTICA Publishing Group



Kerr effect and others show linear variation with the applied electric field following the Pockels effect. The origin of these effects is electronic and therefore they exhibit a fast response; however, these effects are relatively weak, so a large interaction region with the light is required from millimeters to centimeters and large voltages are needed. Liquid crystals (LCs) are composed of anisotropic molecules, usually rod-shaped, and therefore can rotate under the application of small voltage. It is a strong effect showing birefringence modulation typically in the range 0.1–0.28; however, larger values up to 0.4 were also demonstrated in response to 1–10 V and only a few microns thick layer is required to generate 100% modulation. With resonant structures, a very thin LC layer and small index modulation is required to tune the resonance and obtain a large modulation depth. LCs possess a wide variety of EO effects depending on their structure determined by the material, the molecular alignment geometry of the device, and the anchoring strength of the molecules on the surfaces. They can flow and fill nanogaps exhibiting strong thermo-optic and magneto-optic responses, therefore they are ideal for tuning metamaterials. Hence, by combining the two fields, a wide range of new devices with high potential can be generated. Recent review articles [14, 15, 32, 38–42] on tunable MTMs, contain up-to-date information on tuning using liquid crystals, ref. 37 is dedicated to this topic. A short overview is presented below.

Of all the possible tuning methods of liquid crystals, electrical tuning is the most convenient as it requires low voltages and negligible current. Among the first LC tunable MTM devices was the one analyzed by Khoo et al. [43], consisting of nanospheres immersed in the nematic liquid crystal. LiTaO_3 was used as the core material for this purpose, and their effective index properties were calculated using the Maxwell Garnet mixing rule. By using this combination, it was shown that at the frequency of 108 THz, the effective index of the material changes from +1 to −1 as the effective permittivity varied from 2 to 4. Electromagnetically induced transparency (EIT) and absorption resonant structure were demonstrated with the LC layer to shift the resonance up to 0.5 THz [44, 45] with modulation depths of 18.3 dB and 10.5 dB based on different combinations in split ring resonators in the THz range. An all-dielectric metasurface composed of an array of nanodisks was built [46] giving resonance in the SWIR range, and the LC layer on the top induced a shift of about 70 nm and modulation depth of 75%. Another all-dielectric device is the guided mode resonance (GMR) structure we demonstrated [8]. It is composed of thin subwavelength grating on top of a waveguide layer and covered with 2000 nm LC and showed voltage-induced tuning of the resonance by 40 nm and more than 80% modulation depth in the SWIR range. A thick subwavelength TiO_2 grating exhibiting resonances in reflection, like the thin grating GMR, was also investigated by us [47] as a refractive index sensor. In this case, the grating itself acts as waveguide, thus providing the GMR peak; however, additional resonances were also observed in the simulations such as the bound in the continuum (BIC) ultranarrow resonance. Later, a tunable MTM based on 2-D metal-dielectric composite was reported to operate in the NIR region [48]. Results showed that the metamaterial exhibits a negative index band between 1.37 μm and 1.47 μm when ϵ_{LC} is 2. As ϵ_{LC} increases, the negative index band gradually decreases from shorter wavelengths

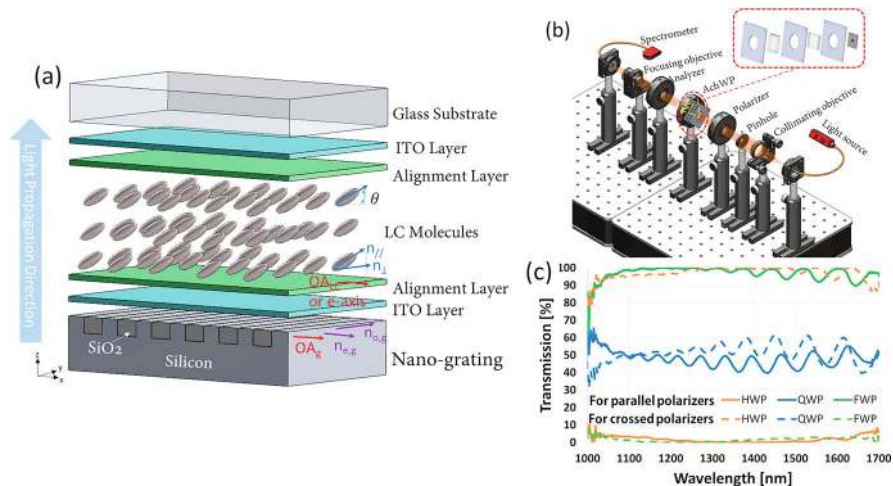


Fig. 3 (a) The designed ideal metasurface combined with the LC layer, transparent electrodes and alignment layers. (b) Experimental setup for device characterization. (c) Measured transmission spectra for the QWP, HWP, and FWP modes between crossed and parallel polarizers

to the longer wavelength side until it completely disappears for $\varepsilon_{\text{LC}} \geq 2.7$. The proposed near-IR MTM can reconfigure the index of refraction over a negative-zero-positive range from $\lambda = 1.37 \mu\text{m}$ to $\lambda = 1.47 \mu\text{m}$, which makes it a promising candidate for applications requiring tunable devices. The study suggests that a minimum practical value for the permittivity of an LC is $\varepsilon_{\text{LC}} = 2$, making this MTM design highly practical. In their work, the negative index nature of the composite structure is analyzed for near IR and extended to the mid-IR range for usability in an extensive spectral range. An LC tunable metal-dielectric-metal cavity structure was demonstrated [49] to create an electrically adjustable LC THz MTM polarization converter. A new MTM composite of nanoporous microparticles (NMPs) in LC was shown by us to act as a voltage tunable scattering device exemplified using p-Si NMPs [50], organic cigar-shaped cochleate NMPs [51], and octa-decanol NMPs [52] doped in small concentrations to the LC. The NMP itself acts as a tunable meta-atom since the LC infiltrates the nanopores and modifies the effective refractive index when an external field is applied. Very recently [53] our group demonstrated a tunable achromatic waveplate based on nanograting made of Si combined with $8 \mu\text{m}$ thin LC layer operating in the SWIR range showing fast tunability between quarter, half, and full waveplates, see Fig. 3.

The group of Chu [54] recently demonstrated a tunable filter based on a 2D array of a-Si nanodisks covering the C-band telecommunication window using the organic photoalignment layer AZB. They showed that photoalignment gives better contrast, but compared to flat surface devices it is still lower by a factor of 4–5. The resonance dip however has a FWHM of more than 30 nm, indicating that it is far from useful in practical applications.

Since LCs have a large thermo-optic effect, the same tunable MTM structures can also be tuned thermally. A thermo-optic LC-MTM was reported by Liu et al. [55] using an electrical split ring resonator structure. In this work, the E7 LC was infiltrated between the MTM and an additional 1-mm-thick quartz cover slip. The maximum shift induced is -12.3 GHz. After infiltration of the metamaterial with LC, the resonant dip shifted to 1.161 THz for the LC-orientation parallel to the split opening and 1.154 THz when the LC is perpendicular to the split opening. The guided mode resonant MTM structure was demonstrated in reference [8] as a potential thermo-optic sensor and filter near the phase transition from nematic to isotropic where the thermo-optic effect is enhanced. Our NMP-LC MTM composite [48–50] was also shown to be tuned by temperature.

LCs also have magnetic anisotropy, and the molecules can rotate in response to a magnetic field. A negative index device was proposed based on SRRs and rods arranged in a periodic manner by Pendry [56]. By utilizing a similar design of MTM, Zhang et al. [57] developed a magnetically tunable LC MTM device operating in the GHz range. Resonance shift was analyzed showing that the effective index change in the composite structure is linearly dependent on the LC index change. Using a photoelastic LC elastomer with a plasmonic metasurface on top, Liu et al. demonstrated tuning of the plasmonic dip by more than 200 nm in the SWIR range optically [58].

One of the attractive MTM devices is flat lenses, which can be engineered with a radial refractive index profile achieved by varying the density of the unit cells (photonic atoms) of the MTM. The index profile can be continuous as with glass lenses or discrete as with diffractive lenses. By infiltrating LC in between and within the unit cells, it is then possible to vary the focal length. One potential application of varifocal flat lenses is in the field of virtual and augmented reality. By incorporating these lenses into head-mounted displays, it could be possible to provide a more realistic and immersive experience to users by dynamically adjusting the focal length of the lenses to match the distance of virtual objects in the display. Bosch et al. demonstrated bifocal metalens tunable with LC in the vis-NIR range [59]. A remarkable work by Leninger et al., studied the LC infiltration within the nanoapertures of a 2D metasurface with a radially variable effective index using three nematic LC mixtures [60]. For more information on tunable metalenses, the reader is referred to the recent [39] review article. A closely related topic to tunable metalenses is the beam steering devices based on LC-MTMs with the common feature of both being phase-only spatial light modulators. Using a metasurface made of TiO_2 nanoantenna covered with 1500 nm LC layer, Li et al., demonstrated an SLM with improved pixel size down to one micron because most of the phase modulation originates from the resonant metasurface rather than from the LC [61]. They found a $\pm 11^\circ$ controlled beam deflection and a 36% modulation in transmission.

As we can see from this short review, photonic MTM devices that tune over a wide spectral range, with high modulation depth, fast speed, narrowband, high light throughput, and easily constructed do not exist yet. The demonstrations done so far use nematic LCs, which are limited in their response time to the tens of

msec range. In addition, there is an alignment problem of the LC molecules inside nanoapertures in the specific direction required, which was partially solved using photoalignment polymers deposited by spin coating—problematic when done on nanostructured surfaces. In our opinion it is possible to resolve these problems using unique MTM designs, using photoalignment of thin solid films prepared by physical vapor deposition, using unidirectional nanopatterning with ultrashort pulsed laser, and oblique angle deposition combined with photolithography, as well as materials selection. Based on the existing state of the art, we can summarize the reasons for the limited performance of the demonstrated LC tunable PMM devices as follows:

- (a) LC molecules alignment in the desired orientation inside nanoapertures is not well controlled. Recent experiments showed that LC can infiltrate nanoapertures [62], though the nature of the alignment inside and how to control it is not a resolved problem. For long wavelengths in the THz or microwaves region, the apertures can be as large as microns or more, therefore it is much easier to control the LC alignment for such devices [1]. However, controlling the LC alignment is not easy for the optical regime where the apertures are in the order of 100 nm to submicron.
- (b) Nematic LCs, which are optimized for displays, are limited in their response time to the tens of msec range and increase with the thickness d following d^2 behavior. Although adding a separate few microns thick LC layer to the PMM was shown to improve PMM device properties as a tunable device compared to the equivalent device not containing MTM, the switching speed is still limited, therefore there is a need to resolve the problems associated with LC alignment within nanogaps, not only for nematic LCs but also other fast modes as well.
- (c) Existing resonant PMMs, particularly those with high quality factors (high-Q resonances) usually have a short dynamic range, thus limiting the tunability to a maximum spectral range of a few tens of nm. Hence, novel resonant PMM designs that exhibit broadband tuning are needed.
- (d) Nonresonant PMMs usually behave as anisotropic materials and therefore special care should be taken to tune them with liquid crystals as the relative orientation of the principal axis of the two media is crucial for tunability. Hence there is a need to resolve the LC alignment problem in nanoapertures.
- (e) Large-scale production of existing PMMs in the optical frequency regime is problematic because the structures contain complex nanoscale features in the lateral dimension.

2.2 Obtaining Faster High-Quality LC PMM Devices

Since the nematic LC response time decreases inversely with the square of LC layer thickness, PMM-based devices are expected to be faster by two orders of magnitude than the existing LC devices. Ultrafast LC modes such as the ferroelectric and electroclinic (chiral smectic A) LCs can be integrated to generate tunable

devices having micro- and nanosecond switching times. The PMM architectures can enhance these LC materials' electro-optic response while maintaining their large speed. In standard LC devices, usually, the electro-optic response and speed compete analogously to the time-energy uncertainty principle, while here we propose to break this limitation by combining LCs and other EO materials with PMMs. Notably, the ubiquitous LC display has LC-cells or panels, in which the liquid crystal must be perfectly aligned over large areas, up to square meters. Therefore, the simplest, highest symmetry, LC phase (nematic) is used, which allows high yield in manufacturing. However, it is well known that the response speed of nematic LCs is limited to about 10 ms, which is just about good enough for active-matrix video displays [63]. About 100 to 1000 times faster switching can be found in ferroelectric and antiferroelectric liquid crystal (FLCs and AFLCs, respectively) modes [64]. FLCs and AFLCs are, with their layered (smectic) structures, unfortunately much more challenging than nematics in terms of alignment, which has put them on the sideline in the display arena, except for in some high-performance FLC microdisplays, where the small area ($<1\text{cm}^2$) allows for high yield. Hence there is a place to explore and develop high speed LC modes, for use in small, ultrafast LC photonic MTM devices and demonstrate their suitability for medical diagnostics, bio and chemical analytes sensing, and remote sensing.

Nematic-Based Liquid Crystals Conventional LCs (nematic) respond to an applied electric field via their dielectric anisotropy. The switching (or relaxation) back to the field-free state is driven solely by elastic forces, making the relaxation time proportional to the square of the LC layer thickness. The switching times for nematic LCs are generally limited to the msec range [65], although several complex methodologies have been applied in attempts to effectively reduce the switching time such as: (i) driving voltage waveform manipulation [66] (ii) dividing the device into several thinner (and therefore faster) sub-devices (iii) optimizing material parameters [67], (iv) optimizing the anchoring strength and pretilt on the surfaces, (v) vertically aligned [68], in-plane switching mode [69], twisted alignment, asymmetric alignment [70–72], (vi) the use of dual frequency mode [73], blue phase Kerr effect [74, 75], the flexoelectro-optic mode [76–78] in short pitch chiral nematic (cholesteric) phase, (vii) using nano- or microstructured LC networks [79] such as the nano-polymer dispersed LCs (nPDLCs) and stressed LCs [80, 81], and (viii) working at elevated temperatures to reduce the LC viscosity (see Fig. 4 for some illustrations). In the Kerr effect in the isotropic phase, just above the nematic phase, or when the switching is caused by the electric field-induced modification of the order parameters and not due to reorientation of the optic axis, the response becomes closer to the nsec range [82, 83], but the effect is very small producing birefringence changes in the order of 0.001–0.01 at applied voltages of the order of kV.

The cases of submsec switching and below are limited in their applicability because the associated electro-optic effects become weak as in the Kerr effect case:

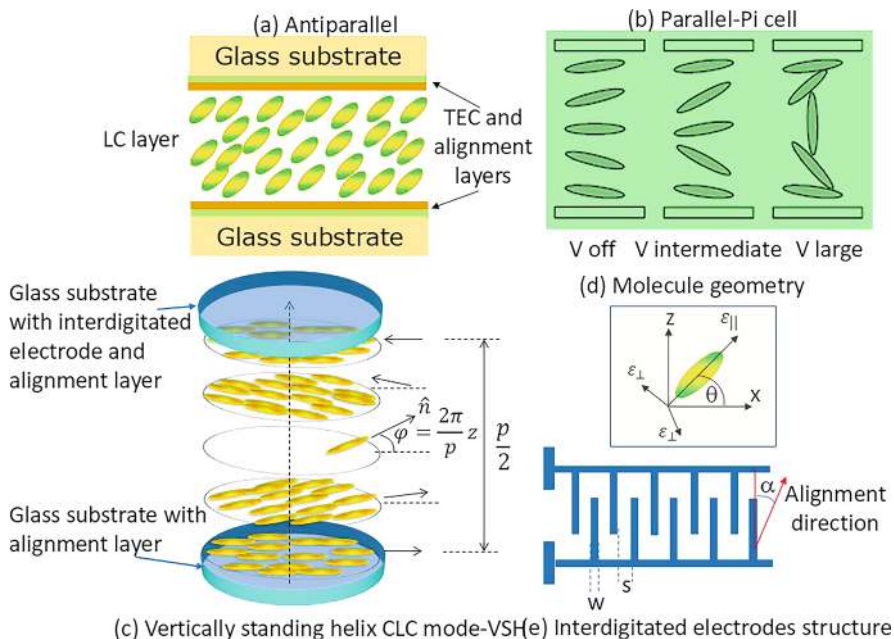


Fig. 4 Schematics illustrating some important configurations for: **(a)** typical nematic LC device in the parallel alignment geometry, **(b)** parallel alignment geometry, which gives slightly faster speed, showing also the deformed structure as the voltage increases, **(c)** vertically aligned short pitch cholesteric LC with a field applied in the plane of the substrates using interdigitated electrodes, which gives speeds in the sub-msec range in what is called the flexo-electro-optic effect, **(d)** geometry of LC principal dielectric constants, and **(e)** interdigitated electrode structure on one substrate, showing also the alignment direction at an angle usually $\alpha \sim 10^\circ$ with respect to the electrode fingers

high voltages are needed and usually, heating is required, which is not desirable in optical systems as it produces instabilities and noise, and finally increasing the number of LC elements (such as in the Lyot-based [84, 85] LC tunable filter (LCTF) configuration) makes the device bulky and lossy. A relatively faster Lyot-based approach was proposed recently with higher light throughput and more compact, however, it is suitable only for multispectral operation [86].

Nevertheless, some of these improvements are useful and their potential can be evaluated by trying further improvements for the specific PMM devices. Some resonant LC devices, which have been around for a few decades, require smaller LC layer thicknesses such as the tunable Fabry-Perot [87] or guided mode resonance filter [8]. Nonetheless, the manufacturability of these devices is not easy, their dynamic range is limited to a few tens of nm and the required LC thickness is still in the few mm range, meaning response time in the msec range. In general, resonant structures have a small dynamic range; however, some PMM structures can circumvent this problem by using the broadband nature of lossy surface waves.

Like anisotropic layers inside the waveguide, LCs anisotropy can cause coupling between the TE and TM waves. This may result in the appearance of polarization change and additional resonances at the polarization orthogonal to the incident one [88]. Nevertheless, with LCs where the optic axis is rotating in the same plane as a voltage is applied, it is possible to excite only one mode independent from the other—see analysis of this problem in our earlier article [89]. The polarization-independent modes such as nano-PDLCs and the blue phase Kerr effect can be used; although showing smaller refractive index modulation, with their highly sensitive structure, wide tuning range and large modulation depths can still be achieved. These LC phases are also faster, approaching fractions of microseconds response time. It should be noted that in PMM devices the nanoscale LC gaps allow utilizing the full potential of these fast LC phases at relatively small voltages because the Kerr-induced birefringence is proportional to the square of the applied electric field.

Ferroelectric Liquid Crystal Modes A more direct, and attractive way to reduce the LC response times is to use chiral (*) polar smectic liquid crystals. Smectic LCs are layered media. In the smectic A* phase the director is parallel to the smectic layer normal \mathbf{z} , (Fig. 5a) while in smectic C* and C_a*, the molecules are tilted at the angle θ with respect to \mathbf{z} (Fig. 5b–c). In chiral tilted smectics [14], the director makes a helix along \mathbf{z} (Fig. 5b), and in materials with a period (pitch) smaller than the wavelength of light, the average optic axis is along \mathbf{z} . Furthermore, there is a spontaneous polarization density \mathbf{P} normal to the director and to \mathbf{z} , which allows for polar azimuthal switching of \mathbf{n} about \mathbf{z} at fixed θ under the torque $\mathbf{P} \times \mathbf{E}$. The synclitic SmC* phase is ferroelectric while anticlinic SmC_a* is antiferroelectric. The following three electro-optic modes are attractive for incorporation of PMM structures.

- *Deformed helix ferroelectric mode.* In short-pitch FLCs, a field applied normal to \mathbf{z} gives a deformation of the helix, causing a tilt of the optical indicatrix in a plane normal to \mathbf{E} , cf. Figure 5b. This is the deformed helix ferroelectric (DHF) mode [90, 91]. When the period is much less than the wavelength $p < \lambda$, it behaves as a uniaxial medium, which becomes biaxial when a field is applied [92, 93]. In Fig. 5b the mode is called vertically aligned DHF to compare with the standard one where the helix is in the plane of the substrates [94, 95]. The tilt is analogue in the applied field and allows for continuous phase-only tuning. In recent years, novel DHF materials with higher molecular tilt and smaller pitch have been developed, providing faster and higher amplitude switching [40]. Moreover, as $p < \lambda$, any light scattering from the periodic structure is ruled out. Hence, in the DHF mode, the structure behaves effectively as a continuously field-controllable retarder, in a wide region before the helix completely unwinds. Color switching and optically addressed modulators were demonstrated first in reference [96].
- *Surface-stabilized FLC and AFLC modes* where the helix is unwound by surface forces, and therefore providing only binary operation, have been successfully commercialized in high-resolution microdisplays where both grayscale and color are written in the time domain. In these displays, the molecular tilt is

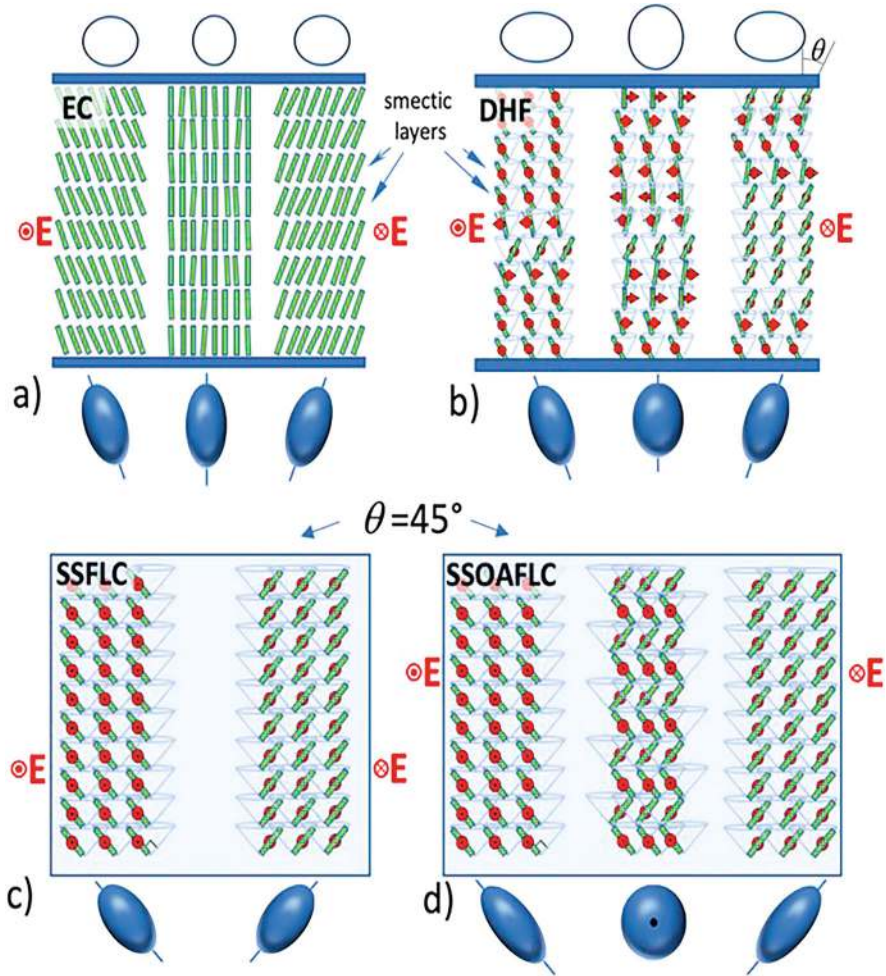


Fig. 5 Schematics of analogue (**a** and **b**), binary (**c**), and ternary (**d**) smectic modes. In the analogue EC and DHF modes the index ellipsoid (blue) rotates in a plane normal to **E** producing an effective ellipsoid (projection onto the substrate plane) depicted as empty ellipses. *NOTE: The picture is highly out of scale. The smectic layers are 2-3 nm thick, the DHF SmC* pitch is about 300 nm, and the LC layer thickness planned is usually < 10 μm . We are grateful to Prof. Per Rudquist for sharing this figure*

ideally 22.5° . For many purposes, one may focus on FLC materials with 45° tilt, which allows for pure phase-only modulation, cf. Figure 5c and d. In the antiferroelectric SmC_a^* phase the structure is anticlinic. Surface-stabilized orthoconic AFLCs [97, 98], ideally provide *three level* phase-only modulation [99], at a slightly lower speed than FLCs. Alignment of the surface stabilized ferroelectric liquid crystal (SSFLC) in a twisted-splayed geometry has been shown to reveal an analogue response and phase-only modulation [100].

- *The electroclinic (EC) effect in SmA** [101] is the fastest useful electro-optic effect in LCs, under certain conditions even providing sub-microsecond switching. This mode has the same geometry as the DHF-mode. The first fast Optically addressed spatial light modulator (OASLM) using this mode was demonstrated by the main PI [102] with a thorough investigation of its electro-optic switching characteristics [92]. The highest electroclinic switching amplitude is found in the so-called deVries smectic A* materials [103, 104].

In some photonic MTM structures, the LC layer is sometimes required to give *phase-only modulation*, for which the analogue vertical alignment FLC modes (DHF and EC) can be used using interdigitated electrodes on one of the substrates to apply the electric field parallel to the plane of the substrate (see Fig. 4e). For certain applications based on switching between two or more wavelengths, SSFLC, and orthoconic AFLCs can be explored.

Aligning the LC molecules on the surfaces of the substrates is a crucial issue in obtaining the desired device quality. All the LC tunable PMM devices reported so far mainly used mechanical rubbing and sometimes only on one surface, though no special attention was devoted to the alignment within the nanoapertures. For a device with light–matter interaction mainly occurring inside the nanogaps, a different alignment strategy should be used to obtain the desired LC director orientation and uniform defect-free structures. Since the interaction region in the waveguide case is relatively large (0.1–1 mm), the LC layer must be free of defects because scattering and losses in such a large region become significant. Recently [54], photoalignment on metasurface made of nanodisks showed some improvement over the standard rubbing technique. However, photoalignment using polymer films needs spin coating, a technique that can produce irregularities on the metasurface, particularly when the lines or disks are a few hundred nm or larger in height because of the walls and edges. This can be the reason why the dips obtained in ref. [54] are a few tens of nm wide since defects broaden the resonance and reduce its contrast. We identified three alignment strategies that need to be investigated further to resolve the problem as follows (Table 1):

- Photoalignment using nano-dimensional chalcogenide glass film:* This is based on the permanent photoalignment we discovered [105–108] a few years ago using 30–50 nm films of chalcogenide glass (As_2S_3 , As_2Se_3 , ...) deposited using physical vapor deposition. A thin film of 30–60 nm is deposited on the surface and then irradiated with linearly polarized blue light. The LC molecules on the surface tend to align along the polarization direction due to the photo-induced anisotropy on the surface. Other photosensitive materials showing high photoinduced anisotropy, which should be investigated, are a-Se and GST.
- Unidirectional surface nanostructuring using ultrashort pulsed lasers:* In this methodology, polarized femtosecond laser pulses are shone on the surface at energies just above the ablation threshold (typically few tens of pulses at 1030 nm wavelength, pulse width of the order of 100–200fs and energy of 10–100nJ). A nanograting pattern appears with the lines perpendicular to the polarization direction. We have proved this on the ITO electrode layer

Table 1 Overview of the faster LC modes

LC mode	Typical rise time	Typical decay time	Comments
Pretilt angle control	Reduces the rise time by up to 50% for small pretilt angle, the effect vanishes at high voltages	Increases the decay time by up to 30%	Can be applied with other modes, but not for all applications
Drive scheme	Hundreds of microseconds up to few msec depending on the overshooting voltage	Few msec till tens of msec, depending on thickness as d^2	Can be applied with all other modes
Dual frequency LCs	Few hundreds of microseconds depending mainly on the LC material	>500 μ s up to few msec, varies with thickness as d^2	
Nano-polymer dispersed LC (Nano-PDLC)	From sub-msec up to ten msec, depending on the LC used, the polymer matrix, voltage applied, and thickness of the cell	Few msec till hundreds of msec, depend mainly on the composite materials and thickness as d^2	
Anti parallel NLC	Few msec till tens of msec, decreases as $1/V^2$	Tens till hundreds of msec, varies with thickness as d^2	
Blue phase	Sub-msec, can be reduced to 100 μ s if doped with orientation polymer-stabilizing dopants	Sub-msec	Have narrow temperature range
Twisted nematic	Few msec till few tens of msec, decreases as $1/V^2$, and depends on thickness d^2 and the LC molecules	Tens of msec, varies with thickness as d^2	
Ferroelectric LCs	Can reach down to microseconds even at low voltage if the pitch is much smaller than the cell thickness	Decay time can be shorter than rise time and reaches down to few microseconds	Operate under DC voltage
Electroclinic LCs	Reaching down to sub-microseconds	Larger than the rise time by a factor of 2	Strong temperature dependence
Flexoelectro-optic effect in short-pitch cholesterics	Few microseconds	Few tens/hundreds of microseconds (\sim ten times slower than rise time)	Optic axis rotates in a plane perpendicular to the applied field
Nanosecond EMOP mode	Nanoseconds	Tens of nanoseconds	Based on electrically induced modification of the order parameters (EMOP) of NLCs rather than on the Frederiks reorientation of \vec{n}

showing excellent molecular alignment along the nanotextured lines [109, 110]. Nanostructuring with ultrafast laser is a well-established methodology on a large group of materials.

- (iii) *Oblique angle deposition of oxides*: This type of deposition at a large angle ($\sim 60^\circ$) produces nano-columns on the surface oriented along the same direction, which causes the LC molecules to align along them. SiO_2 films and other materials of 20–50 nm thickness were shown to give good alignment [111].

3 PMMs for Energy Applications

3.1 Introduction

The need for efficient energy conversion is very necessary to meet the increase in environmentally friendly, renewable energy requirements. From the past decade we have seen many techniques to improve the energy efficiency by utilizing the advancements in the field of plasmonics and various fabrication [112–116]. Solar energy conversion technique paves the way for various applications including solar absorption, water desalination, distillation, wastewater management, etc. [117–119]. However, the main snag in developing solar absorbers is to generate strong spectral selectivity, near-perfect solar absorption, angular independence, and polarization independence. Achieving near-ideal solar thermal energy conversion requires absorbers that exhibit near-perfect absorption from the ultraviolet (UV) to the near-infrared (NIR) regions while minimizing mid-and-far infrared (IR) emissions. Traditional PMM's rely on localized surface plasmon resonance (LSPR) at metal/dielectric interfaces [119, 120], which lacks the broadband operating wavebands. Recent advancements have demonstrated that having impedance matching, slow light PMMs can greatly enhance the broadband spectral absorption. Metamaterial nanostructures, particularly those utilizing metal/dielectric stacks have shown promise in realizing broadband high absorption. These structures, known as hyperbolic metamaterials (HMM), can achieve high absorption efficiencies across a wide spectral range [121–123].

3.2 Design Physics of Metamaterial Photothermal Converters

Metamaterials can either be of periodic or aperiodic structures that are subwavelength, enabling the device to manipulate light in a very peculiar way compared to naturally occurring materials. This property arises solely due to the structural composition rather than material composition. For photothermal applications, metamaterials can be designed to have high absorption across a broad range of wavelengths. This can be achieved by various techniques such as:

3.2.1 Localized Surface Plasmon Resonances (LSPR) PMM

LSPR can significantly enhance the local electromagnetic field, leading to increased absorption of light. Earlier PMM absorbers were developed using LSPR phenomena. The excitation of LSPR at metal/dielectric interfaces results in strong absorption peaks, which can be tuned by adjusting the size, shape, and material composition of the nanostructures. In order to attain broadband absorption a simultaneous excitation of magnetic and electric resonances resulting from localized surface plasmon resonance at metal/dielectric interfaces is required [124, 125]. In one of the promising works, a near-ideal total solar-thermal conversion efficiency of up to 90.32% at 373.15 K was reported for solar absorbers, with an ideal efficiency of 95.6% [125]. According to the results obtained, it shows that geometric parameter adjustment can sustain efficient solar thermal conversions at greater operating temperatures. The structure has shown near perfect absorption at broader angle range of up to ± 60 degrees, hence the absorber has a huge potential to be used for solar energy harvesting applications irrespective of the incident polarization. There have been published works that combine the additional MM layer with these multilayer topologies. One such design has shown broadband ideal absorption in the solar spectrum region [126]. The design of the ultra-wideband (UWB) ideal solar energy absorber is based on a Ti ring with a $\text{SiO}_2\text{-Si}_3\text{N}_4\text{-Ti}$ thin film layered structure. This absorber has a total thickness of 620 nm and a basic structure (in this case a ring shape), making it relatively straightforward to build. It can also overcome the constraints of typical solar energy absorbers, such as poor average absorption rate and perfect absorption bandwidth. The absorptivity at 3683 nm is greater than 90% in the 300–4000 nm range; the average absorptivity is 95.0%, and the weighted absorptivity under air mass (AM) 1.5 is 97.0%. Perfect absorption values of 99.9% and 99.7% were specifically attained at wavelengths of 483 and 2380 nm. The metal used in this work is very ideal for the photothermal conversion studies as Ti is very stable at room temperatures and its boiling point is as high as 1668°. Similar to typical lossy metals, Ti also has large dielectric loss term, which also assists in the absorption efficiency (Fig. 6).

Having a thick layer of Ti at the bottom of the design ensures that almost all the EM signals are blocked from passing through the structure. This design technique has become quite common in almost all the PMM absorbers reported recently, as it eliminates the possibility of transmission through the device. It is observed that absorption in the visible spectrum is caused by the resonance inside the Ti ring while the absorption at the NIR region is caused largely by the resonance in the outer ring regions.

3.2.2 PMM Based on Dipole Interaction

In metamaterials, magnetic polaritons can be excited to achieve high absorption over a broad range of wavelengths. Magnetic polaritons are hybrid quasiparticles resulting from the strong coupling between electromagnetic waves and magnetic

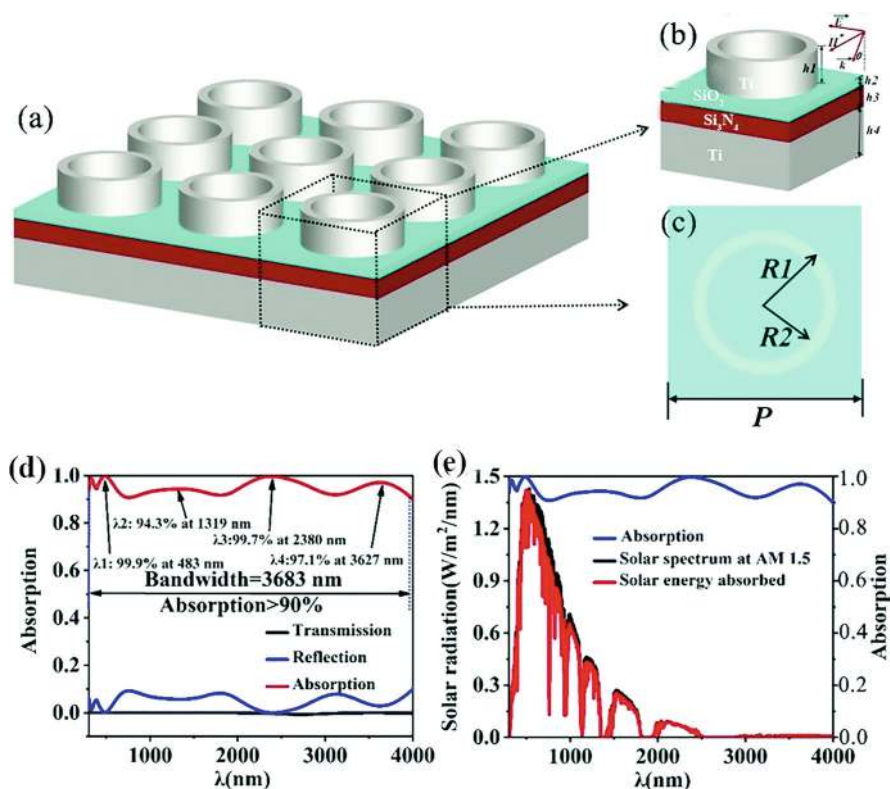


Fig. 6 (a)–(c) 3-D schematic diagram of the UWB solar energy absorber. (d) Comparison of the solar energy absorption of the standard solar radiation spectrum AM 1.5 (black line) and the UWB solar energy absorber under AM 1.5 (red line). (e) spectrum of the solar energy absorber. Reproduced from Ref. 126 with permission from the Royal Society of Chemistry

dipole excitations in a material. These polaritons can be excited in metamaterials through specific resonant structures, which support magnetic dipole resonances. This phenomenon will usually occur at metal/dielectric interfaces as well as on the surface of the PMM metal structures. Surface currents formed across the structure will define the excitation of magnetic or electric dipole formation.

As mentioned before for every metal/dielectric PMM device, it is very common to have a thick block of EM signal blocking material placed on it to block the transmission of light through the device. For HMMs, increasing the layers of metal/dielectric stack will eliminate the need of a metal block. Having layers of meta-atoms arranged in parallel or perpendicular to the incident light, it is possible to create dipole effect in the PMM structure. When combined with multi-material MM layers, it was shown that both electric and magnetic polaritons can be excited simultaneously to generate broadband absorption [127].

Here a three-layer structure with an array of nano-cylinders made up of two different materials (Ti and Cr) is chosen to act as the meta-atom layer. Al_2O_3 is chosen as the spacer between the top layer and the bottom reflective thick Au metal layer. There is an additional brown carbon layer added between the nano-array and dielectric spacer to enhance the absorption.

It is observed that the absorber presents a good absorption performance and wide absorption bandwidth in the wavelength range of 300–1200 nm, which accounts for 82.74% of solar energy. Absorber has been found to have strong absorption capabilities and a broad absorption bandwidth within the wavelength range of 300–1200 nm, which is responsible for 82.74% of solar radiation. In the visible spectrum, the absorbers made of various materials show an absorbance of about 100%. Circulating current is shown in Fig. 7(ii) (a) at the interface between the Cr nano-cylinder and the Al_2O_3 layer at the wavelength of 300 nm, the currents inside of the two nanostructures are in opposite directions, leading to the fact that there is a clockwise circular current flow between these two nanostructures. Meanwhile, there is an anticlockwise current flow within the carbon layers. All these current flows in turn create the strong magnetic field explaining the large absorption in the visible region. Similarly, for other wavelengths 900 nm and 1200 nm, there is current flow unidirectionally indicating the weaker electric and magnetic plasmonic resonance, which explains why absorbance is reduced with the increase in the wavelength. Hence it can be noted from results that the formation of magnetic and electric polaritons is due to the peculiar patterning of the metal layers. Similar technique is utilized in many of the THz and GHz MM device studies published earlier. This is due to the fact that for most of such cases, there are metal/dielectric patterning done on the surface to create circulating surface current according to the shape of the pattern.

3.2.3 Hyperbolic PMMs

Absorption properties of hyperbolic PMM's (HPMMs) are primarily determined by their ability to support high-k modes, which are surface plasmon polaritons (SPPs) or bulk plasmon polaritons (BPPs) that propagate along the interfaces of the material. These modes lead to enhanced electromagnetic field confinement and, consequently, increased absorption. The high density of photonic states in HMMs also contributes to their superior absorption characteristics. HMMs can achieve near-perfect absorption over a wide range of EM spectrum ranging from mm waves to nm range [128]. For instance, absorbers based on metal/dielectric multilayer structures or self-assembled metal nanoparticles often exhibit high thermal radiation in the mid- and far-IR regions, reducing their total solar-thermal energy conversion efficiency. These structures are a good candidates for water desalination. Porous plasmonic absorber can float naturally on water surface, efficiently absorb a broad solar spectrum (>96%), and focus the absorbed energy at the surface of the water to enable efficient (~90%) and effective desalination. In the study conducted by

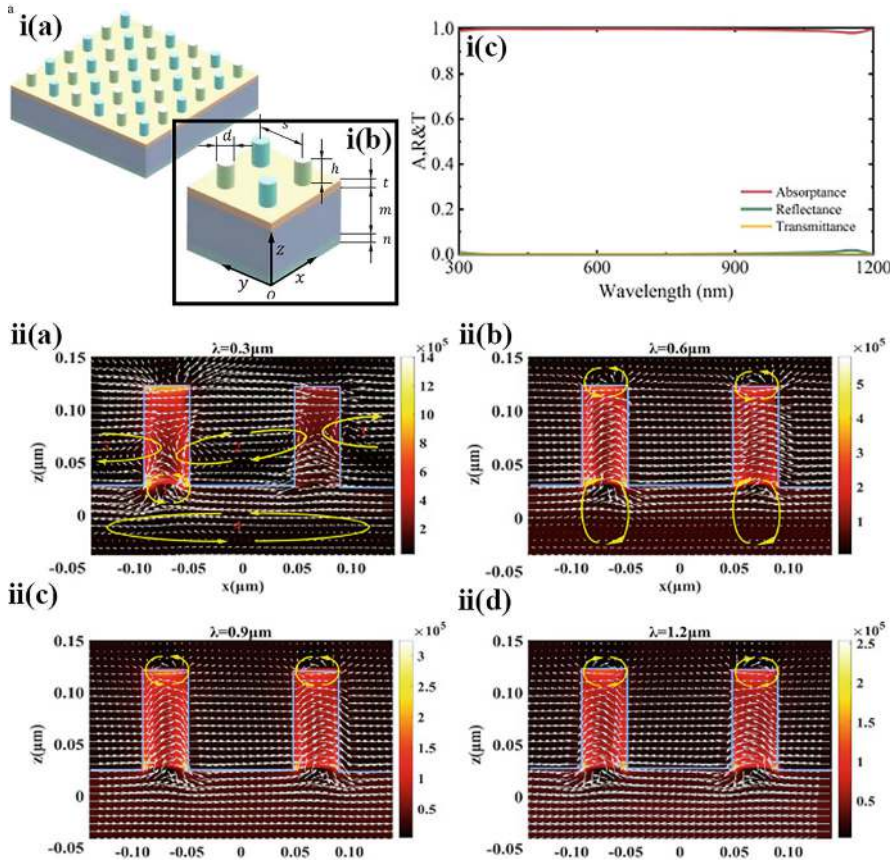


Fig. 7 (i) 3D design parameters of the PMM absorber (a) schematic of the PMM array. (b) unit cell of the absorber with geometric parameters, the height of the nanostructures is denoted by h and their diameter is d . The thicknesses of the Al_2O_3 layer, carbon layer, and Au layer are represented by t , m , and n , respectively ($n = 100$ nm, $m = 5000$ nm, $t = 30$ nm, $d = 40$ nm, $h = 100$ nm, and $s = 140$ nm.). (c) absorption spectra for the designed structure (ii) The current density vector distributions of the absorber on the plane of $y = -70$ nm. (a) Current density vector distribution at 300 nm. (b) Current density vector distribution at 600 nm. (c) Current density vector distribution at 900 nm. (d) Current density vector distribution at 1200 nm. Reproduced from ref. [127] with permission from Elsevier

Zhou et al. [129]. according to the study conducted by the authors, aluminum-based porous structure has shown larger durability and efficiency in water desalination. Design consists of nanoporous anodic aluminum oxide membrane and aluminum nanoparticles aligned on the side walls of aluminum oxide membrane. These closely packed nanoparticles create a strong plasmon hybridization effect and high-density surface plasmon resonances, which result in broadband absorption. The spontaneous formation of an oxide layer on aluminum nanoparticles (NPs) serves a dual purpose.

Firstly, it acts as a protective barrier, enhancing the particle's stability without requiring additional protection methods. Secondly, this oxide layer substantially alters the dielectric properties of the surrounding environment. This change in dielectric characteristics results in an extended absorption bandwidth, particularly toward the infrared (IR) spectrum.

3.2.4 Interfacial Photothermal Converters

Perfect absorber PMM can be an ideal candidate for interfacial photothermal conversion. These structures can be used to implement the water desalination process very effectively as most of the EM wave gets absorbed at the surface of the metamaterial layer. Though these structures work on the same basic principle as impedance matching, typical devices have thermal loss and deterioration over the prolonged period of use. In our lab we have developed a simple PMM structure for the interfacial photothermal conversion [130]. The structure consists of a typical metal/dielectric/metal layer, where the bottom metal layer will act as a reflector. A spacer made up of Si_3Ni_4 is used as a spacer. While considering the design we have chosen Si_3Ni_4 as a spacer since it is a good candidate to absorb IR range EM waves. Also, Silicon nitride is chemically stable and compatible with various fabrication processes, making it a reliable material for integrating into complex photonic and metamaterial structures. We have chosen tungsten(W) as the metal bottom layer as well as top MM patterning. A simple to fabricate mesh structure is designed with a thickness of 7 nm. These lines are designed in such a way that asymmetry is created in the mesh to facilitate broadband absorption. The period of the unit cell is 500 nm, the thickness of the bottom layer W is 170 nm, and the spacer layer thickness is 110 nm (Fig. 8).

For the IR region EM wave oscillates between the top pattern and the bottom layer while in the visible range, there is a significant amount of field localization at the surface and edges of the design. This enables the device to be used as a near-perfect interfacial photothermal converter.

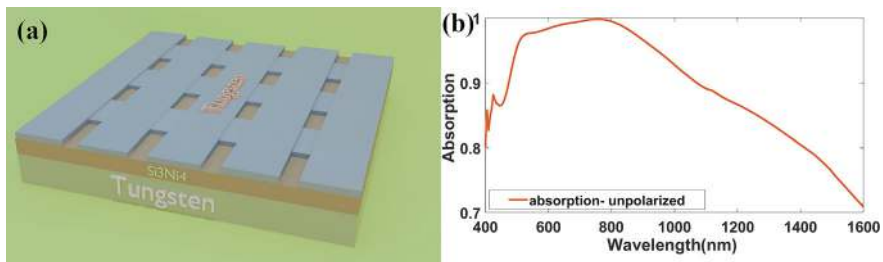


Fig. 8 (a) is the unit cell schematic of the designed PMM device. (b) absorption spectra for the unpolarized light from visible to SWIR region

3.3 Challenges and Future Directions

Even if metamaterials have a lot to offer in terms of photothermal conversion, problems still need to be solved. These include the complexity of design, the requirement for scalability, and the material's resilience at elevated temperatures. Research in the future is probably going to center on creating new materials and frameworks that can get over these obstacles. For instance, because all-dielectric metamaterials do not experience the same losses as structures made of metal, researchers are looking at using them. Furthermore, efforts are still on to create metamaterials that can adapt their properties dynamically under changing environmental circumstances. Finally, metamaterial photothermal converters are a major development in solar energy collection technology, water desalination, etc. They are excellent prospects for a variety of applications due to their near-perfect absorption, spectrum selectivity, and great thermal efficiency. With further study addressing issues related to durability, fabrication, and system integration, metamaterial-based solar thermal technologies have the potential to become more significant components of renewable energy systems.

4 PMMs for Sensing Applications

In the above sections, we have seen that using metamaterial surface one can easily modulate the light properties and can be used to concentrate the electric field for energy applications. In addition, the metasurfaces provide the feasibility to significantly tune the resonant electromagnetic (EM) spectra, which are influenced by the surrounding environment. Due to these resonant properties, the refractive index (RI) of nearby biomolecular analytes can be assessed by observing changes in the scattered output spectra. Therefore, designing sensitive meta atoms (MAs) for specific target wavelengths and configurations is crucial. Additionally, photonic metamaterial (PMM)-based RI sensing platforms offer several advantages over traditional optical biosensors including surface plasmon resonance (SPR), lossy mode resonance-based biosensors [131–134]. First, since RI changes are detected through macroscopic optical responses, primarily reflection or transmission of focused input beams, PMM-based sensors generally provide better fabrication tolerance and signal stability compared to SPR-based sensors. Second, the periodic arrangement of photonic unit cells leads to reduced radiative damping and higher quality factors, facilitated by phenomena such as plasmon-induced transparency and Fano resonances [135]. Finally, the functionality of a single nanophotonic RI sensor can be enhanced by incorporating PMMs. Carefully designed arrays of various photonic unit cells or supercells can produce multiple resonances and broadband slow light effects, which are difficult to achieve with SPR-based sensors. In addition, by analyzing interference between multiple beams, anisotropic scattering, and dispersive responses from certain EM devices, fundamental properties of incident

EM waves can be detected and analyzed. Key characteristics of interest for PMMs include polarization and spectral composition, which are commonly analyzed using commercial bulk-optic devices such as polarimeters and spectrometers. As the demand for compact and integrated light-sensing components in electronic devices has surged, PMMs are emerging as promising platforms for implementing these functions in a compact and lightweight form [18, 136]. In this section of the chapter, we will discuss a few examples of using PMMs for sensing applications showing their potential for real-world applications along with challenges and future directions.

4.1 Surface-Enhanced Raman Scattering Using PMMs

The inelastic scattering of electromagnetic waves with the molecules produces the signature of molecular vibrational modes that occur due to the emission of new photons through a process called Raman scattering. It shows the broad range of advantages (i) unique fingerprint signature of the analyte causing high selectivity, (ii) easy sample preparation method, (iii) no signal interference from the water, (iv) single molecule detection, (v) feasibility of the multiplexed sensing with a single laser beam, and (vi) high throughput and point of care (POC) applicability by using commercially available portable Raman microscope. Raman scattering typically produces very weak signals due to low scattering cross-section ($1/10^{12}$), which makes it challenging to detect with standard experimental methods. To address this challenge, Surface-Enhanced Raman Scattering (SERS) has been developed as a technique to significantly amplify the Raman signal. SERS relies on two primary mechanisms to achieve this enhancement: electromagnetic enhancement and chemical enhancement [137]. In the first method, the enhancement of the electromagnetic field at the nanometallic surface is utilized to improve the signal intensity up to the orders of 10^8 . This enhancement occurs when the wavelength of the incident light matches with the resonance wavelength corresponding to the Localized Surface Plasmon (LSP) resonance of the nanometallic substrate. LSP resonance refers to the collective oscillation of electrons at the surface of metallic nanoparticles, which intensifies the local electromagnetic field. The geometry of the nanoparticles plays a critical role here such as nanoparticles with sharp edges or tips can produce particularly strong SERS signals because these geometrical features enhance the local electromagnetic field more effectively [138, 139]. The later factor, which plays a significant role for enhancing the Raman signal is chemical enhancement. This mechanism involves interactions between the metal surface and the analyte molecules and occurs due to the charge transfer or the formation of chemical bonds between the metal and the molecules being studied. These interactions increase the polarizability of the molecules, which enhances the Raman scattering signal [140, 141]. Essentially, the nanometallic surface can modify the electronic properties of the analyte molecules, making them more responsive to the incident light. Numerous studies have been reported in literature utilizing specially designed PMMs for

enhanced electromagnetic field provided SERS-based applications [135, 142]. In addition, configurations that enable coupling between extended surface plasmons (ESP) and localized SP (LSP) can result in even greater signal enhancements. Studies have demonstrated that certain geometries, such as those with closely spaced metal structures or nanoparticles with specific shapes, can significantly boost the Raman signal through this coupling effect [143, 144]. A simplified model for understanding Raman scattering enhancement involves calculating the field enhancement near a single isolated particle. This model provides a way to estimate the total enhancement factor by multiplying the enhancements of both the incident and scattered fields. An example of this calculation for a SERS enhancement factor per molecule can be found in the supplementary materials of Ref. [144]. For a comprehensive overview of current developments and future directions in SERS technology, refer to the recent review in Ref. [138]. This review discusses the latest advancements in the field, including new materials, techniques, and applications. A few studies using PMMs for SERS applications will be discussed in Sect. 4.3.

4.2 Surface-Enhanced Fluorescence (SEF) Using PMMs

Like SERS, SEF is one of the important applications where enhanced electromagnetic field is used to improve the fluorescence intensity of the fluorophore when kept near PMMs. Fluorescence is a phenomenon observed in molecules known as fluorophores, where the molecular structures are capable of absorbing light at one wavelength (the excitation wavelength) and emitting it at a longer wavelength (the emission wavelength). When fluorophores are placed near metallic nanostructures, their fluorescence properties can change significantly. Appropriate selection of fluorophore is very important to ensure that optical absorption of the fluorophore and metal overlaps. The energy transfer between fluorophore and enhanced electromagnetic field due to PMMs is dominated by dipole–dipole interaction as follows if the distance between the PMMs and the fluorophore lies within 1–10 nm, the non-radiative localized field of the plasmon dipole can excite that of fluorophore [145, 146]. In addition, the lifetime of the excited state can be shortened in the vicinity of the PMMs. This reduction occurs because the metal can facilitate faster energy transfer processes, such as enhanced radiative decay, making the fluorophore return to its ground state more quickly. This phenomenon is also called Förster resonance energy transfer (FRET). Understanding and controlling these interactions between fluorophores and PMMs are crucial for applications in fields such as biosensing, imaging, and molecular detection, where fluorescence signals are used to obtain detailed information about molecular interactions and concentrations. In the next sections, we will be discussing a few studies reported in literature applying PMMs for SERS- and SEF-based sensing applications.

4.3 Studies Reported Using PMMs for Sensing Applications

4.3.1 Ag Nanosculptured Thin Films (nSTFs) for SERS Applications

Nanosculptured thin films (nSTFs) are the group of materials prepared by the oblique or the glancing angle deposition technique in forms of nanocolumns, nanoscrews, nanozigzags, and many other nanoshapes. Silver (Ag) nSTFs exhibit remarkable localized plasmonic properties that make them a promising substrate for enhanced spectroscopies such as SERS, SEF, etc. [147, 148]. These enhanced signals strongly depend on the morphological nature of n-STF metasurfaces such as nanorod diameter, height, pore size, etc., which depends upon the substrate properties, preparation conditions, etc. Their long-term stability in the water environment makes them suitable candidates for biosensing in water. A nanobiosensor chip leveraging surface-enhanced Raman spectroscopy (SERS) on Ag nSTFs was developed to detect *Escherichia coli* (*E. coli*) bacteria at concentrations as low as a single bacterium [149]. The sensor was based on capitalizing highly enhanced plasmonic properties of silver nSTFs on a silicon substrate, significantly amplifying the Raman signals, as verified with adsorbed 4-aminothiophenol molecules. To ensure specificity, T-4 bacteriophages were immobilized on the sensor's surface, enabling the targeted capture of *E. coli* bacteria. Figure 9 represents the used Raman setup and the corresponding enhanced Raman signal with varying bacterial concentrations on the Ag n-STF substrate.

Results shown in Fig. 9 revealed that the sensor facilitates rapid, accurate, and stable detection of *E. coli*, even at ultralow concentrations, down to the level of a single bacterium within a 10 μ l sample volume. This level of sensitivity and specificity positions the sensor as a powerful tool for detecting *E. coli* in various applications, offering both precision and reliability.

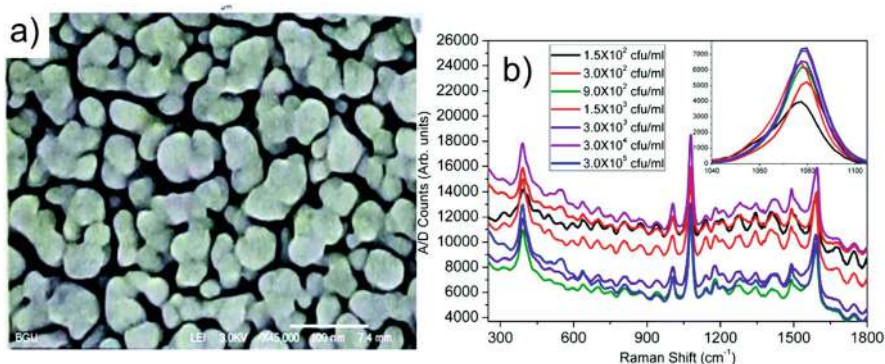


Fig. 9 (a) SEM image of fabricated n-STF substrate (top view), and (b) SERS spectra with varying *E. coli*. Concentration over the Ag n-STF substrate. (Reproduced with permission from Ref. [149])

4.3.2 LSPR-SPR Coupled Plasmonic Metasurface for SERS Applications

As mentioned earlier, SERS is usually achieved when the Raman active molecule is brought near metal nanostructures-mediated plasmonic hot spots, it enhances the Raman signal up to a million times (even more, depending on nanostructure morphology). In addition, the signal can further be enhanced when the plasmonic nanostructure is kept near the metallic thin film causing the coupling of the propagating surface plasmon resonance (SPR) and localized SPR (LSPR) [150–152]. For example, in a study reported by Srivastava et al., an approach is demonstrated to create extremely high electromagnetic hot spots using a configuration that couples propagating (or extended) and localized SPR [144]. In the study, conventional Kretschmann-Raether configuration is employed as shown in Fig. 10.

The metasurface chip is fabricated by spin coating of Au nanoparticle over the Ag (silver) coated glass surface that enables the coupling the extended plasmon wave due to Ag thin film with localized plasmons in gold nanoparticles that are dispersed on top of the silver film. When the extended plasmon wave interacts with the gold nanoparticles, it excites localized plasmons within them. This interaction between the extended and localized plasmons leads to a substantial increase in the electromagnetic field, creating the extremely high hot spots necessary for enhanced sensing. A critical factor in achieving maximum enhancement is the interparticle gap—the distance between neighboring gold nanoparticles. The study highlights that the SERS enhancement is highly dependent on this gap ensuring the generation of the strongest possible hot spots. To test the SERS efficacy of the proposed configuration, a monomolecular layer of 4-aminothiophenol as a test molecule is placed between the silver film and gold nanoparticles. Figure 4(a) shows the electromagnetic enhancement with respect to interparticle gap while 4(b) represents

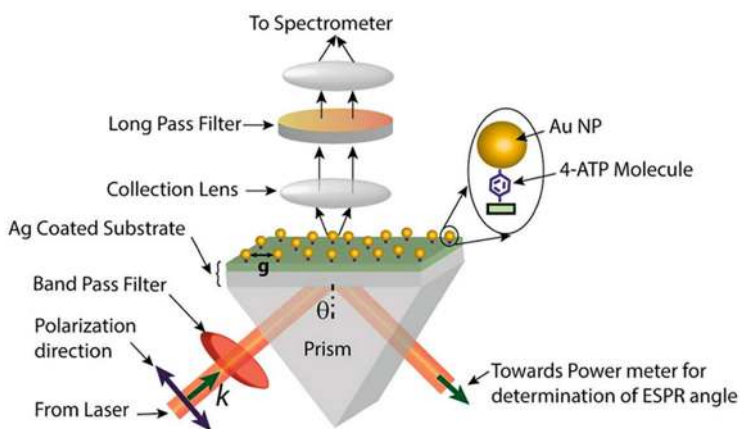


Fig. 10 Schematic of the experimental setup for ESP-LSP coupled metasurface. (Reproduced with permission from Ref. [144])

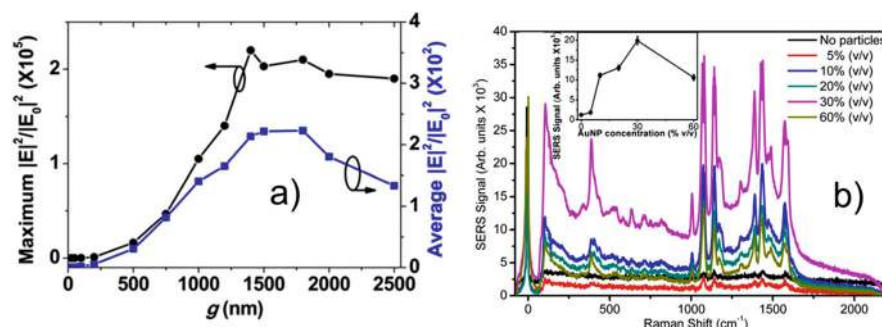


Fig. 11 (a): Maximum electric field intensity vs. interparticle gap of optimization of ESP-LSP enhancement and (b) SERS spectra obtained for 4-ATP biomolecules with varying nanoparticle concentrations over Ag surface. (Reproduced with permission from Ref. [144])

the SERS spectra obtained for 4-ATP molecule using varying concentrations of Au nanoparticles over the Ag surface (Fig. 11).

From Fig. 4b, it is evident that an extraordinary SERS enhancement factor of the order of 10^{10} per molecule was found allowing for the detection of extremely low concentrations of molecules, which is vital for sensitive analytical techniques. The study's findings have broad implications beyond just SERS. The ability to create ultrahigh electromagnetic hot spots can enhance the performance of optoelectronic devices, such as solar cells and photodetectors, by increasing their interaction with light. Additionally, this technology could be applied in energy systems, where plasmonic enhancements might improve the efficiency of energy conversion and storage devices, such as in plasmon-enhanced photocatalysis. In continuation, several studies have been reported to develop plasmonic metasurfaces leveraging the benefits of extended surface plasmons and localized surface plasmon coupling for metal enhanced spectroscopies and their applications for sensing.

4.3.3 Self-Referenced Refractive Index Sensor Using Thin Dielectric Grating on Thin Metal Film (TDGTMF) Metasurface

Recently, our group has been pioneering a self-referenced PMM, featuring a thin dielectric grating with a thickness of less than 200 nm atop a thin metal film measuring under 50 nm [153–155]. These studies highlighted that employing a very thin metallic grating, in the range of approximately 20–40 nm, can significantly enhance optical transmission, resulting in the emergence of two distinct transmission peaks [156]. The TDGTMF geometry, as illustrated in Fig. 12, was found to support the excitation of two distinct optical modes [153, 154]. The first mode arises from the guided mode resonance induced by the dielectric grating. The observed dip in the reflection spectrum, rather than a peak, is attributable to the presence of the

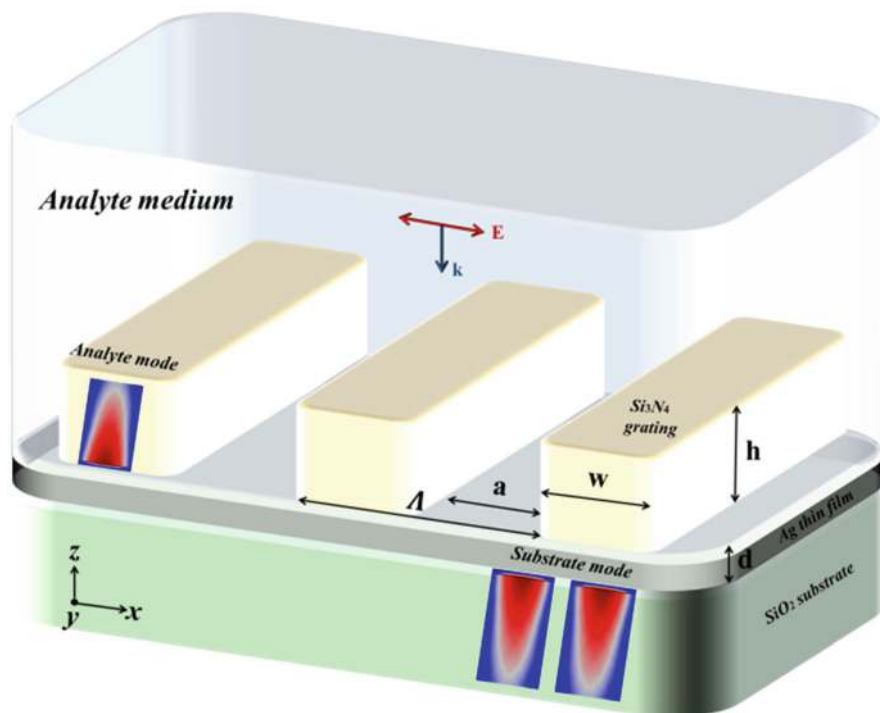


Fig. 12 Diagram of the self-referenced RI sensor utilizing the TDGTMF geometry. (Reproduced with permission from Ref. [4])

metal film beneath the grating. This mode predominantly manifests in the analyte medium and is referred to as the analyte mode. In contrast, the second optical mode is the ESP mode, which is excited at the interface between the metal film and the substrate, known as the substrate mode [154, 155]. Simulations of field distributions reveal how the presence and behavior of these fields relate to the sensitivity of each resonance to changes in the refractive index (RI) of the surrounding material. Since the substrate mode is minimally sensitive to the RI of the analyte, it can serve as a reference for detecting changes in the analyte RI. This is illustrated in the reflection RI- λ map of the TDGTMF geometry, with a grating thickness of $h = 175$ nm and a metal film thickness of $d = 40$ nm (see Fig. 13a). Notably, as the analyte RI increases, the substrate mode begins to diminish and nearly vanishes when the analyte RI approaches the RI of the SiO₂ substrate (1.443–1.445 within the specified spectral range) [153]. The substrate mode, which has a greater penetration depth compared to the analyte mode [154, 155], is associated with localized resonant surface plasmon (LRSP) excitation, making it suitable for detecting larger biological entities such as cells and bacteria. The thickness of the metal film plays a crucial role in the excitation of the substrate mode (Fig. 13b).

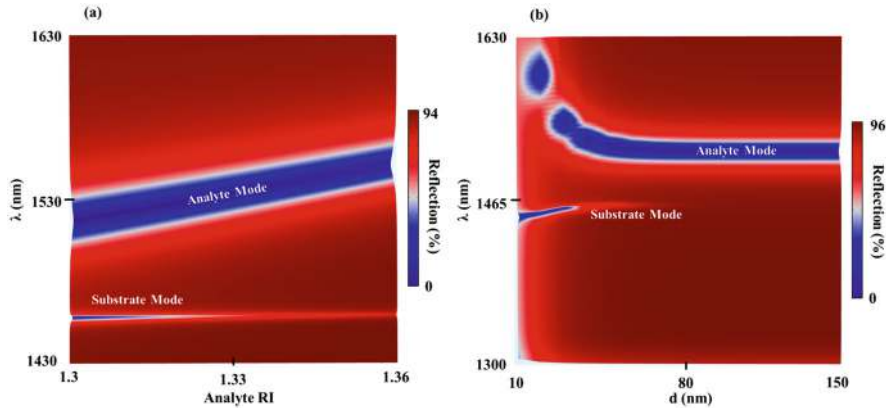


Fig. 13 (a) Reflection map of analyte RI vs. wavelength (λ) for the TDGTMF geometry with a grating thickness $h = 175$ nm and a metal film thickness $d = 40$ nm. (b) Reflection map of grating thickness d vs. wavelength (λ) with a grating thickness $h = 175$ nm. Simulations used TM-polarized light at normal incidence, applied to a Si_3N_4 grating with a periodicity $\Lambda = 1000$ nm and grating spacings of 450 nm in both (a) and (b). Water and SiO_2 were used as the superstrate (analyte) and substrate materials, respectively. (Reproduced with permission from Ref. [153])

This work was then utilized to achieve multimodal sensing using thin dielectric grating by optimizing the metallic grating properties for desired applications like for surface-enhanced fluorescence (SEF) and SERS, the resonance wavelength should match with the laser wavelength used. The grating was fabricated using e-beam lithography method and utilized for SEF/SERS applications as follows:

To estimate SEF enhancement, firstly, fluorescent signal was measured using a spectrometer. However, capturing fluorescence from granules on the sample proved challenging because the beam covered only part of the grating, potentially introducing noise. To address this issue, a fluorescent microscope was used to obtain an image of a cleaner area of the sample, avoiding granules (see Fig. 14a). This area was selected (marked by the blue rectangle in Fig. 14a) and converted into a 2D gray-level image (Fig. 14b). The 1D gray-level plot along the red dashed line in Fig. 14c showed no saturation, ensuring reliable SEF enhancement estimation. Although the microscope (50 \times magnification and 0.8 numerical aperture) did not use polarizers or a single illumination angle, the captured image qualitatively demonstrated the reflecting grating's SEF potential. The fluorescent signal was about an order of magnitude higher in the grating areas compared to the spaces, with the field also present within the grating spaces, as simulations indicated. Conversely, the signal in off-grating areas was much lower, exceeding a two-order magnitude difference compared to the grating lines. Note that due to structural imperfections, the EF (enhancement factor) varied depending on the fluorescent signal location, as seen in Fig. 14.

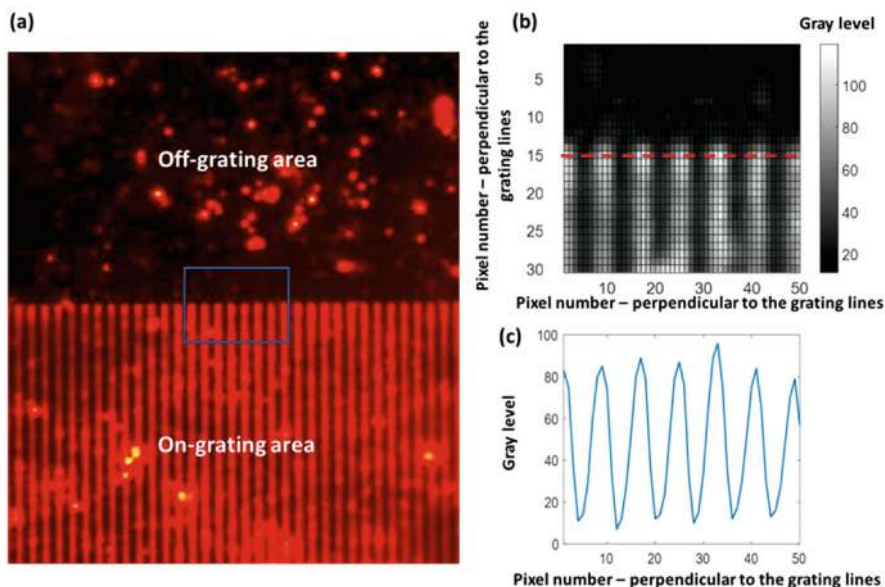


Fig. 14 : (a) Fluorescent image of the structure. (b) 2D gray-level map of the area highlighted by the blue rectangle in (a). (c) 1D gray-level profile along the red dashed line shown in (b). (Reproduced with permission from Ref. [157])

To demonstrate multimodal sensing, SERS measurement was also studied in the Ag grating. It is worth noticing SERS measurements on the same chip in air due to a lack of resonance at 785 nm (laser wavelength). Using a higher RI medium could achieve resonance wavelength, matching with the laser wavelength. In addition, it may also be noted that although a medium with a higher refractive index could create a resonance at 785 nm, this approach was not pursued due to the sensitivity of Ag to water and its tendency to oxidize. Consequently, an Au grating was fabricated with parameters shown in the atomic force microscopy (AFM) images in Fig. 15a. The AFM images indicate that the grating period Λ , groove width w , and thickness h were kept as approximately 720 nm, 340 nm, and 215 nm, respectively, with a wall angle of about 50° . The reflection spectrum in Fig. 15b shows a resonance at 794 nm, broad enough to overlap with the 785 nm laser, making it suitable for SERS. Figure 15c compares SERS signals from 4-aminothiophenol (4-ATP) on a flat Au film (blue curve), an Au grating on Au film (red curve), and Ag sculptured thin films (STF) (green curve). A 4-ATP monolayer was used in all cases due to its known self-assembly into a single layer on metal surfaces at low concentrations ($<1\%$ in ethanol or methanol).

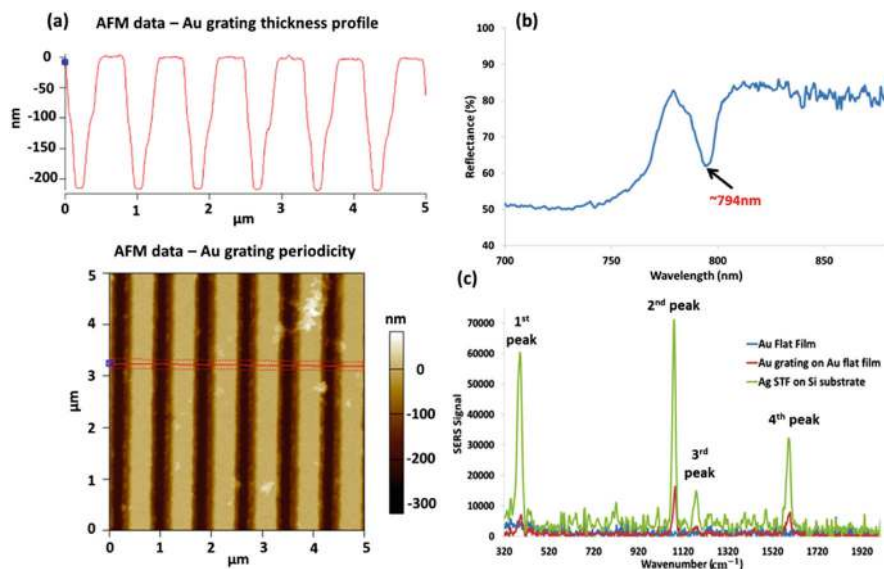


Fig. 15 (a) Atomic force microscopy (AFM) images of the fabricated Au grating. (b) Reflection spectra of the Au grating on an Au film. (c) Comparison of SERS signals: 4-ATP monolayer on a flat Au film (blue curve), 4-ATP on an Au grating on an Au film (red curve), and 4-ATP on Ag-STF on a Si substrate (green curve). (Reproduced with permission from Ref. [157])

4.3.4 Two-Dimensional Metallic Grating-Based PMM for Multimodal Sensing

In previous studies, the subwavelength grating has shown a great potential for designing sensors for multimodal sensing for realizing SERS and SEF. However, these gratings suffer from higher variability as affected by several parameters such as ununiform surface, polarization dependent with respect to incident light, ambient temperature, etc. Among these mentioned factors, to eliminate the first two factors, our group has also introduced 2-D Ag grating with Au nano cubes on top of it [158]. The 2D structure eliminates the polarization dependency of the incident light, ensuring polarization-independent SERS, hence higher reproducibility along the periodic substrate gives ultrahigh SERS enhancement due to coupling between localized and extended plasmons, while its uniform surface minimizes signal variability. The substrate is designed using the finite element method (FEM) to achieve similar enhancement for both TE and TM polarized light. The chip is fabricated using electron beam lithography and characterized for surface-enhanced fluorescence (SEF) and SERS using R6G as the target indicator molecule. Figure 16 shows the schematic of designed chip and corresponding curve depicting the overlap of resonance dip wavelength and laser wavelength.

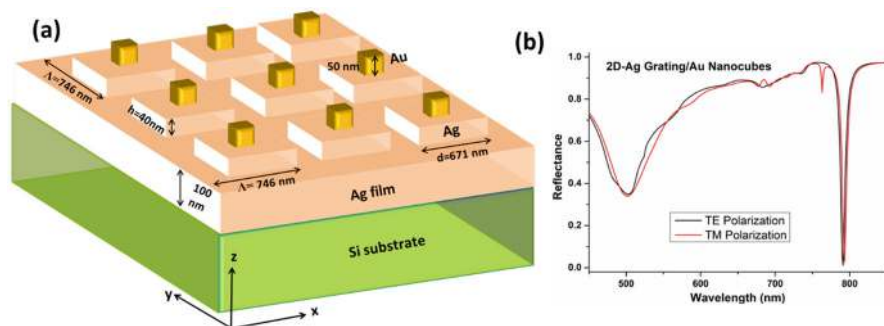


Fig. 16 (a) Schematic diagram of designed 2D grating chip and (b) Reflectance spectra for fabricated chip showing almost similar response for TE and TM polarized light minimizing polarization-dependent effect. (Reproduced with permission from Ref. [158])

The results show an eightfold enhancement compared to a bare Ag thin film for SEF and a staggering enhancement of 2.5×10^6 times for SERS. To evaluate the chemical sensing performance of the sensor surface, the chip was characterized with varying concentrations of picric acid (PA) detection and found the minimum detection limit up to the orders of few nM.

4.3.5 Terahertz Plasmonic Metasurfaces for Sensing Applications

Terahertz (THz) plasmonic metamaterials have garnered significant interest in recent years, particularly in the field of biosensing due to their noninvasive, nondestructive, and harmless interaction with biological tissues [159, 160]. These materials operate in the THz frequency range, which lies between the microwave and infrared regions of the electromagnetic spectrum, making them ideal for probing biological samples without causing damage. The ability to interact with biological tissues in both in vivo and in vitro environments positions THz plasmonic metamaterials as powerful tools for quick infection diagnosis, cost-effective pharmacological studies, and real-time monitoring of biological processes. For example, toroidal metamaterials have emerged as a particularly promising class, owing to their ability to support high-quality, sharp resonance modes. These resonance modes are highly sensitive to changes in the surrounding environment, making toroidal metamaterials excellent candidates for the development of highly sensitive biosensors. In this context, Arash et al. explore the development of a THz metasensor based on a plasmonic surface consisting of metamolecules that support ultra-narrow toroidal resonances toward its application for the detection of virus-envelope proteins (ZIKV-EPs), which are relevant in the diagnosis of viral infections such as Zika virus [161]. Toroidal metamaterials represent a novel class of artificial materials that exhibit unique electromagnetic properties not found in natural materials. These metamaterials are engineered to support toroidal dipole

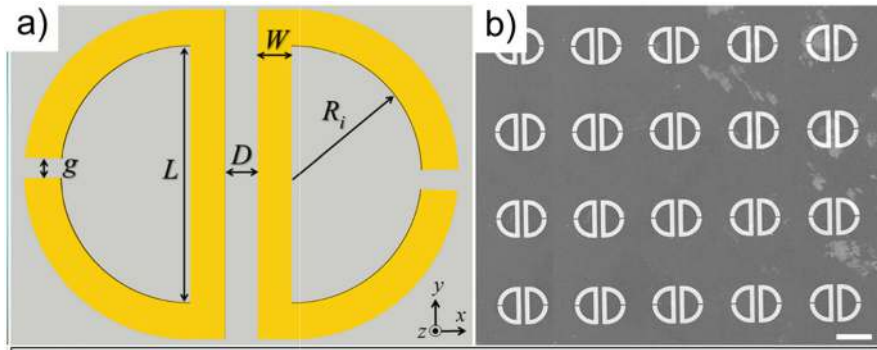


Fig. 17 (a) Schematic image of the unit cell and (b) SEM image of toroidal metasurface. (Reproduced with permission from Ref. [161])

moments, which are distinct from the traditional electric and magnetic dipoles. The toroidal dipole moment arises from a specific arrangement of currents that flow in a toroidal (doughnut-shaped) pattern, leading to the formation of sharp and highly localized resonance modes. These resonance modes are characterized by their ultra-narrow linewidths, which are indicative of high-quality factors (Q-factors). The high Q-factor of toroidal resonances makes them highly sensitive to perturbations in the surrounding environment, such as changes in the refractive index or the presence of biomolecules, making them ideal for sensing applications.

In the study, the metasurface was composed of an array of metamolecules, engineered to support toroidal resonances when excited by THz radiation. The design process involved extensive numerical simulations to optimize the geometry and arrangement of the metamolecules, ensuring that the metasurface exhibits the desired electromagnetic response. Once the design was finalized, the metasurface was fabricated using standard microfabrication lithography techniques. After fabrication, the metasurface is functionalized by immobilizing antibodies specific to the target biomarker, in this case, ZIKV-EPs. The antibodies are attached to the surface of the metamolecules, enabling the selective binding of the biomarker when it is present in the surrounding medium. Figure 17 shows the schematic representation of the proposed metasurface and SEM image of fabricated one using lithography method.

Further, the sensing application of the proposed metasurface is based on the detection of shifts in the toroidal resonance frequency as a result of biomarker binding. When the target biomarker, ZIKV-EPs, binds to the functionalized surface of the metamolecules, it induces a change in the local refractive index around the metamolecules. This change in refractive index perturbs the electromagnetic environment of the toroidal resonance, leading to a measurable shift in the resonance frequency, as shown in Fig. 18.

It is worth mentioning, when the GNPs are introduced into the medium surrounding the metasurface, they increase the local concentration of the biomarker

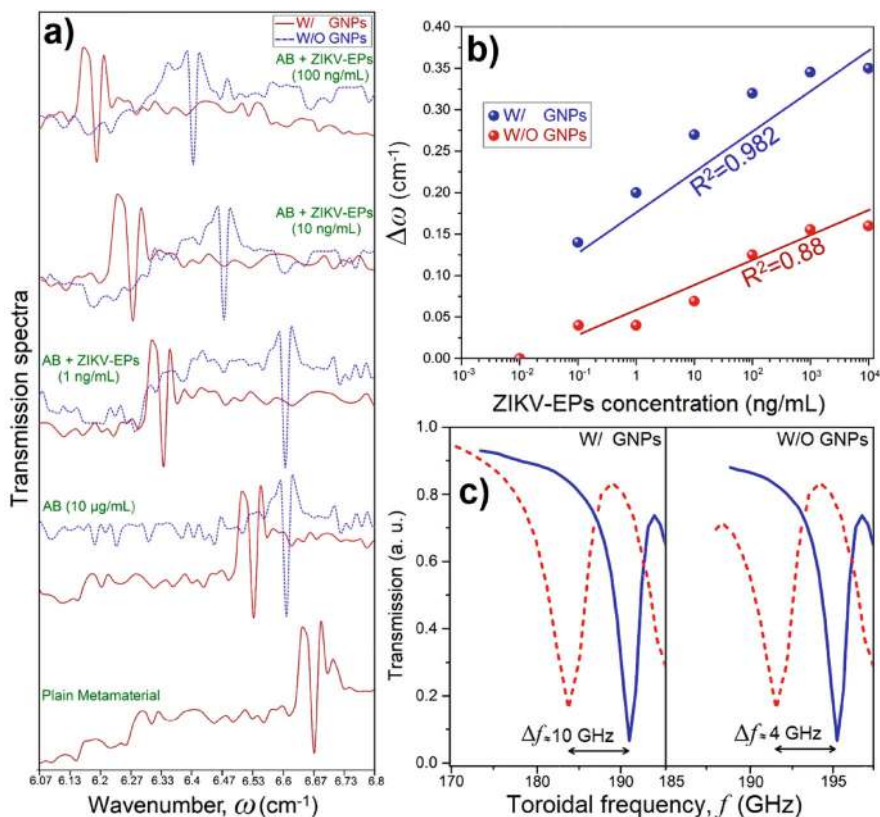


Fig. 18 (a) The transmission amplitude spectra for the fabricated metasurfaces for with and without gold nanoparticles (GNPs) for varying concentrations of ZIKV-AB and ZIKV-EPs variants. (b) Calibration curve representing the toroidal resonance shift vs. ZIKV-EPs concentration for with and without GNPs. (c) The magnified transmission spectra as a function of frequency. (Reproduced with permission from Ref. [161])

near the metamolecules. This results in a more pronounced perturbation of the toroidal resonance, leading to a larger shift in the resonance frequency. By measuring the shift of the toroidal dipolar momentum (up to $\Delta\omega \sim 0.35 \text{ cm}^{-1}$) for different concentrations of the biomarker, it was possible to analyze the sensitivity, repeatability, and limit of detection (LoD) of the enhanced metasensor. In the initial experiments, the metasensor was used to sense and quantify ZIKV-EPs by measuring the spectral shifts of the toroidal resonances as the concentration of the biomarker varied. The results showed that the metasensor was capable of detecting very low concentrations of the biomarker, with a high degree of sensitivity and specificity. The detection process is rapid, making the metasensor suitable for real-time monitoring of biomolecular interactions. In conclusion, the THz metasensor based on toroidal plasmonic metamaterials represents a powerful and versatile tool

for biosensing, with the potential to revolutionize various fields by enabling the detection of low concentrations of biomarkers with unprecedented sensitivity.

4.4 Concluding Remarks

In conclusion, metasurface sensors represent a significant leap forward in optical sensing technology. Unlike conventional optical sensors, which often face challenges related to sensitivity, size, and complexity, metasurfaces offer a solution through their unique design and material properties. Metasurfaces are engineered materials with nanostructures that allow for unprecedented manipulation of light. By precisely tailoring these nanostructures, metasurfaces can achieve exceptional levels of sensitivity, enabling the detection of subtle environmental changes or minute quantities of analytes. This chapter has summarized various metal sensors, including those based on STFs, ESP-LSP coupled metasurfaces, thin gratings, and toroidal metasurfaces, all of which demonstrate significant potential for developing sensors that are miniaturized, cost-effective, and capable of lower detection limits. However, challenges such as precise fabrication, stability, and signal variability still exist. With ongoing technological advancements, these limitations can be addressed, paving the way for the practical applications of metasurface sensors in real-world scenarios.

Acknowledgments The funding from the following sources was very helpful: NATO Science for Peace and Security Programme under contract number MYP G5814 for supporting the project titled: “Nanomaterials for explosive traces detection with SERS” (NOOSE); the European Union’s Horizon 2020 research and innovation program under the Marie Skłodowska-Curie grant agreement No 872662; the Israel Ministry of Innovation, Science and Technology, and the Ministry of Energy.

References

1. R.C. McPhedran, I.V. Shadrivov, B.T. Kuhlmei, Y.S. Kivshar, Metamaterials and metaoptics. *NPG Asia Mater.* **3**, 100–108 (2011). <https://doi.org/10.1038/asiamat.2011.146>
2. K. Wang, M. Chekhova, Y. Kivshar, Metamaterials for quantum technologies. *Phys. Today* **75**(8), 38 (2022). <https://doi.org/10.1063/PT.3.5062>
3. R. Bridgelall, J.B. Rafert, D. Atwood, D.D. Tolliver, Hyperspectral range imaging for transportation systems. *Proc. SPIE* **9803**, 98032Y (2016)
4. G. ElMasry, D.-W. Sun, Principles of hyperspectral imaging technology, in *Hyperspectral Imaging for Food Quality Analysis and Control*, ed. by D.-W. Sun, (Academic, San Diego, 2010), pp. 3–43
5. J. O’Brien, A. Furusawa, J. Vučković, Photonic quantum technologies. *Nat. Photonics* **3**, 687 (2009) <http://www.nature.com/doifinder/10.1038/nphoton.2009.229>
6. M. Humar, M. Ravnik, S. Pajk, I. Musčević, Electrically tunable liquid crystal microresonators. *Nat. Photonics* **3**, 595 (2009). <https://doi.org/10.1038/nphoton.2009.170>

7. I.-C. Benea-Chelms, M.L. Meretska, D.L. Elder, M. Tamagnone, L.R. Dalton, F. Capasso, Electro-optic spatial light modulator from an engineered organic layer. *Nat. Commun.* **12**, 5928 (2021). <https://doi.org/10.1038/s41467-021-26035-y>
8. I. Abdulhalim, Optimized guided mode resonant structure as thermo-optic sensor and liquid crystal tunable filter. *Chin. Opt. Lett.* **7**(8), 667 (2009) <https://opg.optica.org/col/abstract.cfm?URI=col-7-8-667>
9. W. Cai, V.M. Shalaev, *Optical Metamaterials* (Springer, 2010)
10. M. Kadic, G.W. Milton, M. Wegener, 3D metamaterials. *Nat. Rev. Phys.* **1**, 198 (2019)
11. Y. Liu, X. Zhang, Metamaterials: A new frontier of science and technology. *Chem. Soc. Rev.* **40**, 2494 (2011)
12. H.-T. Chen, A.J. Taylor, N. Yu, A review of metasurfaces: Physics and applications. *Rep. Prog. Phys.* **79**(7), 076401 (2016) <https://iopscience.iop.org/article/10.1088/0034-4885/79/7/076401/meta#:~:text=DOI%2010.1088/0034%2D4885/79/7/076401>
13. S. Nie, I.F. Akyildiz, Metasurfaces for multiplexed communication. *Nature Electronics* **4**(3), 177–178 (2021)
14. C.-W. Lee, H.J. Choi, H. Jeong, Tunable metasurfaces for visible and SWIR applications, *Nano. Convergence* **7**(3) (2020). <https://doi.org/10.1186/s40580-019-0213-2>
15. Y. Tian, A. Ghanekar, M. Ricci, M. Hyde, O.J. Gregory, Y. Zheng, A review of tunable wavelength selectivity of metamaterials in near-field and far-field radiative thermal transport. *Materials* **11**, 862 (2018)
16. X. Zhao, Z. Sun, L. Zhang, Z. Wang, R. Xie, J. Zhao, R. You, Y. Zheng, Review on metasurfaces: An alternative approach to advanced devices and instruments. *Adv. Devices Instrum.* **2022**, 9765089, 19 (2022). <https://doi.org/10.34133/2022/9765089>
17. J.-Y. Ou, E. Plum, J. Zhang, N.I. Zheludev, Giant nonlinearity of an optically reconfigurable plasmonic metamaterial. *Adv. Mater.* **28**, 729–733 (2015)
18. N. Yu, F. Capasso, Flat optics with designer metasurfaces. *Nat. Mater.* **13**(2), 139 (2014)
19. J.Y. Ou, E. Plum, J. Zhang, N.I. Zheludev, An electromechanically reconfigurable plasmonic metamaterial operating in the near-infrared. *Nat. Nanotechnol.* **8**, 252 (2013)
20. W. Chen, W. Liu, Y. Jiang, M. Zhang, N. Song, N.J. Greybush, J. Guo, A.K. Estep, K.T. Turner, R. Agarwal, C.R. Kagan, Ultrasensitive, mechanically responsive optical metasurfaces via strain amplification. *ACS Nano* **12**(11), 10683–10692 (2018). <https://doi.org/10.1021/acsnano.8b04889>
21. E. Arbabi, A. Arbabi, S.M. Kamali, Y. Horie, M.S. Faraji-Dana, A. Faraon, MEMS-tunable dielectric metasurface lens. *Nat. Commun.* **9**, 812 (2018)
22. S.J. Foland, J.-B. Lee, A highly-compliant asymmetric 2D guided-mode resonance sensor for simultaneous measurement of dual-axis strain, in *2013 IEEE 26th international conference on micro electro mechanical systems (MEMS)*, (2013). <https://doi.org/10.1109/memsys.2013.6474329>
23. Y. Zhu, X. Hu, Y. Fu, H. Yang, Q. Gong, Ultralow-power and ultrafast all-optical tunable plasmon-induced transparency in metamaterials at optical communication range. *Sci. Rep.* **3**, 2338 (2013)
24. J. Kim, E.G. Carnemolla, C. DeVault, A.M. Shaltout, D. Faccio, V.M. Shalaev, A.V. Kildishev, M. Ferrera, A. Boltasseva, Dynamic control of nanocavities with tunable metal oxides. *Nano Lett.* **18**, 740–746 (2018)
25. M.X. Ren, W. Wu, W. Cai, B. Pi, X.Z. Zhang, J.J. Xu, Reconfigurable metasurfaces that enable light polarization control by light. *Light. Sci. Appl.* **6**, e16254 (2017)
26. Y. Yang, J. Lu, A. Manjavacas, T.S. Luk, H. Liu, K. Kelley, J.-P. Maria, E.L. Runnerstrom, M.B. Sinclair, S. Ghimire, I. Brener, High-harmonic generation from an epsilon-near-zero material. *Nat. Phys.* **15**, 1022–1026 (2019)
27. B. Gholipour, J. Zhang, K.F. MacDonald, D.W. Hewak, N.I. Zheludev, An all-optical, non-volatile, bidirectional, phase-change meta-switch. *Adv. Mater.* **25**, 3050 (2013)
28. B. Gholipour, D. Piccinotti, A. Karvounis, K.F. MacDonald, N.I. Zheludev, Reconfigurable ultraviolet and high-energy visible dielectric metamaterials. *Nano Lett.* **19**, 1643–1648 (2019)

29. Z. Zhu, P.G. Evans, R.F. Haglund, J.G. Valentine, Dynamically reconfigurable metadvice employing nanostructured phase-change materials. *Nano Lett.* **17**, 4881–4885 (2017)
30. Z. Chen, X. Wang, Y. Qi, S. Yang, J.A.N.T. Soares, B.A. Apgar, R. Gao, R. Xu, Y. Lee, X. Zhang, J. Yao, L.W. Martin, Self-assembled, nanostructured, tunable metamaterials via spinodal decomposition. *ACS Nano* **10**, 10237–10244 (2016)
31. S. Bhupathi, S. Wang, M. Abutoama, I. Balin, L. Wang, P.G. Kazansky, Y. Long, I. Abdulhalim, Femtosecond laser-induced vanadium oxide metamaterial nanostructures and the study of optical response by experiments and numerical simulations. *ACS Appl. Mater. Interfaces* **12**, 37 (2020). <https://doi.org/10.1021/acsami.0c03844>
32. S. Bhupathi, M. Abutoama, Y. Long, I. Abdulhalim, Sculptured thin film vanadium dioxide Thermochromic coatings grown by oblique angle deposition: Investigation of transmittance response and modulation enhancement by experiment and theoretical modeling. *J. Mater. Chem. C* **9**, 13304–1316p (2021). <https://doi.org/10.1039/d1tc02649f>
33. Y. Huang, J. Li, G. Wen, Active and tunable metamaterials, Chapter 2, in *Metamaterials—Devices and Applications*, (Intech, 2017). <https://doi.org/10.5772/67198>
34. Y.J. Huang, G.J. Wen, Y.J. Yang, et al., Tunable dual-band ferrite-based metamaterials with dual negative refractions. *Appl. Phys. A Mater. Sci. Process.* **106**, 79–86 (2012)
35. H. Zhao, J. Zhou, Q. Zhao, et al., Magneto-tunable left-handed material consisting of yttrium iron garnet slab and metallic wires. *Appl. Phys. Lett.* **91**, 131107 (2007)
36. Y.J. Huang, G.J. Wen, T.Q. Li, et al., Design and characterization of tunable terahertz metamaterials with broad bandwidth and low loss. *IEEE Antenn. Wireless Propaga. Lett.* **11**, 264 (2012)
37. A. Caratenuto, F. Chen, Y. Tian, M. Antezza, G. Xiao, Y. Zheng, Magnetic field-induced emissivity tuning of InSb-based metamaterials in the terahertz frequency regime. *Opt. Mater. Express* **11**(9), 3141 (2021). <https://doi.org/10.1364/ome.433003>
38. K. Fan, R.D. Averitt, W.J. Padilla, Active and tunable nanophotonic metamaterials. *Nano* **11**(17), 3769–3803 (2022). <https://doi.org/10.1515/nanoph-2022-0188>
39. X. Jing, R. Yang, Y. Fan, F. Quanhong, F. Zhang, A review of tunable electromagnetic metamaterials with anisotropic liquid crystals. *Front. Phys.* **9**, 633104 (2021). <https://doi.org/10.3389/fphy.2021.633104>
40. S. Bang, J. Kim, G. Yoon, T. Tanaka, J. Rho, Recent advances in tunable and reconfigurable metamaterials. *Michromachines* **9**, 560 (2020)
41. J. Kim, J. Seong, Y. Yang, S.-W. Moon, T. Badloe, J. Rho, Tunable metasurfaces towards versatile metalenses and metaholograms: a review. *Adv. Photonics* **4**(2), 024001 (2022). <https://doi.org/10.1117/1.AP.4.2.024001>
42. H. Hajlan, A. Ghobadi, B. Butun, E. Ozbay, Active metamaterial nearly perfect light absorbers: A review. *J. Amer. Optical Soc. B* **36**(8), F131–F143 (2022). <https://doi.org/10.1364/JOSAB.36.00F131>
43. I.C. Khoo, D.H. Werner, X. Liang, A. Diaz, B. Weiner, Nanosphere dispersed liquid crystals for tunable negative-zero-positive index of refraction in the optical and terahertz regimes. *Opt. Lett.* **31**, 2592 (2006)
44. L. Yang, F. Fan, M. Chen, X. Zhang, S.-J. Chang, Active terahertz metamaterials based on liquid-crystal induced transparency and absorption. *Opt. Commun.* **382**, 42–48 (2017)
45. Z. Shen, S. Zhou, S. Ge, W. Duan, P. Chen, L. Wang, et al., Liquid-crystal-integrated metadvice: Towards active multifunctional terahertz wave manipulations. *Opt. Lett.* **43**(19), 4695 (2018)
46. A. Komar, Z. Fang, J. Bohn, J. Sautter, M. Decker, A. Miroshnichenko, et al., Electrically tunable all-dielectric optical metasurfaces based on liquid crystals. *Appl. Phys. Lett.* **110**, 071109 (2017)
47. S. Isaacs, A. Hajoj, M. Abutoama, A. Kozlovsky, E. Golan, I. Abdulhalim, Resonant grating without a planar waveguide layer as a refractive index sensor. *Sensors* **19**(13), 30003 (2019)
48. D.H. Werner, D.H. Kwon, I.C. Khoo, A.V. Kildishev, V.M. Shalaev, Liquid crystal clad near-infrared metamaterials with tunable negative-zero-positive refractive indices. *Opt. Express* **15**(6), 3342 (2007)

49. B. Vasić, D.C. Zografopoulos, G. Isić, R. Beccherelli, R. Gajić, Electrically tunable terahertz polarisation converter based on overcoupled metal-isolator-metal metamaterials infiltrated with liquid crystals. *Nanotechnology* **28**, 124002 (2017)
50. P. Lakshmi Madhuri, R.J. Martín-Palma, B. Martín-Adrados, I. Abdulhalim, Voltage controlled scattering from porous silicon Mie-particles in liquid crystals. *J. Molec. Liq.* **281**, 108–116 (2019). <https://doi.org/10.1016/j.molliq.2019.02.085>
51. P.L. Madhuri, Z. Shuddhodana, M.A. Judeh, I. Abdulhalim, Cochleate-doped liquid crystal as switchable metamaterial window mediated by molecular orientation modified aggregation. *Part. Part. Syst. Charact.* **37**(5), 2000067(8p) (2020). <https://doi.org/10.1002/ppsc.202000067>
52. I. Abdulhalim, P.L. Madhuri, M. Diab, T. Mokari, Novel easy to fabricate liquid crystal composite with potential for electrically or thermally controlled transparency windows. *Opt. Express* **27**(12), 17387–17401 (2019)
53. M.A. Aisheh, M. Abutoama, M. Abuleil, I. Abdulhalim, Fast tunable metamaterial liquid crystal achromatic waveplate. *Nanophotonics* **12**(6), 1115–1127 (2023). <https://doi.org/10.1515/nanoph-2022-0656>
54. X. Chang, M. Pivnenko, P. Shrestha, W. Weijie, W. Zhang, D. Chu, Electrically tuned active metasurface towards metasurface-integrated liquid crystal on silicon (meta-LCoS) devices. *Opt. Express* **31**(4), 5378 (2023)
55. L. Liu, I.V. Shadrivov, D.A. Powell, M. Rezaur Raihan, H.T. Hattori, M. Decker, E. Mironov, D.N. Neshev, Temperature control of terahertz metamaterials with liquid crystals. *IEEE Trans. Terahertz Sci. Technol.* **3**(6), 827 (2013)
56. J.B. Pendry, D.R. Smith, The quest for the superlens. *Sci. Am.* **295**, 60–67 (2006)
57. F. Zhang, L. Kang, Q. Zhao, J. Zhou, X. Zhao, D. Lippens, Magnetically tunable left handed metamaterials by liquid crystal orientation. *Opt. Express* **17**(6), 4360 (2009)
58. J. Liu, H. Zeng, M. Cheng, Z. Wang, J. Wang, M. Cen, D. Luo, A. Priimagi, Y.J. Liu, Photoelastic plasmonic metasurfaces with ultra-large near infrared spectral tuning. *Materials Horizons* **9**, 942–952 (2022)
59. M. Bosch, M.R. Shcherbakov, K. Won, H.-S. Lee, Y. Kim, G. Shvets, Electrically actuated varifocal lens based on liquid-crystal-embedded dielectric Metasurfaces. *Nano Lett.* **21**(9), 3849–3856 (2021)
60. A. Liningera, A.Y. Zhub, J.-S. Parkb, G. Palermmod, S. Chatterjee, J. Boyda, F. Capasso, G. Strangi, Optical properties of metasurfaces infiltrated with liquid crystals. *PNAS* **117**(34), 20390–20396 (2020). <https://doi.org/10.1073/pnas.2006336117>
61. S.-Q. Li, X. Xuewu, R.M. Veetil, V. Valuckas, R. Paniagua-Domínguez, A.I. Kuznetsov, Phase-only transmissive spatial light modulator based on tunable dielectric metasurface. *Science* **364**, 1087–1090 (2019)
62. S. Mor, V. Torres-Costa, R.J. Martín-Palma, I. Abdulhalim, Planar polar liquid crystalline alignment in nanostructured porous silicon one dimensional photonic crystals. *Appl. Phys. Lett.* **97**, 113106 (2010). <https://doi.org/10.1063/1.3489428>
63. D.-K. Yang, W. Shin-Tson, *Fundamental of Liquid Crystal Devices* (Wiley, 2006)
64. S.T. Lagerwall, *Ferroelectric and Antiferroelectric Liquid Crystals* (Wiley-VCH, Weinheim, 1999)
65. P. Bos, Fast-switching liquid-crystal effects for displays. *Inf. Display.* **23**, 20–25 (2007)
66. T.-H. Choi, J.-W. Kim, T.-H. Yoon, Wide-temperature high-speed operation of a nematic liquid crystal cell, in *Proceedings SPIE 10125, Emerging Liquid Crystal Technologies XII, 101251H*, (2017). <https://doi.org/10.1117/12.2253681>
67. F. Gou, H. Chen, M.C. Li, S.L. Lee, S.T. Wu, Submillisecond-response liquid crystal for high-resolution virtual reality displays. *Opt. Express* **25**(7), 7984–7997 (2017)
68. Y. Iwata, M. Murata, K. Tanaka, A. Jinda, T. Ohtake, T. Shinomiya, H. Yoshida, Novel super-fast response, ultra-wide temperature range VA-LCD. *SID Symp. Dig. Tech. Pap.* **44**, 431–434 (2013). <https://doi.org/10.1002/j.2168-0159.2013.tb06239.x>
69. T. Matsushima, K. Okazaki, Y. Yang, K. Takizawa, New fast response time in plane switching liquid crystal mode. *SID Symp. Dig. Tech. Pap.* **46**, 648–651 (2015). <https://doi.org/10.1002/sdtp.10237>

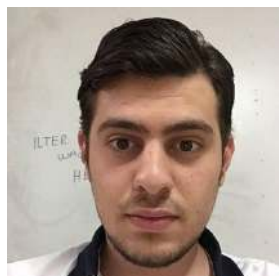
70. M. Tokita, O. Sato, Y. Inagaki, A. Nomura, Y. Tsujii, S. Kang, T. Fukuda, J. Watanabe, High-density poly(methyl methacrylate) brushes as anchoring surfaces of nematic liquid crystals. *Jpn. J. Appl. Phys.* **50**(7), 071701 (2011)
71. O. Sato, N. Iwata, J. Kawamura, T. Maeda, Y. Tsujii, J. Watanabe, M. Tokita, An in-plane switching liquid crystal cell with weakly anchored liquid crystals on the electrode substrate. *J. Mater. Chem. C* **5**(18), 4384–4387 (2017)
72. Y. Choi, S.-W. Oh, T.-N. Choi, H.-J. Sohn, S.-I.N. Do, T.-H. Yoon, Liquid crystal cell asymmetrically anchored for high transmittance and triggered with a vertical field for fast switching. *Opt. Express* **28**(14), 20553 (2020)
73. A.B. Golovin, S.V. Shiyankovskii, O.D. Lavrentovich, Fast switching dual-frequency liquid crystal optical retarder, driven by an amplitude and frequency modulated voltage. *Appl. Phys. Lett.* **83**, 3864–3866 (2003). <https://doi.org/10.1063/1.1625114>
74. H. Choi, H. Higuchi, H. Kikuchi, Fast electro-optic switching in liquid crystal blue phase II. *Appl. Phys. Lett.* **98**, 131905 (2011). <https://doi.org/10.1063/1.3564896>
75. Y. Hisakado, H. Kikuchi, T. Nagamura, T. Kajiyama, Large electro-optic Kerr effect in polymer-stabilized liquid-crystalline blue phases. *Adv. Mater.* **17**, 96–98 (2005). <https://doi.org/10.1002/adma.200400639>
76. P. Rudquist, L. Komitov, S. Lagerwall, Linear electro-optic effect in a cholesteric liquid crystal. *Phys. Rev. E* **50**, 4735–4743 (1994)
77. P. Rudquist, T. Carlsson, L. Komitov, et al., The flexoelectro-optic effect in cholesterics. *Liq. Cryst.* **22**, 445–449 (1997)
78. X. Wang, J.A.J. Fells, C. Welch, M.-G. Tamba, G.H. Mehl, S.M. Morris, S.J. Elston, Characterization of large tilt-angle flexoelectro-optic switching in chiral nematic liquid crystal devices. *Liq. Cryst.* **46**(3), 408–414 (2019). <https://doi.org/10.1080/02678292.2018.1502822>
79. A. Jakli, D.R. Kim, L.C. Chien, A. Saupe, Effect of a polymer network on the alignment and the rotational viscosity of a nematic liquid crystal. *J. Appl. Phys.* **72**, 3161 (1992)
80. O. Kurochkin, O. Buluy, N. Aryasova, V. Nazarenko, J. Varshal, M. Manevich, J.L. West, Y. Reznikov, Concentration dependence of phase retardation and optical response of stressed liquid crystal systems based on nematic liquid crystal pentylcyanobiphenyl. *J. Mol. Liq.* **267**, 115 (2018)
81. J.L. West, G. Zhang, A. Glushchenko, Y. Reznikov, Fast birefringent mode stressed liquid crystal. *Appl. Phys. Lett.* **86**, 31111 (2005). <https://doi.org/10.1063/1.1852720>
82. V. Borshch, S.V. Shiyankovskii, O.D. Lavrentovich, Nanosecond electro-optic switching of a liquid crystal. *Phys. Rev. Lett.* **111**, 107802 (2013)
83. B.-X. Li, V. Borshch, H. Wang, Q. Li, S.V. Shiyankovskii, O.D. Lavrentovich, Enhanced nanosecond electro-optic effect in isotropic and nematic phases of dielectrically negative nematics doped by strongly polar additive. *J. Mol. Liq.* **267**, 450–455 (2018)
84. O. Aharon, I. Abdulhalim, Birefringent tunable filter with wide dynamic range. *Opt. Lett.* **34**, 2114 (2009)
85. O. Aharon, I. Abdulhalim, Liquid crystal tunable filter with extended free spectral range. *Opt. Express* **17**, 11426–11433 (2009)
86. M. Abuleil, I. Abdulhalim, Narrowband multispectral liquid crystal tunable filter. *Opt. Lett.* **51**, 1957 (2016)
87. S. Isaacs, F. Placido, I. Abdulhalim, Investigation of liquid crystal fabry perot tunable filters: Design, fabrication and polarization independence. *Appl. Opt.* **53**, H91–H101 (2014)
88. D.C. Zografopoulos, R. Asquini, E.E. Kriezis, A. d'Alessandro, R. Beccherelli, Guided-wave liquid-crystal photonics. *Lab Chip* **12**, 3598–3610 (2012)
89. I. Abdulhalim, Anisotropic layers in waveguides for mode tuning and tunable filtering, in *Proceedings SPIE 6135, Liquid Crystal Materials, Devices, and Applications XI*, 61350R, (2006). <https://doi.org/10.1117/12.660572>
90. E.P. Pozhidaev, V. Chigrinov, A. Murauski, V. Molkin, D. Tao, H.S. Kwok, V-shaped electro-optical mode based on deformed-helix ferroelectric liquid crystal with subwavelength pitch. *J. SID* **5**, 273 (2012)

91. E.P. Pozhidaev, V.V. Vashchenko, V.V. Mikhailenko, A.I. Krivoshey, V.A. Barbashov, L. Shi, A.K. Srivastava, V.G. Chigrinov, H.S. Kwok, Ultrashort helix pitch antiferroelectric liquid crystals based on chiral esters of terphenyldicarboxylic acid. *J. Mat. Chem.* **C 4**, 10339e10346 (2016)
92. I. Abdulhalim, G. Moddel, Switching behavior and electro-optic response due to the soft mode ferroelectric effect in chiral Smectic A liquid crystals. *Liq. Crys.* **9**(4), 493 (1991)
93. I. Abdulhalim, Highly promising electrooptic material: Distorted helix ferroelectric liquid crystal with a specific tilt angle. *Appl. Phys. Lett.* **101**, 141903 (5pp) (2012)
94. E.P. Pozhidaev, A.D. Kiselev, A.K. Srivastava, V.G. Chigrinov, H.-S. Kwok, M.V. Minchenko, Orientational Kerr effect and phase modulation of light in deformed-helix ferroelectric liquid crystals with subwavelength pitch. *Phys. Rev. E* **87**, 052502 (2013)
95. A.K. Srivastava, E.P. Pozhidaev, V.G. Chigrinov, H.S. Kwok, Vertically aligned ferroelectric liquid crystals with high Kerr constant for field sequential color displays. *Mol. Liq.* **295**, 111054 (2019)
96. I. Abdulhalim, G. Moddel, Optically and electrically controlled light modulation and color switching using helix Distorsion of ferroelectric liquid crystals. *Mol. Cryst. Liq. Cryst.* **200**, 79 (1991)
97. K. D'havé, P. Rudquist, S.T. Lagerwall, H. Pauwels, W. Drzewinski, R. Dabrowski, Solution of the dark state problem in antiferroelectric liquid crystal displays. *Appl. Phys. Lett.* **76**, 3528–3520 (2000)
98. P. Rudquist, Orthoconic antiferroelectric liquid crystals. *Liq. Cryst.* **40**, 1678–1697 (2013)
99. D. Engström, J. Per Rudquist, S. Bengtsson, Galt three level phase- modulator based on orthoconic antiferroelectric liquid crystals. *Opt. Lett.* **31**, 3158–3160 (2006)
100. I. Abdulhalim, Continuous phase-only or amplitude light modulation using ferroelectric liquid crystals with fixed boundary orientations. *Optic. Communi.* **108**, 219 (1994)
101. S. Garoff, R.B. Meyer, Electroclinic effect at the A-C phase change ion a chiral smectic liquid crystal. *Phys. Rev. Lett.* **38**, 848 (1977)
102. I. Abdulhalim, G. Moddel, K.M. Johnson, High speed analog spatial light modulator using an a-Si: H photosensor and an electroclinic liquid crystal. *Appl. Phys. Lett.* **55**, 1603 (1989)
103. N.A. Clark, T. Bellini, R.F. Shao, D. Coleman, S. Bardou, D.R. Link, J.E. MacLennan, X.H. Chen, M.D. Wand, D.M. Walba, P. Rudquist, S.T. Lagerwall, Electro-optic characteristics of de Vries tilted smectic liquid crystals: Analog behavior in the smectic A(*) and smectic C-* phases. *Appl. Phys. Lett.* **80**, 4097 (2002)
104. P. Rudquist, M. Osipov, F. Giesselmann, On the orientational distribution functions in de Vries-type smectic liquid crystals. *Liq. Cryst.* **45**, 2097–2108 (2019)
105. M. Gelbaor, M. Klebanov, V. Lyubin, I. Abdulhalim, Photoinduced permanent alignment of liquid crystal on nanostructured chalcogenide thin film. *Appl.Phys.Lett.* **98**, 071909 (2011)
106. I. Abdulhalim, M. Gelbaor, M. Klebanov, V. Lyubin, Photoinduced phenomena in nano-dimensional glassy As₂S₃ films. *Opt. Mater. Express* **1**, 1192–1201 (2011)
107. M.G. Kirzhner, T.A. Kumar, A. Chaudhary, M. Klebanov, I. Abdulhalim, Polar anchoring energy measurement of photoaligned nematic liquid crystal on nanodimensional chalcogenide glass films. *J. Mol. Liq.* **267**, 182–186 (2018)
108. A.K. Tatipamula, M.G. Kirzhner, A. Chaudhary, M. Klebanov, I. Abdulhalim, Electro-Optical properties of photoaligned Liquid Crystal cells prepared with obliquely irradiated Chalcogenide glasses. *Mol. Liq.* **349**, 118087 (2022). <https://doi.org/10.1016/j.molliq.2021.118087>
109. A. Solodar, A. Cerkaskaite, R. Drevinskas, P.G. Kazansky, I. Abdulhalim, Ultrafast laser induced nanostructured ITO for liquid crystal alignment and higher transparency electrodes. *Appl. Phys. Lett.* **113**, 081603 (2018) Also in [arXiv:1802.09757](https://arxiv.org/abs/1802.09757) [physics.optics]
110. I. Cerkaskaite, R. Drevinskas, A. Solodar, I. Abdulhalim, P.G. Kazansky, Form-birefringence in ITO thin films engineered by ultrafast laser nanostructuring. *ACS Photonics* **4**, 2944–2951 (2017)
111. K. Takatoh, *Alignment Technologies and Applications of Liquid Crystal Devices* (Taylor & Francis, London/New York, 2005)

112. D. Wu, Y. Liu, Z. Xu, Z. Yu, L. Yu, L. Chen, C. Liu, R. Li, R. Ma, J. Zhang, H. Ye, Numerical study of the wide-angle polarization-independent ultra-broadband efficient selective solar absorber in the entire solar spectrum. *RRL Solar* **1**(7), 1700049 (2017)
113. Y. Cui, K.H. Fung, J. Xu, H. Ma, Y. Jin, S. He, N.X. Fang, Ultrabroadband light absorption by a sawtooth anisotropic metamaterial slab. *Nano Lett.* **12**(3), 1443–1447 (2012)
114. A. Tittl, M.G. Harats, R. Walter, X. Yin, M. Schäferling, N. Liu, R. Rapaport, H. Giessen, Quantitative angle-resolved small-spot reflectance measurements on plasmonic perfect absorbers: Impedance matching and disorder effects. *ACS Nano* **8**(10), 10885–10892 (2014)
115. Q. Liang, T. Wang, Z. Lu, Q. Sun, Y. Fu, W. Yu, Metamaterial-based two-dimensional Plasmonic subwavelength structures offer the broadest waveband light harvesting. *Adv. Opt. Mater.* **1**(1), 43–49 (2013)
116. P. Feng, W.D. Li, W. Zhang, Dispersion engineering of plasmonic nanocomposite for ultrathin broadband optical absorber. *Opt. Express* **23**(3), 2328–2338 (2015)
117. Z. Wang, Y. Wei, C. Zhang, Flexible broadband absorber for solar energy harvesting. *Plasmonics* **19**, 215–225 (2024)
118. Y. Yuan, C. Dong, J. Gu, Q. Liu, J. Xu, C. Zhou, G. Song, W. Chen, L. Yao, D. Zhang, A scalable Nickel–cellulose hybrid metamaterial with broadband light absorption for efficient solar distillation. *Adv. Mater.* **32**, 1907975 (2020)
119. L. Zhou, Y. Tan, J. Wang, et al., 3D self-assembly of aluminium nanoparticles for plasmon-enhanced solar desalination. *Nature Photon* **10**, 393–398 (2016)
120. C.Y. Chang, H.T. Lin, M.S. Lai, T.Y. Shieh, C.C. Peng, M.H. Shih, Y.C. Tung, Flexible localized surface plasmon resonance sensor with metal-insulator-metal nanodisks on PDMS substrate. *Sci Rep.* **8**(1), 11812 (2018)
121. J.K. Behera, K. Liu, M. Liana, T. Cao, A reconfigurable hyperbolic metamaterial perfect absorber. *Nanoscale Adv.* **3**, 1758–1766 (2021)
122. P. Shekhar, J. Atkinson, Z. Jacob, Hyperbolic metamaterials: Fundamentals and applications. *Nano Convergence* **1**, 14 (2014)
123. D. Lee, S. So, H. Guangwei, M. Kim, T. Badloe, H. Cho, J. Kim, H. Kim, C.-W. Qiu, J. Rho, Hyperbolic metamaterials: Fusing artificial structures to natural 2D materials. *eLight* **2**, 1 (2022)
124. W. Pinghui, Z. Chen, H. Jile, C. Zhang, X. Danyang, L. Lv, An infrared perfect absorber based on metal-dielectric-metal multi-layer films with nanocircle holes arrays. *Results Phys.* **16**, 102952 (2020)
125. W. Dong, C. Liu, Y. Liu, X. Zenghui, Y. Zhongyuan, Y. Li, L. Chen, R. Ma, J. Zhanga, H. Ye, Numerical study of a wide-angle polarization-independent ultra-broadband efficient selective metamaterial absorber for near-ideal solar thermal energy conversion. *RSC Adv.* **8**(38), 21054–21064 (2018)
126. F. Zhou, F. Qin, Z. Yi, W. Yao, Z. Liu, X. Wu, P. Wu, Ultra-wideband and wide-angle perfect solar energy absorber based on Ti nanorings surface plasmon resonance. *Phys. Chem. Chem. Phys.* **23**, 17041–17048 (2021)
127. Z. Wang, Z. Liu, G. Duan, L. Fang, H. Duan, Ultrahigh broadband absorption in metamaterials with electric and magnetic polaritons enabled by multiple materials. *Int. J. Heat Mass Transf.* **185**, 122355 (2022)
128. Y.I. Abdulkarim, A. Mohanty, O.P. Acharya, B. Abppasani, M.S. Khan, S.K. Mohapatra, F.F. Muhammadsharif, J. Dong, A review on metamaterial absorbers: Microwave to optical. *Front. Phys.* **10**, 893791 (2022)
129. L. Zhou, Y. Tan, J. Wang, et al., 3D self-assembly of aluminium nanoparticles for plasmon-enhanced solar desalination. *Nat. Photonics* **10**, 393–398 (2016)
130. C.K. Amaljith, I. Abdulhalim, Metamaterial devices for tunability and energy management in the SWIR region, in *Proceedings Volume PC12990, Metamaterials XIV; PC129901U*, (2024)
131. I. Abdulhalim, M. Zourob, A. Lakhtakia, Surface plasmon resonance for biosensing: A mini-review. *Electromagnetics* **28**(3), 214–242 (2008). <https://doi.org/10.1080/02726340801921650>

132. S. Balbinot, A.M. Srivastav, J. Vidic, I. Abdulhalim, M. Manzano, Plasmonic biosensors for food control. *Trends Food Sci. Technol.* **111**, 128–140 (2021)
133. I. Del Villar et al., Optical sensors based on lossy-mode resonances. *Sensors Actuators B Chem.* **240**, 174–185 (2017). <https://doi.org/10.1016/j.snb.2016.08.126>
134. S.P. Usha, A.M. Shrivastav, B.D. Gupta, A contemporary approach for design and characterization of fiber-optic-cortisol sensor tailoring LMR and ZnO/PPY molecularly imprinted film. *Biosens. Bioelectron.* **87** (2017). <https://doi.org/10.1016/j.bios.2016.08.040>
135. Y. Lee, S.J. Kim, H. Park, B. Lee, Metamaterials and metasurfaces for sensor applications. *Sensors (Switzerland)* **17**(8) (2017). <https://doi.org/10.3390/s17081726>
136. S. Jahani, Z. Jacob, All-dielectric metamaterials. *Nat. Nanotechnol.* **11**(1), 23–36 (2016). <https://doi.org/10.1038/nnano.2015.304>
137. V. Shvalya, G. Filipič, J. Zavašnik, I. Abdulhalim, U. Cvelbar, Surface-enhanced Raman spectroscopy for chemical and biological sensing using nanoplasmonics: The relevance of interparticle spacing and surface morphology. *Appl. Phys. Rev.* **7**(3) (2020). <https://doi.org/10.1063/5.0015246>
138. M. Moskovits, Surface-enhanced Raman spectroscopy: A brief retrospective. *J. Raman Spectrosc.* **36**(6–7), 485–496 (2005). <https://doi.org/10.1002/jrs.1362>
139. I. Abdulhalim, Plasmonic sensing using metallic nano-sculptured thin films. *Small* **10**(17), 3499–3514 (2014). <https://doi.org/10.1002/sml.201303181>
140. P. Li, F. Long, W. Chen, J. Chen, P.K. Chu, H. Wang, Fundamentals and applications of surface-enhanced Raman spectroscopy-based biosensors. *Curr. Opin. Biomed. Eng.* **13**, 51–59 (2020). <https://doi.org/10.1016/j.cobme.2019.08.008>
141. S.M. Morton, L. Jensen, Understanding the molecule-surface chemical coupling in SERS. *J. Am. Chem. Soc.* **131**(11), 4090–4098 (2009). <https://doi.org/10.1021/ja809143c>
142. A.M. Shrivastav, U. Cvelbar, I. Abdulhalim, A comprehensive review on plasmonic-based biosensors used in viral diagnostics. *Commun. Biol.* **4**(1), 1–12 (2021). <https://doi.org/10.1038/s42003-020-01615-8>
143. M. Abutoama et al., Ultrahigh field enhancement optimization versus Rabi splitting investigated using au Nano-bipyramids on metal films. *J. Phys. Chem. C* **123**(20), 12984–12996 (2019). <https://doi.org/10.1021/acs.jpcc.9b01201>
144. S.K. Srivastava, A. Li, S. Li, I. Abdulhalim, Optimal interparticle gap for ultrahigh field enhancement by LSP excitation via ESPs and confirmation using SERS. *J. Phys. Chem. C* **120**(50), 28735–28742 (2016). <https://doi.org/10.1021/acs.jpcc.6b08276>
145. P.K. Jain, K.S. Lee, I.H. El-Sayed, M.A. El-Sayed, Calculated absorption and scattering properties of gold nanoparticles of different size, shape, and composition: Applications in biological imaging and biomedicine. *J. Phys. Chem. B* **110**(14), 7238–7248 (2006). <https://doi.org/10.1021/jp057170o>
146. H. Yu, Y. Peng, Y. Yang, Z.Y. Li, Plasmon-enhanced light-matter interactions and applications. *NPJ Comput. Mater.* **5**(1), 1–14 (2019). <https://doi.org/10.1038/s41524-019-0184-1>
147. A. Shalabney, C. Khare, J. Bauer, B. Rauschenbach, I. Abdulhalim, Detailed study of surface-enhanced Raman scattering from metallic nanosculptured thin films and their potential for biosensing. *J. Nanophotonics* **6**(1), 061605–061601 (2012). <https://doi.org/10.1117/1.jnp.6.061605>
148. S.K. Srivastava, A. Shalabney, I. Khalaila, C. Grüner, B. Rauschenbach, I. Abdulhalim, SERS biosensor using metallic nano-sculptured thin films for the detection of endocrine disrupting compound biomarker vitellogenin. *Small* **10**(17), 3579–3587 (2014). <https://doi.org/10.1002/sml.201303218>
149. S.K. Srivastava et al., Highly sensitive and specific detection of *E. coli* by a SERS nanobiosensor chip utilizing metallic nanosculptured thin films. *Analyst* **140**(9), 3201–3209 (2015). <https://doi.org/10.1039/c5an00209e>

150. N. Singh, A.M. Shrivastav, N. Vashistha, I. Abdulhalim, 3D plasmonic hot spots network via gold decorated deep micro-porous silicon exhibiting ultrahigh-SERS enhancement with application to explosives detection. *Sensors Actuators B Chem.* **374**, 132813 (2023). <https://doi.org/10.1016/J.SNB.2022.132813>
151. I. Abdulhalim, Coupling configurations between extended surface electromagnetic waves and localized surface plasmons for ultrahigh field enhancement. *Nano* **7**(12), 1891–1916 (2018). <https://doi.org/10.1515/nanoph-2018-0129>
152. S.Y. Ding, E.M. You, Z.Q. Tian, M. Moskovits, Electromagnetic theories of surface-enhanced Raman spectroscopy. *Chem. Soc. Rev.* **46**(13), 4042–4076 (2017). <https://doi.org/10.1039/c7cs00238f>
153. M. Abutoama, M.J. Abuleil, I. Abdulhalim, Resonant subwavelength and Nano-scale grating structures. *Sensors (Switzerland)* **21**, 4523 (2021)
154. M. Abutoama, I. Abdulhalim, Self-referenced biosensor based on thin dielectric grating combined with thin metal film. *Opt. Express* **23**(22), 28667 (2015). <https://doi.org/10.1364/oe.23.028667>
155. M. Abutoama, I. Abdulhalim, Angular and intensity modes self-referenced refractive index sensor based on thin dielectric grating combined with thin metal film. *IEEE J. Sel. Top. Quantum Electron.* **23**(2), 72–80 (2017). <https://doi.org/10.1109/JSTQE.2016.2520878>
156. S.K. Srivastava, I. Abdulhalim, Self-referenced sensor utilizing extra-ordinary optical transmission from metal nanoslits array. *Opt. Lett.* **40**(10), 2425 (2015). <https://doi.org/10.1364/ol.40.002425>
157. M. Abutoama, A. Bajaj, D. Li, Y. Wang, L. Jiang, I. Abdulhalim, Resonant modes of reflecting gratings engineered for multimodal sensing. *APL Photonics* **5**(7) (2020). <https://doi.org/10.1063/5.0011306>
158. I. Abdulhalim, A.M. Shrivastav, M. Abutoama, 3D periodic metal nanostructure for multimodal sensing with application for explosives detection using SERS, in *Optical Sensing and Detection VIII*, (2024), p. 129991K
159. H.T. Chen, W.J. Padilla, J.M.O. Zide, A.C. Gossard, A.J. Taylor, R.D. Averitt, Active terahertz metamaterial devices. *Nature* **444**(7119), 597–600 (2006). <https://doi.org/10.1038/nature05343>
160. S. Tabassum, S.K. Nayemuzzaman, M. Kala, A. Kumar Mishra, S.K. Mishra, Metasurfaces for sensing applications: Gas, bio and chemical. *Sensors* **22**(18) (2022). <https://doi.org/10.3390/s22186896>
161. A. Ahmadvand et al., Extreme sensitive metasensor for targeted biomarkers identification using colloidal nanoparticles-integrated plasmonic unit cells. *Biomed. Opt. Express* **9**(2), 373 (2018). <https://doi.org/10.1364/boe.9.000373>



Majd Abu Aisheh graduated from the Department of Mechanical Engineering of Middle East Technical University in Ankara, Turkey. During his MSc studies from 2016 to 2018 he worked as a research assistant and focused on the study of fires in tunnels to develop fire extinguishing systems. He is a PhD candidate in the Department of Electro-Optics and Photonics Engineering at Ben-Gurion University, where his research focuses on enhancing the response time of photonic devices.



Amaljith CK graduated from the Department of Nuclear Physics at the University of Madras, Chennai, India, in 2018. From 2018 to 2021, he served as a research assistant in the same department. During this time, he worked on the development of THz metamaterial devices. He is pursuing a PhD in the Department of Electro-Optics and Photonics Engineering at Ben-Gurion University, where his research focuses on tunable metamaterial devices for various electro-optic applications.



Dr. Anand M. Shrivastav obtained his Ph.D. Degree from Physics Department, Indian Institute of Technology Delhi in 2018. He worked as postdoctoral fellow in The Hong Kong Polytechnique University (Hong Kong), Ben Gurion University of Negev (Israel) and Public University of Navarra (Spain). He has received several awards and fellowships such as PBC postdoc fellowship (Israel) and Marie Curie Postdoc Fellowship (Spain), Distinction in doctoral thesis award, etc. He has authored 35+ research articles in peer reviewed journals, one book (Optical Sensors for Environmental Monitoring and Biomedical Diagnostics) and about 14+ conference papers. He holds the memberships of SPIE, The Optical Society (OSA) and Optical Society of India (OSI). Current research area is focused on plasmonics and nanophotonics for biosensing applications. Currently, he is working as research track Assistant Professor in SRM Institute of Science and Technology, Kattankulathur, Chennai, India.



Prof. Ibrahim Abdulhalim is a professor in the Department of Electro-Optics and Photonics Engineering at Ben Gurion University. He has worked in research and development in variety of academic institutions and industrial companies such as: the Optoelectronic Computing Systems Center in the University of Colorado at Boulder, USA, the Optoelectronics Research Center of Southampton University, England, the Thin Films Center of the University of Western Scotland, KLA-Tencor and Nova measuring instruments, and in GWS-Photonics. In October 2005, he joined the Department of Electro-Optic Engineering at Ben Gurion University and acted as the department head between 2006 and 2014. His current research activities involve liquid crystal devices for photonic applications, nanophotonic and plasmonic structures for biosensing, biomedical optical imaging techniques such as spectropolarimetric imaging and full-field optical coherence tomography. Prof. Abdulhalim has published over 220 journal articles, 70 conference proceedings

papers, 11 book chapters, coauthored 1 book titled: Integrated Nanophotonic Devices (Micro and Nano Technologies), co-edited a book titled: Signal Amplification in Optical Biosensing, and has 22 granted patents. He became a fellow of the Institute of Physics, UK in 2004, SPIE fellow in 2010, and senior member of Optica in 2016. He was an associate editor of the SPIE Journal of NanoPhotonics, and presently acting for the Journals of Sensors, and Biosensors, and a topical editor for Applied Optics. In 2014 he founded a company called Photonicsys, specialized in optical and photonic devices for biosensing, and in 2019 a company called Photoliqsys, specialized in liquid crystal devices and applications.

The Role of Maxwell's Equations in Design of Metamaterials and in 3D Imaging



Partha P. Banerjee, Austin M. Scott, and Guo Chen

1 Introduction

This chapter summarizes two applications of Maxwell's equations which we have been actively pursuing in our Holography and Metamaterials Lab over the last few years. One area of interest is the design of metamaterials with negative index for subwavelength imaging, as well as the design of metamaterials for use as bandpass filters with given center wavelength and cutoffs. The other area is 3D imaging using interferometric (holographic) and non-interferometric techniques for applications in the 3D mapping of topography of surfaces, viz., cracks, deformations, and most recently fingerprints.

Metamaterials, which are nano-engineered artificial structures, have shown potential as versatile platforms for achieving various functions, including sensing [1], waveguiding [2], and sub-diffraction imaging [3]. A typical application is the nano-scale metallo-dielectric (MD) bandpass filters, which have garnered significant interest due to their ability to achieve high miniaturization [4], flexible and broadband transmission [5], and sharp-edge profiles [6].

To analyze the optical properties of MD structures, one important method is to use the dispersion relation for electromagnetic (EM) waves through the periodic MD structure. Just as in quantum mechanics, the dispersion relation provides valuable insights into the passbands and stopbands within a crystal lattice [7], the dispersion relation for EM waves offers the potential to engineer the complex refractive index of a proposed structure [8], and enables control over the group velocity of propagating waves [9]. It will be seen that this topological dispersion relation, arising from the structure of the metamaterial, suitably modified to include the

P. P. Banerjee (✉) · A. M. Scott · G. Chen
Electro-Optics and Photonics, University of Dayton, Dayton, OH, USA
e-mail: pbanerjee1@udayton.edu

material dispersion relation of the metal and the dielectric, can adequately describe the frequency response of the finite MD filter.

Digital holography (DH) is an interferometric technique of obtaining phase information whereby holograms are recorded on a CCD or CMOS detector and numerically reconstructed using a computer [10]. Allowing both 3D and quantitative phase images of objects to be recovered, DH has been successfully employed in non-destructive testing and metrology [11], microscopy [12], 3D imaging of biological samples [13], 3D image encryption [14], 3D object recognition [15], and 3D tomographic imaging [16], to name a few. Various system architectures exist for DH, such as phase-shifting DH [17] where the object and reference beams are nominally copropagating to the image sensor, and multiple holograms are recorded with a phase shift applied to the reference beam between each recording, and off-axis DH [18] where a slight angle is introduced between the object and reference beams as they propagate to the image sensor. Reconstruction of the digital hologram is done using the law of Fresnel propagation, either in the space or spatial frequency domain, which is also derived from the Helmholtz equation.

Regarding reconstruction, the phase reconstructed from the digital hologram is a wrapped phase, meaning it must be unwrapped to obtain the true phase. This can be done using a phase unwrapping algorithm such as the Phase Unwrapping Max-flow Algorithm, or PUMA [19]. An alternative is using the transport of intensity technique, which is a non-interferometric method for phase retrieval capable of recovering the true phase of an object without the need for phase unwrapping [20]. The transport of intensity equation (TIE) is also derived from the Helmholtz equation under the paraxial approximation [21, 22], and is a deterministic phase retrieval method requiring a minimum of two axially separated intensity images. Multiple intensity images are required to estimate the axial intensity derivative using finite difference methods.

2 Metallo-Dielectric Structures: Metamaterials for Optical Filters

Previous research has successfully derived the dispersion relations for periodic one-dimensional (1D) MD structures [23], where the presence of metallic films introduces unique optical properties distinct from straightforward metal absorption [24]. In related research on bandpass filters, the potential of engineering the reflectance spectra using multilayer structures has been discussed, including dielectric layer structures with graphene monolayers [25] and plasma photonic crystal structures [26]. Among these works, Qiao et al. [27] pointed out that using photonic crystal layers along with highly absorptive metal films can realize one or multiple highly reflected peaks, even achieving enhanced transmission in narrowband regions. The introduction of the metal offers great flexibility in designing essential reflection or transmission optical devices in the visible and near-infrared ranges. Therefore,

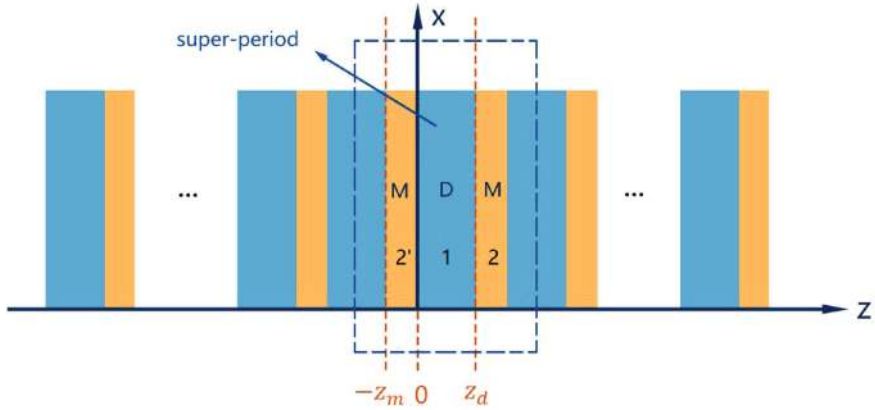


Fig. 1 Schematic of a 1D periodic MD structure, where the symbol “M” corresponds to a metal layer with a thickness of z_m , while “D” represents a dielectric layer with a thickness of z_d . The periodic MD structure can be considered as an extended repetition of the dark blue block, also referred to as the “super-period” $[\frac{z_d}{2}; z_m; z_d; z_m; \frac{z_d}{2}]$. The significance of the super-period is explained in Ref. [28], and multiple super-periods are expressed in $[\frac{z_d}{2}; z_m; z_d; z_m; \frac{z_d}{2}]^q$, with q refers to the number of super-periods

it is crucial to combine the studies on MD structure dispersion relations with the engineering of MD structure transmittance and reflectance.

None of the work mentioned above uses the dispersion relation in an infinite periodic structure to predict the transmittance features of a finite multilayer structure. Additionally, many prior studies have employed the transfer matrix method (TMM) to find the dispersion relation [23–25, 27]. We have suggested an alternative and perhaps more fundamental approach that involves solving the Helmholtz equation with appropriate boundary conditions. By employing Bloch's theorem to express the periodicity of solutions, this method parallels the quantum mechanical analysis of a 1D periodic potential barrier. This technique reveals the intrinsic relationship between layer thickness, material properties, and the ultimate optical characteristics of an infinite periodic structure, such as transmission characteristics, in a concise and efficient manner.

Consider an MD structure with infinite extension along the z -direction. This structure consists of a dielectric layer within the range $z \in [0, z_d]$ (designated as region 1) and a metal layer within the range $z \in [z_d, z_m]$ (denoted as region 2), as illustrated in Fig. 1. The adjacent metal layer within the range $z \in [-z_m, 0]$ is labeled as region 2'. Both the dielectric and metal layers extend periodically on both sides of regions 2 and 2'. Assume for now that light propagates along the z -axis.

As shown in Ref. [28], the exponential form of the dispersion relation for normal incidence takes the form

$$\frac{1}{8k_1k_2} \left[(k_1 + k_2)^2 \left(e^{j(k_1z_d + k_2z_m)} + e^{-j(k_1z_d + k_2z_m)} \right) \right]$$

$$\begin{aligned}
& - (k_1 - k_2)^2 \left(e^{j(k_1 z_d - k_2 z_m)} + e^{-j(k_1 z_d - k_2 z_m)} \right) \Big] \\
& = \frac{1}{2} \left(e^{jk_{\text{eff}}(z_d + z_m)} + e^{-jk_{\text{eff}}(z_d + z_m)} \right). \quad (1)
\end{aligned}$$

Here, k_1 and k_2 represent the propagation constants in region 1 and 2 (2'), respectively, and are defined as $k_{1,2} = \tilde{n}_{1,2}k_0 = \sqrt{\epsilon_{r1,2}}k_0$, where k_0 is the propagation constant in free-space, $\tilde{n}_{1,2}$ and $\epsilon_{r1,2}$ refer to the complex refractive indices and relative permittivities, respectively, of the dielectric and metal layers. The complex refractive index can be represented as $\tilde{n} = n - jk$, where the real part n corresponds to the refractive index, and the magnitude of the imaginary part is k , which is the absorption coefficient. Solving Eq. (1) enables the determination of k_{eff} . By defining $k_{\text{eff}} = \beta - j\alpha$, the real part of the effective propagation constant β can be determined from $\text{Re}(k_{\text{eff}})$, and the effective attenuation constant α can be obtained by taking $-\text{Im}(k_{\text{eff}})$. It is important to note that for forward propagating waves, the value of α should be positive. Eq. (1) can be further simplified into its trigonometric form:

$$\cos(k_1 z_d) \cos(k_2 z_m) - \frac{k_1^2 + k_2^2}{2k_1 k_2} \sin(k_1 z_d) \sin(k_2 z_m) = \cos(k_{\text{eff}}(z_d + z_m)). \quad (2)$$

Typically, for most wavelengths of interest, the absorption coefficient of metals, k_m , is dominant compared to the refractive index ($k_m > n_m$). Conversely, the absorption coefficient of dielectrics is generally close to zero ($k < n_d$). To simplify the analysis, it can be assumed that for a metal, $\tilde{n}_2 = -jk_m$, and for a dielectric, $\tilde{n}_1 = n_d$. With such an assumption, which will be called “ideal case” throughout, Eq. (2) can now be expressed as

$$\begin{aligned}
& \cos(n_d k_0 z_d) \cosh(k_m k_0 z_m) + \left(\frac{k_m^2 - n_d^2}{2n_d k_m} \right) \sin(n_d k_0 z_d) \sinh(k_m k_0 z_m) \\
& = \cos(k_{\text{eff}}(z_d + z_m)), \quad (3)
\end{aligned}$$

which is the dispersion relation in the ideal case. The RHS of the equation is a cosine function, which takes values in the range $[-1, 1]$. This constrains the values of the left-hand side (LHS) of the equation. Specifically, $\text{LHS} \in [-1, 1]$ defines the passbands, while $\text{LHS} \in (-\infty, -1) \cup (1, \infty)$ defines the stopbands for a MD structure. By setting the LHS of the equation to zero ($\text{LHS} = 0$), we can determine the center wavelength. Additionally, the cutoff wavelengths can be determined by setting $\text{LHS} = \pm 1$. With the given thicknesses z_d, z_m , and material properties n_d, k_m , these featured wavelengths can be determined directly, and important information about the optical characteristics of the MD structure can be obtained accordingly. Details of this along with various examples of different metals and dielectrics have

been shown in Ref. [28] along with the relationship between predictions from the dispersion relation with the transmittance of a finite MD structure, computed using TMM. It has been also shown that the LHS of the dispersion relation for the ideal case is close to the LHS of the real part of the dispersion relation for the actual case ($n_m \neq 0$, $k_d \approx 0$), so that inferences about the center wavelength and cutoffs can be adequately ascertained from the plots for the ideal case ($n_m = 0$, $k_d = 0$).

The dispersion relations for normal incidence represent the simplest and most unique case. TE and TM polarized waves exhibit identical behavior. For oblique incidence, we first consider TE polarization, where we assume the electric field is in the y - z plane. We define the unit vectors in the x , y , and z directions as $\hat{\mathbf{a}}_x$, $\hat{\mathbf{a}}_y$, and $\hat{\mathbf{a}}_z$, respectively. When considering oblique incident TE waves and accounting for both forward and backward propagating components, the general solutions in regions 1, 2', and 2 are given by:

$$\mathbf{E}_1 = \left(A e^{-jk_{1z}z} + B e^{jk_{1z}z} \right) e^{-jk_{1x}x} \hat{\mathbf{a}}_y, \quad (4)$$

$$\mathbf{E}_{2'} = \left(C e^{-jk_{2z}z} + D e^{jk_{2z}z} \right) e^{-jk_{2x}x} \hat{\mathbf{a}}_y, \quad (5)$$

$$\mathbf{E}_2 = \mathbf{E}_{2'}(z - (z_d + z_m)) \exp(-jk_{z\text{eff}}(z_d + z_m)). \quad (6)$$

where \mathbf{E}_1 , \mathbf{E}_2 , and $\mathbf{E}_{2'}$ represent the electric fields in regions 1, 2', and 2, respectively. $k_{1,2x}$ and $k_{1,2z}$ correspond to the x and z components of $k_{1,2}$, respectively, while $k_{z\text{eff}}$ represents the z component of k_{eff} . Starting from Maxwell's equations, the boundary conditions can be derived, and are expressed as follows:

$$E_{y1}(0) = E_{y2'}(0), \quad \frac{dE_{y1}(0)}{dz} = \frac{dE_{y2'}(0)}{dz}; \quad (7a)$$

$$E_{y1}(z_d) = E_{y2'}(z_d), \quad \frac{dE_{y1}(z_d)}{dz} = \frac{dE_{y2'}(z_d)}{dz}. \quad (7b)$$

Here, $E_{y1,2'}$ represent the y -components of the electric field $\mathbf{E}_{2'}$. Similarly, the subscripts x and z denote the x - and z -components, respectively. After some extensive algebra, which involves the use of the boundary conditions and setting the determinant of the ensuing matrix to zero, the dispersion relation becomes

$$\cos(k_{1z}z_d) \cos(k_{2z}z_m) - \frac{k_{1z}^2 + k_{2z}^2}{2k_{1z}k_{2z}} \sin(k_{1z}z_d) \sin(k_{2z}z_m) = \cos(k_{z\text{eff}}(z_d + z_m)), \quad (8)$$

which has the same form as the dispersion relation for normal incidence, as in Eq. (2), except that the propagation constants are now replaced with their corresponding z components.

Similarly, when considering TM polarization, the polarization is in the x - z plane. Eqs. (4–6) undergo the following changes:

$$\mathbf{E}_1 = \left[a (\cos \theta_1 \hat{\mathbf{a}}_x - \sin \theta_1 \hat{\mathbf{a}}_z) e^{-jk_{1z}z} + b (\cos \theta_1 \hat{\mathbf{a}}_x + \sin \theta_1 \hat{\mathbf{a}}_z) e^{jk_{1z}z} \right] e^{-jk_{1x}x}, \quad (9)$$

$$\mathbf{E}_{2'} = \left[c (\cos \theta_2 \hat{\mathbf{a}}_x - \sin \theta_2 \hat{\mathbf{a}}_z) e^{-jk_{1z}z} + d (\cos \theta_2 \hat{\mathbf{a}}_x + \sin \theta_2 \hat{\mathbf{a}}_z) e^{jk_{2z}z} \right] e^{-jk_{2x}x}, \quad (10)$$

$$\mathbf{E}_2 = \mathbf{E}_{2'}(z - (z_d + z_m)) \exp(-jk_{z\text{eff}}(z_d + z_m)), \quad (11)$$

where $\theta_{1,2}$ represent the angles between the propagation direction and the z -axis in regions 1 and 2' (2), respectively. It is important to note that the value of $\theta_{1,2}$ can be mathematically complex in this context. We can also use exponential form to express the general solutions to avoid the use of complex angles. Starting again from Maxwell's equations, the boundary conditions can be derived as follows:

$$D_{z1}(0) = D_{z2'}(0), E_{x1}(0) = E_{x2'}(0); \quad (12a)$$

$$D_{z1}(z_d) = D_{z2}(z_d), E_{x1}(z_d) = E_{x2}(z_d). \quad (12b)$$

Once again as before, by setting the determinant of the matrix to zero and utilizing Snell's law ($k_1 \sin \theta_1 = k_2 \sin \theta_2$) as well as the relation $k_{1,2}^2 = \epsilon_{r1,2} k_0^2 = k_{1,2x}^2 + k_{1,2z}^2$, one can derive the dispersion relation for oblique incident TM polarized waves as

$$\begin{aligned} \cos(k_{1z}z_d) \cos(k_{2z}z_m) - \frac{\epsilon_{r2}^2 k_{1z}^2 + \epsilon_{r1}^2 k_{2z}^2}{2\epsilon_{r1}\epsilon_{r2}k_{1z}k_{2z}} \sin(k_{1z}z_d) \sin(k_{2z}z_m) \\ = \cos(k_{z\text{eff}}(z_d + z_m)). \end{aligned} \quad (13)$$

It is worth noting that the x component of the propagation constant, k_x , remains unchanged during propagation according to Snell's law. For a finite multilayer structure, if the incident angle in air θ_0 is given, the unchanged x component can be expressed as $k_x = k_{1x} = k_{2x} = k_0 \sin \theta_0$. After solving for the z component $k_{z\text{eff}}$ using Eq. (8) or Eq. (13), the effective propagation constant can be calculated as $k_{\text{eff}}^2 = k_x^2 + k_{z\text{eff}}^2$. Through some straightforward algebra, it can be verified that when the incident angle is zero, implying normal incidence, both Eq. (8) and Eq. (13) are equivalent to Eq. (2).

2.1 Frequency Response of MD Filters

As discussed above, the dispersion relation allows us to determine the center wavelength and cutoff wavelengths by setting $LHS = 0$ and $LHS = \pm 1$. The accuracy of this method can be verified using TMM. Figure 2 displays the agreement between the featured wavelengths obtained from the LHS of the ideal dispersion relation and those obtained from the TMM. A one-super-period MD structure in ideal case is considered with Ag as the metal and TiO_2 as the dielectric, with layer thicknesses of $z_d = 100$ nm and $z_m = 40$ nm. Even when using only one super-period for the TMM simulation, we can observe a good match between the featured wavelengths of the infinite structure and the finite structure. The predicted center wavelength precisely corresponds to the peak position, and the cutoff wavelengths indicate the edges of the passband, thereby defining the bandwidth. It is also worth noting that with ideal materials, the maximum transmittance reaches one, indicating a lossless structure.

In our prior work [28, 29, 32], we have demonstrated that increasing the number of super-periods does not change the bandwidth or the center wavelength (which represents the position of the central peak). However, with an increase in the number of super-periods, there is a noticeable increase in oscillations across the passband, which occur due to the Fabry-Perot effect. As shown in Ref. [28], an increase in the number of super-periods results in a longer overall length, which decreases the spacing between each peak, leading to more oscillation peaks within the same passband.

Furthermore, MD layers are typically deposited on a substrate with a much larger thickness (on the millimeter scale) compared to the MD layers (which are

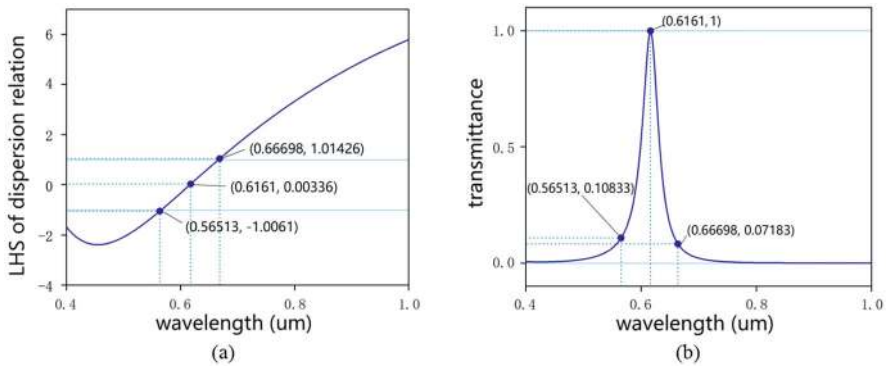


Fig. 2 (a) LHS of the dispersion relation of an infinite multilayers periodic structure in ideal case. (b) Transmittance spectrum plotted TMM using one super-period finite structure $[\frac{z_d}{2}; z_m; z_d; z_m; \frac{z_d}{2}]$. Thicknesses $z_d = 100$ nm, $z_m = 40$ nm, and ideal materials are considered ($n_m = 0$, $k_d = 0$). The metal is Ag and the dielectric is TiO_2 , and the refractive index parameters of them are obtained from published values [30, 31]

on the micron scale). The existence of the substrate can lead to even more dense oscillations that are undetectable using a spectrometer.

Instead of the number of super-periods, the material properties and layer thicknesses have a significant impact on the dispersion relation and, consequently, the featured wavelengths. According to heuristic formulas presented in Ref. [28, 29], the center wavelength is approximately proportional to n_d . Moreover, the values of k_m (and more importantly $dk_m/d\lambda$) can influence both the center and the cutoff wavelengths. By controlling the variables mathematically, it is shown that k_m should have a more pronounced effect on the cutoff wavelengths, while n_m primarily influences transmittance, as outlined in Ref. [32]. Results in Ref. [28] involving different metals (Ag, Au, Al) with constant layer thicknesses also revealed that metals with larger k_m values (such as Al) have smaller bandwidths and shorter center wavelengths, whereas metals with smaller k_m values (like Au) have larger bandwidths and longer center wavelengths.

Similar comparisons can be done for oblique incidence with TE and TM polarizations. As shown in Fig. 3, two super-period MD structures in the ideal case is considered for oblique incidence, with Ag as the metal and TiO_2 as the dielectric, with layer thicknesses of $z_d = 100$ nm and $z_m = 20$ nm. The characteristic wavelengths still align with the TMM transmittance results, even when considering different incident angles and different polarizations. For normal incidence, the simulation results are the same for both TE and TM polarizations, as expected.

There are only small changes in the center and cutoff wavelengths of the main passband (in the visible spectrum) with increasing incidence angle. Figure 3a shows that for TE waves the LHS of the dispersion shifts slightly with increasing angles, while the shape generally remains the same. While for TM waves, as shown in Fig. 3c, we can hardly observe the shift, however the shape of the LHS will change when the wavelength is below 350 nm.

The main difference lies in the extent of transmittance oscillations within a passband. For TM waves, as shown in Fig. 3d, in the main passband, the transmittance values exhibit more severe oscillations (with a smaller ratio of the minimum over the maximum) as the incident angle increases. Conversely, the lower sideband displays less severe oscillations with increasing angle. This indicates that the two passbands can exhibit distinctly different behaviors as the incident angle varies. It is evident that the oscillations become more pronounced in both passbands, and the transmittance peak decreases significantly for the sideband with a large incident angle.

3 Interferometric and Non-Interferometric Methods for Phase Retrieval

A hologram is simply the interference pattern between the light reflected from or transmitted through an object and a reference beam. Assuming the object field is

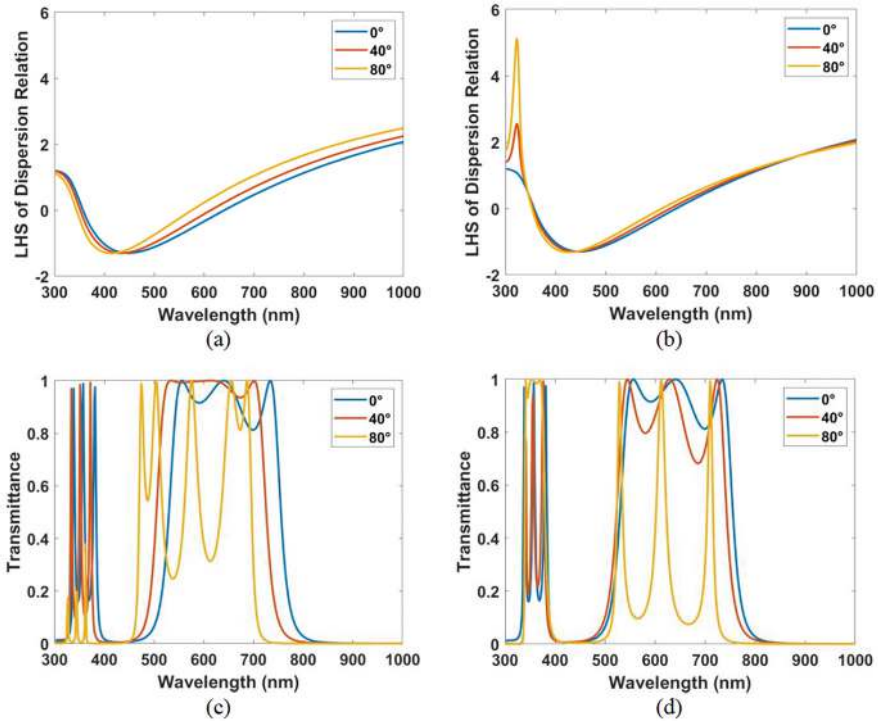


Fig. 3 LHS of the dispersion relations of an infinite MD structure using (**a**) TE waves and (**b**) TM waves. TMM-simulated transmittance spectra of a two super-periods MD structure $\left[\frac{z_d}{2}; z_m; z_d; z_m; \frac{z_d}{2} \right]^2$ for (**c**) TE waves and (**d**) TM waves. Various incidence angles are used, and the materials are assumed to be ideal ($n_m = 0, k_d = 0$). Thicknesses of dielectric and metal are $z_d = 100$ nm and $z_m = 20$ nm, respectively, with Ag as the metal (using data from Wu et al. [30]) and TiO₂ as the dielectric (using data from Siefke et al. [33])

$E_o(x, y)$ and the reference field is a plane wave simply written as E_R , the intensity profile of the interference pattern, also referred to as the hologram function can be written as

$$h(x, y) \propto |E'_o(x, y) + E_R|^2, \quad (14)$$

where $E'_o(x, y)$ is the Fresnel propagated field to the recording (CCD) plane, located at a distance, say, d , from the object plane.

Intensity and phase reconstructions of the digital hologram are accomplished numerically using Fresnel propagation as follows. If locations at the hologram plane and the reconstruction plane are denoted by (x', y') and (x, y) , respectively, the reconstructed optical field in the reconstruction plane can be written using the Fresnel diffraction formula. The Fresnel diffraction formula for paraxial propagation can be derived starting from the paraxial wave equation, which is derived in turn

from the Helmholtz equation. Solution of the paraxial wave equation can be readily done using Fourier transforms and yields the transfer function of propagation $\tilde{H}(k_x, k_y; z)$. The inverse transform is the impulse response for propagation $\tilde{h}(x, y; z)$ and is equivalent to the radiation from a point source. The diffracted field, for instance, $E'_o(x, y)$ above is the convolution of the original field $E(x, y)$ and the impulse response. This integral is useful in calculating the propagated field from the hologram illuminated by a reading beam, and is given by the integral

$$E(x, y) = \frac{j}{\lambda d} \exp\left(-j \frac{2\pi}{\lambda} d\right) \exp\left[-j \frac{\pi}{\lambda d} (x^2 + y^2)\right] \int_{-\infty}^{\infty} \int_{-\infty}^{\infty} h(x', y') E_R^* \\ \times \exp\left[-j \frac{\pi}{\lambda d} (x'^2 + y'^2)\right] \exp\left[j \frac{2\pi}{\lambda d} (xx' + yy')\right] dx' dy', \quad (15)$$

where λ is the illumination wavelength in free space and E_R^* is the complex conjugate of the optical field of the reference beam used when recording the hologram. The integral on the right side of Eq. (15) can be recognized as the inverse Fourier transform $\mathcal{F}^{-1}\{\bullet\}$. Accordingly, Eq. (15) can be re-expressed as

$$E(x, y) = \frac{j}{\lambda d} \exp\left(-j \frac{2\pi}{\lambda} d\right) \exp\left[-j \frac{\pi}{\lambda d} (x^2 + y^2)\right] \\ \times \mathcal{F}^{-1}\left\{E_R^*(x', y') h(x', y') \exp\left[j \frac{\pi}{\lambda d} (x'^2 + y'^2)\right]\right\}. \quad (16)$$

The intensity of the reconstructed hologram is given by

$$I(x, y) = |E(x, y)|^2, \quad (17)$$

and the phase by

$$\phi(x, y) = \tan^{-1}\left(\frac{\text{Im}[E(x, y)]}{\text{Re}[E(x, y)]}\right). \quad (18)$$

Note that in Eq. (18), the use of the inverse tangent function implies that the phase calculated is modulo 2π , and therefore, wrapped. There are commonly used techniques, e.g., PUMA that perform phase unwrapping to yield the exact phase, except when there are large phase excursions with large gradients [34]. Another technique to find the unwrapped phase is through the use of the transport of intensity equation (TIE), more of which is discussed below. Here, defocused image intensities are computed around the reconstruction plane and used to find the unwrapped phase directly, since it does not make use of the inverse tangent function. Alternatively, a multiwavelength technique can be used, where holograms

are recorded and reconstructed using dual wavelengths $\lambda = \lambda_1$ and $\lambda = \lambda_2$. The reconstructed wrapped phases are then subtracted to give an equivalent phase, which now to the synthetic wavelength

$$\Lambda = \frac{\lambda_1 \lambda_2}{|\lambda_1 - \lambda_2|}. \quad (19)$$

Clearly, Λ can be very large or very small. Large synthetic wavelengths of the order of 50 μm can be achieved by using two wavelengths, one of which is acousto-optically generated [35]. Very small synthetic wavelengths, generated by using widely different wavelengths, have been used for mapping surfaces of semiconductors such as silicon chips and shown to have resolution in the order of tens of nanometers [36]. For the example of 3D topography of fingerprints, we have used $\lambda_1 = 514.5 \text{ nm}$ and $\lambda_2 = 457.9 \text{ nm}$, thereby generating $\Lambda = 4.1624 \mu\text{m}$. The use of two wavelengths allows for the flexibility to adjust the synthetic wavelength for a wide range of depths D of the object; in our experiments, a synthetic wavelength of around $4 \mu\text{m}$ allowed for good discrimination of the level-3 details in the topograms of fingerprints.

In what follows, we describe a technique, which is nonholographic and simply relies on imaging. This is, after all, the concept behind TIE, mentioned above. The TIE is a partial differential equation (PDE) derived from the Helmholtz equation under the paraxial approximation and constitutes the conservation of energy of a propagating electromagnetic wave. Derived independently by Teague [21] and Banerjee et al. [22], the PDE is given by

$$\nabla_{\perp}^2 \phi(x, y; z = z_0) + \frac{k_0}{I(x, y; z = z_0)} \frac{\partial I(x, y; z = z_0)}{\partial z} \approx 0, \quad (20)$$

where ∇_{\perp}^2 denotes the Laplacian operator in the transverse dimensions x and y , $\phi(x, y; z = z_0)$ and $I(x, y; z = z_0)$ are, respectively, the phase and intensity of the optical field at the image plane $z = z_0$, and $k_0 = 2\pi/\lambda$ where λ is the wavelength. For phase objects it can generally be assumed that the intensity near the image plane is effectively constant, which allows Eq. (20) to be solved for the phase at the image plane, using the relation

$$\phi(x, y; z = z_0) = \mathcal{F}^{-1} \left\{ \frac{1}{k_x^2 + k_y^2} \mathcal{F} \left\{ \frac{k_0}{I(x, y; z = z_0)} \frac{\partial I(x, y; z = z_0)}{\partial z} \right\} \right\}, \quad (21)$$

where \mathcal{F} and \mathcal{F}^{-1} denote the forward and inverse Fourier transform operators, and k_x and k_y are spatial frequencies in the x and y dimensions, respectively. Implementation of the TIE for phase retrieval requires a minimum of two intensity images symmetrically defocused about the (in-focus) image plane, taken here to be

at $z = z_0 = 0$. Taking the defocusing distance to be $\pm \Delta z$, the two defocused intensity images $I(x, y; z = z_0 \pm \Delta z) = I_{\pm \Delta z}$ are used to estimate the derivative of the image-plane intensity in Eq. (21) by a finite difference method, as well as the image plane intensity using the average of the defocused intensities.

3.1 Applications to 3D Fingerprint Mapping

Visualization of fingerprints is an important aspect of criminal investigations for the identification of individuals present at the scene. Methods for developing and analyzing fingerprints are numerous, and choosing the optimal one is usually dependent on the underlying surface and environmental conditions including temperature, humidity, and aging time. For those fingerprints proving difficult or impossible to develop with traditional methods like dusting powders or chemical reactions, columnar thin films (CTFs) deposited onto the sebaceous residue have been shown to preserve the 3D profile of the fingerprint with high fidelity [37, 38]. Subsequent analysis of the CTF-coated fingerprint is necessary for visualization and characterization of uniquely identifying details, which can be done using phase imaging techniques. Digital holography (DH) [39] and a combination of DH and the TIE [40] are phase imaging methods requiring the recording of one or more digital holograms followed by isolation of the object field and numerical back-propagation to obtain the phase of the object, from which the 3D topogram can be reconstructed. Both DH and DH + TIE have been used to recover the topograms of CTF-coated fingerprint samples, which are either transparent or nicely reflecting [40]. For nontransparent samples exhibiting strong scattering, however, recording of the digital hologram becomes quite difficult due to the rapid spatial scattering of the object beam after reflection from the sample. Additionally, using lenses and recording the digital hologram very close to the object plane increases the difficulty of separating the object information from the background light (dc) and twin image. Here, we propose using TIE alone to recover the 3D topogram of CTF-coated fingerprint samples on opaque substrates that exhibit strong surface scattering. This approach requires a series of through-focus intensity images of the object, thus allowing the use of imaging optics to control the scattering, and, subsequently, enabling recovery of the 3D topogram.

The setup used for the TIE-based phase retrieval is shown in Fig. 4a. Figure 4b, c show intensity images of a sample S2C2D2 (chalcogenide 1000 nm CTF-coated fingerprint on brass aged for 7 days at 5 °F) taken at defocused planes $z = \mp \Delta z$, with $\Delta z = 10 \mu\text{m}$, and Fig. 4d shows the recovered topogram. After acquiring the phase from the recorded intensity images using Eq. (21), residual phase curvature is removed and noise is reduced using MATLAB local functions “detrend” and “medfilt2,” respectively. The depth profile, and thus, the topogram is then calculated using $h_\phi = \phi_0/k_0$. A single representative topogram is shown here as an example (Fig. 4d), however, many more have been recovered using DH, DH + TIE, and TIE.

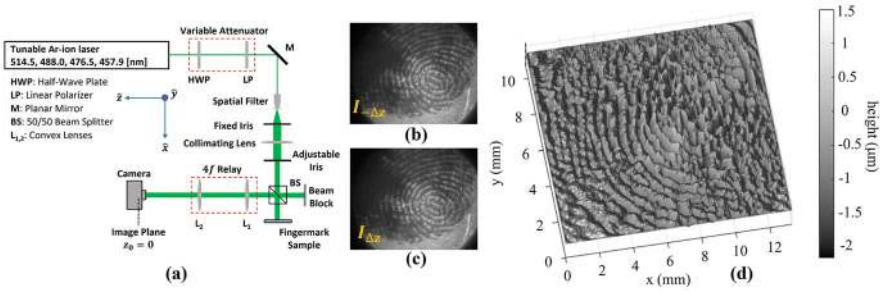


Fig. 4 (a) Schematic of experimental setup for TIE-based topography. (b) Intensity at plane $z = -\Delta z$. (c) Intensity at plane $z = \Delta z$. (d) recovered 3D topogram of the fingerprint [41]

4 Concluding Remarks

This chapter summarizes selected work from our group in the area of metamaterials and 3D imaging using DH and TIE. As is readily seen, Maxwell's equations and the resulting Helmholtz equation are indeed the backbone of the results presented.

Incorporating the concept of the Fourier transform and the angular spectrum concept is useful in solving many of the problems regarding propagation of optical beams in various environments. For instance, the transfer function of propagation provides a convenient method to solve diffraction problems [42, 43]. An extension to this technique to analyze propagation of the longitudinal component of the optical field during beam propagation has been conveniently derived using the transfer function concept [44]. The concept of dispersion relations provides a convenient way to explore plane wave and beam propagation in negative index materials [45–48]. The eikonal equations in the presence of diffraction is the basis of TIE and TPE (transport of phase equation) [22, 43] and is useful in analyzing beam propagation in nonlinear systems. The transfer matrix method (TMM) and the Berreman method, also derived from the Helmholtz equation is useful in analyzing optical propagation through liquid crystals and metamaterials [49–51]. Maxwell's equations are also used to analyze nonlinear self-organization in photorefractive materials [52–55]. Holographic interferometry and DH, all consequences of Maxwell's equations and the Helmholtz equation, have been used by our group to determine object deformations in various scenarios [56–60].

The list of topics that can be handled by Maxwell's equations is indeed endless. Maxwell's equations have truly changed the world!

Acknowledgments Parts of this work (fingermarks) have been funded by the U.S. Department of Homeland Security under Grant Award No. 17STCIN00001-05-00. The work on metamaterials has been partially supported from a Summer Faculty Fellowship Award from the Air Force. The authors would like to thank the participation of the following individuals who contributed to the contents of this Chapter: Akhlesh Lakhtakia and Muhammad Faryad from Penn State; and Hammid Al-Ghezi from University of Dayton.

Appendix: Helmholtz Equation, Transfer Function for Propagation, Transport of Intensity

The Helmholtz equation for the optical field phasor E follows from the wave equation for the real optical field E resulting from Maxwell's equations. For a scalar optical field, it takes the form

$$\nabla^2 E_p + k_0^2 E_p = 0, \quad (\text{A1})$$

Now writing $E_p = E_e \exp -jk_0 z$, where E_e is called the envelope, and invoking the slowly varying approximation, the paraxial wave equation follows [42, 43]:

$$2jk_0 \frac{\partial E_e}{\partial z} = \frac{\partial^2 E_e}{\partial x^2} + \frac{\partial^2 E_e}{\partial y^2}. \quad (\text{A2})$$

Using Fourier transforms, this PDE can be solved to give the transfer function for propagation

$$\hat{H}(k_x, k_y; z) = \exp \left(\frac{j}{2k_0} (k_x^2 + k_y^2) z \right). \quad (\text{A3})$$

The inverse transform of this is the transfer function for propagation given as

$$h(x, y; z) = \mathcal{F}_{xy}^{-1} [H(k_x, k_y)] = \frac{jk_0}{2\pi z} \exp \left[-jk_0 (x^2 + y^2) / 2z \right]. \quad (\text{A4})$$

Alternatively, the optical field paraxial wave equation can be decomposed into its magnitude and phase:

$$E_e = \sqrt{I} e^{-j\varphi}. \quad (\text{A5})$$

Substituting into (A2) and separating imaginary and real parts, the TIE and TPE are obtained [22, 43]:

$$\vec{\nabla}_{\perp} \cdot (I \vec{\nabla}_{\perp} \varphi) = -k_0 \frac{\partial I}{\partial z}, \quad (\text{A6})$$

$$\vec{\nabla}_{\perp} \varphi \cdot \vec{\nabla}_{\perp} \varphi + 2k_0 \left(\frac{\partial \varphi}{\partial z} \right) = \frac{\vec{\nabla}_{\perp}^2 \sqrt{I}}{\sqrt{I}}. \quad (\text{A7})$$

References

1. P. Kabashin, P. Evans, S. Pastkovsky, W. Hendren, G. Wurtz, R. Atkinson, R. Pollard, V. Podolskiy, A. Zayats, Plasmonic nanorod metamaterials for biosensing. *Nat. Mater.* **8**, 867–871 (2009)
2. A. Goyadinov, V.A. Podolskiy, Metamaterial photonic funnels for subdiffraction light compression and propagation. *Phys. Rev. B* **73**, 155108-1–155108-5 (2006)
3. Z. Liu, H. Lee, Y. Xiong, C. Sun, X. Zhang, Far-field optical hyperlens magnifying subdiffraction-limited objects. *Science* **315**, 1686–1686 (2007)
4. J. Garcia-Garcia, J. Bonache, I. Gil, F. Martin, M.D. Velazquez-Ahumada, J. Martel, Miniaturized microstrip and CPW filters using coupled metamaterial resonators. *IEEE Trans. Microwave Theory Tech.* **54**, 2628–2635 (2006)
5. J. Han, J. Gu, X. Lu, M. He, Q. Xing, W. Zhang, Broadband resonant terahertz transmission in a composite metal-dielectric structure. *Opt. Express* **17**(19), 16527–16534 (2009)
6. N. Jin, J. Li, Terahertz wave bandpass filter based on metamaterials. *Microw. Opt. Tech. Lett.* **53**(8), 1858–1860 (2010)
7. A. Alex-Amor, A. Palomares-Caballero, F. Mesa, O. Quevedo-Teruel, P. Padilla, Dispersion analysis of periodic structures in anisotropic media: Application to liquid crystals. *IEEE Trans. Antennas Prop.* **70**, 2811–2821 (2021)
8. J.P. Dowling, M.B. Charles, Anomalous index of refraction in photonic bandgap materials. *J. Mod. Opt.* **41**(2), 345–351 (1994)
9. M. de Dios-Leyva, C. Drake-Pérez Julio, Properties of the dispersion relation in finite one-dimensional photonic crystals. *J. Appl. Phys.* **109**, 1–10 (2011)
10. G. Nehmetallah, P. Banerjee, Application of digital and analog holography in three-dimensional imaging. *Adv. Opt. Photon.* **4**, 472–553 (2012)
11. T. Kreis, Application of digital holography for nondestructive testing and metrology: A review. *IEEE Trans. Industr. Inform.* **12**(1), 240–247 (2016)
12. Y. Takaki, H. Kawai, H. Ohzu, Hybrid holographic microscopy free of conjugate and zero-order images. *Appl. Opt.* **38**(23), 4990–4996 (1999)
13. W. Xu, M.H. Jericho, I.A. Meinertzhagen, H.J. Kreuzer, Digital in-line holography for biological applications. *PNAS* **98**(20), 11301–11305 (2001)
14. A. Alfalou, C. Brosseau, Optical image compression and encryption methods. *Adv. Opt. Photon.* **1**, 589–636 (2009)
15. B. Javidi, E. Tajahuerce, Three-dimensional object recognition by use of digital holography. *Opt. Lett.* **25**(9), 610–612 (2000)
16. T. Noda, S. Kawata, S. Minami, Three-dimensional phase-contrast imaging by a computed-tomography microscope. *Appl. Opt.* **31**(5), 670–674 (1992)
17. T. Tahara, R. Yonesaka, S. Yamamoto, T. Kakue, P. Xia, Y. Awatsuji, K. Nishio, S. Ura, T. Kubota, O. Matoba, High-speed three-dimensional microscope for dynamically moving biological objects based on parallel phase-shifting digital holographic microscopy. *IEEE J. Sel. Top. Quantum Electron.* **18**(4), 1387–1393 (2012)
18. E. Sanchez-Ortiga, A. Doblas, G. Saavedra, M. Martinez-Corral, J. Garcia-Sucerquia, Off-axis digital holographic microscopy: Practical design parameters for operating at diffraction limit. *Appl. Opt.* **53**(10), 2058–2066 (2014)
19. J.M. Bioucas-Dias, G. Valadao, Phase unwrapping via graph cuts. *IEEE Trans. Image Process.* **16**(3), 698–709 (2007)
20. A.K. Gupta, N.K. Nishchal, Transport of intensity equation for phase imaging: A review. *Asian J. Phys.* **28**(10–12), 777–786 (2019)
21. M.R. Teague, Deterministic phase retrieval: A Green's function solution. *J. Opt. Soc. Am.* **73**(11), 1434–1441 (1983)
22. P.P. Banerjee, A. Korpel, K.E. Lonngren, Self-refraction of nonlinear capillary-gravity waves. *Phys. Fluids* **26**(9), 2393–2398 (1983)

23. D. Soto-Puebla, M. Xiao, F. Ramos-Mendieta, Optical properties of a dielectric–metallic superlattice: The complex photonic bands. *Phys. Lett. A* **326**, 273–280 (2004)
24. A. Alejo-Molina, J.J. Sánchez-Mondragón, D.A. May-Arrijo, D. Romero, J. Escobedo-Alatorre, A. Zamudio-Lara, Complex dispersion relation of 1D dielectric photonic crystal with thin metallic layers. *Microelectron. J.* **40**, 459–461 (2009)
25. C.H. Costa, F.C.P. Luiz, G.B. Claudionor, Light propagation in quasiperiodic dielectric multilayers separated by graphene. *Phys. Rev. B* **96**, 125412–125421 (2017)
26. Z. Rahmani, N. Rezaee, The reflection and absorption characteristics of one-dimensional ternary plasma photonic crystals irradiated by TE and TM waves. *Optik* **184**, 134–141 (2019)
27. B. Guo, M.Q. Xie, L. Peng, Photonic band structures of one-dimensional photonic crystals doped with plasma. *Phys. Plasmas* **19**, 10–17 (2012)
28. P.P. Banerjee, H. Al-Ghezi, G. Chen, J. Slagle, M. Rumi, R. Gnawali, D.R. Evans, Prediction of metallo-dielectric transmission filter performance based on underlying dispersion relations. *J. Opt. Soc. Amer. B* **41**, 698–711 (2024)
29. P.P. Banerjee, H. Al-Ghezi, G. Chen, Prediction of metallo-dielectric transmission filter performance based on dispersion relations, in *invited talk, Weiglhofer Symposium on Electromagnetic Theory*, (Edinburgh, 2022)
30. Y. Wu, C. Zhang, N.M. Estakhri, Y. Zhao, J. Kim, M. Zhang, X.X. Liu, G.K. Pribil, A. Alù, C.K. Shih, X. Li, Intrinsic optical properties and enhanced plasmonic response of epitaxial silver. *Adv. Mater.* **26**, 6106–6110 (2014)
31. S. Sarkar, V. Gupta, M. Kumar, J. Schubert, P.T. Probst, J. Joseph, T.A.F. König, Hybridized guided-mode resonances via colloidal plasmonic self-assembled grating. *ACS Appl. Mater. Interfaces* **11**, 13752–13760 (2019)
32. G. Chen, *Analysis of Propagation across Multilayered Metamaterials for Subwavelength Focusing and Bandpass Filtering Applications*, MS thesis (University of Dayton, 2022)
33. T. Siefke, S. Kroker, K. Pfeiffer, O. Puffky, K. Dietrich, D. Franta, I. Ohlidal, A. Szeghalmi, E.-B. Kley, A. Tünnermann, Materials pushing the application limits of wire grid polarizers further into the deep ultraviolet spectral range. *Adv. Opt. Mater.* **4**, 1780–1786 (2016)
34. H. Zhou, M.M.R. Hussain, P.P. Banerjee, A review of the dual-wavelength technique for phase imaging and 3D topography. *Light: Adv. Manuf.* **3**(17), 1 (2022)
35. U. Abeywickrema, D. Beamer, P. Banerjee, T.-C. Poon, Holographic topography using acousto-optically generated large synthetic wavelengths, in *Proceedings SPIE9771, Practical Holography XXX: Materials and Applications, 97710C*, (2016)
36. D. Claus, D.J. Robinson, D.G. Chetwynd, Y. Shuo, W.T. Pike, J.J.D.J.T. Garcia, J.M. Rodenburg, Dual wavelength optical metrology using ptychography. *J. Opt.* **15**, 035702 (2013)
37. R.C. Shaler, A. Lakhtakia, J.W. Rogers, D.P. Pulsifer, R.J. Martin-Palma, Columnar-thin-film acquisition of fingerprint topology. *JNP* **5**, 051509 (2011)
38. S.A. Muhlberger, D.P. Pulsifer, A. Lakhtakia, R.J. Martin-Palma, R.C. Shaler, Optimized development of sebaceous fingerprints on nonporous substrates with conformal columnar thin films. *J. Forensic Sci.* **59**(1), 94–102 (2014)
39. U. Abeywickrema, P. Banerjee, A. Kota, S.E. Swiontek, A. Lakhtakia, High-resolution topograms of fingerprints using multiwavelength digital holography. *Opt. Eng.* **56**(3), 034117 (2017)
40. N.A. Alanazi, A.M. Scott, H. Al-Ghezi, M. Faryad, A. Lakhtakia, P.P. Banerjee, Transport of intensity and phase: Applications to digital holography [invited]. *Appl. Opt.* **63**(7), 2436–2454 (2024)
41. A.M. Scott, P.P. Banerjee, M. Faryad, A. Lakhtakia, 3D topographic imaging of columnar-thin-film-coated fingerprints using transport of intensity, in *Presented at Optica Digital Holography and Three-Dimensional Imaging Conference*, (2024)
42. P.P. Banerjee, A simple derivation of the Fresnel diffraction formula. *Proc. IEEE* **73**, 1959–1960 (1985)
43. P.P. Banerjee, T.-C. Poon, *Principles of Applied Optics* (CRC, 1991)

44. P.P. Banerjee, G. Cook, D.R. Evans, A q-parameter approach to analysis of propagation, focusing, and waveguiding of radially polarized Gaussian beams. *J. Opt. Soc. Am. A* **26**, 1366–1374 (2009)
45. P.P. Banerjee, G. Nehmetallah, Linear and nonlinear propagation in negative index materials. *J. Opt. Soc. Amer. B* **23**, 2348–2355 (2006)
46. P.P. Banerjee, R. Aylo, G. Nehmetallah, Baseband and envelope propagation in media modeled by a class of complex dispersion relations. *J. Opt. Soc. Amer. B* **25**, 990–994 (2008)
47. R. Aylo, P.P. Banerjee, Modeling propagation in negative index media using causal complex dispersion relations. *J. Opt. Soc. Amer. B* **27**, 1583–1588 (2010)
48. G. Nehmetallah, R. Aylo, P. Powers, A. Sarangan, J. Gao, H. Li, A. Achari, P.P. Banerjee, Co-sputtered SiC + ag nanomixtures as visible wavelength negative index metamaterials. *Opt. Exp.* **20**, 7095–7100 (2012)
49. R. Gnawali, P.P. Banerjee, J.W. Haus, V. Reshetnyak, D.R. Evans, Berreman approach to optical propagation through anisotropic metamaterials: Application to metallo-dielectric stacks. *Opt. Comm.* **425**, 71–79 (2018)
50. R. Gnawali, A. Kota, P.P. Banerjee, J.W. Haus, V. Reshetnyak, D.R. Evans, A simplified transfer function approach to beam propagation in anisotropic metamaterials. *Opt. Comm.* **461**, 125235 (2020)
51. H. AL-Ghezi, R. Gnawali, P.P. Banerjee, L. Sun, J. Slagle, D.R. Evans, 2×2 anisotropic transfer matrix approach for optical propagation in uniaxial transmission filter structures. *Opt. Exp.* **28**, 35761–35783 (2020)
52. P.P. Banerjee, H.-L. Yu, D. Gregory, N. Kukhtarev, H.J. Caulfield, Self-organization of scattering in photorefractive KNbO_3 in a hexagonal spot array. *Opt. Lett.* **20**, 10–12 (1995)
53. T. Honda, P.P. Banerjee, Threshold for spontaneous pattern formation in reflection-grating-dominated photorefractive media with mirror feedback. *Opt. Lett.* **21**, 779–781 (1996)
54. J.O. Dimmock, P.P. Banerjee, F.L. Madarasz, N.V. Kukhtarev, Steady state analysis of self-organization of light into a scattering ring due to induced reflection gratings in photorefractive materials. *Opt. Comm.* **175**, 433–446 (2000)
55. M.A. Saleh, P.P. Banerjee, J.L. Carns, G. Cook, D.R. Evans, Stimulated photorefractive backscatter leading to six-wave mixing and phase conjugation in iron doped lithium niobate. *Appl. Opt.* **46**, 6151–6160 (2007)
56. P.P. Banerjee, G. Nehmetallah, N. Kukhtarev, S. Praharaj, Dynamic holographic interferometry of diffuse objects and its application to determination of airplane attitudes. *Appl. Opt.* **47**, 3877–3887 (2008)
57. G. Nehmetallah, P.P. Banerjee, N. Kukhtarev, “SHOT: Single-beam holographic tomography”, invited contribution. *SPIE Newsroom* (2011). <https://doi.org/10.1117/2.1201102.003474>. <http://spie.org/x47311.xml?ArticleID=x47311>
58. L. Williams, G. Nehmetallah, P.P. Banerjee, Digital tomographic compressive holographic reconstruction of three-dimensional objects in transmissive and reflective geometries. *Appl. Opt.* **52**, 1702–1710 (2013)
59. L. Williams, P.P. Banerjee, G. Nehmetallah, S. Praharaj, Holographic volume displacement calculations via multiwavelength digital holography. *Appl. Opt.* **53**, 1597–1603 (2014)
60. H. Zhou, E. Stoykova, M. Hussain, P.P. Banerjee, Performance analysis of phase retrieval using transport of intensity with digital holography [invited]. *Appl. Opt.* **60**, A73–A83 (2021)

Nanophotonics Applications of Gradient Surface Electromagnetic Waves



Igor I. Smolyaninov and Vera N. Smolyaninova

1 Introduction

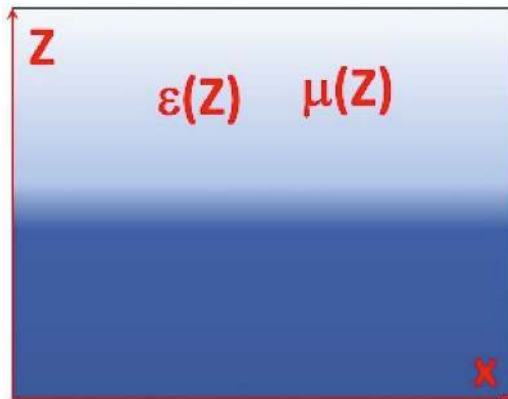
Surface electromagnetic wave (SEW) solutions of macroscopic Maxwell equations, such as surface plasmon polaritons (SPP) at sharp metal-dielectric boundaries [1] and Zenneck waves at sharp boundaries between high-loss and low-loss dielectrics [2], have been known for some time. More recently, SEW solutions have also been discovered in low-loss [3] and even very high-loss [4, 5] gradient dielectric media, such as the surface of seawater and various underground sediment layers. This discovery was both surprising and practically useful, as these SEWs may be utilized in broadband underwater radio [6] and video [7] communication. Another potential application of this finding is in UV nanophotonics [8], as virtually all materials behave as very high-loss dielectrics at UV frequencies. Additionally, this result has broad fundamental physics implications, complementing recent observations of loss-enhanced transmission due to PT-symmetry in non-Hermitian optical systems [9].

Unfortunately, these newly discovered SEW solutions still suffer from relatively short propagation ranges. Although their propagation range is considerably longer than their wavelength, it remains short in practical terms, limiting their applications. The goal of this chapter is to extend the theoretical considerations in refs. [4, 5] to a more general case where a highly lossy gradient medium exhibits surface gradients of both its dielectric permittivity $\epsilon(z)$ and its magnetic permeability $\mu(z)$,

I. I. Smolyaninov (✉)
Saltenna LLC, McLean, VA, USA
e-mail: igor.smolyaninov@saltenna.com

V. N. Smolyaninova
Department of Physics Astronomy and Geosciences, Towson University, Towson, MD, USA
e-mail: vsmolyaninova@towson.edu

Fig. 1 Gradient interface problem considered in this chapter. The dielectric permittivity $\varepsilon(z)$ and the magnetic permeability $\mu(z)$ of the medium are continuous and depend only on z coordinate, which is illustrated schematically by halftones



as illustrated in Fig. 1. We will demonstrate that novel lower-loss propagating surface wave solutions may be found in some of these situations. Potentially, these new results may be applied in practical underwater and underground communication systems, establishing broadband radio communication channels along the surfaces of rusty pipes deployed in underwater and underground oil and gas fields. The developed theory also has important implications in the field of metamaterial optics, where the negative effect of metamaterial losses on signal propagation remains a significant problem. The usefulness of the developed approach will be illustrated by several newly found examples of gradient geometries where the surface wave problem can be solved analytically. Finally, we will present several examples of practically useful novel surface wave geometries, ranging from radio communication underwater to UV nanophotonics.

2 General Theoretical Framework

Let us examine the solutions to the macroscopic Maxwell equations in a scenario where the dielectric permittivity and magnetic permeability of a medium vary with the z coordinate: $\varepsilon = \varepsilon(z) = \varepsilon'(z) + i\varepsilon''(z)$ and $\mu = \mu(z) = \mu'(z) + i\mu''(z)$, as illustrated in Fig. 1. Both $\varepsilon = \varepsilon(z)$ and $\mu = \mu(z)$ functions are assumed to be continuous and the effects of spatial dispersion are neglected.

These functions are derived from experimental measurements. (Note that typical sources of spatial dispersion in electromagnetism include anisotropic material responses due to crystal structure or optical activity in solutions of chiral molecules. Spatial dispersion is also significant in collisional damping in plasmas. None of these factors are present in the experimental situations studied in our work). Under these conditions, the spatial variables in the Maxwell equations separate, and without loss of generality, we can assume electromagnetic mode propagation in the x direction, resulting in field dependencies proportional to $e^{i(kx - \omega t)}$ (see also

ideologically similar derivations in [4, 5]). The macroscopic Maxwell equations then straightforwardly lead to a wave equation

$$-\nabla^2 \vec{E} - \vec{\nabla} \left(E_z \frac{\partial \varepsilon}{\partial z} \right) = \frac{\omega^2 \varepsilon \mu}{c^2} \vec{E} + \left(\vec{\nabla} \mu \right) \times \left(\frac{\vec{\nabla} \times \vec{E}}{\mu} \right) \quad (1)$$

where E_z is the z component of electric field. For the TE polarization this wave equation may be written as

$$-\nabla^2 E_y = \frac{\omega^2 \varepsilon \mu}{c^2} E_y - \frac{1}{\mu} \left(\frac{\partial \mu}{\partial z} \right) \left(\frac{\partial E_y}{\partial z} \right) \quad (2)$$

If an effective “wave function” $E_y = \psi \mu^{1/2}$ is introduced, the wave Eq. (2) may be rewritten in the form of one-dimensional Schrodinger equation

$$-\frac{\partial^2 \psi}{\partial z^2} + \left(-\frac{\varepsilon(z) \mu(z) \omega^2}{c^2} - \frac{1}{2} \frac{\partial^2 \mu}{\mu \partial z^2} + \frac{3}{4} \frac{(\partial \mu / \partial z)^2}{\mu^2} \right) \psi = -\frac{\partial^2 \psi}{\partial z^2} + V \psi = -k^2 \psi \quad (3)$$

On the other hand, for the TM polarization of greater interest to us, the wave equation may be written in the form of a similar one-dimensional Schrodinger equation

$$-\frac{\partial^2 \psi}{\partial z^2} + \left(-\frac{\varepsilon(z) \mu(z) \omega^2}{c^2} - \frac{1}{2} \frac{\partial^2 \varepsilon}{\varepsilon \partial z^2} + \frac{3}{4} \frac{(\partial \varepsilon / \partial z)^2}{\varepsilon^2} \right) \psi = -\frac{\partial^2 \psi}{\partial z^2} + V \psi = -k^2 \psi \quad (4)$$

where the effective “wave function” $E_z = \psi / \varepsilon^{1/2}$ has been introduced. In both Eqs. 3 and 4, the $-k^2$ term serves as the effective energy in the corresponding Schrödinger equation. It is important to note that the continuity of $D_z = \psi \varepsilon^{1/2}$ necessitates the continuity of $\psi(z)$, provided that $\varepsilon(z)$ is continuous and $\varepsilon = \varepsilon' + i\varepsilon'' \neq 0$.

The most intriguing result from refs. [4, 5] arose from examining the TM polarized solutions within a medium with an almost purely imaginary dielectric permittivity, $\varepsilon(z) \approx i\varepsilon''(z) = i\sigma(z)/\varepsilon_0\omega$, where ε_0 is the dielectric permittivity of vacuum, $\varepsilon''\varepsilon''$ is very large, and the medium’s conductivity $\sigma(z)$ is given in practical SI units. Based on Eq. 4, the effective potential in this scenario can be written as

$$V(z) = -\frac{i\sigma\mu\omega}{\varepsilon_0 c^2} - \frac{1}{2} \frac{\partial^2 \sigma}{\sigma \partial z^2} + \frac{3}{4} \frac{(\partial \sigma / \partial z)^2}{\sigma^2} \quad (5)$$

As observed in [4, 5], the second and third terms in Eq. 5 remain real even when ε'' is very large, and they can become much larger than the first term if the medium's conductivity changes rapidly enough near the surface as a function of z . When these terms dominate the first one, a propagating SEW solution may emerge in a highly lossy system. However, if μ is real, the first term in Eq. 5 (which equals $\text{Im}(V)$) limits the propagation length of such an SEW solution, except at very low frequencies.

The key insight of the current work is that the SEW propagation length can be significantly enhanced if $\mu(z)$ also becomes an almost purely imaginary function (while the effective potential well described by Eq. 5 remains deep enough to support an SEW mode). This can occur in materials with near-zero permeability ($\mu \approx 0$, MNZ) [10], and in any material where $\mu' \approx 0$ (with μ'' not necessarily being small). MNZ conditions are typically found in split-ring resonator (SRR) array metamaterials, whose effective permeability is defined [11] as

$$\mu_{\text{eff}}(\omega) = 1 - \frac{1 - (\omega_s/\omega_p)^2}{1 - (\omega_s/\omega)^2 - i\gamma/\omega}, \quad (6)$$

where ω_s is the resonant frequency of SRR, ω_p is the magnetic plasma frequency of the array, and $\gamma \ll \omega_s$ is the damping constant. It is assumed that $\omega_p > \omega_s$ so that $\mu'' > 0$ at all frequencies. The MNZ conditions are observed around $\omega \approx \omega_p$, and in this frequency range

$$\mu_{\text{eff}}(\omega) \approx \frac{i\gamma\omega_p}{\omega_p^2 - \omega_s^2} \quad (7)$$

If a gradient medium incorporates such an SRR array metamaterial, the surface potential described by Eq. 5 becomes almost purely real:

$$V \approx \frac{\sigma\gamma\omega_p^2}{\varepsilon_0 c^2 (\omega_p^2 - \omega_s^2)} - \frac{1}{2} \frac{\partial^2 \sigma}{\sigma \partial z^2} + \frac{3}{4} \frac{(\partial \sigma / \partial z)^2}{\sigma^2} \quad (8)$$

(the practical SI units of conductivity are used in this equation.) Moreover, if the damping constant is small, the second and third terms in Eq. 8 become much larger than the first one, ensuring that the SEW eigenstate remains unperturbed.

Besides SRR metamaterial geometries, MNZ conditions may also be found in natural materials, such as yttrium iron garnet (YIG) near the ferromagnetic resonance (FMR) [12]. Since FMR is also present in surface-oxidized iron [13], our theoretical results could potentially be applied to practical underwater and underground communication systems. In these systems, broadband (MHz compared to KHz range acoustic communication) SEW radio communication channels could be established along the surfaces of rusty pipes used in underwater and underground oil and gas production fields. While this promising possibility warrants a detailed

investigation of its own, we will now focus on several analytical SEW problems that can be solved using the general formalism outlined.

3 Analytical Solutions of SEW Problem in Gradient Media

In a general arbitrary case, the effective Schrödinger equations (Eqs. 3 and 4) describing the SEW problem in gradient media must be solved numerically (see examples in [4, 5, 8]). However, several important simple geometries can be solved analytically. Let us begin by demonstrating that the gradient terms in Eqs. 3 and 4 cannot be neglected. Indeed, if we assume that

$$-\frac{1}{2} \frac{\partial^2 \varepsilon}{\varepsilon \partial z^2} + \frac{3}{4} \frac{(\partial \varepsilon / \partial z)^2}{\varepsilon^2} = 0 \quad (9)$$

this differential equation may be solved analytically, and the most general solution of this equation is either a constant, or

$$\varepsilon(z) = \frac{c_2}{(c_1 + z)^2} \quad (10)$$

where c_1 and c_2 are constants. It is evident that such a solution cannot accurately represent a step-like function, which is characteristic of a real interface between two distinct materials.

Now, let us examine two nonmagnetic gradient media geometries, as schematically illustrated in Fig. 2. Figure 2a corresponds to a gradual metal–dielectric interface. Let us assume that.

$$\varepsilon' = az \text{ for } |z| < \xi \quad (11)$$

and that ε' stays constant outside this region. We will neglect the second derivative of ε' near $z = \pm \xi$. We also assume that $\varepsilon'' = \delta > \varepsilon'$, and it stays constant across the interface. Under these assumptions, in the limit of small ω , the effective potential $V(z)$ given by Eq. 4 becomes a rectangular potential well which depth is:

$$V = -\frac{3\alpha^2}{4\delta^2} \quad (12)$$

This potential well contains at least one bound SEW state, resembling a surface plasmon-like SEW solution. It is important to note that the typically derived SPP solution [1] corresponds to the limit where $\xi \rightarrow 0$ and $\delta = 0$, resulting in a discontinuous $\varepsilon(z)$. In this scenario, $V \rightarrow -\infty$ and the continuity of ψ at $z = 0$ cannot be maintained. Under these special conditions, the derivation of the conventional SPP solution reverts to the more common approach described in [1].

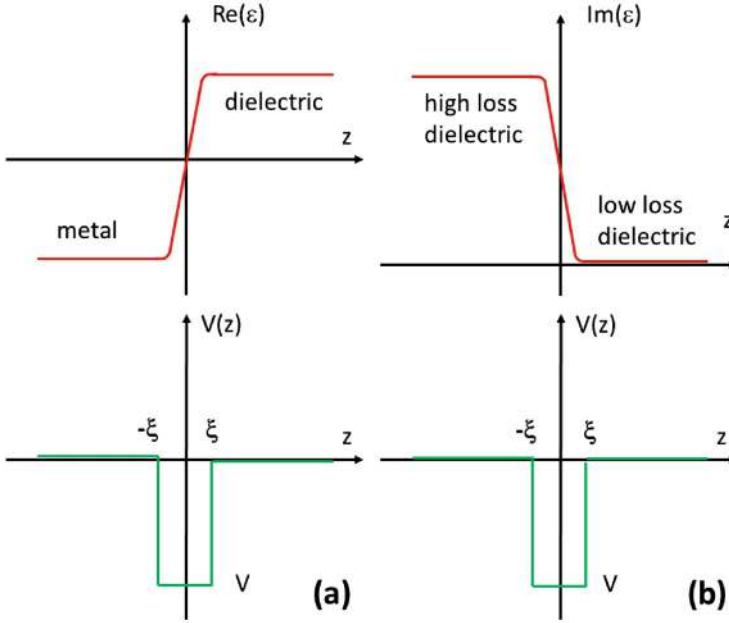


Fig. 2 Two kinds of gradient interfaces which produce a rectangular potential well at the interface. **(a)** A metal–dielectric interface which leads to a surface plasmon-like SEW solution. **(b)** An interface between low-loss and high-loss dielectric which leads to Zenneck-like SEW solution

Another example, depicted in Fig. 2b, involves a gradient interface between high-loss and low-loss dielectrics, where

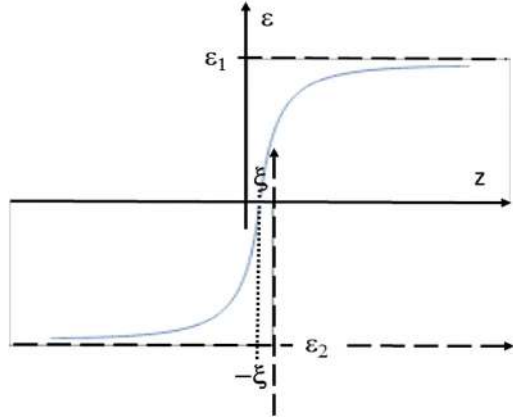
$$\varepsilon'' = -\alpha z + \alpha \xi \text{ for } |z| < \xi \quad (13)$$

and ε'' stays constant outside this region. Once again, we neglect the second derivative of ε'' near $z = \pm \xi$. We also assume that $\varepsilon' = \delta \gg \varepsilon''$, and it remains constant across the interface. Under these assumptions, the effective potential $V(z)$ given by Eq. 4 again forms a rectangular potential well, with its depth defined by Eq. 12. Similar to the scenario in Fig. 2a, this potential well possesses at least one bound SEW state, corresponding to a Zenneck-like SEW solution.

In principle, almost any 1D surface potential $V(z)$ can be emulated by appropriate (metamaterial) engineering of either the $\varepsilon(z)$ or $\mu(z)$ profile. As an example, consider a 1D Coulomb potential and the case of an engineered $\varepsilon(z)$. The required profile can be obtained by solving a differential equation.

$$-\frac{1}{2} \frac{\partial^2 \varepsilon}{\varepsilon \partial z^2} + \frac{3}{4} \frac{(\partial \varepsilon / \partial z)^2}{\varepsilon^2} = -\frac{\alpha}{z} \quad (14)$$

Fig. 3 A Coulomb-like potential well at an interface of two media may be constructed approximately from two $\varepsilon(z)$ profiles given by Eq. 15. The $1/z$ divergences are cut off at $z = \pm\xi$



where a is an arbitrary positive constant. This equation has been solved using ordinary differential equation solver Wolfram Alpha [14], which gives the following approximate solution:

$$\varepsilon(z) = c_2 \exp \left(\int_1^z \frac{c_1 J_1(2\sqrt{\alpha\zeta}) + \sqrt{\alpha\zeta} ((c_1 - 2) J_0(2\sqrt{\alpha\zeta}) - c_1 J_2(2\sqrt{\alpha\zeta}))}{\zeta J_1(2\sqrt{\alpha\zeta}) (1 - c_1)} d\zeta \right) \quad (15)$$

where c_1 and c_2 are constants, and $J_n(z)$ is the Bessel function of the first kind.

Since $1/z \rightarrow 0$ in the limit of large z , this solution tends to a constant in this limit (see discussion of solutions of Eq. 9 above). On the other hand, $\varepsilon(z)$ diverges near $z = 0$. Thus, an interface between two media may be engineered as shown in Fig. 3, so that near the interface $\varepsilon(z)$ may be approximated with a cutoff 1D Coulomb potential. In the limit of small ω such a potential well will support a set of Rydberg-like SEW states—see for example ref. [15].

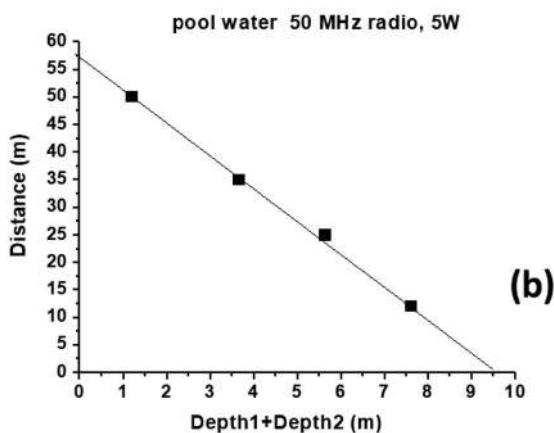
The analytical results outlined above support results of [4, 5, 8] which indicate that SEW modes are ubiquitous, and they can be found and utilized in all kinds of electromagnetic environments. Below we will illustrate several examples of such applications in the cases of radio communication underwater in the MHz frequency range, Wi-Fi communication through steel pipes in the GHz frequency range, and UV nanophotonics.

4 Radio Frequency Applications of Gradient Surface Electromagnetic Waves

4.1 Underwater Radio Communication at MHz Frequencies

Let's begin with the application of SEWs in underwater radio communication. These experiments utilized SEW antennas [6] operating in the MHz frequency

Fig. 4 (a) Photo of an underwater radio communication experiment performed at 50 MHz in pool water (skin depth $\eta = 0.1$ m). The lateral positions of two divers underwater are marked by two red plastic buoys. (b) Experimental results plotted as communication distance vs. the sum of depths of the two radios underwater. Note that radio communication was achieved over distances of many hundreds of skin depth



range. A SEW antenna specifically excites the propagation mode supported by a dielectric (or magnetic) discontinuity when positioned nearby. Unlike traditional antennas, a SEW antenna does not radiate or support free space electromagnetic fields. In the MHz frequency range underwater, they exhibited efficient radio communication over distances spanning several hundred skin depths. An example of the experimental setup for a typical 50 MHz underwater radio communication experiment performed in chlorinated pool water (in which skin depth at 50 MHz equals $\eta = 0.1$ m) is depicted in Fig. 4a. In these experiments two Yaesu VX-8 radios operated at 50 MHz at 5 W output power were connected to their respective SEW antennas (as described in detail in [6]), and used for voice communication between two divers, while both divers and all the components of their radio systems were completely submerged underwater.

Quantitative analysis of these experiments provides strong evidence of the SEW transmission mechanism underwater. When plotted as distance L versus the sum of diver depths D_1 and D_2 underwater (see Fig. 4b), the experimental datapoints exhibit a linear dependence. The slope of this dependence clearly points at the

SEW communication mechanism. Indeed, in the absence of external RF noise, radio communication underwater is limited by the constant radio receiver sensitivity, so that

$$e^{-\frac{D_1}{\eta'}} e^{-\frac{D_2}{\eta'}} e^{-\frac{L}{\eta^*}} \approx \text{const} \quad (16)$$

where η' is the SEW penetration depth into water, and η^* is the SEW propagation length along the water surface (note that neither of these parameters should necessarily be equal to the skin depth η , and in fact both η' and η^* exceed η considerably). The logarithm of Eq. 16 gives rise to the linear dependence observed in the experiment:

$$L \approx C - \frac{\eta^*}{\eta'} (D_1 + D_2) \quad (17)$$

Based on the experimental data points in Fig. 4b, it appears that $\eta^*/\eta' > 6$, confirming the SEW-mediated mechanism of underwater radio communication. This explains the observed combinations of communication depths and distances that far exceed the conventional limit set by the bulk skin depth η of pool water. At 50 MHz, pool water is considered a highly lossy dielectric. With a typical conductivity of $\sigma \approx 0.5$ S/m, the imaginary part of its dielectric permittivity $\epsilon'' \approx 180$ significantly surpasses the real part $\epsilon' \approx 81$. The ability of SEW-based underwater radios to achieve communication distances of approximately 60 m, or about 600 skin depths (and around 100 wavelengths in pool water at 50 MHz), clearly demonstrates the low-loss propagation of SEW modes compared to bulk radio wave propagation underwater. Additionally, due to their very large bandwidth (6 MHz at a 30 MHz carrier frequency), SEWs enable the transmission of live high-definition video signals underwater (see Fig. 5 and a detailed report in [7]), which is impossible to achieve with traditional acoustic communications typically operating in the KHz range [16].

4.2 Radio Communication Through Metal at GHz Frequencies

Another intriguing application of the developed theoretical framework involves common metals in the GHz frequency range. In this range, all metals behave as very high-loss dielectrics due to their extremely high conductivities, typically in the range of 10^6 – 10^7 S/m. Considering the relationship between ϵ'' and material conductivity σ as mentioned above:

$$\epsilon''(z) = \sigma(z)/\epsilon_0\omega, \quad (18)$$

Fig. 5 Transmission of live high-definition video image underwater using SEW antennas operating at 30 MHz carrier frequency. As indicated in (a), the video signal bandwidth is 6 MHz. Positions of the underwater video camera and the SEW antenna are indicated by arrows in (b)



we see that metals in the GHz range are analogous to seawater in the KHz and lower MHz ranges. The simplest way to demonstrate the potential of GHz-range SEWs in high-loss metal environments is to consider the propagation of SEW-mediated signals through metal enclosures.

SEWs are known to significantly enhance signal transmission through arrays of deeply subwavelength holes in metal surfaces [17]. The physical mechanism behind this effect is believed to involve the coupling of incoming electromagnetic waves to SEWs propagating along the opposite metal-dielectric interfaces of a metal layer. Although the original observations in ref. [17] were made in the visible frequency range, similar effects have recently been observed with SEW antennas operating in the GHz range [18]. Several interesting and practical applications of this effect are shown in Figs. 6 and 7.

Figure 6 demonstrates the transmission of a live Wi-Fi video signal through a steel riser pipe, typically used in the oil and gas industry, which was sealed tightly at both ends with thick aluminum shields. Notably, the pipe is visibly rusty, indicating that both gradients of $\epsilon(z)$ and $\mu(z)$ must be considered in a comprehensive theoretical description of this experiment. Figure 7 provides further examples of GHz-range SEW signal transmission through metal plates.

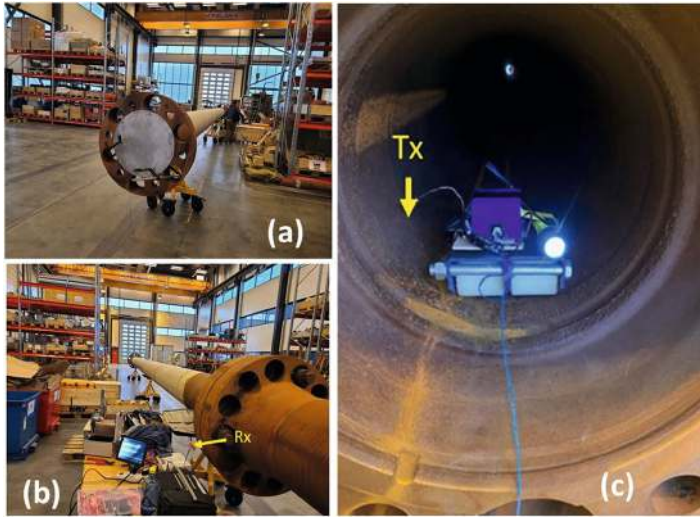


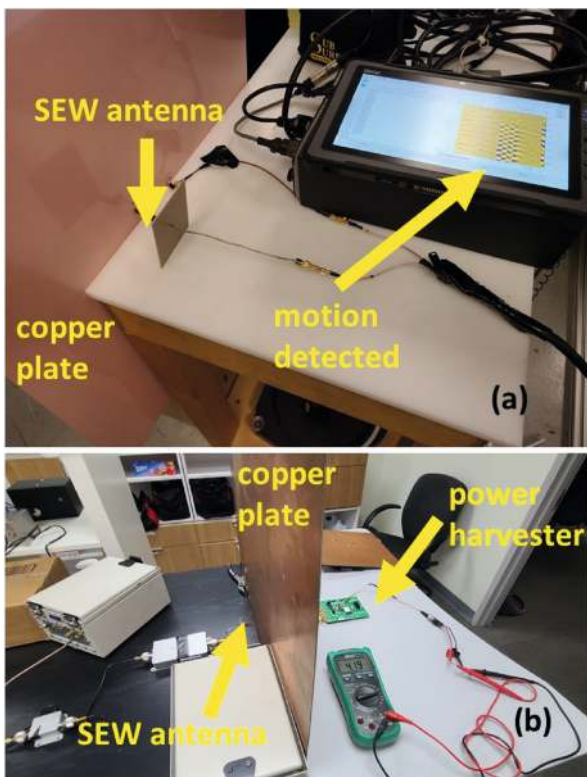
Fig. 6 SEW-mediated transmission of Wi-Fi video signal through a 32 m long section of a steel riser pipe. The pipe was tightly closed on both ends with thick aluminum shields (a). The Wi-Fi video transmitter was moved through the length of the pipe, while live video (seen on the monitor in image (b)) was transmitted from inside the pipe (c) with no interruption

In the first example shown in Fig. 7a, a SEW antenna was connected to a commercial ground-penetrating radar (GPR), enabling motion detection through a metal plate. A very clear signal, produced by a slight hand wave behind the copper plate, is seen in Fig. 7a. It was verified that the native conventional antennas of this GPR could not detect any similar hand motion behind the same copper plate.

As an extension of this experiment, we confirmed that wireless power transmission through metal walls is also possible in the “SEW mode” (see Fig. 7b). In this experiment, we used the P2110-EVAL-01 power harvester circuit from Powercast Corporation. A 2.45 GHz SEW antenna in contact with a large copper shield was used on the receiving side of the experiment. On the transmitting side, we used the same SEW Wi-Fi transmitter as in Fig. 6, with the signal amplified to 10 W by a commercial outdoor Wi-Fi amplifier. The transmitting SEW antenna was placed in close contact with the metal surface on the other side of the large copper shield. As seen on the multimeter screen in Fig. 7b, the power harvester circuit achieved 4.19 V charging when connected to the SEW antenna.

These experiments highlight the significant potential of SEW antennas and signals in wireless communication and power transfer. Unlike conventional radio systems, which cannot transmit signals through metal obstacles, such previously prohibitive situations seem ideal for SEW-based remote communication and power transfer.

Fig. 7 (a) Plasmonic antenna connected to a commercial GPR (QM1020 made by USRadar) detects hand motion behind a copper plate. (b) Plasmonic antenna connected to a commercial power harvester (P2110-EVAL-01 made by Powercast Corporation) enables wireless power transmission through a copper plate

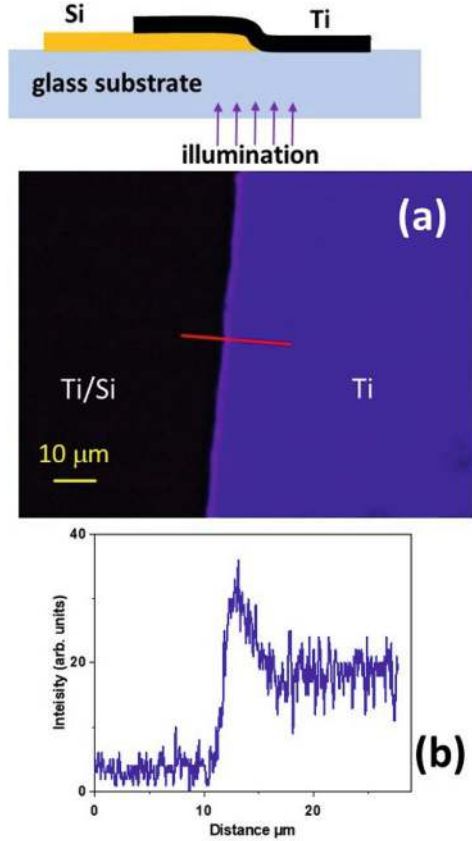


5 Nanophotonics Applications of Gradient Surface Electromagnetic Waves

5.1 UV Silicon Nanophotonics

Let's now explore several examples of nanophotonics applications of gradient surface electromagnetic waves (SEWs). First, consider the use of SEW solutions in highly lossy dielectric media for UV nanophotonics. Since almost all materials behave as highly lossy dielectrics in the UV range, TM polarized SEW propagation must occur at numerous material interfaces. These SEW solutions will have a k -vector larger than the k -vector of photons in each adjacent medium, making them akin to surface plasmon polaritons (SPPs). The presence of such large k -vector SEW modes across various material geometries can lead to novel opportunities in UV nanophotonics and environmental sensing. Unlike typical plasmonic metals, which are challenging to use in nanofabrication with CMOS techniques, many silicon-based SEW geometries will become feasible. Indeed, at around 300 nm UV light wavelength, doping silicon with metals like nickel or titanium alters the dielectric constant's absolute magnitude while it remains almost purely imaginary.

Fig. 8 (a) Transmission optical microscope image of an overlap region between a 260 nm thick silicon and a 230 nm thick titanium film. The image size is $117\ \mu\text{m} \times 88\ \mu\text{m}$. Note the stripe of enhanced transmission, which goes in parallel with the silicon–titanium interface. Its cross-section measured along the red line is shown in the plot (b). The top inset in (a) shows experimental geometry



Our theoretical and experimental findings strongly support the existence of these novel SEW modes in the UV-VIS domain, as demonstrated at the silicon–titanium interface (see Figs. 8 and 9). In the experiment shown in Fig. 8, we examined UV transmission in the overlap region between a 260 nm thick silicon film and a 230 nm thick titanium film. A stripe of enhanced transmission parallel to the silicon–titanium interface is clearly visible. According to Fermi’s golden rule, the increased light transmission at the silicon–titanium junction indicates a higher density of electromagnetic states (DOS) in the junction area, which becomes accessible to photons tunneling through the thick composite conductive film. Thus, the significant increase in light transmission near the Si/Ti junction strongly suggests the presence of SEW interfacial modes in the UV range.

Numerical modeling of the effective potential $V(z)$ at the silicon–titanium interface (see Fig. 9) for 300 nm UV light also reveals the existence of a SEW state. Assuming a 20 nm thick Si/Ti transition region (Fig. 9a), where the dielectric permittivity gradually shifts from bulk silicon to bulk titanium values (compare Fig. 9a with Fig. 3), the resulting effective potential shown in Fig. 9b features a distinct

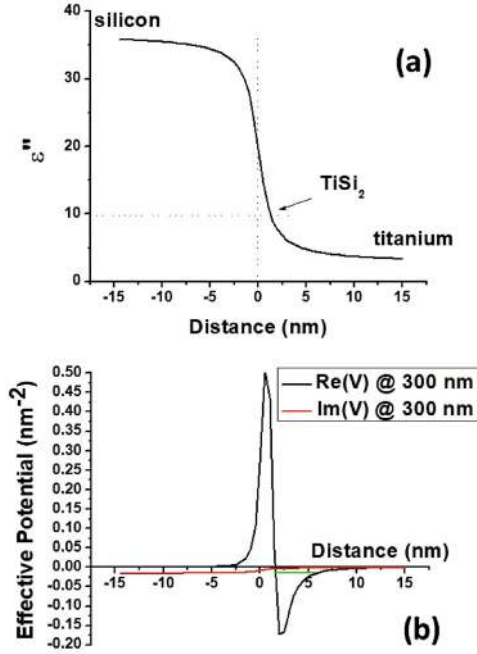


Fig. 9 (a) Plot of an assumed 20 nm thick planar transition layer between silicon and titanium formed due to diffusion of Ti into Si during deposition. The permittivity of the transition region was assumed to follow a simple arctan law: $\varepsilon'' = A \arctan(z/\xi) + B$, where $A = (\varepsilon''_{Si} - \varepsilon''_{Ti})/\pi$ and $B = (\varepsilon''_{Si} + \varepsilon''_{Ti})/2$. The magnitude of $\varepsilon''(z)$ is shown at $\lambda_0 = 300$ nm. The titanium silicide number is indicated by an arrow. (b) The corresponding effective potential energy (both real and imaginary parts) at the silicon interface defined by Eq. 4 (for TM light) plotted at $\lambda_0 = 300$ nm. The numerically obtained effective energy level is shown in green

potential well where $\text{Im}(V) \ll \text{Re}(V)$, supporting a SEW state indicated in green. Note the Coulomb-like character of $V(z)$ at $z > 0$, as expected based on Fig. 3. This bound state yields at least one solution with an almost purely real wave vector k , corresponding to a surface electromagnetic mode with a long propagation length.

Figure 10 presents numerical simulations of surface wave excitation and scattering in a Si/Ti gradient waveguide at $\lambda_0 = 300$ nm. In these simulations, performed using the COMSOL Multiphysics solver, the UV light field in the Si/Ti gradient surface waveguide is excited by a dipole radiation source placed 7 nm above the junction and scattered by a 4 nm diameter metal defect at the 100 nm point, resulting in a pattern of standing surface waves. This simulation illustrates SEW propagation over lateral distances that significantly exceed the SEW wavelength.

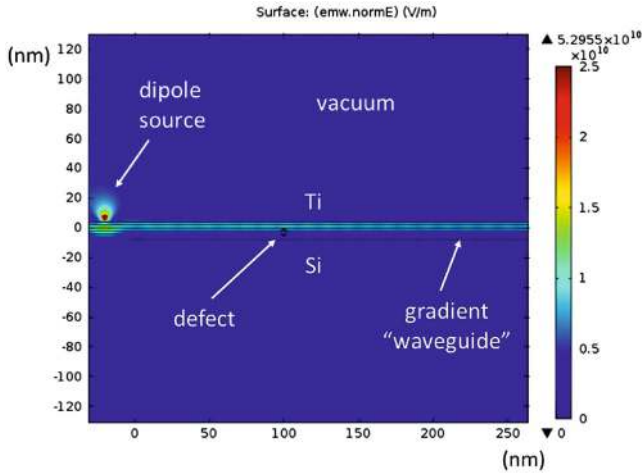


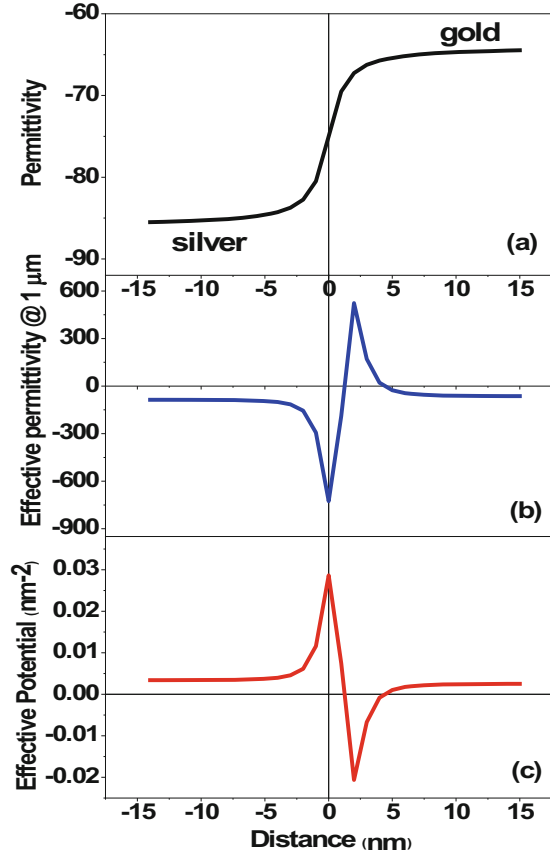
Fig. 10 COMSOL Multiphysics simulations of surface wave excitation in a Si/Ti junction at $\lambda_0 = 300$ nm. The UV light field in the effective gradient waveguide is excited by a dipole radiation source located 7 nm above the junction. A small defect is placed inside the junction at the 100 nm point, resulting in a pattern of standing surface waves. This simulation illustrates SEW propagation over lateral distances, which far exceed the SEW wavelength

5.2 Experimental Observation of Surface Wave States at the Gold–Silver Interface

While the strongly lossy case may be very interesting in UV nanophotonics applications, let us now consider a gradual interface between two different good low-loss metals, such as gold and silver (see Fig. 11). Let’s demonstrate that a gradual interface between gold and silver may also support propagation of a gradient surface electromagnetic wave, which is different from the more well-known surface plasmon polaritons. The existence of such surface waves leads to a paradoxical situation in which a continuous metal barrier, which does not have any pinholes, may exhibit considerably increased light transmission if the barrier is made of two different metals.

In the visible and near-infrared regions, as depicted in Fig. 11a, the dielectric permittivity $\varepsilon(z)$ of such a system will be large, negative, and predominantly real [21]. For instance, the transition region between gold and silver shown in Fig. 11a is assumed to be approximately 10 nm thick. This gradual inter-diffusion layer would naturally form if a silver film is deposited on top of a gold film through thermal evaporation. The resulting effective potential $V(z)$, calculated using Eq. (4), is illustrated in Fig. 11c. We will assess whether a propagating SEW solution can be expected for such a potential well.

Fig. 11 (a) Assumed gradual transition region separating gold and silver films. (b) Corresponding effective permittivity calculated using Eq. (19) at $\lambda = 1 \text{ mm}$ (c) Effective potential of the transition region calculated using Eq. (4)



To demonstrate the existence of such a SEW solution, we can start by defining the effective permittivity of the transition layer as

$$\varepsilon_{\text{eff}}(z) = \varepsilon(z) + \frac{c^2}{\omega^2} \left(\frac{1}{2} \frac{\partial^2 \varepsilon}{\partial z^2} - \frac{3}{4} \frac{(\partial \varepsilon / \partial z)^2}{\varepsilon^2} \right), \quad (19)$$

thus incorporating the gradient terms from Eq. (4) into the “effective” permittivity. The so obtained effective dielectric permittivity of the transition layer is plotted in Fig. 11b. The latter plot demonstrates that a gradual interface between gold and silver is equivalent to a parallel plate metallic waveguide, which is known to have no cutoff frequency for the TM-polarized light, and which always supports a TM_0 guided mode (note the region of positive ε_{eff} in between the two negative ε_{eff} regions in Fig. 11b). Indeed, using the Numerov method [22], Eq. (4) may be solved numerically for the geometry depicted in Fig. 11. At the free space wavelength of $\lambda_0 = 1 \text{ μm}$ such a numerical solution results in $-k^2 = -0.00345 \text{ nm}^{-2}$, which leads

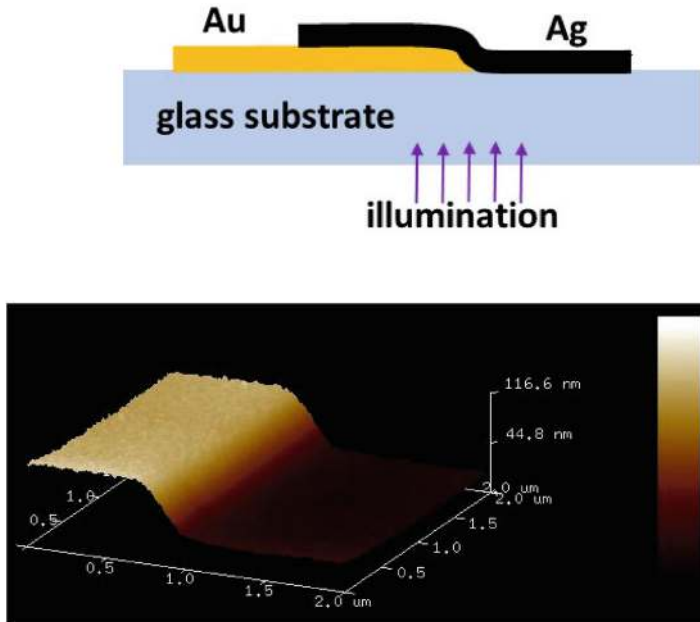


Fig. 12 Schematic geometry of our samples (top) and an AFM image (bottom) of the composite film near the gold-silver edge. The AFM image demonstrates that the sample integrity was not compromised near edge

to $k = 0.059 \text{ nm}^{-1}$ and $\lambda = 106 \text{ nm}$ for the guided TM-polarized SEW mode. While the SEW propagation length for a perfectly flat interface is defined by $\text{Im}(k)$, in most practical situations the propagation length will be defined by surface roughness.

Our experimental results on light propagation through gold-silver interfaces appear to be consistent with theoretical predictions and numerical simulations described above. Since direct probing of the SEW field at the gold-silver interface using scanning probe technique is not possible, we investigated light transmission through composite gold-silver films fabricated on glass slides using thermal evaporation. These experimental results are summarized in Figs. 12 and 13.

The composite gold-silver films were fabricated on top of glass slides overcoated with thin (5 nm) chromium layer for adhesion, as illustrated in Fig. 12. The sample shown in Fig. 13a consisted of 80 nm gold film (on the left) overcoated with an overlap with 88 nm silver film. The schematic geometry of this sample is illustrated in Fig. 12. Optical microscope images of the overlap region obtained in reflection (Fig. 13a) and transmission (Fig. 13b–d) using white light illumination are shown in these figures. As clearly seen in Fig. 13b, a stripe of strongly enhanced light transmission is observed near the edge of the gold-silver overlap region, which goes in parallel with the edge. Figures 13c–f summarize results of our spectroscopic studies of this effect. It appears that the red light transmission far exceeds transmission of blue light through the Au/Ag junction. This is clear from

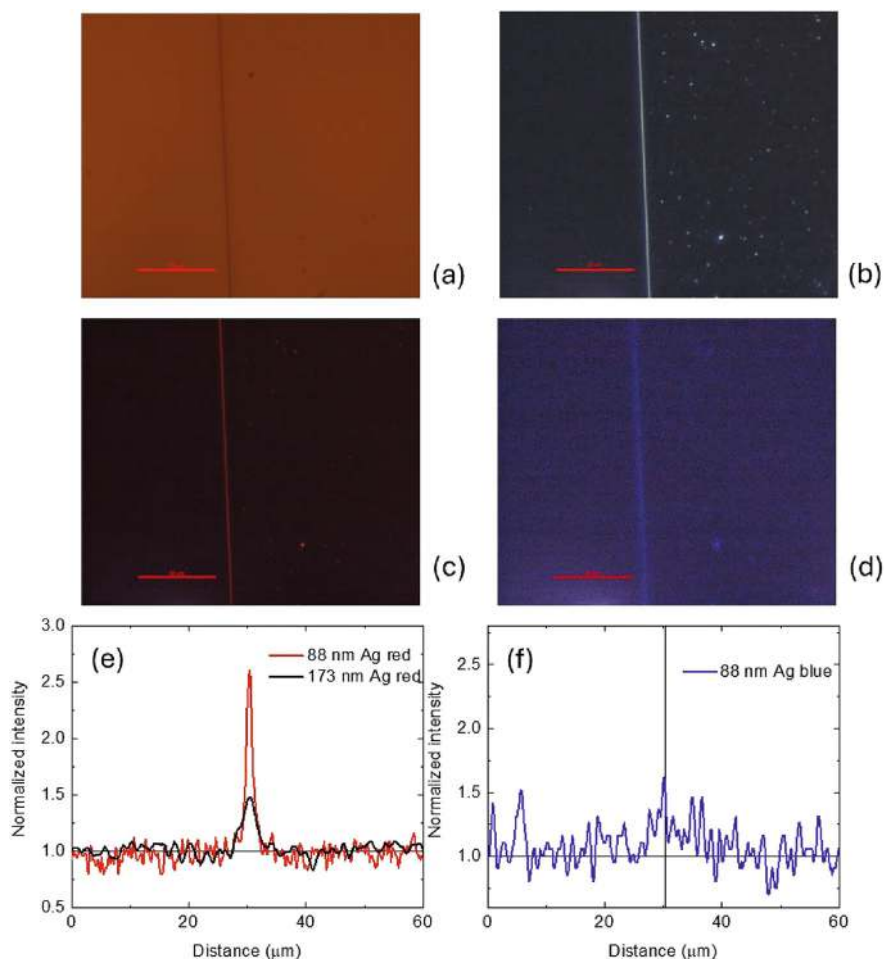


Fig. 13 (a) Reflection microscopic image of an overlap region between 88 nm thick silver and 80 nm thick gold films. The scale bar corresponds to 50 nm. (b) Corresponding transmission image obtained using white light illumination. Note the stripe of strongly enhanced transmission, which coincides with the gold–silver interface. (c) Transmission image of the same sample obtained using a red filter ($>75\%$ avg. transmission for 615–730 nm wavelengths and $<1\%$ avg. transmission for 380–550 nm wavelengths). (d) Transmission image of the same sample obtained using a blue filter (center wavelength 440 nm, FWHM = 85 nm). (e) and (f) show the near edge cross-sections of the transmission images (c) and (d), respectively. The black curve in (e) corresponds to a different sample in which the silver film thickness was increased to 173 nm

both transmission images obtained with color filters and from comparison of their cross-sectional plots presented in Fig. 13e and Fig. 13f through the stripe region. Moreover, when the silver film thickness is increased to 173 nm, transmission of red light through the junction remains quite considerable (see Fig. 13e), while the blue light transmission becomes undetectable at the current sensitivity of our

experiments. These results are consistent with the novel theoretical mechanism discussed above. Indeed, based on Eq.(4), the effective potential $V(z)$ at the Au/Ag interface is mostly real at longer wavelengths, where the dielectric permittivity of both gold and silver are large, negative, and mostly real. On the other hand, $V(z)$ acquires considerable imaginary part toward the blue light wavelengths. Note that these results are drastically different from the naïve expectations based on the known wavelength-dependent skin depth in gold and silver. Note that the skin depth of silver at red light 600 nm wavelength equals about 14 nm. This means that based on conventional expectations light would need to be transmitted through at least 12 skin depths, which makes this effect somewhat similar to the previous experimental observations of enhanced SEW transmission underwater (see Sect. 4.1).

We verified using AFM imaging (see the bottom part of Fig. 12) that the integrity of the composite gold-silver film was not compromised in any way near the gold-silver edge (it did not contain any pinholes or crevices near the edge). Therefore, the effect of enhanced optical transmission near the gold-silver edge cannot be attributed to defects of the composite film.

Based on the obtained theoretical and experimental information, we must conclude that the effect of enhanced light transmission through the composite gold-silver film may be connected to the existence of novel SEW modes at the gold-silver interface. Similar to SPP-mediated light transmission through nanohole arrays [17], these novel SEW modes may facilitate transmission of light through a continuous composite metal film. Indeed, according to the Fermi's golden rule, the increased transmission of light at the gold-silver junction indicates an increased density of photonic states (DOS) in the general area of the junction, which become available to the photons tunneling through the composite metal film. This increase may occur due to the surface topography step (see Fig. 12), which breaks the momentum conservation law and facilitates coupling between photons and surface plasmons of the metal films. However, this mechanism is excluded by our control experiments with Ag/Ag junctions in which a silver film of similar thickness was overcoated with another silver film and no enhanced transmission was observed (see Fig. 14—compare with Fig. 13a,c). The newly discovered interfacial states of the gold-silver interface are another source of the DOS increase, which becomes available to the tunneling photons. Therefore, a strong increase in light transmission near the Au/Ag junction (in the demonstrated absence of the topographical effects) is a strong indication in favor of our theoretical model.

6 Discussion and Conclusion

Table 1 below illustrates the common feature of our experiments on SEW propagation in various material systems. In all these situations $\varepsilon'' > \varepsilon'$ in the relevant frequency range, while $\varepsilon''(z)$ exhibits considerable gradients near surface. Note that in the GHz frequency range typical metals are described by complex conductivities, so that $\sigma'' \approx \omega\tau\sigma'$, where the inverse relaxation time τ^{-1} is typically in the infrared



Fig. 14 (a) Reflection microscopic image of an overlap region between 75 nm thick silver film on top of 80 nm thick silver film. The scale bar corresponds to 50 μm . (b) Corresponding transmission image obtained using white light illumination and the same red filter as in Fig. 13c

Table 1 Dielectric permittivity of relevant high loss materials

Pool water @50 MHz [6]		Steel@3 GHz	Si @300 nm [19, 20]
ε'	81	$\sim 10^3$	1.7
ε''	180	8.7×10^6 , see [18]	36

frequency range [23]. Therefore, as was noted above, the case of metals in the GHz range basically corresponds to the case of seawater in the KHz and lower MHz ranges. Table 1 provides us with a strong assurance that the experimental cases considered in Sects. 4 and 5 may be treated in a similar fashion.

In conclusion, we have demonstrated that novel low-loss propagating surface wave solutions can exist in a gradient medium in which both dielectric permittivity and magnetic permeability are dominated by their imaginary parts. In addition, we have studied several examples of gradient geometries in which the surface wave problem may be solved analytically. Our results indicate practical ways in which broadband radio communication channels may be established along the surfaces of rusty pipes deployed in underwater and underground oil and gas producing fields. The developed theory also has important implications in the fields of nanophotonics and metamaterial optics, where the negative effect of metamaterial losses on signal propagation remains a major problem. We presented several experimental examples of practically useful novel surface wave geometries spanning the range of frequencies from MHz range radio communication underwater to Wi-Fi communication through steel pipes in the GHz frequency range, and to UV nanophotonics.

References

1. A.V. Zayats, I.I. Smolyaninov, A. Maradudin, Nano-optics of surface plasmon-polaritons. *Phys. Rep.* **408**, 131–314 (2005)
2. S.K. Oruganti, F. Liu, D. Paul, J. Liu, J. Malik, K. Feng, H. Kim, Y. Liang, T. Thundat, F. Bien, Experimental realization of Zenneck type wave-based non-radiative, non-coupled wireless power transmission. *Sci. Rep.* **10**, 925 (2020)
3. A. Shvartsburg, V. Kuzmiak, G. Petite, Optics of subwavelength gradient nanofilms. *Phys. Rep.* **452**, 33–88 (2007)
4. I.I. Smolyaninov, Surface electromagnetic waves at gradual interfaces between lossy media. *PIER* **170**, 177–186 (2021)
5. I.I. Smolyaninov, Surface electromagnetic waves in lossy conductive media: Tutorial. *JOSA B* **39**, 1894–1901 (2022)
6. I.I. Smolyaninov, Q. Balzano, C.C. Davis, D. Young, Surface wave based underwater radio communication. *IEEE Antennas Wirel. Propag. Lett.* **17**, 2503–2507 (2018)
7. I.I. Smolyaninov, Q. Balzano, M. Barry, Transmission of high-definition video signals underwater using surface electromagnetic waves. *arXiv*, 2210.06296 [eess.SP] (2022)
8. I.I. Smolyaninov, Gradient-index nanophotonics. *J. Opt.* **23**, 095002 (2021)
9. A. Guo, G.J. Salamo, D. Duchesne, R. Morandotti, M. Volatier-Ravat, V. Aimez, G.A. Siviloglou, D.N. Christodoulides, Observation of PT-symmetry breaking in complex optical potentials. *Phys. Rev. Letters* **103**, 093902 (2009)
10. S. Zhong, S. He, Ultrathin and lightweight microwave absorbers made of mu-near-zero metamaterials. *Phys. Rep.* **3**, 2083 (2013)
11. J.B. Pendry, A.J. Holden, D.J. Robbins, W.J. Stewart, Magnetism from conductors and enhanced nonlinear phenomena. *IEEE Trans. on Microw. Theory Tech.* **47**, 2075–2084 (1999)
12. J. Krupka, P. Aleshkevych, B. Salski, P. Kopyt, A. Pacewicz, Ferromagnetic resonance revised—Electrodynamic approach. *Sci. Rep.* **7**, 5750 (2017)
13. Z. Frait, D. Fraitová, R. Gemperle, FMR in surface oxidized iron single crystals. *Czechoslovak J. Phys. B* **25**, 906–915 (1975)
14. www.wolframalpha.com
15. J.A. Reyes, M. del Castillo-Mussot, 1D Schrödinger equations with coulomb-type potentials. *J. Phys. A Math. Gen.* **32**, 2017 (1999)
16. A. Song, M. Stojanovic, M. Chitre, Editorial: Underwater acoustic communications: Where we stand and what is next? *IEEE J. Ocean. Eng.* **44**, 1 (2019)
17. T.W. Ebbesen, H.J. Lezec, H.F. Ghaemi, T. Thio, P.A. Wolff, Extraordinary optical transmission through sub-wavelength hole arrays. *Nature* **391**, 667–669 (1998)
18. I.I. Smolyaninov, Q. Balzano, D. Young, Surface wave-based radio communication through conductive enclosures. *PIER M* **85**, 21–28 (2019)
19. Z. Dong, T. Wang, X. Chi, J. Ho, C. Tserkezis, et al., Ultraviolet interband plasmonics with Si nanostructures. *Nano Lett.* **19**, 8040–8048 (2019)
20. M. Amiotti, A. Borghesi, G. Guizzetti, F. Nava, Optical properties of polycrystalline nickel silicides. *Phys. Rev. B* **42**, 8939 (1990)
21. D.R. Lide (ed.), *CRC Handbook of Chemistry and Physics* (CRC Press, Boca Raton, 2005)
22. B.V. Numerov, A method of extrapolation of perturbations. *Mon. Not. R. Astron. Soc.* **84**, 592–601 (1924)
23. N. Ashcroft, D. Mermin, *Solid State Physics* (Holt, Rinehart and Winston, New York, 1976)

The Circular Bragg Phenomenon Updated



Akhlesh Lakhtakia 

1 Introduction

The circular Bragg phenomenon is the circular-polarization-state-selective reflection of plane waves in a spectral regime called the circular Bragg regime that depends on the direction of incidence [1, 2]. This phenomenon is displayed by structurally chiral materials (SCMs) exemplified by chiral liquid crystals [3–9] and chiral sculptured thin films [10–12]. These linear materials are periodically nonhomogeneous along a fixed axis, their constitutive dyadics rotating either clockwise or counterclockwise at a fixed rate about that axis [13, 14]. The reflection is very high when left-circularly polarized (LCP) light is incident on a left-handed SCM, which is periodically nonhomogeneous along the thickness direction, provided that (i) the direction of incidence is not too oblique with respect to the thickness direction, (ii) the free-space wavelength lies in the circular Bragg regime, and (iii) the number of periods in SCM is sufficiently large; however, when right-circularly polarized light (RCP) is incident on a left-handed SCM, the reflectance is very low in the circular Bragg regime [1, 12, 15, 16]. An analogous statement holds for right-handed SCMs. The circular Bragg phenomenon is resilient against structural disorder [17] and the tilt of the axis of periodicity [18, 19].

An expository and detailed review of the literature on circular Bragg phenomenon was published in 2014 [1], to which the interested reader is referred. During the subsequent decade, several novel results—both experimental [11, 12, 20, 21] and theoretical [22, 23]—on the plane-wave response of SCMs have emerged,

A. Lakhtakia (✉)

Department of Engineering Science and Mechanics, The Pennsylvania State University,
University Park, PA, USA

School of Mathematics, University of Edinburgh, Edinburgh, UK

e-mail: akhlesh@psu.edu

which prompted me to compile this album of theoretical numerical results on the plane-wave response of SCMs. Of course, no novelty can be claimed for these results, but this album is expected to guide relevant research for the next decade.

This chapter is organized as follows. Section 2 provides the essentials of the boundary-value problem underlying the plane-wave response of an SCM of finite thickness. Section 3 provides illustrative results on the spectral variations of intensity-dependent observable quantities, and Sect. 4 is focused similarly on phase-dependent observable quantities, in the reflection half-space as well as in the transmission half-space, in relation to the polarization state and the direction of propagation of the incident plane wave.

An $\exp(-i\omega t)$ dependence on time t is implicit, where ω is the angular frequency and $i = \sqrt{-1}$. With ε_0 and μ_0 , respectively, denoting the permittivity and permeability of free space, the free-space wavenumber is denoted by $k_0 = \omega\sqrt{\varepsilon_0\mu_0}$, and $\lambda_0 = 2\pi/k_0$ is the free-space wavelength. The Cartesian coordinate system (x, y, z) is adopted. Vectors are in boldface and unit vectors are additionally decorated by a caret on top. Dyadics [24] are double underlined. Column vectors are underlined and enclosed in square brackets. The asterisk (*) denotes the complex conjugate and the dagger (\dagger) denotes the conjugate transpose.

2 Boundary-Value Problem

The half-space $z < 0$ is the region of incidence and reflection, while the half-space $z > L$ is the region of transmission. The region $0 < z < L$ is occupied by an SCM.

2.1 Relative Permittivity Dyadic of SCM

The relative permittivity dyadic of the SCM is given by [10]

$$\begin{aligned} \underline{\underline{\varepsilon}}_{\text{rel}}(z) = & \underline{\underline{S}}_z(h, \Omega, z) \bullet \underline{\underline{S}}_y(\chi) \bullet [\varepsilon_a \hat{\mathbf{z}}\hat{\mathbf{z}} + \varepsilon_b \hat{\mathbf{x}}\hat{\mathbf{x}} + \varepsilon_c \hat{\mathbf{y}}\hat{\mathbf{y}}] \\ & \bullet \underline{\underline{S}}_y^{-1}(\chi) \bullet \underline{\underline{S}}_z^{-1}(h, \Omega, z), \quad z \in (0, L). \end{aligned} \quad (1)$$

The frequency-dependent relative permittivity scalars ε_a , ε_b , and ε_c embody local orthorhombicity [25]. The tilt dyadic

$$\underline{\underline{S}}_y(\chi) = \hat{\mathbf{y}}\hat{\mathbf{y}} + (\hat{\mathbf{x}}\hat{\mathbf{x}} + \hat{\mathbf{z}}\hat{\mathbf{z}}) \cos \chi + (\hat{\mathbf{z}}\hat{\mathbf{x}} - \hat{\mathbf{x}}\hat{\mathbf{z}}) \sin \chi \quad (2)$$

contains $\chi \in [0, \pi/2]$ as an angle of inclination with respect to the xy plane. The structural handedness of the SCM is captured by the rotation dyadic

$$\underline{\underline{S}}_z(h, \Omega, z) = \hat{\mathbf{z}}\hat{\mathbf{z}} + (\hat{\mathbf{x}}\hat{\mathbf{x}} + \hat{\mathbf{y}}\hat{\mathbf{y}}) \cos\left(h \frac{\pi z}{\Omega}\right) + (\hat{\mathbf{y}}\hat{\mathbf{x}} - \hat{\mathbf{x}}\hat{\mathbf{y}}) \sin\left(h \frac{\pi z}{\Omega}\right), \quad (3)$$

where 2Ω is the structural period in the thickness direction (i.e., along the z axis), whereas $h \in \{-1, 1\}$ is the structural-handedness parameter, with $h = -1$ for structural left-handedness and $h = 1$ for structural right-handedness.

The foregoing equations apply to chiral sculptured thin films [10–12] and chiral smectic liquid crystals [6–8], with $\varepsilon_a \neq \varepsilon_b \neq \varepsilon_c$ and $\chi > 0^\circ$. They also apply to cholesteric liquid crystals with $\varepsilon_a \neq \varepsilon_b = \varepsilon_c$ and $\chi = 0^\circ$ [4, 5] and heliconical cholesteric liquid crystals [9] with $\varepsilon_a \neq \varepsilon_b = \varepsilon_c$ and $\chi \in (0^\circ, 90^\circ)$.

2.2 Incident, Reflected, and Transmitted Plane Waves

A plane wave, propagating in the half-space $z < 0$ at an angle $\theta_{\text{inc}} \in [0, \pi/2)$ with respect to the z axis and at an angle $\psi \in [0, 2\pi)$ with respect to the x axis in the xy plane, is incident on the SCM of thickness L . The electric field phasor associated with the incident plane wave is represented as [10]

$$\begin{aligned} \mathbf{E}^{\text{inc}}(\mathbf{r}) &= (a_s \mathbf{s} + a_p \mathbf{p}_+) \exp[i\kappa (x \cos \psi + y \sin \psi)] \exp(ik_0 z \cos \theta_{\text{inc}}) \quad (4a) \\ &= \left[\frac{(i\mathbf{s} - \mathbf{p}_+)}{\sqrt{2}} a_L - \frac{(i\mathbf{s} + \mathbf{p}_+)}{\sqrt{2}} a_R \right] \exp[i\kappa (x \cos \psi + y \sin \psi)] \\ &\quad \times \exp(ik_0 z \cos \theta_{\text{inc}}), \quad z < 0, \end{aligned} \quad (4b)$$

where

$$\left. \begin{aligned} \kappa &= k_0 \sin \theta_{\text{inc}} \\ \mathbf{s} &= -\hat{\mathbf{x}} \sin \psi + \hat{\mathbf{y}} \cos \psi \\ \mathbf{p}_\pm &= \mp (\hat{\mathbf{x}} \cos \psi + \hat{\mathbf{y}} \sin \psi) \cos \theta_{\text{inc}} + \hat{\mathbf{z}} \sin \theta_{\text{inc}} \end{aligned} \right\}. \quad (5)$$

The amplitudes of the perpendicular- and parallel-polarized components, respectively, are denoted by a_s and a_p in Eq. (4a). The amplitudes of the LCP and the RCP components of the incident plane wave are denoted by a_L and a_R , respectively, in Eq. (4b).

The electric field phasor of the reflected plane wave is expressed as

$$\begin{aligned} \mathbf{E}^{\text{ref}}(\mathbf{r}) &= (r_s \mathbf{s} + r_p \mathbf{p}_-) \exp[i\kappa (x \cos \psi + y \sin \psi)] \exp(-ik_0 z \cos \theta_{\text{inc}}) \quad (6a) \\ &= - \left[\frac{(i\mathbf{s} - \mathbf{p}_-)}{\sqrt{2}} r_L - \frac{(i\mathbf{s} + \mathbf{p}_-)}{\sqrt{2}} r_R \right] \exp[i\kappa (x \cos \psi + y \sin \psi)] \\ &\quad \times \exp(-ik_0 z \cos \theta_{\text{inc}}), \quad z < 0, \end{aligned} \quad (6b)$$

and the electric field phasor of the transmitted plane wave is represented as

$$\mathbf{E}^{\text{tr}}(\mathbf{r}) = (t_s \mathbf{s} + t_p \mathbf{p}_+) \exp[i\kappa(x \cos \psi + y \sin \psi)] \exp[ik_0(z - L) \cos \theta_{\text{inc}}] \quad (7a)$$

$$= \left[\frac{(i\mathbf{s} - \mathbf{p}_+)}{\sqrt{2}} t_L - \frac{(i\mathbf{s} + \mathbf{p}_+)}{\sqrt{2}} t_R \right] \exp[i\kappa(x \cos \psi + y \sin \psi)] \\ \times \exp[ik_0(z - L) \cos \theta_{\text{inc}}], \quad z > L. \quad (7b)$$

Linear reflection amplitudes are denoted by r_s and r_p in Eq. (6a), whereas the circular reflection amplitudes are denoted by r_L and r_R in Eq. (6b). Similarly, t_s and t_p are the linear transmission amplitudes in Eq. (7a), whereas t_L and t_R are the circular transmission amplitudes in Eq. (7b).

2.3 Reflection and Transmission Coefficients

The reflection amplitudes r_s and r_p as well as the transmission amplitudes t_s and t_p (equivalently, r_L , r_R , t_L , and t_R) are unknown. A boundary-value problem must be solved in order to determine these amplitudes in terms of a_s and a_p (equivalently, a_L and a_R). Several numerical techniques exist to solve this problem [26–29]. The most straightforward technique requires the use of the piecewise uniform approximation of $\underline{\underline{\varepsilon}}_{\text{rel}}(z)$ followed by application of the 4×4 transfer-matrix method [30]. The interested reader is referred to Ref. 10 for a detailed description of this technique.

Interest generally lies in determining the reflection and transmission coefficients entering the 2×2 matrixes on the left side in each of the following four relations [10]:

$$\begin{bmatrix} r_s \\ r_p \end{bmatrix} = \begin{bmatrix} r_{ss} & r_{sp} \\ r_{ps} & r_{pp} \end{bmatrix} \begin{bmatrix} a_s \\ a_p \end{bmatrix}, \quad (8a)$$

$$\begin{bmatrix} t_s \\ t_p \end{bmatrix} = \begin{bmatrix} t_{ss} & t_{sp} \\ t_{ps} & t_{pp} \end{bmatrix} \begin{bmatrix} a_s \\ a_p \end{bmatrix}, \quad (8b)$$

$$\begin{bmatrix} r_L \\ r_R \end{bmatrix} = \begin{bmatrix} r_{LL} & r_{LR} \\ r_{RL} & r_{RR} \end{bmatrix} \begin{bmatrix} a_L \\ a_R \end{bmatrix}, \quad (8c)$$

and

$$\begin{bmatrix} t_L \\ t_R \end{bmatrix} = \begin{bmatrix} t_{LL} & t_{LR} \\ t_{RL} & t_{RR} \end{bmatrix} \begin{bmatrix} a_L \\ a_R \end{bmatrix}. \quad (8d)$$

These coefficients are doubly subscripted: those with both subscripts identical refer to co-polarized, while those with two different subscripts denote cross-polarized,

reflection or transmission. Clearly from Eqs. (4a)–(7b), the coefficients defined *via* Eqs. (8a) and (8b) are simply related to those defined *via* Eqs. (8c) and (8d).

2.4 Parameters Chosen for Calculations

An album of numerical results is presented in the remainder of this chapter, with the frequency-dependent constitutive parameters

$$\varepsilon_{a,b,c}(\lambda_0) = 1 + \frac{p_{a,b,c}}{1 + (N_{a,b,c}^{-1} - i\lambda_0^{-1}\lambda_{a,b,c})^2} \quad (9)$$

chosen to be single-resonance Lorentzian functions [31], this choice being consistent with the requirement of causality [32–34]. The oscillator strengths are determined by the values of p_ℓ , $\lambda_\ell(1 + N_\ell^{-2})^{-1/2}$ are the resonance wavelengths, and λ_ℓ/N_ℓ are the resonance linewidths, $\ell \in \{a, b, c\}$. Values of the parameters used for all theoretical results reported in this chapter are as follows: $p_a = 2.3$, $p_b = 3.0$, $p_c = 2.2$, $\lambda_a = \lambda_c = 260$ nm, $\lambda_b = 270$ nm, and $N_a = N_b = N_c = 130$. Furthermore, $\chi = 37^\circ$, $L = 30\Omega$, and $\Omega = 150$ nm.

The album comprising Figs. 1, 2, 3, 4, 5, 6, 7, 8, 9, 10, and 11 contains 2D plots of the theoretically calculated spectral variations of diverse observable quantities in the reflection and transmission half-spaces for either

- $\theta_{\text{inc}} \in [0^\circ, 90^\circ)$ and $\psi = 0^\circ$ or
- $\theta_{\text{inc}} = 0^\circ$ and $\psi \in [0^\circ, 360^\circ)$.

These plots are provided for both $h = 1$ and $h = -1$ to facilitate easy comparison of the effect of structural handedness.

3 Intensity-Dependent Quantities

3.1 Circular Remittances

The square of the magnitude of a circular reflection or transmission coefficient is the corresponding circular reflectance or transmittance; thus, $R_{LR} = |r_{LR}|^2 \in [0, 1]$ is the circular reflectance corresponding to the circular reflection coefficient r_{LR} , $T_{LR} = |t_{LR}|^2 \in [0, 1]$ is the circular transmittance corresponding to the circular transmission coefficient t_{LR} , and so on. The total circular reflectances are given by

$$\left. \begin{aligned} R_L &= R_{LL} + R_{RL} \in [0, 1] \\ R_R &= R_{RR} + R_{LR} \in [0, 1] \end{aligned} \right\} \quad (10)$$

and the total circular transmittances by

$$\left. \begin{aligned} T_L &= T_{LL} + T_{RL} \in [0, 1] \\ T_R &= T_{RR} + T_{LR} \in [0, 1] \end{aligned} \right\}. \quad (11)$$

As the principle of conservation of energy must be satisfied by the presented formalism, the inequalities [10]

$$R_\ell + T_\ell \leq 1, \quad \ell \in \{L, R\}, \quad (12)$$

hold, with the equalities relevant only if the SCM is non-dissipative at a particular frequency of interest.

The Bragg phenomenon was discovered as a reflection phenomenon, so that its chief signature comprises high-reflectance spectral regimes [35–37]. The same is true of the circular Bragg phenomenon, which has been confirmed by time-domain simulations [38–40].

In addition, the circular Bragg phenomenon is best manifested as the circular-polarization-state-selective reflection of light. Therefore, it is best to begin the album with the spectral variations of the circular reflectances $R_{\mu\nu}(\lambda_0, \theta_{\text{inc}}, \psi)$, $\mu \in \{L, R\}$ and $\nu \in \{L, R\}$. These are presented in Fig. 1 for $h = \pm 1$.

Note the presence of a high-reflectance ridge in the plots of R_{RR} for $h = 1$ and in the plots of R_{LL} for $h = -1$ in Fig. 1. For fixed ψ , the high-reflectance ridge curves toward shorter wavelengths as θ_{inc} increases, which has been experimentally verified [11, 12, 20]. For fixed θ_{inc} , the high-reflectance ridge is more or less invariant with respect to ψ . The ridge is absent in the plots of R_{LL} for $h = 1$ and in the plots of R_{RR} for $h = -1$; however, the ridge is vestigially present in the plots of both cross-polarized reflectances.

The fraction of the power density of the incident plane wave that is not reflected is either transmitted into the half-space $z > L$ or absorbed in the SCM ($0 < z < L$). Since $\text{Im}(\varepsilon_\ell) > 0$, $\ell \in \{a, b, c\}$, there is some absorption [11, 20]. Accordingly, in Fig. 2, the circular Bragg phenomenon is manifested as a low-transmittance trough in the plots of T_{RR} for $h = 1$ and in the plots of T_{LL} for $h = -1$, that trough being absent in the plots of T_{LL} for $h = 1$ and in the plots of T_{RR} for $h = -1$. Vestigial presence of the trough in the plots of T_{LR} and T_{RL} for $h = \pm 1$ should also be noted.

3.2 Linear Remittances

The square of the magnitude of a linear reflection or transmission coefficient is the corresponding linear reflectance or transmittance; thus, $R_{\text{sp}} = |r_{\text{sp}}|^2 \in [0, 1]$ is the linear reflectance corresponding to the linear reflection coefficient r_{sp} and $T_{\text{ps}} = |t_{\text{ps}}|^2 \in [0, 1]$ is the linear transmittance corresponding to the linear transmission coefficient t_{ps} , etc. The total linear reflectances are given by

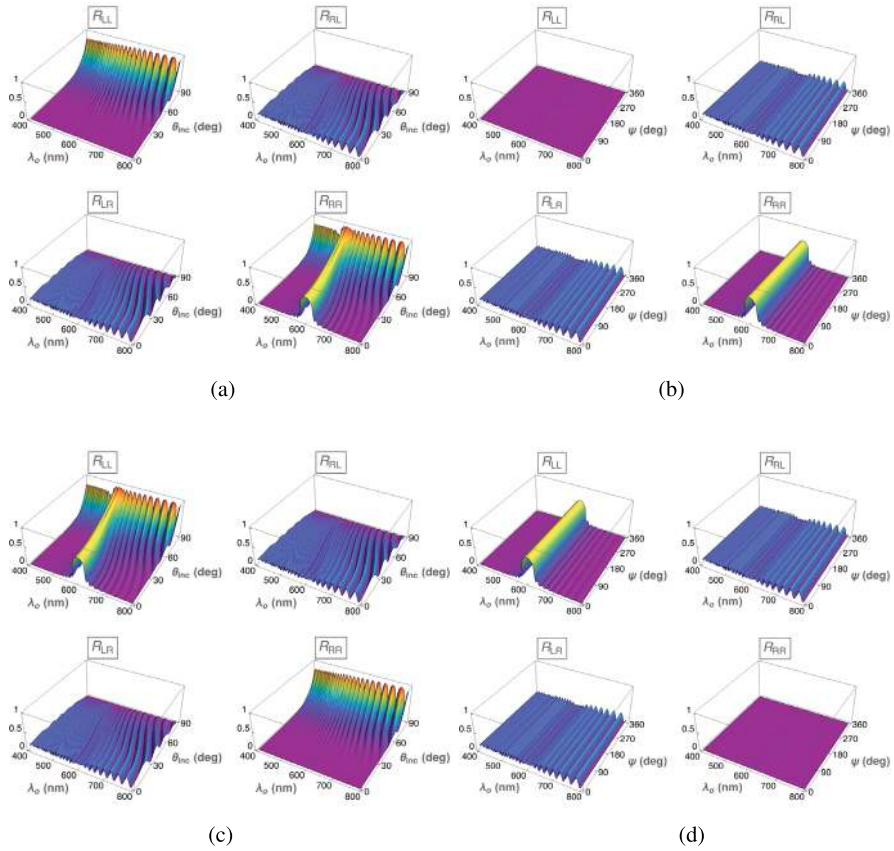


Fig. 1 Spectral variations of circular reflectances $R_{\mu\nu}(\lambda_0, \theta_{inc}, \psi)$, $\mu \in \{L, R\}$ and $\nu \in \{L, R\}$, when (a), (b) $h = 1$ and (c), (d) $h = -1$. (a), (c) $\theta_{inc} \in [0^\circ, 90^\circ]$ and $\psi = 0^\circ$; (b), (d) $\theta_{inc} = 0^\circ$ and $\psi \in [0^\circ, 360^\circ]$. (a) $h = 1$, $\theta_{inc} \in [0^\circ, 90^\circ]$, and $\psi = 0^\circ$. (b) $h = 1$, $\theta_{inc} = 0^\circ$, and $\psi \in [0^\circ, 360^\circ]$. (c) $h = -1$, $\theta_{inc} \in [0^\circ, 90^\circ]$, and $\psi = 0^\circ$. (d) $h = -1$, $\theta_{inc} = 0^\circ$, and $\psi \in [0^\circ, 360^\circ]$

$$\left. \begin{aligned} R_s &= R_{ss} + R_{ps} \in [0, 1] \\ R_p &= R_{pp} + R_{sp} \in [0, 1] \end{aligned} \right\} \quad (13)$$

and the total linear transmittances by

$$\left. \begin{aligned} T_s &= T_{ss} + T_{ps} \in [0, 1] \\ T_p &= T_{pp} + T_{ps} \in [0, 1] \end{aligned} \right\} \quad (14)$$

The inequalities (12) still hold with $\ell \in \{s, p\}$ and convert to equalities only if the SCM is non-dissipative at a particular frequency of interest.

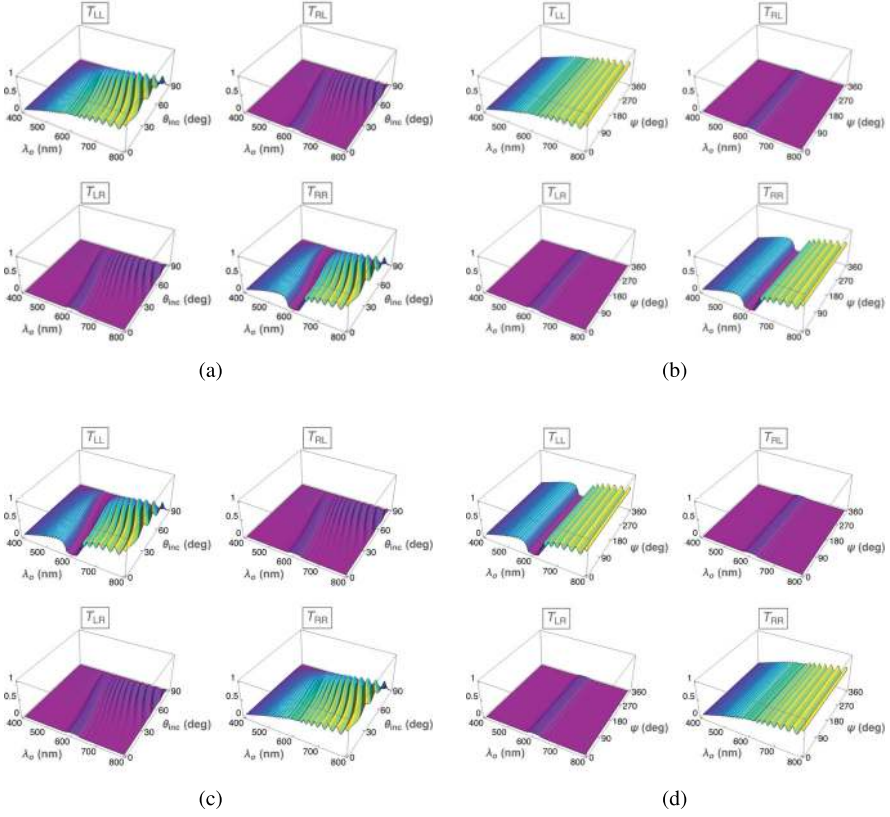


Fig. 2 Spectral variations of circular transmittances $T_{\mu\nu}(\lambda_0, \theta_{\text{inc}}, \psi)$, $\mu \in \{L, R\}$ and $\nu \in \{L, R\}$, when (a), (b) $h = 1$ and (c), (d) $h = -1$. (a), (c) $\theta_{\text{inc}} \in [0^\circ, 90^\circ]$ and $\psi = 0^\circ$; (b), (d) $\theta_{\text{inc}} = 0^\circ$ and $\psi \in [0^\circ, 360^\circ]$. (a) $h = 1$, $\theta_{\text{inc}} \in [0^\circ, 90^\circ]$, and $\psi = 0^\circ$. (b) $h = 1$, $\theta_{\text{inc}} = 0^\circ$, and $\psi \in [0^\circ, 360^\circ]$. (c) $h = -1$, $\theta_{\text{inc}} \in [0^\circ, 90^\circ]$, and $\psi = 0^\circ$. (d) $h = -1$, $\theta_{\text{inc}} = 0^\circ$, and $\psi \in [0^\circ, 360^\circ]$

Linear reflectances can be written in terms of circular reflectances [10]. Therefore, the circular Bragg regime is evident in the spectral variations of both co-polarized linear reflectances as a medium-reflectance ridge and in the spectral variations of both cross-polarized reflectances as a low-reflectance ridge [11, 20], in Fig. 3 for both $h = 1$ and $h = -1$. For fixed ψ , the ridge curves toward shorter wavelengths as θ_{inc} increases. For fixed θ_{inc} , the low-reflectance ridge in the plots of R_{ps} and R_{sp} is more or less invariant with respect to ψ ; but the medium-reflectance ridge in the plots of R_{ss} and R_{pp} has two periods of undulations.

Linear transmittances can be written in terms of circular transmittances [10, 22]. The spectral variations of both co-polarized linear transmittances exhibit a medium-transmittance trough and both cross-polarized linear transmittances show a low-reflectance ridge [11, 20], in Fig. 4 for both $h = 1$ and $h = -1$. Indicative of the circular Bragg phenomenon, these features curve toward shorter wavelengths as θ_{inc}

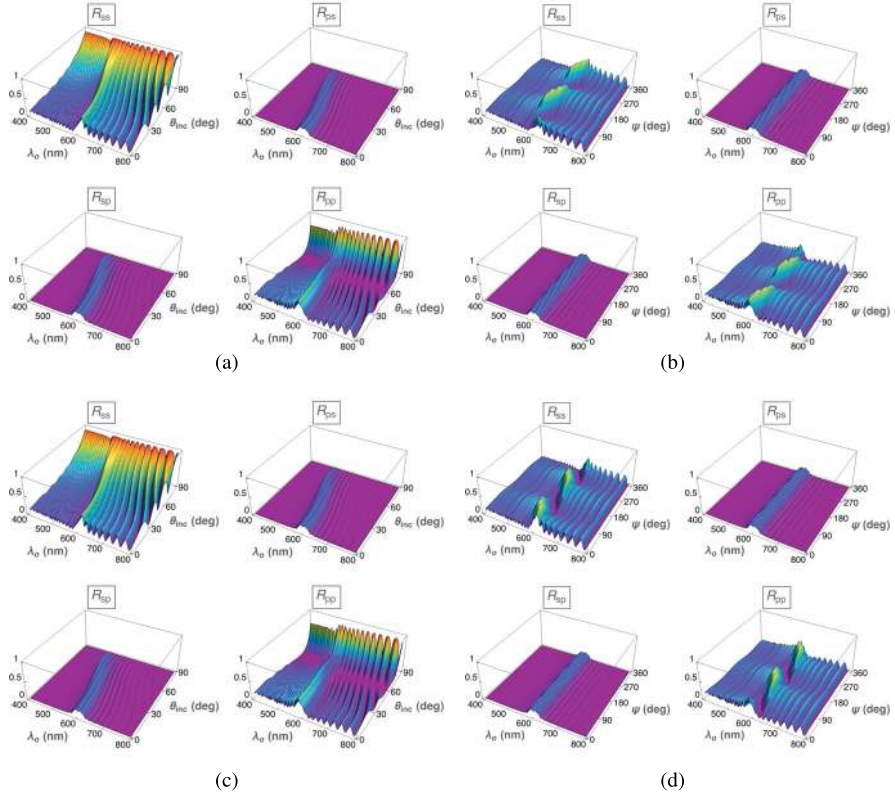


Fig. 3 Spectral variations of linear reflectances $R_{\mu\nu}(\lambda_0, \theta_{inc}, \psi)$, $\mu \in \{s, p\}$ and $\nu \in \{s, p\}$, when (a), (b) $h = 1$ and (c), (d) $h = -1$. (a), (c) $\theta_{inc} \in [0^\circ, 90^\circ]$ and $\psi = 0^\circ$; (b), (d) $\theta_{inc} = 0^\circ$ and $\psi \in [0^\circ, 360^\circ]$. (a) $h = 1$, $\theta_{inc} \in [0^\circ, 90^\circ]$, and $\psi = 0^\circ$. (b) $h = 1$, $\theta_{inc} = 0^\circ$, and $\psi \in [0^\circ, 360^\circ]$. (c) $h = -1$, $\theta_{inc} \in [0^\circ, 90^\circ]$, and $\psi = 0^\circ$. (d) $h = -1$, $\theta_{inc} = 0^\circ$, and $\psi \in [0^\circ, 360^\circ]$

increases when ψ is held fixed. For fixed θ_{inc} but variable ψ , the low-transmittance ridge in the plots of T_{ps} and T_{sp} and the medium-transmittance trough in the plots of T_{ss} and T_{pp} have two periods of undulations.

3.3 Circular and Linear Dichroisms

With

$$\left. \begin{aligned} A_L &= 1 - (R_L + T_L) \in [0, 1] \\ A_R &= 1 - (R_R + T_R) \in [0, 1] \end{aligned} \right\} \quad (15)$$

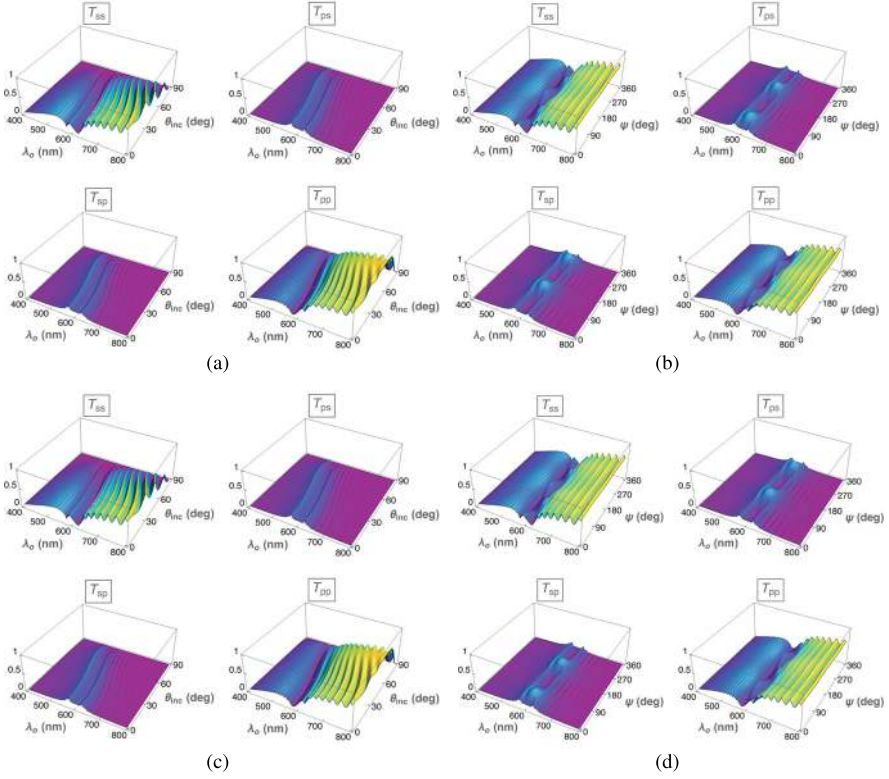


Fig. 4 Spectral variations of linear transmittances $T_{\mu\nu}(\lambda_0, \theta_{inc}, \psi)$, $\mu \in \{s, p\}$ and $\nu \in \{s, p\}$, when (a), (b) $h = 1$ and (c), (d) $h = -1$. (a), (c) $\theta_{inc} \in [0^\circ, 90^\circ]$ and $\psi = 0^\circ$; (b), (d) $\theta_{inc} = 0^\circ$ and $\psi \in [0^\circ, 360^\circ]$. (a) $h = 1$, $\theta_{inc} \in [0^\circ, 90^\circ]$, and $\psi = 0^\circ$. (b) $h = 1$, $\theta_{inc} = 0^\circ$, and $\psi \in [0^\circ, 360^\circ]$. (c) $h = -1$, $\theta_{inc} \in [0^\circ, 90^\circ]$, and $\psi = 0^\circ$. (d) $h = -1$, $\theta_{inc} = 0^\circ$, and $\psi \in [0^\circ, 360^\circ]$

as the circular absorbances,

$$CD_{\text{tru}} = \sqrt{A_R} - \sqrt{A_L} \in [-1, 1] \quad (16)$$

is the *true* circular dichroism, which quantitates the circular-polarization-dependence of absorption. The *apparent* circular dichroism

$$CD_{\text{app}} = \sqrt{T_R} - \sqrt{T_L} \in [-1, 1] \quad (17)$$

is a measure of the circular-polarization-state-dependence of transmission [11]. Whereas CD_{app} may not equal zero for a non-dissipative SCM, CD_{tru} must be.

Figure 5 contains plots of the spectral variations of both CD_{app} and CD_{tru} in relation to the direction of plane-wave incidence. The circular Bragg phenomenon is evident as a trough in all plots of CD_{app} and CD_{tru} for $h = 1$, and as a ridge in

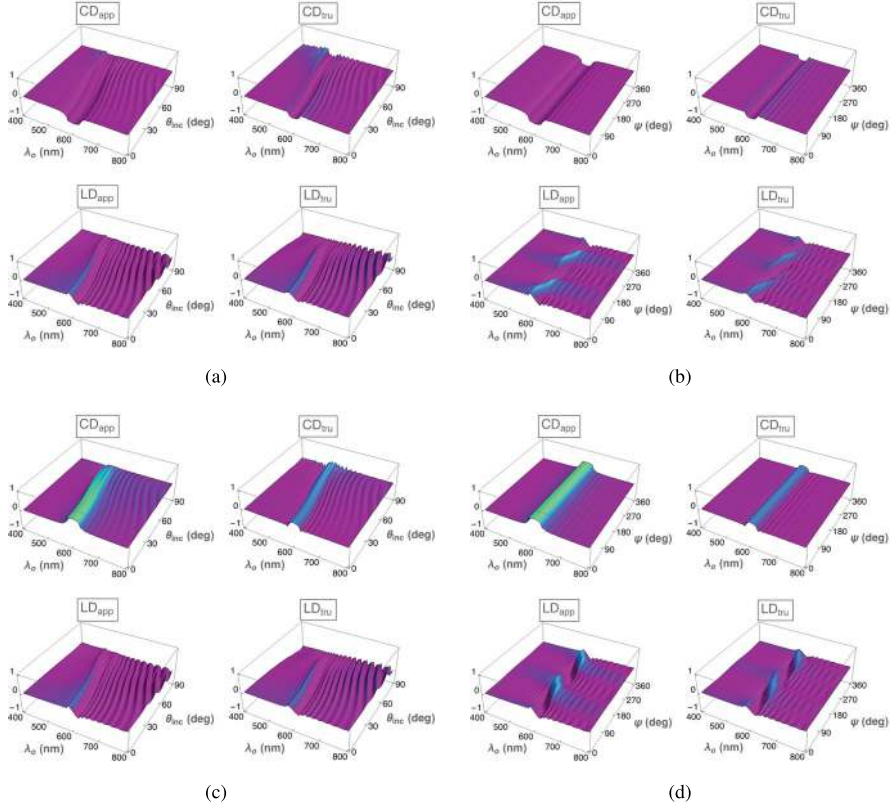


Fig. 5 Spectral variations of apparent circular dichroism $CD_{app}(\lambda_0, \theta_{inc}, \psi)$, true circular dichroism $CD_{tru}(\lambda_0, \theta_{inc}, \psi)$, apparent linear dichroism $LD_{app}(\lambda_0, \theta_{inc}, \psi)$, and true linear dichroism $LD_{tru}(\lambda_0, \theta_{inc}, \psi)$, when (a), (b) $h = 1$ and (c), (d) $h = -1$. (a), (c) $\theta_{inc} \in [0^\circ, 90^\circ]$ and $\psi = 0^\circ$; (b), (d) $\theta_{inc} = 0^\circ$ and $\psi \in [0^\circ, 360^\circ]$. (a) $h = 1$, $\theta_{inc} \in [0^\circ, 90^\circ]$, and $\psi = 0^\circ$. (b) $h = 1$, $\theta_{inc} = 0^\circ$, and $\psi \in [0^\circ, 360^\circ]$. (c) $h = -1$, $\theta_{inc} \in [0^\circ, 90^\circ]$, and $\psi = 0^\circ$. (d) $h = -1$, $\theta_{inc} = 0^\circ$, and $\psi \in [0^\circ, 360^\circ]$

all plots of CD_{app} and CD_{tru} for $h = -1$. Furthermore, the quantities hCD_{app} and hCD_{tru} are invariant if the sign of h is changed. These features curve toward shorter wavelengths as θ_{inc} increases while ψ is held fixed, as has been experimentally verified [11]. For normal incidence (i.e., $\theta_{inc} = 0^\circ$), the effect of ψ is minimal.

Similarly to the circular absorbances,

$$\left. \begin{aligned} A_s &= 1 - (R_s + T_s) \in [0, 1] \\ A_p &= 1 - (R_p + T_p) \in [0, 1] \end{aligned} \right\} \quad (18)$$

are the linear absorbances. The *true* linear dichroism is defined as [11]

$$LD_{\text{tru}} = \sqrt{A_s} - \sqrt{A_p} \in [-1, 1] \quad (19)$$

and the *apparent* linear dichroism as

$$LD_{\text{app}} = \sqrt{T_s} - \sqrt{T_p} \in [-1, 1]. \quad (20)$$

Whereas $LD_{\text{tru}} \equiv 0$ for a non-dissipative SCM, LD_{app} may not be null valued.

Figure 5 also contains plots of the spectral variations of both LD_{app} and LD_{tru} in relation to the direction of plane-wave incidence. The circular Bragg phenomenon is featured in all plots. For fixed ψ , the feature curves toward shorter wavelengths as θ_{inc} increases, which has been experimentally verified [11]. For normal incidence, the feature has two undulations with increasing ψ , and the replacement $h \rightarrow -h$ affects both LD_{app} and LD_{tru} non-trivially.

4 Phase-Dependent Quantities

4.1 Ellipticity and Optical Rotation

The most general plane wave in free space is elliptically polarized [41]. Signed ellipticity functions

$$\left. \begin{aligned} EF^{\text{inc}} &= -2 \frac{\text{Im}(a_s a_p^*)}{|a_s|^2 + |a_p|^2} \\ EF^{\text{ref}} &= -2 \frac{\text{Im}(r_s r_p^*)}{|r_s|^2 + |r_p|^2} \\ EF^{\text{tr}} &= -2 \frac{\text{Im}(t_s t_p^*)}{|t_s|^2 + |t_p|^2} \end{aligned} \right\} \quad (21)$$

characterize the shapes of the vibration ellipses of the incident, reflected, and transmitted plane waves.

Note that $EF^\ell \in [-1, 1]$, $\ell \in \{\text{inc}, \text{ref}, \text{tr}\}$. The magnitude of EF^ℓ is the ellipticity of the plane wave labeled ℓ . The vibration ellipse simplifies to a circle when $|EF^\ell| = 1$ (circular polarization state), and it degenerates into a straight line when $EF^\ell = 0$ (linear polarization state). The plane wave is left-handed for $EF^\ell > 0$ and right-handed for $EF^\ell < 0$.

The major axes of the vibration ellipses of the incident and the reflected/transmitted plane waves may not coincide, the angular offset between the two major axes known as optical rotation. The auxiliary vectors [10]

$$\left. \begin{aligned} \mathbf{F}^{\text{inc}} &= \left\{ 1 + \left[1 - (EF^{\text{inc}})^2 \right]^{1/2} \right\} \text{Re} (a_s \mathbf{s} + a_p \mathbf{p}_+) + EF^{\text{inc}} \text{Im} (a_s \mathbf{p}_+ - a_p \mathbf{s}) \\ \mathbf{F}^{\text{ref}} &= \left\{ 1 + \left[1 - (EF^{\text{ref}})^2 \right]^{1/2} \right\} \text{Re} (r_s \mathbf{s} + r_p \mathbf{p}_-) + EF^{\text{ref}} \text{Im} (r_s \mathbf{p}_- - r_p \mathbf{s}) \\ \mathbf{F}^{\text{tr}} &= \left\{ 1 + \left[1 - (EF^{\text{tr}})^2 \right]^{1/2} \right\} \text{Re} (t_s \mathbf{s} + t_p \mathbf{p}_+) + EF^{\text{tr}} \text{Im} (t_s \mathbf{p}_+ - t_p \mathbf{s}) \end{aligned} \right\} \quad (22)$$

are parallel to the major axes of the respective vibration ellipses. Therefrom, the angles τ^{inc} , τ^{ref} , and τ^{tr} are calculated using the following expressions:

$$\left. \begin{aligned} \cos \tau^\ell &= (\mathbf{F}^\ell \cdot \mathbf{s}) / |\mathbf{F}^\ell|, & \ell \in \{\text{inc}, \text{ref}, \text{tr}\} \\ \sin \tau^\ell &= (\mathbf{F}^\ell \cdot \mathbf{p}_+) / |\mathbf{F}^\ell|, & \ell \in \{\text{inc}, \text{tr}\} \\ \sin \tau^{\text{ref}} &= (\mathbf{F}^{\text{ref}} \cdot \mathbf{p}_-) / |\mathbf{F}^{\text{ref}}| \end{aligned} \right\}. \quad (23)$$

The optical rotation of the reflected/transmitted plane wave then is the angle

$$OR^\ell = \begin{cases} \tau^\ell - \tau^{\text{inc}} + \pi, & \text{if } -\pi \leq \tau^\ell - \tau^{\text{inc}} \leq -\pi/2, \\ \tau^\ell - \tau^{\text{inc}}, & \text{if } |\tau^\ell - \tau^{\text{inc}}| < \pi/2, \\ \tau^\ell - \tau^{\text{inc}} - \pi, & \text{if } \pi/2 \leq \tau^\ell - \tau^{\text{inc}} \leq \pi, \end{cases} \quad \ell \in \{\text{ref}, \text{tr}\}. \quad (24)$$

The ellipticity function of the reflected/transmitted plane wave is denoted by EF_s^ℓ and EF_p^ℓ , respectively, and the optical rotation of the reflected/transmitted plane wave is denoted by OR_s^ℓ and OR_p^ℓ , respectively, for incident perpendicular-polarized and parallel-polarized plane waves, $\ell \in \{\text{ref}, \text{tr}\}$.

Figure 6 provides the spectral variations of $EF_{s,p}^{\text{ref}}$ and $OR_{s,p}^{\text{ref}}$, and Fig. 7 the spectral variations of $EF_{s,p}^{\text{tr}}$ and $OR_{s,p}^{\text{tr}}$. A feature representing the circular Bragg phenomenon is clearly evident in all 32 plots in the two figures. For fixed ψ , the feature curves toward shorter wavelengths as θ_{inc} increases. For normal incidence, the feature has two undulations with increasing ψ . Although measurements of optical rotation and ellipticity of the transmitted plane wave for normal incidence have been reported for over a century [42–44], comprehensive experimental investigations for oblique incidence are very desirable in the near future.

4.2 Geometric Phases of Reflected and Transmitted Plane Waves

The Stokes parameters of the incident plane wave are given by Jackson [45]

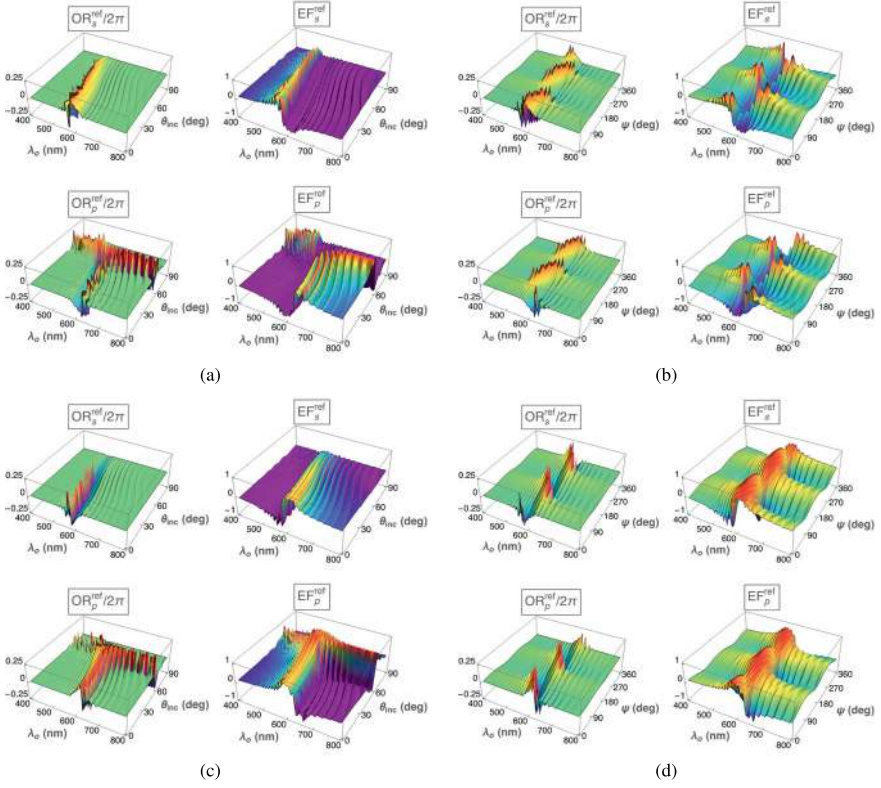


Fig. 6 Spectral variations of the optical rotation $OR_\mu^{\text{ref}}(\lambda_0, \theta_{\text{inc}}, \psi)$ and ellipticity function $EF_\mu^{\text{ref}}(\lambda_0, \theta_{\text{inc}}, \psi)$, $\mu \in \{s, p\}$, of the reflected plane wave, when (a), (b) $h = 1$ and (c), (d) $h = -1$. (a), (c) $\theta_{\text{inc}} \in [0^\circ, 90^\circ)$ and $\psi = 0^\circ$; (b), (d) $\theta_{\text{inc}} = 0^\circ$ and $\psi \in [0^\circ, 360^\circ)$. (a) $h = 1$, $\theta_{\text{inc}} \in [0^\circ, 90^\circ)$, and $\psi = 0^\circ$. (b) $h = 1$, $\theta_{\text{inc}} = 0^\circ$, and $\psi \in [0^\circ, 360^\circ)$. (c) $h = -1$, $\theta_{\text{inc}} \in [0^\circ, 90^\circ)$, and $\psi = 0^\circ$. (d) $h = -1$, $\theta_{\text{inc}} = 0^\circ$, and $\psi \in [0^\circ, 360^\circ)$

$$\left. \begin{aligned} s_0^{\text{inc}} &= |a_L|^2 + |a_R|^2 = |a_s|^2 + |a_p|^2 \\ s_1^{\text{inc}} &= 2 \operatorname{Re}(a_L a_R^*) = |a_p|^2 - |a_s|^2 \\ s_2^{\text{inc}} &= 2 \operatorname{Im}(a_L a_R^*) = 2 \operatorname{Re}(a_s a_p^*) \\ s_3^{\text{inc}} &= |a_R|^2 - |a_L|^2 = 2 \operatorname{Im}(a_s a_p^*) \end{aligned} \right\}. \quad (25)$$

The Poincaré spinor $[\underline{\phi}^{\text{inc}}]$ of the incident plane wave can then be obtained from Eqs. (26) and (27) in the Appendix.

After making the changes $\{a_L \rightarrow r_L, a_R \rightarrow r_R, a_s \rightarrow r_s, a_p \rightarrow r_p\}$, Eqs. (25) can be used to determine the Stokes parameters $s_0^{\text{ref}}, s_1^{\text{ref}}, s_2^{\text{ref}}$, and s_3^{ref} of the reflected

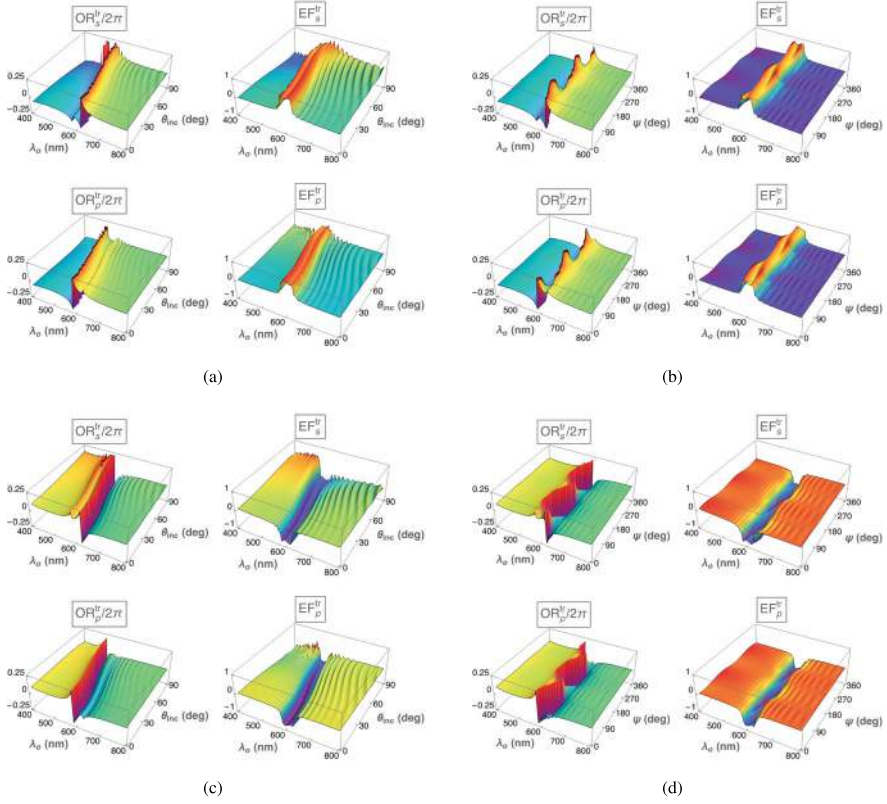


Fig. 7 Spectral variations of the optical rotation $OR_{\mu}^{\text{tr}}(\lambda_0, \theta_{\text{inc}}, \psi)$ and ellipticity function $EF_{\mu}^{\text{tr}}(\lambda_0, \theta_{\text{inc}}, \psi)$, $\mu \in \{s, p\}$, of the transmitted plane wave, when (a), (b) $h = 1$ and (c), (d) $h = -1$. (a), (c) $\theta_{\text{inc}} \in [0^\circ, 90^\circ]$ and $\psi = 0^\circ$; (b), (d) $\theta_{\text{inc}} = 0^\circ$ and $\psi \in [0^\circ, 360^\circ]$. (a) $h = 1$, $\theta_{\text{inc}} \in [0^\circ, 90^\circ]$, and $\psi = 0^\circ$. (b) $h = 1$, $\theta_{\text{inc}} = 0^\circ$, and $\psi \in [0^\circ, 360^\circ]$. (c) $h = -1$, $\theta_{\text{inc}} \in [0^\circ, 90^\circ]$, and $\psi = 0^\circ$. (d) $h = -1$, $\theta_{\text{inc}} = 0^\circ$, and $\psi \in [0^\circ, 360^\circ]$

plane wave, and the Poincaré spinor $[\underline{\phi}^{\text{ref}}]$ of the reflected plane wave can then be obtained from Eqs. (26) and (27). Calculation of the Poincaré spinor $[\underline{\phi}^{\text{tr}}]$ of the transmitted plane wave follows the same route [46].

Thereafter, the reflection-mode geometric phase Φ_{ℓ}^{ref} and the transmission-mode geometric phase Φ_{ℓ}^{tr} , $\ell \in \{s, p, R, L\}$, can be calculated with respect to the incident plane wave using Eq. (28) in available in the Appendix. The subscript ℓ in both quantities indicates the polarization state of the incident plane wave: perpendicular (s), parallel (p), left-circular (L), or right-circular (R).

Note that $\Phi_{\text{R}}^{\text{ref}} = \Phi_{\text{R}}^{\text{tr}} \equiv 0$ because of the structure of $[\underline{\phi}^{\text{inc}}]$ for an incident RCP plane wave [22, 23]. The other six geometric phases Φ_{ℓ}^{ref} and Φ_{ℓ}^{tr} , $\ell \in \{s, p, L\}$, are generally non-zero in Figs. 8, 9, 10, and 11; furthermore, their spectral dependencies

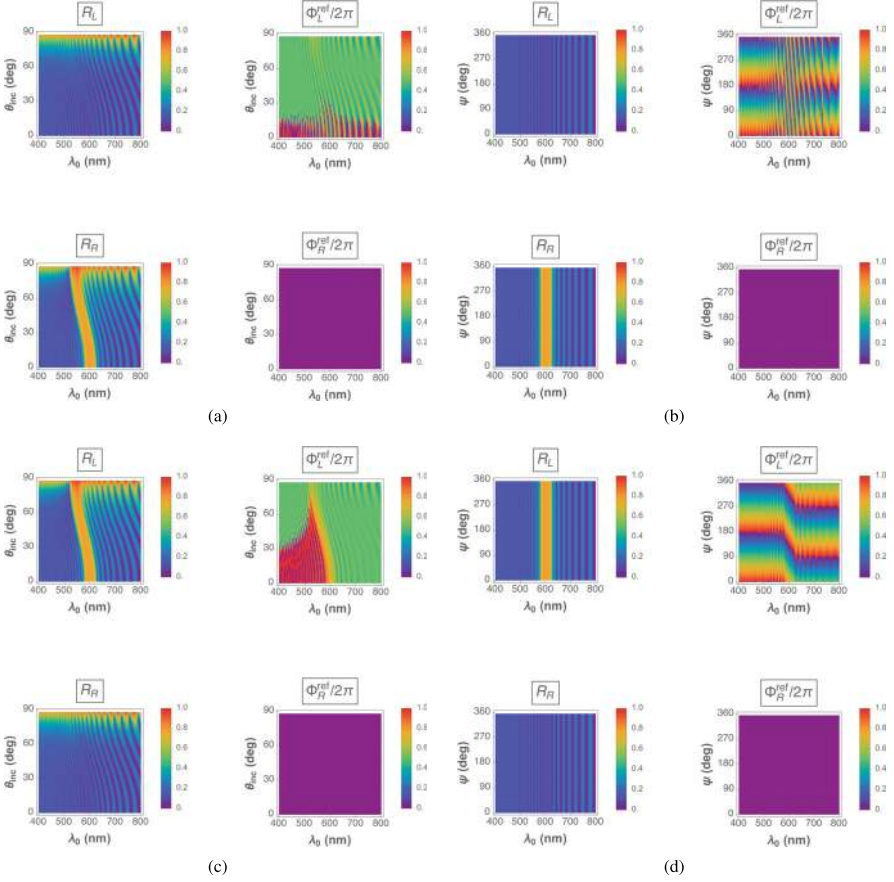


Fig. 8 Spectral variations of the total circular reflectance $R_\mu(\lambda_0, \theta_{\text{inc}}, \psi)$ and reflection-mode geometric phase $\Phi_\mu^{\text{ref}}(\lambda_0, \theta_{\text{inc}}, \psi)$, $\mu \in \{L, R\}$, when (a), (b) $h = 1$ and (c), (d) $h = -1$. (a), (c) $\theta_{\text{inc}} \in [0^\circ, 90^\circ)$ and $\psi = 0^\circ$; (b), (d) $\theta_{\text{inc}} = 0^\circ$ and $\psi \in [0^\circ, 360^\circ)$. (a) $h = 1$, $\theta_{\text{inc}} \in [0^\circ, 90^\circ)$, and $\psi = 0^\circ$. (b) $h = 1$, $\theta_{\text{inc}} = 0^\circ$, and $\psi \in [0^\circ, 360^\circ)$. (c) $h = -1$, $\theta_{\text{inc}} \in [0^\circ, 90^\circ)$, and $\psi = 0^\circ$. (d) $h = -1$, $\theta_{\text{inc}} = 0^\circ$, and $\psi \in [0^\circ, 360^\circ)$

have some resemblance to those of the corresponding total remittances defined in Eqs. (10), (11), (13), and (14). Indeed, a feature representing the circular Bragg phenomenon is clearly evident in the plots of Φ_ℓ^{ref} and Φ_ℓ^{tr} , $\ell \in \{s, p, L\}$. The feature curves toward shorter wavelengths as θ_{inc} increases while ψ is fixed, and the feature has two undulations with increasing ψ for normal incidence.

Although the geometric phase of the transmitted plane wave has been measured for normal incidence on a chiral sculptured thin film [21], that was done only at a single value of λ_0 , that too in the long-wavelength neighborhood of the circular Bragg regime. Hopefully, experimental verification of the features evident in Figs. 8, 9, 10, and 11 will be carried out soon and the role of structural handedness clarified.

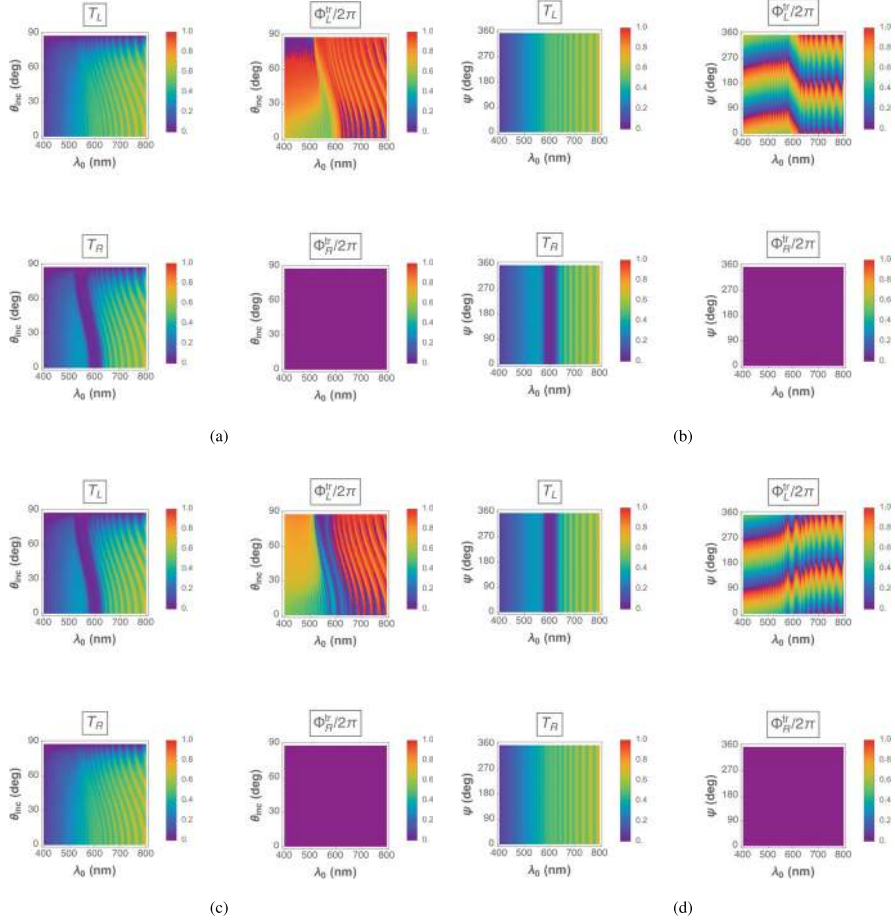


Fig. 9 Spectral variations of the total circular transmittance $T_\mu(\lambda_0, \theta_{\text{inc}}, \psi)$ and transmission-mode geometric phase $\Phi_\mu^{\text{tr}}(\lambda_0, \theta_{\text{inc}}, \psi)$, $\mu \in \{L, R\}$, when (a), (b) $h = 1$ and (c), (d) $h = -1$. (a), (c) $\theta_{\text{inc}} \in [0^\circ, 90^\circ]$ and $\psi = 0^\circ$; (b), (d) $\theta_{\text{inc}} = 0^\circ$ and $\psi \in [0^\circ, 360^\circ]$. (a) $h = 1$, $\theta_{\text{inc}} \in [0^\circ, 90^\circ]$, and $\psi = 0^\circ$. (b) $h = 1$, $\theta_{\text{inc}} = 0^\circ$, and $\psi \in [0^\circ, 360^\circ]$. (c) $h = -1$, $\theta_{\text{inc}} \in [0^\circ, 90^\circ]$, and $\psi = 0^\circ$. (d) $h = -1$, $\theta_{\text{inc}} = 0^\circ$, and $\psi \in [0^\circ, 360^\circ]$

5 Final Remark

Measurement of intensity-dependent observable quantities such as reflectances and transmittances was instrumental in the identification of the circular Bragg phenomenon [44, 47] and continues to be undertaken [11, 12, 20]. However, measurement of phase-dependent quantities, especially for oblique incidence, has been identified in this update as an arena for comprehensive research in the near future.

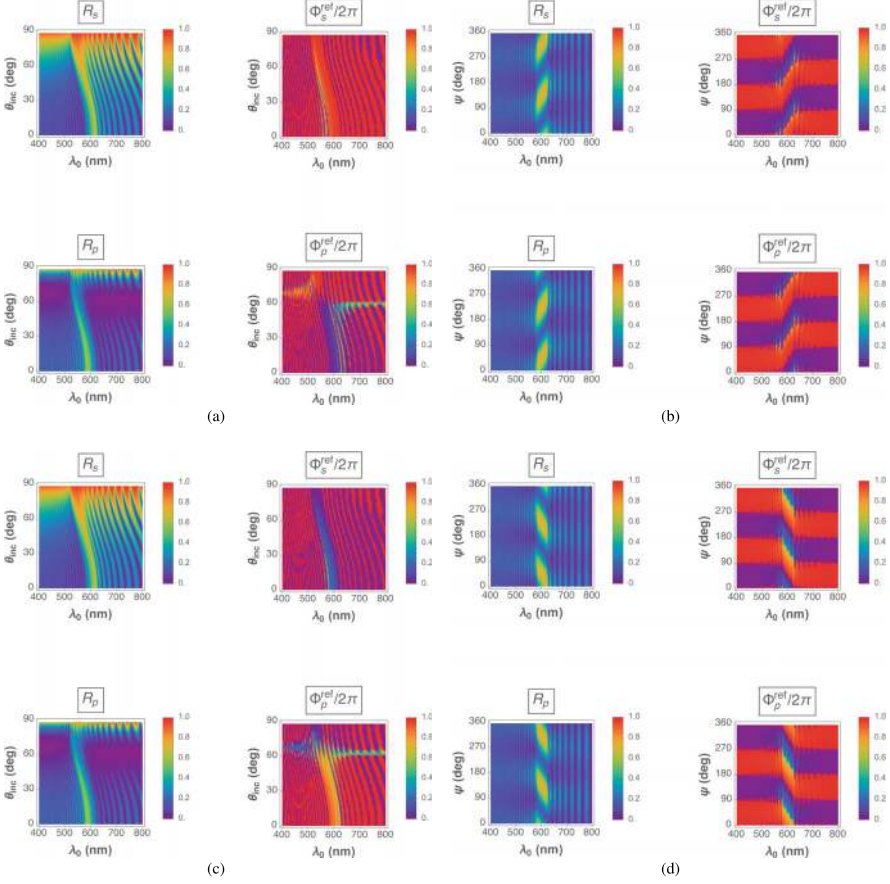


Fig. 10 Spectral variations of the total linear reflectance $R_\mu(\lambda_0, \theta_{\text{inc}}, \psi)$ and reflection-mode geometric phase $\Phi_\mu^{\text{ref}}(\lambda_0, \theta_{\text{inc}}, \psi)$, $\mu \in \{s, p\}$, when (a), (b) $h = 1$ and (c), (d) $h = -1$. (a), (c) $\theta_{\text{inc}} \in [0^\circ, 90^\circ]$ and $\psi = 0^\circ$; (b), (d) $\theta_{\text{inc}} = 0^\circ$ and $\psi \in [0^\circ, 360^\circ]$. (a) $h = 1$, $\theta_{\text{inc}} \in [0^\circ, 90^\circ]$, and $\psi = 0^\circ$. (b) $h = 1$, $\theta_{\text{inc}} = 0^\circ$, and $\psi \in [0^\circ, 360^\circ]$. (c) $h = -1$, $\theta_{\text{inc}} \in [0^\circ, 90^\circ]$, and $\psi = 0^\circ$. (d) $h = -1$, $\theta_{\text{inc}} = 0^\circ$, and $\psi \in [0^\circ, 360^\circ]$

Appendix: Poincaré Spinor and Geometric Phase

Any uniform plane wave propagating in free space can be represented as a point on the surface of the Poincaré sphere $s_1^2 + s_2^2 + s_3^2 = s_0^2$, where s_0 , s_1 , s_2 , and s_3 are the four Stokes parameters. The plane wave's location is identified by the longitude $\alpha \in [0, 2\pi)$ and the latitude $\beta \in [-\pi/2, \pi/2]$ defined through the relations

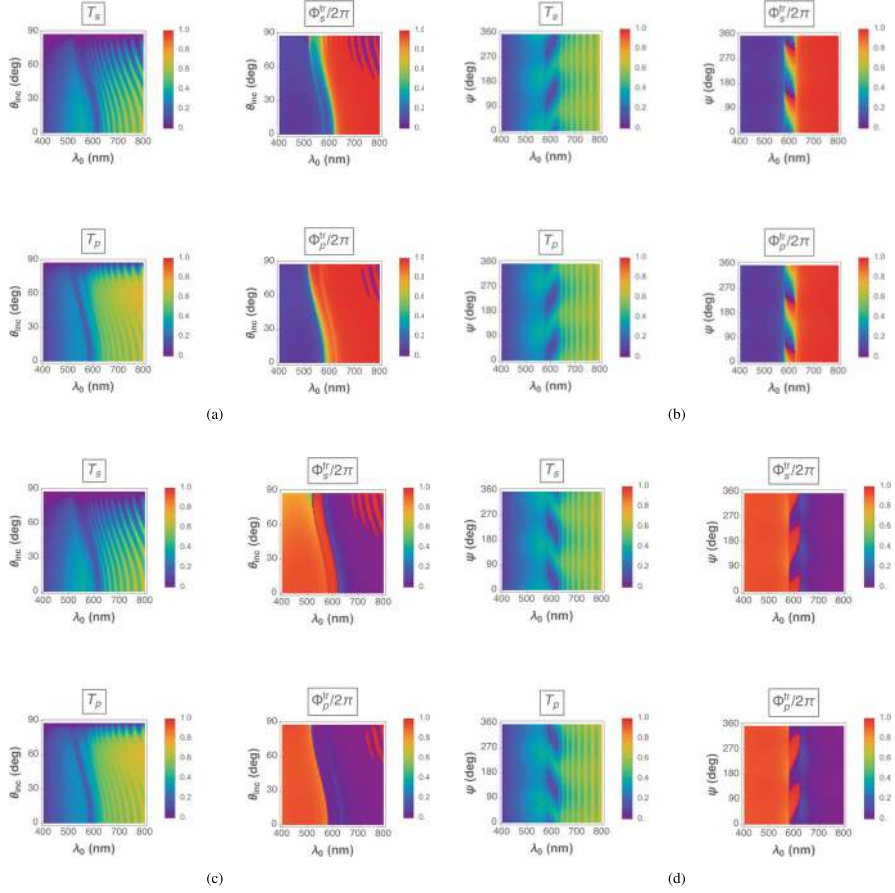


Fig. 11 Spectral variations of the total linear transmittance $T_\mu(\lambda_0, \theta_{\text{inc}}, \psi)$ and transmission-mode geometric phase $\Phi_\mu^{\text{tr}}(\lambda_0, \theta_{\text{inc}}, \psi)$, $\mu \in \{s, p\}$, when (a), (b) $h = 1$ and (c), (d) $h = -1$. (a), (c) $\theta_{\text{inc}} \in [0^\circ, 90^\circ]$ and $\psi = 0^\circ$; (b), (d) $\theta_{\text{inc}} = 0^\circ$ and $\psi \in [0^\circ, 360^\circ]$. (a) $h = 1$, $\theta_{\text{inc}} \in [0^\circ, 90^\circ]$, and $\psi = 0^\circ$. (b) $h = 1$, $\theta_{\text{inc}} = 0^\circ$, and $\psi \in [0^\circ, 360^\circ]$. (c) $h = -1$, $\theta_{\text{inc}} \in [0^\circ, 90^\circ]$, and $\psi = 0^\circ$. (d) $h = -1$, $\theta_{\text{inc}} = 0^\circ$, and $\psi \in [0^\circ, 360^\circ]$

$$\left. \begin{aligned} s_1 &= s_0 \cos \beta \cos \alpha \\ s_2 &= s_0 \cos \beta \sin \alpha \\ s_3 &= s_0 \sin \beta \end{aligned} \right\}. \quad (26)$$

The angles α and β appear in the Poincaré spinor

$$[\underline{\phi}] = \begin{bmatrix} \cos\left(\frac{\pi}{4} - \frac{\beta}{2}\right) \\ \sin\left(\frac{\pi}{4} - \frac{\beta}{2}\right) \exp(i\alpha) \end{bmatrix}. \quad (27)$$

With respect to a plane wave labeled “1”, the geometric phase of a plane wave labeled “2” is defined as the angle

$$\Phi_{21} = \text{Arg} \left\{ \left[\underline{\phi}_1 \right]^\dagger \cdot \left[\underline{\phi}_2 \right] \right\}. \quad (28)$$

Acknowledgments This chapter is in appreciation of the national cricket team of U.S.A. that acquitted itself very well during the T20 World Cup tournament held jointly in U.S.A. and West Indies in 2024. The author thanks the Charles Godfrey Binder Endowment at Penn State for supporting his research from 2006 to 2024.

References

1. M. Faryad, A. Lakhtakia, The circular Bragg phenomenon. *Adv. Opt. Photon.* **6**, 225–292 (2014)
2. A. Lakhtakia, V.C. Venugopal, On Bragg reflection by helicoidal bianisotropic mediums. *Archiv für Elektronik und Übertragungstechnik* **53**, 287–290 (1999)
3. S. Chandrasekhar, *Liquid Crystals*, 2nd edn. (Cambridge University, Cambridge, 1993)
4. P.G. De Gennes, J.A. Prost, *The Physics of Liquid Crystals*, 2nd edn. (Oxford University, Oxford, 1993)
5. R. Nityananda, On the theory of light propagation in cholesteric liquid crystals. *Mol. Cryst. Liq. Cryst.* **21**, 315–331 (1973)
6. O. Parodi, Light propagation along the helical axis in chiral smectics C. *J. Phys. Colloq.* **36**, C1-325–C1-326 (1975)
7. S. Garoff, R.B. Meyer, R. Barakat, Kinematic and dynamic light scattering from the periodic structure of a chiral smectic C liquid crystal. *J. Opt. Soc. Am.* **68**, 1217–1225 (1978)
8. I. Abdulhalim, L. Benguigui, R. Weil, Selective reflection by helicoidal liquid crystals. Results of an exact calculation using the 4×4 characteristic matrix method. *J. Phys. Paris* **46**, 815–825 (1985)
9. J. Xiang, Y. Li, Q. Li, D.A. Paterson, J.M.D. Storey, C.T. Imrie, O.D. Lavrentovich, Electrically tunable selective reflection of light from ultraviolet to visible and infrared by heliconical cholesterics. *Adv. Mater.* **27**, 3014–3018 (2015)
10. A. Lakhtakia, R. Messier, *Sculptured Thin Films: Nanoengineered Morphology and Optics* (SPIE, Bellingham, 2005); Chap. 9
11. P.D. McAtee, A. Lakhtakia, Experimental and theoretical investigation of the co-occurrence of linear and circular dichroisms for oblique incidence of light on chiral sculptured thin films. *J. Opt. Soc. Am. A* **35**, 1131–1139 (2018). Replace “ $-(z-L)$ ” by “ $+(z-L)$ ” in Eq. (8b)
12. S. Erten, A. Lakhtakia, G.D. Barber, Experimental investigation of circular Bragg phenomenon for oblique incidence. *J. Opt. Soc. Am. A* **32**, 764–770 (2015)
13. A. Lakhtakia, W.S. Weiglhofer, Axial propagation in a magnetic-dielectric cholesteric medium. *Liq. Cryst.* **15**, 659–667 (1993)
14. A. Lakhtakia, W.S. Weiglhofer, Axial propagation in general helicoidal bianisotropic media. *Microw. Opt. Technol. Lett.* **6**, 804–806 (1993)
15. W.D. St. John, W.J. Fritz, Z.J. Lu, D.-K. Yang, Bragg reflection from cholesteric liquid crystals. *Phys. Rev. E* **51**, 1191–1198 (1995)
16. A. Lakhtakia, Reflection of an obliquely incident plane wave by a half space filled by a helicoidal bianisotropic medium. *Phys. Rev. E* **374**, 3887–3894 (2010)

17. A. Lakhtakia, Resilience of circular-polarization-state-sensitive reflection against morphological disorder in chiral structures. *J. Nanophotonics* **18**, 036005 (2024)
18. F. Wang, A. Lakhtakia, R. Messier, Coupling of Rayleigh–Wood anomalies and the circular Bragg phenomenon in slanted chiral sculptured thin films. *Eur. Phys. J. Appl. Phys.* **20**, 91–103 (2002)
19. K. Yin, T. Zhan, J. Xiong, Z. He, S.-T. Wu, Polarization volume gratings for near-eye displays and novel photonic devices. *Crystals* **10**, 561 (2020)
20. R.A. Fiallo, *Architecting One-dimensional and Three-dimensional Columnar Morphologies of Chiral Sculptured Thin Films*, Doctoral Thesis (Pennsylvania State University, Pennsylvania, 2024)
21. A. Das, S. Mandal, R.A. Fiallo, M.W. Horn, A. Lakhtakia, M. Pradhan, Geometric phase and photonic spin Hall effect in thin films with architected columnar morphology. *J. Opt. Soc. Am. B* **40**, 2418–2428 (2023). Replace “tan” by “sin” in Eq. (5b)
22. A. Lakhtakia, Transmission-mode geometric-phase signatures of circular Bragg phenomenon. *J. Opt. Soc. Am. B* **41**, 500–507 (2024)
23. A. Lakhtakia, Geometric phase in plane-wave transmission by a dielectric structurally chiral slab with a central phase defect. *Phys. Rev. A* **109**, 053517 (2024)
24. H.C. Chen, *Theory of Electromagnetic Waves: A Coordinate-free Approach* (TechBooks, Fairfax, 1992)
25. J.F. Nye, *Physical Properties of Crystals: Their Representation by Tensors and Matrices* (Oxford University, Oxford, 1985)
26. R. Dreher, G. Meier, Optical properties of cholesteric liquid crystals. *Phys. Rev. A* **8**, 1616–1623 (1973)
27. A. Sugita, H. Takezoe, Y. Ouchi, A. Fukuda, E. Kuze, N. Goto, Numerical calculation of optical eigenmodes in cholesteric liquid crystals by 4×4 matrix method. *Jpn. J. Appl. Phys.* **21**, 1543–1546 (1982)
28. C. Oldano E. Miraldi, P. Taverna Valabrega, Dispersion relation for propagation of light in cholesteric liquid crystals. *Phys. Rev. A* **27**, 3291–3299 (1983)
29. A. Lakhtakia, W.S. Weiglhofer, Further results on light propagation in helicoidal bianisotropic mediums: oblique propagation. *Proc. R. Soc. Lond. A* **453**, 93–105 (1997)
30. T.G. Mackay, A. Lakhtakia, *The Transfer-Matrix Method in Electromagnetics and Optics* (Morgan & Claypool, San Ramon, 2020)
31. F. Wooten, *Optical Properties of Solids* (Academic, New York, 1972); Sec. 3.1
32. M. Frisch, ‘The most sacred tenet’? Causal reasoning in physics. *Br. J. Philos. Sci.* **60**, 459–474 (2009)
33. H. Silva, B. Gross, Some measurements on the validity of the principle of superposition in solid dielectrics. *Phys. Rev.* **60**, 684–687 (1941)
34. P. Kinsler, How to be causal: time, spacetime and spectra. *Eur. J. Phys.* **32**, 1687–1700 (2011)
35. W.H. Bragg, W.L. Bragg, The reflection of X-rays by crystals. *Proc. R. Soc. Lond. A* **88**, 428–438 (1913)
36. W.H. Bragg: The reflection of X-rays by crystals. *Nature* **91**, 477 (1913)
37. P.P. Ewald, Zur Begründung der Kristalloptik; Teil II: Theorie der Reflexion und Brechung. *Annalen der Physik Series 4* **49**, 117–143 (1916)
38. J.B. Geddes III, M.W. Meredith, A. Lakhtakia, Circular Bragg phenomenon and pulse bleeding in cholesteric liquid crystals. *Opt. Commun.* **182**, 45–57 (2000)
39. M.W. Meredith, A. Lakhtakia, Time-domain signature of an axially excited cholesteric liquid crystal. Part I: Narrow-extent pulses. *Optik* **111**, 443–453 (2000)
40. J.B. Geddes III, A. Lakhtakia, Time-domain signature of an axially excited cholesteric liquid crystal. Part II: Rectangular wide-extent pulses. *Optik* **112**, 62–66 (2000)
41. M. Born, E. Wolf, *Principles of Optics*, 6th edn. (Cambridge University, Cambridge, 1980); Sec. 1.4.2
42. E. Reusch, Untersuchung über Glimmercombinationen. *Annalen der Physik und Chemie (Leipzig)* **138**, 628–638 (1869)

43. E. Reusch, Optical investigations on periodic multilayers of mica, in *More Adventures in Contemporary Electromagnetic Theory*, ed. by F. Chiadini, V. Fiumara (Springer, Cham, 2025); (This is an English translation of Ref. 42.)
44. J.-P. Mathieu, Examen de quelques propriétés optiques fondamentales des substances cholestériques. *Bulletin de la Société Française de Minéralogie* **41**, 174–195 (1938)
45. J.D. Jackson, *Classical Electrodynamics*, 3rd edn. (Wiley, New York, 1999); Sec. 7.2
46. A. Lakhtakia, Geometric phase and nanoscale architected morphology of Reusch piles, in *More Adventures in Contemporary Electromagnetic Theory*, ed. by F. Chiadini, V. Fiumara (Springer, Cham, 2025)
47. J.L. Ferguson, Cholesteric structure—I Optical properties. *Mol. Cryst.* **1**, 293–307 (1966)



Akhlesh Lakhtakia received his B.Tech. (1979) and D.Sc. (2006) degrees from the Banaras Hindu University and his M.S. (1981) and Ph.D. (1983) degrees from the University of Utah. He joined the Department of Engineering Science and Mechanics at The Pennsylvania State University in 1983, where he is now Evan Pugh University Professor of Engineering Science and Mechanics. He is also a Visiting Professor of Mathematics at the University of Edinburgh and an Honorary International Chair Professor at National Taipei University of Technology. Dr. Lakhtakia has been elected a fellow of Optical Society of America, SPIE, Institute of Physics (UK), American Association for the Advancement of Science, American Physical Society, Institute of Electrical and Electronics Engineers, Royal Society of Chemistry, Royal Society of Arts, and Sigma Xi. He has been designated a Distinguished Alumnus of both of his *almae matres* at the highest level. Awards at Penn State include: Outstanding Research Award, Outstanding Advising Award, Premier Research Award, Outstanding Teaching Award, and the Faculty Scholar Medal in Engineering. He received the 2010 SPIE Technical Achievement Award, the 2016 Walston Chubb Award for Innovation, the 2022 Smart Structures and Materials Lifetime Achievement Award, the 2022 IEEE Antennas and Propagation Society Distinguished Achievement Award, the 2022 Radio Club of America Lifetime Achievement Award, and the 2024 SPIE Gold Medal. He has served as a Sigma Xi Distinguished Lecturer (2022–24) and a Jefferson Science Fellow at the US State Department (2022–23). His current research interests include electromagnetic scattering, surface multiplasmonics, photovoltaic solar cells, sculptured thin films, mimunes, engineered biomimicry, and forensic science.

Computational Plasmonics: Boundary Integral Equation Methods in Scattering Problems



Christos Mystilidis, Guy Vandenbosch, and Xuezhi Zheng

1 Introduction

Maxwell's equations supplemented by appropriate boundary conditions and (an often phenomenological) description of matter constitute all that is necessary to study even the most complicated of electromagnetic problems. The development, refinement, and application of methods to probe such problems numerically, when analytical approaches fall short due to complications of the geometry or the material, define the research domain of *Computational Electromagnetics* (CEM). We can boldly state that CEM is the workhorse of modern electromagnetics; the field enjoys an unprecedented level of maturity with numerous well-established recipes [1–3] being routinely employed and sharpened [4–8], further enabled by formidable hardware. The success of CEM has spilled from the scientific sphere and is felt by the general public (the ultimate goal and *raison d' être* of every scientific discipline): CEM is instrumental for the design of modern telecommunication systems (such as massive MIMO and WIFI networks [9]). It is undoubtedly playing an essential role in forging modern society.

The field of *plasmonics* concerns the study of collective free-electron oscillations (plasmons), initially in metals but also in more exotic materials [10] that support free carriers, and their coupling with electromagnetic radiation (plasmon-polaritons). Classical electromagnetics have been employed with impressive success in the nanoscale [11] to offer physical explanations to exotic optical phenomena: the squeezing of light in nanometric scales has allowed the overcome of the diffraction

C. Mystilidis · X. Zheng (✉)

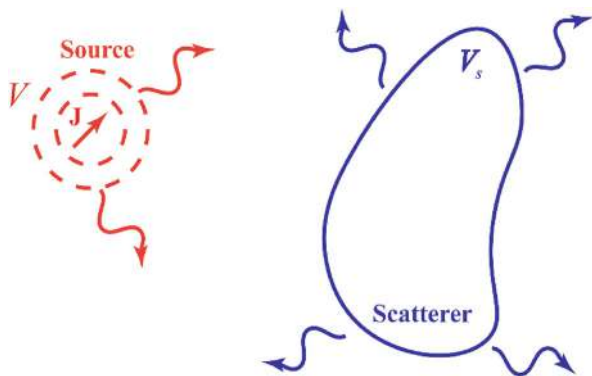
Department of Electrical Engineering, KU Leuven, Leuven, Belgium

G. Vandenbosch

Katholieke Universiteit Leuven, Leuven, Belgium

e-mail: guy.vandenbosch@ku.leuven.be

Fig. 1 Illustration of a scattering problem. An external source, in the figure a current \mathbf{J} (see the red arrow) occupies a volume in space V_s and radiates an incident field (see the red curved lines) in space. The incident field impinges on a scatterer, which occupies a volume V and induces a scattered field (see the blue curved lines)



limit [12] and as such offers plenty opportunities for applications ranging from efficient light harvesting [13] to plasmonic-assisted chemical reactions [14], single molecule sensing [15], and promising biomedical applications [16]. CEM follows closely and is routinely updated to tackle problems in the nanoscale and the optical spectrum, a notable difference from its beginnings in microwave frequencies [17]. In this chapter, we discuss CEM applied in plasmonics and in particular in *scattering problems*. As is the conventional wisdom, we define such problems as follows. An object is illuminated by external sources, that is, currents and charges occupying a volume in space. The said sources generate an incident field, which impinges upon the object (the latter introduces an inhomogeneity in space due to different material properties from the background). Part of the radiation is transmitted inside the *scatterer*, while part of it is bouncing off its surface (the scattered field). The definition is shown in Fig. 1.

Despite the great variety of computational algorithms that have been published through the years, we can distinguish two main categories: *differential equation-based* (DE) and *integral equation-based* (IE) approaches. In the first, the discretization and subsequent manipulations to extract the solution concern the differential equations of the problem; the latter include an additional step of transforming the working differential to integral equations and subsequently attacking the resulting equations. DE-based algorithms (notably the Finite Element Method, FEM, and the Finite Difference Time Domain, FDTD) are characterized by high flexibility, being able to treat spatial and material inhomogeneities and nonlinearities [18]. From a technical side, the implementation of such codes is relatively straightforward and as such multiple instances of commercial software have appeared (such as Lumerical and COMSOL), which are used routinely by the community [11, 19, 20]. Further, such techniques can be applied easily to coupled systems of differential equations, allowing *multiphysics* simulations to be set up; this in turn renders them indispensable for *semiclassical* simulations, where the quantum mechanical nature of the electron gas is partially admitted through material differential equations [21, 22] (we will elaborate on this later) or in microwave heating studies [23].

At the same time, such methods are unable to intrinsically account for infinite domain situations, which pertain exactly to the scattering problems at hand. The computational domain must be then closed with appropriate boundary conditions (such as scattering boundary conditions or Perfectly Matched Layers), which unavoidably introduce artifacts (though the relevant research has come a long way to minimize such issues [24]) and most importantly empirical decisions, which lack rigorousness. A potentially important drawback is the very high number of spatial or temporal samples required [18]. This issue is underlined in nanoscale scenarios where, as we mentioned before, extreme localization of the electromagnetic field can happen (close to geometrical singularities or nanoscopic gaps [21, 25]), far beyond the (optical) wavelength scale, requiring a locally very high mesh density. As such not only a refined but further an *adaptive* mesh is required.

IE-based methods act in a complementary manner to DE-based ones. The reformulation of the initial problem in integral (or integrodifferential) equation format is achieved through the concept of *Green's functions* [26], which are the impulse response functions of the electromagnetic system. The action of the infinite background is included in these functions naturally; there is no need to enter in empirical discussions or suffer artificial error. Of course, Green's functions are analytically available only in certain setups (geometries and materials), effectively limiting the exploration space for such methods. Since Green's functions account for the background, IE-based methods attack explicitly only the scatterer and as such result in *Boundary Integral Equation* (BIE) or *Volume Integral Equation* (VIE) formalisms. This is a particularly appealing characteristic in plasmonic setups where only the hotspot of plasmonic activity, the scatterer, is discretized; the number of unknowns is smaller (compared to DE approaches) and the method is close to the physics. The integral equations are transformed to linear (note that IE methods dealing with nonlinearities are quite more involved [27, 28]) systems routinely through the *Method of Moments* (MoM). MoM (and by extension BIE and VIE) is characterized by intense analytical work, is very accurate as the integral equations are formally exact, and requires quite sophisticated implementations. Hybrid methods harvesting the strong points of each family of methods have also been developed [18]. In this work, from all that pertains to CEM in scattering problem of plasmonics, we present BIE formalisms together with MoM.

We can further distinguish two levels of accuracy when it comes to a CEM method. For one, there is (what we call) numerical accuracy: the CEM method has to be accurate with respect to the assumptions taken to set it up. For example, for a well-posed problem a numerically inaccurate CEM method is due to too sparse discretization or neglect proper treatment of the singularities or simply mistakes in the implementation thereof. At a more fundamental level there is the physical accuracy: the algorithm hinges upon a set of physical laws or reasonable models. When these equations fall outside of the range of their validity, it is reasonable to expect that the solutions provided by CEM would be inaccurate (no matter how meticulous an analysis or careful an implementation has been carried out). As we discussed in our first paragraph, the description of matter is often *phenomenological*. Typically, we assign a material response function, for example,

a *bulk permittivity*, to a piece of material (this response function is the fingerprint of the said material). The past two decades have rendered plasmonic devices of ever-decreasing size experimentally available [21, 29–32]. This shrinking has seriously challenged the constitutive equations (see (3) below): a bulk permittivity is not anymore capable of capturing adequately the material response, where quantum mechanical effects contribute significantly. In principle, a full quantum mechanical treatise should be used to extract the full solution. Nonetheless, the solution of Schrödinger’s equation for every degree of freedom of a nanoscopic system, in the deep nanometric (deep-nm) regime (1–10 nm), is a formidable computational task. Alternative *ab initio* approaches based on the Density Functional Theory (DFT), as the Time-Dependent DFT (TDDFT) shift the focus on the electron density, a collective property [33]; nonetheless, the exploration space of plasmonic devices is still severely limited. At the same time, it is worth asking whether it is possible to treat this regime (optical frequencies and deep-nm) as an intermediate one, where the conventional approach of Maxwell’s equations coupled with a material equation can accept quantum corrections (even if *ad hoc*) and explain accurately and intuitively experimental findings [10]. Indeed, *semiclassical models* appear as attractive alternatives: relatively simple, intuitive, and accurate (when applied with caution). Despite their *relative* simplicity, such models depart significantly from the standard base of *macroscopic* CEM recipes: a reconciliation of the CEM discipline with such models is highly sought for, with immense interest both from a numerical and engineering side for the obvious reasons, but also from the viewpoint of physicists as such methods constitute *enabling technology* for probing new physics.

Here we focus on one such model, the *Hydrodynamic Drude Model* (HDM), which has become recently particularly popular among the nanoplasmonics community; we motivate our choice more persuasively in the third section of our chapter, where we additionally present in detail a BIE formalism for nonlocal media within this model.

For all our discussions below, we note that a harmonic $e^{-i\omega t}$ time dependence is assumed and subsequently suppressed throughout. The magnetic permeability of the scatterers is assumed equal to the vacuum unit value reflecting the very weak magnetic effects in optical frequencies in natural media (such as metals). We use Gaussian units; though this may alienate some readers, we wish to continue along the lines of the seminal works in BIEs in the field [34–36].

2 Boundary Integral Equation Formalism: Local Media

In this section we discuss how to construct a BIE formalism and elaborate on the MoM and on critical details of the numerical implementation such as the notion of *singularity extraction*.

We note that there are multiple integral equation formalisms pertinent to plasmonics [37–41], however we opt to follow the one presented by García de Abajo and Howie [25], developed explicitly for plasmonics and Electron Energy Loss Spectroscopy (EELS); there an electron beam passing by the vicinity (or even

through [42]), the scatterer of interest is used to excite modes that conventional illumination by light cannot probe (and thus referred to as *dark modes*). This is a potential-based formulation. We motivate our choice by four reasons:

1. [36] is very much celebrated among the plasmonics community as evidenced by the high number of citations of this work.
2. [36] is the mathematical formulation behind the equally celebrated and used MATLAB toolbox MNPBEM [43].
3. [36] is the predecessor of a string of publications from our group [44–48], which extend the original method to treat nonlocal media (see Section 3).
4. a potential-based formulation has particularly appealing advantages from a computational viewpoint and seems pertinent to quantum electromagnetics [49, 50].

2.1 Potential-Based Formalism

The first step is to recast Maxwell's equations in a potential-based format. We assume that an electromagnetic field distribution arises in a homogeneous space due to the action of the external sources ρ and \mathbf{J} , which in turn occupy a domain V . This distribution is a solution of the following set of equations

$$\begin{aligned} \nabla \cdot \mathbf{D} &= 4\pi\rho, \nabla \cdot \mathbf{B} = 0, \\ \nabla \times \mathbf{E} &= ik_0\mathbf{B}, \nabla \times \mathbf{H} = \frac{4\pi}{c}\mathbf{J} - ik_0\mathbf{D}. \end{aligned} \quad (1)$$

As usual, \mathbf{E} denotes the electric field, \mathbf{H} the magnetic field, \mathbf{B} is the magnetic induction, \mathbf{D} is the electric shift, c is the speed of light in vacuum, and k_0 is the free space wavenumber.

The link between the fundamental (\mathbf{E}, \mathbf{H}) and the secondary (\mathbf{D}, \mathbf{B}) fields is the *constitutive* or *material* equations. As we have discussed, the assumption of very weak magnetism is tantamount to

$$\mathbf{B}(\mathbf{r}) = \mathbf{H}(\mathbf{r}). \quad (2)$$

Above \mathbf{r} is the position vector of an observation point in space.¹ For the case of electric fields, we adopt a similar phenomenological approach to (2), however we allow the relative electric permittivity ϵ to be frequency dependent (and the associated medium/metal chromatically dispersive), that is

$$\mathbf{D}(\mathbf{r}, \omega) = \epsilon(\mathbf{r}, \omega) \mathbf{E}(\mathbf{r}, \omega). \quad (3)$$

¹ We note that we include or neglect the arguments \mathbf{r} and ω rather liberally; we include them when they are critical to the point made (e.g., the local character of (3)) and we neglect them to make the formalism friendlier.

Within the parlance of the nanoplasmonics community the equation above (admittedly an equation most electrical engineers in the business of electromagnetics are very familiar with) is known as the *Local Response Approximation* (LRA). This can be easily appreciated as follows: the reason (electric field) gives rise to a response (electric displacement) *exactly at the point of application* \mathbf{r} . It seems that the material (represented by ϵ and unit permeability) does not admit any long-range correlation [10]. Later we will relax such familiar but strict assumption to allow for a description of some scale regimes, deep in the nanometric scale that became experimentally accessible more recently and where such an assumption is ill-advised.

For now, we will continue with the LRA (with which the reader is assumed to feel more comfortable) and we will introduce the *scalar electric potential* ϕ and the *vector magnetic potential* \mathbf{A} in the manner conventional to electromagnetics textbooks [26]

$$\mathbf{E} = ik_0\mathbf{A} - \nabla\phi, \mathbf{B} = \nabla \times \mathbf{A}. \quad (4)$$

The ambiguity in the definition of the potentials is resolved by the *Lorenz gauge*

$$\nabla \cdot \mathbf{A} = ik_0\epsilon\phi, \quad (5)$$

which in turn enables us to construct *wave equations* for the potentials

$$\nabla^2\phi + k^2\phi = -4\pi\frac{\rho}{\epsilon}, \nabla^2\mathbf{A} + k^2\mathbf{A} = -\frac{4\pi}{c}\mathbf{J}, \quad (6)$$

where $k = \omega\sqrt{\mu\epsilon} = k_0\sqrt{\epsilon}$ is the wavenumber of the material occupying volume V . Equations (6) become the working equations, the ones we need to solve in order to find the electromagnetic fields in V .

We include additional complexity by assuming now that the translational invariance of the space V is interrupted by a surface B . In other words, an *interface* separates V in two regions, 1 and 2, as shown in Fig. 2. External sources may appear on one region, on both or neither. To reconcile the different potentials in each region, we introduce appropriate *boundary conditions*. It is well-known [36] that these are

$$\phi_1 = \phi_2, \mathbf{A}_1 = \mathbf{A}_2, \quad (7)$$

$$\frac{\partial\mathbf{A}_1}{\partial n} - \mathbf{n}ik_0\epsilon_1\phi_1 = \frac{\partial\mathbf{A}_2}{\partial n} - \mathbf{n}ik_0\epsilon_2\phi_2, \epsilon_1\mathbf{n} \cdot (ik_0\mathbf{A}_1 - \nabla\phi_1) = \epsilon_2\mathbf{n} \cdot (ik_0\mathbf{A}_2 - \nabla\phi_2). \quad (8)$$

Above, \mathbf{n} is the vector normal to the interface (with direction from in to out; this is arbitrary but once a convention is set, it should be followed throughout) and $\partial/\partial n$ is the directional derivative along its direction. Equations (7) stem from the continuity

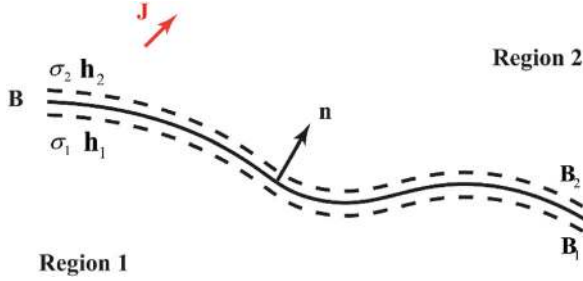


Fig. 2 Illustration of Huygens' principle. A boundary B separates Region 1 from Region 2 and the normal of the boundary points from Region 1 to Region 2. An external source J is in Region 2. Equivalent sources, i.e., σ_1, \mathbf{h}_1 and σ_2, \mathbf{h}_2 , that generate the correct scattered fields in Region 1 and Region 2, are impressed on two fictitious boundaries, B_1 and B_2 , which are just inside and just outside the boundary B

of the tangential components of the \mathbf{E} and \mathbf{H} . The more involved (8) are statements of the Lorenz gauge and the continuity of the normal component of \mathbf{D} .

We have reformulated our electromagnetic problem in terms of potentials. We proceed with introducing the BIE formalism; this hinges upon the concept of Green's functions.

2.2 Boundary Integral Equation Formalism

The sources that may exist in regions 1 and 2 create corresponding potentials (and of course, fields). The material contrasts on the interface introduce potentials due to scattering in either side. The total potential in each region is the superposition of these two contributions. To study them we will avoid discussing the external sources and the material contrasts explicitly. Instead, we will follow another way.

Let's momentarily retreat to the homogeneous space (though, as it will be made clear below, the same applies for a single region). We have defined Green's functions as impulse functions for our electromagnetic system, formally [26]

$$\nabla^2 g(\mathbf{r}, \mathbf{r}') + k^2 g(\mathbf{r}, \mathbf{r}') = -4\pi \delta(\mathbf{r} - \mathbf{r}'), \quad (9)$$

where $g(\mathbf{r}, \mathbf{r}')$ is the Green's functions, $\delta(\mathbf{r} - \mathbf{r}')$ is a Dirac delta, and \mathbf{r}' is the position vector of a source point. In other words, $g(\mathbf{r}, \mathbf{r}')$ reveals the response at point \mathbf{r} due to a point-like excitation at \mathbf{r}' . We explicitly mention a homogeneous space, since then the analytical form of $g(\mathbf{r}, \mathbf{r}')$ is available [26]

$$g(\mathbf{r}, \mathbf{r}') = \frac{e^{ikr}}{r}, \quad (10)$$

for a 3D space and

$$g(\mathbf{r}, \mathbf{r}') = \frac{16\pi}{i} H_0^{(1)}(kr), \quad (11)$$

for a 2D space. Above $r = |\mathbf{r} - \mathbf{r}'|$ is the distance between source and observation point and $H_0^{(1)}$ is the Hankel function of the first kind. We note for later that when the observation point approaches infinitesimally the source point (or $r \rightarrow 0$) both (10) and (11) become *singular* (the latter due to the logarithmic singularity of the Neumann function).

Using the superposition principle, the action of a source distribution can be stated through Green's functions. For externally applied charge and current sources, the resultant imposed potentials are

$$\varphi^e(\mathbf{r}) = \frac{1}{\varepsilon} \int_V g(\mathbf{r}, \mathbf{r}') \rho(\mathbf{r}') d\mathbf{r}', \quad \mathbf{A}^e(\mathbf{r}) = \frac{1}{c} \int_V g(\mathbf{r}, \mathbf{r}') \mathbf{J}(\mathbf{r}') d\mathbf{r}', \quad (12)$$

where the integration is carried out on the source volume. These are actual sources. We can construct similar expressions for virtual or auxiliary ones.

For the case of Fig. 2, we imagine two surfaces B_1 and B_2 , contained by regions 1 and 2, respectively, which are similar to the actual interface B^2 . We further assume that charge and current distributions σ_1 and σ_2 , and \mathbf{h}_1 and \mathbf{h}_2 lay on these surfaces. These sources are blind across the interface. In other words, they radiate exclusively in the region where they belong and there they reconstruct the scattered potentials (originally created by the interface and the material contrasts). Alternatively, we can think that these sources radiate as if in a homogeneous space, completely filled by the material of their attached region. However, the potentials (and fields) they construct in the region(s) they are not attached to are completely unphysical and should be dropped. By this line of reasoning, equivalent problems to the original one are built; their superposition reconstructs the sought after solution (the reader may have noticed that we have just described the *Huygens equivalence principle*; for a visual representation thereof see Fig. 3).

Using the same token as in (12), the potentials constructed by these virtual sources are

$$\varphi_i^{\text{scat}}(\mathbf{r}) = \int_{B_i} g_i(\mathbf{r}, \mathbf{r}') \sigma_i(\mathbf{r}') d\mathbf{r}', \quad i = 1, 2, \quad (13)$$

² This is intuitive and pertains to the case of Fig. 2, however it is not necessary; note that the first step, where virtual sources are placed on surfaces attached to each region serves mostly an educational purpose. As we discuss below, eventually the two surfaces will fall onto the actual interface; the details of this limiting procedure are not of importance. Note that the particular shape of these auxiliary surfaces is essential for another (similar) method, the *Method of Auxiliary Sources* [51]; the ambiguity in the shape of the surfaces is the price to pay for bypassing surface integral singularities that we will encounter down the line.

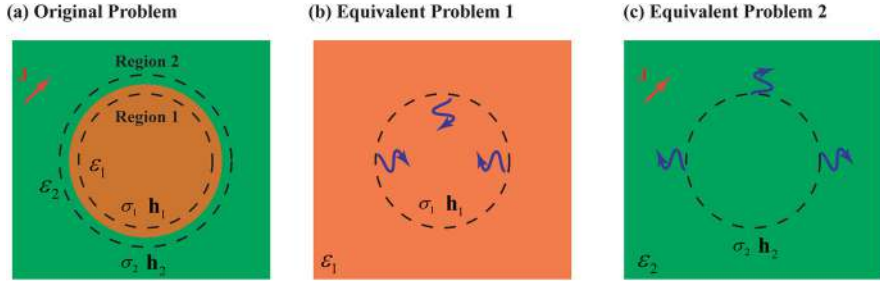


Fig. 3 Illustration of the original problem (a) and the two associated equivalent problems (b), (c). In (a), the original problem: a scatterer with a permittivity ε_1 sits in a space filled with a material whose permittivity, ε_2 , is shown. The scatterer occupies a volume, i.e., Region 1, while the rest of the space is as Region 2. A source current \mathbf{J} is imposed in Region 2, and again two sets of equivalent sources σ_1, \mathbf{h}_1 , and σ_2, \mathbf{h}_2 are impressed on two boundaries (see the dashed lines in (a)) just inside and outside the boundary of the scatterer to correctly account for the scattered field. In (b) and (c), the two equivalent problems are demonstrated. The equivalent problem 1 in (b) (2 in (c)) assumes that σ_1, \mathbf{h}_1 (σ_2, \mathbf{h}_2) are the sources that radiate into a homogeneous space, which is filled by the material of Region 1 (Region 2), and can generate the true scattered fields in Region 1 (Region 2)

and

$$\mathbf{A}_i^{\text{scat}}(\mathbf{r}) = \int_{B_i} g_i(\mathbf{r}, \mathbf{r}') \mathbf{h}_i(\mathbf{r}') d\mathbf{r}', \quad i = 1, 2. \quad (14)$$

In each region, the total potentials are then

$$\varphi_i = \varphi_i^e + \varphi_i^{\text{scat}}, \quad (15)$$

and

$$\mathbf{A}_i = \mathbf{A}_i^e + \mathbf{A}_i^{\text{scat}}. \quad (16)$$

Through a limiting procedure B_1 and B_2 overlap with each other and eventually with B . Then, (13) and (14) cannot be arbitrary but have to abide by the working principles, which are the boundary conditions (7) and (8) we presented above. Combining (12), (13), (14), (15), and (16) with the boundary conditions (7) and (8) we get

$$\int_{B_1} g_1(\mathbf{r}, \mathbf{r}') \sigma_1(\mathbf{r}') d\mathbf{r}' - \int_{B_2} g_2(\mathbf{r}, \mathbf{r}') \sigma_2(\mathbf{r}') d\mathbf{r}' = \varphi^e, \quad (17)$$

and

$$\int_{B_1} g_1(\mathbf{r}, \mathbf{r}') \mathbf{h}_1(\mathbf{r}') d\mathbf{r}' - \int_{B_2} g_2(\mathbf{r}, \mathbf{r}') \mathbf{h}_2(\mathbf{r}') d\mathbf{r}' = \mathbf{A}^e, \quad (18)$$

and

$$\int_{B_1} \frac{\partial g_1(\mathbf{r}, \mathbf{r}')}{\partial n} \mathbf{h}_1(\mathbf{r}') d\mathbf{r}' - \int_{B_2} \frac{\partial g_2(\mathbf{r}, \mathbf{r}')}{\partial n} \mathbf{h}_2(\mathbf{r}') d\mathbf{r}' - \mathbf{n} i k_0 \left(\varepsilon_1 \int_{B_1} g_1(\mathbf{r}, \mathbf{r}') \sigma_1(\mathbf{r}') d\mathbf{r}' - \varepsilon_2 \int_{B_2} g_2(\mathbf{r}, \mathbf{r}') \sigma_2(\mathbf{r}') d\mathbf{r}' \right) = \boldsymbol{\alpha}^e, \quad (19)$$

and

$$\varepsilon_1 \int_{B_1} \frac{\partial g_1(\mathbf{r}, \mathbf{r}')}{\partial n} \sigma_1(\mathbf{r}') d\mathbf{r}' - \varepsilon_2 \int_{B_2} \frac{\partial g_2(\mathbf{r}, \mathbf{r}')}{\partial n} \sigma_2(\mathbf{r}') d\mathbf{r}' - \mathbf{n} \cdot i k_0 \left(\varepsilon_1 \int_{B_1} g_1(\mathbf{r}, \mathbf{r}') \mathbf{h}_1(\mathbf{r}') d\mathbf{r}' - \varepsilon_2 \int_{B_2} g_2(\mathbf{r}, \mathbf{r}') \mathbf{h}_2(\mathbf{r}') d\mathbf{r}' \right) = D^e. \quad (20)$$

The quantities ϕ^e , \mathbf{A}^e , $\boldsymbol{\alpha}^e$, and D^e are all due to the excitation (as indicated by the superscript). They are defined as

$$\varphi^e = \varphi_2^e - \varphi_1^e, \quad \mathbf{A}^e = \mathbf{A}_2^e - \mathbf{A}_1^e, \quad (21)$$

$$\boldsymbol{\alpha}^e = \frac{\partial \mathbf{A}_2^e}{\partial n} - \frac{\partial \mathbf{A}_1^e}{\partial n} + i k_0 \mathbf{n} (\varepsilon_1 \varphi_1^e - \varepsilon_2 \varphi_2^e), \quad (22)$$

$$D^e = \mathbf{n} \cdot [\varepsilon_1 (i k_0 \mathbf{A}_1^e - \nabla \varphi_1^e) - \varepsilon_2 (i k_0 \mathbf{A}_2^e - \nabla \varphi_2^e)]. \quad (23)$$

We have reached what we have set for: Eqs. (17), (18), (19), and (20) are all boundary integral equations (notice the surface integrals involved); the system consists of two scalar and two vector equations for an equal number of unknowns and is, in principle, solvable. To solve it, we will employ a standard MoM, however it is necessary to simplify our formalism, which is admittedly rather cumbersome.

We introduce the following operators:

$$\begin{aligned} G_i f &= \int_{B_i} g_i(\mathbf{r}, \mathbf{r}') f(\mathbf{r}') d\mathbf{r}', \quad i = 1, 2, \\ H_i f &= \frac{\partial}{\partial n} G_i f = \int_{B_i} \frac{\partial g_i(\mathbf{r}, \mathbf{r}')}{\partial n} f(\mathbf{r}') d\mathbf{r}', \quad i = 1, 2, \end{aligned} \quad (24)$$

where f is the equivalent charges or a cartesian component of the equivalent currents, which render the formalism much more appealing. Using (24) in (17), (18), (19), and (20) we get [36]

$$G_1 \sigma_1 - G_2 \sigma_2 = \varphi^e, \quad (25)$$

$$G_1 \mathbf{h}_1 - G_2 \mathbf{h}_2 = \mathbf{A}^e, \quad (26)$$

$$H_1 \mathbf{h}_1 - H_2 \mathbf{h}_2 - \mathbf{n} i k_0 (\varepsilon_1 G_1 \sigma_1 - \varepsilon_2 G_2 \sigma_2) = \boldsymbol{\alpha}^e, \quad (27)$$

$$\varepsilon_1 H_1 \sigma_1 - \varepsilon_2 H_2 \sigma_2 - \mathbf{n} \cdot i k_0 (\varepsilon_1 G_1 \mathbf{h}_1 - \varepsilon_2 G_2 \mathbf{h}_2) = D^e. \quad (28)$$

We proceed with discretizing the boundaries and performing the MoM.

2.3 Method of Moments

The importance of the MoM in CEM cannot be overstated. Numerous textbooks or educational papers are written explicitly or contain chapters for it. It is not our goal to review its essential steps, but rather present them for the case we are interested in here. The transformation of the integral to linear equations is the same for each of (25), (26), (27), and (28). As such, we present it exclusively for (25) to avoid repetition.

The first essential step is to expand the charges on each side of the interface (see Fig. 2) in terms of appropriate *basis functions*. There is no recipe for choosing such functions; one needs to guess functions that approximate the best the actual behavior of the function to be expanded (e.g., they should vanish at the ends of a wire antenna). At the same time, they should be simple enough in order to facilitate both analytical manipulations and further (and perhaps most importantly) numerical evaluation. As such, a compromise is often made. Since the scatterer whose surface is to be discretized is deeply subwavelength, the basis functions are supported by elements whose maximum dimensions is much smaller than the excitation's wavelength. As such, simple pulses can be used to approximate locally the charges and currents. In particular,

$$\begin{aligned} \sigma_1(\mathbf{r}) &= \sum_{i=1}^N a_i p_i(\mathbf{r}), \\ \sigma_2(\mathbf{r}) &= \sum_{i=1}^N b_i p_i(\mathbf{r}), \end{aligned} \quad (29)$$

where

$$p_i(\mathbf{r}) = \begin{cases} 1, & \mathbf{r} \in \Delta B_i \\ 0, & \mathbf{r} \notin \Delta B_i \end{cases}, \quad (30)$$

a_i and b_i are the weights and N the number of basis functions chosen to cover the surface of the scatterer. In turn, the surface is discretized in N subdomains (subsurfaces) ΔB_i ³. Substituting (29) and (30) into (25) does little to solve the

³ To be more precise, triangles for 3D scatterers and linear segments for 2D ones.

problem. On the contrary it creates a single equation with $2N$ unknowns. In order for (29) to be a formal approximation of σ_1 and σ_2 a certain index must be selected. In MoM we select to minimize the *weighted residuals*. We select a set of *testing functions*. Their selection can be arbitrary; however it is convenient (and often beneficial, assuming that we can exploit orthogonality properties certain basis/testing functions may dispose) to assume a Galerkin approach, according to which the testing function has the same form as the basis functions do. Here

$$t_j(\mathbf{r}) = p_j(\mathbf{r}), \quad (31)$$

where $j = 1, \dots, N$ an independent index from i . We subsequently take (25), multiply by t_j and integrate along each element that supports t_j . This results in (we use the formalism of (17) for clarity)

$$\begin{aligned} \int_{\Delta B_{1,j}} t_j(\mathbf{r}) \int_{B_1} g_1(\mathbf{r}, \mathbf{r}') \sum_{i=1}^N a_i p_i(\mathbf{r}') d\mathbf{r}' d\mathbf{r} \\ - \int_{\Delta B_{2,j}} t_j(\mathbf{r}) \int_{B_2} g_2(\mathbf{r}, \mathbf{r}') \sum_{i=1}^N b_i p_i(\mathbf{r}') d\mathbf{r}' d\mathbf{r} = \int_{\Delta B_{1,j}} t_j(\mathbf{r}) \varphi^e(\mathbf{r}) d\mathbf{r}, \end{aligned} \quad (32)$$

or (using (30), exchanging the sum and integral signs, and admitting $B_1 \rightarrow B_2 \rightarrow B$)

$$\begin{aligned} \int_{\Delta B_j} p_j(\mathbf{r}) \sum_{i=1}^N a_i \int_{\Delta B_i} g_1(\mathbf{r}, \mathbf{r}') p_i(\mathbf{r}') d\mathbf{r}' d\mathbf{r} \\ - \int_{\Delta B_j} p_j(\mathbf{r}) \sum_{i=1}^N b_i \int_{\Delta B_i} g_2(\mathbf{r}, \mathbf{r}') p_i(\mathbf{r}') d\mathbf{r}' d\mathbf{r} = \int_{\Delta B_j} p_j(\mathbf{r}) \varphi^e(\mathbf{r}) d\mathbf{r}, \end{aligned} \quad (33)$$

where ΔB_j are the subsurfaces for the testing (observation) and ΔB_i for the basis (source). We introduce the following matrices, using additionally (30)

$$\mathbf{V}[v_j], \quad v_j = \int_{\Delta B_j} \varphi^e(\mathbf{r}) d\mathbf{r}, \quad (34)$$

the $N \times 1$ excitation vector, $\mathbf{a}[a_i]$ and $\mathbf{b}[b_i]$ the two $N \times 1$ coefficient vectors, and

$$\begin{aligned} \mathbf{Z}_a \begin{bmatrix} z_{ij}^a \end{bmatrix}, z_{ij}^a = \int_{\Delta B_j} \int_{\Delta B_i} g_1(\mathbf{r}, \mathbf{r}') d\mathbf{r}' d\mathbf{r}, \\ \mathbf{Z}_b \begin{bmatrix} z_{ij}^b \end{bmatrix}, z_{ij}^b = \int_{\Delta B_j} \int_{\Delta B_i} g_2(\mathbf{r}, \mathbf{r}') d\mathbf{r}' d\mathbf{r}, \end{aligned} \quad (35)$$

the two $N \times N$ reciprocal capacitance matrices, leading to

$$\mathbf{Z}_a \mathbf{a} + \mathbf{Z}_b \mathbf{b} = \mathbf{V}. \quad (36)$$

We evaluate (34) and (35) purely numerically; the integrands are well-behaving functions in the bounded subsurfaces ΔB_j and ΔB_i . The exception is when the two different subsurfaces coincide (the observation points fall on the source points) when the singular behavior of the Green's function reveals itself. We will give details in the next subsection. We note that a similar procedure can be carried out for all remaining integral equations; the result is the linear system we have been discussing from the start. There are numerous recipes to solve such systems, direct or iterative, which for well-conditioned system are equivalent⁴.

2.4 Singularity Extraction

In this subsection we will discuss the special treatment of the case when an observation point/surface/linear segment coincides with a source one. Then, as can be easily seen from (10) (the same applies for (11); the 3D case will be our example here) the Green's function becomes singular ($r = 0$ is a pole for this function) and the matrix elements (35) diverge. If we could locate the pathological terms, extract them from the integrand of (35), apply a quadrature for the residue and attack analytically the pathology, our problem would be solved. This is exactly what a singularity extraction method is, and there are numerous such instances in the literature [52–55].

As such, we Taylor expand the exponential in the numerator of (10) around $r = 0$, getting

$$\frac{e^{ikr}}{r} = \frac{1}{r} + ik - \frac{k^2}{2}r - \frac{ik^3}{6}r^2 + O(r^3). \quad (37)$$

Above, the big-oh O symbol means that r^3 is the next leading term in the Taylor series. We recognize the pole in the first term. As such, we write the elementary (but so essential in the singularity extraction method) relation

$$\frac{e^{ikr}}{r} = \left(\frac{e^{ikr}}{r} - \frac{1}{r} \right) + \frac{1}{r}, \quad (38)$$

where the first term is analytic in $r = 0$ (the pole degenerates to a removable singularity) and as such is integrated numerically, while the second analytically,

⁴ The direct linear equation solvers have an easier implementation; the iterative solvers require a reasonable first guess, which may be hard to find. On the other hand, iterative solvers tend to be faster, asymptotically behaving like $O(MN)$, where M is the number of iterations versus $O(N^2)$ for the direct. A MoM nonetheless (especially for the tiny physical system we discuss herein) is associated with dense but of low rank matrices. The asymptotic behavior is not reached, and the efficiency benefits are not really felt.

based on well-established formulas, depending also on the shape of elements [52–55].

The method we showcased above is sufficient for most purposes. Let's linger around (38) a bit more. Though the first term has avoided the singularity, it has a discontinuous first derivative. Naturally, we prefer to feed numerical integrators *smooth* integrands to improve convergence. Removing and subsequently adding another term is along this line of reasoning, eventually writing

$$\frac{e^{ikr}}{r} = \left(\frac{e^{ikr}}{r} - \frac{1}{r} + \frac{k^2 r}{2} \right) + \frac{1}{r} - \frac{k^2 r}{2}. \quad (39)$$

Now, the first term has a continuous first derivative, since it behaves from (37) as r^2 . The second term is analytically handled as before.

3 Boundary Integral Equation Formalism: Nonlocal Corrections

In this section we discuss the ramifications the admission of the nonlocal character of the electron gas in metals has in the BIE formalism we presented in the previous section, as well as in the numerics. The HDM is used to include nonlocality in the material response.

3.1 The Hydrodynamic Drude Model

The HDM has a long history with significant and many contributions during the 1960s, 1970s, and 1980s [56–60], a relative slowdown during the 1990s and 2000s, and subsequent resurgence that is still going strong [21, 61–67]. The HDM is conceptually very simple: the electron gas is treated as charged fluid, which is driven by the quantum (or exclusion) pressure, a result of the Pauli exclusion principle [68] and the fact that the electron gas is compressible [10]. Thus, a classical convective flow equation is used to account for a quantum mechanical effect [65]. The material equation is [68],

$$\frac{\beta^2}{\omega(\omega + i\gamma)} \nabla (\nabla \cdot \mathbf{P}_f(\mathbf{r})) + \mathbf{P}_f(\mathbf{r}) = -\frac{1}{4\pi} \frac{\omega_p^2}{\omega(\omega + i\gamma)} \mathbf{E}(\mathbf{r}), \quad (40)$$

where \mathbf{P}_f is the free-electron polarization density, γ is the phenomenological damping rate ($\gamma \propto \tau^{-1}$, the scattering time of free-electrons), which includes various sources of loss, ω_p is the plasma frequency, and $\beta = \sqrt{3/5}v_F$ is the hydrodynamic parameter, here with the high-frequency ($\omega \gg \gamma$) value [69]. It is clear, that the strength of the nonlocal effect is determined by β . Nonetheless, far

from a fitting parameter, β is a physical constant of the system. If we, however, chose to take $\beta \rightarrow 0$, then the local and very familiar $\mathbf{P}_f(\mathbf{r}) = \chi_f(\omega)\mathbf{E}(\mathbf{r})$, where $\chi_f(\omega) = -\frac{\omega_p^2}{[4\pi(\omega^2 + i\omega\gamma)]}$, the Drude susceptibility, is recovered. We finally note that the nonlocal character of (40) is evident by the spatial derivatives that act on \mathbf{P}_f , while the quantum nature of the correction the first term brings is admitted by the Fermi velocity. Equation (40) must be coupled to (1) (or most often to the electric wave equation) to acquire the behavior of the semiclassical material.

The discussion revolving around (40) concerns exclusively free electrons. *Bound* electrons exist in noble metals (the primary materials of application of HDM) and they offer an alternative interaction between light and matter [69], which is often treated locally (though more recent works argue for a more rigorous approach [22]), as follows

$$\mathbf{P}_{bd}(\mathbf{r}) = \chi_{bd}(\omega)\mathbf{E}(\mathbf{r}). \quad (41)$$

Above, \mathbf{P}_{bd} is the bound-electron polarization density and χ_{bd} is the accompanying bound-electron susceptibility; this is either inferred from experimental data [70, 71] or is described by more complicated (e.g., Lorentz-Drude) models [72, 73].

The HDM is used in our work both for its simplicity (analytical or semi-analytical solutions are available for this semiclassical model [57, 63, 74–76]) but also for its accuracy with respect to experimental findings. In particular, HDM when applied to systems consisting of noble metals (such as gold and silver, essential building blocks for plasmonic architectures) is able to predict limitations to the near-field enhancement [21], spectrum shifts of the scattering/absorption cross-sections [77–79], and further the existence of longitudinal modes [80], which are homogeneous solutions of the Maxwell's equations, should one admit the wavevector dependence of the permittivity [81]. From an engineering perspective, despite the possibly dense vocabulary of new terms we used above, the HDM is quite close to the classical picture: multiple (and significant) quantum mechanical phenomena are not accounted for, such as quantum tunneling and electron spill-out [68]. The latter is equivalent to introducing hard-wall boundaries, as in the classical perception. Though these simplifications render HDM conceptually simpler, they are the reasons behind significant shortcomings of applications of HDM in alkali metals [82, 83].

3.2 Potential-Based Formalism for Nonlocal Media

We aim here to introduce the potential-based formalism we described before for the case of nonlocal media. As before, we start with a very simple geometry of a homogeneous space filled with a nonlocal material. Sources ρ and \mathbf{J} may exist in a domain V_s ; however, to simplify the analysis, we assume a source-free space. The admission of the nonlocal character of the material, which is equivalent to the

admission of a wavevector dependence of the permittivity, gives rise to additional, longitudinal solutions for the Maxwell's Equations in (1). As such, the total field \mathbf{F} has two components: a transverse (predicted classically) and a longitudinal (predicted due to nonlocality). Transverse and longitudinal fields are not coupled with each other (but are reconciled at the interface to be discussed later) and as such the Helmholtz theorem can be applied

$$\mathbf{F} = \mathbf{F}^T + \mathbf{F}^L. \quad (42)$$

Note, that assuming that (2) still holds (with the same rationale as before), (42) concerns exclusively electric fields. *Transverse* and *longitudinal* are characterizations based on the following differential relations

$$\nabla \cdot \mathbf{F}^T = 0, \nabla \times \mathbf{F}^T \neq 0, \quad (43)$$

and

$$\nabla \cdot \mathbf{F}^L \neq 0, \nabla \times \mathbf{F}^L = 0. \quad (44)$$

From (43) we can appreciate the Gauss law as the origin of the transverse behavior of classical waves, while from (44) we can appreciate the semi-static nature of the longitudinal plasma waves; (44) provides an important hint for the potentials selected to represent such fields.

Based on (42) we can construct two independent sets of Maxwell's equations: one for the transverse distribution (from this point forward $\mathbf{F} = \mathbf{E}$)

$$\begin{aligned} \nabla \cdot \mathbf{D}^T &= 0, \nabla \cdot \mathbf{B}^T = 0, \\ \nabla \times \mathbf{E}^T &= ik_0 \mathbf{B}^T, \nabla \times \mathbf{H}^T = -ik_0 \mathbf{D}^T, \end{aligned} \quad (45)$$

and one for the longitudinal distribution

$$\begin{aligned} \nabla \cdot \mathbf{D}^L &= 0, \mathbf{B}^L = \mathbf{0}, \\ \nabla \times \mathbf{E}^L &= \mathbf{0}, ik_0 \mathbf{D}^L = 0. \end{aligned} \quad (46)$$

Let us analyze each system, (45) and (46), further. For (45), the constitutive relations read

$$\mathbf{D}^T = \mathbf{E}^T + 4\pi \mathbf{P}_f^T + 4\pi \mathbf{P}_{bd}^T, \quad (47)$$

$$\mathbf{P}_{bd}^T = \chi_{bd} \mathbf{E}^T, \quad (48)$$

$$\mathbf{P}_f^T = \chi_f^T \mathbf{E}^T = -\frac{1}{4\pi} \frac{\omega_p^2}{\omega(\omega + i\gamma)} \mathbf{E}^T. \quad (49)$$

We can introduce a *total* transverse permittivity by combining the separate contributions of (47) as follows:

$$\mathbf{D}^T = \varepsilon^T \mathbf{E}^T, \quad (50)$$

where

$$\varepsilon^T = 1 + 4\pi\chi_{bd} - \frac{\omega_p^2}{\omega(\omega + i\gamma)}. \quad (51)$$

We can then construct a wave equation for the electric field as per usual

$$\nabla \times \nabla \times \mathbf{E}^T - k^2 \mathbf{E}^T = \mathbf{0}. \quad (52)$$

For the longitudinal system (46) the constitutive relations become

$$\mathbf{D}^L = \mathbf{E}^L + 4\pi\mathbf{P}_f^L + 4\pi\mathbf{P}_{bd}^L, \quad (53)$$

$$\mathbf{P}_{bd}^L = \chi_{bd} \mathbf{E}^L, \quad (54)$$

$$\frac{\beta^2}{\omega(\omega + i\gamma)} \nabla^2 \mathbf{P}_f^L + \mathbf{P}_f^L = -\frac{1}{4\pi} \frac{\omega_p^2}{\omega(\omega + i\gamma)} \mathbf{E}^L. \quad (55)$$

As for the transverse case, we can derive a wave equation for \mathbf{E}^L . This is

$$\nabla^2 \mathbf{E}^L + \kappa^2 \mathbf{E}^L = \mathbf{0}. \quad (56)$$

Above [65]

$$\kappa^2 = \frac{1}{\beta^2} \left[\omega^2 + i\omega\gamma - \frac{\omega_p^2}{\varepsilon_{bd}} \right], \quad (57)$$

is the *longitudinal* wavenumber and $\varepsilon_{bd} = 1 + 4\pi\chi_{bd}$ is the bound-electron permittivity. We note that the longitudinal wavenumber remains predominantly imaginary below the plasma frequency, with the real part emerging (and dominating) beyond it [84]. As such longitudinal modes are evanescent in the frequency regime below the plasma frequency and become propagating above it. Though this may seem like an argument against incorporating such fields in the optical response in the first frequency regime, we will see in the examples that nonlocality affects spectra even around the dipole resonance (situated at $\omega_p/\sqrt{3}$ for a simple-metal spherical scatterer). It is interesting to discuss the magnitude of κ or rather, the associated wavelength. This, for noble metals and in the optical frequencies we are

interested in, is below 1 nm [85]. Later, we will discuss the important complication this causes to numerics. Further, the mere existence of a longitudinal wavenumber makes a clear statement: despite the semi-static nature of longitudinal modes, (44), and (56) are accounts of the *dynamics* of such systems (see [62] for an account of the consequences should one fully embrace, at first glance reasonable, the full quasistatic approximation).

Naturally, we are more interested in reformulating (45) and (46) in terms of appropriate potentials. Since (45) is identical to (1) (with elimination of the sources), we anticipate that the transverse potentials will be very similar in definition to the local ones we defined in (4), (5), and (6). As such, our main task is to deduce potentials for the longitudinal modes. Exploiting their curl-free nature, we introduce

$$\mathbf{E}^L = -\nabla\varphi^L. \quad (58)$$

The computational benefits of the potential-based formalism, evident from the local case, are here underlined. The emergence of an additional degree of freedom (longitudinal modes) is accompanied by increased computational cost. Nonetheless, the approach presented here seems to alleviate to an extent the problem: a single scalar is all that must be additionally calculated. This scalar function satisfies another wave equation, in particular

$$\nabla^2\varphi^L + \kappa^2\varphi^L = 0. \quad (59)$$

To recapitulate, in a region of space filled with a nonlocal material we introduce three potentials: \mathbf{A} , φ , and φ^L . The latter two are combined to give the total potential $\varphi^{\text{tot}} = \varphi + \varphi^L$. We underline that the possibility to introduce longitudinal and transverse potentials separately is enabled by the independence of the respective field distributions far from interfaces.

Let us depart from the homogeneous space and introduce an interface, splitting effectively the space in two regions 1 and 2; region 1 remains nonlocal⁵, however we fill region 2 with a local medium, essentially simulating an architecture where a metallic nanoparticle is enveloped by a local background (say vacuum). Boundary conditions must be then applied at the interface to reconcile the wave equations we derived. As a new degree of freedom has arisen, we expect that an *additional boundary condition* (ABC) will be needed to render the system solvable. Alternatively, it is only natural to supplement the new differential equation in (40) with a boundary condition. As such, we maintain the boundary conditions (7) and (8), though including φ_1^L (region 2 is local and as such does not support a longitudinal mode nor potential), in particular

⁵ All our analysis holds should we invert the nature of the regions, i.e., from nonlocal—local to local—nonlocal.

$$\varphi_1 + \varphi_1^L = \varphi_2, \mathbf{A}_1 = \mathbf{A}_2, \quad (60)$$

$$\varepsilon_{1,bd} \mathbf{n} \cdot \left(\frac{\partial \mathbf{A}_1}{\partial n} - \mathbf{n} i k_0 \varepsilon_1 \varphi_1 = \frac{\partial \mathbf{A}_2}{\partial n} - \mathbf{n} i k_0 \varepsilon_2 \varphi_2, \right. \\ \left. \varepsilon_{1,bd} \mathbf{n} \cdot (i k_0 \mathbf{A}_1 - \nabla [\varphi_1 + \varphi_1^L]) = \varepsilon_2 \mathbf{n} \cdot (i k_0 \mathbf{A}_2 - \nabla \varphi_2) \right). \quad (61)$$

Note that the longitudinal potential is not involved in the first Eq. (61), as it is not involved in the Lorenz gauge. The second Eq. (61) is derived, as is the second equation of (8), from the continuity of the normal component of the electric displacement. However, only what concerns the bound electrons is involved in region 1. This puzzling aspect of (61) is resolved immediately upon revelation of the pertinent ABC.

The best choice of ABCs has been the subject of a recent review [86] and of numerous older papers in the 1970s and 1980s [58, 81, 87–89]. However, the choice is not arbitrary: it has to be derived from the physical arguments that were used to derive (40), that is, the ABC must be consistent with the material equation [62]. The statement we made earlier, that in the HDM electron-spill out is suppressed, essentially a hard-wall assumption, is equivalent to the Sauter ABC at the boundary B [86]

$$\mathbf{n} \cdot \mathbf{P}_f = 0. \quad (62)$$

This is the reason there is no free-electron contribution regarding region 1 in the second Eq. (61). The potential reformulation of (62) is

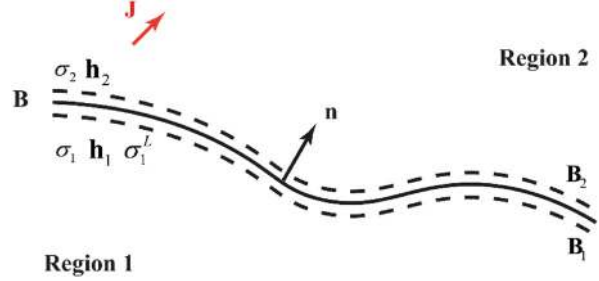
$$\chi_{1,f} \mathbf{n} \cdot (i k_0 \mathbf{A}_1 - \nabla \varphi_1) + \frac{\varepsilon_{1,bd}}{4\pi} \mathbf{n} \cdot \nabla \varphi_1^L = 0, \quad (63)$$

where $\chi_{1,f}$ is the transverse free-electron susceptibility (given by the Drude model).

3.3 Boundary Integral Equation Formalism

As for the local case, the main aim is to construct surface integral equations for the newly defined potentials. We repeat the geometry in Fig. 4, which is identical to that of the local case. However we assume that a region (say, region 1) is filled with a nonlocal medium (for the physically hard to interpret nonlocal-nonlocal case, see [47, 48]). As before, auxiliary sources, charges σ_1 and σ_2 and currents \mathbf{h}_1 and \mathbf{h}_2 are placed on two surfaces B_1 and B_2 just inside region 1 and region 2, respectively. As we have mentioned before, these sources radiate as if in a homogeneous space; they produce meaningful results only in their attached region (their results in the rest region(s) are discarded). Eventually, the total potentials (and fields) are a superposition of the contribution of all sources.

Fig. 4 Illustration of Huygens' principle for a boundary that encloses a nonlocal medium. The whole setup is the same as the one in Fig. 2 with the only difference that an equivalent source σ_1^L is imposed on B_1 to take the longitudinal wave into account



Following from the Helmholtz decomposition, and the independence of transverse from longitudinal (and vice versa) fields, we distinguish between sources that generate exclusively transverse fields and sources that generate exclusively longitudinal fields. The first are actually the ones we have already discussed. The latter we call *longitudinal charges* σ_1^L (such charges should be placed on appropriate surfaces in all regions filled with nonlocal media). They radiate in the same manner as the transverse charges and sources and their radiation is captured by a Green's function, that is

$$\varphi_1^{L,\text{scat}} = \int_{B_1} g_1^L(\mathbf{r}, \mathbf{r}') \sigma_1^L(\mathbf{r}') d\mathbf{r}', \quad (64)$$

where the longitudinal Green's function g_1^L is defined as in (10) or (11), with the wavenumber given by (57). This simple statement in concert with our discussion about the magnitude of the longitudinal wavenumber betrays serious numerical complications in modeling nonlocal media. In particular, in such media, we have to resolve (in terms of the spatial discretization used) the transverse waves, with the length scale defined by the wavelength of the incident field (subwavelength scale) and the longitudinal ones, with the length scale defined by the longitudinal wavelength (subnanometric scale). A nonlocal simulation is, by its very nature, a *multiphysics* and *multiscale* numerical effort [68]. By using a BIE, that is, by focusing exclusively on the boundaries of the architecture we avoid the burden of reconciling two different length scales and the concomitant adaptive meshing that FEM implementations have reported [90]. At the same time, taking into consideration that the effects of nonlocality manifest strongly within angstroms inside the interface (defined by the aforesaid nonlocal length scale) a surface approach, as the one discussed here, seems close to the physics [85]. As such the computational benefits of a BIE approach are underlined in a nonlocal setting and the adoption of such a method seems motivated by the physics of the problem.

Returning to the formulation and using the same argument in favor of simplicity as before, we introduce the operator

$$G_1^L f = \int_{B_1} g_1^L(\mathbf{r}, \mathbf{r}') f(\mathbf{r}') d\mathbf{r}', \quad (65)$$

which acts on the arbitrary scalar function f , which here represents longitudinal charges. Performing the limiting procedure B_1 and $B_2 \rightarrow B$, we reconcile all included sources via the boundary conditions (60), (61), and (63). In this manner, upon introduction of (24) and (65) we acquire our modified system of BIEs

$$G_1\sigma_1 + G_1^L\sigma_1^L - G_2\sigma_2 = \varphi^e, \quad (66)$$

$$G_1\mathbf{h}_1 - G_2\mathbf{h}_2 = \mathbf{A}^e, \quad (67)$$

$$H_1\mathbf{h}_1 - H_2\mathbf{h}_2 - \mathbf{n}ik_0(\varepsilon_1G_1\sigma_1 - \varepsilon_2G_2\sigma_2) = \boldsymbol{\alpha}^e, \quad (68)$$

$$\varepsilon_1H_1\sigma_1 - \varepsilon_2H_2\sigma_2 - \mathbf{n} \cdot ik_0(\varepsilon_1G_1\mathbf{h}_1 - \varepsilon_2G_2\mathbf{h}_2) = D^e, \quad (69)$$

$$4\pi\chi_{f,1}(\mathbf{n} \cdot ik_0G_1\mathbf{h}_1 - H_1\sigma_1) + \varepsilon_{bd,1}H_1^L\sigma_1^L = 0. \quad (70)$$

We solve the system (66), (67), (68), (69), and (70) (note that these three scalar and two vector equations are used to extract an equal number of scalar and vector variables) using the MoM we have described previously. We use pulse basis functions for the expansion of σ_1^L using the same rationale as before: for sufficiently dense discretization (this means here resolving the subnanometric rather than subwavelength field variations; see [48] for a nice graphical depiction of this statement) the longitudinal charge can be considered piecewise constant. In the next section, we show certain examples that result by the algorithm we described in this and the previous sections.

4 Examples

In this section, two examples are demonstrated. For the first, we consider a sodium (Na) sphere. The radius of the sphere is 2 nm. The sphere is excited by a normally incident TM (transverse magnetic) polarized plane wave (see the inset of Fig. 5a). The frequency of the incident field spans from 3 to 8 electron volts (eVs) with 201 sampling points in the range. Two material models are considered: one is a local response model (the Drude model with a plasma frequency 5.89132 eV and a damping rate 0.1 eV); the other is the nonlocal hydrodynamic model (where the Fermi velocity is 1.06×10^6 m/s).

We compare the absorption and scattering cross-sections [91] from the discussed BIE implementation with the Mie theory. It can be seen from Fig. 5 that the results

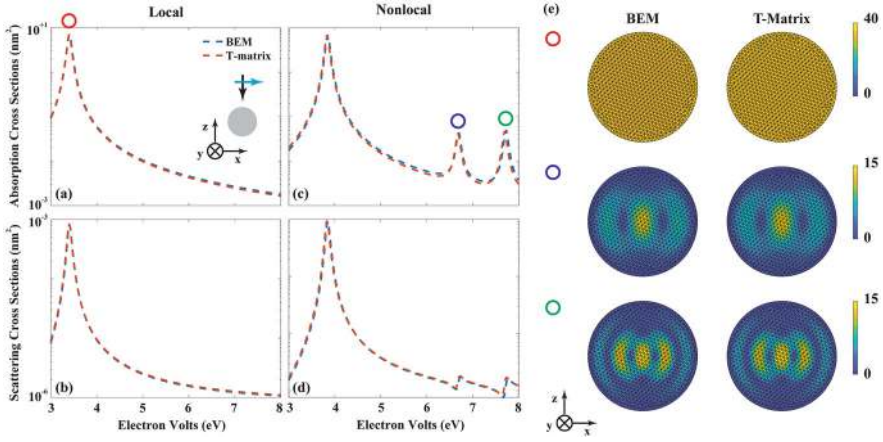


Fig. 5 Comparison between the results from the discussed BIE algorithm and the Mie theory for the scattering of a sodium (Na) sphere. In (a)–(d), the absorption cross-sections and the scattering cross-sections are demonstrated. The results from the BIE algorithm are marked by blue dashed lines, while the ones from the Mie theory are marked by red dashed lines. The scattering problem is illustrated in (a). In (a) the main resonance is highlighted by a red circle, while the resonances of the longitudinal modes are highlighted by a blue and a green circle. The electric field distributions at these resonances are shown in (e). There, the magnitudes of the fields are shown and coded by the colors from blue to yellow

agree well for both the local and the nonlocal cases. To quantify, we define relative errors,

$$\text{err}_{\text{sca}} = \frac{|\sigma_{\text{sca}}^{\text{Mie}} - \sigma_{\text{sca}}^{\text{BEM}}|}{\sigma_{\text{sca}}^{\text{Mie}}} \times 100\%, \quad \text{err}_{\text{abs}} = \frac{|\sigma_{\text{abs}}^{\text{Mie}} - \sigma_{\text{abs}}^{\text{BEM}}|}{\sigma_{\text{abs}}^{\text{Mie}}} \times 100\%. \quad (71)$$

For the local case, the maximum relative error of the scattering cross-sections and the one of the absorption cross-sections are 3.9‰ and 1.3‰. For the nonlocal case, the maximum relative errors are 5‰ and 0.4‰. We also evaluate the electric fields at resonances and compare the fields evaluated numerically with the ones by the Mie theory. For this, we define a relative error,

$$\text{err}_{|\mathbf{E}|} = \frac{||\mathbf{E}^{\text{Mie}}| - |\mathbf{E}^{\text{BEM}}||}{|\mathbf{E}^{\text{Mie}}|} \times 100\%. \quad (72)$$

For the local case, the electric field distribution (see the first row of Fig. 5e) at the main resonance (i.e., 3.4 eV) exhibits a maximum relative error of 0.35‰. For the nonlocal case, the electric field distribution (see the second and the third row of Fig. 5e) at the resonance of longitudinal modes (i.e., 6.7 eV and 7.7 eV) exhibits a maximum relative error of 0.04‰ and 0.02‰.

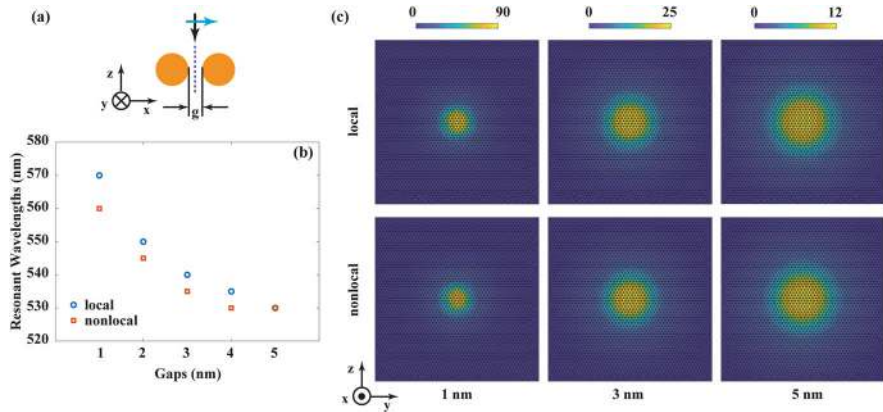


Fig. 6 Scattering of a gold (Au) dimer for different gap sizes. (a) shows the configuration of the scattering problem and (b) illustrates the spectral positions of the main resonances in the scattering spectra of the dimers with difference gap sizes. For the local response model, the positions are marked by the blue circles, while for the nonlocal model, the positions are marked by the red squares. The magnitudes of the electric fields on a cut, which is marked by the black dashed lines in (a), in the mid of the gap region are plotted in (c) for the gap sizes of 1 nm, 3 nm, and 5 nm at the corresponding resonances. The magnitudes of the fields are coded by the colors from blue to yellow. The cut is square with a side of 51 nm and the cut is discretized by triangles (whose maximum area is 0.5696 nm^2) and the electric fields are evaluated at the centers of the triangles

For the second, we look at gold (Au) dimers with different gap sizes. Here, the radius of the spheres is 20 nm and we consider five gap sizes (see g in Fig. 6) from 1 nm to 5 nm with 1 nm as a step. The dimers are excited by a normally incident TM (transverse magnetic) polarized plane wave (see the inset of Fig. 6a). The wavelengths of the plane waves span from 400 nm to 800 nm with 81 sampling points in between. Au is modeled by both the local and the nonlocal models with the effects of bound electrons taken into account (see the relevant parameters in [72] and for the Fermi velocity $1.40 \times 10^6 \text{ m/s}$). On the one hand, we extract the wavelengths of the main resonances in the scattering spectra of the dimers (see Fig. 6a). For small gap sizes, we indeed see a systematic blue shift when comparing the resonant wavelengths of the nonlocal model with the ones of the local model. Eventually, for the gap size of 5 nm, the difference vanishes, which agrees well with previous studies [21, 90]. Further, we plot the electric field distributions on a cut in the middle of the gap region (see the black dashed lines in Fig. 6a) for the gap sizes of 1 nm, 3 nm, and 5 nm (see Fig. 6b). Especially, for the gap size of 1 nm and the nonlocal model, the maximum electric field enhancement (with respect to the magnitude of the incident field which is assumed to be 1) is reduced with respect to the local response model (from 90 to 70), which is due to the fact that the quantum pressure included in the nonlocal model tends to smoothen field singularities.

5 Conclusion

We reviewed a potential-based BIE method particularly tailored to plasmonics. Though each step was presented for the method at hand, the line of reasoning remains the same for other methods of the same category (e.g., construction of BIEs, MoM, singularity extraction). Under the relatively new lens of semiclassical models, which admit the quantum nature of electrons, something necessary at the length scales that contemporary plasmonic research is dwelling, and in particular the HDM, BIE methods appear as a very strong and even natural candidate. As HDM changes essentially only the charge distribution (and also near-fields) close to the interface, a method that focuses exactly on the surface seems to be particularly fitting. Despite the objective limitations by the potential lack of knowledge of the Green's function, the method shown herein and BIEs in general, are able to tackle plasmonics problems that monopolize the interest of the community, such as the spherical dimer we showcased in the second example and thus prove themselves as essential tools for the nanoplasmonics community.

References

1. K. Yee, Numerical solution of initial boundary value problems involving maxwell's equations in isotropic media. *IEEE Trans. Antennas Propag.* **14**(3), 302–307 (1966). <https://doi.org/10.1109/TAP.1966.1138693>
2. J.H. Argyris et al., Finite element method—The natural approach. *Comput. Methods Appl. Mech. Eng.* **17–18**, 1–106 (1979). [https://doi.org/10.1016/0045-7825\(79\)90083-5](https://doi.org/10.1016/0045-7825(79)90083-5)
3. R.F. Harrington, *Field Computation by Moment Methods* (Wiley-IEEE Press, 1993)
4. R.N. Simpson, Z. Liu, R. Vázquez, J.A. Evans, An isogeometric boundary element method for electromagnetic scattering with compatible B-spline discretizations. *J. Comput. Phys.* **362**, 264–289 (2018). <https://doi.org/10.1016/j.jcp.2018.01.025>
5. H.T.B. Do, D.W. Jun, Z. Mahfoud, W. Lin, M. Bosman, Electron dynamics in plasmons. *Nanoscale* **13**(5), 2801–2810 (2021). <https://doi.org/10.1039/D0NR07025D>
6. H.-C. Lin, Z. Wang, C.W. Hsu, Fast multi-source nanophotonic simulations using augmented partial factorization. *Nat. Comput. Sci.* **2**(12), 815–822 (2022). <https://doi.org/10.1038/s43588-022-00370-6>
7. J. Jeong, L. Tsang, X. Xu, S.H. Yueh, S.A. Margulis, Full-wave electromagnetic model simulations of P-band radio signal propagation through forest using the fast hybrid method. *IEEE J. Sel. Top. Appl. Earth Obs. Remote Sens.* **16**, 6711–6722 (2023). <https://doi.org/10.1109/JSTARS.2023.3292324>
8. M. Kouroublikis, N.L. Tsitsas, G. Fikioris, Fundamentals of a null field method-surface equivalence principle approach for scattering by dielectric cylinders. *Eng. Anal. Bound. Elem.* **168**, 105911 (2024). <https://doi.org/10.1016/j.enganabound.2024.105911>
9. V. Ranjbar, R. Beerten, M. Moonen, S. Pollin, Cell-free massive MIMO with sequential Fronthaul architecture and limited memory access points. *IEEE Trans. Commun.* **72**, 1–1 (2024). <https://doi.org/10.1109/TCOMM.2024.3422184>
10. N.A. Mortensen, Mesoscopic electrodynamics at metal surfaces:—From quantum-corrected hydrodynamics to microscopic surface-response formalism. *Nanophotonics* **10**(10), 2563–2616 (2021). <https://doi.org/10.1515/nanoph-2021-0156>

11. H. Duan, A.I. Fernández-Domínguez, M. Bosman, S.A. Maier, J.K.W. Yang, Nanoplasmonics: Classical down to the nanometer scale. *Nano Lett.* **12**(3), 1683–1689 (2012). <https://doi.org/10.1021/nl3001309>
12. D.K. Gramotnev, S.I. Bozhevolnyi, Plasmonics beyond the diffraction limit. *Nat. Photonics* **4**(2), Art. no. 2 (2010). <https://doi.org/10.1038/nphoton.2009.282>
13. H.A. Atwater, A. Polman, Plasmonics for improved photovoltaic devices. *Nat. Mater.* **9**(3), 205–213 (2010). <https://doi.org/10.1038/nmat2629>
14. E. Cortés, R. Grzeschik, S.A. Maier, S. Schlücker, Experimental characterization techniques for plasmon-assisted chemistry. *Nat. Rev. Chem.* **6**(4), 259–274 (2022). <https://doi.org/10.1038/s41570-022-00368-8>
15. R. Chikkaraddy et al., Single-molecule strong coupling at room temperature in plasmonic nanocavities. *Nature* **535**(7610), 127–130 (2016). <https://doi.org/10.1038/nature17974>
16. M. Kim, J.-H. Lee, J.-M. Nam, Plasmonic photothermal nanoparticles for biomedical applications. *Adv. Sci.* **6**(17), 1900471 (2019). <https://doi.org/10.1002/adv.201900471>
17. G.A.E. Vandenbosch, V. Volski, N. Verellen, V.V. Moshchalkov, On the use of the method of moments in plasmonic applications. *Radio Sci.* **46**(5) (2011). <https://doi.org/10.1029/2010RS004582>
18. T.K. Sarkar, A.R. Djordjevic, B.M. Kolundzija, Method of moments applied to antennas, in *Handbook of Antennas in Wireless Communications*, (CRC Press, 2002)
19. J.B. Lassiter et al., Plasmonic waveguide modes of film-coupled metallic nanocubes. *Nano Lett.* **13**(12), 5866–5872 (2013). <https://doi.org/10.1021/nl402660s>
20. C. Ciraci, Y. Urzhumov, D.R. Smith, Far-field analysis of axially symmetric three-dimensional directional cloaks. *Opt. Express* **21**(8), 9397–9406 (2013). <https://doi.org/10.1364/OE.21.009397>
21. C. Ciraci et al., Probing the ultimate limits of plasmonic enhancement. *Science* **337**(6098), 1072–1074 (2012). <https://doi.org/10.1126/science.1224823>
22. Q. Zhou, W. Li, Z. He, P. Zhang, X.-W. Chen, Quantum hydrodynamic model for noble metal nanoplasmonics. *Phys. Rev. B* **107**(20), 205413 (2023). <https://doi.org/10.1103/PhysRevB.107.205413>
23. M. Martinic, D. Schreurs, T. Markovic, B. Nauwelaers, Model-based frequency adaptive microwave heating for PCR applications. *IEEE J. Electromagn. RF Microw. Med. Biol.*, 1–7 (2024). <https://doi.org/10.1109/JERM.2024.3383225>
24. G.A.E. Vandenbosch, A. Vasylychenko, A practical guide to 3D electromagnetic software tools, in *Microstrip Antennas*, (IntechOpen, 2011). <https://doi.org/10.5772/14756>
25. Y. Bian, Z. Zheng, Y. Liu, J. Liu, J. Zhu, T. Zhou, Hybrid wedge plasmon polariton waveguide with good fabrication-error-tolerance for ultra-deep-subwavelength mode confinement. *Opt. Express* **19**(23), 22417–22422 (2011). <https://doi.org/10.1364/OE.19.022417>
26. W.C. Chew, *Waves and Fields in Inhomogeneous Media* (Wiley-IEEE Press, 1995)
27. J.T. Katsikadelis, The analog equation method: A boundary-only integral equation method for nonlinear static and dynamic problems in general bodies. *Theor. Appl. Mech.* **27**, 13–38 (2002)
28. P.W. Partridge, C.A. Brebbia, L.C. Wrobel, *Dual Reciprocity Boundary Element Method* (Springer Science & Business Media, 2012)
29. J.M. Yuk et al., High-resolution EM of colloidal nanocrystal growth using graphene liquid cells. *Science* **336**(6077), 61–64 (2012). <https://doi.org/10.1126/science.1217654>
30. J.A. Scholl, A. García-Etxarri, A.L. Koh, J.A. Dionne, Observation of quantum tunneling between two plasmonic nanoparticles. *Nano Lett.* **13**(2), 564–569 (2013). <https://doi.org/10.1021/nl304078v>
31. B. Song et al., Probing gap plasmons down to subnanometer scales using collapsible nanofingers. *ACS Nano* **11**(6), 5836–5843 (2017) <https://doi.org/10.1021/acsnano.7b01468>
32. W. Chen et al., Probing the limits of plasmonic enhancement using a two-dimensional atomic crystal probe. *Light Sci. Appl.* **7**(1), Art. no. 1 (2018). <https://doi.org/10.1038/s41377-018-0056-3>
33. A. Liebsch, *Electronic Excitations at Metal Surfaces* (Springer Science & Business Media, New York, 1997)

34. F.J. García de Abajo, J. Aizpurua, Numerical simulation of electron energy loss near inhomogeneous dielectrics. *Phys. Rev. B* **56**(24), 15873–15884 (1997). <https://doi.org/10.1103/PhysRevB.56.15873>
35. F.J. García de Abajo, A. Howie, Relativistic electron energy loss and electron-induced photon emission in inhomogeneous dielectrics. *Phys. Rev. Lett.* **80**(23), 5180–5183 (1998). <https://doi.org/10.1103/PhysRevLett.80.5180>
36. F.J. García de Abajo, A. Howie, Retarded field calculation of electron energy loss in inhomogeneous dielectrics. *Phys. Rev. B* **65**(11), 115418 (2002). <https://doi.org/10.1103/PhysRevB.65.115418>
37. J.-W. Liaw, Simulation of surface plasmon resonance of metallic nanoparticles by the boundary-element method. *JOSA A* **23**(1), 108–116 (2006). <https://doi.org/10.1364/JOSAA.23.000108>
38. I.D. Mayergoyz, Z. Zhang, The computation of extinction cross sections of resonant metallic nanoparticles subject to optical radiation. *IEEE Trans. Magn.* **43**(4), 1681–1684 (2007). <https://doi.org/10.1109/TMAG.2007.892500>
39. J. Jung, T.G. Pedersen, T. Søndergaard, K. Pedersen, A.N. Larsen, B.B. Nielsen, Electrostatic plasmon resonances of metal nanospheres in layered geometries. *Phys. Rev. B* **81**(12), 125413 (2010). <https://doi.org/10.1103/PhysRevB.81.125413>
40. M.T.H. Reid, S.G. Johnson, Efficient computation of power, force, and torque in BEM scattering calculations. *IEEE Trans. Antennas Propag.* **63**(8), 3588–3598 (2015). <https://doi.org/10.1109/TAP.2015.2438393>
41. U. Hohenester, N. Reichelt, G. Unger, Nanophotonic resonance modes with the nanobem toolbox. *Comput. Phys. Commun.* **276**, 108337 (2022). <https://doi.org/10.1016/j.cpc.2022.108337>
42. P.E. Stamatopoulou et al., Electron beams traversing spherical nanoparticles: Analytic and numerical treatment. *Phys. Rev. Res.* **6**(1), 013239 (2024). <https://doi.org/10.1103/PhysRevResearch.6.013239>
43. U. Hohenester, A. Trügler, MNPBEM—A Matlab toolbox for the simulation of plasmonic nanoparticles. *Comput. Phys. Commun.* **183**(2), 370–381 (2012). <https://doi.org/10.1016/j.cpc.2011.09.009>
44. X. Zheng, M. Kupresak, R. Mittra, G.A.E. Vandenbosch, A boundary integral equation scheme for simulating the nonlocal hydrodynamic response of metallic antennas at deep-nanometer scales. *IEEE Trans. Antennas Propag.* **66**(9), 4759–4771 (2018). <https://doi.org/10.1109/TAP.2018.2851290>
45. X. Zheng, M. Kupresak, V.V. Moshchalkov, R. Mittra, G.A. Vandenbosch, A potential-based formalism for modeling local and hydrodynamic nonlocal responses from plasmonic waveguides. *IEEE Trans. Antennas Propag.* **67**(6), 3948–3960 (2019)
46. X. Zheng, Dedicated boundary element modeling for nanoparticle-on-Mirror structures incorporating nonlocal hydrodynamic effects. *Adv. Theory Simul.* **5**(12), 2200480 (2022). <https://doi.org/10.1002/adts.202200480>
47. X. Zheng, C. Mystilidis, A. Xomalis, G.A.E. Vandenbosch, A boundary integral equation formalism for modeling multiple scattering of light from 3D nanoparticles incorporating nonlocal effects. *Adv. Theory Simul.* **5**(12), 2200485 (2022). <https://doi.org/10.1002/adts.202200485>
48. C. Mystilidis, X. Zheng, A. Xomalis, G.A.E. Vandenbosch, A potential-based boundary element implementation for modeling multiple scattering from local and nonlocal plasmonic nanowires. *Adv. Theory Simul.* **6**(3), 2200722 (2023). <https://doi.org/10.1002/adts.202200722>
49. W.C. Chew, A.Y. Liu, C. Salazar-Lazaro, W.E.I. Sha, Quantum electromagnetics: A new look—Part I. *IEEE J. Multiscale Multiphysics Comput. Tech.* **1**, 73–84 (2016). <https://doi.org/10.1109/JMMCT.2016.2617018>
50. W.C. Chew, A.Y. Liu, C. Salazar-Lazaro, W.E.I. Sha, Quantum electromagnetics: A new look—Part II. *IEEE J. Multiscale Multiphysics Comput. Tech.* **1**, 85–97 (2016). <https://doi.org/10.1109/JMMCT.2016.2614800>
51. D.I. Kaklamani, H.T. Anastassiou, Aspects of the method of auxiliary sources (MAS) in computational electromagnetics. *IEEE Antennas Propag. Mag.* **44**(3), 48–64 (2002). <https://doi.org/10.1109/MAP.2002.1028734>

52. D. Wilton, S. Rao, A. Glisson, D. Schaubert, O. Al-Bundak, C. Butler, Potential integrals for uniform and linear source distributions on polygonal and polyhedral domains. *IEEE Trans. Antennas Propag.* **32**(3), 276–281 (1984). <https://doi.org/10.1109/TAP.1984.1143304>
53. R. Graglia, Static and dynamic potential integrals for linearly varying source distributions in two- and three-dimensional problems. *IEEE Trans. Antennas Propag.* **35**(6), 662–669 (1987). <https://doi.org/10.1109/TAP.1987.1144160>
54. R.D. Graglia, On the numerical integration of the linear shape functions times the 3-D Green's function or its gradient on a plane triangle. *IEEE Trans. Antennas Propag.* **41**(10), 1448–1455 (1993). <https://doi.org/10.1109/8.247786>
55. P. Yla-Oijala, M. Taskinen, Calculation of CFIE impedance matrix elements with RWG and n/spl times/RWG functions. *IEEE Trans. Antennas Propag.* **51**(8), 1837–1846 (2003). <https://doi.org/10.1109/TAP.2003.814745>
56. A.R. Melnyk, M.J. Harrison, Resonant excitation of plasmons in thin films by electromagnetic waves. *Phys. Rev. Lett.* **21**(2), 85–88 (1968). <https://doi.org/10.1103/PhysRevLett.21.85>
57. R. Ruppin, Optical properties of a plasma sphere. *Phys. Rev. Lett.* **31**(24), 1434–1437 (1973). <https://doi.org/10.1103/PhysRevLett.31.1434>
58. F. Forstmann, H. Stenschke, Electrodynamics at metal boundaries with inclusion of plasma waves. *Phys. Rev. Lett.* **38**(23), 1365–1368 (1977). <https://doi.org/10.1103/PhysRevLett.38.1365>
59. A.D. Boardman, B.V. Paranjape, The optical surface modes of metal spheres. *J. Phys. F Met. Phys.* **7**(9), 1935 (1977). <https://doi.org/10.1088/0305-4608/7/9/036>
60. B.B. Dasgupta, R. Fuchs, Polarizability of a small sphere including nonlocal effects. *Phys. Rev. B* **24**(2), 554–561 (1981). <https://doi.org/10.1103/PhysRevB.24.554>
61. C. David, F.J. García de Abajo, Spatial nonlocality in the optical response of metal nanoparticles. *J. Phys. Chem. C* **115**(40), 19470–19475 (2011). <https://doi.org/10.1021/jp204261u>
62. S. Raza, G. Toscano, A.-P. Jauho, M. Wubs, N.A. Mortensen, Unusual resonances in nanoplasmonic structures due to nonlocal response. *Phys. Rev. B* **84**(12), 121412 (2011). <https://doi.org/10.1103/PhysRevB.84.121412>
63. A.I. Fernández-Domínguez, A. Wiener, F.J. García-Vidal, S.A. Maier, J.B. Pendry, Transformation-optics description of nonlocal effects in plasmonic nanostructures. *Phys. Rev. Lett.* **108**(10), 106802 (2012). <https://doi.org/10.1103/PhysRevLett.108.106802>
64. D. Yoo et al., Modeling and observation of mid-infrared nonlocality in effective epsilon-near-zero ultranarrow coaxial apertures. *Nat. Commun.* **10**(1), 4476 (2019). <https://doi.org/10.1038/s41467-019-12038-3>
65. M.K. Svendsen, C. Wolff, A.-P. Jauho, N.A. Mortensen, C. Tserkezis, Role of diffusive surface scattering in nonlocal plasmonics. *J. Phys. Condens. Matter* **32**(39), 395702 (2020). <https://doi.org/10.1088/1361-648X/ab977d>
66. S. Boroviks et al., Extremely confined gap plasmon modes: When nonlocality matters. *Nat. Commun.* **13**(1), Art. no. 1 (2022). <https://doi.org/10.1038/s41467-022-30737-2>
67. M.H. Eriksen, C. Tserkezis, N.A. Mortensen, J.D. Cox, Nonlocal effects in plasmon-emitter interactions. *Nanophotonics* **13**(15), 2741–2751 (2024). <https://doi.org/10.1515/nanoph-2023-0575>
68. C. Ciraci, J.B. Pendry, D.R. Smith, Hydrodynamic model for plasmonics: A macroscopic approach to a microscopic problem. *ChemPhysChem* **14**(6), 1109–1116 (2013). <https://doi.org/10.1002/cphc.201200992>
69. S. Raza, S.I. Bozhevolnyi, M. Wubs, N.A. Mortensen, Nonlocal optical response in metallic nanostructures. *J. Phys. Condens. Matter* **27**(18), 183204 (2015). <https://doi.org/10.1088/0953-8984/27/18/183204>
70. P.B. Johnson, R.W. Christy, Optical constants of the noble metals. *Phys. Rev. B* **6**(12), 4370–4379 (1972). <https://doi.org/10.1103/PhysRevB.6.4370>
71. R.L. Olmon et al., Optical dielectric function of gold. *Phys. Rev. B* **86**(23), 235147 (2012). <https://doi.org/10.1103/PhysRevB.86.235147>

72. A.D. Rakić, A.B. Djurišić, J.M. Elazar, M.L. Majewski, Optical properties of metallic films for vertical-cavity optoelectronic devices. *Appl. Opt.* **37**(22), 5271–5283 (1998). <https://doi.org/10.1364/AO.37.005271>
73. P.G. Etchegoin, E.C. Le Ru, M. Meyer, An analytic model for the optical properties of gold. *J. Chem. Phys.* **125**(16), 164705 (2006). <https://doi.org/10.1063/1.2360270>
74. J. Benedicto, R. Pollès, C. Ciraci, E. Centeno, D.R. Smith, A. Moreau, Numerical tool to take nonlocal effects into account in metallo-dielectric multilayers. *JOSA A* **32**(8), 1581–1588 (2015). <https://doi.org/10.1364/JOSAA.32.001581>
75. T. Dong, Y. Shi, H. Liu, F. Chen, X. Ma, R. Mittra, Investigation on plasmonic responses in multilayered nanospheres including asymmetry and spatial nonlocal effects. *J. Phys. Appl. Phys.* **50**(49), 495302 (2017). <https://doi.org/10.1088/1361-6463/aa9257>
76. C. Mystilidis, X. Zheng, G.A.E. Vandenbosch, OpenSANS: A semi-analytical solver for nonlocal plasmonicS. *Comput. Phys. Commun.* **284**, 108609 (2023). <https://doi.org/10.1016/j.cpc.2022.108609>
77. S. Raza et al., Blueshift of the surface plasmon resonance in silver nanoparticles studied with EELS. *Nanophotonics* **2**(2), 131–138 (2013). <https://doi.org/10.1515/nanoph-2012-0032>
78. S. Raza, W. Yan, N. Stenger, M. Wubs, N.A. Mortensen, Blueshift of the surface plasmon resonance in silver nanoparticles: Substrate effects. *Opt. Express* **21**(22), 27344–27355 (2013). <https://doi.org/10.1364/OE.21.027344>
79. D. Doyle et al., Tunable subnanometer gap plasmonic metasurfaces. *ACS Photonics* **5**(3), 1012–1018 (2018). <https://doi.org/10.1021/acsphotonics.7b01314>
80. I. Lindau, P.O. Nilsson, Experimental verification of optically excited longitudinal plasmons. *Phys. Scr.* **3**(2), 87 (1971). <https://doi.org/10.1088/0031-8949/3/2/007>
81. F. Forstmann, R.G. Gerhardt, *Metal Optics Near the Plasma Frequency* (Springer, Berlin, 1986)
82. L. Stella, P. Zhang, F.J. García-Vidal, A. Rubio, P. García-González, Performance of nonlocal optics when applied to plasmonic nanostructures. *J. Phys. Chem. C* **117**(17), 8941–8949 (2013). <https://doi.org/10.1021/jp401887y>
83. T.V. Teperik, P. Nordlander, J. Aizpurua, A.G. Borisov, Robust subnanometric plasmon ruler by rescaling of the nonlocal optical response. *Phys. Rev. Lett.* **110**(26), 263901 (2013). <https://doi.org/10.1103/PhysRevLett.110.263901>
84. T. Christensen, W. Yan, S. Raza, A.-P. Jauho, N.A. Mortensen, M. Wubs, Nonlocal response of metallic nanospheres probed by light, electrons, and atoms. *ACS Nano* **8**(2), 1745–1758 (2014). <https://doi.org/10.1021/nn406153k>
85. W. Yan, N.A. Mortensen, M. Wubs, Green's function surface-integral method for nonlocal response of plasmonic nanowires in arbitrary dielectric environments. *Phys. Rev. B* **88**(15), 155414 (2013). <https://doi.org/10.1103/PhysRevB.88.155414>
86. M. Kupresak, X. Zheng, G.A.E. Vandenbosch, V.V. Moshchalkov, Comparison of hydrodynamic models for the electromagnetic nonlocal response of nanoparticles. *Adv. Theory Simul.* **1**(12), 1800076 (2018). <https://doi.org/10.1002/adts.201800076>
87. A.R. Melnyk, M.J. Harrison, Theory of optical excitation of plasmons in metals. *Phys. Rev. B* **2**(4), 835–850 (1970). <https://doi.org/10.1103/PhysRevB.2.835>
88. A.D. Boardman, R. Rupp, The boundary conditions between spatially dispersive media. *Surf. Sci.* **112**(1), 153–167 (1981). [https://doi.org/10.1016/0039-6028\(81\)90339-3](https://doi.org/10.1016/0039-6028(81)90339-3)
89. P. Jewsbury, Electrodynamical boundary conditions at metal interfaces. *J. Phys. F Met. Phys.* **11**(1), 195 (1981). <https://doi.org/10.1088/0305-4608/11/1/021>
90. G. Toscano, S. Raza, A.-P. Jauho, N.A. Mortensen, M. Wubs, Modified field enhancement and extinction by plasmonic nanowire dimers due to nonlocal response. *Opt. Express* **20**(4), 4176–4188 (2012). <https://doi.org/10.1364/OE.20.004176>
91. J.D. Jackson, *Classical Electrodynamics*, 2nd edn. (Wiley, 1975)

On a List of Problems for Research in Generalized Lorenz-Mie Theories, More Generally T-Matrix Approach for Structured Beams: The State-of-the-Art



G rard Gouesbet

1 Introduction

The generalized Lorenz-Mie theory (GLMT), *stricto sensu*, describes the interaction between an incident structured electromagnetic beam (specifically a laser beam) and a homogeneous spherical particle, therefore generalizing the classical Mie theory dated 1908 [1, 2] devoted to the case of plane wave illumination to the case when the particle is illuminated by a laser, e.g., [3, 4] and references therein dating back to 1982 [5]. The expression “generalized Lorenz-Mie theory” is used more generally to deal with the interaction of laser beams with particles having a sufficient degree of symmetry to allow the use of the method of separation of variables to deal with Maxwell’s equations, namely, multilayered spheres [6, 7], cylinders with circular and elliptical cross-sections [8–11], assemblies of spheres and aggregates [12], spheres incorporating an eccentrically located spherical inclusion [13, 14], and spheroids [15–17], to quote a few papers devoted to these different particles, see as well references therein. An entry for more complete references to these different opportunities is available from a textbook [18], and from review papers such as [19–21], and references therein, with the consequence that GLMT may be used with the plural GLMTs.

While the GLMTs are rigorous analytical theories, there exist another approach most often named the Extended Boundary Condition Method (EBCM), but which can as well be called the Null-Field Method [22], usually denoted as a semi-analytical method, and which can deal with symmetrical particles allowing one to use the method of separation of variables, but which can deal as well with other

G. Gouesbet (✉)

Institut National des Sciences Appliqu es de Rouen, Rouen, France

e-mail: gouesbet@coria.fret

kinds of less symmetrical particles [23, 24], although it can become ill-conditioned for the case of highly elongated or flattened particles [22–27].

Both GLMTs and EBCM have a common point, namely, that the incident beam is expanded in terms of vector spherical functions, more particularly in terms of Vector Spherical Wave Functions (VSWFs) in the case of spherical coordinates. Moreover, “EBCM” is very often taken as synonymous of “T-matrix method.” As discussed by several authors, such as Doicu et al. [22], Bates and Wall [28], Hackman and Lim [29], Doicu and Wriedt [30], Nieminen et al. [27, 31], Zakharova et al. [32], Alonso et al. [33], with a somewhat extended discussion in the introduction of [20], this identification, although traditional, may be misleading. Indeed, it happens, for instance, that the GLMT as well is a T-matrix method, e.g., [34, 35], a feature which may provide a better understanding of the title of the present paper, see as well pages 266–268 in [18].

Now, it happens that, in 2012, the Optical Society of America celebrated the 50th anniversary of *Applied Optics*, and then provided an open access to the 50 most cited *Applied Optics* articles of all time, a listing of the 50 most published authors in *Applied Optics* of all time, and published three special issues to end its retrospective of *Applied Optics*’ 50 years. Gouesbet and Lock, pertaining to the Top-50 list of the most-published authors, have then been invited to prepare an article, which has been published in 2013 [36]. This article, with 230 references, discussed 35 problems for future research in GLMTs (and EBCM). After more than a decade, the present chapter discusses these problems, some having been solved while others have not been solved or have not been considered, therefore providing the state-of-the-art of the current situation. New problems are discussed as well. It is to be noted that, while the original paper was signed by two authors, the present one is signed by one author only, the reason why being available, which much regret, from [37].

2 Old Problems

2.1 Problem 1

See subsection 2.B of [36]. In GLMTs and EBCM, the incident fields are expanded over a set of basis functions, namely, VSWFs when spherical coordinates are used. These expansions are defined by coefficients named beam shape coefficients (BSCs), which encode the structure of the beam. In spherical coordinates, these BSCs are denoted $g_{n, TM}^m$ and $g_{n, TE}^m$ in which *TM* stands for “Transverse Magnetic,” *TE* stands for “Transverse Electric,” *n* ranges from 1 to infinity, and *m* from (−*n*) to (+*n*).

We may distinguish two different methods, namely, intrinsic and extrinsic methods, to evaluate the BSCs, as follows: “Intrinsic methods evaluate BSCs of a GLMT posed in a certain coordinate system in terms of quantities pertaining to the same coordinate system. Conversely, extrinsic methods evaluate BSCs of a GLMT

posed in a certain coordinate system in terms of BSCs in a different coordinate system.”

To illustrate these definitions, let us mention that the GLMT *stricto sensu*, i.e., for a homogeneous sphere, used an intrinsic method. Conversely, the GLMT for spheroids used an extrinsic method in which the BSCs in spheroidal coordinates are expressed in terms of the BSCs in spherical coordinates, e.g., [15] and references therein dating back to 2001 [38, 39] and 2002 [40, 41]. In such a context, Problem 1 was defined as: “Develop a general theory of coordinate transformations for extrinsic evaluations of beam shape coefficients,” i.e., express BSCs in a certain coordinate system in terms of BSCs in another coordinate system.

This problem, in its generality, was certainly too ambitious. However, many uses of an extrinsic method have been reviewed in [19–21]. To provide a few examples, besides the use of the extrinsic method to deal with the scattering by spheroidal particles, such a method has been used as well to deal with the scattering by cylinders [42, 43], by spherical particles with a spheroidal inclusion at the center [44], to the study of reflection and transmission of beams by a slab [45], and to the scattering of a particle above a plane surface [46]. A review on intrinsic and extrinsic methods is available from the introduction of [47], together with a discussion of the extrinsic method relating spherical and spheroidal coordinates. Also, the evaluation of spheroidal BSCs using either intrinsic or extrinsic methods is discussed in [48].

2.2 Problem 2

See section 3 of [36]. As a consequence of the use of extrinsic methods to deal with the scattering by spheroidal particles, Problem 2 was defined as: “Develop an intrinsic method for evaluating beam shape coefficients in spheroidal coordinates.” A first solution to this problem has been provided in [49], in the general case of an off-axis formulation. The solution is much more complicated than in the case of spherical coordinates for two reasons (i) vector spheroidal wave functions to be used are more complicated to handle than vector spherical wave functions and (ii) both Transverse Magnetic (TM) and Transverse Electric (TE) coefficients occur in spheroidal radial field components in contrast with the fact that, in spherical coordinates, only TM-coefficients occur in the expanded description of the radial electric field component and TE coefficients occur in the expanded description of the magnetic field component (see Chapter 3 in [18]), as a result of the fact that the Bromwich method, which can be used to build the GLMT in spherical coordinates, cannot be used to build the GLMT in spheroidal coordinates [50]. As a consequence of these new difficulties, the solution to the intrinsic BSCs has been found under the form of an infinite number of equations and an infinite number of unknowns, which might be solved by studying a series of successive approximations. The numerical implementation of such an algorithm has not been achieved.

In view of the difficulties associated above with the off-axis case, a subsequent paper restricted the ambition to the study of an intrinsic method for the evaluation

of spheroidal BSCs in the case of an on-axis standard configuration [51] and has been able to provide numerical results for the fifth-order Gaussian Davis beams [52], for plane waves taken as a limit of fifth-order Gaussian Davis beams when the beam waist radius tends to infinity, and for a Gaussian beam described by using a localized approximation (localized approximations will be discussed below), with comparisons between spheroidal BSCs obtained using either the intrinsic or the extrinsic techniques. The on-axis standard configuration corresponds, in the language of the theory of transformations of BSCs through rotations of coordinate systems [53], to Euler angles equal to 0, e.g., section 6 in [54]. For an application to the case of the scattering of a zeroth-order Bessel beam by spheroid, the reader may refer to [55].

The case of oblique illumination has afterward been considered in [56]. Numerical results are provided for plane waves and Gaussian beams, with an agreement between the extrinsic and intrinsic methods. It would remain to return to the general off-axis case such as depicted, e.g., in [49] or possibly by starting from the on-axis case and using addition theorems in spheroidal coordinates.

2.3 Problem 3

See subsection 4.A of [36]. This problem and others below are related to what is called a localized approximation. It happens that several methods can be used to evaluate BSCs, namely, quadratures [57, 58], finite series [59–61], localized approximations (to be discussed below), and the angular spectrum decomposition (ASD), or angular spectrum representation (ASR) [62, 63] with a review in [64], see as well references therein.

Among these methods, the most popular has been the localized approximation (with variants) due to its flexibility, its easy implementation, and its computing time efficiency. For a review sufficient to the purpose of the present subsection, the reader may refer to [65]. We now define the on-axis and off-axis cases by referring to a scattering problem in which a spherical scatterer is illuminated by a beam with an axis of symmetry. For an on-axis beam, the center of the target particle is located on the beam's symmetry axis, while it is transversely displaced from the symmetry axis for an off-axis beam.

There is a special on-axis case when the center of the beam waist of a Gaussian beam is located at the center of the scattering sphere, let us call it the waist-center case. Then, the phase fronts are locally plane and we may rely on the van de Hulst principle of localization [66], which has been originally used and published in 1986 to design what has then be called a localized approximation, for a Gaussian beam in the waist-center case [67]. Generalizations have been made for more general on-axis incidence and for off-axis incidence, furthermore justified without having to rely any more on the van de Hulst principle of localization [68, 69]. More generally, the case of arbitrary-shaped beams has been considered and a general localized

approximation has been established, including the off-axis case, without having to rely on the van de Hulst principle of localization [70].

When dealing with BSCs for a general on-axis beam and for an off-axis beam, we then have two possibilities (i) use a localized approximation, which has been used without using the van de Hulst principle of localization or (ii) use this principle to deal with the waist-center case and deduce the BSCs so obtained to derive the BSCs in more general situations by using translational addition theorems [71–73]. Therefore, strategy (ii) shows that the van de Hulst principle may be used in the most general configurations, although it becomes hidden when we depart from the waist-center case with strategy (i). Hence Problem 3: “Examine how the localized interpretation propagates through the mathematics using translation addition theorems,” or under another formulation: “Track the localized interpretation throughout the use of the translational addition theorems, and reveal what is hidden.” This was stated as being expectably a difficult problem, and has not been worked out.

2.4 Problem 4

See subsection 4.B of [36]. At the time when the list of problems was published, we possessed several versions of the localized approximation in spherical coordinates, namely (i) an original localized approximation obtained by using the van de Hulst principle of localization and justified by empirical tests [74], (ii) a modified localized approximation for Gaussian beams deduced from a rigorous justification for Gaussian beams [68, 69], and (iii) a second modified localized approximation deduced again from a rigorous justification but valid for arbitrary-shaped beams (excluding however beams with axicon angles and/or topological charges) [70], each new variant proposing an improvement with respect to the previous one. Localized BSCs are obtained using a procedure involving a prefactor ($i/L^{1/2}$), whatever the harmonic time dependence used, i.e., either of the form $\exp(+i\omega t)$ or $\exp(-i\omega t)$ [75]. The quantity L reads as:

$$L = (n - m)(n + m + 1) \quad (1)$$

for the modified localized approximation and:

$$L = (n - |m|)(n + |m| + 1) \quad (2)$$

for the second modified localized approximation. Therefore, if $n = m$ or $n = |m|$ for the modified localized approximation and for the second modified localized approximation, respectively, then the localized BSCs diverge. In [36], remedies to this situation were discussed but it was stated that, nevertheless, it was a loose end that should be cleaned up. Hence, Problem 4 stated: “Complement the second modified localized approximation.” This problem is solved in [76].

2.5 Problem 5

See subsection 4.C in [36]. Localized approximations in spherical coordinates having been very popular and efficient, it was desirable to possess as well localized approximations in spheroidal coordinates, hence Problem 5: “Design an intrinsic localized approximation in spheroidal coordinates.” The extrinsic method already allowed one to implement a localized approximation in spheroidal coordinates because, once the spheroidal BSCs are obtained in terms of the spherical BSCs, it is possible to evaluate these spherical BSCs using a localized approximation, so that the spheroidal BSCs as well are expressed in terms of a localized approximation. But this is an indirect extrinsic procedure. It is expected that a direct intrinsic procedure would be more efficient. The design of intrinsic procedures to evaluate spheroidal procedures (Problem 2 above) was believed to be a necessary step to the design of intrinsic spheroidal localized approximations. Problem 5 is however still an open problem even if Problem 2 already received solutions.

2.6 Problem 6

See subsection 4.D in [36]. Assume that we possess spherical BSCs $g_{n,X}^m$ ($X = \text{TM}$ or TE) by referring, for instance, to the second modified localized approximation. The derivation of the justification of this localized approximation in [70] was however not valid for arbitrary orientation of the illuminating beam but for a specific orientation (non-oblique) called the standard orientation. If we want to obtain localized BSCs for oblique orientation, we must then use a two-step procedure in which (i) we first design a localized approximation for the standard orientation and then (ii) derive the localized BSCs for oblique orientation by applying an operator on the localized BSCs for standard orientation, e.g., [53]. In other words, we first localize and afterward rotate. Alternatively, we might rotate first and localize after. However, these two different procedures do not yield to the same result because localization and rotation are transformations that do not commute [77]. Let us note that these two procedures—which localize first and rotate, or rotate first and localize—are both two-step procedures. Hence Problem 6: “Design a one-step procedure for a localized approximation in spherical coordinates for arbitrary-shaped beams having an arbitrary orientation.” This problem is still open.

2.7 Problem 7

See subsection 4.E in [36]. There exists a variant of localized approximation named integral localized approximation (ILA), which may be viewed as a hybrid method using both a single quadrature and a localization procedure [78]. It is fair to

state that, among the different variants of localization procedure that have been developed, this one is likely the most popular. It exhibits good properties of speed, flexibility, and stability. Although it uses a quadrature, it has been observed that, in some cases, the ILA may be much less time consuming than nonintegral localized approximations. But the ILA has been introduced using the original localization procedure, rather than the modified variants, hence Problem 7: “Revisit the integral localized approximation to implement modified localized approximations.”

2.8 Problem 8

See subsection 4.F of [36]. The rigorous justification of the second modified localized approximation relies on what can be called an N -beam procedure [70] in which an N -beam is defined by relying on the following expansion of the electric field reading as:

$$E_i = E_0 \exp(-iZ) \sum_{p=0}^{\infty} \sum_{q=0}^{\infty} \sum_{l=0}^{\infty} E_{pql}^i X^p Y^q Z^l \quad (3)$$

in which X , Y , Z are rescaled Cartesian coordinates. An N -beam is then obtained from Eq. 3 by a truncation in which all terms for $(p + q + l) > N$ are set to 0. It is then found that the BSCs obtained from the second modified localized approximation is exactly equal to rigorous BSCs obtained from quadratures for N small enough, hence the justification of the word “approximation” since this agreement is no more observed for higher-order N -beams. It was then suggested to deal with the Taylor expansions of actual beams to see how the localized BSCs of N -beams obtained from these actual beams compare with the rigorous BSCs of these N -beams obtained by quadratures, leading to Problem 8 expressed as: “Examine the behavior of localized approximations for Maxwellian beams,” with a subproblem to possibly have a better understanding of the reason why the first terms of the Taylor series are sufficient to design a localized approximation.

For this problem, it is important to deal with Maxwellian beams, i.e., beams whose description exactly satisfies Maxwell’s equations. This excludes, for instance, the case of Gaussian beams described by the Davis scheme of approximations, which is not Maxwellian [79, 80], Bessel-Gauss beams [81], or Laguerre-Gauss beams freely propagating [82–86]. For examples of Maxwellian beams, [36] referred to papers by Neves et al. [87, 88], and Moreira et al. [89]. Other examples of Maxwellian beams are Bessel beams [90, 91], and subsection 4.1 in [92], Lommel beams [93], Laguerre-Gauss beams focused by a lens, e.g., [61] and references therein, and frozen waves, e.g., [94, 95] and references therein.

2.9 Problem 9

See subsection 4.G. in [36]. This subsection deals with top-hat beams, which has been used for optical sizing [96–98]. It has been found interesting to examine whether the localized approximation technique could correctly reconstruct such kinds of beams in the GLMT framework. Using a modified localization procedure, it is found that a reasonable reconstruction could be achieved, but for large amplitude oscillations at the location of the top-hat sharp cutoffs when the field intensities jump from the top-hat level down to 0 [99]. The question is to know whether the use of the second modified localized approximation could help to decrease the amplitude of these oscillations, hence Problem 9: “Implement the second modified localized approximation for modeling top-hat beams.”

2.10 Problem 10

See subsection 4.G. and 4.H. in [36]. Problem 9 could be completed if we found a way to improve the second modified localization procedure to a third localization procedure. It has been observed that, when applied to Gaussian beams, the quality of the localization procedures decreases when the focusing of the beam increases. This may be understood by considering the plane wave spectrum of the beam, which is a second way, besides the use of BSCs, to deal with the description of a laser beam. Although inefficient when it has to be used numerically, e.g., pages 52–54 of [18, 64, 100], it is efficient when it can be handled analytically, e.g., [62] and references therein.

Furthermore, it has the conceptual advantage to easily explain a few important features such as the failure of the optical theorem, e.g., [101] or the fact that the speed of a laser light is smaller than the speed of light, even in vacuum [102]. Another feature, relevant to the present subsection, is that the plane wave spectrum is made of plane waves, which are more or less tilted with respect to the direction of propagation. Now, the more a beam is focused, the more the quantity of tilted waves in the spectrum. It has then been independently demonstrated that, when the tilt of a plane wave increases, the efficiency of a localization procedure applied to this plane wave decreases [77, 103].

Therefore, to solve Problem 10, namely, “Design improved localized approximations,” the theory of transformations discussed in [77, 103], and references therein, might provide an entry, the issue being to examine whether we may build a new localized approximation, which would commute with rotation (see Problem 6) and improve the quality of the localized treatment of tilted waves.

2.11 Problems 11 and 12

See subsection 4.H.1 in [36]. One way to deal with the plane wave spectrum approach requires to use a two-step process, (i) make the angular spectrum decomposition in terms of plane waves and (ii) carry out a partial wave expansion of each plane wave, followed by a summation of plane wave partial wave expansions to obtain the partial wave expansion (and the BSCs) of the whole wave. GLMT however may be viewed as a one-step process in which the expansion of the whole wave is directly obtained thanks to the use of BSCs. Problem 11 was then: “Assess the relative convenience or inconvenience of a two-step process for determining the BSCs relative to a one-step process.” Since the enunciation of this problem, many uses of the ASD to evaluate BSCs have been published, see again [62, 63], and references therein, and also many papers that may easily be reached by using keywords (such as ASD, or “angular”) in [20, 21]. This makes Problem 11 solved (or obsolete). The same is true for Problem 12: “Study computational issues related to the plane wave spectrum approach.”

2.12 Problems 13 and 14

See subsection 4.H.2 in [36]. Problem 13 was “Implement a localized approximation in the EBCM” while Problem 14 “Extend the EBCM to arbitrary-shaped beams with the use of beam shape coefficients.” The origin of these problems is that EBCM has been mainly used for plane wave illumination, or possibly using an ASD in early ages, see a review in [34]. However, the use of EBCM using BSCs was lacking. Insofar as both GLMT and EBCM describe the incident fields using VSWFs, Problem 14 was expected to be fairly easy. Furthermore, Problem 13 may be viewed as a subproblem of Problem 14 in which BSCs used in EBCM would be expressed in terms of a localized approximation.

Indeed, several papers using EBCM to describe the interaction of laser beams with particles, in which the expansion over VSWFs were expressed using BSCs, have been published since then. What I believe to be a fairly exhaustive list of papers dealing with EBCM and BSCs is as follows: (i) Mackowski and Mischenko dealt with discrete random media illuminated by on-axis Gaussian beams with BSCs evaluated using a localized approximation [104], (ii) Chen et al. dealt with uniaxial anisotropic objects illuminated by on-axis Gaussian beams [105], (iii) Wang et al. dealt with optically anisotropic particles illuminated by a Gaussian beam [106], (iv) and (v) Zheng et al. dealt with arbitrary chiral objects illuminated by on-axis Gaussian beams, viewing the method used as a combination of EBCM and GLMT, or with objects with a chiral inclusion [107, 108], to be complemented by subsections 9.4 in [19], 8.1 in [20], and 11.1 in [21].

2.13 Problems 15 and 16

See subsection 4.H.3 in [36]. Descriptions of electromagnetic beams may be Maxwellian or non-Maxwellian, i.e., they exactly satisfy or not Maxwell's equations, see Problem 8 above. In both cases, we may evaluate BSCs. The fields obtained with the aid of these BSCs generate a beam that exactly satisfies Maxwell's equations. For a Maxwellian beam, the beam reconstructed using the BSCs identifies with the original beam. Conversely, for a non-Maxwellian beam, we obtain a conversion from the non-Maxwellian beam to a Maxwellian beam. This process is named a beam remodeling, hence Problem 15: "Examine the angular process of the angular spectrum representation" and Problem 16: "Examine the angular process of the angular spectrum representation for the particular case of a Gaussian beam." We have several examples of discussions of beam remodeling using the other methods (quadratures, finite series, localized approximations), e.g., [81, 85] and more specifically [68, 69], for Gaussian beams. Problems 15 and 16 would actually ask for the examination of similar examples when using the angular spectrum representation. In view of the extensive literature published since then related to the use of ASD in GLMT, and comparisons with different approaches, e.g., references in Problems 11 and 12, we may consider that Problems 15 and 16 are obsolete.

2.14 Problem 17

See subsection 4.H.3 in [36]. Let us consider a beam propagating in the z -direction and its formulation with respect to x and y in the focal plane $z = 0$, and assume that we have an expression for the fields in this focal plane. We may then determine spectral components from these fields using a Fourier transform. Thereafter, because the fields satisfy Helmholtz equation, we can determine the fields in whole space, see Goodman [109] and a detailed discussion page 3 of [102], from Eq. (8) to Eq. (10). We may therefore safely focus on the description of the beam in the focal plane. This description may be non-Maxwellian or Maxwellian, hence Problem 17: "Discuss profiles of non-Maxwellian beams in the focal plane, and draw consequences". An entry for this problem might be to examine the descriptions of various beams, either non-Maxwellian or Maxwellian, in the focal plane, to possibly generate a first intuition "to the solution likely relevant to the remodelling issue of non-Maxwellian beams".

2.15 Problem 18

See subsection 4.H.4 in [36]. To describe a beam in terms of an ASD, we may start from the specification of the electric and magnetic fields in the $z = 0$ plane, see

Problem 17. It is however furthermore necessary to include all boundary conditions the beam is subject to. This was defined as Problem 18: “Study the boundary conditions for the applicability of the angular spectrum method.” Due to problems currently investigated concerning the ASD, and soon available in the literature, this problem may be viewed as obsolete.

2.16 Problem 19

The expressions to evaluate BSCs using double quadratures [57] contain a r -dependent prefactor, e.g., Eqs. (3.13) and (3.20) in [18]. For instance, the expression for the TM -coefficients reads as:

$$g_{n,TM}^m = f(n, m) \frac{r}{j_n(kr)} \int_0^\pi \int_0^{2\pi} E_r P_n^{ImI}(\cos \theta) \exp(-im\varphi) \sin \theta d\theta d\varphi \quad (4)$$

in which $f(n, m)$ is a function which is irrelevant in the context of the present paper, (r, θ, φ) are spherical coordinates, $j_n(kr)$ in which k is a wavenumber denotes spherical Bessel functions of the first kind, P_n^{ImI} are associated Legendre functions, and E_r is the radial component of the electric field. Since BSCs are complex numbers, the double quadrature must be proportional to $j_n(kr)/r$ in order to eliminate the r -dependent prefactor. This is demonstrated in particular by Neves et al. in two papers already quoted [87–88]. However, the demonstration in these papers assume that all plane waves used in the proof are oscillatory, without containing any evanescent wave.

But tightly focused beams may contain evanescent components. It is then interesting to examine how the contributions of these evanescent waves allow one to cancel the prefactors occurring in the quadrature expressions of the BSCs. This defines Problem 19: “Examine the prefactor cancellation process for evanescent components of the angular spectrum method,” which could be better reworded with a more general formulation as: “Examine the prefactor cancellation process for evanescent components.”

2.17 Problem 20

See subsection 4.I. in [36]. This problem was written as: “Review the literature devoted to the scattering of tightly focused beams” with a literature background provided in the relevant subsection 4.I. The idea was that such a review might serve as a springboard for further developments. Retrospectively, I am not sure any more whether such a review would be useful and I would therefore consider Problem 20 as being obsolete.

2.18 Problem 21

See subsection 4.I. in [36]. The case of tightly focused beams has nevertheless the interest that the quality of the localization procedures decreases when the beam is more focused, as already discussed in Problem 10. It is then of interest to examine how the various variants of localized approximations behave for tightly focused beams, particularly when we approach the theoretical limit where the transverse beam dimension is comparable to the wavelength. As an example Fig. 2 of [69] displayed electric field profiles of off-axis localized Gaussian beams for a wavelength of $0.6328\ \mu\text{m}$ and a beam waist of $1\ \mu\text{m}$, for various off-axis x -locations, exhibiting in particular ghost bumps, which are the consequence of the modified localization procedure used to build these profiles, hence Problem 21 reading as: “Examine the behavior of the original and the second modified localized approximations for tightly focused beams, and compare with similar results already obtained for the modified localized approximation.”

2.19 Problem 22

See subsection 4.I. in [36]. The actual beam in the laboratory may depart from the ideal intended beam, as exemplified in [110, 111]. As a consequence, disagreements between theoretical and experimental results might be interpreted in an erroneous way. Therefore, the possibility of measuring BSCs of actual beams in the laboratory would be welcome. This issue has been considered theoretically in [112–114] and successfully tested experimentally [114]. These studies have however been restricted to the case of on-axis illuminations, hence Problem 22: “Theoretically and experimentally investigate techniques of measurements in the laboratory of the beam shape coefficients of off-axis beams.”

2.20 Problem 23

See section 5 in [36]. After Askin’s work, it has been very common to consider optical forces as the summation of two kinds of forces, namely, gradient forces and scattering forces, see review in [48]. In 2013, a few papers were already published using GLMT to calculate optical forces (and also torques), namely, [115–121], and to use them for levitation experiments [122–124]. However, there was only one paper dealing with the decomposition of optical forces in terms of gradient and scattering forces in the GLMT framework [125], nevertheless restricted to Gaussian beams in the weak diffraction limit. Hence Problem 23: “Derive various physically motivated contributions to radiation forces and torques for arbitrary-shaped beams as limiting cases of GLMTs.”

Although this problem has not yet been considered in the case of torques, a thorough analysis of the decomposition of optical forces exerted on spherical particles in a GLMT framework has been considered in the recent years, starting with Rayleigh particles (more generally dipolar particles) [126–136], continuing with small magnetodielectric particles [137, 138], with quadrupoles [139, 140], ending with arbitrary-shaped particles [141], with a review in [142]. One of the many results from this series is that gradient and scattering forces have to be completed by nonstandard forces, which have not been detected by Ashkin due to the fact that GLMT was not yet available at this time. Therefore, as far as optical forces are concerned, Problem 23 is completed.

2.21 Problem 24

See section 5 in [36]. After [125] dealing with Rayleigh particles, it has been *erroneously* stated that “it would not be fruitful to attempt to derive Rayleigh scattering from a GLMT.” This statement was erroneous because [125] examined a weak confinement limit. Actually, if there is no restriction on the amount of focusing, i.e., without considering the weak confinement limit, papers devoted to Rayleigh scattering in the previous subsection demonstrated the existence of nonstandard forces. Problem 24 has then been listed as a consequence of the erroneous statement as: “Derive Rayleigh-Gans theory, or other similar theories, for arbitrary-shaped beams as limiting cases of GLMTs.” Although motivated by an erroneous statement, Problem 24 is still valid. It has not been worked out.

2.22 Problem 25

See subsection 6.A. in [36]. We may consider ray optics approximations of wave optics and focus on the internal fields inside a particle (forgetting fields leaking outside of the particle), producing what is called a billiard. The simplest case is a billiard corresponding to a spherical particle, leading to what is called a circular billiard. Such a simple billiard only produces periodic and quasiperiodic trajectories. More complicated behaviors, namely, chaotic trajectories, may be produced if we consider more complicated enclosures, such as in the case of asymmetric resonant cavities [143–147].

Such behaviors and prospects were published in 2000 in a review paper [148]. At this time, known microcavities leading to chaotic behavior (asymmetric resonant cavities as above, stadium, ovals), e.g., [149] for an example relying on an analogy between light and quantum mechanical scattering, were not compatible with the use of separable coordinate systems for the associated electromagnetic problem and, therefore, could not be investigated in the framework of any GLMT.

This led to the question to know whether we could find a microcavity which would generate chaotic behaviors, that is to say that would not be integrable in the mechanical sense, and nevertheless could receive an analytical treatment in the framework of a GLMT. The answer is positive by considering a circular disk with one eccentrically located circular inclusion, then generating an annular billiard. From the point of view of GLMT, the corresponding problem is the one of a spherical particle containing a spherical inclusion which, indeed, has been solved including with numerical computations [13, 14, 150, 151]. The point of view of the associated billiard generating Hamiltonian chaos has been examined in [152–154]. However, there has not yet been any effort done to connect these two lines of research, i.e., to search in the electromagnetic distribution of energy inside the particle any fingerprint reminiscent of the Hamiltonian behavior, which, expectably, should play some kind of ray skeleton for the complete field structures. This is Problem 25: “Search for optical chaos in the electromagnetic problem associated with the annular billiard, and in other similar electromagnetic problems.”

2.23 Problem 26

See subsection 6.B. in [36]. Instead of dealing with billiards with trajectories confined inside an enclosure, we may consider Hamiltonian trajectories that come from infinity enter an interaction region, and eventually leave back to infinity. It happens that, in some cases, outgoing trajectories may have very complicated, say chaotic behaviors, depending on the incoming trajectory parameters. Technically, we arrive to the definition of irregular (chaotic) scattering reading as: “A scattering system is chaotic if the deflection function or any other convenient property of the final asymptote [outgoing trajectory] is discontinuous on a fractal subset of its domain, which is the set of all incoming asymptotes [in-coming trajectories]” [155]. Examples of configurations leading to such chaotic behaviors are N -hill potentials where at least three hills are present [156], which is to be contrasted with the case where wells rather than hills are considered, with the fact that two wells are sufficient to generate chaotic scattering [157]. Furthermore, smooth potentials may be deformed to hard-edge potentials, so that associated electromagnetic problems could be associated with the case of assemblies of spheres and aggregates [12, 158]. In particular, the simplest case to be considered would be the one of a three-hard disc scattering problem, corresponding to the electromagnetic problem of the scattering by an assembly of three spheres, as described in [148]. The case of three parallel cylinders under perpendicular illumination would be suitable as well. Similarly, as for the case of Hamiltonian chaos in Problem 25, the case of irregular scattering could be worked out, leading to Problem 26: “Examine irregular (chaotic)scattering in electromagnetic situations.”

2.24 Problem 27

See section 7 in [36]. GLMT may be used in the case of pulsed illumination, as discussed in [159–167], see as well [168–172]. Relying on this literature prior to [36], it was obvious that pulsed lasers offered new possibilities for new experiments and applications, including in the field of optical particle characterization, all these opportunities being gathered under the name of pulsometry, hence Problem 27 reading as: “Theoretical and experimental developments in pulsometry.”

An example was by Bakic et al. [169] dealing with time-integrated detection of femtosecond laser pulses scattered by small droplets, demonstrating that rainbow refractometry is feasible under ultrashort pulse illumination. Since then, many aspects of Problem 27 have been published in the literature, which can be retrieved from section 5 in [19], subsection 3.6 in [20], and subsection 4.8 in [21]. It is therefore possible to state that Problem 27 is basically solved, in the course of an indefinite development.

2.25 Problem 28

See section 7 in [36]. When dealing with the interaction of laser pulses and particles, it has been observed that, inside the particle, the light could be focused to light hot spots traveling faster than light. If the material of the particle is modified by the intensity of the hot spots, it has been suggested that this could lead to the occurrence of quasi-particles traveling faster than the speed of light, and therefore generating Cerenkov radiation, which could possibly be observed outside of the particle [173], hence Problem 28: “Pursue theoretical investigations, to be complemented by experiments, concerning the possibility of Cerenkov radiation generation in the case of ultrashort laser pulse scattering.” This problem may be viewed as a subproblem of Problem 27.

2.26 Problem 29

See section 7 in [36]. Another subproblem of Problem 27 has been motivated by a numerical simulation for two-photon absorption and fluorescence in a spherical microcavity under illumination by two laser pulses [174]. This last paper exemplifies the fact that, although GLMTs describe elastic scattering, they allow to evaluate fields inside the scatterer which, rather being passive, can be viewed as excitation fields for other phenomena, in particular nonelastic phenomena, hence Problem 29: “Develop applications of GLMTs outside of the range of elastic linear phenomena.”

2.27 Problem 30

See subsection 8.A. in [36]. Assume for instance that you deal with a case when two Gaussian beams interfere as in laser-Doppler velocimeters or phase-Doppler instruments. You may use GLMT to predict the behavior of such an instrument, to design it, and to interpret data. One way to deal with this problem using GLMT—the obvious one—is to evaluate the BSCs of each incoming beam, then the behavior of each beam in the instrument, and to superpose these behaviors to obtain the response of the instrument. This approach, by the way, has been the first genuine application of GLMT, particularly concerning phase-Doppler instruments for a fairly long-term adventure, e.g., from 1992 to 2003 [175–187].

Another approach would be to directly evaluate the BSCs of the two illuminating beams taken as a single beam, i.e., we may use a one-step approach (superposition of beams viewed as a single beam in its own right) or a two-step approach (considering separately each incoming beam before superposing the responses from each individual beam).

In Problem 30, each incoming beam possessed the same frequency. Actually, a more general problem has been solved in which each illuminating beam possesses its own frequency, independently from the other beams, leading to a polychromatic GLMT, in which BSCs are replaced by field shape spectra (FSSs) [188, 189]. Problem 30 could then be viewed as a special case of the polychromatic GLMT, although a direct approach using only BSCs could be more illuminating concerning the physics of the problem.

2.28 Problem 31

See subsection 8.B. in [36]. Subsection 8.B. provides a history of the development of GLMTs, from the case of spherical particles, which required about 15 years before being able to deal with genuine applications, specifically in the field of optical particle characterization as discussed in Problem 30, then 5 years for the case of circular cylindrical particles, from a formal paper in 1994 [190] to the publication of numerical results in 1997 and 1999 [8, 9], and only about 3 years for the case of elliptical cylindrical cylinders, e.g., [10, 191–193], with a review in [11]. This short discussion provides a testimony of an acceleration of the production of GLMTs for various kinds of particle shapes (and morphologies), hence Problem 31: “Produce and study other GLMTs.”

This problem has been completed much more efficiently than it was expected. Besides the case of multilayered spheres [6, 7], assemblies of spheres and aggregates [12], spheres with an eccentrically located spherical inclusion [13, 14], and spheroids [15–17], already quoted above, let us mention a few other cases dealing with BSCs: cylinders with coating [42], particles with uniaxial and chiral material [194], particles with negative (metamaterial) refractive index [195], spheroids with

inclusions [196], spherical particles with a spheroidal inclusion at the center [44], spheroids with coatings [197], assemblies of cylindrical particles [198], charged particles [199], layers and slabs [200], particles above a surface [46], cylinders with inclusions [201], particles made from a PEMC material, i.e., man-made metamaterial acting as a perfect reflector of electromagnetic waves [202], with many other examples and discussions in [19–21].

2.29 Problems 32 and 33

See subsection 8.B. in [36]. Problem 32 may be viewed as a subproblem of Problem 31 concerning light scattering by a slab, asking whether this problem could not be solved by taking the case of a large sphere in the limit of infinite radius, assuming that a sphere with infinite radius might behave as a slab, hence Problem 32: “Compare scattering by a very large sphere to scattering by a slab.”

Another subcase of Problem 31 is Problem 33 reading as: “Compare scattering by a particle near a surface with scattering by a bisphere for which one of the spheres is much larger than the other.”

Problems 32 and 33 have many variants such as using scattering cylinders instead of scattering spheres in Problem 32 and using a scattering bicylinder instead of a scattering bisphere in Problem 33.

2.30 Problem 34

See subsection 8.C. in [36]. Numerical computations for the GLMT for elliptical cylinders illuminated by arbitrary beams have been published in a PhD thesis by Méès [192], but they have not been published in the archival literature because they do not perfectly agree with results published by Yeh in the case of plane wave illumination [203]. It has been conjectured that Yeh’s results might be slightly inaccurate due to the fact that these results, obtained more than three decades ago, might have not benefitted the more recent advances concerning the computation of the involved Mathieu functions, hence Problem 34 was required before publishing Méès’ results, namely: “Confirm previously obtained computations concerning the GLMT for elliptical cylinders.”

2.31 Problem 35

See subsection 8.D. in [36]. This problem deals with the case of scattering by assemblies of spheres and aggregates already discussed above in the framework of a GLMT in which the assembly is considered as a single particle, instead of

considering this situation as a situation of multiple or even dependent scattering, particularly when they are touching [204]. Let us assume that we have a large number of particles whose positions are only statistically known. One approach used is to deal with a mean-field approximation to electromagnetic scattering in which the statistical positions of the scatterers are used to generate a statistical distribution of BSCs [205]. This seems to be an appealing approach for the case of arbitrary-shaped beam illumination, hence Problem 35: “Develop a mean-field approach for electromagnetic multiple scattering by a statistical assembly of spheres for arbitrary-shaped beam illumination” implying, obviously, specific applications for specific beams.

3 New Problems

It is the fate of scientific research to have problems left behind while, for some reasons, new problems appeared on the stage. It may even happen that solving one problem reveals the opportunity for several other unexpected problems. I therefore intend to complement the discussion of old problems with some new problems consecutively numbered.

3.1 Problem 36

This problem should have been actually already proposed in [36]. It deals with the contents of a paper by Lock [206], more precisely with its Appendix, which proposes a “derivation of the localized approximation for an on-axis Gaussian beam.” This was actually the first rigorous formal derivation of the localized approximation (restricted to Gaussian beams). It relies on a mathematical method known as the stationary phase method allowing one to deal approximately but precisely with quadratures when integrands possess what is called a stationary point. However, the method, successful when dealing with on-axis beams, failed in the case of off-axis situations, hence Problem 36: “Understand the failure of the stationary phase method to the demonstration of a rigorous approach to validate the localized approximation in the case of Gaussian beams, under an off-axis configuration and, if possible, correct the approach to make it feasible.”

3.2 Problem 37

Problem 37 is similar to Problem 29 devoted to nonlinear effects. Internal fields, instead of being excitation fields for nonlinear phenomena, could be excitation

fields for quantum phenomena, hence Problem 37: “Examine quantum phenomena produced by fields inside scattering particles in the framework of GLMT or EBCM.”

3.3 Problem 38

Problem 38 is more a research program than a problem, strictly speaking. It relies on the fact that, under certain conditions, acoustical fields may be expressed in terms of an expansion over basic functions, similar to the one used in GLMT and EBCM, allowing one to define acoustical BSCs $g_{n,A}^m$, in which the subscript A stands for “acoustical,” similar to the electromagnetic BSCs. However, since acoustical fields are scalar fields instead of vectorial fields, we have to deal with a single set of acoustical BSCs $g_{n,A}^m$ instead of two sets of electromagnetic BSCs $g_{n,TM}^m$ and $g_{n,TE}^m$. In particular, the quadrature expression to evaluate acoustical BSCs is similar to Eq. 4 used to express electromagnetic BSCs.

Problem 38 may then be defined as: “Transfer the results obtained in GLMT (and EBCM) to the case of acoustical fields.” Results already obtained for this “problem” have been published in [207–209].

3.4 Problem 39

Returning to electromagnetic issues, structured beams may propagate an infinite amount of energy, like Bessel beams, or a finite amount of energy like Gaussian beams or Bessel-Gauss beams. All these kinds of beams may be encoded using BSCs, hence Problem 39: “How can we, from the expressions for BSCs, determine whether the beam propagates a finite or an infinite amount of energy.”

3.5 Problem 40

As a consequence of Problem 23, the existence of a new kind of optical forces, named “non-standard forces,” has been established. As a consequence of the listed solutions to Problem 23, it has been demonstrated that these nonstandard forces may be isolated, at least in the case of Rayleigh scattering, from spin-curl forces, which have a physical meaning. These spin-curl forces may actually be separated into two parts, namely, (i) scattering forces and (ii) nonstandard forces. But nonstandard forces alone do not yet receive any direct physical meaning, hence Problem 40: “Establish the physical meaning of non-standard forces.”

3.6 Problem 41

Electromagnetic scattering is usually studied in the case when the medium external to the particle is lossless. Problem 41 may then be defined as: “Study light scattering issues when the medium external to the particle is not lossless.” This problem is proposed with the intuitive idea that it could be approached by considering a two-layer particle with the external layer being absorbing, with a radius tending to infinity.

4 Conclusion

About 10 years ago, a list of problems related to GLMTs has been published. As we may see from Sect. 2, some of these problems have been solved or became obsolete. A new set of problems has been defined in Sect. 3. Problem 41 relies on an intuitive feeling and might be possibly poorly defined. I possess a complementary set of problems, which is not discussed here because they might still be more intuitive and more badly defined. This statement has an obvious interest concerning the psychology of researchers, with the likely correct idea that we all begin to deal with a problem with intuitive, poorly defined images, which shall be progressively refined up to a final satisfactory solution. Another moral to the story is that the front of research between what is known and what is unknown possesses a somewhat corrugated frontier due to the fact that well-posed problems have not been considered and left behind while new problems, often unexpected, appeared on the stage. Finally, I hope that the problems proposed in the present chapter might be a motivation for other researchers. Problems should not remain as a hidden treasure for oneself but must better be shared to the interest of the scientific community, particularly when we know that, due to the limited amount of time available, one would not be able to solve all the problems we might have in mind. Research is then a mixture of satisfaction when a problem is solved and of frustration facing all the problems that are not yet solved.

References

1. G. Mie, Beiträge zur Optik trüber Medien, speziell kolloidaler Metalösungen. *Ann. der Phys.* **25**, 377–452 (1908)
2. G. Mie, *Contributions to the Optics of Turbid Media, Particularly of Colloidal Metal Solutions*, Technical Report (Royal Aircraft Establishment, Library Translation 1873, 1976)
3. G. Gouesbet, B. Maheu, G. Gréhan, Light scattering from a sphere arbitrarily located in a Gaussian beam, using a Bromwich formulation. *J. Opt. Soc. Am. A* **5**(9), 1427–1443 (1988)
4. B. Maheu, G. Gouesbet, G. Gréhan, A concise presentation of the generalized Lorenz-Mie theory for arbitrary location of the scatterer in an arbitrary incident profile. *J. Opt. (Paris)* **19**(2), 59–67 (1988)

5. G. Gouesbet, G. Gréhan, Sur la généralisation de la théorie de Lorenz-Mie. *J. Opt.* **13**(2), 97–103 (1982)
6. F. Onofri, G. Gréhan, G. Gouesbet, Electromagnetic scattering from a multilayered sphere located in an arbitrary beam. *Appl. Opt.* **34**(30), 7113–7124 (1995)
7. Z.S. Wu, L.X. Guo, K.F. Ren, G. Gouesbet, G. Gréhan, Improved algorithms for electromagnetic scattering of plane waves and shaped beams by multilayered spheres. *Appl. Opt.* **36**(21), 5188–5198 (1997)
8. K.F. Ren, G. Gréhan, G. Gouesbet, Scattering of a Gaussian beam by an infinite cylinder in the framework of a GLMT, formulation and numerical results. *J. Opt. Soc. Am. A* **14**(11), 3014–3025 (1997)
9. L. Méès, K.F. Ren, G. Gréhan, G. Gouesbet, Scattering of a Gaussian beam by an infinite cylinder with arbitrary location and arbitrary orientation: Numerical results. *Appl. Opt.* **38**(9), 1867–1876 (1999)
10. G. Gouesbet, L. Méès, Generalized Lorenz-Mie theory for infinitely long elliptical cylinders. *J. Opt. Soc. Am. A* **16**(6), 1333–1341 (1999)
11. G. Gouesbet, L.A. Ambrosio, Interactions between arbitrary electromagnetic shaped beams and circular and elliptical infinite cylinders: A review. *J. Quant. Spectrosc. Radiat. Transf.* **286**, Article 108181 (2022)
12. G. Gouesbet, G. Gréhan, Generalized Lorenz-Mie theory for assemblies of spheres and aggregates. *J. Opt. A Pure Appl. Opt.* **1**(6), 706–712 (1999)
13. G. Gouesbet, G. Gréhan, Generalized Lorenz-Mie theory for a sphere with an eccentrically located spherical inclusion. *J. Mod. Opt.* **47**(5), 821–837 (2000)
14. J. Wang, G. Gouesbet, G. Gréhan, S. Saengkaew, Morphology-dependent resonances in an eccentrically layered sphere illuminated by a tightly focused off-axis Gaussian beam. *J. Opt. Soc. Am. A* **28**(9), 1849–1859 (2011)
15. G. Gouesbet, F. Xu, Y. Han, Expanded description of electromagnetic arbitrary shaped beam in spheroidal coordinates for use in light scattering theories: A review. *J. Quant. Spectrosc. Radiat. Transf.* **112**, 2249–2267 (2011)
16. L. Han, Y.P. Han, J. Wang, Z.W. Cui, Internal and near-surface electromagnetic fields for a dielectric spheroid illuminated by a zero-order Bessel beam. *J. Opt. Soc. Am. A* **31**(9), 1946–1955 (2014)
17. L. Han, Y.P. Han, G. Gouesbet, J. Wang, G. Gréhan, Photonic jet generated by spheroidal particle with Gaussian-beam illumination. *J. Opt. Soc. Am. B* **31**(7), 1476–1483 (2014)
18. G. Gouesbet, G. Gréhan, *Generalized Lorenz–Mie Theories*, 3rd edn. (Springer, 2023)
19. G. Gouesbet, Latest achievements in generalized Lorenz-Mie theories: A commented reference database. *Ann. Phys.* **526**(11–12), 461–489 (2014)
20. G. Gouesbet, T-matrix methods for electromagnetic structured beams: A commented reference database for the period 2014–2018. *J. Quant. Spectrosc. Radiat. Transf.* **230**, 247–281 (2019)
21. G. Gouesbet, T-matrix methods for electromagnetic structured beams: A commented reference database for the period 2019–2023. *J. Quant. Spectrosc. Radiat. Transf.* **322**, Article 109015 (2024)
22. A. Doicu, T. Wriedt, Y.A. Eremin, *Light Scattering by Systems of Particles* (Springer, Berlin, 2006)
23. P.C. Waterman, Symmetry, unitarity, and geometry in electromagnetic scattering. *Phys. Rev. D* **3**(4), 825–839 (1971)
24. M.I. Mishchenko, L.D. Travis, A.A. Lacis, *Scattering, Absorption, and Emission of Light by Small Particles* (Cambridge University Press, Cambridge, 2002)
25. M.I. Mishchenko, J.W. Hovenier, L.D. Travis (eds.), *Light Scattering by Nonspherical Particles: Theory, Measurements and Applications* (Academic Press, 2000)
26. M.I. Mishchenko, *Electromagnetic Scattering by Particles and Particle Groups, an Introduction* (Cambridge University Press, Cambridge, 2014)
27. T.A. Nieminen, V.L.Y. Loke, A.B. Stilgoe, N.R. Heckenberg, H. Rubinsztein-Dunlop, T-matrix method for modelling optical tweezers. *J. Mod. Opt.* **58**(5–6), 528–544 (2011)

28. R. Bates, D. Wall, Null field approach to scalar diffraction. I. General method. *Philos. Trans. R. Soc. Lond. Ser. A* **287**(1339), 45–78 (1977)
29. R. Hackman, R. Lim, Development and application of the spheroidal coordinate based T-matrix solution to elastic wave scattering. *Radio Sci.* **29**(4), 1035–1049 (1994)
30. A. Doicu, T. Wriedt, Formulations of the extended boundary condition method for incident Gaussian beams using multiple-multipole expansions. *J. Mod. Opt.* **44**(4), 785–801 (1997)
31. T.A. Nieminen, H. Rubinsztein-Dunlop, N.R. Heckenberg, Calculation of the T-matrix: General considerations and applications of the point-matching method. *J. Quant. Spectrosc. Radiat. Transf.* **79**, 1019–1029 (2003)
32. N.T. Zakharova, G. Videen, N.G. Khlebtsov, Comprehensive T-matrix reference database: A 2009–2011 update. *J. Quant. Spectrosc. Radiat. Transf.* **113**, 1844–1852 (2012)
33. M. Alonso, R. Gutiérrez-Cuevas, N. Moore, Lorenz-Mie theory scattering of focused light via complex focus fields: An analytic treatment. *Phys. Rev.* **97**(5), Article 053848 (2018)
34. G. Gouesbet, J.A. Lock, On the electromagnetic scattering of arbitrary shaped beams by arbitrary shaped particles: A review. *J. Quant. Spectrosc. Radiat. Transf.* **162**, 31–49 (2015)
35. G. Gouesbet, J.A. Lock, On the description of electromagnetic arbitrary shaped beams. The relationship between beam shape coefficients and plane wave spectra. *J. Quant. Spectrosc. Radiat. Transf.* **162**, 18–30 (2015)
36. G. Gouesbet, J.A. Lock, List of problems for future research in generalized Lorenz-Mie theories and related topics, review and prospectus: Commemorative invited paper, for the 50th anniversary of “Applied optics”. *Appl. Opt.* **52**(5), 897–916 (2013)
37. G. Gouesbet, F. Xu, P. Marston, Professor James Albert Lock (1948–2023): A life of honor and work of excellence. *J. Quant. Spectrosc. Radiat. Transf.* **313**, Article 108893 (2024)
38. Y. Han, Z.S. Wu, The expansion coefficients of a spheroidal particle illuminated by Gaussian beam. *IEEE Trans. Antennas Propag.* **49**(4), 615–620 (2001)
39. Y.P. Han, Z.S. Wu, Scattering of a spheroidal particle illuminated by a Gaussian beam. *Appl. Opt.* **40**(15), 2501–2509 (2001)
40. Y.P. Han, Z.S. Wu, Absorption and scattering by an oblate particle. *J. Opt. A Pure Appl. Opt.* **4**(1), 74–77 (2002)
41. Y.P. Han, L. Méès, K.F. Ren, G. Gouesbet, S.Z. Wu, G. Gréhan, Scattering of light by spheroids: The far field case. *Opt. Commun.* **210**, 1–9 (2002)
42. M. Wang, H. Zhang, Y. Han, Y. Li, Scattering of shaped beam by a conducting infinite cylinder with dielectric coating. *Appl. Phys. B* **96**, 105–109 (2009)
43. Y. Zhai, Y. Sun, H.Y. Zhang, On-axis Gaussian beam scattering by an eccentrically coated conducting cylinder. *J. Quant. Spectrosc. Radiat. Transf.* **113**, 1441–1445 (2012)
44. H.Y. Zhang, T.Q. Liao, Scattering of Gaussian beam by a spherical particle with a spheroidal inclusion. *J. Quant. Spectrosc. Radiat. Transf.* **112**(9), 1486–1491 (2011)
45. M.J. Wang, H.Y. Zhang, G.S. Liu, Y.L. Li, Q.F. Dong, Reflection and transmission of Gaussian beam by a uniaxial anisotropic slab. *Opt. Express* **22**(3), 3705–3711 (2014)
46. H.Y. Zhang, Y. Yuan, M. Li, Z. Huang, Gaussian beam scattering by a particle above a plane surface. *J. Quant. Spectrosc. Radiat. Transf.* **217**, 22–28 (2018)
47. L. Han, G. Gouesbet, Y.P. Han, Intrinsic method for the evaluation of beam shape coefficients in spheroidal coordinates for oblique illumination. *J. Quant. Spectrosc. Radiat. Transf.* **224**, 312–318 (2019)
48. G. Gouesbet, Generalized Lorenz-Mie theories and mechanical effects of laser light, on the occasion of Arthur Ashkin’s receipt of the 2018 Nobel prize in physics for his pioneering work in optical levitation and manipulation: A review. *J. Quant. Spectrosc. Radiat. Transf.* **225**, 258–277 (2019)
49. G. Gouesbet, J. Wang, Y. Han, Solution to the intrinsic method for the evaluation of beam shape coefficients in spheroidal coordinates. *Opt. Commun.* **294**, 29–35 (2013)
50. G. Gouesbet, J. Wang, On the structures of some light scattering theories depending on whether or not the Bromwich formulation may be used, e.g. spherical versus spheroidal coordinates. *Opt. Commun.* **285**(21–22), 4200–4206 (2012)

51. L. Han, G. Gouesbet, Y. Han, G. Gréhan, J. Wang, Intrinsic method for the evaluation of beam shape coefficients in spheroidal coordinates for on-axis standard configuration. *Opt. Commun.* **310**, 125–137 (2014)
52. J.P. Barton, D.R. Alexander, Fifth-order corrected electromagnetic field components for fundamental Gaussian beams. *J. Appl. Phys.* **66**(7), 2800–2802 (1989)
53. G. Gouesbet, J. Wang, Y.P. Han, Transformations of spherical beam shape coefficients in generalized Lorenz-Mie theories through rotations of coordinate system. I. General formulation. *Opt. Commun.* **283**(17), 3218–3225 (2010)
54. J. Wang, G. Gouesbet, Y.P. Han, Transformations of spherical beam shape coefficients in generalized Lorenz-Mie theories through rotations of coordinate system. II. Axisymmetric beams. *Opt. Commun.* **283**(17), 3226–3234 (2010)
55. L. Han, Y.P. Han, Z.W. Cui, J. Wang, Expansion of a zero-order Bessel beam in spheroidal coordinates by generalized Lorenz-Mie theory. *J. Quant. Spectrosc. Radiat. Transf.* **147**, 279–287 (2014)
56. L. Han, G. Gouesbet, Y. Han, Intrinsic method for the evaluation of beam shape coefficients in spheroidal coordinates for oblique illumination. *J. Quant. Spectrosc. Radiat. Transf., LIP2018 special issue* **224**, 312–318 (2019)
57. G. Gouesbet, C. Letellier, K.F. Ren, G. Gréhan, Discussion of two quadrature methods of evaluating beam shape coefficients in generalized Lorenz-Mie theory. *Appl. Opt.* **35**(9), 1537–1542 (1996)
58. G. Gouesbet, L.A. Ambrosio, J.A. Lock, On an infinite number of quadratures to evaluate beam shape coefficients in generalized Lorenz-Mie theory and extended boundary condition method for structured EM fields. *J. Quant. Spectrosc. Radiat. Transf.* **242**, Article 196779 (2020)
59. G. Gouesbet, G. Gréhan, B. Maheu, Expressions to compute the coefficients g_n^m in the generalized Lorenz-Mie theory, using finite series. *J. Opt. (Paris)* **19**(1), 35–48 (1988)
60. L.A. Ambrosio, G. Gouesbet, Modified finite series technique for the evaluation of beam shape coefficients in the T-matrix methods for structured beams with application to Bessel beams. *J. Quant. Spectrosc. Radiat. Transf.* **248**, Article 107007 (2020)
61. L.F.M. Votto, L.A. Ambrosio, G. Gouesbet, J. Wang, Finite series algorithm design for lens-focused Laguerre-Gauss beams in the generalized Lorenz-Mie theory. *J. Quant. Spectrosc. Radiat. Transf., virtual special issue of LIP2020* **261**, Article 107 488 (2021)
62. J. Shen, Y. Wang, H. Yu, L.A. Ambrosio, G. Gouesbet, Angular spectrum representation of the Bessel-Gauss beam and its approximation: A comparison with the localized approximation. *J. Quant. Spectrosc. Radiat. Transf.* **284**, Article 108167 (2022)
63. J. Shen, J. Liu, Y. Wang, Z. Liu, H. Yu, Cylindrical wave spectrum decomposition method for evaluating the expansion coefficients of the shaped beam in spherical coordinates. *J. Quant. Spectrosc. Radiat. Transf.* **283**, Article 108138 (2022)
64. G. Gouesbet, J.A. Lock, Y. Han, J. Wang, Efficient computation of arbitrary beam scattering on a sphere: Comments and rebuttal, with a review on the angular spectrum decomposition. *J. Quant. Spectrosc. Radiat. Transf.* **276**, Article 107913 (2021)
65. G. Gouesbet, J.A. Lock, G. Gréhan, Generalized Lorenz-Mie theories and description of electromagnetic arbitrary shaped beams: Localized approximations and localized beam models, a review. *J. Quant. Spectrosc. Radiat. Transf.* **112**, 1–27 (2011)
66. H.C. van de Hulst, *Light Scattering by Small Particles* (Wiley, New York, 1957)
67. G. Gréhan, B. Maheu, G. Gouesbet, Scattering of laser beams by Mie scatter centers: Numerical results using a localized approximation. *Appl. Opt.* **25**(19), 3539–3548 (1986)
68. J.A. Lock, G. Gouesbet, Rigorous justification of the localized approximation to the beam shape coefficients in generalized Lorenz-Mie theory. I. On-axis beams. *J. Opt. Soc. Am. A* **11**(9), 2503–2515 (1994)
69. G. Gouesbet, J.A. Lock, Rigorous justification of the localized approximation to the beam shape coefficients in generalized Lorenz-Mie theory. II. Off-axis beams. *J. Opt. Soc. Am. A* **11**(9), 2516–2525 (1994)

70. G. Gouesbet, Validity of the localized approximation for arbitrary shaped beams in generalized Lorenz-Mie theory for spheres. *J. Opt. Soc. Am. A* **16**(7), 1641–1650 (1999)
71. A. Doicu, T. Wriedt, Computation of the beam shape coefficients in the generalized Lorenz-Mie theory by using the translational addition theorem for spherical vector wave functions. *Appl. Opt.* **36**(13), 2971–2978 (1997)
72. H.Y. Zhang, Y.P. Han, Addition theorem for the spherical vector wave functions and its application to the beam shape coefficients. *J. Opt. Soc. Am. B* **25**(2), 255–260 (2008)
73. L. Boyde, K.J. Chalut, J. Guck, Exact analytical expansion of an off-axis Gaussian laser beam using the translation theorems for the vector spherical harmonics. *Appl. Opt.* **50**(7), 1023–1033 (2011)
74. G. Gouesbet, G. Gréhan, B. Maheu, Localized interpretation to compute all the coefficients g_n^m in the generalized Lorenz-Mie theory. *J. Opt. Soc. Am. A* **7**(6), 998–1007 (1990)
75. J. Wang, G. Gouesbet, Note on the use of localized beam models for light scattering theories in spherical coordinates. *Appl. Opt.* **51**(17), 3832–3836 (2012)
76. G. Gouesbet, Second modified localized approximation for use in generalized Lorenz-Mie theories and other theories revisited. *J. Opt. Soc. Am. A* **30**(4), 560–564 (2013)
77. G. Gouesbet, J.A. Lock, J. Wang, G. Gréhan, Transformations of spherical beam shape coefficients in generalized Lorenz-Mie theories through rotations of coordinate system. V. Localized beam models. *Opt. Commun.* **284**(1), 411–417 (2011)
78. K.F. Ren, G. Gouesbet, G. Gréhan, Integral localized approximation in generalized Lorenz-Mie theory. *Appl. Opt.* **37**(19), 4218–4225 (1998)
79. L.W. Davis, Theory of electromagnetic beams. *Phys. Rev.* **19**(3), 1177–1179 (1979)
80. G. Gouesbet, J. Shen, L.A. Ambrosio, Diverging and converging schemes of approximations to describe fundamental EM Gaussian beams beyond the paraxial approximation. *J. Quant. Spectrosc. Radiat. Transf.* **291**, Article 108344 (2022)
81. N.L. Valdivia, L.F.M. Votto, G. Gouesbet, J. Wang, L.A. Ambrosio, Bessel-Gauss beams in the generalized Lorenz-Mie theory using three remodeling techniques. *J. Quant. Spectrosc. Radiat. Transf.* **256**, Article 107292 (2020)
82. A.E. Siegman, *An Introduction to Lasers and Masers* (McGraw-Hill Book Company, New-York, 1971)
83. A.E. Siegman, *Lasers* (University Science Books, Sausalito, 1986)
84. G. Gouesbet, L.F.M. Votto, L.A. Ambrosio, Finite series expressions to evaluate the beam shape coefficients of a Laguerre-Gauss beam freely propagating. *J. Quant. Spectrosc. Radiat. Transf.* **227**, 12–19 (2019)
85. L.F.M. Votto, L.A. Ambrosio, G. Gouesbet, Evaluation of beam shape coefficients of paraxial Laguerre-Gauss beam freely propagating by using three remodeling methods. *J. Quant. Spectrosc. Radiat. Transf.* **239**, Article 106618 (2019)
86. L.F.M. Votto, G. Gouesbet, L.A. Ambrosio, A framework for the finite series method of the generalized Lorenz-Mie theory and its application to freely propagating Laguerre-Gaussian beams. *J. Quant. Spectrosc. Radiat. Transf.* **309**, Article 108706 (2023)
87. A.A.R. Neves, A. Fontes, L.A. Padilha, E. Rodriguez, C.H. de Brito Cruz, L.C. Barbosa, C.L. Cesar, Exact partial wave expansion of optical beams with respect to an arbitrary origin. *Opt. Lett.* **31**(16), 2477–2479 (2006)
88. A.A.R. Neves, L.A. Padilha, A. Fontes, E. Rodriguez, C.H.B. Cruz, L.C. Barbosa, C.L. Cesar, Analytical results for a Bessel function times Legendre polynomials class integrals. *J. Phys. A Math. Gen.* **39**, L293–L296 (2006)
89. W.L. Moreira, A.A.R. Neves, M.K. Garbos, T.G. Euser, P. St. J. Russell, C.L. Cesar, Expansion of arbitrary electromagnetic fields in terms of vector spherical wave functions. *Opt. Express* **24**(3), 2370–2382 (2016)
90. J. Durnin, Exact solutions for nondiffracting beams. I. The scalar theory. *J. Opt. Soc. Am. A* **4**(4), 651–654 (1987)
91. J. Durnin Jr., J.J. Miceli, J.H. Eberly, Diffraction-free beams. *Phys. Rev. Lett.* **58**(15), 1499–1501 (1987)

92. G. Gouesbet, L.F.M. Votto, L.A. Ambrosio, J. Wang, Poynting vector and beam shape coefficients: On new families of symmetries (non-dark axisymmetric beams of the second kind and dark axisymmetric beams). *J. Quant. Spectrosc. Radiat. Transf.* **271**, Article 107745 (2021)
93. A. Chafiq, A. Belafhal, Scattering of Lommel beams by homogeneous spherical particle in generalized Lorenz-Mie theory. *Opt. Quant. Electron.* **2**, 2018 (2018)
94. L.A. Ambrosio, M. Zamboni-Rached, G. Gouesbet, Discrete vector frozen waves in generalized Lorenz-Mie theory: Linear, azimuthal and radial polarization. *Appl. Opt.* **57**(12), 3293–3300 (2018)
95. L.A. Ambrosio, M. Zamboni Rached, G. Gouesbet, Zeroth-order continuous vector frozen waves for light scattering: Exact multipole expansion in the generalized Lorenz-Mie theory. *J. Opt. Soc. Am. B* **36**(1), 81–89 (2019)
96. D. Allano, G. Gouesbet, G. Gréhan, D. Lisiecki, Droplet sizing using a top-hat laser beam technique. *J. Phys. D. Appl. Phys.* **17**, 43–58 (1984)
97. G. Gréhan, G. Gouesbet, Simultaneous measurements of velocities and sizes of particles in flows using a combined system incorporating a top-hat beam technique. *Appl. Opt.* **25**(19), 3527–3538 (1986)
98. F. Corbin, G. Gréhan, G. Gouesbet, Top-hat beam technique: Improvements and application to bubble measurements. *Part. Part. Syst. Charact.* **8**, 222–228 (1991)
99. G. Gouesbet, J.A. Lock, G. Gréhan, Partial wave representations of laser beams for use in light scattering calculations. *Appl. Opt.* **34**(12), 2133–2143 (1995)
100. J.A. Lock, Improved Gaussian beam-scattering algorithm. *Appl. Opt.* **34**(3), 559–570 (1995)
101. G. Gouesbet, P.L. Marston, Failures of the classical optical theorem under arbitrary-shaped beam incidence in electromagnetism, acoustics, and quantum mechanics: Motivation and a review. *Front. Phys.* (2023). <https://doi.org/10.3389/fphy.2023.1271555>
102. G. Gouesbet, J.A. Lock, Consequences of the angular spectrum decomposition of a focused beam including slower than c beam propagation. *J. Quant. Spectrosc. Radiat. Transf.* **178**, 142–151 (2016)
103. G. Gouesbet, J. Wang, Y.P. Han, Transformations of spherical beam shape coefficients in generalized Lorenz-Mie theories through rotations of coordinate system. IV. Plane waves. *Opt. Commun.* **283**(17), 3244–3254 (2010)
104. D.W. Mackowski, M.I. Mishchenko, Direct simulation of multiple scattering by discrete random media illuminated by Gaussian beams. *Phys. Rev. A* **83**, Article number 013804 (2011)
105. Z. Chen, H.Y. Zhang, Z. Huang, X. Wu, Scattering of on-axis Gaussian beam by a uniaxial anisotropic object. *J. Opt. Soc. Am. A* **31**(11), 2545–2550 (2014)
106. J. Wang, A. Chen, Y. Han, P. Briard, Light scattering from an optically anisotropic particle illuminated by an arbitrary shaped beam. *J. Quant. Spectrosc. Radiat. Transf.* **167**, 135–144 (2015)
107. M. Zheng, H.Y. Zhang, Y.F. Sun, Z.G. Wang, Scattering of on-axis Gaussian beam by an arbitrarily shaped chiral object. *J. Quant. Spectrosc. Radiat. Transf.* **151**, 192–197 (2015)
108. M. Zheng, H.Y. Zhang, Y.F. Sun, On-axis Gaussian beam scattering by an object with a chiral inclusion. *J. Quant. Spectrosc. Radiat. Transf.* **151**, 269–274 (2015)
109. J.W. Goodman, *Introduction to Fourier Optics* (McGraw-Hill, San Francisco, 1968)
110. J.T. Hodges, G. Gréhan, G. Gouesbet, C. Presser, Forward scattering of a Gaussian beam by a nonabsorbing sphere. *Appl. Opt.* **34**(12), 2120–2132 (1995)
111. J.A. Lock, J.T. Hodges, Far-field scattering of an axisymmetric laser beam of arbitrary profile by an on-axis spherical particle. *Appl. Opt.* **35**, 4283–4290 (1996)
112. G. Gouesbet, Measurements of beam shape coefficients in generalized Lorenz-Mie theory and the density-matrix approach. I. Measurements. *Part. Part. Syst. Charact.* **14**, 12–20 (1997)
113. G. Gouesbet, Measurements of beam shape coefficients in generalized Lorenz-Mie theory and the density-matrix approach. II. The density-matrix approach. *Part. Part. Syst. Charact.* **14**, 88–92 (1997)

114. H. Polaert, G. Gouesbet, G. Gréhan, Laboratory determination of beam shape coefficients for use in generalized Lorenz-Mie theory. *Appl. Opt.* **40**(10), 1699–1706 (2001)
115. K.F. Ren, G. Gréhan, G. Gouesbet, Radiation pressure forces exerted on a particle arbitrarily located in a Gaussian beam by using the generalized Lorenz-Mie theory, and associated resonance effects. *Opt. Commun.* **108**(4–6), 343–354 (1994)
116. K.F. Ren, G. Gréhan, G. Gouesbet, Prediction of reverse radiation pressure by generalized Lorenz-Mie theory. *Appl. Opt.* **35**(15), 2702–2710 (1996)
117. H. Polaert, G. Gréhan, G. Gouesbet, Improved standard beams with applications to reverse radiation pressure. *Appl. Opt.* **37**(12), 2435–2440 (1998)
118. H. Polaert, G. Gréhan, G. Gouesbet, Forces and torques exerted on a multilayered spherical particle by a focused Gaussian beam. *Opt. Commun.* **155**(1–3), 169–179 (1998)
119. F. Xu, K.F. Ren, G. Gouesbet, X. Cai, G. Gréhan, Theoretical prediction of radiation pressure force exerted on a spheroid by an arbitrarily shaped beam. *Phys. Rev. E* **75**, Art 026613:1–14 (2007)
120. F. Xu, J.A. Lock, G. Gouesbet, C. Tropea, Radiation torque exerted on a spheroid: Analytical solution. *Phys. Rev. A* **78**, Art 013843:1–17 (2008)
121. F. Xu, J.A. Lock, G. Gouesbet, C. Tropea, Optical stress on the surface of a particle. I. Homogeneous sphere. *Phys. Rev. A* **79**, Article number: 053808 (2009)
122. F. Guilloteau, G. Gréhan, G. Gouesbet, Optical levitation experiments to assess the validity of the generalized Lorenz-Mie theory. *Appl. Opt.* **31**(15), 2942–2951 (1992)
123. G. Martinot-Lagarde, B. Pouligny, M.I. Angelova, G. Gréhan, G. Gouesbet, Trapping and levitation of a dielectric sphere with off-centred Gaussian beams. II. GLMT-analysis. *Pure Appl. Opt.* **4**(5), 571–585 (1995)
124. G. Martinot-Lagarde, M.I. Angelova, B. Pouligny, G. Gréhan, G. Gouesbet, Laser trappings of micron particles and dynamometrical applications. *Ann. Phys.* **20**(2), 127–128 (1995)
125. J.A. Lock, Calculation of the radiation trap force for laser tweezers by use of generalized Lorenz-Mie theory. II. On-axis trapping force. *Appl. Opt.* **43**, 2545–2554 (2004)
126. G. Gouesbet, Gradient, scattering and other kinds of longitudinal optical forces exerted by off-axis Bessel beams in the Rayleigh regime in the framework of generalized Lorenz-Mie theory. *J. Quant. Spectrosc. Radiat. Transf.* **246**, Article 106913 (2020)
127. G. Gouesbet, L.A. Ambrosio, Axicon terms associated with gradient optical forces in generalized Lorenz-Mie theory. *J. Quant. Spectrosc. Radiat. Transf.* **257**, Article 107260 (2020)
128. G. Gouesbet, L.A. Ambrosio, Axicon optical forces and other kinds of transverse optical forces exerted by off-axis Bessel beams in the Rayleigh regime in the framework of generalized Lorenz-Mie theory. *J. Quant. Spectrosc. Radiat. Transf., virtual special issue of LIP2020* **258**, Article 107356 (2021)
129. G. Gouesbet, Optical forces exerted by on-axis Bessel beams on Rayleigh particles in the framework of the generalized Lorenz-Mie theory. *J. Quant. Spectrosc. Radiat. Transf.* **260**, Article 107471 (2021)
130. L.A. Ambrosio, G. Gouesbet, On transverse radiation pressure cross-sections in the generalized Lorenz-Mie theory and their numerical relationships with the dipole theory of forces. *J. Quant. Spectrosc. Radiat. Transf.* **261**, Article 107491 (2021)
131. L.A. Ambrosio, G. Gouesbet, On longitudinal radiation pressure cross-sections in the generalized Lorenz-Mie theory and their numerical relationship with the dipole theory of forces. *J. Opt. Soc. Am. B* **38**(3), 825–833 (2021)
132. L.A. Ambrosio, G. Gouesbet, On the Rayleigh limit of the generalized Lorenz-Mie theory and its formal identification with the dipole theory of forces. I. The longitudinal case. *J. Quant. Spectrosc. Radiat. Transf.* **262**, Article 107531 (2021)
133. L.A. Ambrosio, G. Gouesbet, On the Rayleigh limit of the generalized Lorenz-Mie theory and its formal identification with the dipole theory of forces. II. The transverse case. *J. Quant. Spectrosc. Radiat. Transf.* **266**, Article 107591 (2021)
134. G. Gouesbet, L.A. Ambrosio, Rayleigh limit of the generalized Lorenz-Mie theory for on-axis beams and its relationship with the dipole theory of forces. Part I. Non dark axisymmetric

- beams of the first kind, with the example of Gaussian beams. *J. Quant. Spectrosc. Radiat. Transf.* **266**, Article 107569 (2021)
135. G. Gouesbet, L.A. Ambrosio, Rayleigh limit of generalized Lorenz-Mie theory: Axicon terms revisited. *J. Quant. Spectrosc. Radiat. Transf.* **270**, Article 107691 (2021)
 136. G. Gouesbet, L.A. Ambrosio, Rayleigh limit of generalized Lorenz-Mie theory for on-axis beams and its relationship with the dipole theory of forces. Part II: Non-dark axisymmetric beams of the second kind and dark axisymmetric beams, including a review. *J. Quant. Spectrosc. Radiat. Transf.* **273**, Article 107836 (2021)
 137. G. Gouesbet, V.S. de Angelis, L.A. Ambrosio, Optical forces and optical force categorizations on small magnetodielectric particles in the framework of generalized Lorenz-Mie theory. *J. Quant. Spectrosc. Radiat. Transf.* **279**, Article 108046 (2022)
 138. L.A. Ambrosio, V.S. de Angelis, G. Gouesbet, The generalized Lorenz-Mie theory and its identification with the dipole theory of forces for particles with electric and magnetic properties. *J. Quant. Spectrosc. Radiat. Transf.* **281**, Article 108104 (2022)
 139. V.S. de Angelis, L.A. Ambrosio, G. Gouesbet, Comparative numerical analysis between the multipole expansion of optical force up to quadrupole terms and the generalized Lorenz-Mie theory. *J. Opt. Soc. Am. B* **38**(8), 2353–2361 (2021)
 140. G. Gouesbet, V.S. De Angelis, L.A. Ambrosio, Optical forces and optical force categorizations exerted on quadrupoles in the framework of generalized Lorenz-Mie theory. *J. Quant. Spectrosc. Radiat. Transf.* **298**, Article 108487 (2023)
 141. G. Gouesbet, V. de Angelis, L.A. Ambrosio, Optical forces and optical force partitions exerted on arbitrary sized spherical particles in the framework of generalized Lorenz-Mie theory. *J. Quant. Spectrosc. Radiat. Transf.* **307**, Article 108661 (2023)
 142. G. Gouesbet, L.A. Ambrosio, Optical force categorization in the framework of generalized Lorenz-Mie theory, in *Light, Particles and Plasmonics*, (Elsevier, 2023). <https://doi.org/10.1016/B978-0-323-99901-4.00016-0>
 143. J.U. Nöckel, A.R. Stone, Chaotic light: A theory of asymmetric resonant cavities, in *Optical Processes in Microcavities*, (World Scientific Publication, Singapore, 1996), pp. 389–426
 144. J.U. Nöckel, A.D. Stone, Ray and wave chaos in asymmetric resonant optical cavities. *Lett. Nat.* **385**, 45–47 (1997)
 145. A.D. Stone, J.U. Nöckel, Asymmetric resonant optical cavities. *Opt. Photon. News* **8**, 37–38 (1997)
 146. A. Mekis, J.U. Nöckel, G. Chen, A.D. Stone, R.K. Chang, Ray chaos and Q spoiling in lasing droplets. *Phys. Rev. Lett.* **75**, 2682–2685 (1995)
 147. J.U. Nöckel, A.D. Stone, R.K. Chang, Q-spoiling and directionality in deformed ring cavities. *Opt. Lett.* **19**, 1693–1695 (1994)
 148. G. Gouesbet, G. Gréhan, Generalized Lorenz-Mie theories, from past to future. *Atomization Sprays* **10**(3–5), 277–333 (2000)
 149. J.M. Jensen, Chaotic scattering of light by a dielectric cylinder. *J. Opt. Soc. Am. A* **10**, 1204–1208 (1993)
 150. J. Wang, G. Gouesbet, Y.P. Han, G. Gréhan, Study of scattering from a sphere with an eccentrically located spherical inclusion by generalized Lorenz-Mie theory: Internal and external field distributions. *J. Opt. Soc. Am. A* **28**(1), 24–39 (2011)
 151. J. Wang, L. Han, Y.P. Han, G. Gouesbet, X.C. Wu, Y.C. Wu, Shaped beam scattering from a single lymphocyte cell by generalized Lorenz-Mie theory. *J. Quant. Spectrosc. Radiat. Transf.* **133**, 72–80 (2014)
 152. G. Gouesbet, S. Meunier-Guttin-Cluzel, G. Gréhan, Generalized Lorenz-Mie theory for a sphere with an eccentrically located spherical inclusion, and optical chaos. Part. Part. Syst. Charact. **18**, 190–195 (2001)
 153. G. Gouesbet, S. Meunier-Guttin-Cluzel, G. Gréhan, Periodic orbits in Hamiltonian chaos of the annular billiard. *Phys. Rev. E* **65**(1), Art 016212:1–18 (2001)
 154. G. Gouesbet, S. Meunier-Guttin-Cluzel, G. Gréhan, Morphology-dependent resonances and/or whispering gallery modes for a two-dimensional dielectric cavity with an eccentricity

- located spherical inclusion, a Hamiltonian point of view with Hamiltonian (optical) chaos. *Opt. Commun.* **201**(4–6), 223–242 (2002)
155. C. Jung, S. Pott, Classical cross section for chaotic potential scattering. *J. Phys. A* **22**, 2925–2938 (1989)
 156. S. Bleher, C. Grebogi, E. Ott, Bifurcation to chaotic scattering. *Phys. D* **46**, 87–121 (1990)
 157. V. Daniels, M. Vallières, J.M. Yuan, Chaotic scattering on a double well: Periodic orbits, symbolic dynamics, and scaling. *Chaos* **3**, 475–485 (1993)
 158. P. Briard, Y.P. Han, Z. Chen, X. Cai, J. Wang, Scattering of aggregated particles illuminated by a zeroth-order Bessel beam. *Opt. Commun.* **391**, 42–47 (2017)
 159. G. Gouesbet, G. Gréhan, Generic formulation of a generalized Lorenz-Mie theory for a particle illuminated by laser pulses. *Part. Part. Syst. Charact.* **17**(5–6), 213–224 (2000)
 160. G. Gouesbet, L. Méès, G. Gréhan, Generic formulation of a generalized Lorenz-Mie theory for pulsed laser illumination, in *Laser Techniques for Fluid Mechanics*, ed. by Adrian, Durao, Durst, Heitor, Maeda, Whitelaw, (Springer, 2002), pp. 175–188
 161. L. Méès, G. Gréhan, G. Gouesbet, Time-resolved scattering diagrams for a sphere illuminated by plane wave and focused short pulses. *Opt. Commun.* **194**(1–3), 59–65 (2001)
 162. L. Méès, G. Gouesbet, G. Gréhan, Scattering of laser pulses (plane wave and focused Gaussian beams) by spheres. *Appl. Opt.* **40**(15), 2546–2550 (2001)
 163. L. Méès, G. Gouesbet, G. Gréhan, Interaction between femtosecond pulses and a spherical microcavity: Internal fields. *Opt. Commun.* **199**(1–4), 33–38 (2001)
 164. L. Méès, G. Gouesbet, G. Gréhan, Numerical predictions of microcavity internal fields created by femtosecond pulses, with emphasis on whispering gallery modes. *J. Opt. A Pure Appl. Opt.* **4**, S150–S153 (2002)
 165. Y.P. Han, L. Méès, K.F. Ren, G. Gréhan, Z.S. Wu, G. Gouesbet, Far scattered field from a spheroid under a femtosecond pulsed illumination in a generalized Lorenz-Mie theory framework. *Opt. Commun.* **231**(1–6), 71–77 (2004)
 166. L. Méès, G. Gouesbet, G. Gréhan, Transient internal and scattered fields from a multi-layered sphere illuminated by a pulsed laser. *Opt. Commun.* **282**(21), 4189–4193 (2009)
 167. L. Han, Y.P. Han, J. Wang, G. Gouesbet, Internal and near-surface field distributions for a spheroidal particle illuminated by a focused Gaussian beam: On-axis case. *J. Quant. Spectrosc. Radiat. Transf.* **126**, 38–43 (2013)
 168. A.R. Jones, Some calculations on the scattering efficiencies of a sphere illuminated by an optical pulse. *J. Phys. D* **40**(23), 7306–7312 (2007)
 169. S. Bakic, F. Xu, N. Damaschke, C. Tropea, Feasibility of extending rainbow refractometry to small particles using femtosecond laser pulses. *Part. Part. Syst. Charact.* **26**(1–2), 34–40 (2009)
 170. Y.E. Geints, A.A. Zemlyanov, E.K. Panina, Whispering-gallery mode excitation in a micro-droplet illuminated by a train of chirped ultrashort laser pulses. *Appl. Opt.* **48**(30), 5842–5848 (2009)
 171. L.P. Su, S.Y. Chen, W.J. Zhao, D.M. Ren, Scattering properties of ultrashort laser pulses by air bubbles in the sea water. *Proc. SPIE* **8192**, 8192K (2011)
 172. C. Calba, L. Méès, C. Rozé, T. Girasole, Ultrashort pulse propagation through a strongly scattering medium: Simulation and experiments. *J. Opt. Soc. Am. A* **25**, 1541–1550 (2008)
 173. M. Brunel, L. Méès, G. Gouesbet, G. Gréhan, Cerenkov-based radiation from superluminal excitation in microdroplets by ultra-short pulses. *Opt. Lett.* **26**(20), 1621–1623 (2001)
 174. L. Méès, J.P. Wolf, G. Gouesbet, G. Gréhan, Two-photon absorption and fluorescence in a spherical micro-cavity illuminated by using two laser pulses: Numerical simulations. *Opt. Commun.* **208**(4–6), 371–375 (2002)
 175. G. Gréhan, G. Gouesbet, A. Naqwi, F. Durst, Trajectory ambiguities in phase Doppler systems: Use of polarizers and additional detectors to suppress the effect. In *Proceedings of the 6th International Symposium on Applications of Laser Techniques to Fluid Mechanics, and Workshop on Computers in Flow Measurements*, Lisbon, 20th–23th July 1992
 176. G. Gréhan, G. Gouesbet, A. Naqwi, F. Durst, Particle trajectory effects in phase-Doppler systems: Computations and experiments. *Part. Part. Syst. Charact.* **10**(6), 332–338 (1993)

177. G. Gréhan, G. Gouesbet, A. Naqwi, F. Durst, Trajectory ambiguities in phase-Doppler systems: Study of a near-forward and a near-backward geometry. Part. Part. Syst. Charact. **11**(2), 133–144 (1994)
178. G. Gréhan, K.F. Ren, G. Gouesbet, A. Naqwi, F. Durst, Evaluation of a particle sizing technique based on laser sheets. Part. Part. Syst. Charact. **11**(1), 101–106 (1994)
179. G. Gréhan, F. Onofri, G. Gouesbet, Anémométrie phase-Doppler en milieux multiphasiques: Vers de nouvelles possibilités. La Houille Blanche **1/2**, 98–104 (1996)
180. F. Onofri, D. Blondel, G. Gréhan, G. Gouesbet, On the optical diagnosis and sizing of spherical coated and multilayered particles with phase-Doppler anemometry. Part. Part. Syst. Charact. **13**(2), 104–111 (1996)
181. H. Mignon, G. Gréhan, G. Gouesbet, T.H. Xu, C. Tropea, Measurement of cylindrical particles with phase-Doppler anemometry. Appl. Opt. **35**(25), 5180–5190 (1996)
182. F. Onofri, T. Girasole, G. Gréhan, G. Gouesbet, G. Brenn, J. Domnick, T.H. Xu, C. Tropea, Phase-Doppler anemometry with the dual burst technique for measurement of refractive index and absorption coefficient simultaneously with size and velocity. Part. Part. Syst. Charact. **13**(2), 112–124 (1996)
183. N. Gauchet, T. Girasole, K.F. Ren, G. Gréhan, G. Gouesbet, Application of generalized Lorenz-Mie theory for cylinders to cylindrical particle characterization by phase-Doppler anemometry. Opt. Diagn. Eng. **2**(1), 1–10 (1997)
184. H. Bultynck, G. Gouesbet, G. Gréhan, A miniature monoblock backward phase-Doppler unit. Meas. Sci. Technol. **9**, 161–170 (1998)
185. N. Damaschke, G. Gouesbet, G. Gréhan, H. Mignon, C. Tropea, Response of phase Doppler anemometer systems to non-spherical droplets. Appl. Opt. **37**(10), 1752–1761 (1998)
186. D. Blondel, H. Bultynck, G. Gouesbet, G. Gréhan, Phase-Doppler measurements with compact monoblock configurations. Part. Part. Syst. Charact. **18**, 79–90 (2001)
187. K.F. Ren, T. Girasole, A.K.M.P. Taylor, G. Gouesbet, G. Gréhan, Theoretical evaluation of a shadow Doppler velocimeter. Opt. Commun. **220**, 269–280 (2003)
188. L.A. Ambrosio, J.O. de Sarro, G. Gouesbet, An approach for a polychromatic generalized Lorenz-Mie theory. J. Quant. Spectrosc. Radiat. Transf. **312**, Article 108824 (2024)
189. L.A. Ambrosio, J.O. de Sarro, G. Gouesbet, Corrigendum to “an approach for a polychromatic generalized Lorenz-Mie theory” [J. Quant. Spectrosc. Radiat. Transfer, 31 (2024), 108824] J. Quant. Spectrosc. Radiat. Transf. **319**, Article 108963 (2024)
190. G. Gouesbet, G. Gréhan, Interaction between shaped beams and an infinite cylinder, including a discussion of Gaussian beams. Part. Part. Syst. Charact. **11**, 299–308 (1994)
191. G. Gouesbet, L. Méès, G. Gréhan, Partial-wave description of shaped beams in elliptical-cylinder coordinates. J. Opt. Soc. Am. A **15**(12), 3028–3038 (1998)
192. Loïc Méès. Diffusion de la lumière par des objets cylindriques: simulations par théorie de Lorenz–Mie généralisée et applications métrologiques. PhD thesis, Faculté des Sciences de l'Université de Rouen, 2000
193. G. Gouesbet, L. Méès, Generalized Lorenz-Mie theory for infinitely long cylinders with elliptical cross-sections. Erratum. J. Opt. Soc. Am. A **22**(3), 574–575 (2005)
194. Z.S. Wu, Q.K. Yuan, Y. Pen, Z.J. Li, Internal and external electromagnetic fields for on-axis Gaussian beam scattering from a uniaxial anisotropic sphere. J. Opt. Soc. Am. A **26**(8), 1779–1788 (2009)
195. L.A. Ambrosio, H.E. Hernandez-Figueroa, Fundamentals of negative refractive index optical trapping: Forces and radiation pressures exerted by focused Gaussian beams using the generalized Lorenz-Mie theory. Biomed. Opt. Express **1**(5), 1284–1301 (2010)
196. B. Yan, H.Y. Zhang, C.H. Liu, Gaussian beam scattering by a spheroidal particle with an embedded conducting sphere. J. Infrared Millim. Terahertz Waves **32**(1), 126–133 (2011)
197. F.G. Mitri, Optical Bessel beam illumination of a subwavelength prolate gold (Au) spheroid coated by a layer of plasmonic material: Radiation force, spin and orbital torques. J. Phys. Commun. **1**(1), Paper 015 001. (13 pp) (2017)
198. F.G. Mitri, Pushing, pulling and electromagnetic radiation force cloaking by a pair of conducting cylindrical particles. J. Quant. Spectrosc. Radiat. Transf. **206**, 142–150 (2018)

199. S. Gong, R. Li, Y. Liu, J. Zhang, Scattering of a vector Bessel vortex beam by a charged sphere. *J. Quant. Spectrosc. Radiat. Transf.* **215**, 13–24 (2018)
200. H. Li, J. Liu, L. Bai, Z. Wu, Deformations of circularly polarized Bessel vortex beam reflected and transmitted by a uniaxial anisotropic slab. *Appl. Opt.* **57**(25), 7353–7362 (2018)
201. H.Y. Zhang, K. Chen, Z. Huang, M. Wang, Gaussian beam scattering by an infinite cylinder with a spherical inclusion. *J. Quant. Spectrosc. Radiat. Transf.* **245**, Article 106866 (2020)
202. H. Tang, R. Li, S. Gong, B. Wei, L. Yang, Z. Zhu, Y. Wu, F.G. Mitri, Scattering of arbitrary-shaped optical polarized beams by a PEMC. *J. Quant. Spectrosc. Radiat. Transf.* **281**, Article 108101 (2022)
203. C. Yeh, The diffraction of waves by a penetrable ribbon. *J. Math. Phys.* **4**, 65–71 (1963)
204. J.B. Guidt, G. Gouesbet, J.N. Le Toulouzan, An accurate validation of visible infra-red double extinction simultaneous measurements of particle sizes and number-densities by using densely laden standard media. *Appl. Opt.* **29**(7), 1011–1022 (1990)
205. R. Botet, P. Rannou, M. Cabane, Mean-field approximation of Mie scattering by fractal aggregates of identical spheres. *Appl. Opt.* **36**, 8791–8797 (1997)
206. J.A. Lock, Contribution of high-order rainbows to the scattering of a Gaussian laser beam by a spherical particle. *J. Opt. Soc. Am. A* **10**(4), 693–706 (1993)
207. G. Gouesbet, L.A. Ambrosio, Rigorous justification of a localized approximation to encode on-axis Gaussian acoustical waves. *J. Acoust. Soc. Am.* **154**(2), 1062–1072 (2023)
208. G. Gouesbet, L.A. Ambrosio, Description of acoustical Gaussian beams from the electromagnetic Davis scheme of approximations and the on-axis localized approximation. *J. Acoust. Soc. Am.* **155**(2), 1583–1592 (2024)
209. L.A. Ambrosio, G. Gouesbet, Finite series approach for the calculation of beam shape coefficients in ultrasonic and other acoustic scattering. *J. Sound Vib.* **585**, Article 118461 (2024)

Sum Rules and Physical Bounds for a Particulate Slab



Gerhard Kristensson 

1 Introduction

In recent years, many useful sum rules and physical bounds have been developed for electromagnetic applications. Examples of these applications are radar absorbers [22], periodic structures (frequency selective surfaces) [7, 18], passive scatterers [24], antennas [6], metamaterials [5], and high-impedance surfaces [2, 4]. The underlying mathematical theory behind the sum rules is covered by many authors [1, 19]. These references also contain additional, relevant literature on the topic.

In general, the scattered field by a collection of randomly distributed particles consists of a coherent (ensemble averaged) part and an incoherent part. The coherent field is of paramount importance in many radar applications, and here we develop some new bandwidth results based on the average transmitted field by a particulate slab. Specifically, we cover some important consequences of causality and the passivity of the (lossless or lossy) particles, which constitute the cornerstones of the sum rule based on transmission. These sum rules contain both low- and high-frequency expansions of the transmission coefficient. As a bonus and an effect of the sum rule results, we also get a possibility to check the accuracy in the numerical implementation of the theory.

In this chapter, we develop two sum rules and corresponding physical bounds for the coherent transmitted electromagnetic field by a particulate slab. One main question of this chapter is to find a limit or to predict the bandwidth of the coherent transmitted field for a given transmission level and thickness of the slab. To answer this question, we use the obtained physical bounds.

G. Kristensson (✉)
Lund University, Lund, Sweden
e-mail: gerhard.kristensson@telia.com

The underlying theory and the numerical implementation of the coherent reflected and transmitted fields by a random collection of particles in a slab geometry are very well investigated in a series of papers [8, 9, 11, 13, 15, 16].

The calculation of the transmission coefficient by a slab is reviewed in Sect. 2, and in Sect. 3, the analytic properties of the transmission coefficient are analyzed. This section also contains two sum rules and physical bounds of the transmission coefficient of the coherent field. A few numerical examples are presented in Sect. 4, and the results are summarized in Sect. 5. A series of appendices concludes the chapter.

2 Coherent Transmitted Field by a Particulate Slab in the Frequency-Domain

The geometry of the problem is depicted in Fig. 1, and for the application in this chapter, we specialize to an incident plane wave at normal incidence polarized in the x -direction, i.e.,

$$E_i(z) = E_0 \hat{x} e^{ikz}$$

The background medium is characterized by a real permittivity ϵ and permeability μ . The background wavenumber is denoted k . This is the description of the incident field in the frequency domain with angular frequency $\omega = kc$ (background wave velocity c) and suppressed time convention $\exp(-i\omega t)$.

For simplicity and to fix ideas, we assume that all particles are identical and spherical. The material of particles is assumed consist of homogeneous dielectric material. Generalizations to non-spherical particles and optically active materials are possible. The common radius of the particles is denoted a .

The material is confined to the slab $z \in [z_1 - a, z_2 + a]$, and we adopt the notation $d = z_2 - z_1$ and $D = d + 2a$. Note the difference between the slab containing the local origins, $[z_1, z_2]$ (thickness d), and the material confinement, $[z_1 - a, z_2 + a]$ (thickness D), see Fig. 1.

The expressions of the total coherent (average) fields on both sides of the slab for an incident plane wave are [11]

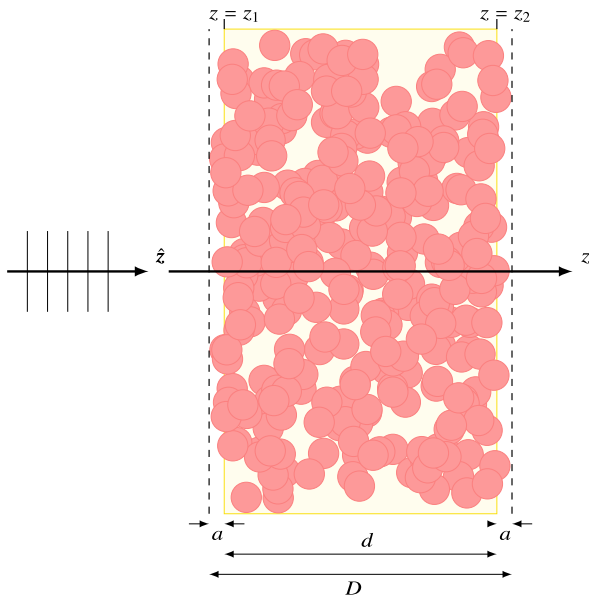
$$\langle E_r(z) \rangle = r(k) E_0 \hat{x} e^{-ikz}, \quad z < z_1 - a, \quad \langle E_t(z) \rangle = t(k) E_0 \hat{x} e^{ikz}, \quad z > z_2 + a$$

where $r(k)$ and $t(k)$ are the reflection and transmission coefficients of the slab, respectively.

The transmission coefficient $t(k)$ of the slab is [11]¹

¹ The reflection coefficient $r(k)$ is computed in a similar manner [11], but we do not give the details here, since focus is on the transmitted field.

Fig. 1 The geometry of the material region $z \in [z_1 - a, z_2 + a]$. In three dimensions, the spheres do not intersect. However, in this two-dimensional graph, some of the projections of the spheres overlap. The yellow region denotes the region of possible locations of local origins, i.e., the interval $[z_1, z_2]$



$$t(k) = 1 + \frac{2\pi n_0}{k^3 E_0} \sum_{\tau=1}^2 \sum_{l=1}^{\infty} i^{-l+\tau-1} \sqrt{\frac{2l+1}{8\pi}} y_{\tau l}(k) \quad (1)$$

where the coefficients $y_{\tau l}(k)$ are

$$y_{\tau l}(k) = k \int_{z_1}^{z_2} e^{-ikz'} f_{\tau l}(z') dz' \quad (2)$$

The number density of the particles, i.e., the number of particles per unit volume, is denoted n_0 . The volume fraction of the particles φ and the number density n_0 are related by [15]

$$\varphi = n_0 \frac{4\pi a^3}{3} \left(1 - \frac{2a}{D}\right) = n_0 \frac{4\pi a^3}{3} \frac{d}{D} \quad (3)$$

Under the assumption of the Quasi Crystalline Approximation (QCA) [17], the coefficients $f_{\tau l}(z)$ satisfy the following system of integral equations [11]:

$$f_{\tau l}(z) = t_{\tau l} i^{l-\tau+1} \sqrt{2\pi(2l+1)} E_0 e^{ikz} + \frac{n_0}{k^2} t_{\tau l} \sum_{\tau'=1}^2 \sum_{l'=1}^{\infty} \int_{z_1}^{z_2} K_{\tau l \tau' l'}(z - z') f_{\tau' l'}(z') dz', \quad z \in [z_1, z_2] \quad (4)$$

where the transition matrix of the spherical particles is denoted $t_{\tau l}$, and the kernel $K_{\tau l \tau' l'}(z)$ has the form [11]

$$K_{\tau l \tau' l'}(z) = \sum_{\lambda=|l-l'|+|\tau-\tau'|}^{l+l'} \mathcal{A}_{\tau l \tau' l' \lambda} I_{\lambda}(-kz, 2ka) \quad (5)$$

where the real numbers $\mathcal{A}_{\tau l \tau' l' \lambda}$ are calculated in [11], and the values are explicitly given in Appendix 5. The integrals $I_l(kz, \eta)$ are ($\zeta = kz, \eta = 2ka$)

$$I_l(\zeta, \eta) = \int_{b(\zeta)}^{\infty} g(\sqrt{x^2 + \zeta^2}) h_l^{(1)}(\sqrt{x^2 + \zeta^2}) P_l(\zeta/\sqrt{x^2 + \zeta^2}) x \, dx, \quad \zeta \in \mathbb{R}$$

where $h_l^{(1)}(z)$ and $P_l(x)$ denote the spherical Hankel functions of the first kind and Legendre polynomials, respectively, and where

$$b(\zeta) = \begin{cases} \sqrt{\eta^2 - \zeta^2}, & |\zeta| \leq \eta \\ 0, & |\zeta| > \eta \end{cases}$$

and $g(kr)$ is the pair correlation function. These integrals have a closed-form solution for the hole correction (HC), i.e., when $g(kr) = H(kr - \eta)$, see [12]. The Heaviside step function is denoted H . The hole correction prevents the particles to overlap or intersect, and it assumes that the distribution of any two particles is independent, which is an approximation of the actual distribution of the particles. The exact expression of the integral $I_l(\zeta, \eta)$ is reviewed in gray box as follows.

Some effective ways to compute the integrals $I_l(\zeta, \eta)$, $\zeta \in \mathbb{R}$, $\eta \in \mathbb{R}$, $l = 0, 1, 2, \dots$, for the hole correction (HC), are presented in [12]. The definition of the integral is:

$$I_l(\zeta, \eta) = \int_0^{\infty} H(\sqrt{x^2 + \zeta^2} - \eta) h_l^{(1)}(\sqrt{x^2 + \zeta^2}) P_l(\zeta/\sqrt{x^2 + \zeta^2}) x \, dx$$

The result is

$$I_l(\zeta, \eta) = i^l e^{-i\zeta}, \quad \zeta \leq -\eta, \quad I_l(\zeta, \eta) = i^{-l} e^{i\zeta}, \quad \zeta \geq \eta$$

and

$$I_l(\zeta, \eta) = -\eta h_{l+1}^{(1)}(\eta) P_l(\zeta/\eta)$$

(continued)

$$+ \sum_{k=0}^{[l/2]} (-1)^k (2l - 4k + 1) h_{l-2k}^{(1)}(\eta) P_{l-2k}(\zeta/\eta), \quad \zeta \in (-\eta, \eta)$$

which is a finite sum of spherical waves.

A useful property of the $I_l(\zeta, \eta)$ function is the parity property: $I_l(-\zeta, \eta) = (-1)^l I_l(\zeta, \eta)$.

The procedure outlined earlier solves the transmission problem for the coherent (average) field exactly and includes all interaction effects between the particles. For a given configuration (geometry, material parameters, and number density) compute the solution $f_{\tau l}(z)$ to the system of integral equations in (4). Proceed by computing the coefficient $y_{\tau l}(k)$ in (2), and, finally, sum the terms in (1) to get the transmission coefficient $t(k)$. This procedure solves the coherent (average) transmitted field of the slab.

2.1 Low-Frequency Behavior

The low frequency expression of the transmission coefficient for spherical particles of radius a as a function of the complex wavenumber $\kappa = k + i\varsigma$, $k \in \mathbb{R}$, $\varsigma \geq 0$ is, see Appendix 5

$$t(\kappa) = 1 + i\kappa H + O(\kappa^2), \quad \kappa \rightarrow 0 \quad (6)$$

where the constant H is

$$H = -9i\varphi D \left(\frac{t_{11}}{4(\kappa a)^3 + 6i\varphi t_{11} \frac{D}{d}} + \frac{t_{21}}{4(\kappa a)^3 + 6i\varphi t_{21} \frac{D}{d}} \right) + H^{\text{Corr}} \quad (7)$$

The real-valued coefficient H^{Corr} is a small correction term due to boundary effects,² see (14) in Appendix 5. In most situations, the correction term has no practical importance, but becomes important when high precision is required, see Sect. 4.2.1. Note that (6) is the low-frequency expression of the transmission coefficient under the assumption of the hole correction (HC) pair correlation function. The Percus–Yevick approximation leads to more complex expressions, but solvable, and these results are reported in a future publication. Note also that the

² In the numerical illustrations in Sect. 4, the contribution is approximately 0.3%.

low-frequency limit in (6) is not the identical to the homogenization limit, which also requires $a/D \rightarrow 0$.

2.1.1 Non-magnetic Dielectric Sphere

If the spherical particles are non-magnetic, $\mu = 1$, and homogeneous with a permittivity ϵ_1 , then $t_{11} = 0$ (to leading order in κa) and to leading order in powers of κa

$$t_{21} = \frac{2i(\kappa a)^3}{3} y + O((\kappa a)^5)$$

where

$$y = \frac{\epsilon_1 - \epsilon}{\epsilon_1 + 2\epsilon}$$

The constant y can also be written in terms of the polarizability γ_e of the particle [14, Sec. 7.9], i.e.,

$$\gamma_e = 4\pi a^3 y$$

To leading order in powers of κa , the transmission coefficients $t(\kappa)$ for spherical, non-magnetic, homogeneous particles with HC is, see (7)

$$H = \frac{3\varphi D}{2} \frac{y}{1 - \varphi y \frac{D}{d}} + H^{\text{Corr}} \quad (8)$$

where the small correction terms H^{Corr} is

$$H^{\text{Corr}} = \frac{24\varphi y D a}{d} \left(\int_0^1 \frac{dt}{4 - \varphi y \frac{D}{d} (2 + 3t - t^3)} - \frac{1}{4 - 4\varphi y \frac{D}{d}} \right)$$

Numerical calculations show that the difference between H in (8), obtained with the hole correction, and the Percus–Yevick approximation is small, see also [15].³ Note that these low-frequency expressions are not the same as the homogenization expressions, which corresponds to letting $a/d \rightarrow 0$ (or $D/d \rightarrow 1$). In the low frequency limit $\kappa \rightarrow 0$, the structure of the slab remains, i.e., $a/d = \text{constant}$, and the medium is not homogeneous. In the homogenization limit, $H^{\text{Corr}} \rightarrow 0$ and $D/d \rightarrow 1$.

³ The low frequency result with the Percus–Yevick approximation is also tractable, and this result is published in a future publication.

3 Analytic Properties of the Transmission Coefficient in the Time-Domain

In this section, the analytic properties of the transmission coefficient $t(k)$ of a slab, filled with passive particles, are investigated. Some relevant literature on the topic is found in [1, 4, 5, 7, 18, 19].

3.1 Causality

In a time-domain setting, a general incident wave of fixed polarization $\hat{\mathbf{x}}$ impinges normally on a slab $z \in [z_1 - a, z_2 + a]$. The background wave velocity is c , and the wavenumber is denoted $k = \omega/c$. We have

$$E_i(z, t) = \hat{\mathbf{x}} \int_{-\infty}^{\infty} A(k) e^{ikc((z-z_1+a)/c-t)} dk, \quad z < z_1 - a$$

This is the description of the incident field in the time domain.

We assume the incident field $E_i(z_1 - a, t) = 0$, $t < 0$ and that $A(k) \in L^2(\mathbb{R})$. This implies by Titchmarsh's theorem [1, 20] that $A(k)$ has an analytic continuation in the upper complex plane $\mathbb{C}_+ = \{z \in \mathbb{C} : \text{Im } z > 0\}$. The amplitude $A(k)$ is not only in $L^2(\mathbb{R})$ for an argument on the real axis. It is also in $L^2(\mathbb{R})$ on every line in the upper half plane parallel to the real axis. The reflected and transmitted fields are

$$\begin{cases} E_r(z, t) = \hat{\mathbf{x}} \int_{-\infty}^{\infty} r(k) A(k) e^{-ikc((z-z_1+a)/c+t)} dk, & z < z_1 - a \\ E_t(z, t) = \hat{\mathbf{x}} \int_{-\infty}^{\infty} t(k) A(k) e^{ikc((z-z_1+a)/c-t)} dk, & z > z_2 + a \end{cases}$$

The fields $E_i(z, t)$, $E_r(z, t)$, and $E_t(z, t)$ are real quantities, which imply

$$A(k) = A^*(-k), \quad r(k) = r^*(-k), \quad t(k) = t^*(-k), \quad k \in \mathbb{R}$$

We assume the wave front velocity in the slab does not exceed the background velocity c . This assumption excludes the case with particles having an internal wave speed higher than the background wave speed. Assuming causality of the reflected and the transmitted fields, i.e., $E_r(z_1 - a, t) = 0$, $t < 0$ and $E_t(z_2 + a, t + D/c) = 0$, $t < 0$, where $D = z_2 - z_1 + 2a$. This implies that $r(k)$ and $t(k)$ have analytic continuations in \mathbb{C}_+ [20].

On the real axis, energy conservation, $|r(k)|^2 + |t(k)|^2 \leq 1$, implies, $|r(k)| \leq 1$ and $|t(k)| \leq 1$. Since our goal in this chapter is to find sum rules for the transmitted field, we concentrate on the transmission coefficient $t(k)$, and leave the reflection coefficient $r(k)$ to future investigations.

In \mathbb{C}_+ , we have by Cauchy's theorem (note that $tA \in L^2(\mathbb{R})$ if $A \in L^2(\mathbb{R})$) [20]

$$t(\kappa)A(\kappa) = \frac{1}{2\pi i} \int_{-\infty}^{\infty} \frac{t(k')A(k')}{k' - \kappa} dk', \quad \kappa \in \mathbb{C}_+$$

and

$$|t(\kappa)| \leq \frac{1}{2\pi |A(\kappa)|} \int_{-\infty}^{\infty} \frac{|A(k')|}{|k' - \kappa|} dk', \quad \kappa \in \mathbb{C}_+$$

Let $\kappa_1 = k_1 + i\varsigma_1$, $\varsigma_1 > 0$, and $A(\kappa) = 1/(\kappa - \kappa_1^*) = 1/(\kappa - k_1 + i\varsigma_1)$, which is a causal transform and belongs to $L^2(\mathbb{R})$, i.e.,

$$|t(\kappa_1)| \leq \frac{\varsigma_1}{\pi} \int_{-\infty}^{\infty} \frac{1}{(k' - k_1)^2 + \varsigma_1^2} dk' = 1, \quad \kappa_1 \in \mathbb{C}_+$$

and we get

$$|t(\kappa)| \leq 1, \quad \kappa \in \mathbb{C}_+ \cup \mathbb{R}$$

3.2 Sum Rule with the Logarithm

Construct a Herglotz function $h_1(\kappa)$, see Appendix 5 for definition, from the transmission coefficient $t(\kappa)$. Following [7], we obtain in an appropriately chosen branch of the logarithm

$$h_1(\kappa) \stackrel{\text{def}}{=} -i \ln \left(t(\kappa) \prod_{n=1}^N \frac{1 - \kappa/\kappa_n^*}{1 - \kappa/\kappa_n} \right)$$

where $\kappa_n, n = 1, 2, \dots, N$, are the zeros (if any) of the transmission coefficient $t(\kappa)$ in the upper complex plane \mathbb{C}_+ , i.e., $\text{Im } \kappa_n > 0, n = 1, 2, \dots, N$. The product is called a Blaschke product [23]. Note that for real k , all terms in the product have modulus 1, i.e.,

$$\left| \frac{1 - k/\kappa_n^*}{1 - k/\kappa_n} \right| = 1, \quad k \in \mathbb{R}$$

and

$$\text{Im } h_1(k) = -\text{Re } \ln \left(t(k) \prod_{n=1}^N \frac{1 - k/\kappa_n^*}{1 - k/\kappa_n} \right) = -\ln |t(k)|, \quad k \in \mathbb{R}$$

and $\text{Im } h_1(k)$ is an even function of the real argument k .

The low-frequency behavior of $h_1(\kappa)$ becomes

$$\begin{aligned} h_1(\kappa) &= -i \left(\ln t(\kappa) + \sum_{n=1}^N \ln(1 - \kappa/\kappa_n^*) - \sum_{n=1}^N \ln(1 - \kappa/\kappa_n) \right) \\ &= -i\kappa \left(iH + \sum_{n=1}^N \left(\frac{1}{\kappa_n} - \frac{1}{\kappa_n^*} \right) \right) + o(\kappa) = \kappa \left(H + 2 \sum_{n=1}^N \text{Im} \frac{1}{\kappa_n} \right) + o(\kappa), \quad \kappa \rightarrow 0 \end{aligned}$$

where H is real and has dimension length. With the notation introduced in Appendix 5, the asymptotic expansion at the origin is of order $N_0 = 1$, and $a_{-1} = a_0 = 0$, $a_1 = H + 2 \sum_{n=1}^N \text{Im} \frac{1}{\kappa_n}$.

At high frequencies, under the assumption that transmission has a limit value t_∞ , we have

$$h_1(\kappa) = o(\kappa), \quad \kappa \rightarrow \infty$$

With the notation of Appendix 5, the asymptotic expansion at infinity is of order $N_\infty = -1$, and $b_1 = 0$.

Consequently, see Theorem C.2 in Appendix 5

$$-\frac{2}{\pi} \int_0^\infty \frac{\ln |t(k)|}{k^2} dk = \frac{2}{\pi} \int_0^\infty \frac{\text{Im } h_1(k)}{k^2} dk = H + 2 \sum_{n=1}^N \text{Im} \frac{1}{\kappa_n} \leq H$$

The integral is well-behaved. This is the exact value of the sum rule. The sum rule as an integral in the wavelength $\lambda = 2\pi/k$ reads⁴

$$\int_0^\infty \ln \frac{1}{|t(\lambda)|} d\lambda = - \int_0^\infty \ln |t(\lambda)| d\lambda = -2\pi \int_0^\infty \frac{\ln |t(k)|}{k^2} dk \leq \pi^2 H \quad (9)$$

In the next subsection, we use this sum rule to find bounds on the product of the bandwidth and the prescribed transmission rate.

3.2.1 Physical Bound

Estimate the left-hand side of the wavelength integral in (9) as follows. For a given transmission level $t_0 \in (0, 1]$, let $I(t_0)$ be the interval of wavelength where transmission is less than t_0 , i.e., $|t(\lambda)| \leq t_0 \leq 1$, $\lambda \in I(t_0)$. The interval $I(t_0)$ can

⁴ We make a small abuse in notation of the transmission coefficient t as the same function in both k and λ .

consist of a union of disjoint parts. In most situations, it is a connected interval. Then, since the integrand in (9) is a positive function, a crude estimate is

$$|I(t_0)| \ln \frac{1}{t_0} \leq \int_{I(t_0)} \ln \frac{1}{|t(\lambda)|} d\lambda \leq \int_0^\infty \ln \frac{1}{|t(\lambda)|} d\lambda \leq \pi^2 H$$

where $|I(t_0)|$ denotes the length of the interval $I(t_0)$. We get the physical bound

$$|I(t_0)| \leq \frac{\pi^2 H}{\ln \frac{1}{t_0}} = \frac{\pi^2 H}{|\ln t_0|} \quad (10)$$

A similar bound for a periodic array has been reported in [7]. A numerical example of this physical bound is presented in Sect. 4.1. In most practical situations, $|I(t_0)|$ denotes the largest wavelength for which $|t(\lambda)| \leq t_0$, see Sect. 4.1.

3.3 Sum Rule with Pulse Herglotz Function

A more elaborate Herglotz function is the pulse Herglotz function [19], i.e.,

$$h_\Delta(z) = -\frac{1}{\pi} \int_{-\Delta}^{\Delta} \frac{1}{z-t} dt = \frac{1}{\pi} \ln \frac{z-\Delta}{z+\Delta}, \quad \text{Im } z > 0$$

where $\Delta > 0$, and the branch cut of the logarithm is assumed along the negative real axis. Details on this function are presented in Appendix 5.

The asymptotes of $h_\Delta(z)$ are

$$h_\Delta(z) = \begin{cases} i - \frac{2z}{\pi\Delta} + O(z^2), & z \hat{\rightarrow} 0 \\ -\frac{2\Delta}{z\pi} + O(z^{-2}), & z \hat{\rightarrow} \infty \end{cases}$$

The symbol $z \hat{\rightarrow} 0$ stands for the non-tangential limit $|z| \rightarrow 0$ within some Stoltz domain $\{z \in \mathbb{C}_+ : \theta \leq \arg(z) \leq \pi - \theta\}$ with the angle $\theta \in (0, \pi/2]$. For more details, see Appendix 5.

The imaginary part of $h_\Delta(z)$ is non-negative and bounded by unity in the upper half plane \mathbb{C}_+ . Specifically, the inner part of the circle $|z| = \Delta$ in the upper complex half plane maps to $1/2 < \text{Im } h_\Delta(z) < 1$, see Fig. 13. In the region outside the circle $|z| = \Delta$ in the upper complex half plane, we have $0 < \text{Im } h_\Delta(z) < 1/2$.

The Möbius transformation

$$w(z) = i \frac{1+z}{1-z} \quad \Leftrightarrow \quad z(w) = \frac{w-i}{w+i}$$

maps the unit circle to the upper complex half plane. Moreover, a circle centered at the origin with radius $t_0 \in (0, 1]$ in the z -plane is mapped to a circle centered at $w_0 = i(1 + t_0^2)/(1 - t_0^2)$ with radius $r_0 = 2t_0/(1 - t_0^2)$ in the w -plane.

Define the Herglotz function $h_2(\kappa) \stackrel{\text{def}}{=} h_\Delta(w(t(\kappa)))$. The asymptotes of $w(t(\kappa))$ are

$$w(t(\kappa)) = \begin{cases} -\frac{2}{\kappa H} + O(1), & \kappa \hat{\rightarrow} 0 \\ i\frac{1+t_\infty}{1-t_\infty} + O(\kappa^{-1}), & \kappa \hat{\rightarrow} \infty \end{cases}$$

where t_∞ is the assumed high frequency limit of the transmission coefficient, and

$$h_2(\kappa) \stackrel{\text{def}}{=} h_\Delta(w(t(\kappa))) = \begin{cases} \frac{\kappa \Delta H}{\pi} + O(\kappa^2), & \kappa \hat{\rightarrow} 0 \\ o(\kappa), & \kappa \hat{\rightarrow} \infty \end{cases}$$

Note that $w(t(-k)) = w(t^*(k)) = -w^*(t(k))$ and $h_2(-k) = h_\Delta(-w^*(t(k)))$ for $k \in \mathbb{R}$. Since $h_\Delta(-z^*) = -h_\Delta^*(z)$, we get $h_2(-k) = -h_2^*(k)$ for $k \in \mathbb{R}$. With the notation in Appendix 5, the asymptotic expansion at the origin is of order $N_0 = 1$, and $a_{-1} = a_0 = 0$, $a_1 = \Delta H/\pi$, and the asymptotic expansion at infinity is of order $N_\infty = -1$, and $b_1 = 0$.

We now determine the value of the scale factor $\Delta = \Delta(t_0)$. The aim is to find bounds on the bandwidth for transmission $|t| \leq t_0 \in (0, 1]$. The connection between parameter $\Delta(t_0)$ and the suggested threshold $|t| = t_0 \leq 1$ is found by

$$\Delta(t_0) = \frac{1+t_0^2}{1-t_0^2} + \frac{2t_0}{1-t_0^2} = \frac{1+t_0}{1-t_0} > 0$$

This choice of $\Delta(t_0)$ maps the circle $|t| \leq t_0$ to a circle in the w/Δ -plane centered at $i(1+t_0^2)/(1+t_0)^2$ with radius $2t_0/(1+t_0)^2$ (green discs in Fig. 2).

Consequently, see Theorem C.2 in Appendix 5

$$\frac{2}{\pi} \int_0^\infty \frac{\text{Im } h_2(k)}{k^2} dk = \frac{\Delta H}{\pi} = \frac{1+t_0}{1-t_0} \frac{H}{\pi} \quad (11)$$

The integral is well-behaved. The sum rule as an integral in the wavelength $\lambda = 2\pi/k$ reads

$$\int_0^\infty \text{Im } h_2(\lambda) d\lambda = 2\pi \int_0^\infty \frac{\text{Im } h_2(k)}{k^2} dk = \pi \Delta H = \pi \frac{1+t_0}{1-t_0} H \quad (12)$$

This is the exact value of the sum rule with the pulse Herglotz function.

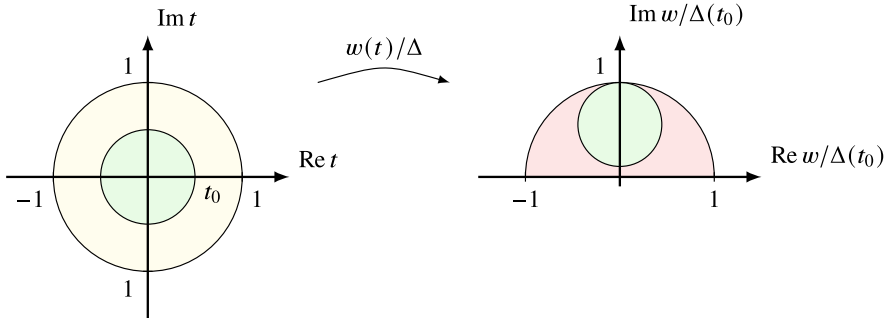


Fig. 2 The Möbius transform $w(t)/\Delta$. The green circle is the image of $|t(k)| \leq t_0 = 0.5$

In the next subsection, we use this sum rule to find a bound on the bandwidth given a certain transmission level t_0 . The sum rule is exact, and it can be used to verify the numerical computations of the transmission coefficient. In fact, for a given particle and transmission level t_0 , the right-hand side of (12) is given, and the integral on the left-hand side is determined.

3.3.1 Physical Bound

We now apply the exact sum rule in (12) to get a physical bound on the bandwidth of the transmission coefficient, given a certain threshold $t_0 \in (0, 1]$. Let the wavelength interval $I(t_0)$ denote the interval where $|t| \leq t_0$. The interval $I(t_0)$ can consist of a union of disjoint parts. In this interval, the integrand in the sum rule is larger than $1/2$ by construction, and we get by estimating the integral

$$\frac{|I(t_0)|}{2} \leq \int_{I(t_0)} \operatorname{Im} h_2(\lambda) \, d\lambda \leq \int_0^\infty \operatorname{Im} h_2(\lambda) \, d\lambda = \pi \frac{1+t_0}{1-t_0} H$$

where $|I(t_0)|$, which is related to the bandwidth of the problem, denotes the length of the interval $I(t_0)$. In summary, we get

$$|I(t_0)| \leq 2\pi \frac{1+t_0}{1-t_0} H \quad (13)$$

A numerical example of this physical bound is presented in Sect. 4.2.

4 Numerical Results

In a series of numerical examples, we illustrate the results in this chapter. Examples of both physical bounds and numerical accuracy are presented.

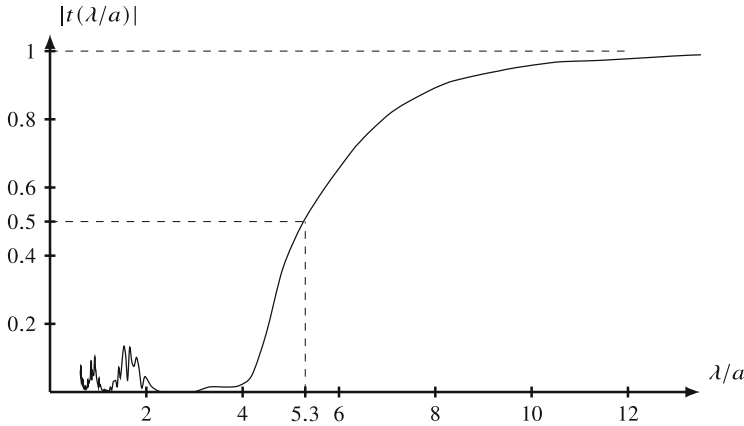


Fig. 3 The absolute value of the transmission coefficient t as a function of the normalized wavelength λ/a for a slab of thickness $D/a = 20$, volume fraction $\varphi = 15\%$, permittivity $\epsilon_1/\epsilon = 4$, and permeability $\mu_1/\mu = 1$

4.1 First Physical Bound

We start with the physical bound obtained in Sect. 3.2. In Figs. 3 and 4, the modulus and the negative logarithm of the modulus of the transmission coefficient, respectively, are depicted as a function of the scaled wavelength λ/a . In all figures⁵ presented in this chapter, the dielectric, spherical particles of radius a have permittivity $\epsilon_1/\epsilon = 4$, and permeability $\mu_1/\mu = 1$, the slab has thickness $D/a = 20$, and the volume fraction is $\varphi = 15\%$.

The value of the transmission coefficients in the complex plane as a function of λ/a along the curve is shown in Fig. 5. We notice that the curve circles around the origin, which indicates that there are several zeros in the upper half plane [10, Th. 4.10a]. The exact behavior at the origin is hard to ensure due to limited numerical precision at low transmission levels.

The area under the entire curve in Fig. 4 is approximately $20.8a$ while $\pi^2 H = 24.1a$. The gap between these two numbers indicates that there are zeros in the upper complex half-plane. If we integrate over frequencies instead for over the wavelength, i.e.,

$$-\int_0^\infty \frac{\ln |t(k)|}{k^2} dk \leq \frac{\pi H}{2}$$

we obtain by numerical integration of the integral on the left-hand side $3.45a$, which should be compared with the value $\pi H/2 = 3.84a$.

⁵ Figure 9 is an exception.

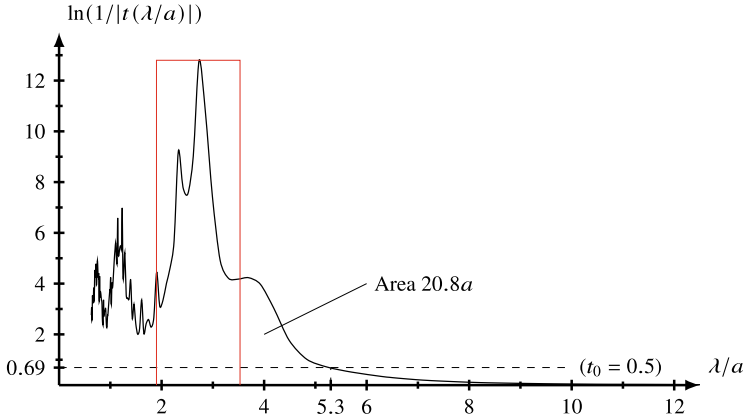
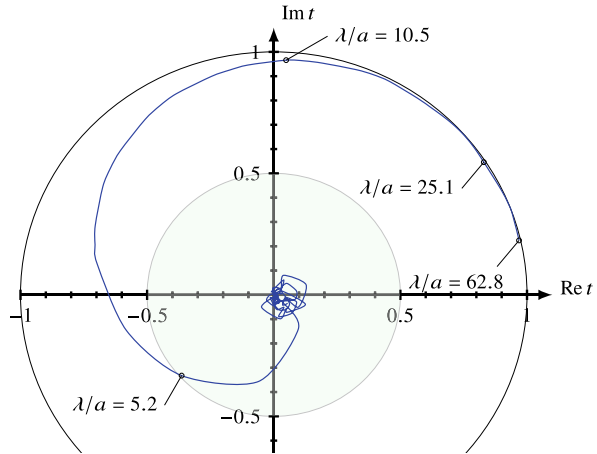


Fig. 4 The function $\ln(1/|t|)$ as a function of the normalized wavelength λ/a for a slab of thickness $D/a = 20$, volume fraction $\varphi = 15\%$, permittivity $\epsilon_1/\epsilon = 4$, and permeability $\mu_1/\mu = 1$. The red box has the same area as the area under the curve ($\approx 20.8a$)

Fig. 5 The complex-valued transmission coefficient, t , in the complex plane as a function of the wavelength λ/a for a slab of thickness $D/a = 20$ and volume fraction $\varphi = 15\%$. The curve starts at $\lambda/a = 0$ circling the origin and ends at 1 as $\lambda/a \rightarrow \infty$. Green disc shows the transmission rate $|t| \leq t_0 = 0.5$



The bandwidth of the peak in Fig. 4 can be estimated by equating a box (red box in the figure) such that the area under the entire curve and that of the box are the same ($\approx 20.8a$). More examples of estimating the bandwidth are presented in e.g., [24]. The length of the wavelength interval of the red box is 1.63 in units of a .

At a transmission threshold of $t_0 = 0.5$, the right-hand side in (10) is calculated to $\pi^2 H / |\ln t_0| = 34.8a$. This value is much larger than the numerical value $|I(t_0)| \approx 5.3a$ obtained in the figure. However, this comes to no surprise, since the sum rule has to hold for all possible configurations, which have the same value of H and t_0 . This illustration shows that our configuration is far from the extreme value.

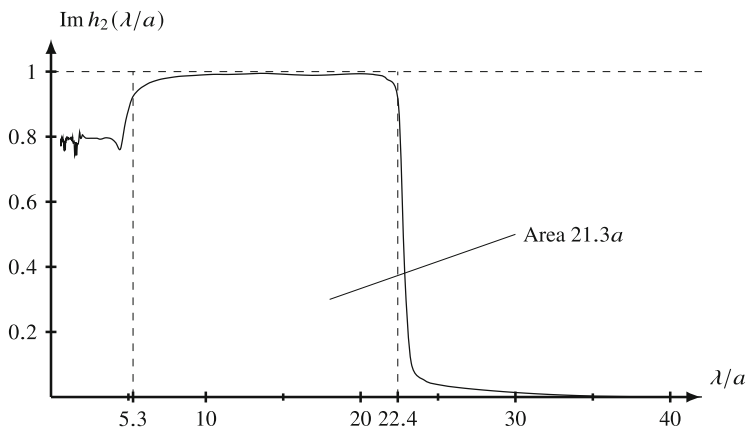


Fig. 6 The function $\text{Im } h_2(\lambda/a)$ for $t_0 = 0.5$ as a function of the normalized wavelength λ/a for a slab of thickness $D/a = 20$, volume fraction $\varphi = 15\%$, permittivity $\epsilon_1/\epsilon = 4$, and permeability $\mu_1/\mu = 1$

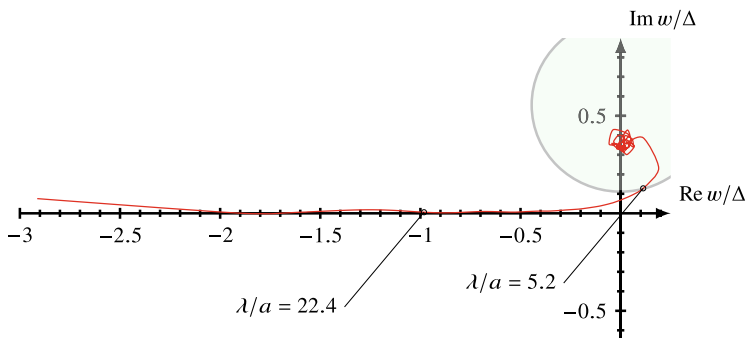


Fig. 7 The components of the complex-valued w/Δ for $t_0 = 0.5$, in the complex plane as a function of the wavelength λ/a for a slab of thickness $D/a = 20$ and volume fraction $\varphi = 15\%$. The curve starts at $\lambda/a = 0$ inside the green circle and ends at $-\infty + i/3$ as $\lambda/a \rightarrow \infty$

4.2 Second Physical Bound

The Herglotz function, $h_2(\kappa)$, defined in Sect. 3.3, is depicted as a function of λ/a in Fig. 6 for the same material data and geometry as in Sect. 4.1. Again, the transmission threshold is $t_0 = 0.5$. The argument $w(t(\kappa))/\Delta$ of the Herglotz function is shown in Fig. 7. Note that the argument in the Herglotz function stays above the negative real axis as $\lambda/a \rightarrow \infty$.

An upper bound of the wavelength interval from (13) is $2\pi H\Delta(t_0) = 46.1a$, which is larger than the limit with the first physical bound in Sect. 3.2, and much larger than the value $|I(t_0)| \approx 5.3a$ obtained from the numerical example. Again,

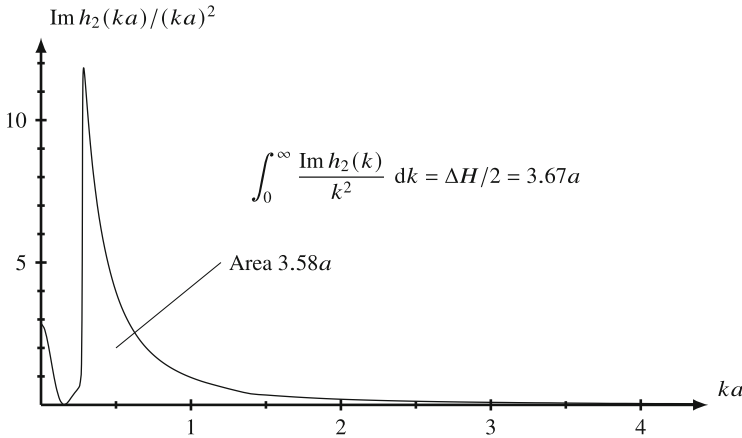


Fig. 8 The function $\text{Im } h_2(ka)/(ka)^2$ for $t_0 = 0.5$ as a function of frequency ka for a slab of thickness $D/a = 20$, volume fraction $\varphi = 15\%$, permittivity $\epsilon_1/\epsilon = 4$, and permeability $\mu_1/\mu = 1$

this is not surprising, since the sum rule holds for all possible configurations having the same value of H and t_0 .

4.2.1 Numerical Accuracy Tested

Numerical integration of the area under the entire curve in Fig. 6 gives a value of approximately $21.3a$. This value is smaller than the exact value $\pi H \Delta(t_0) = 23.0a$, which can be explained by loss of numerical precision at higher frequencies or the choice of numerical integration by the trapezoidal rule. As an alternative, we instead integrate over normalized frequency $x = ka$, see (12), i.e.,

$$\int_0^\infty \frac{\text{Im } h_2(x)}{x^2} dx = \frac{\Delta(t_0)H}{2a}$$

This form of the sum rule weights low frequencies higher and higher frequencies less, see Fig. 8. Low-frequency data have higher numerical precision, which guarantee a more accurate test of the sum rule. With the same data as aforementioned, the right-hand side is $\Delta(t_0)H/2 = 3.67a$, and the left-hand side is by numerical integration approximately $3.58a$. This is less than a 3% discrepancy, which is sufficient for most applications. A numerical test with different transmission levels $t_0 \in (0, 1)$ shows that the agreement gets better for higher values of t_0 .

However, since the sum rule aforementioned is an exact identity, possible sources of error are important to identify. Some potential sources of this discrepancy are listed in Table 1. The integration is performed by both the trapezoidal and Simpson's rule over the interval $ka \in [0.00001, 8]$ (nonuniform points), which seems to suffice. Moreover, potential convergence problems in solving (4) have been eliminated by a

Table 1 Possible explanations of the discrepancies in the sum rule

Possible errors
Missing parts in the integration interval $[0, \infty)$
Inappropriate numerical quadrature
Numerical solution of the system of integral equations
Correct pair correlation function—boundary effects
Effect of QCA

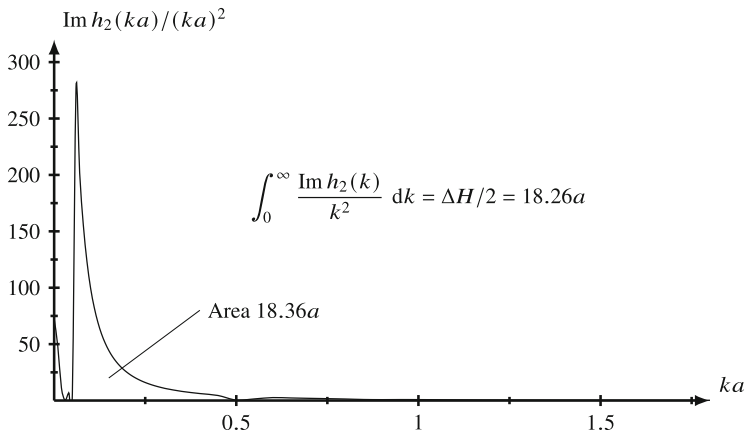


Fig. 9 The function $\text{Im } h_2(ka)/(ka)^2$ for $t_0 = 0.5$ as a function of frequency ka for a slab of thickness $D/a = 100$, volume fraction $\varphi = 15\%$, permittivity $\epsilon_1/\epsilon = 4$, and permeability $\mu_1/\mu = 1$

comparison with an independent implementation [8]. Hence, with some confidence, we can eliminate these causes to the discrepancy.

However, a more likely cause, we find in the choice of the pair correlation function $g(r)$. We assume the pair correlation function (the Percus–Yevick approximation is employed) only depends on the distance between two particles, which definitely is an approximation of the correct pair correlation function depending on two points, i.e., $g(\mathbf{r}, \mathbf{r}')$. Specifically, close to the boundary, there are effects that are not included in our choice of pair correlation function. The importance of these boundary effects is hard to estimate. A thicker slab should make these effects smaller, since then the boundary is a smaller portion of the slab geometry. Indeed, a computation with a thicker slab, $D/a = 100$ (all other parameters the same), confirms this conjecture, and the error is now 0.6%, see Fig. 9.

The importance of the correct pair correlation is further emphasized if we compare the sum rule evaluated by the hole correction (HC) and the Percus–Yevick approximation (PY). The result is displayed in Fig. 10, where numerical integration with the hole correction results in a large error in the sum rule. The hole correction seems not to generate a transmission coefficient that complies with energy conservation [15], which seems to be the cause of the this huge discrepancy.

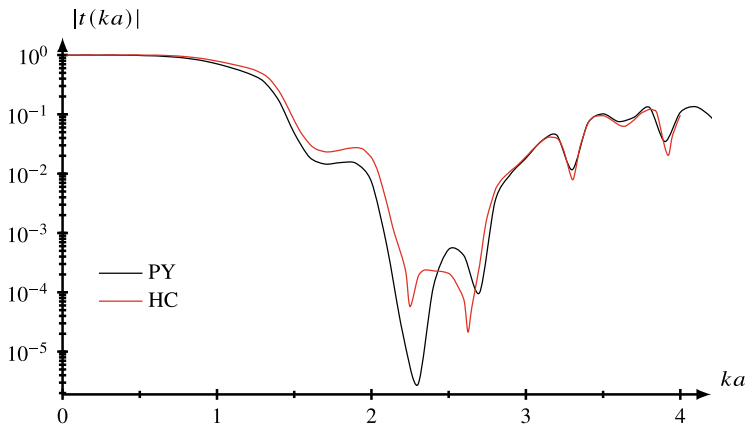


Fig. 10 The transmission coefficient for the hole correction (HC) and Percus–Yevick approximation as a function of frequency ka for a slab of thickness $D/a = 20$, volume fraction $\varphi = 15\%$, permittivity $\epsilon_1/\epsilon = 4$, and permeability $\mu_1/\mu = 1$

Finally, the Quasi Crystalline Approximation is assumed in the derivation of the system of integral equations in (4). How this approximation affects the result, and whether the sum rule can be a test on this assumption is an open question.

5 Discussion and Conclusions

Physical bounds on bandwidth and slab thicknesses are important tools in the design of slab configurations with specific transmission performance. In this chapter, we have developed two different sum rules for the transmission coefficient. The particles of the slab are assumed to be passive, and the system has to satisfy a causality condition. The sum rules are then employed to obtain physical bounds on a combination of bandwidth and transmission rates. The exact sum rule also serves as an independent check on the numerical precision of the numerical calculations. Numerical illustrations show that the physical bound is not obtained, and these examples show that the constructions are far from extreme designs. The test of numerical accuracy shows that the precision is satisfactory.

Acknowledgments The analysis presented in this chapter was made possible by support of the Swedish Defence Research Agency, FOI, which is gratefully acknowledged.

Appendix A: The Expansion Coefficients

In this appendix, the coefficients $\mathcal{A}_{\tau l \tau' l' \lambda}$ in (5) are reviewed [11]. We have

$$\mathcal{A}_{\tau l \tau' l' \lambda} = -2\pi \begin{matrix} \tau'=1 & \tau'=2 \\ \tau=1 & \tau=2 \end{matrix} \begin{pmatrix} C_{ll'\lambda} & -D_{ll'\lambda} \\ D_{ll'\lambda} & C_{ll'\lambda} \end{pmatrix}$$

where

$$C_{ll'\lambda} = \frac{1}{2} i^{l'-l+\lambda} (2\lambda+1) \sqrt{\frac{(2l+1)(2l'+1)}{l(l+1)l'(l'+1)}} \\ \times \begin{pmatrix} l & l' & \lambda \\ 0 & 0 & 0 \end{pmatrix} \begin{pmatrix} l & l' & \lambda \\ 1 & -1 & 0 \end{pmatrix} [l(l+1) + l'(l'+1) - \lambda(\lambda+1)]$$

$$D_{ll'\lambda} = \frac{1}{2} i^{l'-l+\lambda+1} (2\lambda+1) \sqrt{\frac{(2l+1)(2l'+1)}{l(l+1)l'(l'+1)}} \\ \times \begin{pmatrix} l & l' & \lambda-1 \\ 0 & 0 & 0 \end{pmatrix} \begin{pmatrix} l & l' & \lambda \\ 1 & -1 & 0 \end{pmatrix} \sqrt{\lambda^2 - (l-l')^2} \sqrt{(l+l'+1)^2 - \lambda^2}$$

and where $\begin{pmatrix} \cdot & \cdot & \cdot \\ \cdot & \cdot & \cdot \end{pmatrix}$ denotes Wigner's 3j symbol [3]. Both $C_{ll'\lambda}$ and $D_{ll'\lambda}$ are real numbers, due to the properties of the Wigner's 3j symbol. The first non-zero ones are

$$C_{11\lambda} = -\delta_{\lambda,0} + \frac{1}{2}\delta_{\lambda,2}, \quad D_{11\lambda} = \frac{3}{2}\delta_{\lambda,1}$$

Appendix B: Low Frequency Solution

In this appendix, we solve the system of integral equations in (4) in the limit of small $\varepsilon = ka$ for the HC correction under the constraint that d/a (or D/a) is constant.⁶ Only $l = 1$ and $m = 1$ contribute in this limit. Moreover, a polarization of the incident wave in the \hat{x} direction engages only $\{\tau, \sigma\} = \{1, o\}, \{2, e\}$. Therefore, in

⁶ The low frequency behavior under the Percus–Yevick approximation is also solvable, and the results are presented in a future publication.

the analysis, we suppress the σ , m , and l indices, and the equations to solve are [11] ($\zeta = kz$, $\zeta_1 = kz_1$, $\zeta_2 = kz_2$, $kd = \zeta_2 - \zeta_1$):

$$f_\tau(\zeta) = t_{\tau 1} a_\tau e^{i\zeta} + \frac{n_0 t_{\tau 1}}{k^3} \sum_{\tau'=1}^2 \int_{\zeta_1}^{\zeta_2} K_{\tau\tau'}(\zeta - \zeta') f_{\tau'}(\zeta') d\zeta', \quad \zeta \in [\zeta_1, \zeta_2]$$

where

$$a_{\tau 1} = -i^{-\tau} \sqrt{6\pi} E_0$$

and [11]

$$K_{\tau\tau'}(\zeta) = \begin{matrix} \tau'=1 & \tau'=2 \\ \tau=2 \end{matrix} \begin{pmatrix} 2\pi I_0(\zeta, 2\varepsilon) - \pi I_2(\zeta, 2\varepsilon) & -3\pi I_1(\zeta, 2\varepsilon) \\ 3\pi I_1(\zeta, 2\varepsilon) & 2\pi I_0(\zeta, 2\varepsilon) - \pi I_2(\zeta, 2\varepsilon) \end{pmatrix}$$

The explicit values of $I_l(\zeta, \varepsilon)$, $l = 0, 1, 2$ are [11]

$$I_0(\zeta, 2\varepsilon) = \begin{cases} e^{-i\zeta}, & \zeta \leq -2\varepsilon \\ e^{2i\varepsilon} P_0\left(\frac{\zeta}{2\varepsilon}\right), & -2\varepsilon < \zeta < 2\varepsilon \\ e^{i\zeta}, & \zeta \geq 2\varepsilon \end{cases}$$

$$I_1(\zeta, 2\varepsilon) = \begin{cases} ie^{-i\zeta}, & \zeta \leq -2\varepsilon \\ -ie^{2i\varepsilon} P_1\left(\frac{\zeta}{2\varepsilon}\right), & -2\varepsilon < \zeta < 2\varepsilon \\ -ie^{i\zeta}, & \zeta \geq 2\varepsilon \end{cases}$$

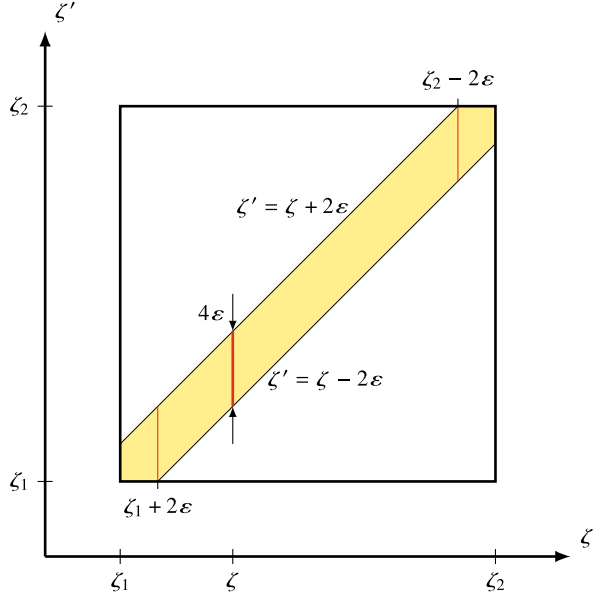
$$I_2(\zeta, 2\varepsilon) = \begin{cases} -e^{-i\zeta}, & \zeta \leq -2\varepsilon \\ e^{2i\varepsilon} \frac{iP_0\left(\frac{\zeta}{2\varepsilon}\right) - (i + 2\varepsilon)P_2\left(\frac{\zeta}{2\varepsilon}\right)}{2\varepsilon}, & -2\varepsilon < \zeta < 2\varepsilon \\ -e^{i\zeta}, & \zeta \geq 2\varepsilon \end{cases}$$

where $P_l(x)$ denotes the Legendre polynomials. The dominant terms of the kernel in the interval (inside the hole correction) $|\zeta| \leq 2\varepsilon$ are

$$K_{\tau\tau'}(\zeta) = \frac{\pi}{2i\varepsilon} \begin{matrix} \tau'=1 & \tau'=2 \\ \tau=2 \end{matrix} \begin{pmatrix} P_0\left(\frac{\zeta}{2\varepsilon}\right) - P_2\left(\frac{\zeta}{2\varepsilon}\right) + O(\varepsilon) & O(\varepsilon) \\ O(\varepsilon) & P_0\left(\frac{\zeta}{2\varepsilon}\right) - P_2\left(\frac{\zeta}{2\varepsilon}\right) + O(\varepsilon) \end{pmatrix}$$

and outside the hole correction the terms are of the order $O(1)$ and therefore contribute to the solution with higher-order powers in ε .

Fig. 11 The domain of integration in ζ' with the hole correction in yellow



Divide the integration interval $[\zeta_1, \zeta_2]$ in a singular hole correction part $\zeta - \zeta' \in [-2\epsilon, 2\epsilon]$ and the remaining interval outside the hole correction. The integrals over the latter interval contain higher order contributions in ϵ and are omitted. We have to leading order

$$f_\tau(\zeta) = t_{\tau 1} a_\tau e^{i\zeta} + \frac{n_0 t_{\tau 1}}{k^3} \int_{|\zeta - \zeta'| \leq 2\epsilon} K_{\tau\tau}(\zeta - \zeta') f_\tau(\zeta') d\zeta', \quad \zeta \in [\zeta_1, \zeta_2], \quad \tau = 1, 2$$

where the domain of integration is depicted in yellow in Fig. 11.

In the integral, we replace $f_{\tau'}(\zeta') \rightarrow f_{\tau'}(\zeta)$ —the difference contributes with higher order terms in ϵ . We have

$$f_\tau(\zeta) = t_{\tau 1} a_\tau e^{i\zeta} + \frac{n_0 t_{\tau 1}}{k^3} f_\tau(\zeta) \int_{|\zeta - \zeta'| \leq 2\epsilon} K_{\tau\tau}(\zeta - \zeta') d\zeta', \quad \zeta \in [\zeta_1, \zeta_2], \quad \tau = 1, 2$$

Integration over the yellow area in Fig. 11 contributes with one integral $I_0(\zeta)$ and two integrals $I_1(\zeta)$, $I_2(\zeta)$ at the boundary. We obtain

$$\begin{aligned} I_0(\zeta) &\stackrel{\text{def}}{=} \frac{\pi}{2i\epsilon} \int_{\zeta-2\epsilon}^{\zeta+2\epsilon} P_0\left(\frac{\zeta - \zeta'}{2\epsilon}\right) - P_2\left(\frac{\zeta - \zeta'}{2\epsilon}\right) d\zeta' = -i\pi \int_{-1}^1 P_0(t) - P_2(t) dt \\ &= -2i\pi, \quad \zeta_1 + 2\epsilon \leq \zeta \leq \zeta_2 - 2\epsilon \end{aligned}$$

The two remaining parts at the boundaries of the slab are

$$\begin{aligned}
 I_1(\zeta) &\stackrel{\text{def}}{=} \frac{\pi}{2i\varepsilon} \int_{\zeta_1}^{\zeta+2\varepsilon} P_0\left(\frac{\zeta-\zeta'}{2\varepsilon}\right) - P_2\left(\frac{\zeta-\zeta'}{2\varepsilon}\right) d\zeta' \\
 &= -\frac{i\pi}{2} \left\{ 3\frac{\zeta-\zeta_1}{2\varepsilon} + 2 - \left(\frac{\zeta-\zeta_1}{2\varepsilon}\right)^3 \right\}, \quad \zeta_1 \leq \zeta \leq \zeta_1 + 2\varepsilon
 \end{aligned}$$

and

$$\begin{aligned}
 I_2(\zeta) &\stackrel{\text{def}}{=} \frac{\pi}{2i\varepsilon} \int_{\zeta-2\varepsilon}^{\zeta_2} P_0\left(\frac{\zeta-\zeta'}{2\varepsilon}\right) - P_2\left(\frac{\zeta-\zeta'}{2\varepsilon}\right) d\zeta' \\
 &= -\frac{i\pi}{2} \left\{ 2 - 3\frac{\zeta-\zeta_2}{2\varepsilon} + \left(\frac{\zeta-\zeta_2}{2\varepsilon}\right)^3 \right\}, \quad \zeta_2 - 2\varepsilon \leq \zeta \leq \zeta_2
 \end{aligned}$$

The set of integral equations simplifies to leading order to

$$f_\tau(\zeta) = t_{\tau 1} a_\tau e^{i\zeta} + \frac{n_0 t_{\tau 1}}{k^3} f_\tau(\zeta) \begin{cases} I_1(\zeta), & \zeta_1 \leq \zeta \leq \zeta_1 + 2\varepsilon \\ I_0(\zeta), & \zeta_1 + 2\varepsilon \leq \zeta \leq \zeta_2 - 2\varepsilon \\ I_2(\zeta), & \zeta_2 - 2\varepsilon \leq \zeta \leq \zeta_2 \end{cases}$$

with solutions

$$f_\tau(\zeta) = \begin{cases} \frac{t_{\tau 1} a_\tau e^{i\zeta}}{1 - C_\tau I_1(\zeta)}, & \zeta_1 \leq \zeta \leq \zeta_1 + 2\varepsilon \\ \frac{t_{\tau 1} a_\tau e^{i\zeta}}{1 - C_\tau I_0(\zeta)}, & \zeta_1 + 2\varepsilon \leq \zeta \leq \zeta_2 - 2\varepsilon \\ \frac{t_{\tau 1} a_\tau e^{i\zeta}}{1 - C_\tau I_2(\zeta)}, & \zeta_2 - 2\varepsilon \leq \zeta \leq \zeta_2 \end{cases}$$

where the constant C_τ is

$$C_\tau = \frac{n_0 t_{\tau 1}}{k^3} = \frac{3\varphi t_{\tau 1}}{4\pi\varepsilon^3} \frac{D}{d}$$

Finally, we can calculate y_τ in (2) for $l = 1$.

$$\begin{aligned}
 y_\tau &= \int_{\zeta_1}^{\zeta_2} f_\tau(\zeta) e^{-i\zeta} d\zeta \\
 &= -i^{-\tau} t_{\tau 1} \sqrt{6\pi} E_0 \left(\int_{\zeta_1}^{\zeta_1+2\varepsilon} \frac{d\zeta}{1 - C_\tau I_1(\zeta)} + \frac{kd - 4\varepsilon}{1 + 2i\pi C_\tau} + \int_{\zeta_2-2\varepsilon}^{\zeta_2} \frac{d\zeta}{1 - C_\tau I_2(\zeta)} \right)
 \end{aligned}$$

$$\begin{aligned}
&= -i^{-\tau} t_{\tau 1} \sqrt{6\pi} E_0 \left(\frac{kd - 4\varepsilon}{1 + 2i\pi C_{\tau}} + 4\varepsilon \int_0^1 \frac{dt}{1 + \frac{i\pi}{2} C_{\tau} (2 + 3t - t^3)} \right) \\
&= -i^{-\tau} t_{\tau 1} \sqrt{6\pi} \varepsilon E_0 \left(\frac{d/a}{1 + 2i\pi C_{\tau}} + A_{\tau}^{\text{Corr}} \right)
\end{aligned}$$

where the correction term A_{τ}^{Corr} is

$$A_{\tau}^{\text{Corr}} = 4 \int_0^1 \frac{dt}{1 + \frac{i\pi}{2} C_{\tau} (2 + 3t - t^3)} - \frac{4}{1 + 2i\pi C_{\tau}}$$

The remaining integral in this expression can be solved analytically by finding the roots of the denominator and a partial fraction of the integrand. In an numerical illustration, it is more convenient to numerically compute the integral than to try to find the analytic solution.

The constant H in (6) can now be determined from the low-frequency limit of the transmission coefficient in (1). The result is

$$\begin{aligned}
H &= \frac{2\pi n_0}{ik^4 E_0} \sum_{\tau=1}^2 i^{\tau-2} \sqrt{\frac{3}{8\pi}} y_{\tau} = \frac{3\pi n_0}{ik^4} \sum_{\tau=1}^2 t_{\tau 1} \varepsilon \left(\frac{d/a}{1 + 2i\pi C_{\tau}} + A_{\tau}^{\text{Corr}} \right) \\
&= -3i\pi a \sum_{\tau=1}^2 C_{\tau} \left(\frac{d/a}{1 + 2i\pi C_{\tau}} + A_{\tau}^{\text{Corr}} \right) = H^{\text{Appr}} + H^{\text{Corr}}
\end{aligned}$$

where

$$\left\{ \begin{aligned} H^{\text{Appr}} &= -3i\pi \sum_{\tau=1}^2 \frac{C_{\tau} d}{1 + 2i\pi C_{\tau}} = -9i\varphi D \sum_{\tau=1}^2 \frac{t_{\tau 1}}{4\varepsilon^3 + 6i\varphi t_{\tau 1} \frac{D}{d}} \\ H^{\text{Corr}} &= -3i\pi a \sum_{\tau=1}^2 C_{\tau} A_{\tau}^{\text{Corr}} \\ &= -36i\varphi \frac{D}{d} a \sum_{\tau=1}^2 \left(\int_0^1 \frac{t_{\tau 1} dt}{4\varepsilon^3 + \frac{3i}{2}\varphi t_{\tau 1} \frac{D}{d} (2 + 3t - t^3)} - \frac{t_{\tau 1}}{4\varepsilon^3 + 6i\varphi t_{\tau 1} \frac{D}{d}} \right) \end{aligned} \right. \quad (14)$$

Appendix C: Herglotz Functions and Integral Identity

In this appendix, we investigate the Herglotz functions and some integral identities with these functions. More technical details can be found in [1, 14, 19, 25].

A Herglotz function $h(z)$ is defined as [19]

Definition C.1 A function $h(z)$ is called a Herglotz function if

1. $h(z)$ is defined and analytic everywhere in the upper complex half-plane, $\mathbb{C}_+ = \{z \in \mathbb{C} : \text{Im } z > 0\}$
2. $\text{Im } h(z) \geq 0$ for all $z \in \mathbb{C}_+$

If $h(z)$ is a Herglotz function, then $-1/h(z)$ is a Herglotz function, and if $h(z)$ and $g(z)$ are Herglotz functions, the composition $h(g(z))$ is a new Herglotz function, provided $g(z)$ does not attain real values for $z \in \mathbb{C}_+$.

We adopt the following definitions [19]:

Definition C.2 If the Herglotz function $h(z)$ satisfies $h(-z^*) = -h^*(z)$, $z \in \mathbb{C}_+$, the Herglotz function is symmetric.

Definition C.3 If for $N \geq -1$, the Herglotz function $h(z)$ satisfies

$$h(z) = \sum_{n=-1}^N b_{-n} z^{-n} + o\left(z^{-N}\right), \quad \text{as } z \hat{\rightarrow} \infty$$

where the constants b_{-n} , $n = -1, 0, \dots, N$ are all **real**, then $h(z)$ admits at $z = \infty$ an asymptotic expansion of order N . The symbol $z \hat{\rightarrow} \infty$ stands for the non-tangential limit $|z| \rightarrow \infty$ within some Stoltz domain $\{z \in \mathbb{C}_+ : \theta \leq \arg(z) \leq \pi - \theta\}$ with the angle $\theta \in (0, \pi/2]$.

Definition C.4 If for $N \geq -1$, the Herglotz function $h(z)$ satisfies

$$h(z) = \sum_{n=-1}^N a_n z^n + o\left(z^N\right), \quad \text{as } z \hat{\rightarrow} 0$$

where the constants a_n , $n = -1, 0, \dots, N$ are all **real**, then $h(z)$ admits at $z = 0$ an asymptotic expansion of order N . The notation $z \hat{\rightarrow} 0$ stands for the non-tangential limit $|z| \rightarrow 0$ within some Stoltz domain $\{z \in \mathbb{C}_+ : \theta \leq \arg(z) \leq \pi - \theta\}$ with the angle $\theta \in (0, \pi/2]$.

The following two theorems are instrumental [1, 19]:

Theorem C.1 Let $h(z)$ be a Herglotz function. Then for some integer $N_\infty \geq 0$ the following integral

$$\lim_{\varepsilon \rightarrow 0^+} \lim_{y \rightarrow 0^+} \int_{\varepsilon < |x| < 1/\varepsilon} x^{2N_\infty} \text{Im } h(x + iy) \, dx$$

exists as a finite number if and only if $h(z)$ admits an asymptotic expansion of order $2N_\infty + 1$ at $z = \infty$. In this case

$$\lim_{\varepsilon \rightarrow 0^+} \lim_{y \rightarrow 0^+} \frac{1}{\pi} \int_{\varepsilon < |x| < 1/\varepsilon} x^n \operatorname{Im} h(x + iy) \, dx = \begin{cases} a_{-1} - b_{-1}, & n = 0 \\ -b_{-n-1}, & 0 < n \leq 2N_\infty \end{cases}$$

holds.

Theorem C.2 *Let $h(z)$ be a Herglotz function. Then for some integer $N_0 \geq 1$ the following integral*

$$\lim_{\varepsilon \rightarrow 0^+} \lim_{y \rightarrow 0^+} \int_{\varepsilon < |x| < 1/\varepsilon} \frac{\operatorname{Im} h(x + iy)}{x^{2N_0}} \, dx$$

exists as a finite number if and only if $h(z)$ admits an asymptotic expansion of order $2N_0 - 1$ at $z = 0$. In this case

$$\lim_{\varepsilon \rightarrow 0^+} \lim_{y \rightarrow 0^+} \frac{1}{\pi} \int_{\varepsilon < |x| < 1/\varepsilon} \frac{\operatorname{Im} h(x + iy)}{x^n} \, dx = \begin{cases} a_1 - b_1, & n = 2 \\ a_{n-1}, & 2 < n \leq 2N_0 \end{cases}$$

holds.

Appendix D: The Pulse Herglotz Function

In this appendix, we analyze the pulse Herglotz function. We have⁷

$$h(z) = -\frac{1}{\pi} \int_{-1}^1 \frac{1}{z - t} \, dt = \frac{1}{\pi} \ln \frac{z - 1}{z + 1}, \quad \operatorname{Im} z \geq 0$$

where the branch cut of the logarithm is assumed along the negative real axis (principal branch cut, $-\pi < \arg z \leq \pi$).

We focus on the imaginary part of this function in the upper complex half plane, $z = x + iy$, $y \geq 0$.

$$\operatorname{Im} h(z) = \frac{1}{\pi} \arg \frac{z - 1}{z + 1}$$

Points $z = x + iy$ with constant phase θ of the expression $(z - 1)/(z + 1)$, see Fig. 12 satisfy

⁷ An alternative expression of the pulse Herglotz function is [21]

$$h(z) = i - \frac{2}{\pi} \operatorname{arctanh}(z), \quad z \in \mathbb{C}_+$$

where the values on the real axis are taken as limits as $y \rightarrow 0^+$ (upper side of the branch cuts).

Fig. 12 The argument $\arg(z-1)/(z+1) = \theta = \theta_1 - \theta_2$ as a function of the angles θ_1 and θ_2

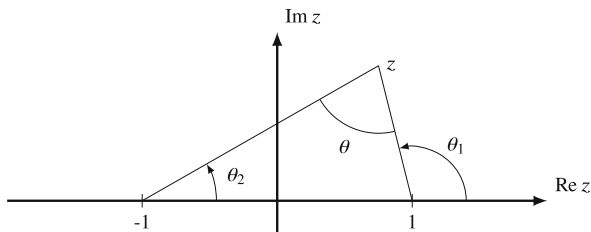
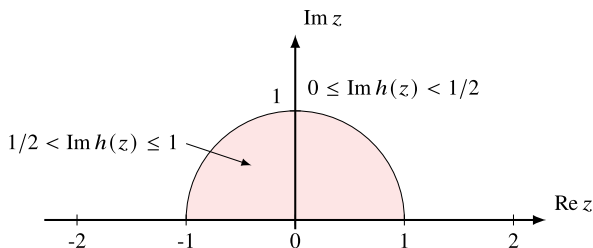


Fig. 13 The value of the imaginary part of the function $h(z)$ in the upper complex half plane



$$\tan \theta = \frac{2y}{x^2 + y^2 - 1}, \quad \theta \in [0, \pi]$$

This is the equation of a circle with center at $z_0 = x_0 + iy_0$ and radius r , where

$$\begin{cases} x_0 = 0 \\ y_0 = \frac{1}{\tan \theta} \\ r = \sqrt{\frac{1}{\tan^2 \theta} + 1} \end{cases} \quad \text{Im } h(z) = \theta/\pi$$

The imaginary part of $h(z)$ is bounded by unity in the upper complex half plane, $0 \leq \text{Im } h(z) \leq 1$. Moreover, inside the unit circle in the upper complex half plane, $1/2 < \text{Im } h(z) \leq 1$, see Fig. 13. On the real axis $z = x$ we have

$$\text{Im } h(z) = \begin{cases} 1, & -1 < x < 1 \\ 0, & (-\infty, -1) \cup (1, \infty) \end{cases}$$

The asymptotes of $h(z)$ are

$$h(z) = \begin{cases} i - \frac{2z}{z^2} + O(z^2), & z \hat{\rightarrow} 0 \\ -\frac{2\pi}{z\pi} + O(z^{-2}), & z \hat{\rightarrow} \infty \end{cases}$$

We also notice that $h(z)$ is a symmetric Herglotz function. In fact, for the principal branch, we have outside the branch cut

$$\ln(z^*) = (\ln z)^*, \quad \ln \frac{1}{z} = -\ln z$$

which leads to

$$h(-z^*) = \frac{1}{\pi} \ln \frac{z^* + 1}{z^* - 1} = \left(\frac{1}{\pi} \ln \frac{z + 1}{z - 1} \right)^* = - \left(\frac{1}{\pi} \ln \frac{z - 1}{z + 1} \right)^* = -h^*(z), \quad z \in \mathbb{C}_+$$

References

1. A. Bernland, A. Luger, M. Gustafsson, Sum rules and constraints on passive systems. *J. Phys. A: Math. Theor.* **44**(14), 145205 (2011). <https://doi.org/10.1088/1751-8113/44/14/145205>
2. C.R. Brewitt-Taylor, Limitation on the bandwidth of artificial perfect magnetic conductor surfaces. *Microwaves Antennas Propag IET* **1**(1), 255–260 (2007)
3. A.R. Edmonds, *Angular Momentum in Quantum Mechanics*, 3rd edn. (Princeton University Press, Princeton, 1974)
4. M. Gustafsson, D. Sjöberg, Physical bounds and sum rules for high-impedance surfaces. *IEEE Trans. Antennas Propag.* **59**(6), 2196–2204 (2011). <https://doi.org/10.1109/TAP.2011.2143688>
5. M. Gustafsson, D. Sjöberg, Sum rules and physical bounds on passive metamaterials. *New J. Phys.* **12**, 043046 (2010). <https://doi.org/10.1088/1367-2630/12/4/043046>
6. M. Gustafsson, C. Sohl, G. Kristensson, Physical limitations on antennas of arbitrary shape. *Proc. R. Soc. A* **463**, 2589–2607 (2007). <https://doi.org/10.1098/rspa.2007.1893>
7. M. Gustafsson, C. Sohl, C. Larsson, D. Sjöberg, Physical bounds on the all-spectrum transmission through periodic arrays. *Europhys. Lett.* **87**(3), 34002 (2009)
8. M. Gustavsson, G. Kristensson, N. Wellander, Multiple scattering by a collection of randomly located obstacles—numerical implementation of the coherent fields. *J. Quant. Spectrosc. Radiat. Transfer* **185**, 95–100 (2016). <https://doi.org/10.1016/j.jqsrt.2016.08.018>
9. M. Gustavsson, G. Kristensson, N. Wellander, *Multiple scattering by a collection of randomly located obstacles. Part II: Numerical implementation—coherent fields*. Technical report LUTEDX/(TEAT-7236)/1–19/(2014), Revision No. 1, January 2021. Department of Electrical and Information Technology, P.O. Box 118, S-221 00 (Lund University, Lund, 2014)
10. P. Henrici, *Applied and Computational Complex Analysis*, vol. 1 (Wiley, New York, 1974)
11. G. Kristensson, Coherent scattering by a collection of randomly located obstacles—an alternative integral equation formulation. *J. Quant. Spectrosc. Radiat. Transfer* **164**, 97–108 (2015). <https://doi.org/10.1016/j.jqsrt.2015.06.004>
12. G. Kristensson, Evaluation of some integrals relevant to multiple scattering by randomly distributed obstacles. *J. Math. Anal. Appl.* **432**(1), 324–337 (2015). <https://doi.org/10.1016/j.jmaa.2015.06.047>
13. G. Kristensson, *Multiple scattering by a collection of randomly located obstacles. Part V: Low order contributions to the coherent fields*. Technical report, LUTEDX/(TEAT-7277)/1–45/(2023). Department of Electrical and Information Technology, P.O. Box 118, S-221 00 (Lund University, Lund, 2023)
14. G. Kristensson, *Scattering of Electromagnetic Waves by Obstacles*. Mario Boella Series on Electromagnetism in Information and Communication (SciTech Publishing, Edison, 2016)
15. G. Kristensson, M. Gustavsson, N. Wellander, The coherent electromagnetic field and the effect of the pair distribution function. *J. Quant. Spectrosc. Radiat. Transfer* **285**, 108178 (2022)

16. G. Kristensson, N. Wellander, Multiple scattering by a collection of randomly located obstacles distributed in a dielectric slab, Chap. 25, in *Advances in Mathematical Methods for Electromagnetics*, ed. by K. Kobayashi, P.D. Smith (SciTech Publishing, 2021), pp. 621–651. <https://digital-library.theiet.org/doi/book/10.1049/sbew528e>
17. M. Lax, Multiple scattering of waves. II. The effective field in dense systems. *Phys. Rev.* **85**, 621–629 (1952). <https://doi.org/10.1103/PhysRev.85.621>
18. A. Ludvig-Osipov, J. Lundgren, C. Ehrenborg, Y. Ivanenko, A. Ericsson, M. Gustafsson, B.L.G. Jonsson, D. Sjöberg, Fundamental bounds on transmission through periodically perforated metal screens with experimental validation. *IEEE Trans. Antennas Propag.* **68**(2), 773–782 (2020)
19. M. Nedic, C. Ehrenborg, Y. Ivanenko, A. Ludvig-Osipov, S. Nordebo, A. Luger, L. Jonsson, D. Sjöberg, M. Gustafsson, Herglotz functions and applications in electromagnetics, Chap. 20, in *Advances in Mathematical Methods for Electromagnetics*, ed. by K. Kobayashi, P.D. Smith (Institution of Engineering and Technology, 2021), pp. 491–514. <https://digital-library.theiet.org/doi/book/10.1049/sbew528e>
20. H.M. Nussenzveig, *Causality and Dispersion Relations* (Academic, London, 1972)
21. F.W.J. Olver, D.W. Lozier, R.F. Boisvert, C.W. Clark, *NIST Handbook of Mathematical Functions* (Cambridge University Press, New York, 2010)
22. K.N. Rozanov, Ultimate thickness to bandwidth ratio of RadarAbsorbers. *IEEE Trans. Antennas Propag.* **48**(8), 1230–1234 (2000). <https://doi.org/10.1109/8.884491>
23. W. Rudin, *Real and Complex Analysis* (McGraw-Hill, New York, 1987)
24. C. Sohl, M. Gustafsson, G. Kristensson, Physical limitations on broadband scattering by heterogeneous obstacles. *J. Phys. A: Math. Theor.* **40**, 11165–11182 (2007). <https://doi.org/10.1088/1751-8113/40/36/015>
25. C. Sohl, M. Gustafsson, G. Kristensson, S. Nordebo, A general approach for deriving bounds in electromagnetic theory, in *Proceedings of the XXIXth URSI General Assembly* (International Union of Radio Science, Chicago, 2008), B01p4

Optics with Tightly Interlaced Matched Ambidextrous Bilayers



Francesco Chiadini , Roberta De Simone , Vincenzo Fiumara ,
and Akhlesh Lakhtakia

1 Introduction

The search for advanced, high-performance optical devices is constantly evolving due to the increasing complexity of systems that are required to deliver high-precision performance, reliability, environmental stability, etc. [1–4]. Often, the key lies in the use of new materials exhibiting special characteristics. Nowadays, researchers focus on artificially engineered materials that offer functionalities not possible with natural materials [5]. A host of such artificial materials, usually made up of subwavelength components such as nano-rods and nano-layers, have been proposed, theoretically investigated, and experimentally characterized. Among these innovative materials, we draw attention to the Tightly Interlaced Matched Ambidextrous Bilayer (TIMAB).

The TIMAB is a non-homogeneous nano-structured material consisting of a cascade of bilayer cells made up of two chiral sculptured thin films (CSTFs) that are identical except for their structural handedness [6, 7]. Simpler than a CSTF is a columnar thin film (CTF), which has a columnar morphology, i.e., it is an assembly of identical nano-columns, all parallel to one another. It is usually grown by physical vapor deposition (PVD) by creating a collimated vapor flux in a low-

F. Chiadini (✉) · R. De Simone

Department of Industrial Engineering, University of Salerno, Fisciano, Italy
e-mail: fchiadini@unisa.it; rodesimone@unisa.it

V. Fiumara

Department of Engineering, University of Basilicata, Potenza, Italy
e-mail: vincenzo.fiumara@unibas.it

A. Lakhtakia

Department of Engineering Science and Mechanics, The Pennsylvania State University,
University Park, PA, USA
e-mail: akhlesh@psu.edu

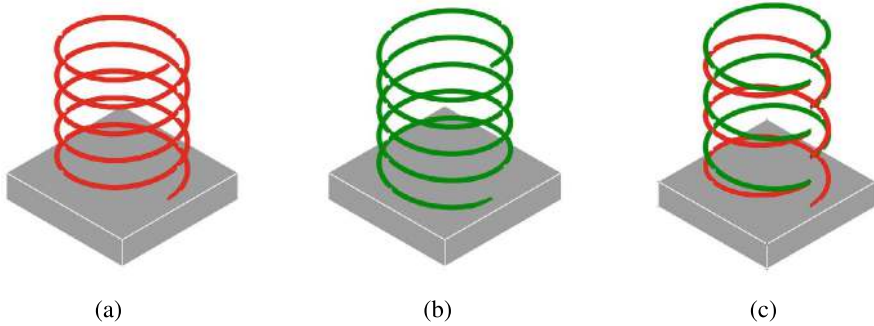


Fig. 1 Schematics of the CSTF and TIMAB morphologies. The red coils are right-handed and the green coils are left-handed. (a) Right-handed CSTF. (b) Left-handed CSTF. (c) TIMAB

pressure chamber. For that purpose, a solid material is placed in a tungsten boat inside the chamber. The boat is resistively heated to allow the material to evaporate and thereby generate a collimated vapor flux directed toward a flat substrate inside the chamber. The direction of the vapor flux is at angle $\chi_v \in (0^\circ, 90^\circ]$ with respect to the substrate plane. The CTF is the assembly of nano-columns, inclined at an angle $\chi \geq \chi_v$ with respect to the substrate plane, which forms on the substrate. The angle χ depends on the angle χ_v according to the relationship $\chi = \tan^{-1}(\gamma \tan \chi_v)$, where the parameter γ depends on the evaporated material [8, 9]. When the substrate is rotated uniformly about a central normal axis passing through it, nano-helices form instead of nano-columns. The resulting film is a CSTF [10].

The structure of a CSTF can be either right-handed or left-handed, depending on the sense of substrate rotation. Whereas the handedness of a CSTF is invariant along the axis normal to the substrate, in the TIMAB, the handedness flips in the center of the bilayer cell so that the cell consists of one period each of two CSTFs, which are identical except in structural handedness [7], as depicted schematically in Fig. 1.

To exemplify the enhancement of device performances leveraged by the use of TIMAB, we present the distinguishing characteristics of two optical phenomena involving this material: (i) surface-plasmon-polariton (SPP) wave propagation guided by a planar metal/TIMAB interface and (ii) polarization-universal bandgap on axial excitation. The first part of this chapter is dedicated to the features of SPP waves propagating guided by the planar interface of a metal and a TIMAB, in terms of phase speed, attenuation rate, and field profile [11]. In the second part of the chapter, we show that a TIMAB can be used to realize a polarization-universal bandgap [6, 7] and that linear chirping of the pitch of TIMAB's CSTF constituents results in a significantly widening of that bandgap [12].

An $\exp(-i\omega t)$ dependence on time t is used, with ω as the angular frequency and $i = \sqrt{-1}$ as the imaginary unity; $k_0 = \omega\sqrt{\epsilon_0\mu_0}$ is the free-space wavenumber and $\lambda_0 = 2\pi/k_0$ is the free-space wavelength, with μ_0 as the free-space permeability and ϵ_0 as the free-space permittivity; $c_0 = 1/\sqrt{\epsilon_0\mu_0}$ is the speed of light in free space; and $\eta_0 = \sqrt{\mu_0/\epsilon_0}$ is the intrinsic impedance of free space. Vectors are

represented in boldface; dyadics are doubly underlined; and Cartesian unit vectors are denoted by \mathbf{u}_x , \mathbf{u}_y , and \mathbf{u}_z . Column vectors are in boldface and bracketed, and matrices are double underlined and bracketed.

2 Tightly Interlaced Matched Ambidextrous Bilayer (TIMAB)

The frequency-domain constitutive relations of a CSTF are written as [8, 10]

$$\mathbf{D}(\mathbf{r}, \omega) = \varepsilon_0 \underline{\underline{\varepsilon}}_{CSTF}(h, z, \Omega, \chi, \omega) \cdot \mathbf{E}(\mathbf{r}, \omega), \quad (1a)$$

and

$$\mathbf{B}(\mathbf{r}, \omega) = \mu_0 \mathbf{H}(\mathbf{r}, \omega), \quad (1b)$$

where

$$\underline{\underline{\varepsilon}}_{CSTF}(h, z, \Omega, \chi, \omega) = \underline{\underline{S}}_z(h, z, \Omega) \cdot \underline{\underline{S}}_y(\chi) \cdot \underline{\underline{\varepsilon}}_{ref}^o(\omega) \cdot \underline{\underline{S}}_y^{-1}(\chi) \cdot \underline{\underline{S}}_z^{-1}(h, z, \Omega) \quad (2)$$

is the relative permittivity dyadic [13]. The dyadic

$$\underline{\underline{S}}_z(h, z, \Omega) = \mathbf{u}_z \mathbf{u}_z + (\mathbf{u}_x \mathbf{u}_x + \mathbf{u}_y \mathbf{u}_y) \cos\left(h \frac{\pi z}{\Omega}\right) + (\mathbf{u}_y \mathbf{u}_x - \mathbf{u}_x \mathbf{u}_y) \sin\left(h \frac{\pi z}{\Omega}\right) \quad (3a)$$

expresses a uniform rotation about the z axis with period 2Ω . The parameter h takes the value 1 for CSTFs with structural right-handedness and the value -1 for CSTFs with structural left-handedness. The dyadic

$$\underline{\underline{S}}_y(\chi) = \mathbf{u}_y \mathbf{u}_y + (\mathbf{u}_x \mathbf{u}_x + \mathbf{u}_z \mathbf{u}_z) \cos \chi + (\mathbf{u}_z \mathbf{u}_x - \mathbf{u}_x \mathbf{u}_z) \sin \chi \quad (3b)$$

expresses a rotation by angle χ about the y axis. Finally, the dyadic

$$\underline{\underline{\varepsilon}}_{ref}^o(\omega) = \varepsilon_a(\omega) \mathbf{u}_z \mathbf{u}_z + \varepsilon_b(\omega) \mathbf{u}_x \mathbf{u}_x + \varepsilon_c(\omega) \mathbf{u}_y \mathbf{u}_y \quad (3c)$$

contains the scalars $\varepsilon_a(\omega)$, $\varepsilon_b(\omega)$, and $\varepsilon_c(\omega)$ as the principal relative permittivities. These scalars depend on the angle χ_v as [9, 14]

$$\varepsilon_{a,b,c}(\omega) = [A_{a,b,c}(\omega) + B_{a,b,c}(\omega) (90 - \chi_v)^2]^2, \quad (4)$$

where the angle χ_v is to be provided in degree. The coefficients $A_{a,b,c}$ and $B_{a,b,c}$ depend on both χ_v and the evaporant material.

2.1 Periodic TIMAB

A TIMAB is a periodic cascade of multiple bilayer cells, each cell containing a layer of a CSTF and a layer of its enantiomer, i.e., a CSTF identical except for structural handedness. Both layers are as thick as the structural period of the CSTF. So, whereas the structural handedness of a CSTF is invariant along the z axis, the structural handedness of a TIMAB flips across an interlayer interface.

Suppose that a TIMAB comprises $N > 1$ bilayer cells. The n th bilayer cell, $n \in [1, N]$, extends from z_{n-1} to z_n , where $z_m = 4m\Omega$. Instead of Eq. (1a), we use [6, 7]

$$\mathbf{D}(\mathbf{r}, \omega) = \varepsilon_0 \underline{\underline{\varepsilon}}_n(h, z, \chi, \omega) \cdot \mathbf{E}(\mathbf{r}, \omega), \quad z \in (z_{n-1}, z_n), \quad n \in [1, N], \quad (5a)$$

where

$$\underline{\underline{\varepsilon}}_n = \begin{cases} \underline{\underline{\varepsilon}}_{CSTF}(h, z, \Omega, \chi, \omega), & z \in (z_{n-1}, z_{n-1} + 2\Omega) \\ \underline{\underline{\varepsilon}}_{CSTF}(-h, z - 2\Omega, \Omega, \chi, \omega), & z \in (z_{n-1} + 2\Omega, z_n) \end{cases}. \quad (5b)$$

2.2 Aperiodic TIMAB

As perviously remarked, the two CSTFs in every bilayer cell are identical except in structural handedness. We can preserve that characteristic but alter the value of Ω from bilayer cell to bilayer cell. For this aperiodic TIMAB, Eq. (5b) is modified to

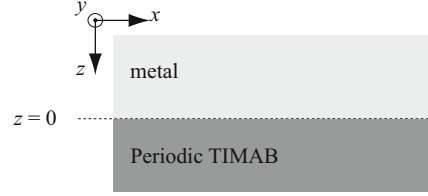
$$\underline{\underline{\varepsilon}}_n = \begin{cases} \underline{\underline{\varepsilon}}_{CSTF}(h, z, \Omega_n, \chi, \omega), & z \in (z_{n-1}, z_{n-1} + 2\Omega_n) \\ \underline{\underline{\varepsilon}}_{CSTF}(-h, z - 2\Omega_n, \Omega_n, \chi, \omega), & z \in (z_{n-1} + 2\Omega_n, z_n) \end{cases}, \quad (6)$$

where $z_0 = 0$ and $z_m = \sum_{j=1}^m 4\Omega_j$.

3 SPP Wave Propagation

SPP waves are electromagnetic waves that are guided by a planar interface of a metal and a dielectric material [15]. The propagation characteristics of such waves are tightly related to the constitutive properties of both partnering mediums [16, 17]. In this section, we recount the optical characteristics of SPP waves propagating at a planar metal/TIMAB interface, the TIMAB being periodic.

Fig. 2 Schematics of the side view ($y = 0$) of the boundary-value problem for SPP wave propagation



3.1 Boundary-Value Problem

We consider the canonical boundary-value problem schematically illustrated in Fig. 2 where the half space $z < 0$ is occupied by a metal with complex relative permittivity ε_{met} , and the half space $z > 0$ is occupied by a periodic TIMAB described by Eqs. (1b), (5a), and (5b) in the limit $N \rightarrow \infty$. We consider an SPP wave propagating at an angle ψ with respect to the x axis in the transverse xy plane; thus, the direction of propagation is parallel to the unit vector $\mathbf{u}_{\text{prop}} = \mathbf{u}_x \cos \psi + \mathbf{u}_y \sin \psi$, $\psi \in [0^\circ, 360^\circ)$. Moreover, the SPP wave's fields must decay far away from the interface, i.e., as $|z| \rightarrow \infty$.

With q as the generally complex-valued wavenumber, the electric and magnetic phasors can be represented $\forall z \in (-\infty, \infty)$ as

$$\begin{cases} \mathbf{E}(\mathbf{r}) = [e_x(z)\mathbf{u}_x + e_y(z)\mathbf{u}_y + e_z(z)\mathbf{u}_z] \cdot \exp(iq\mathbf{u}_{\text{prop}} \cdot \mathbf{r}) \\ \mathbf{H}(\mathbf{r}) = [h_x(z)\mathbf{u}_x + h_y(z)\mathbf{u}_y + h_z(z)\mathbf{u}_z] \cdot \exp(iq\mathbf{u}_{\text{prop}} \cdot \mathbf{r}) \end{cases}, \quad (7)$$

where the unknown functions $e_x(z)$, $e_y(z)$, $e_z(z)$, $h_x(z)$, $h_y(z)$, and $h_z(z)$ have to be determined. For later use, we define the column vector

$$[\mathbf{f}(z)] = \begin{bmatrix} e_x(z) \\ e_y(z) \\ h_x(z) \\ h_y(z) \end{bmatrix}. \quad (8)$$

In the half space $z < 0$, the SPP wave's fields are of the textbook variety:

$$\begin{cases} \mathbf{E}(\mathbf{r}) = \left[A_1 \mathbf{u}_s + A_2 \left(\frac{\alpha_{\text{met}}}{k_0} \mathbf{u}_{\text{prop}} + \frac{q}{k_0} \mathbf{u}_z \right) \right] \\ \quad \cdot \exp(iq\mathbf{u}_{\text{prop}} \cdot \mathbf{r}) \exp(-i\alpha_{\text{met}}z) \\ \mathbf{H}(\mathbf{r}) = \frac{1}{\eta_0} \left[A_1 \left(\frac{\alpha_{\text{met}}}{k_0} \mathbf{u}_{\text{prop}} + \frac{q}{k_0} \mathbf{u}_z \right) - A_2 \varepsilon_{\text{met}} \mathbf{u}_s \right] \\ \quad \cdot \exp(iq\mathbf{u}_{\text{prop}} \cdot \mathbf{r}) \exp(-i\alpha_{\text{met}}z) \end{cases}, \quad z < 0, \quad (9)$$

where A_1 and A_2 are unknown scalars,

$$\mathbf{u}_s = -\mathbf{u}_x \sin \psi + \mathbf{u}_y \cos \psi \quad (10)$$

is the vector that constitutes the orthogonal coordinate system $\{\mathbf{u}_{\text{prop}}, \mathbf{u}_s, \mathbf{u}_z\}$,

$$\alpha_{\text{met}} = \sqrt{k_0^2 \varepsilon_{\text{met}} - q^2} \quad (11)$$

is the attenuation constant in the z direction with the constraint

$$\text{Im}(\alpha_{\text{met}}) > 0 \quad (12)$$

that must be enforced to ensure that the fields decay exponentially as $z \rightarrow -\infty$. Equations (9) yield

$$[\mathbf{f}(0^-)] = \begin{bmatrix} -\sin \psi & \frac{\alpha_{\text{met}}}{k_0} \cos \psi \\ \cos \psi & \frac{\alpha_{\text{met}}}{k_0} \sin \psi \\ \frac{\alpha_{\text{met}}}{k_0 \eta_0} \cos \psi & \frac{\varepsilon_{\text{met}}}{\eta_0} \sin \psi \\ \frac{\alpha_{\text{met}}}{k_0 \eta_0} \sin \psi & -\frac{\varepsilon_{\text{met}}}{\eta_0} \cos \psi \end{bmatrix} \begin{bmatrix} A_1 \\ A_2 \end{bmatrix}. \quad (13)$$

In the periodic TIMAB, $[\mathbf{f}(z)]$ satisfies the 4×4 -matrix ordinary differential equation [10]

$$\frac{d}{dz} [\mathbf{f}(z)] = i [\underline{\underline{\mathbf{P}}}(s, z)] [\mathbf{f}(z)], \quad (14)$$

where the matrix

$$\begin{aligned} & [\underline{\underline{\mathbf{P}}}(s, z)] \\ &= \omega \varepsilon_0 \begin{bmatrix} 0 & 0 & 0 & \eta_0^2 \\ 0 & 0 & -\eta_0^2 & 0 \\ sh \varepsilon_e \cos\left(\frac{\pi z}{\Omega}\right) \sin\left(\frac{\pi z}{\Omega}\right) & -\left[\varepsilon_e \cos^2\left(\frac{\pi z}{\Omega}\right) + \varepsilon_d\right] & 0 & 0 \\ \left[\varepsilon_e \sin^2\left(\frac{\pi z}{\Omega}\right) + \varepsilon_d\right] & -sh \varepsilon_e \cos\left(\frac{\pi z}{\Omega}\right) \sin\left(\frac{\pi z}{\Omega}\right) & 0 & 0 \end{bmatrix} \end{aligned}$$

$$\begin{aligned}
& + q \frac{\varepsilon_d (\varepsilon_a - \varepsilon_b)}{\varepsilon_a \varepsilon_b} \frac{\sin 2\chi}{2} \\
& \times \begin{bmatrix} \cos\left(\frac{\pi z}{\Omega}\right) \cos \psi \, sh \sin\left(\frac{\pi z}{\Omega}\right) \cos \psi & 0 & 0 \\ \cos\left(\frac{\pi z}{\Omega}\right) \sin \psi \, sh \sin\left(\frac{\pi z}{\Omega}\right) \sin \psi & 0 & 0 \\ 0 & 0 & sh \sin\left(\frac{\pi z}{\Omega}\right) \sin \psi - sh \sin\left(\frac{\pi z}{\Omega}\right) \cos \psi \\ 0 & 0 & -\cos\left(\frac{\pi z}{\Omega}\right) \sin \psi & \cos\left(\frac{\pi z}{\Omega}\right) \cos \psi \end{bmatrix} \\
& + \frac{q^2}{\omega \varepsilon_0} \frac{\varepsilon_d}{\varepsilon_a \varepsilon_b} \begin{bmatrix} 0 & 0 & \cos \psi \sin \psi & -\cos^2 \psi \\ 0 & 0 & \sin^2 \psi & -\cos \psi \sin \psi \\ 0 & 0 & 0 & 0 \\ 0 & 0 & 0 & 0 \end{bmatrix} \\
& + \frac{q^2}{\omega \mu_0} \begin{bmatrix} 0 & 0 & 0 & 0 \\ 0 & 0 & 0 & 0 \\ -\cos \psi \sin \psi & \cos^2 \psi & 0 & 0 \\ -\sin^2 \psi & \cos \psi \sin \psi & 0 & 0 \end{bmatrix} \tag{15}
\end{aligned}$$

with

$$\varepsilon_d = \frac{\varepsilon_a \varepsilon_b}{\varepsilon_a \cos^2 \chi + \varepsilon_b \sin^2 \chi}, \tag{16}$$

$$\varepsilon_e = \varepsilon_c - \varepsilon_d, \tag{17}$$

and

$$s = \begin{cases} +1 & z \in (0, 2\Omega) \cup (4\Omega, 6\Omega) \cup \dots, \\ -1 & z \in (2\Omega, 4\Omega) \cup (6\Omega, 8\Omega) \cup \dots \end{cases} \tag{18}$$

Equation (4) can be used to write [18]

$$\varepsilon_d = [D_0 + D_1(90 - \chi_v) + D_2(90 - \chi_v)^2]^2, \tag{19}$$

where the unit of χ_v is degree and the coefficients $D_{0,1,2}$ depend on both χ_v and the evaporant material.

Equation (14) can be solved numerically by means of a piecewise uniform approximation technique [10, 11, 15] to yield the functional relationship

$$[\mathbf{f}(4\Omega)] = \left[\underline{\underline{Q}} \right] [\mathbf{f}(0^+)] , \quad (20)$$

where the matrix $\left[\underline{\underline{Q}} \right]$ is the characteristic matrix of one period of the TIMAB.

Let us denote the four eigenvalues and the corresponding eigenvectors of $\left[\underline{\underline{Q}} \right]$ by σ_m and $[\mathbf{v}_m]$, $m \in [1, 4]$, where $\text{Re}(\ln \sigma_1) < 0$, $\text{Re}(\ln \sigma_2) < 0$, $\text{Re}(\ln \sigma_3) > 0$ and $\text{Re}(\ln \sigma_4) > 0$. In order to fulfill the condition that the fields must decay as $z \rightarrow \infty$, we must set [15]

$$[\mathbf{f}(0^+)] = [\mathbf{v}_1 \quad \mathbf{v}_2] \begin{bmatrix} B_1 \\ B_2 \end{bmatrix} , \quad (21)$$

where B_1 and B_2 are unknown scalars.

3.2 Dispersion Equation

The use of Eqs. (13) and (21) in the standard boundary conditions

$$[\mathbf{f}(0^+)] = [\mathbf{f}(0^-)] \quad (22)$$

results in the matrix equation

$$\left[\underline{\underline{M}} \right] \begin{bmatrix} A_1 \\ A_2 \\ B_1 \\ B_2 \end{bmatrix} = \begin{bmatrix} 0 \\ 0 \\ 0 \\ 0 \end{bmatrix} , \quad (23)$$

where $\left[\underline{\underline{M}} \right]$ is a 4×4 matrix. This equation has a nontrivial solution only if

$$\det \left[\underline{\underline{M}} \right] = 0 , \quad (24)$$

which serves as the dispersion equation for SPP wave propagation.

For fixed $\psi \in (0^\circ, 360^\circ)$, Eq. (24) has to be numerically solved to determine q . The phase speed of the SPP waves, normalized with respect to the speed of light in vacuum c_0 , is denoted by

$$v_{ph} = \frac{\omega}{c_0 \text{Re}(q)} . \quad (25)$$

The propagation distance

$$\Delta_{\text{prop}} = \frac{1}{\text{Im}(q)} \quad (26)$$

is the distance along the direction of propagation at which the field amplitude reduces to a factor e^{-1} .

After finding q , $[\mathbf{f}(z)]$ can also be determined for all z in terms of a normalization constant. Results reported in the next section were obtained imposing $B_2 = 1$ and calculating A_1 , A_2 , and B_1 by Eq. (23). Thereafter, $e_z(z)$ and $h_z(z)$ can be straightforwardly determined using the Maxwell equations. Finally, the time-averaged Poynting vector

$$\mathbf{P}(\mathbf{r}) = \frac{1}{2} \text{Re} [\mathbf{E}(\mathbf{r}) \times \mathbf{H}^*(\mathbf{r})] \quad (27)$$

can be computed, with the asterisk denoting the complex conjugate.

3.3 Numerical Results

For all calculations, we fixed the free-space wavelength $\lambda_0 = 633$ nm, and $h = +1$. The metal was taken to be silver with relative permittivity $\varepsilon_{\text{met}} = -14.461 + i1.1936$ [19]. The periodic TIMAB was chosen to have $\Omega = 162$ nm, $\varepsilon_a = 6.65313 + i0.0429696$, $\varepsilon_b = 7.35561 + i0.050978$, $\varepsilon_c = 6.53285 + i0.042055$ and $\chi = 50^\circ$, which values emerge from experiments on CSTFs [20].

Several solutions of the dispersion equation (24) exist. The corresponding normalized phase speeds, as defined in Eq. (25), are reported in the polar plot in Fig. 3. The radial coordinate in the polar plot represents the value of v_{ph} while the angular coordinate is the angle ψ in the xy plane indicating the direction of propagation of the SPP wave. For the sake of clarity, the solutions are grouped in branches and labeled from 1 to 13 as displayed in Fig. 3. Branches labeled ℓ' correspond to branches ℓ rotated by 180° , $\ell \in [1, 13]$.

The phase speed of the SPP waves goes from a value of 0.3 up to almost 0.6. For every direction of propagation, at least three solutions can be found. Furthermore, there are angular ranges (highlighted gray in Fig. 3) where a multiplicity of up to six different SPP waves can exist for a fixed propagation direction, namely $\psi \in [4^\circ, 8^\circ] \cup [8^\circ, 20^\circ] \cup [70^\circ, 76^\circ]$. This multiplicity is very useful in sensing applications since multiple SPP waves can allow the simultaneous detection of multiple analytes.

It is worth noting that the role of interlacing in the periodic TIMAB is fundamental to increase the multiplicity of SPP waves possibly guided in a specific direction. In fact, the number of SPP waves, which are solutions of the boundary-

Fig. 3 Normalized phase speed v_{ph} as a function of ψ of SPP waves guided by the planar silver/TIMAB interface. Ranges of ψ with the highest number of SPP waves simultaneously excitable are shaded gray

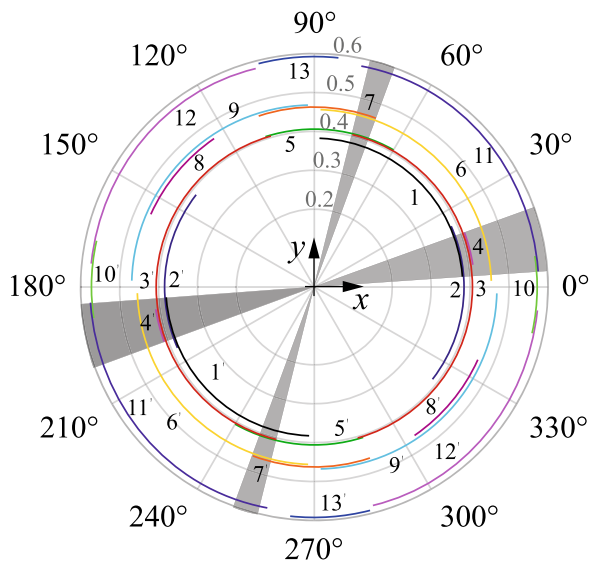
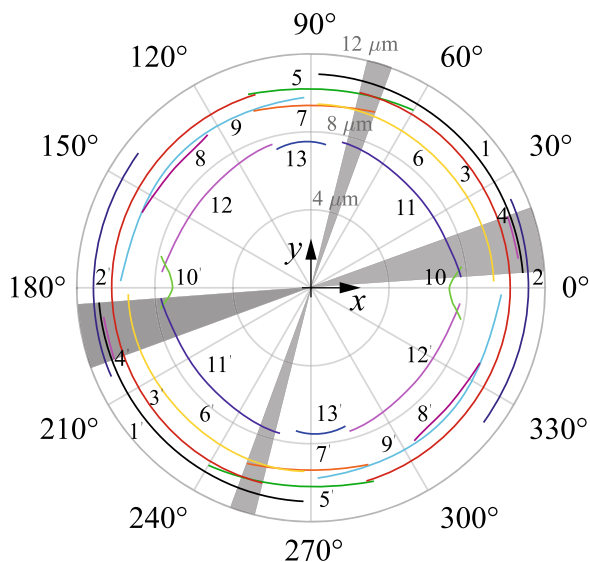


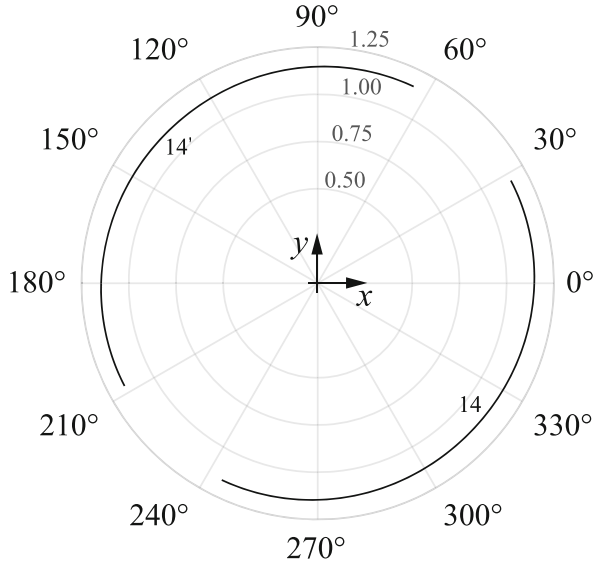
Fig. 4 Propagation distance Δ_{prop} as a function of ψ of SPP waves guided by the planar silver/TIMAB interface. Ranges of ψ with the highest number of SPP waves simultaneously excitable are shaded gray



value problem at the silver/TIMAB interface, turns out to be significantly greater than the number of solutions for the silver/CSTF interface [11].

The propagation distance of the SPP waves, as defined in Eq. (26), is depicted in the polar plot of Fig. 4 for $\ell \in [1, 13]$. In this figure, the radial coordinate represents the propagation distance, which goes from a minimum of $7.09 \mu\text{m}$ up to a maximum of $11.22 \mu\text{m}$ for $\ell \in [1, 13]$.

Fig. 5 Normalized phase speed v_{ph} as a function of ψ of the superluminal SPP wave guided by the planar silver/TIMAB interface



The solutions reported in Figs. 3 and 4 are not exhaustive of all the solutions found. Indeed, an additional solution exists. This additional solution (i.e., $\ell = 14$) is of great importance since it identifies an SPP wave with a phase speed higher than c_0 , thus identifying a superluminal SPP wave. The normalized phase speed is reported in the polar plot in Fig. 5.

The superluminal SPP wave is the solution with the lowest propagation distance, Δ_{prop} being less than $4 \mu\text{m}$, as illustrated in Fig. 6. The angular ranges at which such a solution exists contains the angular ranges shaded gray in Figs. 3 and 4, where a multiplicity of six subluminal solutions was found, thus bringing to seven the total multiplicity for SPP wave propagation in these ranges.

There are solutions in Figs. 3 and 4 with identical propagation distances, identified in Fig. 4 by the points where the branches 3&5, 6&7, 10&11, and 12&10' (and obviously, 3'&5', 6'&7', 10'&11', and 12'&10) cross each other, and with phase speeds so close as to be apparently indistinguishable. SPP waves of these kinds, called *doublets* [21], are distinct SPP waves—which can be inferred by looking at the spatial profiles of the time-averaged Poynting vector for two SPP waves with the same Δ_{prop} . To this end, the spatial profiles along the z axis of the Cartesian components of \mathbf{P} in the coordinate system $\{\mathbf{u}_{prop}, \mathbf{u}_s, \mathbf{u}_z\}$ can be calculated for $x = y = 0$ as follows:

$$P_{prop}(x = 0, y = 0, z) = \mathbf{P}(x = 0, y = 0, z) \cdot \mathbf{u}_{prop}, \quad (28a)$$

$$P_s(x = 0, y = 0, z) = \mathbf{P}(x = 0, y = 0, z) \cdot \mathbf{u}_s, \quad (28b)$$

$$P_z(x = 0, y = 0, z) = \mathbf{P}(x = 0, y = 0, z) \cdot \mathbf{u}_z. \quad (28c)$$

Fig. 6 Propagation distance Δ_{prop} as a function of ψ of the superluminal SPP wave guided by the planar silver/TIMAB interface

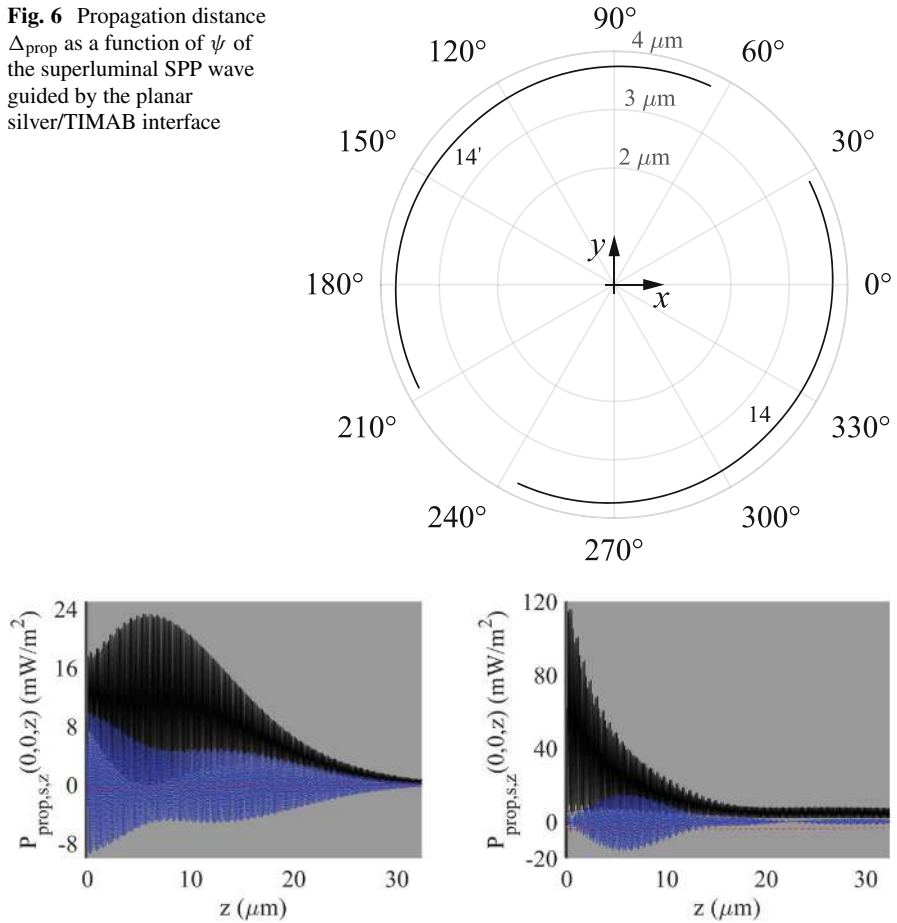


Fig. 7 Variations of $P_{\text{prop}}(0, 0, z)$ (black solid lines), $P_s(0, 0, z)$ (blue dashed-dotted lines), and $P_z(0, 0, z)$ (red dashed lines) with z in the periodic-TIMAB half-space when $\psi = 6.5^\circ$ and $\Delta_{\text{prop}} = 7.642045 \times 10^{-6}$. Left: solution with $v_{\text{ph}} = 0.575835$. Right: solution with $v_{\text{ph}} = 0.571846$

For instance, in Fig. 7, we present the z -variations of the components of \mathbf{P} for the two SPP waves with the same Δ_{prop} at $\psi = 6.5^\circ$. Clearly, components of the SPP wave with the lower phase speed have a higher decay rate along the z axis in the periodic-TIMAB half-space.

But this is not a general conclusion since an analysis of the superluminal solution reveals that the SPP wave with highest phase speed exhibits the highest decay rate along the z axis, as can be seen by examining Fig. 8.

Fig. 8 Variations of $P_{\text{prop}}(0, 0, z)$ (black solid lines), $P_s(0, 0, z)$ (blue dashed-dotted lines), and $P_z(0, 0, z)$ (red dashed lines) with z in the periodic-TIMAB half-space, for the high-phase speed SPP wave guided by the planar silver/TIMAB interface when $\psi = 28^\circ$

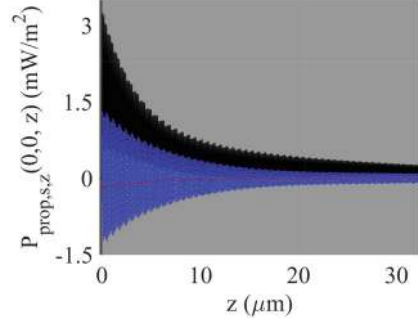
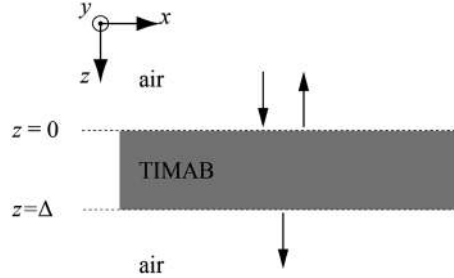


Fig. 9 Schematic of the problem of the plane wave reflection and transmission by a TIMAB slab



4 Polarization-Universal Bandgaps

This section deals with the boundary-value problem of the reflection and transmission of a plane wave normally incident on a TIMAB slab. This problem was first solved for periodic TIMABs described by Eqs. (1b), (5a), and (5b) with finite N [7]. Recently, chirped TIMABs described by Eqs. (1b), (5a), and (6) with finite N were proposed and analyzed [12]. Both architectures were shown to exhibit polarization-universal bandgaps. Here, the main characteristics are illustrated.

4.1 Boundary-Value Problem

Consider a general TIMAB slab consisting of N bilayer cells occupying the region $0 \leq z \leq \Delta$, where $\Delta = \sum_{j=1}^N 4\Omega_j$. The half-spaces $z < 0$ and $z > \Delta$ are vacuums. An arbitrarily polarized plane wave impinges normally on the TIMAB slab from the half-space $z < 0$. The schematic of the boundary-value problem is shown in Fig. 9.

The incident electric field phasor can be written as:

$$\mathbf{E}_i(z) = (a_L \mathbf{u}_+ + a_R \mathbf{u}_-) \exp(ik_0 z), \quad z < 0, \quad (29)$$

where $\mathbf{u}_\pm = (\mathbf{u}_x \pm i\mathbf{u}_y)/\sqrt{2}$, and the subscripts L and R denote the left- and the right-circularly polarized field components with known amplitudes a_L and a_R ,

respectively. The electric field phasor of the plane wave reflected in the half-space $z < 0$ is written as

$$\mathbf{E}_r(z) = (r_R \mathbf{u}_+ + r_L \mathbf{u}_-) \exp(-ik_0 z), \quad z < 0, \quad (30)$$

and the electric field phasor of the plane wave transmitted in the half-space $z > \Delta$ is written as

$$\mathbf{E}_t(z) = (t_L \mathbf{u}_+ + t_R \mathbf{u}_-) \exp[ik_0(z - \Delta)], \quad z > \Delta, \quad (31)$$

where r_L and r_R (t_L and t_R) are the unknown amplitudes of the components of the reflected (transmitted) plane wave.

The boundary-value problem can be solved by using the transfer-matrix method, whose detailed description is provided elsewhere [22]. Here, we only report that the method leads to the 4×4 -matrix relation [10]:

$$[\mathbf{f}(\Delta^+)] = [\underline{\mathbf{A}}_N][\underline{\mathbf{A}}_{N-1}] \cdots [\underline{\mathbf{A}}_2][\underline{\mathbf{A}}_1][\mathbf{f}(0^-)], \quad (32)$$

where

$$[\mathbf{f}(0^-)] = \frac{1}{\sqrt{2}} \begin{bmatrix} (r_L + r_R) + (a_L + a_R) \\ i[(-r_L + r_R) + (a_L - a_R)] \\ -i[(r_L - r_R) + (a_L - a_R)]/\eta_0 \\ -[(r_L + r_R) - (a_L + a_R)]/\eta_0 \end{bmatrix}, \quad (33a)$$

$$[\mathbf{f}(\Delta^+)] = \frac{1}{\sqrt{2}} \begin{bmatrix} t_L + t_R \\ i(t_L - t_R) \\ -i(t_L - t_R)/\eta_0 \\ (t_L + t_R)/\eta_0 \end{bmatrix}, \quad (33b)$$

$$[\underline{\mathbf{A}}_j] = \exp\left(2i\Omega_j[\underline{\mathbf{V}}_j(-1)]\right) \exp\left(2i\Omega_j[\underline{\mathbf{V}}_j(1)]\right), \quad (33c)$$

and

$$[\underline{\mathbf{V}}_j(s)] = \begin{bmatrix} 0 & -ish \frac{\pi}{\Omega_j} & 0 & k_0 \eta_0 \\ ish \frac{\pi}{\Omega_j} & 0 & -k_0 \eta_0 & 0 \\ 0 & -k_0 \eta_0^{-1} \varepsilon_c & 0 & -ish \frac{\pi}{\Omega_j} \\ k_0 \eta_0^{-1} \varepsilon_d & 0 & ish \frac{\pi}{\Omega_j} & 0 \end{bmatrix}. \quad (33d)$$

When the incidence amplitudes $a_{L,R}$ are known, the reflection amplitudes $r_{L,R}$ and the transmission amplitudes $t_{L,R}$ can be obtained by solving Eq. (32). In particular, imposing $a_R = 0$ and giving $a_L \neq 0$, the co- and cross-polarized reflectances $R_{LL} = \left| \frac{r_L}{a_L} \right|^2$ and $R_{RL} = \left| \frac{r_R}{a_L} \right|^2$, as well as the co- and cross-polarized transmittances $T_{LL} = \left| \frac{t_L}{a_L} \right|^2$ and $T_{RL} = \left| \frac{t_R}{a_L} \right|^2$ can be calculated. Similarly, the co- and cross-polarized reflectances $R_{RR} = \left| \frac{r_R}{a_R} \right|^2$ and $R_{LR} = \left| \frac{r_L}{a_R} \right|^2$, as well as the co- and cross-polarized transmittances $T_{RR} = \left| \frac{t_R}{a_R} \right|^2$ and $T_{LR} = \left| \frac{t_L}{a_R} \right|^2$ can be obtained after setting $a_R \neq 0$ and $a_L = 0$.

4.2 Numerical Results

All results presented here were calculated by using $A_c = 1.968$, $B_c = -0.759 \times 10^{-4}$, $D_0 = 1.9749$, $D_1 = -0.0964 \times 10^{-2}$, and $D_2 = -0.7262 \times 10^{-4}$. These values hold at $\lambda_0 = 633$ nm for tantalum-oxide CTFs deposited with $\chi_v = 8^\circ$ [9, 14, 18]. Accordingly, we set $\varepsilon_c = 2.125$ and $\varepsilon_d = 1.981$ and ignored dispersion for $\lambda_0 \in [500, 700]$ nm.

4.2.1 Periodic-TIMAB Slab

Spectra of co- and cross-polarized remittances of a periodic-TIMAB slab with $h = 1$, $N = 50$, and $\Omega_j = 260$ nm $\forall j \in [1, N]$ are shown in Fig. 10 for $\lambda_0 \in [500, 700]$ nm. The spectra of R_{LL} and R_{RR} are almost perfectly superimposable, as also those of T_{RR} and T_{LL} , R_{RL} and R_{LR} , as well as T_{RL} and T_{LR} . The cross-polarized reflectances do not exceed 0.12 for $\lambda_0 \in [500, 700]$ nm, while the cross-polarized transmittances are negligible everywhere in the same spectral regime. Co-polarized reflectances are very high in a narrow spectral regime, which is the polarization-universal Bragg regime, wherein normally incident circularly polarized plane waves are almost totally reflected regardless of their handedness.

The center wavelength λ_{PUB} of the polarization-universal Bragg regime increases with the half structural period Ω , as shown in Figs. 11 and 12, where the spectra of the co- and cross-polarized remittances of periodic TIMABs are presented for $\Omega = 250$ nm and $\Omega = 270$ nm, respectively. As demonstrated by Fig. 13, λ_{PUB} is linearly dependent on Ω .

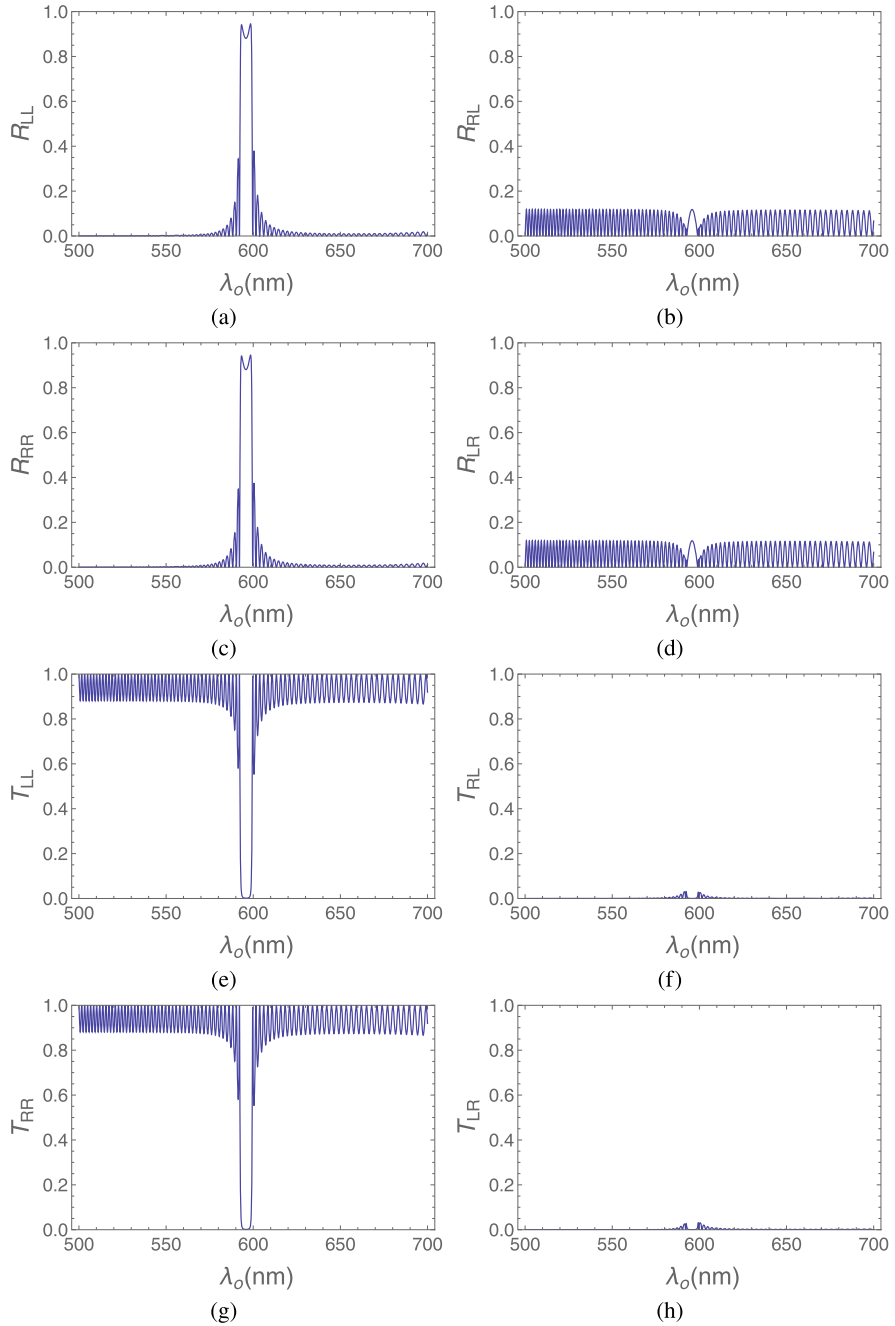


Fig. 10 Spectra of all eight remittances of a periodic-TIMAB slab with $h = 1$, $N = 50$, and $\Omega_j = 260 \text{ nm } \forall j \in [1, N]$

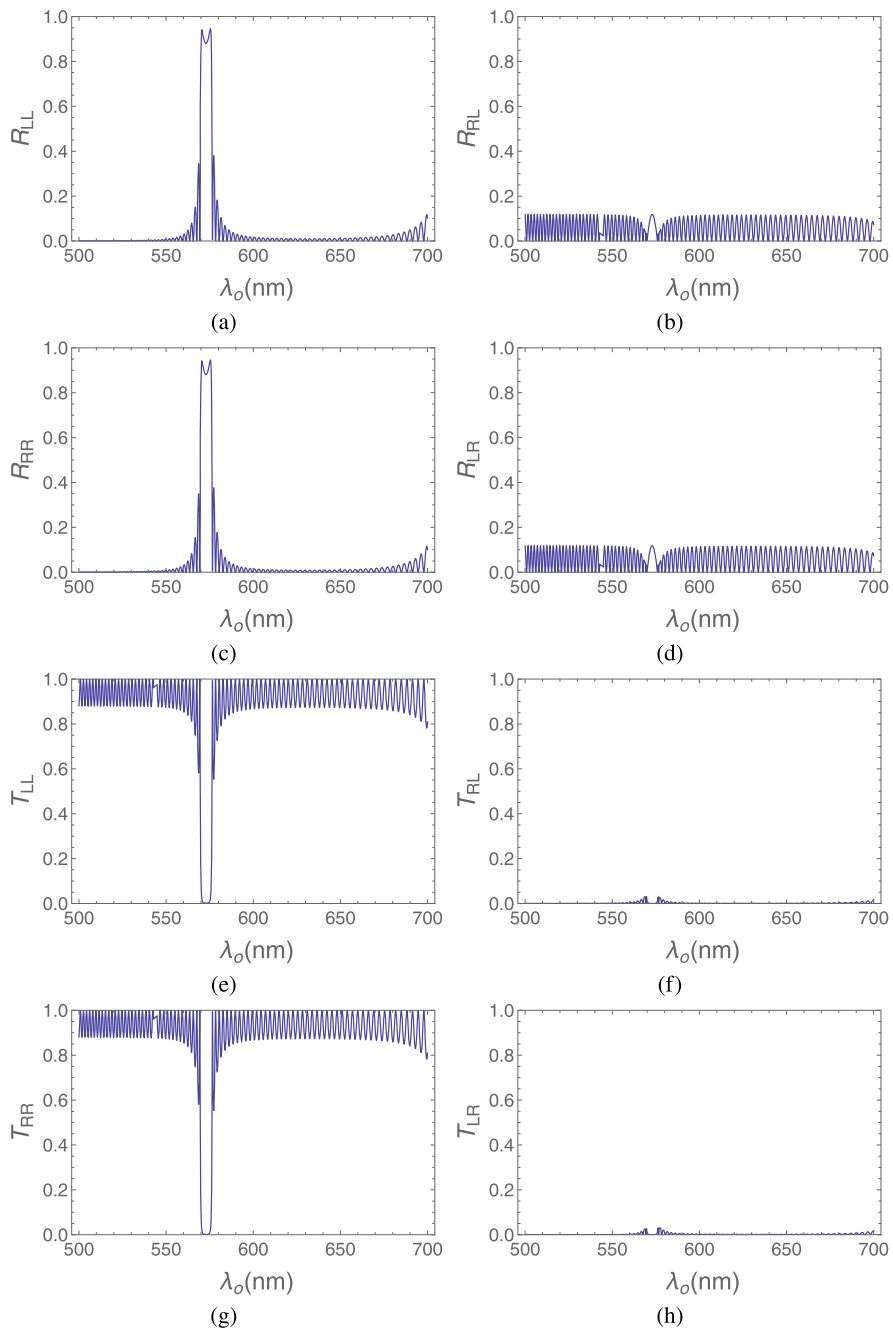


Fig. 11 Spectra of all eight remittances of a periodic-TIMAB slab with $h = 1$, $N = 50$, and $\Omega_j = 250 \text{ nm } \forall j \in [1, N]$

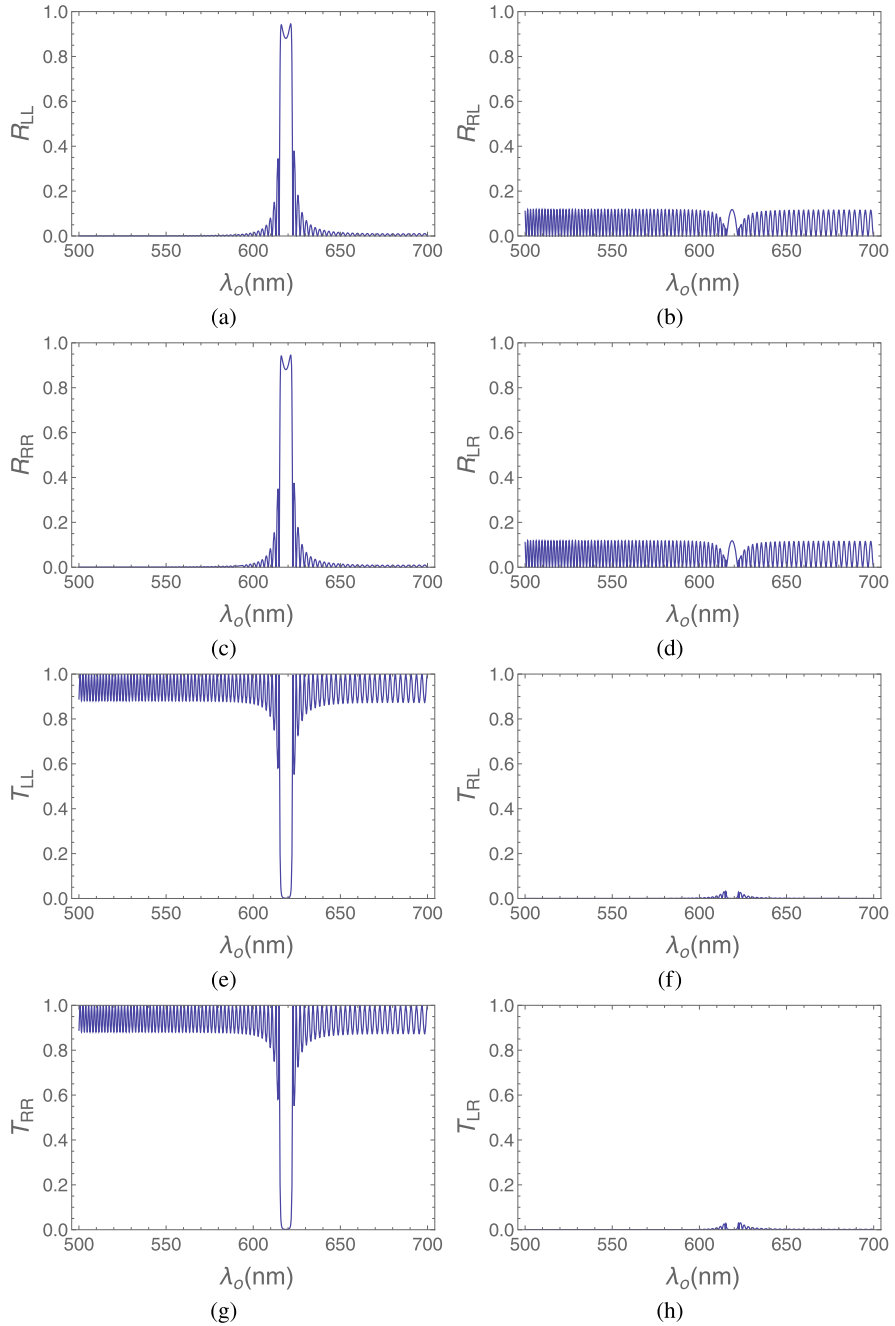
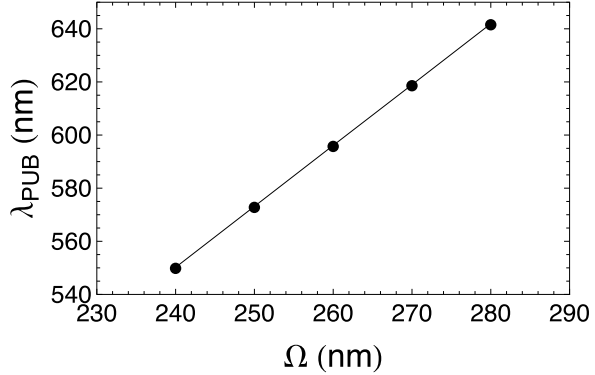


Fig. 12 Spectra of all eight remittances of a periodic-TIMAB slab with $h = 1$, $N = 50$, and $\Omega_j = 270 \text{ nm } \forall j \in [1, N]$

Fig. 13 Center wavelength λ_{PUB} of the universal Bragg regime as a function of Ω for a periodic-TIMAB slab ($\Omega_j = \Omega \text{ nm } \forall j \in [1, N]$)



4.2.2 Linearly Chirped TIMAB Slab

As noted in Sec. 4.2.1, the polarization-universal bandgap exhibited by a periodic TIMAB is very narrow. The full-width-at-half-maximum (FWHM) bandwidth of the co-polarized reflectances in Figs. 10, 11, and 12 is about 7 nm.

Recently, some of us examined linearly chirped TIMAB slabs, which feature a polarization-universal bandgap significantly wider than the periodic-TIMAB slabs [12]. In those chirped TIMABs, Ω_j linearly increases with $j \in [1, N]$, i.e.,

$$\Omega_j = \Omega_{\min} + \frac{\Omega_{\max} - \Omega_{\min}}{N - 1}(j - 1), \quad j \in [1, N]. \quad (34)$$

As an example, spectra of the co- and cross-polarized remittances of a linearly chirped TIMAB with $h = 1$, $N = 50$, lower bound of the chirping range $\Omega_{\min} = 250$ nm, and upper bound of the chirping range $\Omega_{\max} = 270$ nm are shown in Fig. 14. The center wavelength of the bandgap is $\lambda_{UC} = 596$ nm, practically coinciding with the center wavelength λ_{PUB} of the bandgap of the periodic TIMAB with half structural period equal to the central value of the chirping range ($\Omega = 260$ nm). The FWHM bandwidth of the co-polarized reflectance is 40 nm, more than five times the FWHM bandwidth of the periodic TIMAB with the same number of bilayer cells. However, the co-polarized reflectances (transmittances) in the bandgap turn out to be lower (higher) than the co-polarized reflectances (transmittances) of the periodic TIMAB. Similar conclusions have previously been drawn for linearly chirped CSTFs [18].

The values of R_{LL} (T_{LL}) and R_{RR} (T_{RR}) in the bandgap can be increased (decreased) by augmenting the number of bilayers. Spectra of the co- and cross-polarized remittances of a linearly chirped TIMAB with the parameters same as for Fig. 14 but with $N = 80$ are shown in Fig. 15. The center wavelength of the bandgap did not change; but the FWHM of the co-polarized reflectances is 44 nm, which is slightly larger than for $N = 50$, while the average co-polarized reflectances (transmittances) in the bandgap are significantly higher (lower).

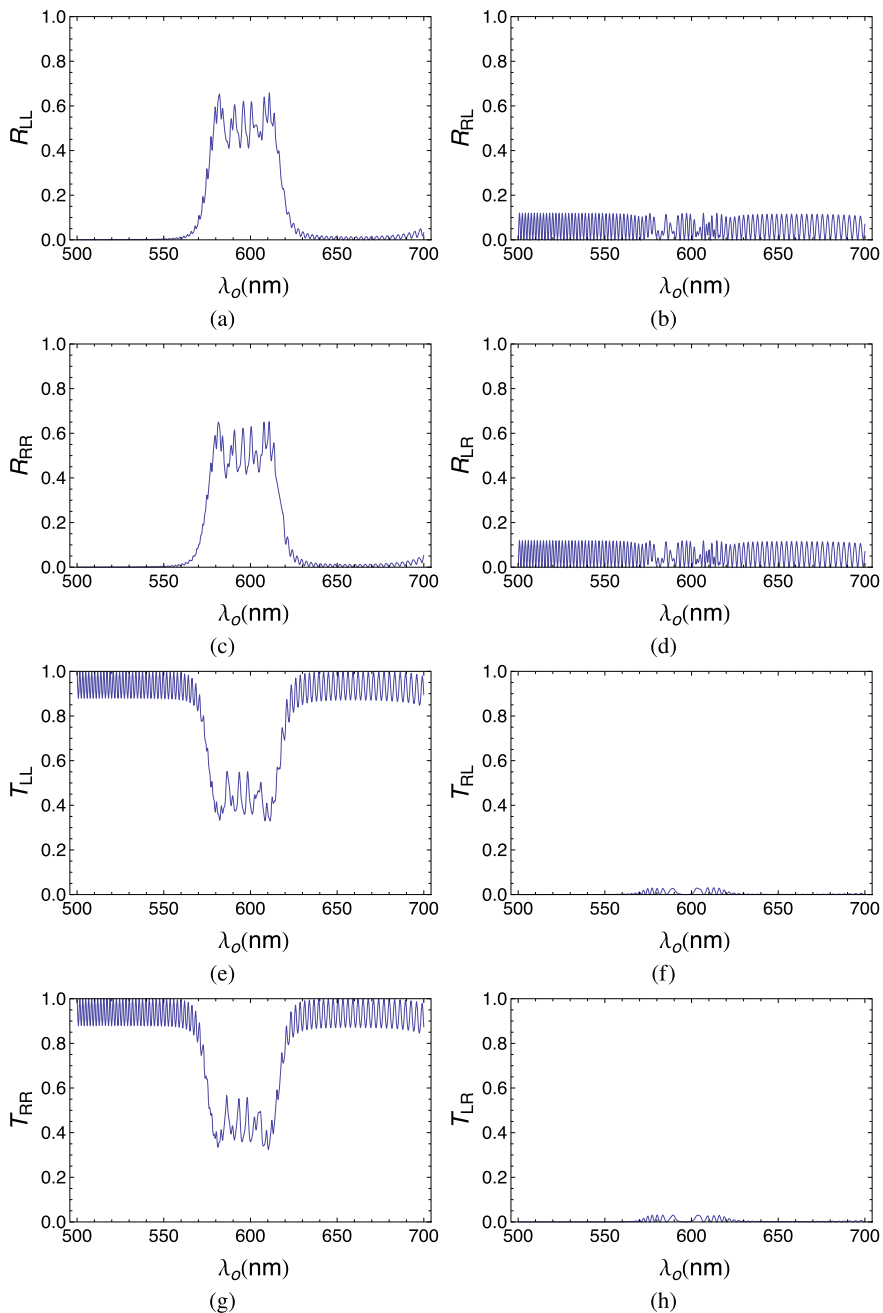


Fig. 14 Spectra of all eight remittances of a linearly chirped TIMAB slab with $h = 1$, $N = 50$, $\Omega_{\min} = 250$ nm, and $\Omega_{\max} = 270$ nm

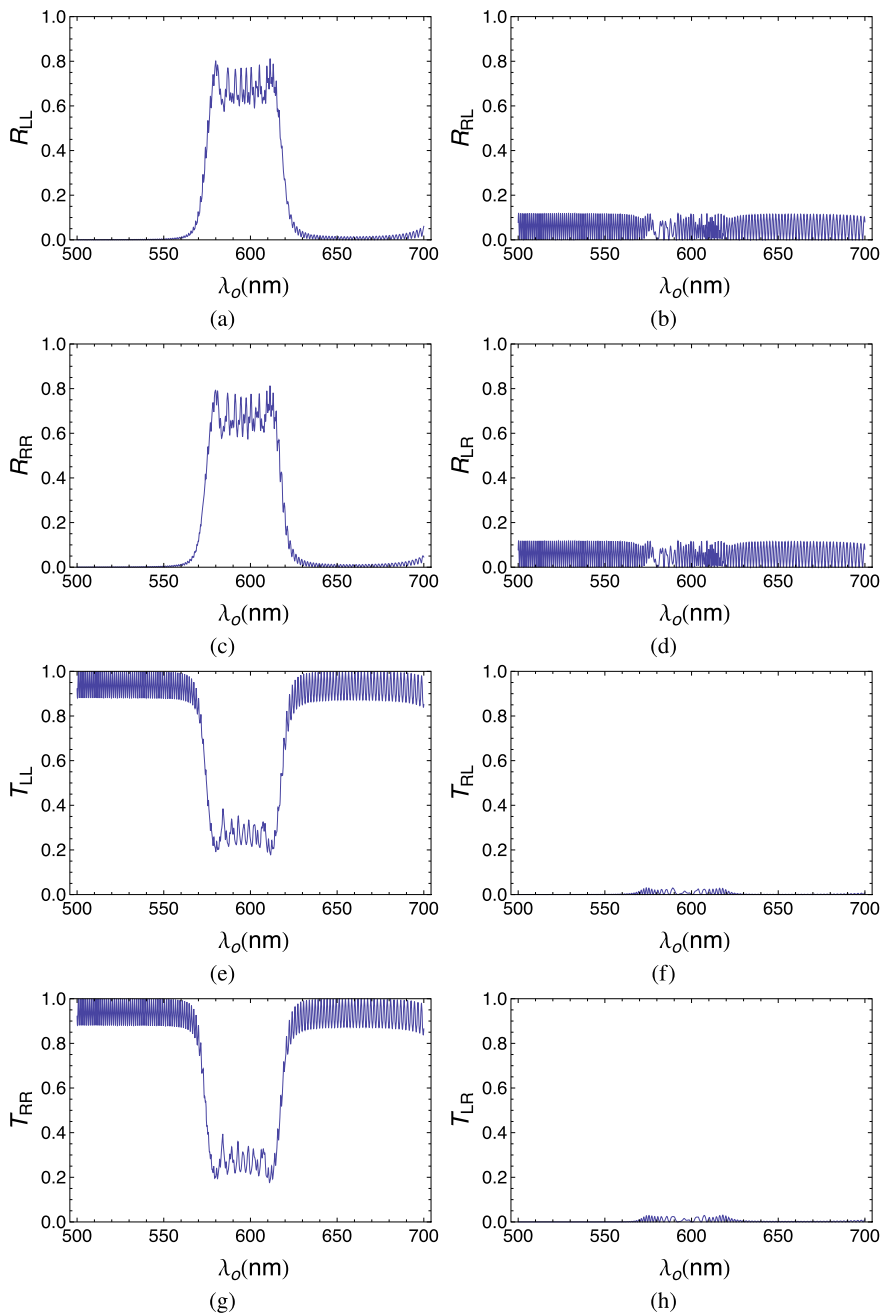


Fig. 15 Spectra of all eight remittances of a linearly chirped TIMAB slab with $h = 1$, $N = 80$, $\Omega_{\min} = 250$ nm, and $\Omega_{\max} = 270$ nm

Another way to increase (decrease) the average co-polarized reflectances (transmittances) in the bandgap requires reduction of the width of the chirping range $\Delta\Omega = \Omega_{\max} - \Omega_{\min}$. Spectra of the co- and cross-polarized remittances of a linearly chirped TIMAB slab with $h = 1$, $N = 50$, and $\Delta\Omega = 10$ nm ($\Omega_{\min} = 255$ nm, $\Omega_{\max} = 265$ nm) are shown in Fig. 16. Since the central value of the chirping range is 260 nm, the central wavelength of the bandgap remains unchanged. The average co-polarized reflectances (transmittances) are significantly higher (lower) than their counterparts for the chirped TIMAB slab with the $\Delta\Omega = 20$ nm, whereas, as expected, the FWHM bandwidth of the bandgap is lower.

The foregoing results allow us to conclude as follows:

- (i) periodic TIMAB slabs exhibit a narrow polarization-universal bandgap;
- (ii) linearly chirped TIMAB slabs exhibit a wider polarization-universal bandgap;
- (iii) increasing the chirping range increases the FWHM bandwidth of the bandgap but decreases (increases) the average co-polarized reflectances (transmittances) in the bandgap; and
- (iv) the average co-polarized reflectances (transmittances) in the bandgap can be increased (decreased) by increasing the number of bilayer cells in the TIMAB slab.

5 Final Remarks

High multiplicity of different SPP waves, including superluminal ones, can exist at metal/TIMAB interface for a fixed propagation direction. Indeed, comparing the solutions of silver/TIMAB and silver/CSTF boundary-value problems for SPP wave-propagation shows that the number of SPP waves that can be guided in a specific direction is significantly increased by interlacing in the TIMAB. Moreover, TIMABs exhibit a polarization-universal bandgap on axial excitation. Periodic TIMAB slabs feature a narrow bandgap with high reflectance. Chirped TIMAB slabs exhibit wider bandgap but reflect less efficiently.

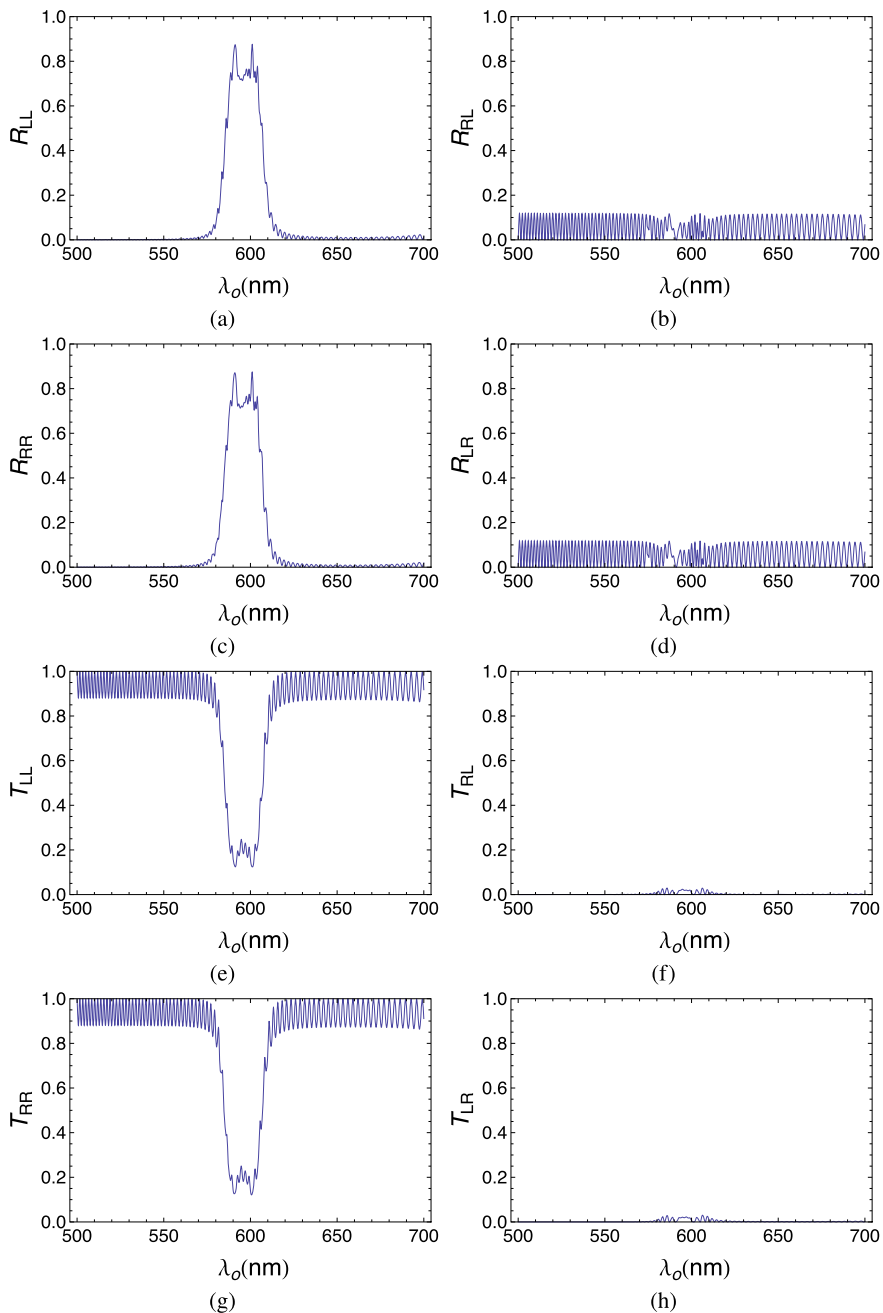


Fig. 16 Spectra of all eight remittances of a linearly chirped TIMAB slab with $h = 1$, $N = 50$, $\Omega_{\min} = 255$ nm, and $\Omega_{\max} = 265$ nm

References

1. V. Pierro, V. Fiumara, F. Chiadini, F. Bobba, G. Carapella, C. Di Giorgio, O. Durante, R. Fittipaldi, E. Mejuto Villa, J. Neilson, M. Principe, I.M. Pinto, On the performance limits of coatings for gravitational wave detectors made of alternating layers of two materials. *Opt. Mater.* **96**, 109269 (2019). <https://doi.org/10.1016/j.optmat.2019.109269>
2. M. Armano, H. Audley, J. Baird, P. Binetruy, M. Born, D. Bortoluzzi, N. Brandt, E. Castelli, A. Cavalleri, A. Cesarini, A.M. Cruise, K. Danzmann, M. de Deus Silva, I. Diepholz, G. Dixon, R. Dolesi, L. Ferraioli, V. Ferroni, E.D. Fitzsimons, R. Flatscher, M. Freschi, I.O. A. García, R. Gerndt, L. Gesa, D. Giardini, F. Gibert, R. Giusteri, C. Grimaldi, J. Grzymisch, F. Guzman, I. Harrison, M.-S. Hartig, G. Heinzl, M. Hewitson, D. Hollington, D. Hoyland, M. Hueller, H. Inchauspé, O. Jennrich, P. Jetzer, U. Johann, B. Johlander, N. Karnesis, B. Kaune, C.J. Killow, N. Korsakova, J.A. Lobo, L. Liu, J.P. López-Zaragoza, R. Maarschalkerweerd, D. Mance, V. Martín, L. Martín-Polo, F. Martín-Porqueras, J. Martino, P.W. McNamara, J. Mendes, L. Mendes, N. Meshksar, A. Monsky, M. Nofrarias, S. Paczkowski, M. Perreux-Lloyd, A. Petiteau, P. Pivato, E. Plagnol, J. Ramos-Castro, J. Reiche, F. Rivas, D.I. Robertson, G. Russano, J. Sanjuan, J. Slutsky, C.F. Sopuerta, F. Steier, T. Sumner, D. Texier, J.I. Thorpe, D. Vetrugno, S. Vitale, V. Wand, G. Wanner, H. Ward, P.J. Wass, W.J. Weber, L. Wissel, A. Wittchen, P. Zweifel, Sensor noise in *LISA Pathfinder*: in-flight performance of the optical test mass readout. *Phys. Rev. Lett.* **126**(13), 131103 (2021). <https://doi.org/10.1103/PhysRevLett.126.131103>
3. E. Semouchkina (ed.), *Dielectric Metamaterials and Metasurfaces in Transformation Optics and Photonics* (Woodhead, Duxford, 2022). <https://doi.org/10.1016/B978-0-12-820596-9.00011-X>
4. O. Durante, M. Magnozzi, V. Fiumara, J. Neilson, M. Canepa, G. Avallone, F. Bobba, G. Carapella, F. Chiadini, R. DeSalvo, R. De Simone, C. Di Giorgio, R. Fittipaldi, A. Micco, I.M. Pinto, A. Vecchione, V. Pierro, V. Granata, Toward the optimization of SiO₂ and TiO₂-based metamaterials: morphological, structural, and optical characterization. *Opt. Mater.* **157**, 116038 (2024). <https://doi.org/10.1016/j.optmat.2024.116038>
5. L. Wang, M. Karaaslan (eds.), *Advanced Metamaterials for Engineers* (IOP Publishing, Bristol, 2023). <https://doi.org/10.1088/978-0-7503-5754-8>
6. R.A. Fiallo, M.W. Horn, A. Lakhtakia, Polarization-universal bandgaps realized with chiral sculptured thin films. *J. Opt. Soc. Am. B* **39**(10), 2697–2704 (2022). <https://doi.org/10.1364/JOSAB.467861>
7. A. Lakhtakia, Axially excited, tightly interlaced, chiral sculptured thin films for polarization-universal bandgaps. *Optik* **119**(4), 175–179 (2008). <https://doi.org/10.1016/j.ijleo.2006.07.013>
8. V.C. Venugopal, A. Lakhtakia, Sculptured thin films: Conception, optical properties, and applications, in *Electromagnetic Fields in Unconventional Materials and Structures*, ed. by O.N. Singh, A. Lakhtakia (Wiley, New York, 2000), pp. 151–216
9. I. Hodgkinson, Q.h. Wu, J. Hazel, Empirical equations for the principal refractive indices and column angle of obliquely deposited films of tantalum oxide, titanium oxide, and zirconium oxide. *Appl. Opt.* **37**(13), 2653–2659 (1998). <https://doi.org/10.1364/AO.37.002653>
10. A. Lakhtakia, R. Messier, *Sculptured Thin Films: Nanoengineered Morphology and Optics* (SPIE Press, Bellingham, 2005). <https://doi.org/10.1117/3.585322>
11. R. De Simone, F. Chiadini, V. Fiumara, A. Lakhtakia, Electromagnetic surface waves guided by the interface of a metal and a tightly interlaced matched ambidextrous bilayer. *J. Opt. (United Kingdom)* **26**(7), 075003 (2024). <https://doi.org/10.1088/2040-8986/ad52a1>
12. R. De Simone, F. Chiadini, V. Fiumara, Polarization-universal bandgap in chirped tightly interlaced matched ambidextrous bilayers. *Opt. Eng.* **63**(11), 117105
13. A. Lakhtakia, The circular Bragg phenomenon updated. *More Adventures in Contemporary Electromagnetic Theory*, ed. by F. Chiadini, V. Fiumara (Springer, Cham, 2024)

14. F. Chiadini, A. Lakhtakia, Extension of Hodgkinson's model for optical characterization of columnar thin films. *Microwave Opt. Technol. Lett.* **42**(1), 72–73 (2004). <https://doi.org/10.1002/mop.20212>
15. J.A. Polo Jr., T.G. Mackay, A. Lakhtakia, *Electromagnetic Surface Waves: A Modern Perspective* (Elsevier, Waltham, 2013). <https://doi.org/10.1016/C2011-0-07510-5>
16. F. Chiadini, V. Fiumara, A. Scaglione, A. Lakhtakia, Compound guided waves that mix characteristics of surface-plasmon-polariton, Tamm, Dyakonov–Tamm, and Uller–Zenneck waves. *J. Opt. Soc. Am. B* **33**(6), 1197–1206 (2016). <https://doi.org/10.1364/JOSAB.33.001197>
17. L. Li, Y. Shi, T.J. Cui, *Electromagnetic Metamaterials and Metasurfaces: From Theory to Applications* (Springer, Singapore, 2024). <https://doi.org/10.1007/978-981-99-7914-1>
18. F. Chiadini, A. Lakhtakia, Design of wideband circular-polarization filters made of chiral sculptured thin films. *Microwave Opt. Technol. Lett.* **42**(2), 135–138 (2004). <https://doi.org/10.1002/mop.20231>
19. Refractive index database <https://refractiveindex.info/>. Accessed 30 May 2024
20. S. Erten, A. Lakhtakia, G.D. Barber, Experimental investigation of circular Bragg phenomenon for oblique incidence. *J. Opt. Soc. Am. A* **32**(5), 764–770 (2015). <https://doi.org/10.1364/JOSAA.32.000764>
21. F. Chiadini, V. Fiumara, A. Scaglione, A. Lakhtakia, Multiple excitations of a surface-plasmon-polariton wave guided by a columnar thin film deposited on a metal grating. *Opt. Eng.* **53**(12), 127105 (2014). <https://doi.org/10.1117/1.OE.53.12.127105>
22. T.G. Mackay, A. Lakhtakia, *The Transfer-Matrix Method in Electromagnetics and Optics* (Springer, Cham, 2020). <https://doi.org/10.1007/978-3-031-02022-3>



Francesco Chiadini is Associate Professor of Electromagnetics in the Department of Industrial Engineering at the University of Salerno, Italy, where he leads the Microwave and Optical Technology Laboratory. He received the Laurea degree in Electronic Engineering and the Ph.D. degree in Information Engineering from the University of Salerno. A Senior Member of the Institute of Electrical and Electronics Engineers, Optica, and SPIE, he has coauthored more than 200 scientific papers of which more than 100 are articles in international peer-reviewed journals. He is currently serving as an Associate Editor of *Microwave and Optical Technology Letters*, and reviews submissions regularly for many journals, conferences, and funding agencies. He is an active member of the LIGO-Virgo-KAGRA Collaboration. His research interests encompass electromagnetic surface waves, antireflection coatings, mirrors for gravitational interferometry, and bioinspired structures.



Roberta De Simone is a Postdoctoral Fellow in Electromagnetics at the University of Salerno, Italy. She leads the teaching activities in the Microwave and Optical Technology Laboratory of the Department of Industrial Engineering, University of Salerno. She received the Laurea degree in Electronic Engineering (with the highest grade) and the Ph.D. degree in Industrial Engineering from the same university. She has coauthored several scientific papers in international peer-reviewed journals, and she is currently serving as a regular reviewer for many journals. She is a member of the LIGO-Virgo-KAGRA Collaboration and the Einstein Telescope (ET) Collaboration. She is also affiliated with the Italian National Institute for Nuclear Physics (INFN).

Her research interests include electromagnetic surface waves, nanostructured thin films, antireflection coatings, and mirrors for gravitational interferometry.



Vincenzo Fiumara received the Laurea degree in Electrical Engineering (*summa cum laude*) and the Ph.D. degree in Applied Electromagnetics from the University of Salerno, Italy, in 1993 and 1997, respectively. In 1998, he was awarded a CNR (Italian National Research Council) Fellowship. He became an Assistant Professor of Electromagnetics in 1999 at the Department of Information Engineering and Electrical Engineering of the University of Salerno. He joined the Department of Engineering at the University of Basilicata in 2005, where he is now full Professor of Electromagnetics. He is a Senior Member of SPIE. He is a member of the LIGO-Virgo-KAGRA Collaboration and the Einstein Telescope (ET) Collaboration, and he is also affiliated with the Italian National Institute for Nuclear Physics (INFN). His current research interests include electromagnetic surface waves, sculptured thin films, mirror coatings for gravitational wave detectors, and disordered photonic structures.



Akhlesh Lakhtakia received his B.Tech. (1979) and D.Sc. (2006) degrees from the Banaras Hindu University and his M.S. (1981) and Ph.D. (1983) degrees from the University of Utah. He joined the Department of Engineering Science and Mechanics at The Pennsylvania State University in 1983, where now he is Evan Pugh University Professor of Engineering Science and Mechanics. He is also a Visiting Professor of Mathematics at the University of Edinburgh.

Dr. Lakhtakia has been elected a Fellow of Optical Society of America (now Optica), SPIE, Institute of Physics (UK), American Association for the Advancement of Science, American Physical Society, Institute of Electrical and Electronics Engineers (IEEE), Royal Society of Chemistry, Royal Society of Arts, and Sigma Xi. He has been designated a Distinguished Alumnus of both of his *almae matres* at the highest level. Awards at Penn State include: Outstanding Research Award, Outstanding Advising Award, Premier Research Award, Outstanding Teaching Award, and the Faculty Scholar Medal in Engineering. Extramural awards include the 2010 SPIE Technical Achievement Award, the 2016 Walston Chubb Award for Innovation, the 2022 Smart Structures and Materials Lifetime Achievement Award, the 2022 IEEE Antennas and Propagation Society Distinguished Achievement Award, the 2022 Radio Club of America Lifetime Achievement Award, and the 2024 SPIE Gold Medal. He has served as a Sigma Xi Distinguished Lecturer (2022–2024) and a Jefferson Science Fellow at the U.S. State Department (2022–2023). His current research interests include electromagnetic scattering, surface multiplasmonics, photovoltaic solar cells, sculptured thin films, mimics, engineered biomimicry, and forensic science.

Analysis of Multiple Scattering by Cylindrical Arrays and Applications to Electromagnetic Shielding



Grigorios P. Zouros , Minas Kouroublakis , and Nikolaos L. Tsitsas 

1 Introduction

Electromagnetic (EM) scattering by finite, infinite, or periodic arrangements of infinite cylinders is essential for understanding wave interactions in structured media, with a richness of applications such as antenna design, active ferromagnetic devices, tunable light transport, plasmonics, metasurfaces, metamaterials, and EM shielding. Various studies have collectively enhanced our understanding of EM interactions by such configurations, showcasing a range of analytical, numerical, and hybrid methods. This diverse methodological toolkit provides a robust foundation for further research and practical applications in various fields of science and engineering. A pioneer investigation of wave scattering by gratings of conducting cylinders was performed in [11] using an integral equation method, where the reflected and transmitted amplitudes were calculated by utilizing the surface field on one element of the array. A finite-difference coupling technique was developed in [10] for arrays of conducting cylinders. This numerical method allowed the calculation of the reflected and transmitted amplitudes directly, without the need of the surface field computation. A point matching technique was presented in [7] for arrays of both conducting and dielectric cylinders, providing a broader perspective on the influence of the size and spacing of the elements to improve the directivity of linear antennas. Multiple scattering by two parallel dielectric cylinders was investigated in [24] via Maxwell's equations solution with appropriate boundary conditions (BCs).

G. P. Zouros

School of Electrical and Computer Engineering, National Technical University of Athens, Athens, Greece

e-mail: zouros@mail.ntua.gr

M. Kouroublakis · N. L. Tsitsas (✉)

School of Informatics, Aristotle University of Thessaloniki, Thessaloniki, Greece

e-mail: ntsitsas@csd.auth.gr

That work provided a detailed mathematical framework for understanding the interactions between closely spaced cylindrical scatterers. Müller's scattering matrix method was employed in [27] for two penetrable cylinders at oblique incidence, and the derived formal solutions were utilized to highlight the complexities introduced by the oblique illumination and the penetrability of the array elements. A nonlinear programming approach was presented in [5] for multiple scattering by a planar array of parallel dielectric cylinders under normal incidence, demonstrating the damping of internal resonance features of the array. A Green's function method for the analysis of EM wave propagation in periodic arrangements of dielectric cylinders was proposed in [1]. The main application concerned the accurate computation of modes propagating in configurations of the so-called holey fibers. A semi-analytical recursive formula was implemented in [9] for periodic arrays of circular cylinders. This method involved the calculation of the reflection and transmission matrices of a periodic array, and then layered structures were examined via this recursive formula. EM scattering from periodic arrays with defects was studied in [26] via a recursive transition-matrix algorithm with pseudo-periodic Fourier transform. This approach focused on the impact of defects within the array, providing valuable insights into the robustness and reliability of periodic structures. Translational symmetries and the discrete Fourier transform were utilized in [13] for arrays featuring axially magnetized parallel plasma columns, highlighting the unique scattering properties of gyrotropic materials, such as the sensitivity response due to slight variations of the external static magnetic field. A volume-integral-equation method employing entire-domain Galerkin techniques was developed in [23] and applied for the investigation of reflection and refraction phenomena by layered all-dielectric gratings in the form of periodic rectangular cylinders. Finally, a hybrid method of auxiliary sources (MAS), combined with the fast multipole method, was presented in [17] and [16] to analyze EM scattering from large perfectly electric conducting (PEC) or dielectric cylindrical arrays, demonstrating a strategy to handle complex large-scale problems with reduced computational cost.

Apart from the key methods employed in notable research works, numerous cylindrical array-based modern applications exist in fields such as active ferromagnetic devices, tunable light transport, plasmonics, metasurfaces, metamaterials, and EM shielding. The design and optimization of devices that rely on ferromagnetic materials were examined in [14], via EM scattering from a finite number of ferromagnetic microwire cylinders. Toroidal dipolar excitations in cylindrical structures were analyzed in [4], aiming at sensing applications. Tunable light transport in disordered systems was examined in [2] by considering energy and negative asymmetry parameters calculations in coated magneto-optical cylindrical arrays, targeting to the development of advanced optical devices capable of controlling light propagation in complex media. The design of plasma-based devices that leverage plasmonic effects was investigated in [8] via a finite array of magnetized plasma cylinders near the frequencies of plasmon resonances. Magnetic mirrors were proposed in [15] by exploiting electric resonances. Reconfigurable wavefront manipulation via gradient metasurfaces was achieved in [22] using elliptical dielectric cylindrical arrays. High transmission and absorption were reported in [21] from metasurfaces

composed of periodically corrugated cylindrical arrays, crucial for the development of devices with tailored EM properties. Systems of polaritonic rods for achieving multifunctional metamaterials were studied in [18]. The effect of gridding an EM shield was examined in [25]. An effective medium approach for multilayered cylindrical metamaterial systems was derived in [19]. The shielding effectiveness (SE) was examined in [12] for various metamaterial cylindrical arrays, aiming at the design of devices for the protection of sensitive electronic equipment from unwanted EM interference (EMI).

In this work, we analyze multiple scattering of EM waves by cylindrical arrays using the MAS. We present the mathematical treatment concerning the application of MAS to conduct full wave scattering analysis by PEC, dielectric and core-shell PEC–dielectric rectangular arrays, using excitations such as a current filament or a plane wave. We also extend the application to the analysis of circular arrays. To highlight the robustness of the developed method, we apply the MAS to demonstrate EM shielding via cylindrical array EM shields (CAES). We define the parameter of SE as a figure of merit and show that rectangular or circular cylindrical arrays may be used to significantly reduce the penetrating fields and thus provide protection to sensitive electronic devices from EMI. The results obtained from MAS are compared to the ones obtained from the HFSS commercial software, and an agreement is met that establishes the verification of the provided method.

Hereinafter, an $\exp(i\omega t)$ time dependence is assumed and suppressed, where ω is the angular frequency.

2 Multiple Scattering by PEC Arrays

Figure 1a illustrates the geometry of a cylindrical rectangular array where each cylindrical element has arbitrary cross section, and the array consists of N_x columns and N_y rows, therefore $N_t = N_x N_y$ cylinders in total. The center of each cylinder lies at

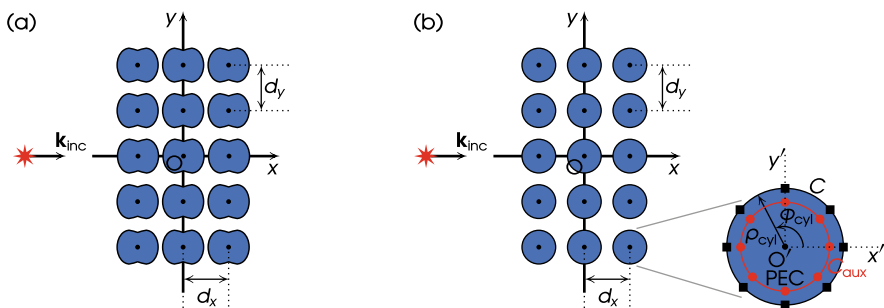


Fig. 1 Rectangular array of PEC cylinders. (a) Elements of arbitrary cross section. (b) Elements of circular cross section

$$x_c^{(n_x, n_y)} = (n_x - 1)d_x - \frac{(N_x - 1)}{2}d_x, \quad (1a)$$

$$y_c^{(n_x, n_y)} = (n_y - 1)d_y - \frac{(N_y - 1)}{2}d_y, \quad (1b)$$

where $n_x = 1, \dots, N_x$ is the column number, $n_y = 1, \dots, N_y$ is the row number, d_x is the distance between the centers of two adjacent cylinders along the x -direction (spatial period along the x -direction), and d_y is the distance between two adjacent cylinders along the y -direction (spatial period along the y -direction).

To simplify the presentation of the MAS formulation, in what follows, we describe the procedure for circular elements, as illustrated in Fig. 1b. Using the global system of coordinates Oxy , the coordinates of each perfectly electric conducting (PEC) cylinder boundary $C^{(n_x, n_y)}$ are given by

$$x_{\text{cyl}}^{(n_x, n_y)} = \rho_{\text{cyl}} \cos \phi_{\text{cyl}} + x_c^{(n_x, n_y)}, \quad (2a)$$

$$y_{\text{cyl}}^{(n_x, n_y)} = \rho_{\text{cyl}} \sin \phi_{\text{cyl}} + y_c^{(n_x, n_y)}, \quad (2b)$$

where ρ_{cyl} is the radius and ϕ_{cyl} is the polar angle of each cylinder's local coordinate system $O'x'y'$, as depicted in Fig. 1b. The structure is illuminated by a TM^z cylindrical wave with incident wavevector \mathbf{k}_{inc} , radiated from an electric current filament source (denoted by the red star in Fig. 1). The incident electric and magnetic fields for this stimulation are given by

$$\mathbf{E}_{\text{inc}}(\mathbf{r}) = -\frac{k_0 Z_0}{4} I H_0^{(2)}(k_0 |\mathbf{r}_f - \mathbf{r}|) \hat{\mathbf{z}}, \quad (3a)$$

$$\mathbf{H}_{\text{inc}}(\mathbf{r}) = -\frac{ik_0}{4} \frac{(y_f - y)\hat{\mathbf{x}} + (x - x_f)\hat{\mathbf{y}}}{|\mathbf{r}_f - \mathbf{r}|} I H_0^{(2)}(k_0 |\mathbf{r}_f - \mathbf{r}|), \quad (3b)$$

where $\mathbf{r} = (x, y)$ is the observation point, $\mathbf{r}_f = (x_f, y_f)$ is the position vector of the current filament, I is the constant electric current amplitude of the filament, $k_0 = \omega\sqrt{\varepsilon_0\mu_0}$ is the free space wavenumber, $Z_0 = \sqrt{\mu_0/\varepsilon_0}$ is free space impedance, and $H_0^{(2)}$ is the Hankel function of the second kind and zeroth order.

The application of MAS on the (n_x, n_y) cylinder of the array is depicted in Fig. 1b. An auxiliary surface $C_{\text{aux}}^{(n_x, n_y)}$ with radius $\rho_{\text{aux}} < \rho_{\text{cyl}}$ is defined, where N auxiliary sources (ASs) in the form of z -directed infinitely long electric current filaments, are homogeneously distributed. In this equivalent situation, the scattered field by each cylinder is the superposition of the fields radiated by the ASs in an unbounded medium filled with the surrounding medium, which in this case is vacuum. Thus, the total scattered field is simply the superposition of the fields radiated by every AS, i.e.,

$$\mathbf{E}_{\text{sc}}(\mathbf{r}) = -\frac{k_0 Z_0}{4} \sum_{n_x=1}^{N_x} \sum_{n_y=1}^{N_y} \sum_{n=1}^N I_n^{(n_x, n_y)} H_0^{(2)}(k_0 |\mathbf{r} - \mathbf{r}_{\text{aux}, n}^{(n_x, n_y)}|) \hat{\mathbf{z}}, \quad (4)$$

where $I_n^{(n_x, n_y)}$ is the unknown complex amplitude of the n -th AS of $C_{\text{aux}}^{(n_x, n_y)}$ and $\mathbf{r}_{\text{aux}, n}^{(n_x, n_y)}$ is the position vector of the n -th AS of $C_{\text{aux}}^{(n_x, n_y)}$.

To calculate the unknown complex amplitudes $I_n^{(n_x, n_y)}$ of the auxiliary currents, we enforce the BCs for the z -directed electric field on N collocation points (CPs) on each cylinder. The local coordinates of these CPs are given by

$$x_{\text{cyl}}^{(m_x, m_y)} = \rho_{\text{cyl}} \cos\left(\frac{2\pi(m-1)}{N}\right) + x_c^{(m_x, m_y)}, \quad m = 1, \dots, N, \quad (5a)$$

$$y_{\text{cyl}}^{(m_x, m_y)} = \rho_{\text{cyl}} \sin\left(\frac{2\pi(m-1)}{N}\right) + y_c^{(m_x, m_y)}, \quad m = 1, \dots, N, \quad (5b)$$

with $m_x = 1, 2, \dots, N_x$, $m_y = 1, 2, \dots, N_y$ and $m = 1, \dots, N$, so as to distinguish between counters pertaining to ASs and CPs. The PEC BC implies that the total z -directed electric field on the boundaries of every cylinder is zero. Therefore, from (3a) and (4), one has

$$\begin{aligned} -\frac{k_0 Z_0}{4} \sum_{n_x=1}^{N_x} \sum_{n_y=1}^{N_y} \sum_{n=1}^N I_n^{(n_x, n_y)} H_0^{(2)}(k_0 |\mathbf{r}_{\text{cyl}, m}^{(m_x, m_y)} - \mathbf{r}_{\text{aux}, n}^{(n_x, n_y)}|) \\ = -\frac{k_0 Z_0}{4} I H_0^{(2)}(k_0 |\mathbf{r}_f - \mathbf{r}_{\text{cyl}, m}^{(m_x, m_y)}|), \end{aligned} \quad (6)$$

with $m_x = 1, \dots, N_x$, $m_y = 1, \dots, N_y$ and $m = 1, \dots, N$, where $\mathbf{r}_{\text{cyl}, m}^{(m_x, m_y)}$ is the position vector of the m -th CP of $C^{(m_x, m_y)}$ in the global coordinate system Oxy . Equation (6) is written in the form of a linear system as follows:

$$\mathbf{Z}\mathbf{I} = \mathbf{V}, \quad (7)$$

where \mathbf{Z} is the matrix of the linear system, \mathbf{I} is the unknown vector of the ASs current amplitudes, and \mathbf{V} is the excitation vector. Solving the aforementioned linear system, we can then compute the total electric field in any position as the superposition of (3a) and (4).

For the case of the TE^z incidence (magnetic current filament source), the equations of the incident cylindrical wave are given by

$$\mathbf{H}_{\text{inc}}(\mathbf{r}) = -\frac{k_0}{4Z_0} K H_0^{(2)}(k_0|\mathbf{r}_f - \mathbf{r}|) \hat{\mathbf{z}}, \quad (8a)$$

$$\mathbf{E}_{\text{inc}}(\mathbf{r}) = \frac{ik_0}{4} \frac{(y_f - y)\hat{\mathbf{x}} + (x - x_f)\hat{\mathbf{y}}}{|\mathbf{r}_f - \mathbf{r}|} K H_0^{(2)}(k_0|\mathbf{r}_f - \mathbf{r}|), \quad (8b)$$

where K is the complex amplitude of the magnetic current filament. The application of MAS in this instance follows the same procedure as in the TM^z case, with the difference that the electric ASs are replaced by magnetic ASs. Hence, the total scattered field is given by

$$\begin{aligned} \mathbf{E}_{\text{sc}}(\mathbf{r}) = & \frac{ik_0}{4} \sum_{n_x=1}^{N_x} \sum_{n_y=1}^{N_y} \sum_{n=1}^N K_n^{(n_x, n_y)} \frac{(x - x_{\text{aux},n}^{(n_x, n_y)})\hat{\mathbf{y}} + (y_{\text{aux},n}^{(n_x, n_y)} - y)\hat{\mathbf{x}}}{|\mathbf{r} - \mathbf{r}_{\text{aux},n}^{(n_x, n_y)}|} \\ & \times H_1^{(2)}\left(k_0|\mathbf{r} - \mathbf{r}_{\text{aux},n}^{(n_x, n_y)}|\right) \hat{\mathbf{z}}, \end{aligned} \quad (9)$$

where $K_n^{(n_x, n_y)}$ is the unknown complex amplitude of the n -th AS of $C_{\text{aux}}^{(n_x, n_y)}$. Subsequently, by applying the BC of nullifying the total electric field at N CPs on each of the cylinders, we obtain

$$\begin{aligned} & -\frac{ik_0}{4} \sum_{n_x=1}^{N_x} \sum_{n_y=1}^{N_y} \sum_{n=1}^N K_n^{(n_x, n_y)} \frac{(y_{\text{aux},n}^{(n_x, n_y)} - y_{\text{cyl},m}^{(m_x, m_y)})t_x + (x_{\text{cyl},m}^{(m_x, m_y)} - x_{\text{aux},n}^{(n_x, n_y)})t_y}{|\mathbf{r}_{\text{cyl},m}^{(m_x, m_y)} - \mathbf{r}_{\text{aux},n}^{(n_x, n_y)}|} \\ & \times H_1^{(2)}\left(k_0|\mathbf{r}_{\text{cyl},m}^{(m_x, m_y)} - \mathbf{r}_{\text{aux},n}^{(n_x, n_y)}|\right) \\ & = \frac{ik_0}{4} \sum_{n=1}^N \frac{(y_f - y_{\text{cyl},m}^{(m_x, m_y)})t_x + (x_{\text{cyl},m}^{(m_x, m_y)} - x_f)t_y}{|\mathbf{r}_f - \mathbf{r}_{\text{cyl},m}^{(m_x, m_y)}|} K H_1^{(2)}\left(k_0|\mathbf{r}_{\text{cyl},m}^{(n_x, n_y)} - \mathbf{r}_f|\right), \end{aligned} \quad (10)$$

where t_x is the x -component of the tangential unit vector on $r_{\text{cyl},m}^{(m_x, m_y)}$ and t_y is the y -component of the tangential unit vector on $r_{\text{cyl},m}^{(m_x, m_y)}$. Equation (10) is a linear system in the form of (7) with unknowns the complex amplitudes $K_n^{(n_x, n_y)}$. The solution of this system leads to the computation of the total field everywhere.

The aforementioned procedure also applies to the case where the incident field is a TM^z or a TE^z plane wave. For TM^z incidence, the incident field is expressed by

$$\mathbf{E}_{\text{inc}}(\mathbf{r}) = E_0 e^{-ik_0(x \cos \phi_{\text{inc}} + y \sin \phi_{\text{inc}})} \hat{\mathbf{z}}, \quad (11a)$$

$$\mathbf{H}_{\text{inc}}(\mathbf{r}) = \frac{1}{Z_0} \hat{\mathbf{k}}_{\text{inc}}(\mathbf{r}) \times \mathbf{E}_{\text{inc}}(\mathbf{r}), \quad (11b)$$

where E_0 is the amplitude of the incident electric field, $\hat{\mathbf{k}}_{\text{inc}}$ is the unit vector of the incident wavevector, and ϕ_{inc} is the azimuth angle of incidence. The respective expressions of the fields for the TE^z incidence are obtained by duality on (11).

An important quantity of interest in scattering problems is the scattering width, defined by [3]

$$\sigma(\phi_{\text{obs}}) = \lim_{r \rightarrow \infty} 2\pi r \frac{|\mathbf{E}_{\text{sc}}(r, \phi_{\text{obs}})|^2}{|\mathbf{E}_{\text{inc}}(r, \phi_{\text{obs}})|^2}, \quad (12)$$

where ϕ_{obs} is the azimuthal observation angle. For the case where the incident wave is a plane wave with unit amplitude, or a cylindrical wave from an excitation source with a unit current amplitude, it can be shown that (12) takes the following forms for TM^z and TE^z incidence, i.e.,

$$\begin{aligned} \sigma_{\text{TM}}(\phi_{\text{obs}}) = \frac{k_0 Z_0^2}{4} & \left| \sum_{n_x=1}^{N_x} \sum_{n_y=1}^{N_y} \sum_{n=1}^N I_n^{(n_x, n_y)} \right. \\ & \times \exp \left[ik_0 (x_{\text{aux}, n}^{(n_x, n_y)} \cos \phi_{\text{obs}} + y_{\text{aux}, n}^{(n_x, n_y)} \sin \phi_{\text{obs}}) \right] \Big|^2, \end{aligned} \quad (13a)$$

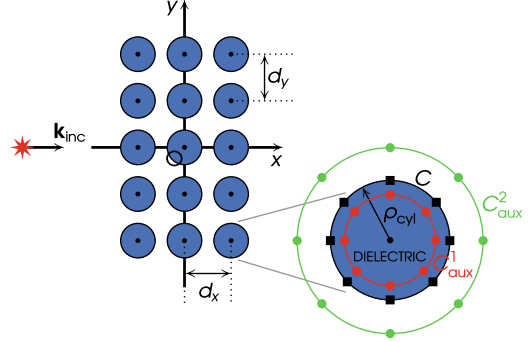
$$\begin{aligned} \sigma_{\text{TE}}(\phi_{\text{obs}}) = \frac{k_0}{4Z_0^2} & \left| \sum_{n_x=1}^{N_x} \sum_{n_y=1}^{N_y} \sum_{n=1}^N K_n^{(n_x, n_y)} \right. \\ & \times \exp \left[ik_0 (x_{\text{aux}, n}^{(n_x, n_y)} \cos \phi_{\text{obs}} + y_{\text{aux}, n}^{(n_x, n_y)} \sin \phi_{\text{obs}}) \right] \Big|^2. \end{aligned} \quad (13b)$$

3 Multiple Scattering by Dielectric Arrays

Figure 2 illustrates the geometry of a cylindrical array where each cylinder is circular (we use circular elements in order to simplify the formulation, although the methodology also supports non-circular cross sections) and dielectric, having permittivity $\varepsilon = \varepsilon_r \varepsilon_0$ and permeability $\mu = \mu_r \mu_0$, where ε_r and μ_r are the respective relative values. The various quantities (e.g., the number of cylinders and the spatial periods) are defined similarly as those in Fig. 1.

For the application of MAS for the (n_x, n_y) cylinder, two auxiliary surfaces $C_{\text{aux}}^{1, (n_x, n_y)}$ and $C_{\text{aux}}^{2, (n_x, n_y)}$ are defined with radii $\rho_{\text{aux}}^{1, (n_x, n_y)}$ and $\rho_{\text{aux}}^{2, (n_x, n_y)}$, respectively. In each surface, a set of N ASs are homogeneously distributed. The scattered field by each cylinder is the superposition of the fields radiated by the sources of $C_{\text{aux}}^{1, (n_x, n_y)}$, while the internal field is the superposition of the fields radiated by the sources of $C_{\text{aux}}^{2, (n_x, n_y)}$. The total scattered electric and magnetic fields equal the

Fig. 2 Rectangular array of circular dielectric cylinders



superposition of the corresponding fields radiated by the sources of all the $C_{\text{aux}}^{1,(n_x,n_y)}$ auxiliary surfaces. Thus, the scattered electric and magnetic fields are expressed by

$$\mathbf{E}_{\text{sc}}(\mathbf{r}) = -\frac{k_0 Z_0}{4} \sum_{n_x=1}^{N_x} \sum_{n_y=1}^{N_y} \sum_{n=1}^N I_n^{1,(n_x,n_y)} H_0^{(2)}(k_0 |\mathbf{r} - \mathbf{r}_{\text{aux},n}^{1,(n_x,n_y)}|) \hat{\mathbf{z}}, \quad (14a)$$

$$\begin{aligned} \mathbf{H}_{\text{sc}}(\mathbf{r}) = & -i \frac{k_0}{4} \sum_{n_x=1}^{N_x} \sum_{n_y=1}^{N_y} \sum_{n=1}^N I_n^{1,(n_x,n_y)} \frac{(x - x_{\text{aux},n}^{1,(n_x,n_y)}) \hat{\mathbf{y}} + (y_{\text{aux},n}^{1,(n_x,n_y)} - y) \hat{\mathbf{x}}}{|\mathbf{r} - \mathbf{r}_{\text{aux},n}^{1,(n_x,n_y)}|} \\ & \times H_1^{(2)}(k_0 |\mathbf{r} - \mathbf{r}_{\text{aux},n}^{1,(n_x,n_y)}|), \end{aligned} \quad (14b)$$

where $I_n^{1,(n_x,n_y)}$ is the complex amplitude of the n -th AS in $C_{\text{aux}}^{1,(n_x,n_y)}$, $\mathbf{r}_{\text{aux},n}^{1,(n_x,n_y)} = (x_{\text{aux},n}^{1,(n_x,n_y)}, y_{\text{aux},n}^{1,(n_x,n_y)})$ is the position vector of the n -th AS on $C_{\text{aux}}^{1,(n_x,n_y)}$ in the global coordinate system Oxy , $\hat{\mathbf{y}}$ is the unit vector along the y -direction of the global coordinate system, $\hat{\mathbf{x}}$ is the unit vector along the x -direction of the global coordinate system, and $H_1^{(2)}$ is the Hankel function of the second kind and first order. The internal field in each cylinder is the superposition of fields radiated by the sources of $C_{\text{aux}}^{2,(n_x,n_y)}$ in an unbounded medium filled with the dielectric material (ϵ, μ), thus it is given by

$$\mathbf{E}_{\text{in}}^{(n_x,n_y)}(\mathbf{r}) = -\frac{kZ}{4} \sum_{n=1}^N I_n^{2,(n_x,n_y)} H_0^{(2)}(k |\mathbf{r} - \mathbf{r}_{\text{aux},n}^{2,(n_x,n_y)}|) \hat{\mathbf{z}}, \quad (15a)$$

$$\begin{aligned} \mathbf{H}_{\text{in}}^{(n_x,n_y)}(\mathbf{r}) = & i \frac{k}{4} \sum_{n=1}^N I_n^{2,(n_x,n_y)} \frac{(x - x_{\text{aux},n}^{2,(n_x,n_y)}) \hat{\mathbf{y}} + (y_{\text{aux},n}^{2,(n_x,n_y)} - y) \hat{\mathbf{x}}}{|\mathbf{r} - \mathbf{r}_{\text{aux},n}^{2,(n_x,n_y)}|} \\ & \times H_1^{(2)}(k |\mathbf{r} - \mathbf{r}_{\text{aux},n}^{2,(n_x,n_y)}|), \end{aligned} \quad (15b)$$

where $k = \omega\sqrt{\varepsilon\mu}$ is the wavenumber in the dielectric material, $Z = \sqrt{\mu/\varepsilon}$ is the dielectric material's wave impedance, $I_n^{2,(n_x,n_y)}$ is the complex amplitude of the n -th AS of $C_{\text{aux}}^{2,(n_x,n_y)}$, and $\mathbf{r}_{\text{aux},n}^{2,(n_x,n_y)} = (x_{\text{aux},n}^{2,(n_x,n_y)}, y_{\text{aux},n}^{2,(n_x,n_y)})$ is the position vector of the n -th AS of $C_{\text{aux}}^{2,(n_x,n_y)}$ in the global coordinate system Oxy .

To calculate the unknown complex amplitudes $I_n^{1,(n_x,n_y)}$ and $I_n^{2,(n_x,n_y)}$, we apply the continuity BCs for the tangential electric and magnetic fields at N CPs of each dielectric boundary $C^{(n_x,n_y)}$. For the case of a TM^z cylindrical wave excitation (electric current filament source), cumbersome manipulations yield

$$\begin{aligned} & -\frac{k_0 Z_0}{4} \sum_{n_x=1}^{N_x} \sum_{n_y=1}^{N_y} \sum_{n=1}^N I_n^{1,(n_x,n_y)} H_0^{(2)}(k_0 |\mathbf{r}_{\text{cyl},m}^{(m_x,m_y)} - \mathbf{r}_{\text{aux},n}^{1,(n_x,n_y)}|) \\ & + \frac{kZ}{4} \sum_{n=1}^N I_n^{2,(n_x,n_y)} H_0^{(2)}(k |\mathbf{r}_{\text{cyl},m}^{(m_x,m_y)} - \mathbf{r}_{2,n}^{n_x,n_y}|) \\ & = \frac{k_0 Z_0}{4} I H_0^{(2)}(k_0 |\mathbf{r}_f - \mathbf{r}_{\text{cyl},m}^{(m_x,m_y)}|), \end{aligned} \quad (16a)$$

$$\begin{aligned} & -\frac{ik_0}{4} \sum_{n_x=1}^{N_x} \sum_{n_y=1}^{N_y} \sum_{n=1}^N I_n^{1,(n_x,n_y)} \frac{\left(y_{\text{aux},n}^{1,(n_x,n_y)} - y_{\text{cyl},m}^{(m_x,m_y)} \right) t_x + \left(x_{\text{cyl},m}^{(m_x,m_y)} - x_{\text{aux},n}^{1,(n_x,n_y)} \right) t_y}{|\mathbf{r}_{\text{cyl},m}^{(m_x,m_y)} - \mathbf{r}_{\text{aux},n}^{1,(n_x,n_y)}|} \\ & \quad \times H_1^{(2)}\left(k_0 |\mathbf{r}_{\text{cyl},m}^{(m_x,m_y)} - \mathbf{r}_{\text{aux},n}^{1,(n_x,n_y)}|\right) \\ & + \frac{ik}{4} \sum_{n=1}^N I_n^{2,(n_x,n_y)} \frac{\left(y_{\text{aux},n}^{2,(n_x,n_y)} - y_{\text{cyl},m}^{(m_x,m_y)} \right) t_x + \left(x_{\text{cyl},m}^{(m_x,m_y)} - x_{\text{aux},n}^{2,(n_x,n_y)} \right) t_y}{|\mathbf{r}_{\text{cyl},m}^{(m_x,m_y)} - \mathbf{r}_{\text{aux},n}^{2,(n_x,n_y)}|} \\ & \quad \times H_1^{(2)}\left(k |\mathbf{r}_{\text{cyl},m}^{(n_x,n_y)} - \mathbf{r}_{\text{aux},n}^{2,(n_x,n_y)}|\right) \\ & = \frac{ik_0}{4} \frac{(y_f - y_{\text{cyl},m}^{(m_x,m_y)})t_x + (x_{\text{cyl},m}^{(m_x,m_y)} - x_f)t_y}{|\mathbf{r}_f - \mathbf{r}_{\text{cyl},m}^{(m_x,m_y)}|} I H_1^{(2)}\left(k_0 |\mathbf{r}_{\text{cyl},m}^{(n_x,n_y)} - \mathbf{r}_f|\right), \end{aligned} \quad (16b)$$

where $m_x = 1, \dots, N_x$, $m_y = 1, \dots, N_y$, $m = 1, \dots, N$, while $\mathbf{r}_{\text{cyl},m}^{(m_x,m_y)} = (x_{\text{cyl}}^{(m_x,m_y)}, y_{\text{cyl}}^{(m_x,m_y)})$ is the position vector of the m -th CP on $C^{(m_x,m_y)}$, t_x is the x component of the tangential unit vector on $r_{\text{cyl},m}^{(m_x,m_y)}$, and t_y is the y component of the tangential unit vector on $r_{\text{cyl},m}^{(m_x,m_y)}$. Equation (16) is a linear system of the form of (7) with unknowns the $2NN_xN_y$ auxiliary current amplitudes. Once it is solved, the total fields are computed everywhere using (3) and (14) for the background region and (15) for the regions inside the dielectric elements.

For the case of a TE^z cylindrical wave excitation (magnetic current filament source), the respective linear system (16) is obtained by duality.

Lastly, the scattering width is given by (13) with $I_n^{(n_x, n_y)}$ and $K_n^{(n_x, n_y)}$ replaced by $I_n^{1, (n_x, n_y)}$ and $K_n^{1, (n_x, n_y)}$, respectively.

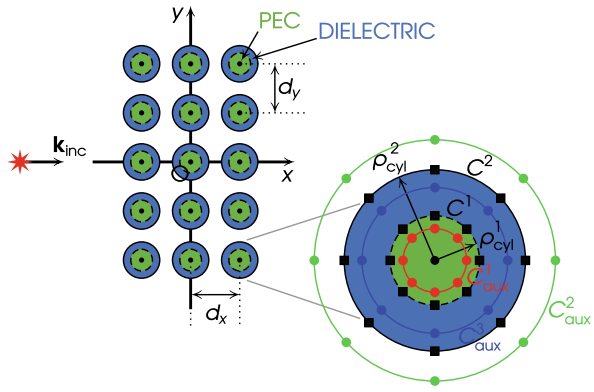
4 Multiple Scattering by Core–Shell PEC–Dielectric Arrays

Figure 3 illustrates the geometry of a cylindrical array where each cylinder has a circular PEC core, coated by a circular dielectric shell with permittivity $\varepsilon = \varepsilon_r \varepsilon_0$ and permeability $\mu = \mu_r \mu_0$. The methodology also supports non-circular core–shell cross sections; however, we focus the presentation on circular ones for simplicity.

The MAS configuration for a single core–shell cylinder is illustrated in Fig. 3. The internal radius is ρ_{cyl}^1 , and the external radius is ρ_{cyl}^2 , corresponding to the boundaries $C^{1, (m_x, m_y)}$ and $C^{2, (m_x, m_y)}$, respectively. We define the three auxiliary surfaces $C_{\text{aux}}^{1, (n_x, n_y)}$, $C_{\text{aux}}^{2, (n_x, n_y)}$ and $C_{\text{aux}}^{3, (n_x, n_y)}$ with respective radii ρ_{aux}^1 , ρ_{aux}^2 and ρ_{aux}^3 . The field in the dielectric shell is the superposition of the fields radiated by the N ASs, which are homogeneously distributed on $C_{\text{aux}}^{1, (n_x, n_y)}$ and $C_{\text{aux}}^{2, (n_x, n_y)}$, while the scattered field is the superposition of the fields radiated by the sources of $C_{\text{aux}}^{3, (n_x, n_y)}$. Thus, the internal fields in each shell are expressed by

$$\mathbf{E}_{\text{in}}^{(n_x, n_y)}(\mathbf{r}) = -\frac{kZ}{4} \sum_{n=1}^N \left[I_n^{1, (n_x, n_y)} H_0^{(2)}(k|\mathbf{r} - \mathbf{r}_{\text{aux}, n}^{1, (n_x, n_y)}|) + I_n^{2, (n_x, n_y)} H_0^{(2)}(k|\mathbf{r} - \mathbf{r}_{\text{aux}, n}^{2, (n_x, n_y)}|) \right] \hat{\mathbf{z}}, \quad (17a)$$

Fig. 3 Rectangular array of circular core–shell PEC–dielectric cylinders



$$\begin{aligned}
\mathbf{H}_{\text{in}}^{(n_x, n_y)}(\mathbf{r}) = & -\frac{ik}{4} \sum_{n=1}^N \left[I_n^{1, (n_x, n_y)} \frac{\left(x - x_{\text{aux}, n}^{1, (n_x, n_y)} \right) \hat{\mathbf{y}} + \left(y_{\text{aux}, n}^{1, (n_x, n_y)} - y \right) \hat{\mathbf{x}}}{|\mathbf{r} - \mathbf{r}_{\text{aux}, n}^{1, (n_x, n_y)}|} \right. \\
& \times H_1^{(2)}(k|\mathbf{r} - \mathbf{r}_{\text{aux}, n}^{1, (n_x, n_y)}|) \\
& + I_n^{2, (n_x, n_y)} \frac{\left(x - x_{\text{aux}, n}^{2, (n_x, n_y)} \right) \hat{\mathbf{y}} + \left(y_{\text{aux}, n}^{2, (n_x, n_y)} - y \right) \hat{\mathbf{x}}}{|\mathbf{r} - \mathbf{r}_{\text{aux}, n}^{2, (n_x, n_y)}|} \\
& \left. \times H_1^{(2)}(k|\mathbf{r} - \mathbf{r}_{\text{aux}, n}^{2, (n_x, n_y)}|) \right]. \quad (17b)
\end{aligned}$$

In addition, the scattered fields are given by

$$\mathbf{E}_{\text{sc}}(\mathbf{r}) = -\frac{k_0 Z_0}{4} \sum_{n_x=1}^{N_x} \sum_{n_y=1}^{N_y} \sum_{n=1}^N I_n^{3, (n_x, n_y)} H_0^{(2)}(k_0|\mathbf{r} - \mathbf{r}_{\text{aux}, n}^{3, (n_x, n_y)}|) \hat{\mathbf{z}}, \quad (18a)$$

$$\begin{aligned}
\mathbf{H}_{\text{sc}}(\mathbf{r}) = & -\frac{ik_0}{4} \sum_{n_x=1}^{N_x} \sum_{n_y=1}^{N_y} \sum_{n=1}^N I_n^{3, (n_x, n_y)} \frac{\left(x - x_{\text{aux}, n}^{3, (n_x, n_y)} \right) \hat{\mathbf{y}} + \left(y_{\text{aux}, n}^{3, (n_x, n_y)} - y \right) \hat{\mathbf{x}}}{|\mathbf{r} - \mathbf{r}_{\text{aux}, n}^{3, (n_x, n_y)}|} \\
& \times H_1^{(2)}(k_0|\mathbf{r} - \mathbf{r}_{\text{aux}, n}^{3, (n_x, n_y)}|), \quad (18b)
\end{aligned}$$

where $I_n^{3, (n_x, n_y)}$ and $\mathbf{r}_{\text{aux}, n}^{3, (n_x, n_y)}$ is the complex amplitude and the position vector, respectively, of the n -th AS of $C_{\text{aux}}^{3, (n_x, n_y)}$.

Next, we apply the BCs at N CPs of $C^{1, (m_x, m_y)}$ and $C^{2, (m_x, m_y)}$, i.e., the continuity of the tangential electric and magnetic field on $C^{2, (m_x, m_y)}$, and the zeroing of the tangential electric field on $C^{1, (m_x, m_y)}$. For the case of a TM^z cylindrical wave excitation (electric current filament source), this procedure leads to

$$\begin{aligned}
& \sum_{n=1}^N I_n^{2, (n_x, n_y)} H_0^{(2)}(k|\mathbf{r}_{\text{cyl}, m}^{1, (m_x, m_y)} - \mathbf{r}_{\text{aux}, n}^{2, (n_x, n_y)}|) \\
& = - \sum_{n=1}^N I_n^{1, (n_x, n_y)} H_0^{(2)}(k|\mathbf{r}_{\text{cyl}, m}^{1, (m_x, m_y)} - \mathbf{r}_{\text{aux}, n}^{1, (n_x, n_y)}|), \quad (19a) \\
& - k_0 Z_0 \sum_{n_x=1}^{N_x} \sum_{n_y=1}^{N_y} \sum_{n=1}^N I_n^{3, (n_x, n_y)} H_0^{(2)}(k|\mathbf{r}_{\text{cyl}, m}^{1, (m_x, m_y)} - \mathbf{r}_{\text{aux}, n}^{3, (n_x, n_y)}|) \\
& + kZ \sum_{n=1}^N I_n^{2, (n_x, n_y)} H_0^{(2)}(k|\mathbf{r}_{\text{cyl}, m}^{1, (m_x, m_y)} - \mathbf{r}_{\text{aux}, n}^{2, (n_x, n_y)}|)
\end{aligned}$$

$$\begin{aligned}
& + kZ \sum_{n=1}^N I_n^{1,(n_x,n_y)} H_0^{(2)}(k|\mathbf{r}_{\text{cyl},m}^{1,(m_x,m_y)} - \mathbf{r}_{\text{aux},n}^{1,(n_x,n_y)}|) \\
& = kZ_0 I H_0^{(2)}(k_0|\mathbf{r}_{\text{cyl},m}^{1,(m_x,m_y)} - \mathbf{r}_f|), \tag{19b} \\
& -k_0 \sum_{n_x=1}^{N_x} \sum_{n_y=1}^{N_y} \sum_{n=1}^N I_n^{3,(n_x,n_y)} \frac{(y_{\text{aux},n}^{3,(n_x,n_y)} - y_{\text{cyl},m}^{2,(m_x,m_y)}) t_x + (x_{\text{cyl},m}^{2,(m_x,m_y)} - x_{\text{aux},n}^{3,(n_x,n_y)}) t_y}{|\mathbf{r}_{\text{cyl},m}^{2,(m_x,m_y)} - \mathbf{r}_{\text{aux},n}^{3,(n_x,n_y)}|} \\
& \quad \times H_1^{(2)}(k_0|\mathbf{r}_{\text{cyl},m}^{(m_x,m_y)} - \mathbf{r}_{\text{aux},n}^{1,(n_x,n_y)}|) \\
& + k \sum_{n=1}^N I_n^{2,(n_x,n_y)} \frac{(y_{\text{aux},n}^{2,(n_x,n_y)} - y_{\text{cyl},m}^{2,(m_x,m_y)}) t_x + (x_{\text{cyl},m}^{2,(m_x,m_y)} - x_{\text{aux},n}^{2,(n_x,n_y)}) t_y}{|\mathbf{r}_{\text{cyl},m}^{2,(m_x,m_y)} - \mathbf{r}_{\text{aux},n}^{2,(n_x,n_y)}|} \\
& \quad \times H_1^{(2)}(k|\mathbf{r}_{\text{cyl},m}^{2,(m_x,m_y)} - \mathbf{r}_{\text{aux},n}^{2,(n_x,n_y)}|) \\
& + k \sum_{n=1}^N I_n^{1,(n_x,n_y)} \frac{(y_{\text{aux},n}^{1,(n_x,n_y)} - y_{\text{cyl},m}^{2,(m_x,m_y)}) t_x + (x_{\text{cyl},m}^{2,(m_x,m_y)} - x_{\text{aux},n}^{1,(n_x,n_y)}) t_y}{|\mathbf{r}_{\text{cyl},m}^{2,(m_x,m_y)} - \mathbf{r}_{\text{aux},n}^{1,(n_x,n_y)}|} \\
& \quad \times H_1^{(2)}(k|\mathbf{r}_{\text{cyl},m}^{2,(m_x,m_y)} - \mathbf{r}_{\text{aux},n}^{1,(n_x,n_y)}|) \\
& = k_0 \frac{(y_f - y_{\text{cyl},m}^{(m_x,m_y)}) t_x + (x_{\text{cyl},m}^{2,(m_x,m_y)} - x_f) t_y}{|\mathbf{r}_{\text{cyl},m}^{2,(m_x,m_y)} - \mathbf{r}_f|} I H_1^{(2)}(k_0|\mathbf{r}_{\text{cyl},m}^{2,(m_x,m_y)} - \mathbf{r}_f|). \tag{19c}
\end{aligned}$$

The linear system (19) is in the form of (7) with unknowns the complex amplitudes of the ASs. Its solution enables the calculation of the total fields everywhere.

For the case of a TE^z cylindrical wave excitation (magnetic current filament source), the BC on the PEC boundary $C^{1,(m_x,m_y)}$ (i.e., null tangential electric field), is expressed as

$$\begin{aligned}
& - \frac{ik}{4} \sum_{n=1}^N K_n^{1,(n_x,n_y)} \frac{(y_{\text{aux},n}^{1,(n_x,n_y)} - y_{\text{cyl},m}^{(m_x,m_y)}) t_x + (x_{\text{cyl},m}^{(m_x,m_y)} - x_{\text{aux},n}^{1,(n_x,n_y)}) t_y}{|\mathbf{r}_{\text{cyl},m}^{(m_x,m_y)} - \mathbf{r}_{\text{aux},n}^{1,(n_x,n_y)}|} \\
& \quad \times H_1^{(2)}(k|\mathbf{r}_{\text{cyl},m}^{(m_x,m_y)} - \mathbf{r}_{\text{aux},n}^{1,(n_x,n_y)}|) \\
& = \frac{ik}{4} \sum_{n=1}^N K_n^{2,(n_x,n_y)} \frac{(y_{\text{aux},n}^{2,(n_x,n_y)} - y_{\text{cyl},m}^{(m_x,m_y)}) t_x + (x_{\text{cyl},m}^{(m_x,m_y)} - x_{\text{aux},n}^{2,(n_x,n_y)}) t_y}{|\mathbf{r}_{\text{aux},n}^{2,(n_x,n_y)} - \mathbf{r}_{\text{cyl},m}^{(m_x,m_y)}|} \\
& \quad \times H_1^{(2)}(k|\mathbf{r}_{\text{cyl},m}^{(m_x,m_y)} - \mathbf{r}_{\text{aux},n}^{2,(n_x,n_y)}|), \tag{20}
\end{aligned}$$

while the BCs on $C^{2,(m_x,m_y)}$ are the dual of (19b) and (19c).

The scattering width is given by (13) with $I_n^{(n_x,n_y)}$ and $K_n^{(n_x,n_y)}$ replaced by $I_n^{3,(n_x,n_y)}$ and $K_n^{3,(n_x,n_y)}$, respectively.

5 Multiple Scattering by Circular Arrays

Figure 4a illustrates the geometry of a circular cylindrical array where each cylindrical element has arbitrary cross section. This array consists of N_ρ circumferences where each circumference has N_ϕ cylinders, therefore $N_t = N_\rho N_\phi$ cylinders in total. The center of each cylinder is positioned at

$$x_c^{(n_\rho,n_\phi)} = a_{n_\rho} \cos\left(\frac{2\pi(n_\phi - 1)}{N_\phi}\right), \quad (21a)$$

$$y_c^{(n_\rho,n_\phi)} = a_{n_\rho} \sin\left(\frac{2\pi(n_\phi - 1)}{N_\phi}\right), \quad (21b)$$

where $n_\rho = 1, \dots, N_\rho$ is the circumference number, $n_\phi = 1, \dots, N_\phi$ is the number of the cylinder on a circumference, and a_{n_ρ} is the radius of the n_ρ -th circumference.

5.1 Circular PEC Arrays

To calculate the total fields, we follow the same procedure discussed in Sec. 2 with the difference that in (4)–(6), n_x, n_y, m_x, m_y, N_x and N_y are replaced by $n_\rho, n_\phi, m_\rho, m_\phi, N_\rho$, and N_ϕ , respectively. As in the rectangular geometry, $m_\rho = 1, 2, \dots, N_\rho$

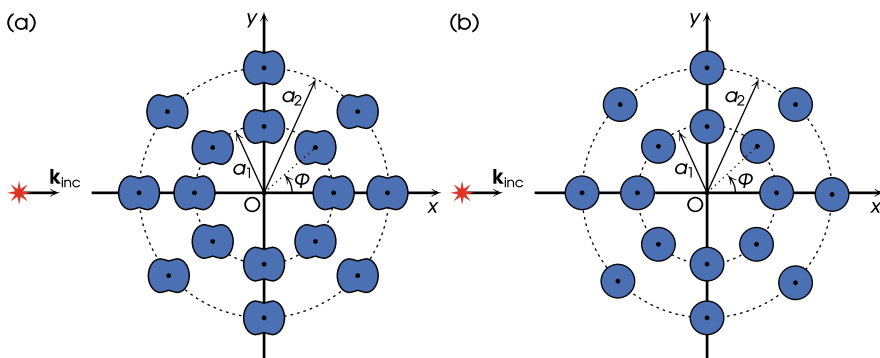


Fig. 4 Circular array of cylinders. Each cylindrical element can be PEC, dielectric, or core-shell PEC-dielectric. (a) Elements of arbitrary cross section. (b) Elements of circular cross section

and $m_\phi = 1, 2, \dots, N_\phi$ in order to distinguish between counters pertaining to ASS and CPs.

5.2 Circular Dielectric and Core–Shell PEC–Dielectric Arrays

To calculate the total fields, we follow the same procedures discussed in Secs. 3 and 4 with the difference that in all equations, n_x, n_y, m_x, m_y, N_x , and N_y are replaced by $n_\rho, n_\phi, m_\rho, m_\phi, N_\rho$, and N_ϕ , respectively.

6 Applications on EM Shielding

One potential application constitutes the CAES for achieving EM shielding. A rectangular array acts as an EM shielding device if the semi-infinite region $x > 0$ in Fig. 1a is shielded from the impinging excitation existing in region $x < 0$. To evaluate a rectangular array as a CAES, we compute the so-called SE [6], in dB, by

$$SE = -20 \log_{10} \frac{|\mathbf{E}_{\text{tot}}(\mathbf{r})|}{|\mathbf{E}_{\text{inc}}(\mathbf{r})|}, \quad (22)$$

where $\mathbf{E}_{\text{tot}}(\mathbf{r})$ is the total electric field in region $x > 0$ of Fig. 1a. The evaluation of SE may be performed at any point \mathbf{r} in region $x > 0$; however, in the calculations that follow, we define such a point on the positive x -axis.

Compared to traditional shields, such as thick metallic slabs, CAES include various advantages, such as light weightiness, optical transparency, and frequency selectivity. Light weightiness can be particularly significant if the EM shield is used in airplanes or drones to facilitate flight. The same applies to portable electronic devices such as mobile phones or laptops. Optical transparency is a particularly important property if optical contact with the protected device or setup is required. Finally, frequency selectivity allows for a selective passage of specific frequency bands.

A drawback of CAES is their limited protection to a single polarization, either TM^z or TE^z . This limitation can be mitigated by positioning a second array adjacent and perpendicular to the initial one. For a comprehensive understanding, a realistic scenario illustrating the utilization of CAES includes a manufacturing plant where a precision electronic control unit (ECU) is responsible for controlling critical processes, as shown in Fig. 5. This ECU is susceptible EMI from nearby machinery, which could lead to malfunctions and production errors. To ensure the reliable operation of the ECU, a cylindrical array embedded in the wall can be employed as an EM shield against TM^z radiation. To mitigate the impact of TE^z radiation, an additional cylindrical array can be positioned adjacent to the initial array, aligning the cylinders along the y -axis, as illustrated in Fig. 5a. If optical contact with the

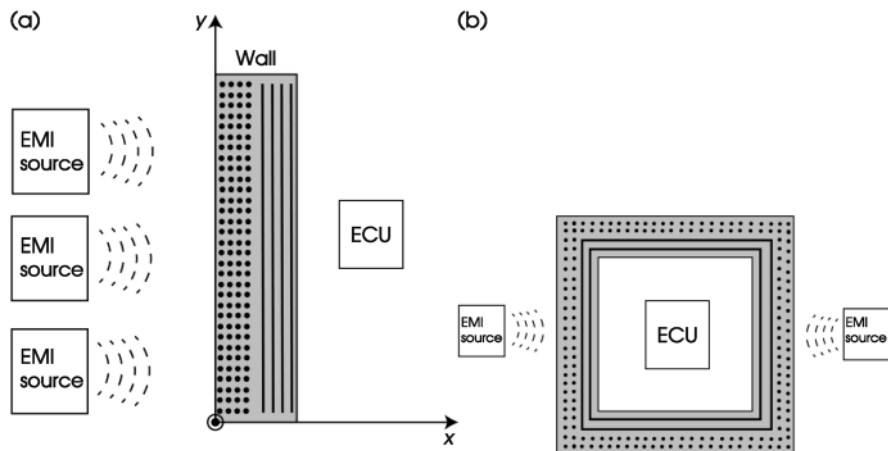


Fig. 5 The application of a double cylindrical array against both TM^z and TE^z incident waves. The black dots represent the cylinders on the z -direction, and the black lines the cylinders on the y -direction. (a) Single wall. (b) Metacage

ECU is required, a wall made of transparent material such as glass or polycarbonate material is used.

If wireless communication between the ECU and devices in other rooms within a particular frequency range is required, a dielectric or a PEC–dielectric array could be employed. This would enable a pass-band within this frequency range while maintaining high SE values outside of it. Lastly, if the ECU is susceptible to interference from all directions, then it can be protected by a metacage, illustrated in Fig. 5b, which means placing cylindrical arrays on all walls surrounding the ECU. Applying the same principles, we can utilize cylindrical arrays to protect the avionics of an aircraft or, on a smaller scale, the EMI-sensitive electronic components of a mobile phone or a laptop.

The optimization of a cylindrical array, as, e.g., to maximize the SE or other figures of merit, poses significant complexities because the quantities of interest depend on a large number of parameters, such as the radius of the PEC or dielectric cylinders or the radii of the core–shell PEC–dielectric configurations. Another parameter is the number of cylinders, which, for the rectangular arrays, is related to the column numbers N_x and the row numbers N_y , while for the circular arrays with the circumference number N_ρ and cylinders per circumference N_ϕ . In addition, the spatial period d_x along the x -direction and the spatial period d_y along the y -direction for a rectangular array, as well as the circumference radius a_{n_ρ} for a circular array, also add to the complexity of the optimization. Other parameters that complicate the optimization is the shape of the cylinders' cross section, the mixture of cylinders with different sizes and shapes, and how they are arranged (alternative array geometries). All these factors show that thoroughly optimizing such setups requires running many simulations to reach a reliable conclusion.

Fig. 6 SE versus f for different values of radius ρ_{cyl} of a rectangular PEC array. Solid curves: MAS. Red squares: HFSS

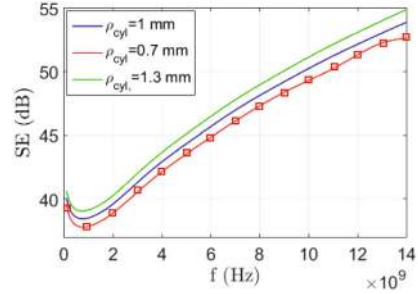


Fig. 7 SE versus f for different values of radius ρ_{cyl} of a rectangular dielectric array. Solid curves: MAS. Red squares: HFSS

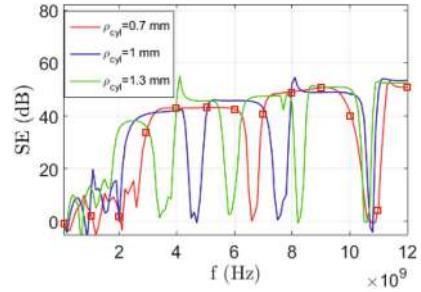
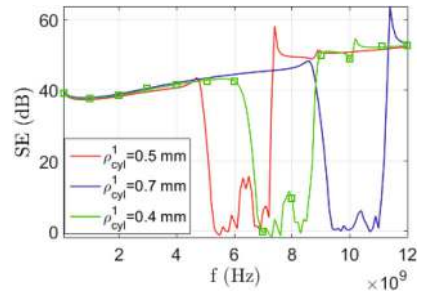


Fig. 8 SE versus f for different values of core radius ρ_{cyl}^1 of a rectangular core-shell PEC-dielectric array. Solid curves: MAS. Green squares: HFSS

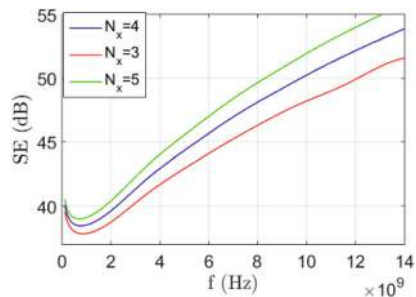


6.1 Shielding via Rectangular Arrays

In what follows, we calculate SE versus operating frequencies f in the range from 100 MHz to 12 GHz from an electric current filament source and discuss the response of PEC, dielectric, and PEC-dielectric rectangular arrays as CAES, by changing some of the various key parameters discussed earlier. The respective relative values for the permittivity and permeability employed for the calculations in both the dielectric and the PEC-dielectric arrays, are $\epsilon_r = 600$ and $\mu_r = 1$.

In Figs. 6, 7, and 8, we investigate how the radius of cylinders affects SE for PEC, dielectric and PEC-dielectric arrays. For the PEC and dielectric arrays we vary ρ_{cyl} by setting the values $\rho_{\text{cyl}} = 0.7$ mm, $\rho_{\text{cyl}} = 1$ mm and $\rho_{\text{cyl}} = 1.3$ mm. For the PEC-dielectric setup, the inner radius is varied as $\rho_{\text{cyl}}^1 = 0.4$ mm, $\rho_{\text{cyl}}^1 = 0.5$ mm and $\rho_{\text{cyl}}^1 = 0.7$ mm, while the outer radius is kept constant at $\rho_{\text{cyl}}^2 = 1$ mm. This

Fig. 9 SE versus f for different number of columns N_x of a rectangular PEC array



effectively changes the thickness of the dielectric coating of the cylinders. The remaining values of parameters are $N_x = 4$, $N_y = 18$, and $d_x = d_y = 5$ mm. From these results we draw the following conclusions. Regarding the PEC array in Fig. 6, the reduction of ρ_{cyl} leads to a decrease in SE. Similarly, the increase of ρ_{cyl} yields an increment in SE. Concerning the dielectric array in Fig. 7, in addition to the decrement or increment of SE, changing the radius also affects the frequency ranges where the array behaves as an effective negative permittivity or double negative (negative in both permittivity and permeability) metamaterial [20] or as a double positive material [3]. This observation is expected as the cylinders resonate at different frequencies for different radii. Finally, regarding the PEC–dielectric configurations in Fig. 8, pass-band frequency windows exist where the SE acquires small values. This equivalently means that the radiation passes through the array from region $x < 0$ to region $x > 0$ without strong reduction. From the plots of Fig. 8, we observe that a thicker dielectric coating moves the pass-band to lower frequencies. Similarly, a thinner coating moves the pass-band to higher frequencies. Therefore, the pass-band window can be shifted by changing the thickness of the dielectric shell.

The results in Figs. 6, 7, and 8, which are depicted by solid curves, were obtained by the developed MAS numerical scheme. To validate the correctness of the MAS scheme, we employ the finite–element method (FEM) of the HFSS commercial software, and we demonstrate validity for a selected number of examples. In particular, the simulations in HFSS are obtained by applying a frequency sweep with a step of 1 GHz. The results are depicted using red squares in Figs. 6 and 7 for the $\rho_{\text{cyl}} = 0.7$ mm case and using green squares in Fig. 8 for the $\rho_{\text{cyl}}^1 = 0.4$ mm case. As evident, the agreement between the MAS and the HFSS is very good, thus providing a convincing validation test.

In Figs. 9, 10, and 11, we investigate how the number of cylinders affects SE by varying N_x from $N_x = 3$ to $N_x = 5$. The study is carried out for PEC, dielectric, and PEC–dielectric arrays. The values of parameters used are $\rho_{\text{cyl}} = 1$ mm, $\rho_{\text{cyl}}^1 = 0.7$ mm, $\rho_{\text{cyl}}^2 = 1$ mm, $N_y = 18$, and $d_x = d_y = 5$ mm. From these plots, we deduce that, when the number of cylinders is decreased, SE also decreases. Yet, when N_x increases, SE also increases. This is expected because reducing for instance N_x , the equivalent thickness of the array decreases.

Fig. 10 SE versus f for different number of columns N_x of a rectangular dielectric array

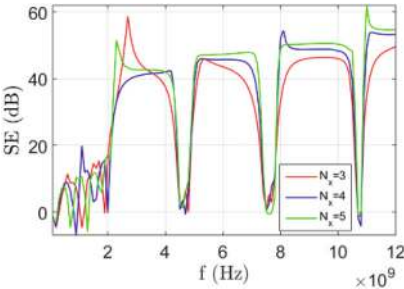


Fig. 11 SE versus f for different number of columns N_x of a rectangular core-shell PEC-dielectric array

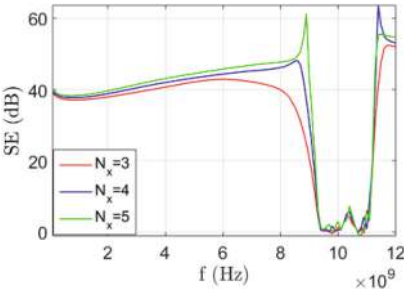


Fig. 12 SE versus f for different values of spatial periods d_x and d_y of a rectangular PEC array

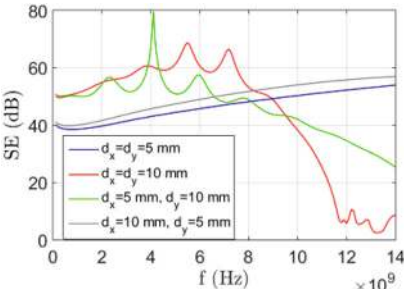
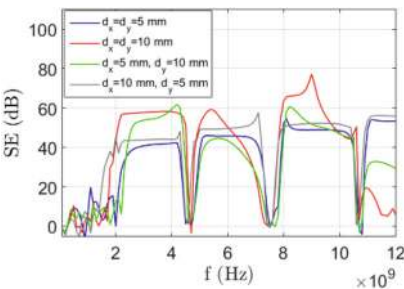
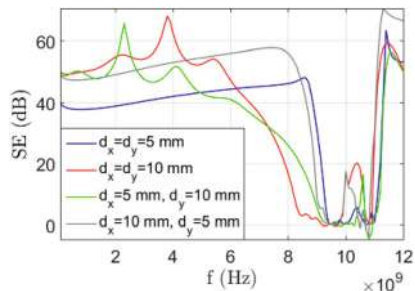


Fig. 13 SE versus f for different values of spatial periods d_x and d_y of a rectangular dielectric array



In Figs. 12, 13, and 14, we explore the dependence of SE on the spatial periods d_x and d_y for three scenarios: by solely increasing d_x while keeping d_y unchanged, by solely increasing d_y while keeping d_x unchanged, and by simultaneously increasing d_x and d_y . These scenarios are investigated for all PEC, dielectric, and PEC-

Fig. 14 SE versus f for different values of spatial periods d_x and d_y of a rectangular core-shell PEC-dielectric array



dielectric configurations. When d_x is solely increased from 5 mm to 10 mm and d_y is fixed at 5 mm, we notice a substantial increase in SE across the entire frequency range. This result indicates that the homogenization of the cylindrical array is not affected significantly by this increase in d_x , at least for frequencies up to 12 GHz. Hence, the large increase of the SE is attributed to the increase of the equivalent thickness of the array. When d_y is solely increased from 5 mm to 10 mm and d_x is fixed at 5 mm, we observe a substantial increase in SE up to a certain frequency for all configurations. Beyond this frequency limit, there is a sharp decline in SE. A qualitative rationale for the increase of the SE is that, as d_y increases, the diffracted field on the testing point (point \mathbf{r} in (22)) is reduced since it is further away from the edges of the partial shield. Regarding the sharp decrease in SE at lower frequencies, it can be attributed to the phenomenon where an increase in the distance d_y between cylinders, leads to a reduction in the maximum frequency at which the incident wave perceives the cylindrical array as a homogeneous entity. Finally, when d_x and d_y are simultaneously increased from 5 mm to 10 mm, we notice a substantial increase in SE up to a certain frequency, somewhat higher than in the previous case. Beyond this frequency, there is a sharp decline in SE. The explanation for this result is the same as that provided for the previous case.

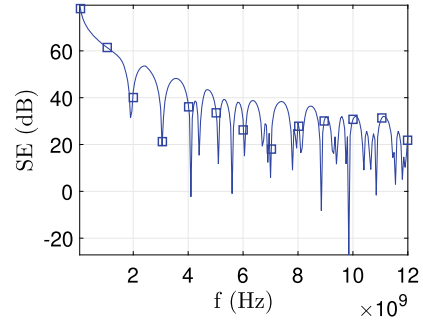
6.2 Shielding via Circular Arrays

As a final demonstration on EM shielding, we examine the use of circular arrays as CAES. In this case, the purpose of the circular array is to shield the internal region (region $\rho < a_1$ in Fig. 4a or b) from sources located in the external region (region $\rho > a_2$ in Fig. 4a or b). The opposite, i.e., to shield the external region from sources located in the internal region, is also applicable.

For this application, we employ a circular PEC array in a vacuum environment using $N_\rho = 2$, $N_\phi = 60$, $a_1 = 6$ cm, and $a_2 = 6.5$ cm. We consider that the whole configuration is exposed to a TM^z plane wave traveling towards the $-x$ -direction in the external region $\rho > a_2$ of Fig. 4b, with an incident electric field given by

$$\mathbf{E}_{\text{inc}}(\mathbf{r}) = E_0 \exp(ik_0 x) \hat{\mathbf{z}}, \quad (23)$$

Fig. 15 SE versus f of a circular PEC array. Solid curves: MAS. Blue squares: HFSS



with $E_0 = 1$ V/m. By employing MAS, we determine the SE shown in Fig. 15. As evident, the MAS is in agreement with HFSS, thus establishing the correctness of the result. It is apparent that SE is notably elevated at low frequencies. Moreover, at specific frequencies, resonances can be observed at which the SE is profoundly reduced.

7 Conclusions and Prospects

We conducted a comprehensive study on the analysis of multiple scattering of EM waves by arrays of infinite cylinders using the MAS. Our analysis encompassed various cylindrical configurations, including PEC, dielectric, and core-shell PEC-dielectric rectangular arrays, as well as circular arrays. The robustness and versatility of MAS were demonstrated through detailed mathematical treatments and practical applications, particularly in the context of EM shielding. Our findings indicate that MAS is a highly effective method for analyzing multiple EM scattering in complex cylindrical arrays. The ability to handle different types of materials and array geometries makes MAS a powerful tool for investigating wave interactions in structured media. We have shown that both rectangular and circular cylindrical arrays can significantly reduce penetrating EM fields, providing effective shielding solutions for protecting sensitive electronic devices from EMI. The comparison of MAS results with those obtained from the HFSS commercial software confirmed the accuracy and reliability of our analysis. The insights gained from this work offer practical guidance for designing advanced EM devices and systems. Applications in antenna design, active ferromagnetic devices, tunable light transport, plasmonics, metasurfaces, metamaterials, and EM shielding, highlight the broad relevance of the presented analysis.

Looking forward, several promising avenues for future research emerge from this study, including further exploration of MAS for more complex configurations, such as irregular or anisotropic cylindrical arrays, and the inclusion of novel materials including metamaterials or hyperbolic media that could open new possibilities for wave manipulation and control. In addition, integrating MAS with optimization

algorithms to design cylindrical arrays with tailored scattering properties for specific applications, could enhance the performance of various devices such as antennas, filters, and cloaking systems.

References

1. E.G. Alivizatos, I.D. Chremmos, N.L. Tsitsas, N.K. Uzunoglu, Green's-function method for the analysis of propagation in holey fibers. *J. Opt. Soc. Am. A* **21**(5), 847–857 (2004)
2. T.J. Arruda, A.S. Martinez, F.A. Pinheiro, Electromagnetic energy and negative asymmetry parameters in coated magneto-optical cylinders: applications to tunable light transport in disordered systems. *Phys. Rev. A (Coll. Park.)* **94**(3), 033825 (2016)
3. C.A. Balanis, *Advanced Engineering Electromagnetics* (John Wiley & Sons, New York, 1989)
4. A.A. Basharin, M. Kafesaki, E.N. Economou, C.M. Soukoulis, V.A. Fedotov, V. Savinov, N.I. Zheludev, Dielectric metamaterials with toroidal dipolar response. *Phys. Rev. X.* **5**(1), 011036 (2015)
5. S.J. Bever, J.P. Allebach, Multiple scattering by a planar array of parallel dielectric cylinders. *Appl. Opt.* **31**(18), 3524–3532 (1992)
6. S. Celozzi, R. Araneo, P. Burghignoli, G. Lovat, *Electromagnetic Shielding: Theory and Applications* (Wiley, Hoboken, 2023)
7. M.Z. El-Gamal, L. Shafai, Scattering of electromagnetic waves by arrays of conducting and dielectric cylinders. *Int. J. Electron.* **65**(5), 1013–1029 (1988)
8. A.V. Ivoninsky, A.V. Kudrin, V.A. Es'kin, Scattering properties of a finite array of magnetized plasma cylinders at the surface plasmon resonances, in *2017 XXXIInd General Assembly and Scientific Symposium of the International Union of Radio Science (URSI GASS)* (IEEE, Piscataway, 2017)
9. V. Gandieri, K. Yasumoto, Analysis of scattering from a finite array of circular cylinders using a model of layered cylindrical arrays. *Opt. Commun.* **284**(18), 4109–4113 (2011)
10. H.A. Kalhor, Electromagnetic scattering by an array of conducting cylinders by finite-difference coupling technique. *J. Appl. Phys.* **48**(4), 1483–1487 (1977)
11. H.A. Kalhor, A. Armand, Scattering of waves by gratings of conducting cylinders. *Proc. Inst. Electr. Eng.* **122**(3), 245 (1975)
12. M. Kouroubakis, G.P. Zouros, N.L. Tsitsas, Shielding effectiveness of metamaterial cylindrical arrays via the method of auxiliary sources. *IEEE Trans. Antennas Propagat.* **72**(7), 5950–5960 (2024)
13. A.V. Kudrin, V.A. Es'kin, T.M. Zaboronkova, Electromagnetic wave scattering by an array of parallel gyrotropic cylinders, in *2014 XXXIth URSI General Assembly and Scientific Symposium (URSI GASS)* (IEEE, Piscataway, 2014)
14. T. Kumar, N. Kalyanasundaram, B.K. Lande, A generalized case of electromagnetic scattering from a finite number of ferromagnetic cylinders. *Adv. Electromagn.* **4**(3), 8 (2015)
15. W. Liu, Generalized magnetic mirrors. *Phys. Rev. Lett.* **119**(12), 123902 (2017)
16. E. Mastorakis, P.J. Papakanellos, H.T. Anastassiou, N.L. Tsitsas, Analysis of electromagnetic scattering from large arrays of cylinders via a hybrid of the method of auxiliary sources (MAS) with the fast multipole method (FMM). *Mathematics* **10**(17), 3211 (2022)
17. E.J. Mastorakis, P.J. Papakanellos, H.T. Anastassiou, N.L. Tsitsas, Hybridization of the method of auxiliary sources (MAS) with the fast multipole method (FMM) for scattering from large arrays of cylinders, in *2019 Photonics & Electromagnetics Research Symposium - Spring (PIERS-Spring)* (IEEE, Piscataway, 2019)
18. C.P. Mavidis, A.C. Tasolamprou, E.N. Economou, C.M. Soukoulis, M. Kafesaki, Polaritonic cylinders as multifunctional metamaterials: single scattering and effective medium description. *Phys. Rev. B.* **102**(15), 155310 (2020)

19. C.P. Mavidis, A.C. Tasolamprou, E.N. Economou, C.M. Soukoulis, M. Kafesaki, Single scattering and effective medium description of multilayer cylinder metamaterials: application to graphene- and to metasurface-coated cylinders. *Phys. Rev. B.* **107**(13), 134120 (2023)
20. A. Pekmezci, L. Sevgi, Properties of metamaterial based electromagnetic absorbers and shields, in *2019 Fifth International Electromagnetic Compatibility Conference (EMC Turkiye)* (IEEE, Piscataway, 2019)
21. Z. Tagay, C. Valagiannopoulos, Highly selective transmission and absorption from metasurfaces of periodically corrugated cylindrical particles. *Phys. Rev. B.* **98**(11), 115306 (2018)
22. O. Tsilipakos, A.C. Tasolamprou, T. Koschny, M. Kafesaki, E.N. Economou, C.M. Soukoulis, Pairing toroidal and magnetic dipole resonances in elliptic dielectric rod metasurfaces for reconfigurable wavefront manipulation in reflection. *Adv. Opt. Mater.* **6**(22), 1800633 (2018)
23. N.L. Tsitsas, Second-kind fredholm integral-equation analysis of scattering by layered dielectric gratings. *IET Microw. Antenn. Propagat.* **15**, 1194–1205 (2021)
24. T.G. Tsuei, P.W. Barber, Multiple scattering by two parallel dielectric cylinders. *Appl. Opt.* **27**(16), 3375–3381 (1988)
25. G.A.E. Vandenbosch, The basic concepts determining electromagnetic shielding. *Am. J. Phys.* **90**(9), 672–681 (2022)
26. K. Watanabe, Y. Nakatake, J. Pištora, Accurate analysis of electromagnetic scattering from periodic circular cylinder array with defects. *Opt. Express* **20**(10), 10646–10657 (2012)
27. H.A. Yousif, S. Köhler, Scattering by two penetrable cylinders at oblique incidence I the analytical solution. *J. Opt. Soc. Am. A Opt. Image Sci. Vis.* **5**(7), 1085 (1988)

Static Bragg-Less and Dynamic Bragg-Like Resonances



Martin W. McCall and Stefanos Fr. Koufidis

1 These Are *Not* the Usual Bragg Gratings

An honest discussion initiates with a straightforward question: is there anything new to be said about Bragg gratings in 2025? Well, concerning *gratings*, as conventionally defined and commonly understood, probably not. But regarding Bragg *resonances*, perhaps there is a story worth telling. In this chapter, we attempt to take the reader through some novel Bragg-type resonances occurring in static and dynamic mediums that have kept us off the streets in recent years.

Scalar coupled-wave theory, a remarkably simple yet quite powerful tool, will be a key approach in most of our derivations, even when exact analytic solutions are attainable. The reasoning is simple: its simplicity. Indeed, such a theory may only apply under corresponding preconditions, but nonetheless, it yields simple formulae and, therefore, straightforward insights into various physical mechanisms. Hence, in Sect. 2, we take a fresh look into coupled-wave equations by leveraging some underlying group-theory symmetries of the differential equation system, which naturally guide us to the so-called Möbius transformation. As we showed in [1], such a transformation reduces the coupled system to a first-order nonlinear differential equation of a single real variable that encodes all relevant spectral information. By exploiting some fundamental geometric properties of the (rather extended) family of conformal mappings, one can obtain the optical response of arbitrarily complex structures, insofar as they can be accurately described via coupled-wave theory. An interesting connection with coupled-oscillator theory will be briefly discussed, and some alternative definitions of the Bragg zone in reciprocal space will be given.

M. W. McCall (✉) · S. F. Koufidis

Department of Physics, Imperial College of Science, Technology and Medicine, London, UK

e-mail: m.mccall@imperial.ac.uk; steven.koufidis20@imperial.ac.uk

Advancing to more physics-pertinent situations, in Sect. 3, we explore an optically active structurally chiral medium. As is well-known, structurally chiral mediums exhibit the circular Bragg phenomenon, whereby a circular state is strongly backscattered when its handedness coincides with that of the medium, while the orthogonal polarization gets transmitted. By infiltrating the structurally chiral medium with a chiral fluid, Ref. [2] numerically showed that these Bragg resonances are shifted linearly with the chirality parameter, which also affects their peaks and corresponding bandwidths. Remarkably, as we derive in [3], when the chirality exceeds the value of the medium's average refractive index, then an additional resonance occurs that backscatters contra-handed light. Hence, a right-handed medium shall reflect both right- and left-handed circular polarizations (referred to hereafter as RCP and LCP, respectively). Additionally, there exists a regime, situated between the two resonances, wherein optical activity precisely counteracts structural chirality, effectively “unwrapping” the medium. Therein, the medium behaves as being purely linearly birefringent, with modes being at once orthogonal and co-handed with the structural scaffold.

In Sect. 4, we discuss the Bragg-less Bragg grating we introduced in [4] by explicitly demonstrating how a Bragg-like response arises in a *uniform* medium without necessitating any kind of refractive index modulation. Instead of wavelength matching, the Bragg condition is stated as a simple parameter tuning. When a medium is simultaneously linearly and circularly birefringent, the chiral circularly polarized eigenstates of pure circular birefringence, propagating at a particular speed, synchronously and alternately sample the co-propagating birefringent eigenaxes of pure linear birefringence, provided that the chirality parameter matches the medium's average refractive index. This periodic sampling gives rise to a polarization-selective Bragg-like resonance, accessible via meta-mediums possessing extreme optical rotation powers. Furthermore, as we elaborated in [5], if the optical axis forms an angle with the direction of wave propagation, this additional degree of freedom offers the possibility of relaxing the aforementioned tuning condition, thus leading to an experimental implementation that does not necessitate (very!) giant chirality. Additionally, for a particular inclination angle, infinite values of the refractive indices are achieved, closely resembling but fundamentally distinct to the singularities discovered by Weiglhofer [6, 7].

Leaving aside the aforesaid static mediums, in Sect. 5, we examine what happens when the permittivity of a conventional Bragg grating is modulated in time in lieu of space. It turns out that in such a temporal analog of a Bragg grating, similar bandgaps are formed. However, by contrast to their static counterparts, these gaps are formed in momentum space, highlighting the underlying physical mechanism of global time modulation: with no broken translational invariance in space, momentum is conserved while energy is not. Hence, these momentum gaps correspond to regimes wherein parametric amplification ensues. Equipped with the rather advanced tool of the Möbius method of Sect. 2, we prove the energy pseudo-conservation relation of Ref. [8], while discussing three illustrative examples of nontrivial temporal modulation: linear chirping, apodization, and phase delineation.

Our contribution concludes with the discussion of the temporal analog of optical activity [9]. In particular, Sect. 6 investigates light propagation in a medium whose permittivity, permeability, and chirality are periodic functions of time. As detailed in [10], unlike static mediums, this dynamic medium only couples co-handed counter-propagating waves. When the impedance varies, two momentum gaps are formed in the Brillouin diagram, leading to parametric amplification with different factors for right- and left-handed modes. Chirality offers control over the centers of the resonances, their associated bandwidths, and their corresponding amplification factors for each handedness, distinctively but not independently. Analytical derivation of the scattering coefficients for a finite time slab of the medium reveals how extreme optical rotation values enable a temporal version of Pendry's chiral route to negative refraction [11]. At its highest point, the study unravels how elliptical polarizations can alter the field orientation upon transmission through a temporal slab while the wave gets, concurrently, parametrically amplified.

2 Geometrical Aspects of Coupled-Wave Theory

Let us start by assuming an archetypal photonic structure, a Bragg grating (cf. Fig. 1), without, however, making any assumptions on whether the profile of its index modulation is uniform or not. Within the context of scalar coupled-wave theory, an incident forward propagating wave, with an amplitude A^+ , will generate a backward propagating one, with an amplitude A^- . The interaction of these two waves is modeled by the system [12]

$$\frac{d}{dz} \begin{pmatrix} A^+ \\ A^- \end{pmatrix} = \begin{pmatrix} 0 & i\kappa e^{-i\varphi(z)} \\ -i\kappa e^{i\varphi(z)} & 0 \end{pmatrix} \begin{pmatrix} A^+ \\ A^- \end{pmatrix}, \quad (1)$$

where the phase term and the coupling coefficient are defined as

$$\varphi(z) = \int_0^z \Phi(z') dz' \quad \text{and} \quad \kappa \approx \pi \frac{\delta \bar{n}}{\lambda_0}, \quad (2)$$

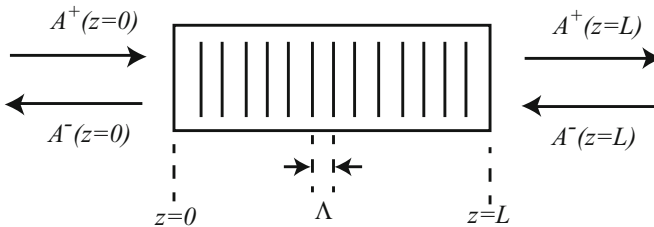
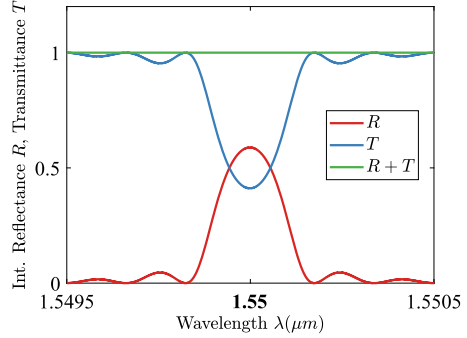


Fig. 1 A Bragg grating lying between $z = 0$ and $z = L$. For an aperiodic grating $\Lambda = \Lambda(z)$

Fig. 2 Exemplary optical spectrum of a uniform Bragg grating: increasing the grating's length L yields steeper curves, while increasing the depth of the refractive index modulation δn widens the Bragg zone



respectively. Here, $\Phi(z) = 2\bar{n}k_0 - K(z)$ accounts for the grating's spatial modulation profile, where \bar{n} is the average refractive index, k_0 is the free-space wavenumber, and $K(z)$ is the local spatial frequency. Additionally, δn denotes the depth of modulation, assumed to be weak for the current purposes, i.e., $\delta n \ll 1$, and λ_0 is the design wavelength. In uniform gratings, $K \equiv K_0 = 2\pi/\Lambda$, where Λ is the pitch; a typical optical response of a uniform Bragg grating is illustrated in Fig. 2.

A pitfall for the unwary is to assume that the general solution to Eq. (1) takes the matrix exponential form. This holds true only on-resonance, i.e., when $\varphi = 0$, where the vectorial-differential equation has constant coefficients. In fact, a system with constant coefficients occurs upon rotating the amplitudes as per $\tilde{A}^+ = e^{i\varphi/2} A^+$ and $\tilde{A}^- = e^{-i\varphi/2} A^-$ —see, e.g., Ref. [13]. Otherwise, since the characteristic matrix does not commute with its integral at every point of its domain of definition, employing the exponential matrix algorithm leads to incorrect results. Such an algorithm can only be used as an approximation in the limiting cases of short gratings and very weak index modulations; of course, “shortness” pertains to the wavelength and “weakness” to the ratio $\delta n/\bar{n}$.

For a grating that extends between $z = 0$ and $z = L$, the solution to Eq. (1) can be cast in terms of a transfer matrix, $\mathbf{S}(z)$, such that $\mathbf{A}(z) = \mathbf{S}(z)\mathbf{A}(0)$. It follows that

$$\frac{d\mathbf{S}}{dz} = \mathbf{M} \cdot \mathbf{S}, \quad (3)$$

with \mathbf{M} being the matrix on the right-hand side of Eq. (1). Two apparent symmetries offer insights into the structure of the system's transfer matrix. Firstly, \mathbf{M} being traceless implies that the determinant of \mathbf{S} is constant as per Liouville's formula. For $\mathbf{S}(0) = \mathbb{I}$, this determinant is unity, irrespective of whether the system has gain or dissipation. We stress, however, that this does not provide conclusions about the system's reciprocity. Secondly, for real system parameters, \mathbf{M} is also Hermitian and anti-diagonal. Therefore, it is straightforward to show that $\mathbf{S}^\dagger \cdot \mathbf{J} \cdot \mathbf{S} = \mathbf{J}$, with $\mathbf{J} = \text{diag}(1, -1)$, which expresses *flux* conservation.

Energy conservation and time-reversal invariance (N.B.— the latter is equivalent to reciprocity in energy-conserving systems—see Byrnes and Foreman's Ref. [14]),

ensure that $\mathbf{S} \in \text{SU}(1, 1)$. The $\text{SU}(1, 1)$ special unitary group has a well-known representation, viz.,

$$\mathbf{S} = \begin{pmatrix} P & Q \\ Q^* & P^* \end{pmatrix}, \quad \text{with } |P|^2 - |Q|^2 = 1. \quad (4)$$

Upon careful inspection of the matrix in Eq. (4), one can see that there is a “natural” conformal mapping between the unit disk (including its boundary) onto itself, achieved via the Möbius transformation $w : \text{SU}(1, 1) \rightarrow \mathbb{C}$:

$$\mathbf{S} = \begin{pmatrix} P & Q \\ Q^* & P^* \end{pmatrix} \longrightarrow w(z) = \frac{Pw_0 + Q}{Q^*w_0 + P^*}, \quad w, w_0 \in \mathbb{C}, \quad (5)$$

which maps the unit disk $\mathcal{D} = \{|w_0| \leq 1, w_0 \in \mathbb{C}\}$ conformally onto itself.

Combining Eqs. (3)–(5), the introduced variable w , akin to the local conductance, evolves according to the Riccati equation

$$\frac{dw}{dz} = i\kappa \left(e^{-i\varphi(z)} + e^{i\varphi(z)} w^2(z) \right). \quad (6)$$

Interestingly, by restricting the action of the transformation (5) to $\partial\mathcal{D}$, the $\text{SU}(1, 1)$ symmetry implies that $|w| = 1$. Thence, setting $w(z) = e^{i\psi(z)}$, $\psi \in \mathbb{R}$, Eq. (6) reduces to the first-order nonlinear differential equation of a single real variable

$$\frac{d\psi}{dz} = 2\kappa \cos(\psi + \varphi). \quad (7)$$

This sole parameter ψ encodes all relevant spectral information, i.e., both amplitude and phase of each element of the transfer matrix (N.B.— \mathbf{S} has three degrees of freedom, independently of the chosen parameterization). Nonetheless, even if Eq. (7) is numerically solved, identifying P and Q remains elusive.

Fortunately, some powerful properties of linear fractional transformations come to the rescue. Indeed, a Möbius transformation

$$w = \frac{aw_0 + b}{cw_0 + d}, \quad \text{where } ad \neq bc,$$

is completely defined by the cross-ratio [15]

$$\frac{(w - w_1)(w_2 - w_3)}{(w - w_3)(w_2 - w_1)} = \frac{(w_0 - w_{01})(w_{02} - w_{03})}{(w_0 - w_{03})(w_{02} - w_{01})},$$

and therefore is uniquely determined by its values at three finite points: $A(w_{01}, w_1)$, $B(w_{02}, w_2)$, $C(w_{03}, w_3)$. Whence, the generally complex coefficients are given by

$$a = \begin{vmatrix} w_{01} w_1 & w_1 & 1 \\ w_{02} w_2 & w_2 & 1 \\ w_{03} w_3 & w_3 & 1 \end{vmatrix}, \quad b = \begin{vmatrix} w_{01} w_1 & w_{01} & w_1 \\ w_{02} w_2 & w_{02} & w_2 \\ w_{03} w_3 & w_{03} & w_3 \end{vmatrix}, \quad c = \begin{vmatrix} w_{01} & w_1 & 1 \\ w_{02} & w_2 & 1 \\ w_{03} & w_3 & 1 \end{vmatrix}, \quad d = \begin{vmatrix} w_{01} w_1 & w_{01} & 1 \\ w_{02} w_2 & w_{02} & 1 \\ w_{03} w_3 & w_{03} & 1 \end{vmatrix}.$$

To fully identify both amplitude and phase of P and Q , we need three pairs of (ψ_{0j}, ψ_j) , where $j = 1, 2, 3$. Thus, we need to solve Eq. (7) three times, each with a different initial condition ψ_{0i} . For convenience, let us choose: $\psi_{01} = 0$, $\psi_{02} = \pi/4$, and $\psi_{03} = \pi/2$; these choices are arbitrary—any finite and discrete points on the unit circle will suffice. The transfer matrix is then

$$\begin{pmatrix} P & Q \\ Q^* & P^* \end{pmatrix} = \frac{1}{\sqrt{ad - bc}} \begin{pmatrix} a & b \\ c & d \end{pmatrix}, \quad (8)$$

with the intensity reflectance and transmittance obtained by applying the boundary condition $A^-(L) = 0$. They read $R = | -Q^*/P^*|^2$ and $T = |1/P^*|^2$, respectively.

Not surprisingly, there is a case wherein Eq. (7) can be solved analytically: none other than linear detuning. In particular, when the phase term of the grating is $\varphi(z) = \delta kz$, where $\delta k = 2\bar{n}k_0 - K_0$ is a detuning parameter, by appropriately changing the variable as $f = \psi + \delta kz$, Eq. (7) reduces to

$$\frac{df}{dz} = 2\kappa \cos f + \delta k. \quad (9)$$

Surprisingly, Eq. (9) is, in fact, the Adler equation from coupled-oscillator theory, with applications in, e.g., Josephson junctions and injection locking, to name a few. The analytic solution to Eq. (9), in terms of ψ , takes the cumbersome form

$$\psi = 2 \tan^{-1} \left[\frac{\frac{\delta k}{2\Delta} \cos \varphi_+ \sinh(\Delta z) + \sin \varphi_+ \cosh(\Delta z) + \frac{\kappa}{\Delta} \cos \varphi_- \sinh(\Delta z)}{-\frac{\delta k}{2\Delta} \sin \varphi_+ \sinh(\Delta z) + \cos \varphi_+ \cosh(\Delta z) + \frac{\kappa}{\Delta} \sin \varphi_- \sinh(\Delta z)} \right],$$

with $\Delta = [\kappa^2 - (\delta k/2)^2]^{1/2}$ and $\varphi_{\pm} = (\psi_0 \mp \varphi)/2$. Setting $w(z) = (1+ui)/(1-ui)$ and $w_0(z) = (1+u_0i)/(1-u_0i)$, where $u = \tan(\psi/2)$ and $u_0 = \tan(\psi_0/2)$, reconstructive surgery reproduces the well-known results:

$$P(z) = e^{-i\varphi/2} p \quad \text{and} \quad Q(z) = e^{-i\varphi/2} q, \quad (10)$$

where

$$p = \cosh(\Delta z) + i \frac{\delta k}{2\Delta} \sinh(\Delta z) \quad \text{and} \quad q = i \frac{\kappa}{\Delta} \sinh(\Delta z). \quad (11)$$

The spatial and spectral evolutions of the variable ψ are depicted in Figs. 3a, b respectively. While these figures may not directly highlight anything about the nature of the Bragg grating, observant readers may discern a pattern: curves within

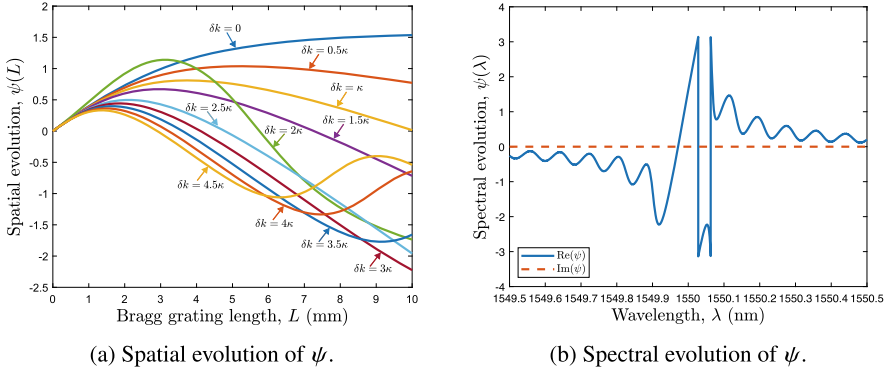


Fig. 3 Two aspects of the variable ψ that encrypts all information related to a Bragg grating. In the uniform index modulation scenario of this example, curves within the Bragg zone exhibit no inflection points, while those outside have at least one (Reprinted with permission from Ref. [1] © American Physical Society)

the Bragg zone, where $\Delta \in \mathbb{R}$, exhibit no inflection points, whereas those outside, where $\Delta = |\Delta|i \in \mathbb{C}$, have at least one. This criterion, easily verifiable by high-school analysis (just check the second derivative test), aligns with the stability condition of the Adler equation, as seen in Ref. [16] and elaborated in Ref. [1].

Converting to the actual fields, one can determine the allowed wavenumbers [1]

$$k = \frac{K_0}{2} + \text{sgn}(\delta k) \left[\left(\bar{n}k_0 - \frac{K_0}{2} \right)^2 - \left(\frac{k_0\delta\bar{n}}{2} \right)^2 \right]^{1/2}. \quad (12)$$

Due to the kinship to the Adler equation, Eq.(12) may be interpreted as the “phase rotation number” of dynamic systems (cf. Eq. (11) in Ref. [16]). For uniform modulation, such a dispersion relation is illustrated in Fig. 4a, where the approximate relation of coupled-wave theory given by Eq.(12) is plotted alongside the exact Floquet–Bloch curve (for the first harmonic). Both theories are in excellent agreement, predicting a regime where the real part of the wavenumber k remains constant while the associated imaginary part is nonzero, signifying strong attenuation.

The photonic bandgap exhibited by (uniform) Bragg gratings has a natural affinity to the Möbius method. In fact, if $w_{\tilde{S}} = e^{iK_0z}w$, where w is that of Eq. (5), the transformation’s fixed points, found on solving $w(\gamma) = \gamma$, lie on the unit circle $\partial\mathcal{D}$ for wavelengths inside the Bragg zone, whereas either inside or outside $\partial\mathcal{D}$ otherwise. Crucially, as we prove in Ref. [1], such a criterion is not restricted to linear detuning, being applicable to any $\text{SU}(1, 1)$ symmetrical structure with arbitrarily complex refractive index modulation.

Another intriguing facet of the photonic bandgap relates to the broader classification of Möbius transformations, as proposed in prior works [17]. Within uniform

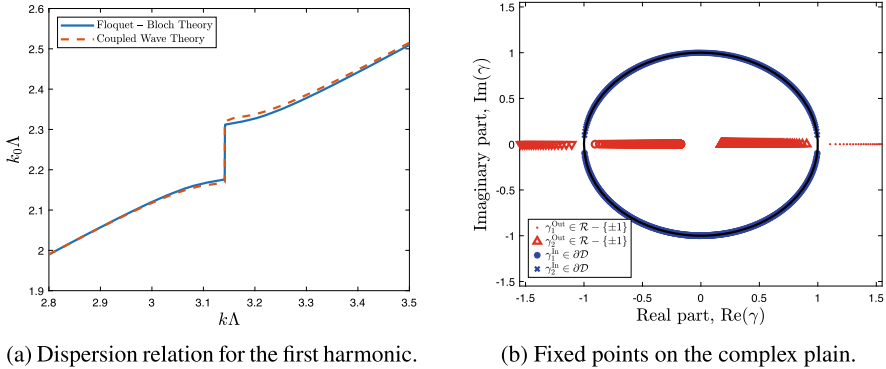


Fig. 4 Dispersion features of a uniform Bragg grating in two different domains (Reprinted with permission from Ref. [1] © American Physical Society)

and loss/gain-free gratings, the real part of the trace of the transfer matrix¹ serves to classify the transformation. Indeed, if $\sigma = \left[\text{trace}(\tilde{\mathbf{S}}) \right]^2$, these transformations can fall into categories such as, e.g., elliptic ($0 \leq \sigma < 4$), parabolic ($\sigma = 4$), or indeed hyperbolic ($4 < \sigma < \infty$). Such a correlation is anticipated due to the known affinity between the trace of transfer matrices, the Bloch angle, and the phase rotation number. Beyond the Bragg zone, the Möbius representation is elliptical; at the edges, it transitions to parabolic, while within, it is hyperbolic.

Hitherto, we have been discussing a fresh perspective on the otherwise well-understood uniform Bragg gratings. Nevertheless, the motivation for developing the Möbius transformation was to examine nontrivial modulation scenarios. To that extent, Fig. 5a illustrates the optical response of a *linearly chirped* Bragg grating, i.e., a grating whose local spatial frequency acquires an additional $\Delta K(z) = (2F/L^2)z$ term, with F being the chirp coefficient. Without further details, one could imagine that the Möbius method could be applicable to more advanced modulation scenarios, such as quadratic chirping and apodization (N.B.— no requirement that the coupling coefficient κ is constant has been imposed, and the definitions seen in Eq. (2) are for purely pedagogical purposes). However, for the sake of brevity, we believe that demonstrating the method's performance in phase discontinuities is a better proof-of-concept. Therefore, in Fig. 5b, we display the optical spectrum of two similar uniform cascaded gratings with slightly dissimilar pitches, Λ_1 and Λ_2 , satisfying the spectral hole condition $1/\Lambda_2 - 1/\Lambda_1 = 1/L$ of Ref. [18]. Around $\lambda = \bar{n}(\Lambda_1 + \Lambda_2)$, a spectral hole ensues, which is indeed successfully captured by the Möbius method.

¹ In this instance, we refer to $\tilde{\mathbf{S}} = (p \ q; q^* \ p^*)$, where p and q are those of Eq. (11).

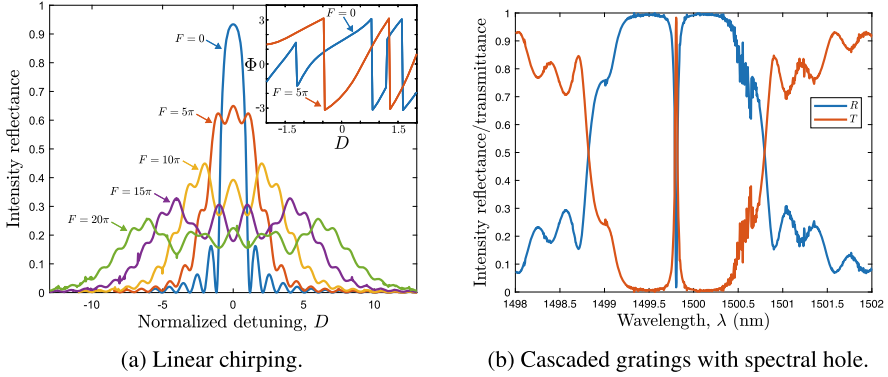


Fig. 5 Optical spectra accessed via the Möbius method for advanced index modulation scenarios (Reprinted with permission from Ref. [1] © American Physical Society)

3 A Circular Bragg Phenomenon for All Handednesses

Equipped with the toolkit of coupled-wave theory of Sect. 2, we proceed to examine a medium that embodies the two primary aspects of chirality: magneto-electric coupling resulting from the absence of mirror symmetry at the molecular scale,² and structural chirality arising from the helical stacking of birefringent layers. Consequently, our complex medium will be aptly christened as optically active structurally chiral. On the one hand, while the term “optical activity” may be somewhat ambiguous, mainly due to its broad context, there is unanimous agreement on the definition of circular birefringence: the propagation of orthogonal circularly polarized states at different speeds. On the other hand, the distinctive response of structurally chiral mediums indicates that a circularly polarized wave, whose handedness coalesces with the structural handedness of the medium, gets strongly backscattered when its wavelength matches the pitch of the scaffold. Conversely, the orthogonal polarization state traverses the medium unaffected, being accountable only to absorption.

A natural question arises: what occurs in mediums where both aspects of chirality coexist? Before attempting to address this question, it is crucial to provide at least some evidence of the existence of such mediums. As it happens, the porous nature of sculptured thin films appears to provide the ideal platform for infiltration by a chiral fluid, as demonstrated by Sherwin and Lakhtakia in Ref. [2]. We revisit such a medium, albeit, instead of employing the Oseen transformation and resorting to the brute force of numerical simulations, we opt for the coupled-wave theory approach—though, we will not spare some symmetries of the exact system!

² To the same order of multipole approximation, electric–electric quadrupole coupling is important in many forms of natural optical activity, such as circular dichroism in oriented mediums—see Chap. 4 of Ref. [19].

If \mathbf{E} , \mathbf{B} are the primitive electromagnetic fields, and \mathbf{D} , \mathbf{H} are their associated stimulated excitation fields, we define the auxiliary fields $\mathbf{b} = (\eta_0/\mu_0)\mathbf{B}$, $\mathbf{d} = \epsilon_0^{-1}\mathbf{D}$, and $\mathbf{h} = \eta_0\mathbf{H}$, which share the same dimensions as the \mathbf{E} -field. Here, ϵ_0 , μ_0 , and $\eta_0 = (\mu_0/\epsilon_0)^{1/2}$ are the free-space permittivity, permeability, and impedance, respectively. For the current purposes, we supplement Maxwell's macroscopic equations with Tellegen's constitutive connections for the simplest reciprocal bi-isotropic medium, viz.,

$$\mathbf{d} = \epsilon \mathbf{E} + i\alpha \mathbf{h} \quad \text{and} \quad \mathbf{b} = -i\alpha \mathbf{E} + \mu \mathbf{h}. \quad (13)$$

In Eq. (13), ϵ , μ , and α are the relative (i.e., dimensionless) permittivity, permeability, and chirality parameters, respectively, with the latter measuring the wavelengths after which the \mathbf{E} -vector of a linearly polarized wave is rotated by 2π . Under this slightly quirky notation, and for an $e^{-i\omega t}$ harmonic excitation, combining Maxwell's macroscopic source-free curl relations leads to the chiral Helmholtz wave equation

$$\frac{d^2 \mathbf{E}}{dz^2} + 2\alpha k_0 \frac{d}{dz} (\hat{\mathbf{z}} \times \mathbf{E}) + k_0^2 (\epsilon \mu - \alpha^2) \mathbf{E} = \mathbf{0}. \quad (14)$$

Structural chirality may then be incorporated into the model by replacing the scalar (relative) permittivity in Eqs. (13) and (14) with the dielectric tensor

$$\epsilon = \mathcal{R} \cdot \hat{\epsilon} \cdot \mathcal{R}^{-1},$$

where $\hat{\epsilon} = \text{diag}(\epsilon_a, \epsilon_b, \epsilon_c)$ is the static dielectric tensor, and \mathcal{R} periodically rotates the medium's eigenaxes about $\hat{\mathbf{z}}$ with a period $\Lambda = 2\pi/p$. In a Cartesian basis,

$$\mathcal{R} = \begin{pmatrix} \cos(pz) & -h \sin(pz) & 0 \\ h \sin(pz) & \cos(pz) & 0 \\ 0 & 0 & 1 \end{pmatrix}, \quad (15)$$

whereby for $h = +1$ (respectively, $h = -1$), the medium is regarded as a right- (respectively, left-) handed. The tensor's transverse projection is expressed as [20]

$$\epsilon_{\perp} = \mathcal{R}_{\perp} \cdot \hat{\epsilon}_{\perp} \cdot \mathcal{R}_{\perp}^{-1}, \quad (16)$$

where $\mathcal{R}_{\perp} = (\sigma/2) e^{ipz} + (\sigma^*/2) e^{-ipz}$, with $\sigma = (1 \ hi; -hi \ 1)$. Here, $\hat{\epsilon}_{\perp} = \bar{\epsilon} \mathbb{I} + \delta\epsilon \mathbb{J}$, with $\bar{\epsilon} = (\tilde{\epsilon} + \epsilon_b)/2$ and $\delta\epsilon = (\tilde{\epsilon} - \epsilon_b)/2$; $\tilde{\epsilon}$ is a function of the background tensor's components and of the rise angle, \mathbb{I} it the unitary matrix, and \mathbb{J} its symplectic form.

If $\bar{n} = (\bar{\epsilon}\mu)^{1/2}$, it proves instructive to expand the transverse part of the electric field in a circular basis as per Jaggard et al. in Ref. [21], namely

$$\mathbf{E}_\perp = \left(A_L^+ e^{ik_0(\bar{n}+\alpha)z} + A_R^- e^{-ik_0(\bar{n}-\alpha)z} \right) \mathbf{Q}_1 + \left(A_R^+ e^{ik_0(\bar{n}-\alpha)z} + A_L^- e^{-ik_0(\bar{n}+\alpha)z} \right) \mathbf{Q}_2, \quad (17)$$

where $\mathbf{Q}_1 = 2^{-1/2} (1 \ i)^\top$ and $\mathbf{Q}_2 = 2^{-1/2} (1 \ -i)^\top$, with \top denoting transpose.³ Under the slowly varying envelope approximation, if we replace in Eq. (14) the permittivity scalar with the tensor of Eq. (16) and substitute Eq. (17), we can phase-match synchronous terms by time-averaging upon several optical cycles. Whence, resolving along \mathbf{Q}_1 and \mathbf{Q}_2 , we obtain, respectively,

$$\begin{aligned} \frac{dA_L^+}{dz} e^{ik_0(\bar{n}+\alpha)z} - \frac{dA_R^-}{dz} e^{-ik_0(\bar{n}-\alpha)z} &= i\kappa A_R^+ e^{i[k_0(\bar{n}-\alpha)-2hp]z} + i\kappa A_L^- e^{-i[k_0(\bar{n}+\alpha)+2hp]z}, \\ \frac{dA_R^+}{dz} e^{ik_0(\bar{n}-\alpha)z} - \frac{dA_L^-}{dz} e^{-ik_0(\bar{n}+\alpha)z} &= i\kappa A_L^+ e^{i[k_0(\bar{n}+\alpha)+2hp]z} + i\kappa A_R^- e^{-i[k_0(\bar{n}-\alpha)-2hp]z}, \end{aligned}$$

where the coupling constant is that of Eq. (2) with $\delta\bar{n} = |\tilde{\epsilon}^{1/2} - \epsilon_b^{1/2}| \in \mathbb{R}$.

We may now concisely cast the aforementioned equations as Eq. (B4) of Ref. [3],

$$\frac{d}{dz} \begin{pmatrix} A_L^+ \\ A_L^- \\ A_R^+ \\ A_R^- \end{pmatrix} = i\kappa \begin{pmatrix} 0 & e^{-i\delta_L z} & e^{-i\delta_c z} & 0 \\ -e^{i\delta_L z} & 0 & 0 & -e^{i\delta_c z} \\ e^{i\delta_c z} & 0 & 0 & e^{-i\delta_R z} \\ 0 & -e^{-i\delta_c z} & -e^{i\delta_R z} & 0 \end{pmatrix} \begin{pmatrix} A_L^+ \\ A_L^- \\ A_R^+ \\ A_R^- \end{pmatrix},$$

where the detuning parameters, $\delta_R = 2k_0(\bar{n} - \alpha) - 2hp$, $\delta_L = 2k_0(\bar{n} + \alpha) + 2hp$, and $\delta_c = 2k_0\alpha + 2hp$, are explicitly linked to the corresponding mode's handedness.

In a right-handed medium, the on-resonance condition for RCP light yields

$$\text{Re}(\delta_R) = 0 \Rightarrow \lambda_0^{\text{Br}} \Big|_{h=+1}^{\text{RCP}} = \Lambda [\text{Re}(\bar{n}) - \alpha], \quad \alpha < \text{Re}(\bar{n}). \quad (18)$$

As anticipated, Eq. (18) is none other than the well-known Bragg condition of the circular Bragg phenomenon, albeit linearly shifted by the presence of the chiral fluid. This result corroborates the findings of Ref. [2]: the fluid's chirality linearly shifts the Bragg resonance toward the red or the blue, depending on the sense of optical rotation (i.e., the sign of α). Such a linear shift is illustrated in Fig. 6a wherein

³ For $|\alpha| < \bar{n}$, the subscripts in the amplitudes, L and R , denote LCP and RCP light, respectively. However, if $|\alpha| > \bar{n}$, which is precisely the condition for entering the negative refraction due to chirality regime, the phase velocity and handedness of counter propagating modes are interchanged—see App. A of Ref. [3].

various circular Bragg resonances are plotted for different values of the chirality parameter. Finally, setting $\delta_c = 0$, we obtain $k_0\alpha = -hp$, corresponding to modes that couple co-propagating cross-handed polarizations.

As per Sect. 2, the coupled-wave system for, say, $\delta_R \approx 0$ has the solution

$$\begin{pmatrix} A_R^+ \\ A_R^- \end{pmatrix}_z = \begin{pmatrix} P & Q \\ Q^* & P^* \end{pmatrix} \begin{pmatrix} A_R^+ \\ A_R^- \end{pmatrix}_{z=0}, \quad (19)$$

with P, Q those of Eq. (10) if $\delta k \equiv \delta_R$. By contrast, at $\delta_c \approx 0$, the solution reads

$$\begin{pmatrix} A_L^+ \\ A_R^+ \end{pmatrix}_z = \begin{pmatrix} e^{-i\frac{\delta_c}{2}z} \tilde{p}^+ & e^{-i\frac{\delta_c}{2}z} \tilde{q} \\ e^{i\frac{\delta_c}{2}z} \tilde{q} & e^{i\frac{\delta_c}{2}z} \tilde{p}^- \end{pmatrix} \begin{pmatrix} A_L^+ \\ A_R^+ \end{pmatrix}_{z=0}. \quad (20)$$

This time, \tilde{p}^\pm and \tilde{q} have the same form as those appearing in Eq. (11), but with the hyperbolic functions being replaced by their associated trigonometric ones (e.g., \sin instead of \sinh etc.); $\Delta_c = [\kappa^2 + (\delta_c/2)^2]^{1/2}$.

Transforming Eq. (20) back to the \mathbf{E} -field on a circular basis, a continuous exchange between LCP and RCP light occurs in the vicinity of the regime where optical activity counterbalances structural chirality. This phenomenon is depicted in Fig. 6b whereby for incident LCP light, the intensity transmittances of LCP-to-LCP and RCP-to-LCP oscillate periodically with the slab's thickness. This evolution originates from linear polarizations in a birefringent medium being resolved onto a circular basis, which is rather mundane. However, what is not mundane at all is that the eigenmodes at λ_0^c ,

$$\mathbf{E}_1 = e^{i\tilde{\epsilon}^{1/2}k_0z} \begin{pmatrix} \cos(pz) \\ h \sin(pz) \end{pmatrix} \quad \text{and} \quad \mathbf{E}_2 = e^{i\epsilon_b^{1/2}k_0z} \begin{pmatrix} -h \sin(pz) \\ \cos(pz) \end{pmatrix},$$

are at once orthogonal and co-handed, inheriting the hosting medium's handedness.

Suppose now that in our right-handed structurally chiral medium, we equate, just for fun,⁴ the detuning parameter corresponding to a left-handed resonance, i.e., δ_L , to zero. The on-resonance wavelength for LCP light would then be

$$\lambda_0^{\text{Br}} \Big|_{h=+1}^{\text{LCP}} = -\Lambda [\text{Re}(\bar{n}) + \alpha]. \quad (21)$$

⁴ After our initial “funny” idea led to the identification of such a reverse circular Bragg phenomenon, we became more astute. We revisited the characteristic matrix of the system resulting from the full analytic electromagnetic analysis and the Oseen transformation, and we reversed the handedness using p instead of h . Thus, by transforming as $(z; \epsilon_b, \tilde{\epsilon}, \mu; k_0; h, p, \alpha) \rightarrow (z; \epsilon_b, \tilde{\epsilon}, \mu; k_0; h, -p, -\alpha)$, following Lakhtakia's method in Ref. [22], we created the illusion that the medium's handedness is reversed, despite h being fixed.

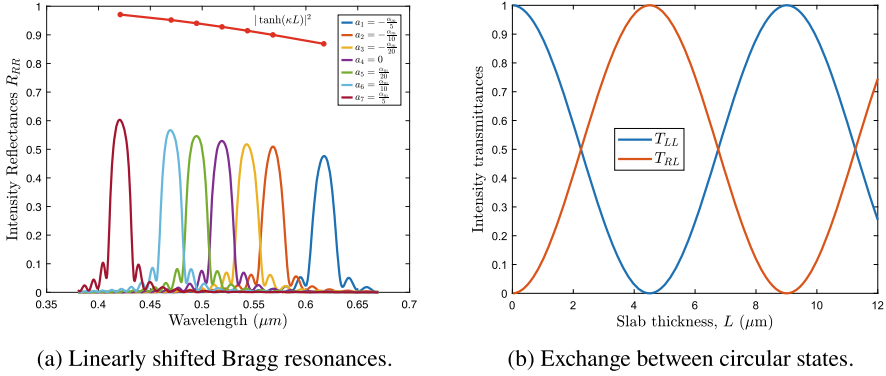


Fig. 6 Optical response of an optically active structurally chiral medium for non-giant chirality. At a specific wavelength, optical activity offsets structural chirality, rendering the medium simply linearly birefringent. There, eigenmodes which are otherwise conveniently represented on a circular basis exchange energy [(b) Is reprinted from Ref. [3] under a Creative Commons CC BY license]

Intriguingly, accessing such a resonance *is* possible when $\alpha < -\text{Re}(\bar{n})$, which also satisfies the condition outlined in Eq. (18) for the “regular” resonance to manifest. Therefore, when $\alpha < -\text{Re}(\bar{n})$, the occurrence of two resonances is anticipated: one for light that aligns with the medium’s handedness, being strongly reflected, and another responsible for backscattering light that is ostensibly contra-handed to the medium.⁵

Considering a finite slab of length L , filled with the medium under consideration, and surrounded by an isotropic dielectric with refractive index n_1 on one side and n_2 on the other, the optical response calculated by full electromagnetic analysis (see Ref. [3]) is illustrated in Fig. 7. Clearly, all spectral characteristics predicted from our analysis are observed. Notably, two resonances emerge: one for RCP light at $\lambda_{\text{Br}}^{\text{RCP}}|_{h=+1} = 1.297 \mu\text{m}$, and the other for LCP at $\lambda_0^{\text{LCP}}|_{h=+1} = 259.55 \text{ nm}$.

In Fig. 7b, the decrease in overall transmittance at shorter wavelengths corresponds to increased absorption due to increasing optical depth. At around λ_0^c , where the transfer of energy between T_{LL} (T_{RR}) and T_{RL} (T_{LR}) peaks, optical activity essentially “unwinds” the medium, rendering it merely birefringent with refractive indices $\tilde{\epsilon}^{1/2}$ and $\epsilon_b^{1/2}$. As the wavelength decreases further, the medium undergoes another “wrapping” but with opposite handedness, potentially leading to a reverse circular Bragg resonance. Despite maintaining its inherent structural handedness, giant chirality may reverse some of the modes’ handedness [3].

⁵ In this chapter, words such as “nominally” and “ostensibly” are selected with precision rather than poetic license. Although the structural handedness remains constant (if you doubt it, just take a snapshot of the helix!), the chirality of the modes changes upon entering negative refracting states.

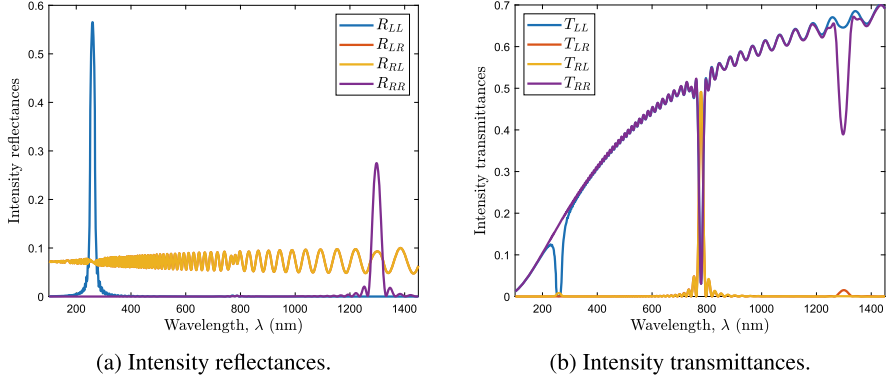


Fig. 7 Optical response of a slab consisting of an optically active right-handed structurally chiral medium with giant chirality $\alpha = -1.5\text{Re}(\tilde{n})$, sandwiched between isotropic dielectrics (Reprinted from Ref. [3] under a Creative Commons CC BY license)

As numerically observed in Ref. [2], optical activity also affects the peak reflectance. To explain this dependence, we may examine the on-resonance approximate expression, $R^{\text{Peak}} = \tanh^2(\kappa L)$. For a particular handedness, say, right, for RCP, we have $k_0^R = p/(\tilde{n} - a)$, while for LCP, $k_0^L = -p/(\tilde{n} + a)$. Thence, for the former,

$$R_{\text{RR}}^{\text{Peak}} = \tanh^2\left(\frac{p}{\tilde{n} - \alpha} \frac{\mu\delta\epsilon}{2\tilde{n}} L\right). \quad (22)$$

It is evident from Eq. (22) that increasing α increases $R_{\text{RR}}^{\text{Peak}}$. On the contrary, for a left-handed medium, increasing α has the opposite impact on $R_{\text{LL}}^{\text{Peak}}$. Figure 6a demonstrates how the reflectance spectrum of a right-handed structurally chiral medium varies with α . Only R_{RR} is shown, as it is only this reflection spectrum that shows the circular Bragg phenomenon for the range of α used in the simulation. In the same plot, the performance of Eq. (22) is also evaluated in the presence of absorption. The deviation from the actual peaks scales with the imaginary part of the dielectric parameters, but clearly demonstrates the monotonic of $R_{\text{RR}}^{\text{Peak}}$ with α .

Furthermore, it is seen in Ref. [2] that optical activity also affects the resonance's bandwidth. This is estimated by coupled-wave theory as $\Delta\lambda_0 = \text{Re}(\delta\tilde{n}) L_p$. Considering the optical rotation, signature of structural chirality, roughly proportional to the square of the local linear birefringence $\delta\tilde{n}$ [23], and by extending the argument to the optical rotation induced by the chiral fluid, we can state that $\Delta\lambda_0 \sim \alpha^2 L_p$. This qualitatively explains the quadratic dependence of Eq. (40) of Ref. [2].

Before turning the page on this section, let us clarify: what sort of value is α ? Is it realistic for the chirality to be comparable to the refractive index of commonly used mediums? The answer is both yes and no. No, because the optical rotatory power of naturally occurring mediums is typically extremely weak (e.g., an optically active crystal may well have a chirality parameter four or five orders of magnitude

less than unity). Nevertheless, experimental efforts in what became known as the “meta-mediums” community led to fascinating demonstrations of artificial mediums exhibiting giant chirality across various realms of the radiation spectrum. For instance, in the visible spectrum, the gammadion nanostructure of Ref. [24] achieves an $\alpha \approx 0.15$ while Katsantonis et al. used in Ref. [25] some three-dimensional U-shaped twisted rings to achieve enhanced and remarkably broadband optical activity in the lower THz region. For a comprehensive discussion on various meta-mediums implementations achieving giant chirality, we recommend Sec. 6 of Ref. [5] and the references therein.

4 Bragg-Less Bragg Gratings

In this section, we will revisit the problem outlined in Sect. 3, only this time, we shall approach it via a flanking maneuver. To that end, we halt the progressive rotation of the eigenaxes along and about the z -axis [i.e., we set $p = 0$ in Eq. (15)], thereby rendering the permittivity tensor equal to the background dielectric tensor.

It proves handy to decompose the fields as $\mathbf{E} = E_{\parallel} \hat{\mathbf{k}} + \mathbf{E}_{\perp}$ and $\mathbf{h} = h_{\parallel} \hat{\mathbf{k}} + \mathbf{h}_{\perp}$, with $\hat{\mathbf{k}}$ being a unit vector in the direction of the wavevector \mathbf{k} , and partition ϵ so that

$$\epsilon \cdot \mathbf{E} = \begin{pmatrix} \hat{\epsilon}_{\perp} \cdot \mathbf{E}_{\perp} + \epsilon_{\parallel} E_{\parallel} \\ \epsilon_{\parallel}^T \cdot \mathbf{E}_{\perp} + \epsilon_s E_{\parallel} \end{pmatrix},$$

where $\hat{\epsilon}_{\perp} : \mathbb{C}^2 \rightarrow \mathbb{C}^2$, $\epsilon_{\parallel} \in \mathbb{C}^2$ and $\epsilon_s \in \mathbb{C}$. Whence, for a monochromatic plane wave, $\mathbf{E} e^{i(\mathbf{k} \cdot \mathbf{r} - \omega t)}$, combining the projections of Maxwell’s source-free macroscopic curl relations, we arrive at Eq. (14) but with the scalar permittivity being replaced by

$$\hat{\epsilon}| = \hat{\epsilon}_{\perp} - \left(\epsilon_s - \frac{\alpha^2}{\mu} \right)^{-1} \epsilon_{\parallel} \epsilon_{\parallel}^T. \quad (23)$$

It is deduced from Eq. (23) that $\hat{\epsilon}|$ depends on the direction of \mathbf{k} . For propagation along a principal direction $\epsilon_{\parallel}^T = \mathbf{0}$, so in this case $\hat{\epsilon}| = \hat{\epsilon}_{\perp}$, which in suitable transverse coordinates can be reduced to $\hat{\epsilon}| = \text{diag}(\epsilon_1, \epsilon_2)$. In the presence of birefringence (say, $\epsilon_1 \neq \epsilon_3$) for general propagation in the $x - z$ plane, the principal indices depend on α . This is a slightly surprising result, given that they do not depend on α for propagation along a principal axis, and soon we will use it to our advantage.

Henceforth, we elect a propagation coordinate system ($\mathbf{k} = k\hat{\mathbf{z}}$) with transverse coordinates (x, y) such that they diagonalize the permittivity tensor as $\hat{\epsilon}| = \text{diag}(\epsilon_1, \epsilon_2)$. Then, the supported by the medium refractive indices turn out to be [4]

$$\pm n^{(\pm)} = \pm \left[\bar{n}^2 + \alpha^2 \pm \left(\Delta\epsilon^2 \mu^2 + 4\alpha^2 \bar{n}^2 \right)^{1/2} \right]^{1/2}, \quad (24)$$

with $\bar{\epsilon} = (\epsilon_1 + \epsilon_2)/2$ and $\Delta\epsilon = (\epsilon_2 - \epsilon_1)/2$.

Scrutinizing Eq. (24) shows that for an ordering $\epsilon_2 > \epsilon_1$, if

$$\epsilon_1 \mu < \alpha^2 < \epsilon_2 \mu, \quad (25)$$

then two branches of $\pm n^{(\pm)}$ become purely imaginary. We thus have evanescence in a bulk dielectric medium! Note that if $\Delta\epsilon = 0$, then the evanescent region disappears. Thus, we can postulate that $\alpha = \bar{n}$ is the “resonant” α yielding the largest imaginary value of $\pm n^{(-)}$. For this value, we find

$$n_L^{\text{res}} \approx 2\bar{n} \quad \text{and} \quad n_R^{\text{res}} \approx i \frac{\Delta\epsilon}{2} \left(\frac{\mu}{\bar{\epsilon}} \right)^{1/2},$$

the approximations being valid for $\Delta\epsilon \ll \bar{\epsilon}$; the subscripts referring to a specific polarization state will be subsequently justified.

Figure 8a depicts all four branches of the refractive indices in Eq. (24) as functions of the chirality parameter. At this point, we want to prevent a potential source of confusion: Fig. 8a is not a typical dispersion diagram but may be interpreted as the variation of the refractive index with the chirality parameter. Current technology is capable of controlling chirality through various methods, such as piezoelectricity [26], external electric fields [27], or conductivity [28] to name a few. Additionally, Fig. 8a illustrates the corresponding polarization of each eigenmode, found on inserting Eq. (24) into Eq. (14) and solving for $E_{\perp y}/E_{\perp x}$. At approximately $\alpha = \pm\bar{n}$, two stopbands emerge [cf. Eq. (25)], wherein the eigenpolarizations are circular with opposite handedness. The affinity of this situation to the one examined in Sect. 3 warrants further investigation.

We won’t be original this time either—we will utilize coupled-wave theory, again! Using the same ansatz as that of Eq. (17), and noting the interesting algebra, $(\times)\mathbf{Q}_1 = -i\mathbf{Q}_1$ and $(\times)\mathbf{Q}_2 = i\mathbf{Q}_2$, we apply the same approximations as in Sect. 2. Thence, upon resolving along \mathbf{Q}_1 and \mathbf{Q}_2 , phase matching at $\alpha = \pm\bar{n}$ leads to

$$\frac{dA_L^+}{dz} = i\kappa A_L^- e^{-ik_0\delta_{(+)}z}, \quad \frac{dA_R^-}{dz} = -i\kappa A_R^+ e^{ik_0\delta_{(-)}z},$$

and

$$\frac{dA_R^+}{dz} = i\kappa A_R^- e^{-ik_0\delta_{(-)}z}, \quad \frac{dA_L^-}{dz} = -i\kappa A_L^+ e^{ik_0\delta_{(+)}z},$$

respectively. In this instance, the identified coupling coefficient is given by

$$\kappa = \frac{k_0 \mu}{2\bar{n}} \Delta\epsilon, \quad (26)$$

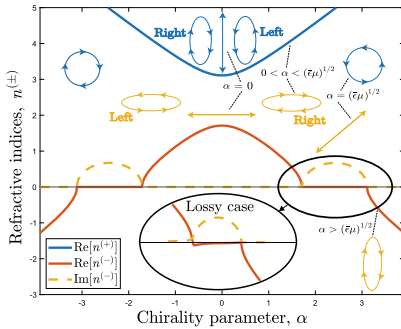
which precisely encapsulates the essence of the coupling mechanism: it disappears when we switch off linear birefringence. The detuning parameters are $\delta_{(\pm)} = 2(\bar{n} \pm \alpha)$, being, crucially, wavelength-independent. It should be noted that at this stage, we do not state that \bar{n} and α are non-dispersive, but rather that there is not a direct wavelength dependence on the tuning condition. Thus, we contend that the proposed mechanism is inherently broadband, with its actual broadband capability being determined by the *differential* dispersion between \bar{n} and α .

The coupled-wave equations derived in this context can be compactly re-expressed as per Eq. (1), i.e., as

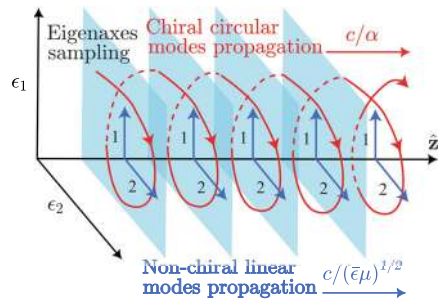
$$\frac{d}{dz} \begin{pmatrix} A_{L,R}^+ \\ A_{L,R}^- \end{pmatrix} = \begin{pmatrix} 0 & i\kappa e^{-i\delta_{L,R}z} \\ -i\kappa e^{i\delta_{L,R}z} & 0 \end{pmatrix} \begin{pmatrix} A_{L,R}^+ \\ A_{L,R}^- \end{pmatrix}, \quad (27)$$

since at $\alpha \approx \bar{n}$ (respectively, $\alpha \approx -\bar{n}$), the A_L^\pm (respectively, A_R^\pm) amplitudes remain constant, while the orthogonals follow a Bragg-like evolution. The solutions to the systems appearing in Eq. (27) are represented by the matrix in Eq. (8), where P and Q correspond to those in Eq. (10) when the suitable detunings and coupling coefficient are substituted.

These two pairs of coupled-wave equations are precisely what we aimed for! They describe a Bragg-like phenomenon centered at $\alpha = \bar{n}$. We also note that within the Bragg regime, circularly polarized light is reflected with the same handedness, making the phenomenon akin to the circular Bragg phenomenon associated with



(a) Chirality-domain dispersion.



(b) Periodic eigenaxes sampling.

Fig. 8 The refractive indices of a linearly and circularly birefringent medium, as functions of the chirality parameter, indicate the existence of two stopbands centered at $\alpha = \pm\bar{n}$, where evanescence occurs. Around $\alpha \approx \bar{n}$, the chiral circularly polarized eigenstates, propagating at speed c/α , synchronously and alternately sample the copropagating birefringent eigenaxes [(a) Is reprinted with permission from Ref. [4] © Optical Society of America; (b) is adapted from ArXiv under a Creative Commons CC BY license]

structurally chiral mediums. However, it is important to highlight that here, there is no need any kind of fabrication (e.g., witting a refractive index profile via a phase mask illuminated by UV light). Furthermore, a significant distinction lies in the fact that in this case, the “Bragg resonance” arises via medium parameters (cf. $\alpha \approx \bar{n}$) rather than through a wavelength condition (cf. $\lambda_0 \approx \bar{n}\Lambda$). In other words, all wavelengths will be reflected whenever $\alpha \approx \bar{n}$, thus justifying our claim for an arbitrarily broadband “grating without a grating.”

The birefringence could be electrically switched on, offering a wide-bandwidth, electro-optic switch. When circularly polarized light propagates at the same speed as light in the absence of both optical activity and birefringence, it encounters the birefringence-induced grating. It is as if the birefringence “grating” is formed by a wave propagating with a refractive index \bar{n} , sampled by a circular polarization rotating at the same rate. Such a heuristic picture is illustrated in Fig. 8b, which shows the non-chiral linear eigenstates propagating with an average speed of c/\bar{n} , and the chiral circularly polarized eigenstates propagating with speed c/α . The latter synchronously and alternately sample the co-propagating birefringent eigenaxes, provided that $\alpha \approx \bar{n}$.

In the coupled-wave theory description outlined in Eq. (27), we can readily compute the optical response of a finite slab of the considered medium. However, we note a minor subtlety: we assume that the surrounding medium is approximately index- (and impedance-) matched with the slab, meaning it has a refractive index $n = \bar{n}$. Otherwise, Fresnel reflections localized at the boundaries would need to be taken into account. While not essential for the layout of our arguments, readers interested in further details can refer to the standard calculations provided in Ref. [29].

When discussing Bragg reflections, it is customary to illustrate the intensity reflectances. However, in Fig. 9a, we present intensity transmittances as functions of the chirality parameter to demonstrate, once again, the exchange between circular states at $\alpha = 0$ (cf. Fig. 6b), where the eigenmodes are purely linear [4]:

$$\frac{\mathbf{E}_\perp(0)}{A_R^+(0)} = \frac{i}{\sqrt{2}} \begin{pmatrix} 1 \\ i \end{pmatrix} + \frac{1}{\sqrt{2}} \begin{pmatrix} 1 \\ -i \end{pmatrix}. \quad (28)$$

The Bragg-like puzzle is completed in Fig. 9b, which shows the on-resonance evolution of T_{RR} transmittance into R_{RR} reflectance as a function of film thickness.

As aforesaid, for off-axis propagation, the principal indices depend on the chirality parameter [cf. Eq. (4)]. This unexpected finding has the potential to relax the $\alpha = \bar{n}$ tuning condition, as it introduces an additional degree of freedom via the inclination angle formed between the optical axis and the direction of wave propagation. Inspired by this observation, we can now generalize the problem further: considering off-axis propagation in uniaxial bi-anisotropic mediums. Consequently, all three scalars in the constitutive connections of Eq. (13) will be replaced by tensors. Additionally, we distinguish the cross-coupling between \mathbf{D} , \mathbf{h} , and \mathbf{b} , \mathbf{E} . In other words, we rewrite the constitutive relations as:

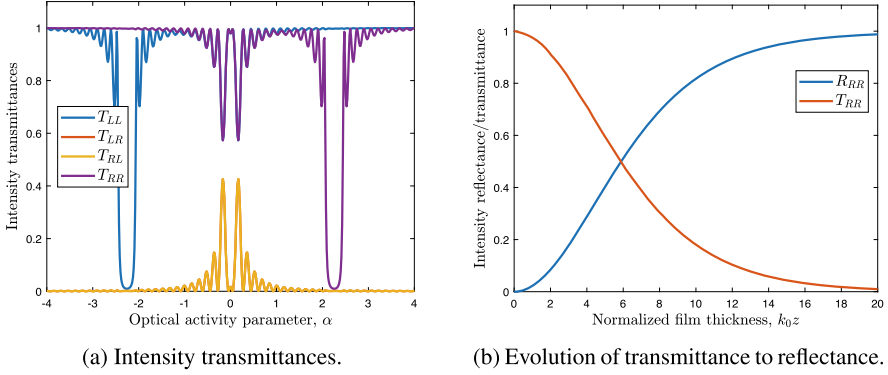


Fig. 9 Bragg-like electromagnetic response achieved in a uniform linearly and circularly birefringent mediums without refractive index modulation. At $\alpha \approx \pm \bar{n}$, one circular polarization state is strongly reflected, while the orthogonal state is transmitted. The evolution from co-transmittance to co-reflectance, as a function of the slab's normalized thickness, mirrors that of uniform Bragg gratings. However, unlike Bragg gratings, there is no coherent superposition of waves originating from distributed local reflections

$$\mathbf{d} = \boldsymbol{\epsilon} \cdot \mathbf{E} + \boldsymbol{\xi} \cdot \mathbf{h} \text{ and } \mathbf{b} = \boldsymbol{\zeta} \cdot \mathbf{E} + \boldsymbol{\mu} \cdot \mathbf{h}, \quad (29)$$

whereby aligning our Cartesian system's z -axis with the optical axis of the medium (cf. Fig. 10a), the components of these tensors are

$$\boldsymbol{\epsilon} = \begin{pmatrix} \epsilon & 0 & 0 \\ 0 & \epsilon & 0 \\ 0 & 0 & \epsilon_z \end{pmatrix}, \quad \boldsymbol{\mu} = \begin{pmatrix} \mu & 0 & 0 \\ 0 & \mu & 0 \\ 0 & 0 & \mu_z \end{pmatrix}, \quad \boldsymbol{\xi} = \begin{pmatrix} \xi & 0 & 0 \\ 0 & \xi & 0 \\ 0 & 0 & \xi_z \end{pmatrix}, \quad \text{and} \quad \boldsymbol{\zeta} = \begin{pmatrix} \zeta & 0 & 0 \\ 0 & \zeta & 0 \\ 0 & 0 & \zeta_z \end{pmatrix}.$$

For a non-reciprocal loss-free medium $\xi = \chi - i\kappa$, $\xi_z = \chi_z - i\kappa_z$, $\zeta = \xi^*$, and $\zeta_z = \xi_z^*$, where $\kappa, \kappa_z \in \mathbb{R}$ are the transverse and axial chirality parameters, respectively, and $\chi, \chi_z \in \mathbb{R}$ are the associated Tellegen coefficients⁶.

Although solving this general problem is quite challenging, as it requires, e.g., rotating the tensors of Eq. (4) so that the direction of propagation in a primed coordinate system coincides with the optical axis,⁷ the recipe is pretty much the same as the one developed earlier; analytic derivations can be found in Ref. [5]. If

⁶ And a little bit of history: While Tellegen mediums are currently widely accepted amongst the scientific community, this was not always the case. In the mid-90s, several theoretical arguments against the existence of non-reciprocal bi-isotropic mediums (see, e.g., Refs. [30, 31]) clashed with several others in favor (see, e.g., Refs. [32, 33]). The initial experimental demonstrations of artificial Tellegen mediums [34], signaled a shift toward including the Tellegen coefficient.

⁷ In fact, as depicted in Fig. 10a, rather than studying oblique incidence, we investigate normal incidence with the optical axis of the medium forming an angle θ with the direction perpendicular to the transverse surfaces of the slab. This approach significantly simplifies matching the fields.

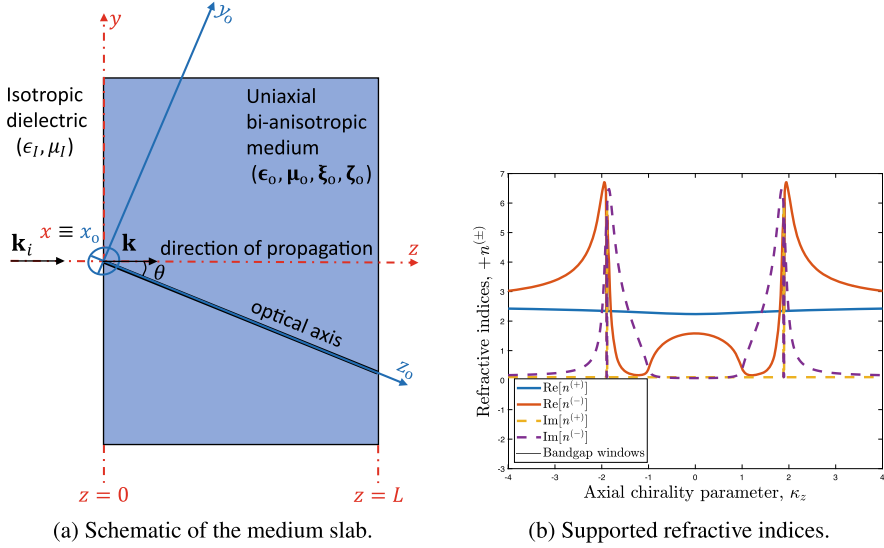


Fig. 10 Off-axis propagation in axially uniaxial bi-anisotropic mediums gives rise to a Bragg-like response in the chirality domain, with the angle formed between the direction of propagation and the optical axis exerting control over the resonances' features (Reprinted with permission from Ref. [5] © Optical Society of America)

$\mu = \mu \mathbb{I}$, the refractive indices of an axially bi-anisotropic uniaxial medium are [35]

$$\pm n^{(\pm)} = \pm \left[\frac{\epsilon \mu (\epsilon_z \mu - |\xi_z|^2)}{\bar{\epsilon} \mu - |\xi_z|^2 \cos^2 \theta \mp \sin^2 \theta (\Delta \bar{\epsilon}^2 \mu^2 + \epsilon \mu |\xi_z|^2)^{1/2}} \right]^{1/2}. \quad (30)$$

In this instance, although the equivalent linear birefringence is $\Delta \bar{\epsilon} = (\epsilon - \epsilon_z)/2$, and thus, it is independent of the inclination angle, the average permittivity

$$\bar{\epsilon} = \frac{\epsilon_z (1 + \cos^2 \theta) + \epsilon \sin^2 \theta}{2},$$

depends on the angle $\theta \in [0, \pi/2]$. The refractive indices of Eq. (30) are plotted as functions of the axial chirality parameter in Fig. 10b.

Detailed algebraic manipulations demonstrate that the center of the resonance, i.e., the value of the chirality parameter for which the purely imaginary refractive indices of Eq. (30) acquire their largest imaginary part is

$$\kappa(\theta, \chi) = \pm \frac{1}{2} \left[\left(\epsilon_z \mu - \chi_z^2 \right)^{1/2} + \left(\frac{\epsilon_s \mu}{\cos^4 \theta} - \chi_z^2 \right)^{1/2} \right]. \quad (31)$$

Hence, by allowing the wave to propagate off-axis and by introducing the Tellegen coefficients, we have achieved not just one but two means of controlling the center of the Bragg-like resonances. Thus, for a specific set of angles, the modified version of our uniform Bragg reflector proves advantageous over the one corresponding to axial propagation. This advantage primarily stems from the ability of θ and χ to significantly alleviate the requirement for giant chirality. However, to avoid boring the readers to death, we set aside analytic arguments, and we urge believers to trust our assertions while inviting non-believers to refer to Fig. 3 of Ref. [5].

The late Weiglhofer, a true expert of wave propagation in uniaxial bi-anisotropic mediums, investigated various singularities, focusing on axially bi-anisotropic mediums in Ref. [6] and transversely bi-anisotropic mediums in Ref. [7]. In these works, he demonstrated that, under specific conditions, certain modes can be suppressed, leading to a transition into negative refractive states due to chirality [11]. As depicted in Fig. 10b, at the upper (respectively, lower) edge of the stopband corresponding to positive (respectively, negative) axial chirality, the refractive indices diverge. In the absence of absorption, the refractive indices become infinite (N.B.— Fig. 10b includes absorption). For the particular value of the inclination angle where such a singularity occurs, $\theta_c \in (0, \pi/2)$, solving the eigenmode problem directly from Maxwell's equations, we find that the Cartesian components of the eigenmodes are:

$$\begin{aligned} \mathbf{E} &= E_0 \begin{pmatrix} 1 & 0 & n_c (\zeta - \xi) \tilde{\tilde{\epsilon}}^{-1} \end{pmatrix}^T, \\ \mathbf{h} &= E_0 \mu^{-1} \begin{pmatrix} -\zeta & n_c & n_c (\xi \zeta - \zeta^2) \tilde{\tilde{\epsilon}}^{-1} \end{pmatrix}^T. \end{aligned}$$

At these singular points, the polarization shifts to linear, while the E_x and E_z components are in quadrature. Since the resonant condition does not implicitly specify any particular wavelength, it theoretically applies to a very broad wavelength range. Additionally, these indices can be controlled by adjusting the inclination angle θ , or, as we show in Ref. [36], via the gyrotropic parameter.

5 Replacing the z's with the t's: Parametric Amplification

It is about time that we abandon the static mediums and move on to their dynamic counterparts. Of course, time-varying mediums are a *very* old business. From Morgenthaler's pioneering work [37] to the most recent and exciting demonstration of the dual to Young's "double-slit" experiment by Sapienza's group [38], the key point remains the same: When a propagating electromagnetic wave encounters an abrupt change in the medium's electromagnetic properties at a specific moment, the conservation of translational symmetry implied by Noether's theorem dictates that momentum is conserved; conversely, energy is not.

As one would suspect, upon replacing the z 's with the t 's, i.e., modulating in time rather than in space, some complications arise: the generation of negative frequencies. If, for the time being, we accept such a nomenclature, for an instantaneously responding medium,⁸ the usual constitutive relations become

$$\mathbf{d} = \epsilon(t)\mathbf{E} \quad \text{and} \quad \mathbf{b} = \mu\mathbf{h}, \quad (32)$$

where the relative permittivity is a periodic function of time with a period T_p .

Considering that momentum is conserved, it is suitable to express the displacement field as a product of its spatial, d_s , and temporal, d_t , part, i.e., $d(z, t; k) = d_s(z; k) d_t(t; k)$. Under such a decomposition, combining Maxwell's curl relations into a wave equation in terms of the total displacement field allows for separation of the variables. Thus, for the spatial part of the field, we obtain the usual Helmholtz wave equation, while for the temporal part of the field, we get

$$\frac{d^2 d_t(t)}{dt^2} + \theta(t) d_t(t) = 0, \quad (33)$$

which is a Hill equation with $\theta(t) = k^2 c^2 / \epsilon(t) \mu$.

In accordance with the coupled-wave theory adaptation for time-varying mediums outlined in Ref. [41], a suitable ansatz for Eq. (33) is

$$d_t(t) = d_t^+(t) e^{i\omega_0 t} + d_t^-(t) e^{-i\omega_0 t}, \quad (34)$$

where ω_0 represents the unperturbed angular frequency, and we have dropped the e^{ikz} term. But what does negative time signify in Eq. (34)? Should we pause here, as we peruse this page, and endeavor to measure the signal of an experiment scheduled for the future? As intriguing as it may seem, negative time, or equivalently, negative frequency, which can be interpreted as phase conjugation [42], is merely a mathematical trick. Indeed, this becomes evident when one observes that the real part of a conventionally backward propagating wave, $E e^{-i(kz+\omega t)}$, is identical to the real part of its complex conjugate, $E^* e^{i(kz+\omega t)}$, that has negative angular frequency.

The modulation profile of the permittivity is chosen as

$$\epsilon(t) = \bar{\epsilon} + \delta\epsilon \cos(\Omega t), \quad (35)$$

where $\Omega = 2\pi/T_p$ is the modulation frequency. Then, by taking the Fourier expansion of the coefficient of Eq. (33), we retain only terms related to the first harmonic and write

⁸ Time-varying mediums that exhibit (almost) instantaneous responses have been experimentally observed in the vicinity of the epsilon-near-zero regime (see, e.g., [39, 40]).

$$\theta(t) \approx \bar{\theta} + \delta\theta \frac{e^{i\Omega t} + e^{-i\Omega t}}{2}. \quad (36)$$

In Eq. (36), the dc-term and the ac-term are given by

$$\bar{\theta} = \frac{c_0^2}{T_p} \int_0^{T_p} \frac{d\tau}{\epsilon(\tau)} \quad \text{and} \quad \delta\theta = -c_0^2 \frac{\delta\epsilon}{\bar{\epsilon}^2},$$

respectively. If we substitute Eqs. (34) and (36) into Eq. (33), phase-matching synchronous terms yields a system similar to that of Eq. (1) albeit with the detuning parameter and the coupling coefficient being, respectively,

$$\delta\omega = \omega_0 - \frac{\Omega}{2} \quad \text{and} \quad \kappa = -\frac{\omega_0}{4} \frac{\delta\epsilon}{\bar{\epsilon}^2}.$$

With all the ingredients at hand, we are well-prepared to examine the temporal analog of Bragg gratings. Turning once again to the dispersion relation of Eq. (12), in this instance, there is a “1-1” projection to the spatial case, namely [8]

$$\omega = \frac{\Omega}{2} + \text{sign}(\delta\omega) \left[\left(\sqrt{\bar{\theta}}k - \frac{\Omega}{2} \right)^2 - \left(\frac{k\delta\theta}{4c_0^2\sqrt{\bar{\theta}}} \right)^2 \right]^{1/2}. \quad (37)$$

The Brillouin diagram illustrating such a dispersion relation is shown in Fig. 11a, where the formation of a momentum gap at $\omega \approx \Omega/2$ is observed. Given the resemblance of Fig. 11a to the dispersion of a static uniform Bragg grating, as seen, e.g., in Fig. 4a, one might hastily conclude that the temporal counterparts of spatially modulated dielectrics also exhibit stopbands where waves are attenuated. Nevertheless, within the gap formed in dynamic mediums, we observe amplification! This claim can be readily supported if one pays due diligence to the harmonic conventions. Indeed, akin to the spatial modulation scheme, within the bandgap, ω acquires an imaginary component. However, in this scenario, setting $\omega = \omega' - i\omega''$ in the wave propagating “backward” in time, $\mathbf{E}e^{-i(kz+\omega t)}$, leads to amplification instead of evanescence.

The next step in unraveling the mystic nature of temporal gratings would be to investigate their optical response. Before doing so, we need to explicitly define the equivalent of a medium slab, essentially giving the term “temporal slab” some meaning. According to Ramaccia et al. in Ref. [43], a temporal slab refers to a specific period of time during which a particular set of constitutive parameters, such as the relative permittivity of a dielectric medium, undergoes modulation (or abrupt variation) before returning to its original state. So far so good... but what about the boundary conditions? Well, in the considered case is perhaps more appropriate to talk about initial conditions, but nonetheless, the latter should include some kind of field matching. As comprehensively elaborated in Ref. [44], field-matching at

temporal boundaries necessitates $\mathbf{d}_t^\pm(0^-, t^-) = \mathbf{d}_t^\pm(0, t)$ ⁹—and that makes all the difference in the world.

Indeed, returning to Eq.(8) of Sect.2, which gives the fundamental matrix that solves the archetypal coupled-wave system of Eq.(1), we now apply the aforementioned initial condition and, therefore, define the forward and backward intensity reflectances

$$R = |Q^*|^2 \quad \text{and} \quad T = |P|^2; \quad (38)$$

nothing in the Möbius method is altered—this is just the final step.

The optical response of the temporal medium under discussion is depicted in Fig. 11b, where the time interval has been selected to ensure ample duration for the amplification process. It's worth noting that choosing a time duration less than twice the period would be insufficient for the waves to extract the required energy from the modulating beam for amplification. This observation is in line with the principles of mechanical oscillation theory, which stipulate that for amplification to occur, the modulation frequency must be double that of the driving force. The behavior of the photonic bandgap resembles typical Bragg gratings, with the primary difference being that elongating the duration does not sharpen the resonance. This occurs because there is no platform where successive reflections from an alternating refractive index can consistently add up coherently in phase. Additionally, Fig. 11b illustrates the energy pseudo-conservation relation $T - R = 1$, which holds true

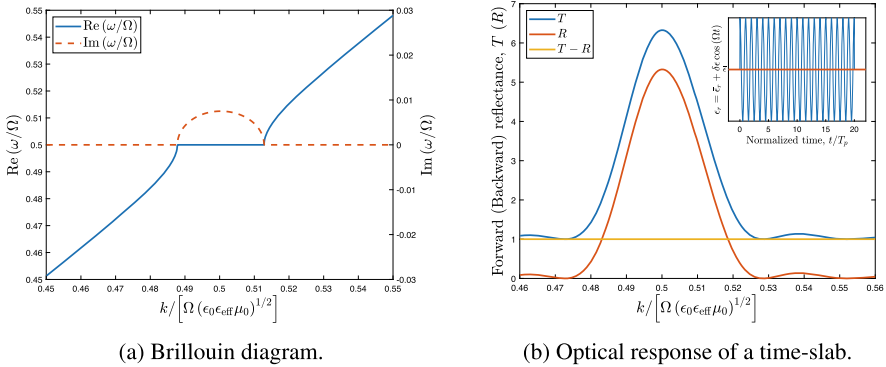


Fig. 11 In the temporal analog of Bragg gratings, the Brillouin diagrams indicate that there are momentum gaps where parametric amplification occurs. There, waves with angular frequencies equal to half the modulation frequency of the slab are amplified (Reprinted with permission from Ref. [8] © Optical Society of America)

⁹ When $\delta\epsilon \ll 1$, the temporal slab approximately attains impedance matching with the pre- and post-modulation “surrounding” medium.

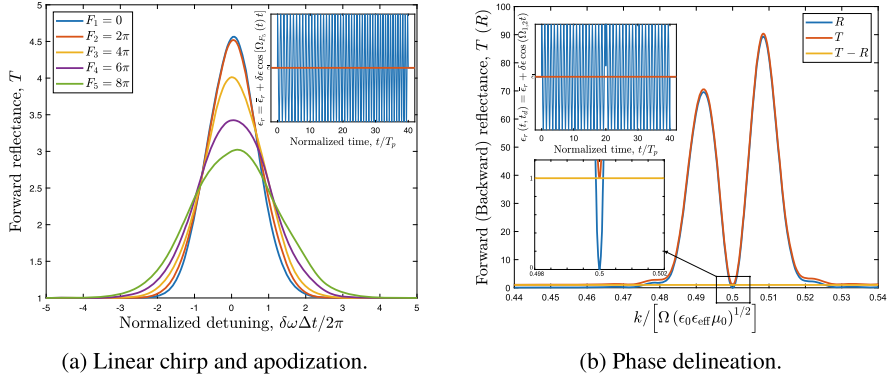


Fig. 12 Exotic time-periodic Bragg grating with even more exotic modulation profiles (Reprinted with permission from Ref. [8] © Optical Society of America)

regardless of the modulation profile. This relation simply follows from the condition stated in Eq. (4).

As emphasized in Sect. 2, we can explore scenarios where linear detuning coexists with apodization without presuming spatial or temporal constancy of the coupling coefficient. In that case, if $\Omega(t) \approx 2\omega_0 + (2F/\Delta t^2)t$ and $\kappa(t) = \kappa e^{[-(4/\Delta t)^2(t-\Delta t/2)^2]}$, the optical spectrum is depicted in Fig. 12a. It appears that the gradual decrease in the coupling of modes toward the beginning and end of the modulation diminishes its amplification capability, and compensation might be necessary.

We conclude this section by discussing the temporal analog of the cascaded grating of equal lengths and slightly dissimilar pitches depicted in Fig. 5b. For the sake of variety, here, instead of “slightly dissimilar pitches,” we will use a phase delineation of $\pi/2$ exactly halfway through the temporal modulation—nothing really changes as these two schemes are mathematically equivalent [20]. As seen in Fig. 12b, a spectral hole also occurs here, around which the phase discontinuity leads to destructive interference. Such a spectral hole finds multiple applications in sensing and might prove beneficial for assessing the precision of the modulation of, say, the permittivity.

6 Optical Rotation While the Signal Gets Amplified

As indicated in the introduction, the two primary origins of chirality are magneto-electric coupling and the helical stacking of birefringent layers. The temporal analog of the former, manifesting as temporal optical activity, appears to have first been discussed in Ref. [9]. Regarding the temporal version of the latter, although not implicitly viewed in this way, it constitutes the so-called Archimedes’ screw for light introduced by Galiffi et al. in Ref. [45]. In this final section, we build upon the

parametric amplifier of Sect. 5 and explore how a time-periodic chirality influences the dispersion features and optical response of the temporal Bragg grating [10].

Once again, the starting point is Tellegen's constitutive relations, as given in Eq. (13) and used for the same purpose in Ref. [9]. However, there is a problematic point: since chirality is inherently dispersive, how could we utilize the Tellegen model for a time-varying medium, which almost directly implies that new frequencies are generated? Within the context of coupled-wave theory, the generation of new frequencies is not an essential concern. But precisely because such a theory can be easily generalized to include higher-order resonances, as demonstrated in Ref. [41], we ought to be exhaustive in our arguments. From all the various propositions in recent and older literature, the most convincing appears to be that of Mostafa et al. in Ref. [46]. In particular, they use the Condon model¹⁰ so that chirality could be regarded as non-dispersive [46] when working at wavelengths much longer than those for which the meta-atoms are resonant.

Hence, we may now write the constitutive connections as

$$\mathbf{d} = \epsilon \mathbf{E} - g c_0 \frac{\partial \mathbf{h}}{\partial t} \quad \text{and} \quad \mathbf{b} = \mu \mathbf{h} + g c_0 \frac{\partial \mathbf{E}}{\partial t}, \quad (39)$$

whereby if ω is an arbitrary frequency, then $g_r = \omega c_0 g$ is dimensionless. Note that although we have kept the notation appearing more frequently in the literature, we underline that g_r corresponds to the dimensionless chirality of previous sections and should not be confused with the gyrotropic parameter of Faraday mediums. Furthermore, for an instantaneously responding medium, the temporal modulation profile of the permittivity, permeability, and chirality is elected to be precisely the one appearing in Eq. (35). Thus, $\bar{\epsilon}$, $\bar{\mu}$, and \bar{g} are the dc-terms of the permittivity, permeability, and chirality, respectively, with $\delta\epsilon$, $\delta\mu$, and δg being the corresponding ac-terms. Again, Ω is the frequency of modulation, common for all three constitutive parameters, and the modulation strengths are presumed to be sufficiently weak.

As if things were not complicated enough, we now have to bear the burden of magneto-electric coupling, which is, moreover, time-dependent. Fortunately, by contrast to the spatial version of our problem (seen, e.g., in Ref. [21]) our medium is, crucially, homogeneous¹¹ Therefore, by employing the so-called wavefields decomposition (see Lindell's et al. [35]), viz.,

$$\mathbf{E}_{(\pm)} = \frac{1}{2} (\mathbf{E} \pm i\eta \mathbf{h}) \quad \text{and} \quad \mathbf{h}_{(\pm)} = \frac{1}{2} [\mathbf{h} \mp (i/\eta) \mathbf{E}], \quad (40)$$

we reduce the bi-isotropic medium to an equivalent isotropic

¹⁰ It should be noted that, as per Silverman's arguments in Ref. [47], the Condon model is indeed an excellent candidate, out of many, as it happens to be invariant under duality transformations.

¹¹ In the global time modulation we are currently working, the medium's electromagnetic parameters change in time for *all* points in space; of course, by all points we refer to those transversed by the wave, which may well be anharmonic.

$$\begin{pmatrix} \mathbf{d}_{(\pm)} \\ \mathbf{b}_{(\pm)} \end{pmatrix} = \begin{pmatrix} \epsilon_{(\pm)}(1, 2) \\ (2, 1)\mu_{(\pm)} \end{pmatrix} \begin{pmatrix} \mathbf{E}_{(\pm)} \\ \mathbf{h}_{(\pm)} \end{pmatrix}, \text{ where } \frac{\epsilon_{(\pm)}}{\epsilon} = \frac{\mu_{(\pm)}}{\mu} = 1 \pm \frac{g_r}{(\epsilon\mu)^{1/2}}. \quad (41)$$

Using exactly the same decomposition of the displacement field into the product of its spatial and temporal parts as in Sect. 5, upon substituting into the wave equation

$$c_0^2 \nabla^2 \mathbf{d}_{(\pm)} = \epsilon_{(\pm)} \frac{\partial \mu_{(\pm)}}{\partial t} \frac{\partial \mathbf{d}_{(\pm)}}{\partial t} + \epsilon_{(\pm)} \mu_{(\pm)} \frac{\partial^2 \mathbf{d}_{(\pm)}}{\partial t^2}. \quad (42)$$

we obtain a second-order differential equation with varying coefficients. Although we could have stopped the preliminary calculations here and regarded this equation as our starting point for the analysis to follow, certain initial conditions satisfied by the coefficients allow for a further reduction. Indeed, if $[\theta_1]_{(\pm)}$ is the coefficient associated with the first time derivative, by defining the auxiliary variable

$$y_{(\pm)}^t = \exp\left(\frac{1}{2} \int_{t_0}^t [\theta_1]_{(\pm)} dt'\right) d_{(\pm)}^t, \quad (43)$$

we are led, once more, to the Hill equation of Eq. (33); of course, this time, the coefficient is slightly more complicated. Nevertheless, it can also be approximated by its first-order Fourier expansion, but this step is omitted for brevity.

Taking the ansatz of Eq. (17) as the basis, we may define $\omega_{0,(\pm)} = \omega_0(1 \mp \bar{g}/\bar{n})$ and substitute

$$\mathbf{y}_{(\pm)}^t = \left[y_{(\pm)}^t \right]^+ e^{-i\omega_{0,(\pm)}t} + \left[y_{(\pm)}^t \right]^- e^{i\omega_{0,(\pm)}t}, \quad (44)$$

into the Hill equation. Under the same underlying ideas and approximations of Sect. 2, algebraic manipulation leads to the coupled-wave system of Eq. (1). In this instance, the coupling coefficients are $\chi_{(\pm)} = -[\delta\theta]_{(\pm)}/4\omega_{0,(\pm)}$, whereas the detuning parameters are $\delta\omega_{0,(\pm)} = \omega_0(1 \mp \bar{g}/\bar{n}) - \Omega/2$; N.B.—the subscript sign notation denotes handedness: “+” for RCP and “−” for LCP.

Therefore, we can now derive a closed-form expression for the supported eigenfrequencies, as shown in Eq. (37), namely

$$\omega_{(\pm)} = \frac{\Omega}{2} + \text{sign}(\delta\tilde{\omega}_{(\pm)}) \left\{ \left[\omega_0 \left(1 \mp \frac{\bar{g}_r}{\bar{n}_r} \right) + \bar{\omega}_{(\pm)} - \frac{\Omega}{2} \right]^2 - \chi_{(\pm)}^2 \right\}^{1/2}. \quad (45)$$

Be that as it may, in this instance, we have two different dispersion curves corresponding to orthogonal polarizations. Both branches are plotted in Fig. 13a, where it is evident that in the presence of chirality, two momentum gaps are formed, each associated with an orthogonal polarization state, with their resonances centered at

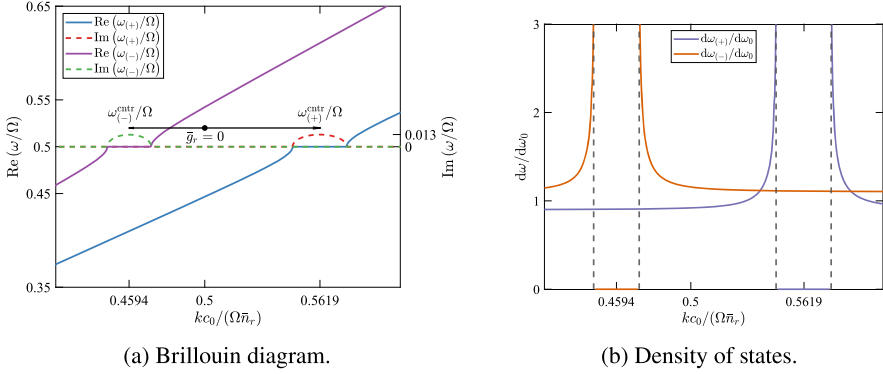


Fig. 13 In the absence of magneto-electric coupling, non-constant impedance due to, say, the temporal modulation of the permittivity leads to the formation of a momentum gap. When chirality is introduced, two parametric amplification regimes emerge, each corresponding to orthogonal polarization states. At the edges of the momentum gaps, where the group velocity diverges, standing waves are formed (Reprinted with permission from Ref. [10] © Optical Society of America)

$$\omega_{(+)}^{\text{cntr}} = \frac{\Omega}{2} \left(1 \mp \frac{\bar{g}_r}{\bar{n}} \right)^{-1}. \quad (46)$$

The result of Eq. (46) is novel, but it should not come as a surprise—we have already seen in Sect. 3 what chirality can do to a resonance! In fact, Eq. (46) demonstrates that it is actually the dc-term of the chirality that induces a shift toward higher or lower frequencies. Of course, such a dependency does not manifest as a linear one, but this is due to the domain in which we examine the resonances. The influence of the ac-term of the chirality has a far more pronounced impact on the bandwidths and the peaks of the resonances, but these details are quite technical and are better suited to be discussed elsewhere.

Furthermore, Fig. 13b illustrates the corresponding density of states, found by differentiating Eq. (45) with respect to the unperturbed frequency, which evidently diverges at the two edges of each momentum gap. Although such a divergence is of utmost importance in distributed feedback lasers, we emphasize that in time-varying mediums, the density of states corresponds to the group velocity and not its inverse as in the spatial case. At any rate, at the diverging points where standing waves are formed, although the group velocity approaches infinity, the signal velocity is always lower than the phase velocity of light in a vacuum.

Once again delving into the optical response of a temporal slab of the medium under consideration, we observe in Fig. 14a that the scattering coefficients, computed using the findings of Sect. 2, confirm the predictions presented in Fig. 14a. Additionally, the “pseudo-conservation” relation discussed in Sect. 5 remains valid, as it is a direct consequence of the underlying $SU(1, 1)$ symmetry described in Sect. 2 [c.f. the condition in Eq. (4)]. For a low degree of magneto-electric coupling, where the two bandgaps may merge, the temporal modulation of permittivity still induces parametric amplifications. In such a case, the levels of the scattering

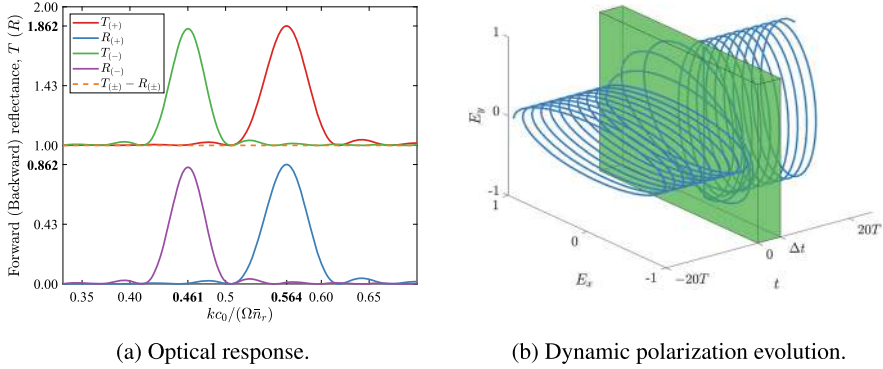


Fig. 14 Optical response of a temporal slab of a time-periodic bi-isotropic medium. For waves of a particular handedness whose angular frequency falls within one of the momentum gaps shown in Fig. 13a, their plane of polarization is rotated upon transmission. The angle of rotation depends on the duration of the temporal modulation (Reprinted with permission from Ref. [10] © Optical Society of America)

coefficients, as depicted in Fig. 14a, resemble those shown in Fig. 11a (assuming equal time durations). However, the influence of weak chirality is more prominent in the rotation of the plane of polarization of a wave residing within the momentum gap. This dynamic evolution is illustrated in Fig. 14b, where the simultaneous rotation of the electric field during wave amplification is evident.

7 Concluding Remarks

In this chapter, we delve into innovative Bragg-like resonances in both static and dynamic mediums, providing fresh insights into the realm of Bragg gratings beyond traditional understandings. Employing scalar coupled-wave theory and conformal mappings, we elucidate the optical responses of intricate structures and their connections to coupled-oscillator theory. Exploring phenomena such as the circular Bragg effect in chiral mediums, we uncover shifts and additional resonances induced by giant chirality. The notion of Bragg-less Bragg gratings challenges conventional ideas by demonstrating resonance without refractive index modulation, showcasing a polarization-selective response without any wavelength-matching requirement. Transitioning to temporal modulation, we discuss momentum gaps formed in time-modulated Bragg gratings, emphasizing parametric amplification and its relationship to energy conservation. Furthermore, we discuss the temporal analog of optical activity, revealing the mechanism by which chirality influences resonances and amplification factors. While purely theoretical, we are confident that our findings not only expand our comprehension of Bragg resonances but also hold relevance across a wide spectrum of the optics community, hopefully engaging both experimentalists and theorists alike.

Acknowledgments Stefanos Fr. Koufidis is financially supported by the Bodossaki Foundation. The development of the concepts presented in Secs. 3 and 4 has benefited from discussions with Prof. Matthew R. Foreman of Nanyang Technological University, Singapore and Dr. Kenny Weir of Imperial College London. The work on time-varying mediums was carried out in collaboration with Dr. Theodoros T. Koutserimpas and Prof. Francesco Monticone of Cornell University Ithaca, New York. Mistakes are ours.

References

1. S.F. Koufidis, M.W. McCall, Möbius transformation and coupled-wave theory: Complete identification of the transfer matrix. *Phys. Rev. A* **106**, 062213 (2022)
2. J.A. Sherwin, A. Lakhtakia, Nominal model for the optical response of a chiral sculptured thin film infiltrated with an isotropic chiral fluid. *Opt. Commun.* **214**, 231–245 (2002)
3. M.W. McCall, S.F. Koufidis, Reverse circular Bragg phenomenon. *Phys. Rev. Res.* **4**, 043154 (2022)
4. M.W. McCall, S.F. Koufidis, Broadband Bragg phenomenon in a uniform birefringent medium. *Opt. Lett.* **48**, 1096–1099 (2023)
5. S.F. Koufidis, M.W. McCall, Wavelength-independent Bragg-like reflection in uniaxial bianisotropic media. *J. Opt. Soc. Am. B* **40**, 2829–2841 (2023)
6. W.S. Weiglhofer, On anomalous propagation in axially uniaxial bianisotropic mediums. *Int. J. Infrared Millim. Waves* **20**, 1277 (1999)
7. W.S. Weiglhofer, On anomalous propagation in transversely uniaxial bianisotropic mediums. *Int. J. Infrared Millim. Waves* **21**, 895 (2000)
8. S.F. Koufidis, T.T. Koutserimpas, M.W. McCall, Temporal analog of Bragg gratings. *Opt. Lett.* **48**, 4500–4503 (2023)
9. S. Yin, Y.-T. Wang, A. Alù, Temporal optical activity and chiral time-interfaces. *Opt. Express* **30**, 47933–47941 (2022)
10. S.F. Koufidis, T.T. Koutserimpas, F. Monticone, M.W. McCall, Electromagnetic wave propagation in time-periodic chiral media. *Opt. Mater. Express* **14**, 3006–3029 (2024)
11. J.B. Pendry, A chiral route to negative refraction. *Science* **306**, 1353 (2004)
12. A. Yariv, Coupled-mode theory for guided-wave optics. *IEEE J. Quantum Electron.* **9**, 919–933 (1973)
13. R. Zengerle, O. Leminger, Phase-shifted Bragg-grating filters with improved transmission characteristics. *J. Light. Technol.* **13**, 2354–2358 (1995)
14. N. Byrnes, M.R. Foreman, Symmetry constraints for vector scattering and transfer matrices containing evanescent components: Energy conservation, reciprocity, and time reversal. *Phys. Rev. Res.* **3**, 013129 (2021)
15. J.W. Brown, R.V. Churchill, *Complex Variables and Applications*, 9th edn. (McGraw-Hill Education, New York, 2014)
16. C. Gong, R. Tönjes, A. Pikovsky, Coupled Möbius maps as a tool to model Kuramoto phase synchronization. *Phys. Rev. E* **102**, 022206 (2020)
17. J.J. Monzón, A.G. Barriuso, L.L. Sánchez-Soto, J.M. Montesinos-Amilibia, Geometrical interpretation of optical absorption. *Phys. Rev. A* **84**, 023830 (2011)
18. M.W. McCall, On the application of coupled mode theory for modeling fiber Bragg gratings. *J. Light. Technol.* **18**, 236 (2000)
19. L.D. Barron, *Molecular Light Scattering and Optical Activity* (Cambridge University Press, Cambridge, 2009)
20. M.W. McCall, A. Lakhtakia, Development and assessment of coupled wave theory of axial propagation in thin-film helicoidal bianisotropic mediums. Part I: Reflectances and transmittances. *J. Mod. Opt.* **47**, 973 (2000)

21. D.L. Jaggard, N. Engheta, M.W. Kowarz, P. Pelet, J.C. Liu, Y. Kim, Periodic chiral structures. *IEEE Trans. Antennas Propag.* **37**, 1447 (1989)
22. A. Lakhtakia, Handedness reversal of circular Bragg phenomenon due to negative real permittivity and permeability. *Opt. Express* **11**, 716 (2003)
23. I. Hodgkinson, Q.H. Wu, B. Knight, A. Lakhtakia, K. Robbie, Vacuum deposition of chiral sculptured thin films with high optical activity. *Appl. Opt.* **39**, 642 (2000)
24. A.Y. Zhu, W.T. Chen, A. Zaidi, Y.-W. Huang, M. Khorasaninejad, V. Sanjeev, C.-W. Qiu, F. Capasso, Giant intrinsic chiro-optical activity in planar dielectric nanostructures. *Light. Sci. Appl.* **7**, 17158 (2018)
25. I. Katsantonis, M. Manousidaki, A.D. Koulouklidis, C. Daskalaki, I. Spanos, C. Kerantzopoulos, A.C. Tasolamprou, C.M. Soukoulis, E.N. Economou, S. Tzortzakos, M. Farsari, M. Kafesaki, Strong and broadband pure optical activity in 3D printed THz chiral metamaterials. *Adv. Opt. Mater.* **11**, 2300238 (2023)
26. W.J. Choi, G. Cheng, Z. Huang, S. Zhang, T.B. Norris, N.A. Kotov, Terahertz circular dichroism spectroscopy of biomaterials enabled by kirigami polarization modulators. *Nat. Mater.* **18**, 820–826 (2019)
27. Q. Zhang, E. Plum, J.-Y. Ou, H. Pi, J. Li, K.F. MacDonald, N.I. Zheludev, Electrogyration in metamaterials: chirality and polarization rotatory power that depend on applied electric field. *Adv. Opt. Mater.* **9**, 2001826 (2021)
28. M. Liu, E. Plum, H. Li, S. Li, Q. Xu, X. Zhang, C. Zhang, C. Zou, B. Jin, J. Han, W. Zhang, Temperature-controlled optical activity and negative refractive index. *Adv. Funct. Mater.* **31**, 2010249 (2021)
29. M.W. McCall, A. Lakhtakia, Explicit expressions for spectral remittances of axially excited chiral sculptured thin films. *J. Mod. Opt.* **51**, 111 (2004)
30. A. Lakhtakia, W.S. Weiglhofer, Constraint on linear, homogeneous, constitutive relations. *Phys. Rev. E* **50**, 5017 (1994)
31. W.S. Weiglhofer, A. Lakhtakia, On the non-existence of linear non-reciprocal bi-isotropic NRBI mediums. *J. Phys. A Math. Theor.* **30**, 2597 (1997)
32. S. Tretyakov, Anything wrong with the naturally non-reciprocal materials? *IEEE Antennas Propag. Mag.* **38**, 84–85 (1996)
33. Y.N. Obukhov, F.W. Hehl, On the boundary-value problems and the validity of the Post constraint in modern electromagnetism. *Optik* **120**, 418 (2009)
34. S.A. Tretyakov, S.I. Maslovski, I.S. Nefedov, A.J. Viitanen, P.A. Belov, A. Sanmartin, Artificial Tellegen particle. *Electromagnetics* **23**, 665 (2003)
35. I.V. Lindell, A.H. Sihvola, S. Tretyakov, A.J. Viitanen, *Electromagnetic Waves in Chiral and Bi-Isotropic Mediums* (Artech House, Norwood, 1994)
36. S.F. Koufidis, M.W. McCall, Gyrotropy-controlled uniform Bragg reflector, in *Seventeenth International Congress on Artificial Materials for Novel Wave Phenomena (Metamaterials)* (IEEE Xplore, 2023), pp. X-171
37. F.R. Morgenthaler, Velocity modulation of electromagnetic waves. *IEEE Trans. Microw. Theory Tech.* **6**, 167–172 (1958)
38. R. Tirole, S. Vezzoli, E. Galiffi, I. Robertson, D. Maurice, B. Tilmann, S.A. Maier, J.B. Pendry, R. Sapienza, Double-slit time diffraction at optical frequencies. *Nat. Phys.* **19**, 999–1002 (2023)
39. S. Saha, O. Segal, C. Fruhling, E. Lustig, M. Segev, A. Boltasseva, V.M. Shalae, Photonic time crystals: a materials perspective [Invited]. *Opt. Express* **31**, 8267–8273 (2023)
40. E. Lustig, O. Segal, S. Saha, E. Bordo, S.N. Chowdhury, Y. Sharabi, A. Fleischer, A. Boltasseva, O. Cohen, V. Shalae, others, Time-refraction optics with single cycle modulation. *Nanophotonics* **12**, 236–242 (2023)
41. T.T. Koutserimpas, Parametric amplification interactions in time-periodic media: coupled waves theory. *J. Opt. Soc. Am. B* **39**, 481–489 (2022)
42. A.M. Shaltout, V.M. Shalae, M.L. Brongersma, Spatiotemporal light control with active metasurfaces. *Science* **364**, 3100 (2019)

43. S. Ramaccia, A. Toscano, F. Bilotti, Light propagation through metamaterial temporal slabs: reflection, refraction, and special cases. *Opt. Lett.* **45**, 5836–5839 (2020)
44. Y. Xiao, D.N. Maywar, G.P. Agrawal, Reflection and transmission of electromagnetic waves at a temporal boundary. *Opt. Lett.* **39**, 574–337 (2014)
45. E. Galiffi, P.A. Huidobro, J.B. Pendry, An Archimedes' screw for light. *Nat. Commun.* **13**, 2523 (2022)
46. M.H. Mostafa, M.S. Mirmoosa, S.A. Tretyakov, Spin-dependent phenomena at chiral temporal interfaces. *Nanophotonics* **12**, 2881 (2023)
47. M.P. Silverman, Reflection and refraction at the surface of a chiral medium: comparison of gyrotropic constitutive relations invariant or noninvariant under a duality transformation. *J. Opt. Soc. Am. A* **178**, 830–837 (1986)



Martin W. McCall is Professor of Theoretical Optics at Imperial College London. After briefly working at Bath University, where he focused on nonlinear dynamics in semiconductor lasers, he moved to Imperial College, where he has remained since. His research has ranged over all things optical and optoelectronic, usually involving gratings in some form or other, e.g. temporal gratings, optical back-planes, and periodically structurally chiral mediums. The thematic of “complex electromagnetic mediums” embraced work on negative refraction and transformation optics, that in 2011 led to his group extending the concept of object cloaking to the so-called “space-time cloaking,” demonstrating that time-modulated mediums could be configured into devices capable of hiding events in space time. More recently, McCall has worked on fundamental aspects of Maxwell’s equations, including questioning the role of traditional constitutive relations and solutions on manifolds with singularities. He is the author of an undergraduate text on classical mechanics and relativity.



Stefanos Fr. Koufidis read Electrical and Computer Engineering at the Aristotle University of Thessaloniki, graduating in 2019. After fulfilling his military service, he was awarded the Arnaoutis Foundation scholarship to pursue the M.Sc. in Optics and Photonics at Imperial College London, which he successfully completed in 2021. Subsequently, he joined Prof. McCall’s group at Imperial as a PhD student, proudly supported by the Bodossaki Foundation. His research interests span various aspects of grating physics, chirality (both structural and non-structural), time-varying mediums, and symmetries in the laws of electrodynamics. He is a member of the Institute of Physics.

Geometric Phase and Nanoscale Architected Morphology of Reusch Piles



Akhlesh Lakhtakia 

1 Introduction

1.1 Poincaré Spinor

Any uniform plane wave propagating in free space can be represented as a point on the surface of the Poincaré sphere $s_1^2 + s_2^2 + s_3^2 = s_0^2$ [1], where s_0 , s_1 , s_2 , and s_3 are the four Stokes parameters [2]. The plane wave's location is identified by the longitude $\alpha \in [0, 2\pi)$ and the latitude $\beta \in [-\pi/2, \pi/2]$ defined through the relations

$$\left. \begin{aligned} s_1 &= s_0 \cos \beta \cos \alpha \\ s_2 &= s_0 \cos \beta \sin \alpha \\ s_3 &= s_0 \sin \beta \end{aligned} \right\}, \quad (1)$$

as shown in Fig. 1. These two angles appear in the Poincaré spinor [3]

$$\left[\underline{\phi} \right] = \begin{bmatrix} \cos \left(\frac{\pi}{4} - \frac{\beta}{2} \right) \\ \sin \left(\frac{\pi}{4} - \frac{\beta}{2} \right) \exp(i\alpha) \end{bmatrix}, \quad (2)$$

where $i = \sqrt{-1}$.

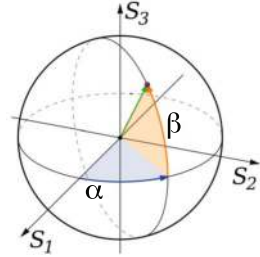
A. Lakhtakia (✉)

Department of Engineering Science and Mechanics, The Pennsylvania State University, University Park, PA, USA

School of Mathematics, University of Edinburgh, Edinburgh, UK

e-mail: akhlesh@psu.edu

Fig. 1 Longitude $\alpha \in [0, 2\pi)$ and latitude $\beta \in [-\pi/2, \pi/2]$ that identify a plane wave on the Poincaré sphere



1.2 Geometric Phase

With respect to a plane wave labeled “1,” the geometric phase of a plane wave labeled “2” is defined as the angle

$$\Phi_{21} = \text{Arg} \left\{ \left[\underline{\phi}_1 \right]^\dagger \cdot \left[\underline{\phi}_2 \right] \right\}, \quad (3)$$

where † denotes the conjugate transpose. The geometric phase is a measure of dissimilarity of two plane waves of the same frequency, even when propagating in the same direction, as was pointed out by Pancharatnam in 1956 [4]. The profound role of geometric phase in classical as well as quantum physics was recognized within the next three decades [5] and it continues to both fascinate researchers [6, 7] and find applications [8–11].

Optical experiments on plane-wave transmission through a columnar thin film [12, 13] and a chiral sculptured thin film [14] have revealed that the geometric phase of the transmitted plane wave depends on the morphology of the thin film [15]. Thin-film morphology can be architected using a variety of fabrication techniques including physical vapor deposition [14, 16], holographic lithography [17], direct laser writing [18], electron tomography [19], hydrothermal method [20], and self assembly [21, 22]. Each technique may produce thin films with similar plane-wave reflectance and transmittance characteristics, but the geometric phase of the reflected and/or transmitted plane wave could contain a signature of the fabrication technique.

1.3 Reusch Piles

An experimental test of the foregoing proposition requires resources currently unavailable to me. So, I chose to establish the rudiments of this proposition theoretically. Chiral sculptured thin films may be considered to be *finely chiral* Reusch piles [23]. Conceived in 1869 [24, 25], a Reusch pile is a periodic multilayer comprising layers of the same homogeneous, uniaxial dielectric material, such that the optic axis in each layer is rotated about the thickness direction (designated to

be parallel to the z axis of a Cartesian coordinate system) with respect to the optic axis in the previous layer by a fixed angle $\Delta\xi$. A delightful artistic interpretation of Reusch piles is available from the sculpture *Segue* created by Anne Huibregtse [26].

In biophysics literature, Reusch piles are eponymously called *Bouligand structures*, following the publication of a 1965 paper [27] wherein Reusch piles in arthropod cuticles were described by Bouligand [28]. A century earlier, Reusch had been inspired not by biological specimen but by artificial structures that today may be called *equichiral* Reusch piles, on which optical experiments had been conducted by Nörremberg, the immediate predecessor of Reusch as professor of physics at the University of Tübingen [24, 25]. The Šolc fan filters of optics [29–32] are also conceptually related to Reusch piles.

A Reusch pile preferentially reflects light of one circular-polarization state in multiple spectral regimes [33, 34], preserving the circular-polarization state of the incident plane wave [35]. These spectral regimes, called *circular Bragg regimes* [36], depend on both the number of layers in one period of the Reusch pile and the dependencies of the constitutive parameters on the frequency [23].

The following classification of Reusch piles was devised in 2004 [23]: Suppose that the period P of a Reusch pile is made up of $2q$, $q \geq 2$, identical layers stacked along the z axis. Then the angular offset of the optic axis of a specific layer with respect to the optic axis of the previous layer is given by

$$\Delta\xi = h \frac{\pi}{q}, \quad q \in \{2, 3, 4, \dots\}, \quad (4)$$

where $h = +1$ for structural right-handedness and $h = -1$ for structural left-handedness. With the assumption that the constitutive parameters are independent of frequency (which is an approximation of limited physical validity [37]), the Reusch pile shall display two families of circular Bragg regimes. Circular Bragg regimes in the *first* family are conjectured to exist with center wavelengths

$$\lambda_0^{1;p,q} = \frac{\lambda_0^{1;0,q}}{pq + 1}, \quad p \in \{0, 1, 2, 3, \dots\}, \quad q \in \{2, 3, 4, \dots\}, \quad (5)$$

whereas circular Bragg regimes in the *second* family are predicted with center wavelengths

$$\lambda_0^{2;p,q} = \frac{\lambda_0^{1;0,q}}{pq + q - 1}, \quad p \in \{0, 1, 2, 3, \dots\}, \quad q \in \{2, 3, 4, \dots\}, \quad (6)$$

where $\lambda_0^{1;0,q}$ depends on the constitutive parameters and period of the Reusch pile and normal incidence has been assumed. Equations (5) and (6) will require modification for frequency-dependent constitutive parameters [38, 39]. Furthermore, there may be circular Bragg regimes that are not captured by the conjectures (5) and (6).

When $h = 1$ and the Reusch pile has a sufficiently large number of periods, the reflectance of an incident right-circularly polarized (RCP) plane wave is very high but that of an incident left-circularly polarized (LCP) plane wave is very low in the first family of circular Bragg regimes, whereas the reflectance of an incident LCP plane wave is very high, but that of an incident RCP plane wave is very low in the second family. When $h = -1$ and the Reusch pile has a sufficiently large number of periods, the reflectance of an incident LCP plane wave is very high, but that of an incident RCP plane wave is very low in the first family, whereas the reflectance of an incident RCP plane wave is very high, but that of an incident LCP plane wave is very low in the second family of circular Bragg regimes. Insertion of central phase defects leads to Reusch piles functioning as spectral hole filters [40].

Since $\lambda_0^{1;p,2} = \lambda_0^{2;p,2} \forall p$, the Reusch pile is classified as *equichiral* for $q = 2$. If $q \geq 3$, the Reusch pile is classified as *ambichiral*. As $q \rightarrow \infty$, the Reusch pile is *finely chiral* with optical reflectance and transmittance characteristics similar to those of chiral liquid crystals [41–44] and chiral sculptured thin films [14, 45, 46]. A microwave analog of a finely chiral Reusch pile was constructed and characterized 50 years ago [47]. Equichiral Reusch piles exhibit the Bragg phenomenon without differentiating between LCP and RCP plane waves [23, 48], as has been experimentally verified recently [49].

Given that $\lambda_0^{1;p+1,q} < \lambda_0^{1;p,q}$ and $\lambda_0^{2;p+1,q} < \lambda_0^{2;p,q}$, it would be arduous to experimentally verify the multiplicity of circular Bragg regimes with a single Reusch pile if $\lambda_0^{1;0,q}$ lies in the visible regime. Still, the exhibition of two adjacent circular Bragg regimes, the ones for $p = 0$ from both families with q fixed, has been experimentally confirmed with some deviation from Eq. (6) due to frequency dependence of the constitutive parameters [23, 50].

1.4 Architected Morphology

With fixed P but increasing q , Reusch piles offer an evolutionary perspective on the roles that architected morphology can play in diverse optical phenomena. Such studies have been undertaken for transmission-mode optical activity [35, 51, 52], circular Bragg phenomenon [50, 53, 54], and surface-wave propagation [55]. In this chapter, I deploy Reusch piles to study the evolution of the geometric phases of the reflected and transmitted plane waves when a Reusch pile is illuminated by a plane wave.

The 2004 classification [23] of Reusch piles excludes (i) columnar thin films [12–14] and (ii) chevronic sculptured thin films [56], because these materials with architected morphology do not exhibit the circular Bragg phenomenon. But their inclusion is necessary to understand the relationship, or lack thereof, between the geometric phase and morphology. Therefore, I augmented Eq. (4) to

$$\Delta\xi = h \frac{2\pi}{N_{\text{lyr}}}, \quad N_{\text{lyr}} \in \{1, 2, 3, 4, \dots\}. \quad (7)$$

Whereas $N_{\text{lyr}} = 1$ for columnar thin films and $N_{\text{lyr}} = 2$ for chevronic thin films, $N_{\text{lyr}} = 4$ for equichiral Reusch piles and $N_{\text{lyr}} \in \{6, 8, 10, \dots\}$ for ambichiral Reusch piles in the 2004 classification [23]. In addition, $N_{\text{lyr}} \in \{3, 5, 7, \dots\}$, which were not explicitly included in the 2004 classification, are also possible while maintaining a full turn of 2π of the optic axes within the thickness P .

The conjectures (5) and (6) still apply with q replaced by $N_{\text{lyr}}/2$, $N_{\text{lyr}} \in \{2, 3, 4, \dots\}$. The case of $N_{\text{lyr}} = 1$ has to be excluded, because a columnar thin film lacks periodicity. Equation (5) indicates that

$$\frac{\lambda_0^{1;p,N_{\text{lyr}}/2}}{\lambda_0^{1;0,N_{\text{lyr}}/2}} \in \begin{cases} \left\{1, \frac{1}{2}, \frac{1}{3}, \frac{1}{4}, \dots\right\}, \\ \left\{1, \frac{2}{5}, \frac{2}{8}, \frac{2}{11}, \dots\right\}, \\ \left\{1, \frac{1}{3}, \frac{1}{5}, \frac{1}{7}, \dots\right\}, \\ \left\{1, \frac{2}{7}, \frac{2}{12}, \frac{2}{17}, \dots\right\}, \\ \left\{1, \frac{1}{4}, \frac{1}{7}, \frac{1}{10}, \dots\right\}, \end{cases} \quad N_{\text{lyr}} = \begin{cases} 2 \\ 3 \\ 4 \\ 5 \\ 6 \end{cases}, \quad (8)$$

and

$$\frac{\lambda_0^{2;p,N_{\text{lyr}}/2}}{\lambda_0^{1;0,N_{\text{lyr}}/2}} \in \begin{cases} \left\{\infty, 1, \frac{1}{2}, \frac{1}{3}, \dots\right\}, \\ \left\{2, \frac{2}{4}, \frac{2}{7}, \frac{2}{10}, \dots\right\}, \\ \left\{1, \frac{1}{3}, \frac{1}{5}, \frac{1}{7}, \dots\right\}, \\ \left\{\frac{2}{3}, \frac{2}{8}, \frac{2}{13}, \frac{2}{18}, \dots\right\}, \\ \left\{\frac{1}{2}, \frac{1}{5}, \frac{1}{8}, \frac{1}{11}, \dots\right\}, \end{cases} \quad N_{\text{lyr}} = \begin{cases} 2 \\ 3 \\ 4 \\ 5 \\ 6 \end{cases}. \quad (9)$$

Thus, the largest finite value of $\lambda_0^{\ell;p,N_{\text{lyr}}/2}$, $\ell \in \{1, 2\}$, is $\lambda_0^{1;0,N_{\text{lyr}}/2}$ with one exception: $\lambda_0^{2;0,3/2} = 2\lambda_0^{1;0,3/2}$. Note that $\lambda_0^{1;p,1} = \lambda_0^{2;p+1,1}$ for chevronic thin films and $\lambda_0^{1;p,2} = \lambda_0^{2;p,2}$ for equichiral Reusch piles, both instances of the two families of circular Bragg regimes not being distinct from each other in their center wavelengths. The sequences in conjectures (8) and (9) will change when the frequency dependence of the constitutive parameters cannot be ignored.

This chapter is organized as follows. Section 2 provides the theoretical framework to calculate the geometric phase of the reflected/transmitted plane wave in relation to the incident plane wave. Numerical results are presented and discussed in Sect. 3, and the chapter ends with key conclusions in Sect. 4. An $\exp(-i\omega t)$ dependence on time t is implicit, where ω as the angular frequency. With ε_0 and μ_0 , respectively, denoting the permittivity and permeability of free space, the free-

space wavenumber is denoted by $k_0 = \omega\sqrt{\varepsilon_0\mu_0}$ and $\lambda_0 = 2\pi/k_0$ is the free-space wavelength. The Cartesian coordinate system (x, y, z) is adopted. Vectors are in boldface, and unit vectors are additionally decorated by a caret on top. Dyadics are double underlined. Column vectors are underlined and enclosed in square brackets. Matrixes are double underlined and enclosed in square brackets.

2 Theory

2.1 Relative Permittivity Dyadic

The Reusch pile is taken to occupy the region $0 < z < NP$, where $N \in \{1, 2, 3, \dots\}$ is the number of periods, and the relative permittivity dyadic

$$\underline{\underline{\varepsilon}}_{\text{rel}}(z + P) = \underline{\underline{\varepsilon}}_{\text{rel}}(z), \quad 0 < z < (N - 1)P, \quad (10)$$

is therefore periodic.

The reference unit cell $0 < z < P$ is subdivided into N_{lyr} layers. The n -th layer, $n \in \{1, 2, \dots, N_{\text{lyr}}\}$, is delimited by the planes $z = z_{n-1}$ and $z = z_n$, where

$$z_m = m \frac{P}{N_{\text{lyr}}}, \quad m \in \{0, 1, 2, \dots, N_{\text{lyr}}\}. \quad (11)$$

The relative permittivity dyadic in the n -th layer of the reference unit cell is given by

$$\underline{\underline{\varepsilon}}_{\text{rel}}(z) = \underline{\underline{Z}}(h; n, N_{\text{lyr}}) \cdot \underline{\underline{Y}}(\chi) \cdot [\varepsilon_a \hat{\mathbf{z}}\hat{\mathbf{z}} + \varepsilon_b \hat{\mathbf{x}}\hat{\mathbf{x}} + \varepsilon_c \hat{\mathbf{y}}\hat{\mathbf{y}}] \cdot \underline{\underline{Y}}^{-1}(\chi) \cdot \underline{\underline{Z}}^{-1}(h; n, N_{\text{lyr}}), \quad z_{n-1} < z < z_n, \quad n \in \{1, 2, \dots, N_{\text{lyr}}\}. \quad (12)$$

The frequency-dependent relative permittivity scalars ε_a , ε_b , and ε_c capture the orthorhombicity [14] of each layer. The tilt dyadic

$$\underline{\underline{Y}}(\chi) = \hat{\mathbf{y}}\hat{\mathbf{y}} + (\hat{\mathbf{x}}\hat{\mathbf{x}} + \hat{\mathbf{z}}\hat{\mathbf{z}}) \cos \chi + (\hat{\mathbf{z}}\hat{\mathbf{x}} - \hat{\mathbf{x}}\hat{\mathbf{z}}) \sin \chi \quad (13)$$

contains $\chi \in [0, \pi/2]$ as an angle of inclination with respect to the xy plane. The structural handedness is captured by the rotation dyadic

$$\begin{aligned} \underline{\underline{Z}}(h; n, N_{\text{lyr}}) &= \hat{\mathbf{z}}\hat{\mathbf{z}} + (\hat{\mathbf{x}}\hat{\mathbf{x}} + \hat{\mathbf{y}}\hat{\mathbf{y}}) \cos \left[(n - 1)h \frac{2\pi}{N_{\text{lyr}}} \right] \\ &+ (\hat{\mathbf{y}}\hat{\mathbf{x}} - \hat{\mathbf{x}}\hat{\mathbf{y}}) \sin \left[(n - 1)h \frac{2\pi}{N_{\text{lyr}}} \right], \quad n \in \{1, 2, \dots, N_{\text{lyr}}\}. \end{aligned} \quad (14)$$

Examination of Eq. (12) reveals the absence of periodicity only for $N_{\text{lyr}} = 1$. However, the structural period is not always P for all values of χ . The structural period is P for $\chi \in (0, \pi/2)$, but $P/2$ for $\chi \in \{0, \pi/2\}$. This distinction has been partially noted earlier [57] for continuously chiral materials (i.e., in the limit $N_{\text{lyr}} \rightarrow \infty$).

Examination of Eq. (12) reveals also the absence of structural handedness for $N_{\text{lyr}} \in \{1, 2\}$. Additionally, structural handedness is absent for $N_{\text{lyr}} = 4$ provided that $\chi \in \{0, \pi/2\}$.

2.2 Boundary-Value Problem

The half-space $z < 0$ is the region of incidence and reflection, while the half-space $z > L$ is the region of transmission. A plane wave, propagating in the half-space $z \leq 0$ at an angle $\theta_{\text{inc}} \in [0, \pi/2)$ with respect to the z axis and at an angle $\psi \in [0, 2\pi)$ with respect to the x axis in the xy plane, is incident on the Reusch pile. The electric field phasor associated with the incident plane wave is represented as [14]

$$\mathbf{E}^{\text{inc}}(\mathbf{r}) = \left[\frac{(i\mathbf{s} - \mathbf{p}_+)}{\sqrt{2}} a_L - \frac{(i\mathbf{s} + \mathbf{p}_+)}{\sqrt{2}} a_R \right] \exp[i\kappa (x \cos \psi + y \sin \psi)] \times \exp(ik_0 z \cos \theta_{\text{inc}}) \quad (15a)$$

$$= (a_s \mathbf{s} + a_p \mathbf{p}_+) \exp[i\kappa (x \cos \psi + y \sin \psi)] \exp(ik_0 z \cos \theta_{\text{inc}}), \quad z < 0, \quad (15b)$$

where

$$\left. \begin{aligned} \kappa &= k_0 \sin \theta_{\text{inc}} \\ \mathbf{s} &= -\hat{\mathbf{x}} \sin \psi + \hat{\mathbf{y}} \cos \psi \\ \mathbf{p}_{\pm} &= \mp (\hat{\mathbf{x}} \cos \psi + \hat{\mathbf{y}} \sin \psi) \cos \theta_{\text{inc}} + \hat{\mathbf{z}} \sin \theta_{\text{inc}} \end{aligned} \right\}. \quad (16)$$

The amplitudes of the LCP and the RCP components of the incident plane wave, denoted by a_L and a_R , respectively, in Eq. (15a) are assumed to be known. Alternatively, a_s and a_p are the known amplitudes of the perpendicular- and parallel-polarized components, respectively, in Eq. (15b).

The electric field phasor of the reflected plane wave is expressed as

$$\mathbf{E}^{\text{ref}}(\mathbf{r}) = - \left[\frac{(i\mathbf{s} - \mathbf{p}_-)}{\sqrt{2}} r_L - \frac{(i\mathbf{s} + \mathbf{p}_-)}{\sqrt{2}} r_R \right] \exp[i\kappa (x \cos \psi + y \sin \psi)] \times \exp(-ik_0 z \cos \theta_{\text{inc}}) \quad (17a)$$

$$= (r_s \mathbf{s} + r_p \mathbf{p}_-) \exp[i\kappa (x \cos \psi + y \sin \psi)] \exp(-ik_0 z \cos \theta_{\text{inc}}), \quad z < 0, \quad (17b)$$

and the electric field phasor of the transmitted plane wave is represented as

$$\mathbf{E}^{\text{tr}}(\mathbf{r}) = \left[\frac{(i\mathbf{s} - \mathbf{p}_+)}{\sqrt{2}} t_{\text{L}} - \frac{(i\mathbf{s} + \mathbf{p}_+)}{\sqrt{2}} t_{\text{R}} \right] \exp[i\kappa(x \cos \psi + y \sin \psi)] \\ \times \exp[ik_0(z - NP) \cos \theta_{\text{inc}}], \quad (18a)$$

$$= (t_{\text{s}}\mathbf{s} + t_{\text{p}}\mathbf{p}_+) \exp[i\kappa(x \cos \psi + y \sin \psi)] \\ \times \exp[ik_0(z - NP) \cos \theta_{\text{inc}}], \quad z > NP. \quad (18b)$$

The reflection amplitudes r_{L} and r_{R} as well as the transmission amplitudes t_{L} and t_{R} (equivalently, r_{s} , r_{p} , t_{s} , and t_{p}) are unknown and require the solution of a boundary-value problem. The most straightforward technique requires the use of the 4×4 transfer-matrix method, whose details are available elsewhere [14, 58]. Thereafter, the total reflectance

$$R = \frac{|r_{\text{L}}|^2 + |r_{\text{R}}|^2}{|a_{\text{L}}|^2 + |a_{\text{R}}|^2} = \frac{|r_{\text{s}}|^2 + |r_{\text{p}}|^2}{|a_{\text{s}}|^2 + |a_{\text{p}}|^2} \quad (19a)$$

and the total transmittance

$$T = \frac{|t_{\text{L}}|^2 + |t_{\text{R}}|^2}{|a_{\text{L}}|^2 + |a_{\text{R}}|^2} = \frac{|t_{\text{s}}|^2 + |t_{\text{p}}|^2}{|a_{\text{s}}|^2 + |a_{\text{p}}|^2} \quad (19b)$$

can be calculated.

2.3 Poincaré Spinors

The Stokes parameters of the incident plane wave are given by [2]

$$\left. \begin{aligned} s_0^{\text{inc}} &= |a_{\text{L}}|^2 + |a_{\text{R}}|^2 = |a_{\text{s}}|^2 + |a_{\text{p}}|^2 \\ s_1^{\text{inc}} &= 2 \operatorname{Re}(a_{\text{L}} a_{\text{R}}^*) = |a_{\text{p}}|^2 - |a_{\text{s}}|^2 \\ s_2^{\text{inc}} &= 2 \operatorname{Im}(a_{\text{L}} a_{\text{R}}^*) = 2 \operatorname{Re}(a_{\text{s}} a_{\text{p}}^*) \\ s_3^{\text{inc}} &= |a_{\text{R}}|^2 - |a_{\text{L}}|^2 = 2 \operatorname{Im}(a_{\text{s}} a_{\text{p}}^*) \end{aligned} \right\}, \quad (20)$$

where $*$ denotes the complex conjugate. The angles α^{inc} and β^{inc} can be calculated using the foregoing equations in Eqs. (1), followed by the Poincaré spinor $[\underline{\phi}^{\text{inc}}]$ from Eq. (2).

The Stokes parameters of the reflected plane wave are given by [2]

$$\left. \begin{aligned} s_0^{\text{ref}} &= |r_L|^2 + |r_R|^2 = |r_s|^2 + |r_p|^2 \\ s_1^{\text{ref}} &= 2 \operatorname{Re}(r_L r_R^*) = |r_p|^2 - |r_s|^2 \\ s_2^{\text{ref}} &= 2 \operatorname{Im}(r_L r_R^*) = 2 \operatorname{Re}(r_s r_p^*) \\ s_3^{\text{ref}} &= |r_R|^2 - |r_L|^2 = 2 \operatorname{Im}(r_s r_p^*) \end{aligned} \right\}, \quad (21)$$

from which the angles α^{ref} and β^{ref} as well as the Poincaré spinor $[\underline{\phi}^{\text{ref}}]$ can be calculated using Eqs. (1) and (2). Calculation of the Stokes parameters of the transmitted plane wave, the angles α^{tr} and β^{tr} , and the Poincaré spinor $[\underline{\phi}^{\text{tr}}]$ follows the same route.

3 Numerical Results

Calculations were made of the total reflectance R_ℓ , total transmittance T_ℓ , reflection-mode geometric phase Φ_ℓ^{ref} , and transmission-mode geometric phase Φ_ℓ^{tr} , $\ell \in \{s, p, R, L\}$. The subscripts in these quantities indicate the polarization state of the incident plane wave: perpendicular (s), parallel (p), left-circular (L), or right-circular (R).

In order to incorporate causal frequency-dependent constitutive parameters [59–61] in calculations, single-resonance Lorentzian functions were assumed for ε_a , ε_b , and ε_c as follows [62]:

$$\varepsilon_\ell(\lambda_0) = 1 + \frac{p_\ell}{1 + \left(\frac{1}{N_\ell} - i \frac{\lambda_\ell}{\lambda_0}\right)^2}, \quad \ell \in \{a, b, c\}. \quad (22)$$

The oscillator strengths are determined by the values of p_ℓ , $\lambda_\ell(1 + N_\ell^{-2})^{-1/2}$ are the resonance wavelengths, and λ_ℓ/N_ℓ are the resonance linewidths. The parameters used for the theoretical results reported here are as follows: $p_a = 2.3$, $p_b = 3.0$, $p_c = 2.2$, $\lambda_a = \lambda_c = 260$ nm, $\lambda_b = 270$ nm, and $N_a = N_b = N_c = 130$. Furthermore, $\chi = 37^\circ$, $N = 15$, and $P = 300$ nm were fixed. Calculations were made for primarily for $\lambda_0 \in [400, 800]$ nm.

Note that $\Phi_R^{\text{ref}} = \Phi_R^{\text{tr}} \equiv 0$ in both Figs. 2 and 3, because of the structure of $[\underline{\phi}^{\text{inc}}]$ for an incident RCP plane wave [63, 64]. The other six geometric phases Φ_ℓ^{ref} and Φ_ℓ^{tr} , $\ell \in \{s, p, L\}$, are generally non-zero, and their spectral dependencies may not follow those of the corresponding total remittances defined in Eqs. (19a) and (19b).

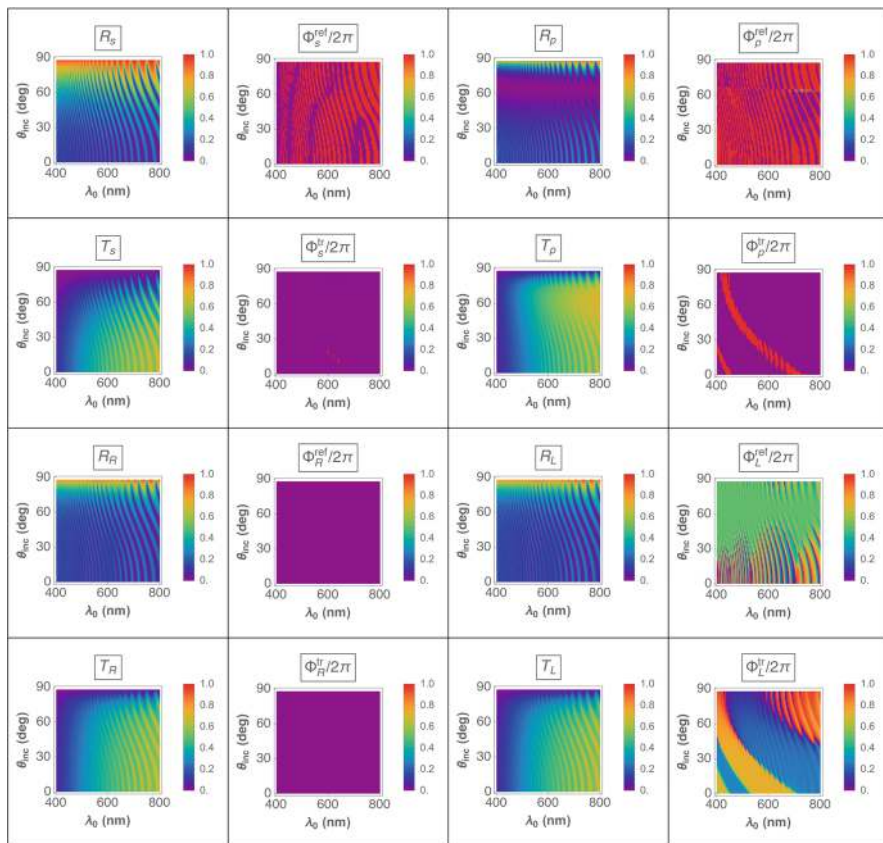


Fig. 2 Spectrums of R_ℓ , T_ℓ , Φ_ℓ^{ref} , and Φ_ℓ^{tr} , $\ell \in \{s, p, R, L\}$, for $\theta_{\text{inc}} \in [0^\circ, 90^\circ)$, when $N_{\text{lyr}} = 1$, $h = \pm 1$, $N = 15$, $P = 300$ nm, and $\psi = 0^\circ$

3.1 Columnar Thin Film ($N_{\text{lyr}} = 1$)

Figure 2 presents the spectrums of R_ℓ , T_ℓ , Φ_ℓ^{ref} , and Φ_ℓ^{tr} , $\ell \in \{s, p, R, L\}$, for $\theta_{\text{inc}} \in [0^\circ, 90^\circ)$ and $\psi = 0^\circ$. Figure 3 presents the analogous spectrums for $\theta_{\text{inc}} = 0^\circ$ and $\psi \in [0^\circ, 360^\circ)$. As the Reusch pile reduces to a single columnar thin film of thickness NP when $N_{\text{lyr}} = 1$, no Bragg phenomenon can be exhibited, the columnar thin film being effectively a homogeneous biaxial-dielectric continuum [12, 65] whose relative permittivity dyadic does not depend on h .

In Figs. 2 and 3, the total linear remittances (i.e., R_s , R_p , T_s , and T_p) depend on the polarization state of the incident linearly polarized plane wave, but the total circular remittances (i.e., R_R , R_L , T_R , and T_L) do not depend on the polarization state of the incident circularly polarized plane wave. The plots of all eight quantities show Fabry–Perot resonances [66], as expected from a homogeneous dielectric slab. The

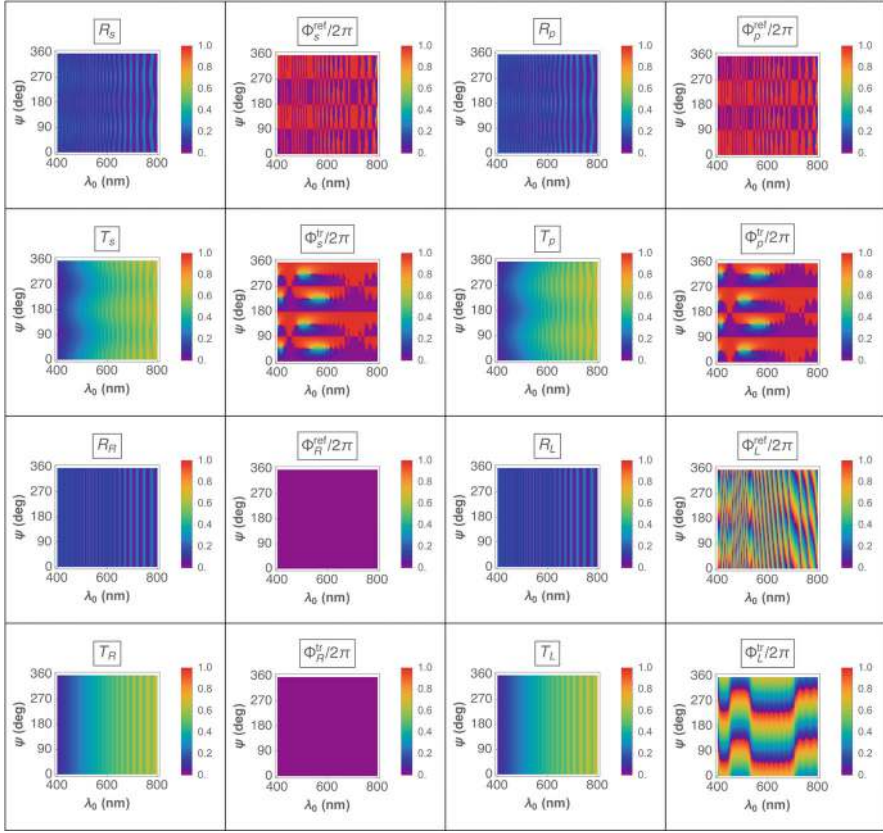


Fig. 3 Spectrums of R_ℓ , T_ℓ , Φ_ℓ^{ref} , and Φ_ℓ^{tr} , $\ell \in \{s, p, R, L\}$, for $\psi \in [0^\circ, 360^\circ)$, when $N_{\text{lyr}} = 1$, $h = \pm 1$, $N = 15$, $P = 300$ nm, and $\theta_{\text{inc}} = 0^\circ$

spectral dependences of Φ_ℓ^{ref} do not follow those of R_ℓ , and the spectral dependences of Φ_ℓ^{tr} do not follow those of T_ℓ , $\ell \in \{s, p, L\}$.

3.2 Chevronic Thin Film ($N_{\text{lyr}} = 2$)

Figure 4 presents the spectrums of R_ℓ , T_ℓ , Φ_ℓ^{ref} , and Φ_ℓ^{tr} , $\ell \in \{s, p, R, L\}$, for $\theta_{\text{inc}} \in [0^\circ, 90^\circ)$ and $\psi = 0^\circ$, and Fig. 5 for $\theta_{\text{inc}} = 0^\circ$ and $\psi \in [0^\circ, 360^\circ)$. Neither the total remittances nor the corresponding geometric phases depend on whether $h = 1$ or $h = -1$ in these two figures, just as in Figs. 2 and 3, because chevronic thin films lack structural handedness.

No trace of the Bragg phenomenon is evident in the plots of the total remittances in Figs. 4 and 5. There is no doubt that the Reusch pile is structurally periodic for

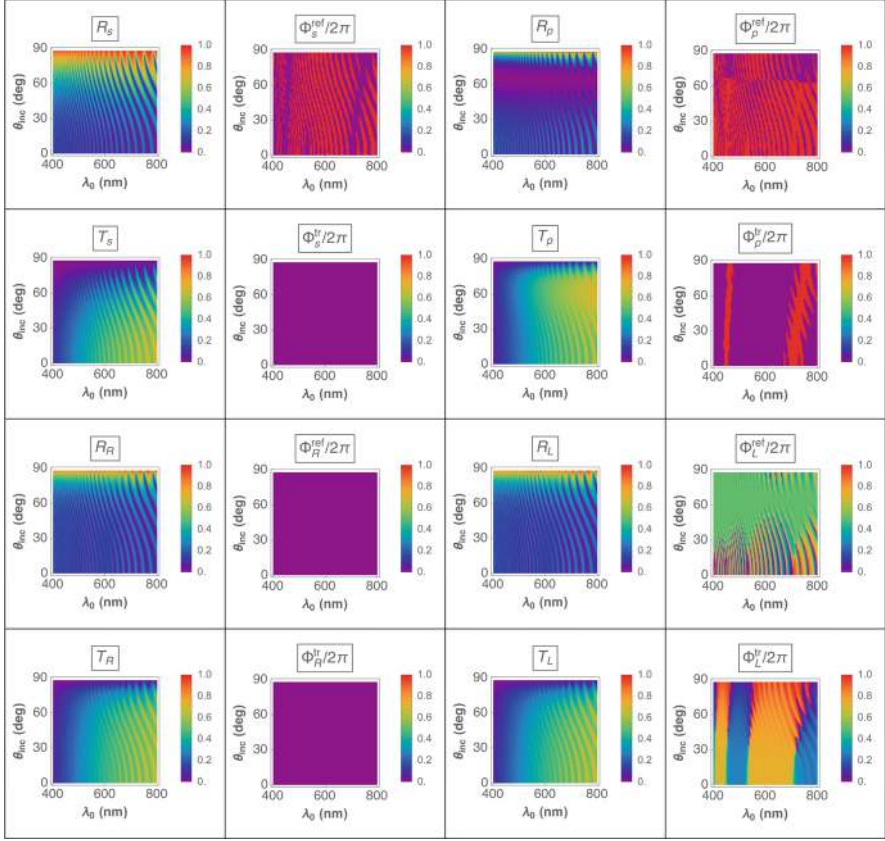


Fig. 4 Spectrums of R_ℓ , T_ℓ , Φ_ℓ^{ref} , and Φ_ℓ^{tr} , $\ell \in \{s, p, R, L\}$, for $\theta_{\text{inc}} \in [0^\circ, 90^\circ]$, when $N_{\text{lyr}} = 2$, $h = \pm 1$, $N = 15$, $P = 300$ nm, and $\psi = 0^\circ$

$N_{\text{lyr}} = 2$, but that structural periodicity does not translate into electromagnetic periodicity for all incidence conditions. Indeed for normal incidence, the interface $z = P/2$ in the reference unit cell is reflectionless [67, 68].

Elsewhere, theoretical research has shown that the Bragg phenomenon is not exhibited by a chevronic thin film for normal and near-normal incidence, which conclusion has been validated experimentally [56]. It is difficult to distinguish between the total remittance plots for $N_{\text{lyr}} = 1$ (Figs. 2 and 3) and $N_{\text{lyr}} = 2$ (Figs. 4 and 5). Theory also indicates that vestigial manifestation of the Bragg phenomenon is possible for highly oblique incidence [56], but a clear signature cannot be discerned in Fig. 4.

The geometric phases Φ_ℓ^{ref} and Φ_ℓ^{tr} , $\ell \in \{s, p, L\}$, are not identically zero in Figs. 4 and 5. Furthermore, although the total remittance plots in Fig. 2 are virtually indistinguishable from their counterparts in Fig. 4, the dependences of $\Phi_{s,p}^{\text{ref}}$, Φ_p^{tr} , and Φ_L^{ref} on θ_{inc} in those two figures show clear differences. These differences

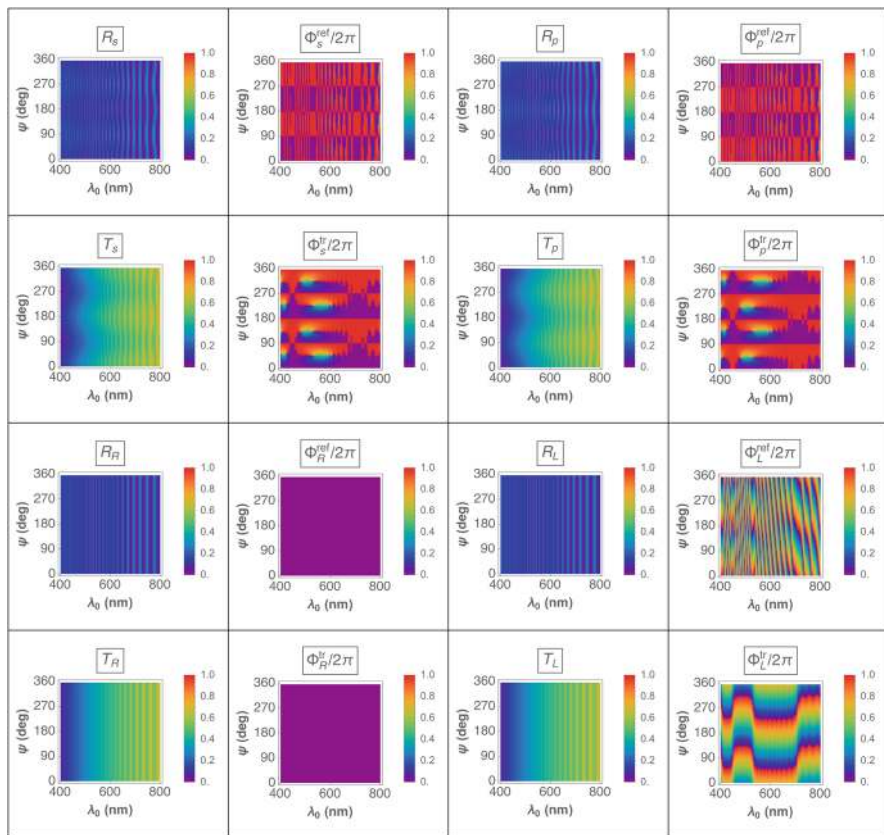


Fig. 5 Spectrums of R_ℓ , T_ℓ , Φ_ℓ^{ref} , and Φ_ℓ^{tr} , $\ell \in \{s, p, R, L\}$, for $\psi \in [0^\circ, 360^\circ)$, when $N_{\text{lyr}} = 2$, $h = \pm 1$, $N = 15$, $P = 300$ nm, and $\theta_{\text{inc}} = 0^\circ$

indicate that the geometric phases of the reflected and the transmitted plane waves are affected by morphology much more than the total remittances, this observation having been previously made only for the geometric phase of the transmitted plane wave [63, 64]. Note, however, that the plots of $\Phi_{s,p}^{\text{ref}}$, Φ_p^{tr} , and Φ_L^{ref} in Figs. 3 and 5 are identical, because the interface $z = P/2$ in the middle of the reference unit cell of the chevronic thin film is electromagnetically inconsequential for normal incidence [67, 68].

3.3 Ambichiral Reusch Pile ($N_{\text{lyr}} = 3$)

A Reusch pile with $N_{\text{lyr}} = 3$ possesses both structural handedness and structural periodicity. Although this Reusch pile was not included in the 2004 classification

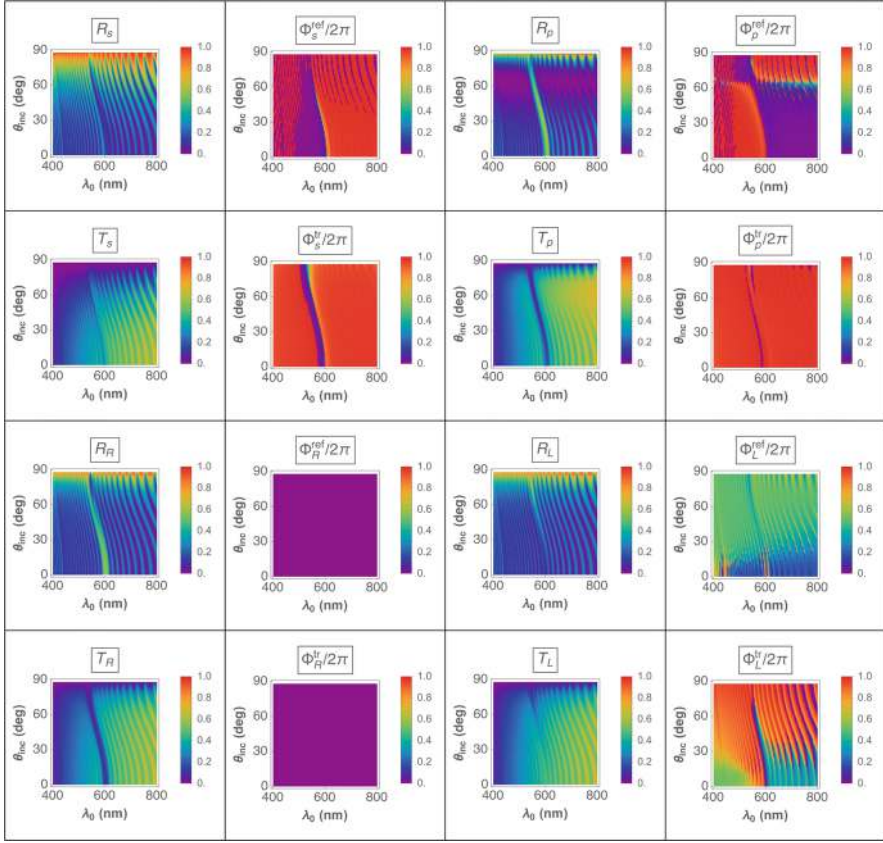


Fig. 6 Spectrums of R_ℓ , T_ℓ , Φ_ℓ^{ref} , and Φ_ℓ^{tr} , $\ell \in \{s, p, R, L\}$, for $\theta_{\text{inc}} \in [0^\circ, 90^\circ]$, when $N_{\text{lyr}} = 3$, $h = 1$, $N = 15$, $P = 300$ nm, and $\psi = 0^\circ$

[23], it should be considered as ambichiral. Figure 6 presents the chosen spectrums for $\theta_{\text{inc}} \in [0^\circ, 90^\circ]$ and $\psi = 0^\circ$, and Fig. 7 for $\theta_{\text{inc}} = 0^\circ$ and $\psi \in [0^\circ, 360^\circ]$, when $h = 1$. The Bragg phenomenon is clearly evident as a deep blue trough in the plots of T_R and a corresponding ridge in the plots of R_R . This trough/ridge is centered at $\lambda_0 = 602$ nm for $\theta_{\text{inc}} = 0^\circ$ and it blueshifts with more oblique incidence [45]. The absence of analogous features in the plots of T_L and R_L supports the conclusion that this is a *circular Bragg phenomenon*. However, in comparison to a chiral sculptured thin film [45], the trough is present in the plots of both T_R and T_L , and the ridge in the plots of both R_R and R_L , for highly oblique incidence.

Analogous spectrums for $h = -1$ are presented in Figs. 8 and 9. The plots of $\{T_R, R_R, T_L, R_L\}$ for fixed ψ are interchanged with those of $\{T_L, R_L, T_R, R_R\}$ for $2\pi - \psi$, in comparison to Figs. 6 and 7; in other words,

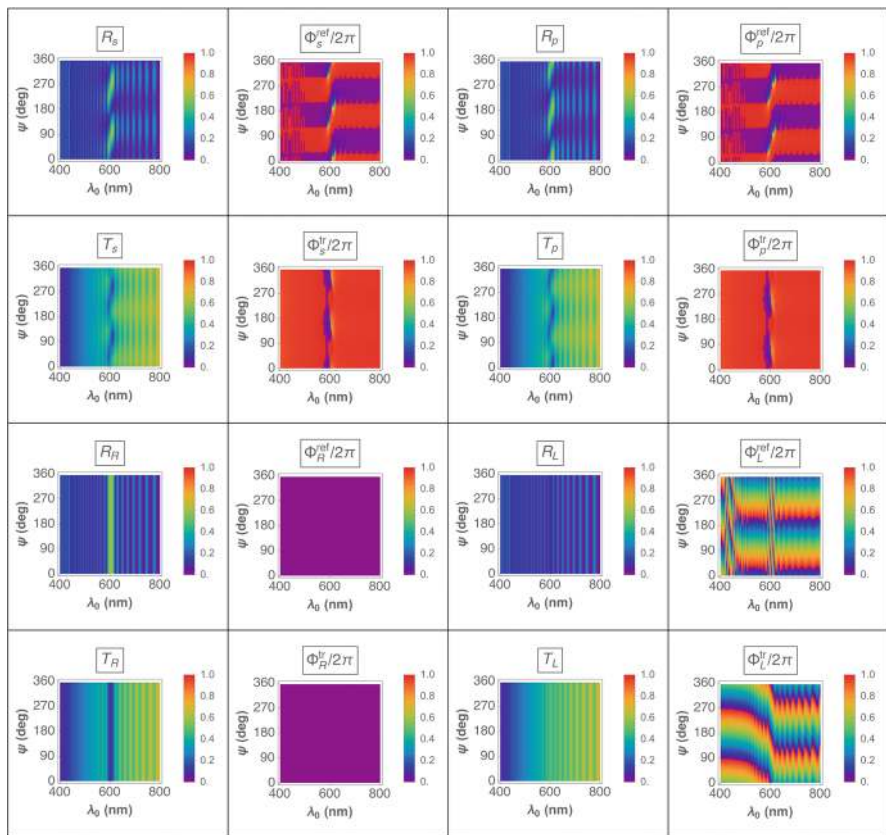


Fig. 7 Spectrums of R_ℓ , T_ℓ , Φ_ℓ^{ref} , and Φ_ℓ^{tr} , $\ell \in \{s, p, R, L\}$, for $\psi \in [0^\circ, 360^\circ)$, when $N_{\text{lyr}} = 3$, $h = 1$, $N = 15$, $P = 300$ nm, and $\theta_{\text{inc}} = 0^\circ$

$$\left. \begin{aligned} R_R(h, \psi) &= R_L(-h, 2\pi - \psi) \\ R_L(h, \psi) &= R_R(-h, 2\pi - \psi) \\ T_R(h, \psi) &= T_L(-h, 2\pi - \psi) \\ T_L(h, \psi) &= T_R(-h, 2\pi - \psi) \end{aligned} \right\}. \quad (23)$$

Since a linearly polarized plane wave can be decomposed into an RCP plane wave and an LCP plane wave, signatures of the circular Bragg phenomenon are also to be found in the plots of linear remittances in Figs. 6, 7, 8, and 9. The following symmetries are exhibited by the linear remittances:

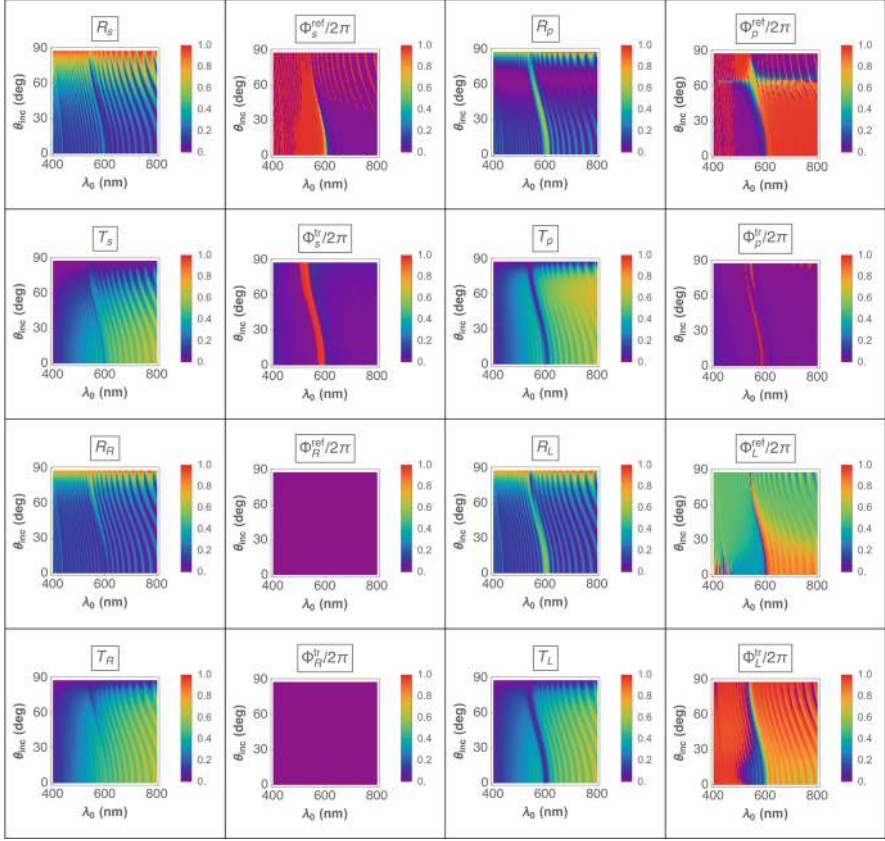


Fig. 8 Spectrums of R_ℓ , T_ℓ , Φ_ℓ^{ref} , and Φ_ℓ^{tr} , $\ell \in \{s, p, R, L\}$, for $\theta_{\text{inc}} \in [0^\circ, 90^\circ]$, when $N_{\text{lyr}} = 3$, $h = -1$, $N = 15$, $P = 300$ nm, and $\psi = 0^\circ$

$$\left. \begin{aligned} R_s(h, \psi) &= R_s(-h, 2\pi - \psi) \\ R_p(h, \psi) &= R_p(-h, 2\pi - \psi) \\ T_s(h, \psi) &= T_s(-h, 2\pi - \psi) \\ T_p(h, \psi) &= T_p(-h, 2\pi - \psi) \end{aligned} \right\}. \quad (24)$$

No symmetries are evident in the plots of geometric phases in Figs. 6, 7, 8, and 9, except that $\Phi_R^{\text{ref}} = \Phi_R^{\text{tr}} \equiv 0$ by virtue of the structure of the Poincaré spinor of an RCP plane wave [63, 64]. The spectrums of Φ_ℓ^{ref} and Φ_ℓ^{tr} , $\ell \in \{s, p, L\}$, are greatly affected when the structural handedness is reversed.

In order to confirm that $N_{\text{lyr}} = 3$ provides the exceptional case $\lambda_0^{2;0, N_{\text{lyr}}/2} > \lambda_0^{1;0, N_{\text{lyr}}/2}$, calculations were also made for λ_0 extending into the near-infrared spectral regime. With $\theta_{\text{inc}} = 0^\circ$ and $\psi = 0^\circ$ fixed, (i) Fig. 10 presents the spectrums

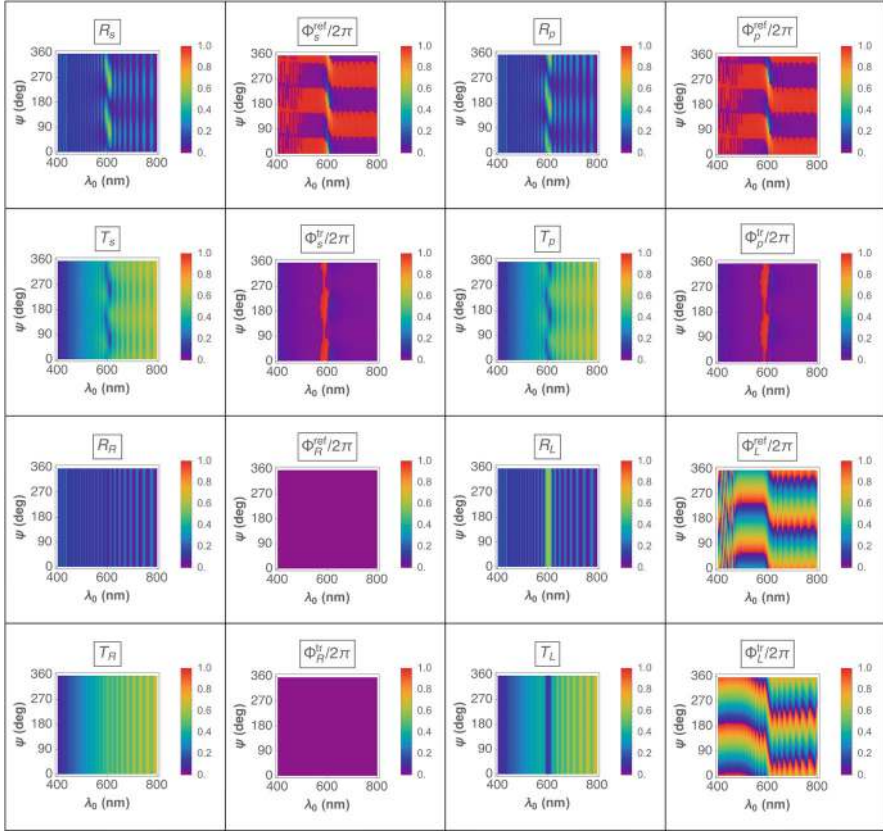


Fig. 9 Spectrums of R_ℓ , T_ℓ , Φ_ℓ^{ref} , and Φ_ℓ^{tr} , $\ell \in \{s, p, R, L\}$, for $\psi \in [0^\circ, 360^\circ)$, when $N_{\text{lyr}} = 3$, $h = -1$, $N = 15$, $P = 300$ nm, and $\theta_{\text{inc}} = 0^\circ$

of R_ℓ , T_ℓ , Φ_ℓ^{ref} , and Φ_ℓ^{tr} , $\ell \in \{s, p, R, L\}$, for $h = 1$, and Fig. 11 presents the same spectrums for $h = -1$. The remittance spectrums in both figures clearly show two circular Bragg regimes. The first is centered at $\lambda_0^{1;0,3/2} = 602$ nm, exactly as in Figs. 6, 7, 8, and 9, and it belongs to the first family described in Sect. 1.3. The second is centered at $\lambda_0^{2;0,3/2} = 1135$ nm and belongs to the second family described in Sect. 1.3. Note that $\lambda_0^{2;0,3/2}$ differs from $2\lambda_0^{1;0,3/2}$ predicted by Eq. (9) because the relative permittivity scalars in Eq. (22) are frequency dependent.

Importantly, the spectral variations of Φ_ℓ^{ref} and Φ_ℓ^{tr} , $\ell \in \{s, p, L\}$, are different in the two circular Bragg regimes in Figs. 10 and 11.

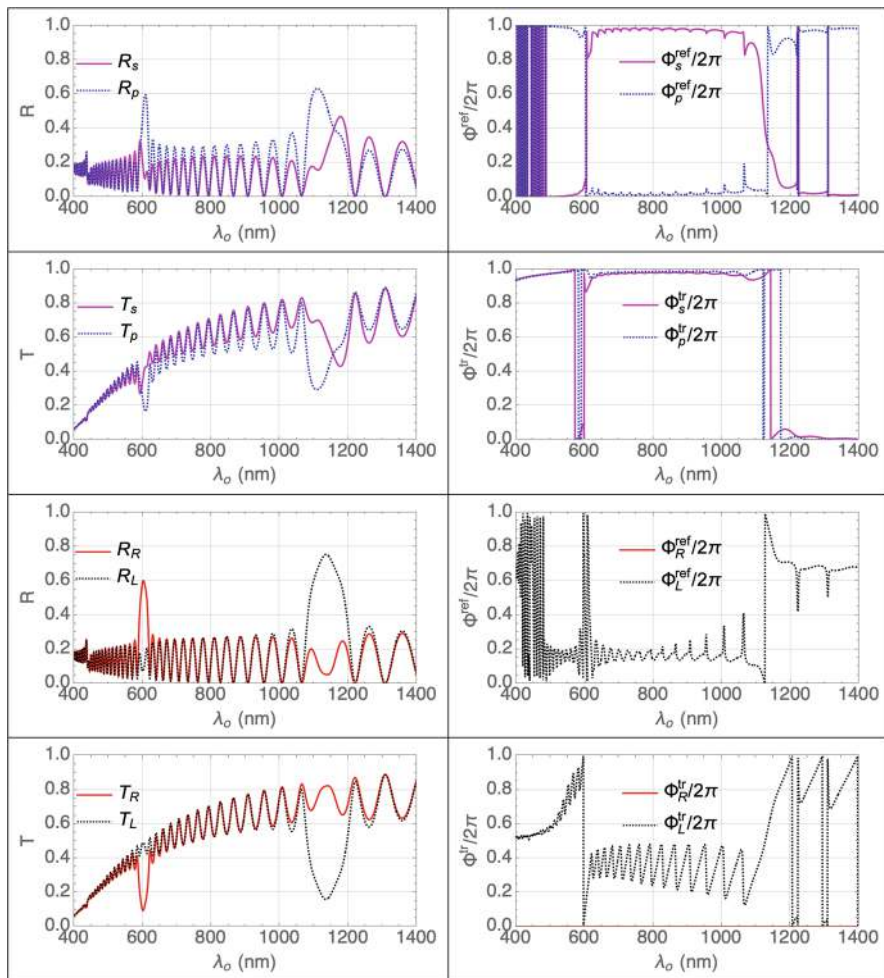


Fig. 10 Spectra of R_ℓ , T_ℓ , Φ_ℓ^{ref} , and Φ_ℓ^{tr} , $\ell \in \{s, p, R, L\}$, for $\theta_{\text{inc}} = 0^\circ$ and $\psi = 0^\circ$, when $N_{\text{lyr}} = 3$, $h = 1$, $N = 15$, and $P = 300$ nm

3.4 Equichiral Reusch Pile ($N_{\text{lyr}} = 4$)

The prefix *equi* in the classification *equichiral* is justified for a Reusch pile with $N_{\text{lyr}} = 4$, since $\lambda_0^{1;p,N_{\text{lyr}}/2} = \lambda_0^{2;p,N_{\text{lyr}}/2} \forall p$ when $N_{\text{lyr}} = 4$. The same Reusch pile is also structurally handed (with period P), so that the suffix *chiral* in the classification *equichiral* is also justified. However, there is a notable exception: the period equals $P/2$, and there is no structural handedness when $\chi \in \{0, \pi/2\}$.

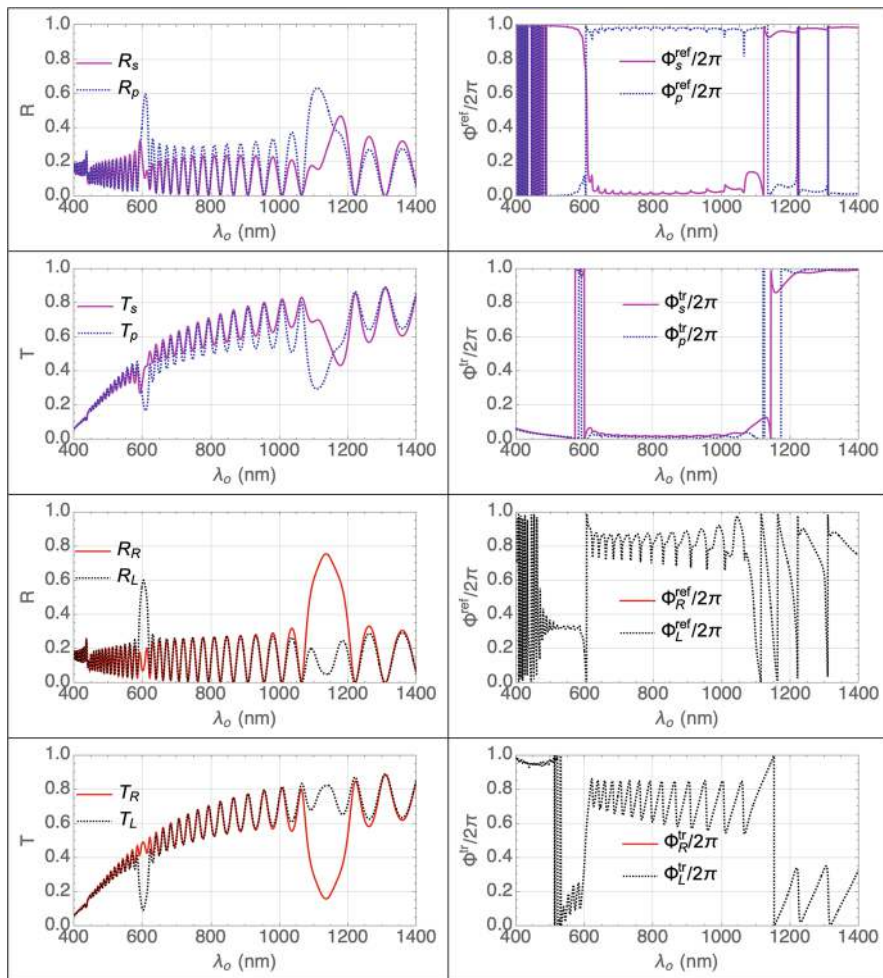


Fig. 11 Spectra of R_ℓ , T_ℓ , Φ_ℓ^{ref} , and Φ_ℓ^{tr} , $\ell \in \{s, p, R, L\}$, for $\theta_{\text{inc}} = 0^\circ$ and $\psi = 0^\circ$, when $N_{\text{lyr}} = 3$, $h = -1$, $N = 15$, and $P = 300$ nm

Figure 12 presents the chosen spectra for $\theta_{\text{inc}} \in [0^\circ, 90^\circ)$ and $\psi = 0^\circ$, and Fig. 13 for $\theta_{\text{inc}} = 0^\circ$ and $\psi \in [0^\circ, 360^\circ)$, when $h = 1$. Figures 14 and 15 are the counterparts of those two figures for $h = -1$. Calculations show that Eqs. (23) and (24) hold for $N_{\text{lyr}} = 4$.

The Bragg phenomenon is clearly evident as a deep blue trough in the plots of both linear and both circular transmittances, and as a corresponding ridge in the plots of both linear and both circular reflectances, regardless of the value of $h \in \{-1, 1\}$. These features are centered about $\lambda_o = 600$ nm for $\theta_{\text{inc}} = 0^\circ$ and blueshift with more oblique incidence. This Reusch pile exhibits a polarization-

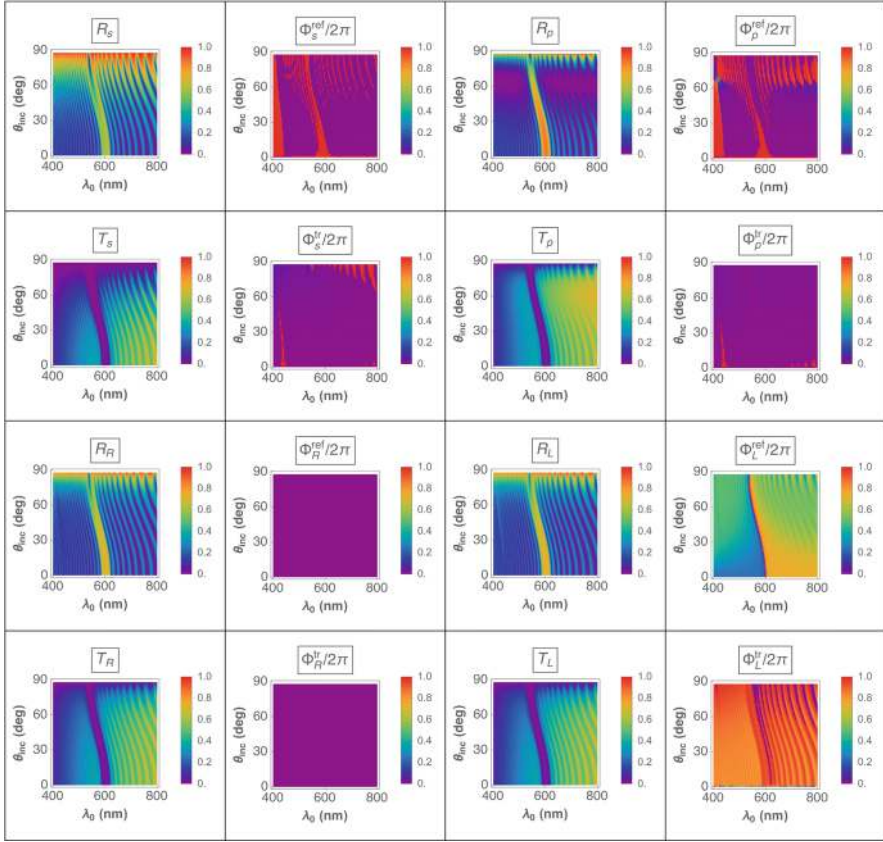


Fig. 12 Spectrums of R_ℓ , T_ℓ , Φ_ℓ^{ref} , and Φ_ℓ^{tr} , $\ell \in \{s, p, R, L\}$, for $\theta_{\text{inc}} \in [0^\circ, 90^\circ]$, when $N_{\text{lyr}} = 4$, $h = 1$, $N = 15$, $P = 300$ nm, and $\psi = 0^\circ$

universal bandgap that can be tuned by adjusting the angle of incidence θ_{inc} , as has been verified experimentally [49].

The plots of Φ_ℓ^{ref} and Φ_ℓ^{tr} , $\ell \in \{s, p, L\}$, in general, contain clear evidence of the polarization-universal bandgap. However, whereas Φ_ℓ^{ref} and Φ_ℓ^{tr} , $\ell \in \{s, p\}$, are greatly affected when the structural handedness is reversed, Φ_L^{ref} and Φ_L^{tr} are affected very little by the same reversal.

3.5 Ambichiral and Finely Chiral Reusch Piles ($N_{\text{lyr}} \geq 5$)

The optical response characteristics for $N_{\text{lyr}} \geq 5$ are similar to those for $N_{\text{lyr}} = 3$, except that Eq.(9) predicts $\lambda_0^{2;0,N_{\text{lyr}}/2}/\lambda_0^{1;0,N_{\text{lyr}}/2} > 1$ for $N_{\text{lyr}} = 3$ but $\lambda_0^{2;0,N_{\text{lyr}}/2}/\lambda_0^{1;0,N_{\text{lyr}}/2} < 1$ for $N_{\text{lyr}} \geq 5$.

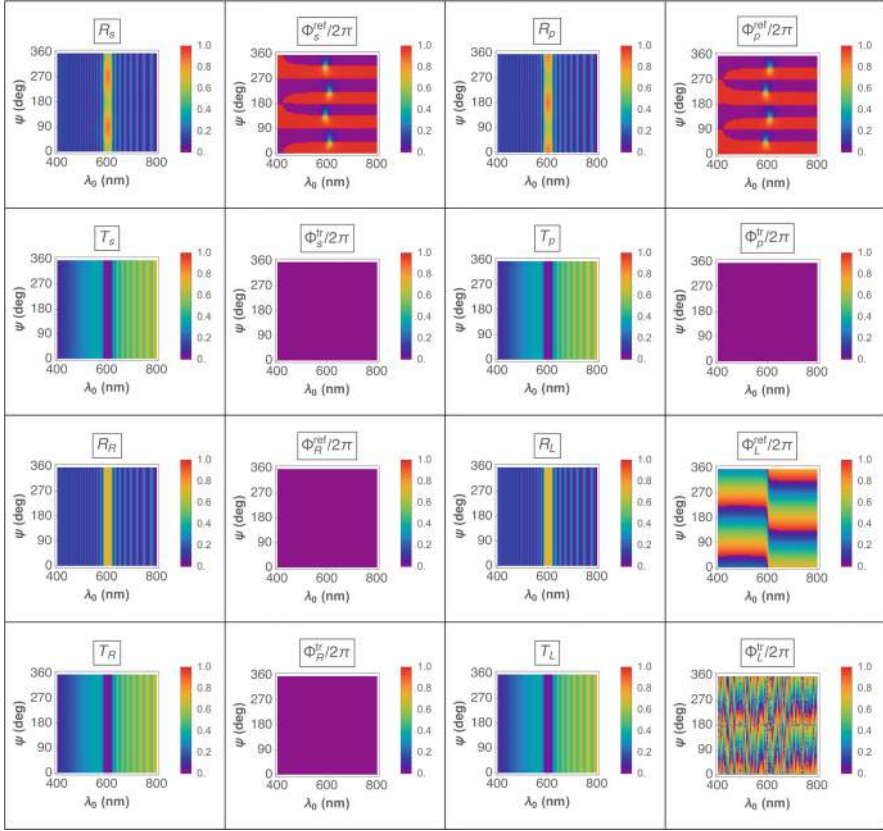


Fig. 13 Spectrums of R_ℓ , T_ℓ , Φ_ℓ^{ref} , and Φ_ℓ^{tr} , $\ell \in \{s, p, R, L\}$, for $\psi \in [0^\circ, 360^\circ)$, when $N_{\text{lyr}} = 4$, $h = 1$, $N = 15$, $P = 300$ nm, and $\theta_{\text{inc}} = 0^\circ$

Figure 16 presents the chosen spectrums for $\theta_{\text{inc}} \in [0^\circ, 90^\circ)$ and $\psi = 0^\circ$, and Fig. 17 for $\theta_{\text{inc}} = 0^\circ$ and $\psi \in [0^\circ, 360^\circ)$, when $N_{\text{lyr}} = 5$ and $h = 1$. Analogous spectrums for $N_{\text{lyr}} = 5$ and $h = -1$ are presented in Figs. 18 and 19. Regardless of whether $h = 1$ or $h = -1$, two distinct circular Bragg regimes are evident in these plots. Whereas $\lambda_0^{1;0,5/2} = 602$ nm for $\theta_{\text{inc}} = 0^\circ$, we have $\lambda_0^{2;0,5/2} = 439$ nm for normal incidence, so that $\lambda_0^{2;0,5/2}/\lambda_0^{1;0,5/2} = 0.729$. This ratio is smaller than 0.667 predicted by Eq. (9), because the relative permittivity scalars in Eq. (22) are frequency dependent.

Equations (23) and (24) hold, but similar symmetries are not evident for the non-zero geometric phases in Figs. 16, 17, 18, and 19. Furthermore, the spectral variations of Φ_ℓ^{ref} and Φ_ℓ^{tr} , $\ell \in \{s, p, L\}$, are different in the two circular Bragg regimes in these figures.

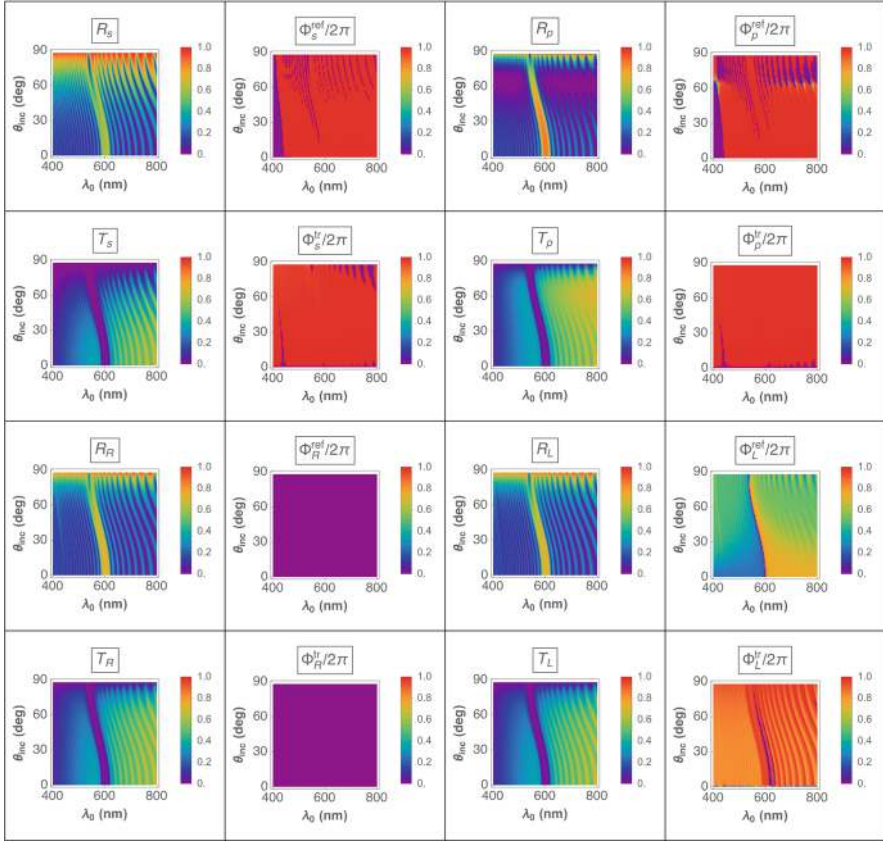


Fig. 14 Spectrums of R_ℓ , T_ℓ , Φ_ℓ^{ref} , and Φ_ℓ^{tr} , $\ell \in \{s, p, R, L\}$, for $\theta_{\text{inc}} \in [0^\circ, 90^\circ]$, when $N_{\text{lyr}} = 4$, $h = -1$, $N = 15$, $P = 300$ nm, and $\psi = 0^\circ$

The Reusch pile becomes finely chiral and $\lambda_0^{2;0,N_{\text{lyr}}/2}$ blueshifts ever farther from $\lambda_0^{1;0,N_{\text{lyr}}/2}$, as N_{lyr} increases significantly beyond 5, and the circular total remittance spectrums begin to converge [53]. A similar convergence is also exhibited by the linear total remittance spectrums. Spectrums of the non-zero geometric phases also appear to converge, except in the vicinity of a circular Bragg regime. This becomes clear from examining the plots of Φ_L^{tr} for $\psi = 0^\circ$, $h = 1$ and $N_{\text{lyr}} \in [1, 50]$ in Fig. 20, wherein the choice of Φ_L^{tr} over other non-zero geometric phases takes into account the fact that T_L is high inside the circular Bragg regime with $\lambda_0^{1;0,N_{\text{lyr}}/2}$ as its center wavelength for $h = 1$. The same conclusion emerges even more strongly from examining the plots of Φ_L^{ref} for $\psi = 0^\circ$, $h = -1$, and $N_{\text{lyr}} \in [1, 50]$ in Fig. 21, the choice of Φ_L^{ref} over other non-zero geometric phases taking into account that R_L is high inside the circular Bragg regime with $\lambda_0^{1;0,N_{\text{lyr}}/2}$ as its center wavelength for $h = -1$.

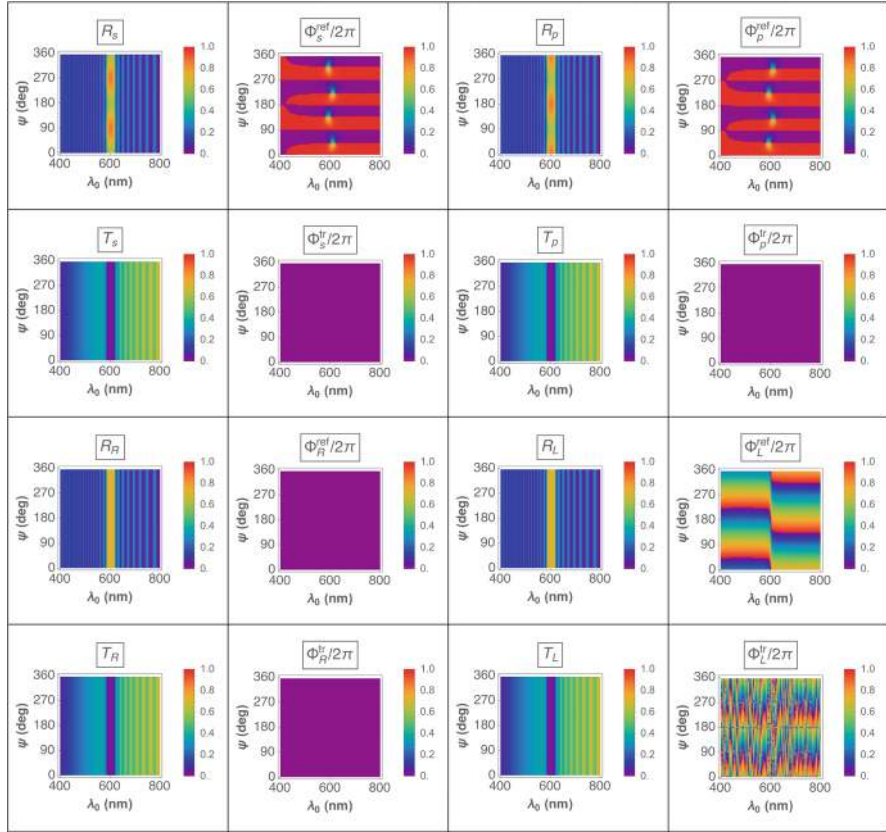


Fig. 15 Spectrums of R_ℓ , T_ℓ , Φ_ℓ^{ref} , and Φ_ℓ^{tr} , $\ell \in \{s, p, R, L\}$, for $\psi \in [0^\circ, 360^\circ)$, when $N_{\text{lyr}} = 4$, $h = -1$, $N = 15$, $P = 300$ nm, and $\theta_{\text{inc}} = 0^\circ$

4 Concluding Remarks

Figures 2, 3, 4, 5, 6, 7, 8, 9, 10, 11, 12, 13, 14, 15, 16, 17, 18, and 19 provide an evolutionary perspective on the nanoscale architected morphology of Reusch piles. Total remittances and geometric phases were presented as functions of the free-space wavelength and the direction of plane-wave incidence for fixed thickness $NP = 4500$ nm with $N = 15$. As N_{lyr} increased from unity, first the Reusch pile became structurally periodic (for $N_{\text{lyr}} \geq 2$) and then structurally handed (for $N_{\text{lyr}} \geq 3$). The layer thickness P/N_{lyr} continued to shrink with increasing N_{lyr} , which can be implemented quite straightforwardly with chiral sculptured thin films [23, 50, 69–72]. Total-remittance values in excess of 0.01 began to converge correct to four decimal digits, as N_{lyr} increased beyond 10 (results not shown).

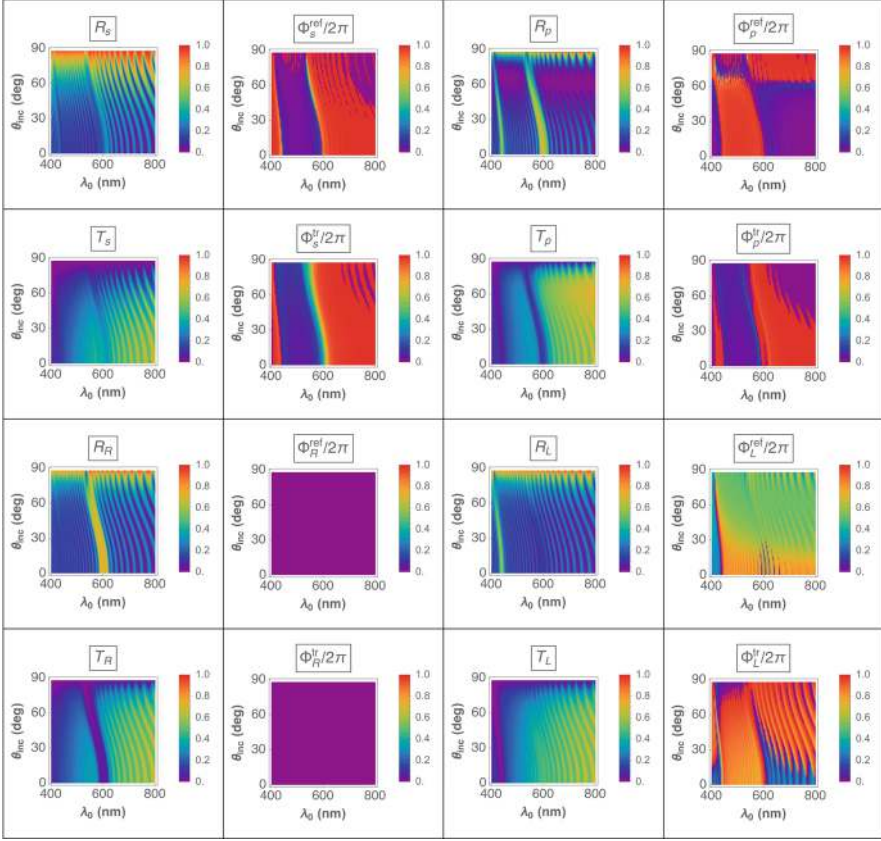


Fig. 16 Spectrums of R_ℓ , T_ℓ , Φ_ℓ^{ref} , and Φ_ℓ^{tr} , $\ell \in \{s, p, R, L\}$, for $\theta_{\text{inc}} \in [0^\circ, 90^\circ]$, when $N_{\text{lyr}} = 5$, $h = 1$, $N = 15$, $P = 300$ nm, and $\psi = 0^\circ$

But that did not turn out to be completely true for the geometric phases. With Φ_L^{tr} selected for $h = 1$ because T_L has a substantial magnitude inside the circular Bragg regime with $\lambda_0^{1;0, N_{\text{lyr}}/2}$ as its center wavelength, and Φ_L^{ref} selected for $h = -1$ because R_L has a substantial magnitude inside the same circular Bragg regime, to facilitate measurements eventually, Figs. 20 and 21 show the emergence of new features in the spectrums of non-zero geometric phases on the short-wavelength side of the chosen circular Bragg regime. Since adjacent layers in a Reusch pile with high N_{lyr} are, at least theoretically identical except for a slight twist about the z axis, the foregoing observation implies that the geometric phases are sensitive to nanoscale morphological changes as a thin film grows. Therefore, geometric phases could contain signatures of nanoscale morphological details that would depend on the fabrication technique. Careful experiments are necessary to establish this possibility.

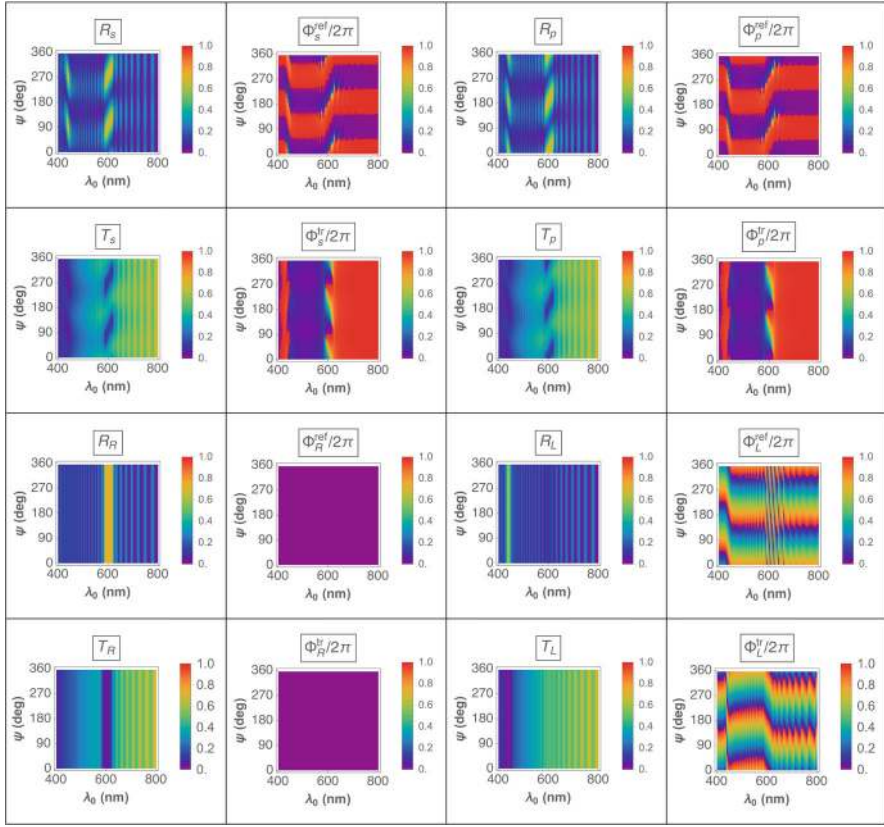


Fig. 17 Spectrums of R_ℓ , T_ℓ , Φ_ℓ^{ref} , and Φ_ℓ^{tr} , $\ell \in \{s, p, R, L\}$, for $\psi \in [0^\circ, 360^\circ)$, when $N_{\text{lyr}} = 5$, $h = 1$, $N = 15$, $P = 300$ nm, and $\theta_{\text{inc}} = 0^\circ$

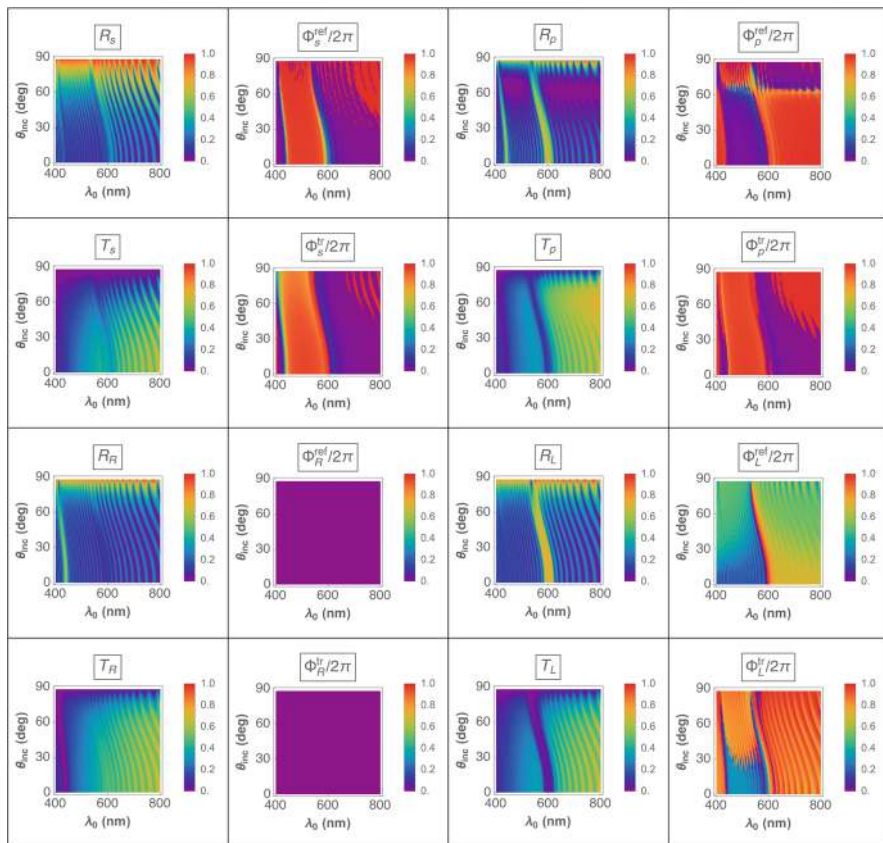


Fig. 18 Spectra of R_ℓ , T_ℓ , Φ_ℓ^{ref} , and Φ_ℓ^{tr} , $\ell \in \{s, p, R, L\}$, for $\theta_{\text{inc}} \in [0^\circ, 90^\circ]$, when $N_{\text{lyr}} = 5$, $h = -1$, $N = 15$, $P = 300$ nm, and $\psi = 0^\circ$

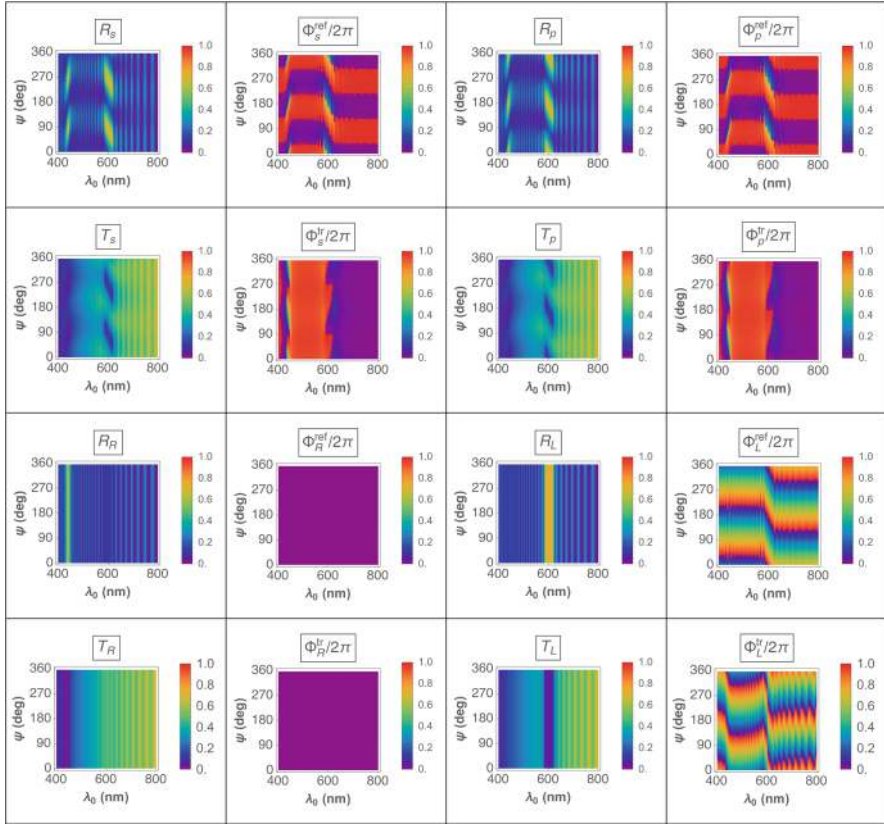


Fig. 19 Spectrums of R_ℓ , T_ℓ , Φ_ℓ^{ref} , and Φ_ℓ^{tr} , $\ell \in \{s, p, R, L\}$, for $\psi \in [0^\circ, 360^\circ)$, when $N_{\text{lyr}} = 5$, $h = -1$, $N = 15$, $P = 300$ nm, and $\theta_{\text{inc}} = 0^\circ$

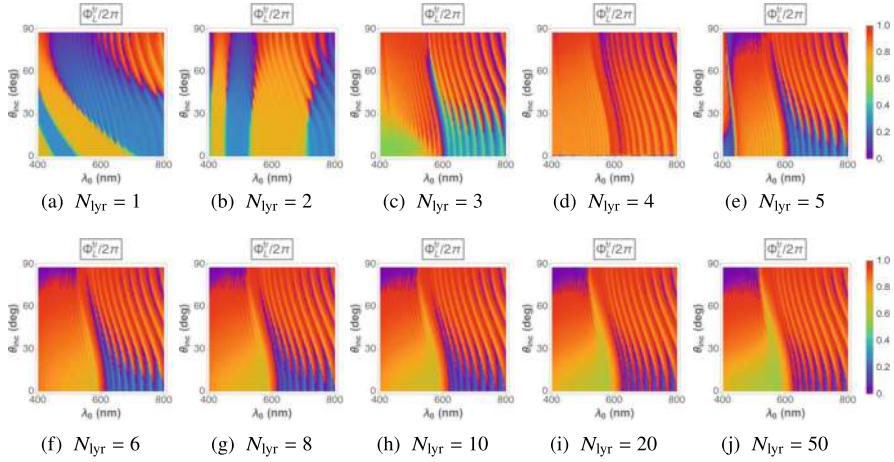


Fig. 20 Spectrums of Φ_L^F for $\theta_{\text{inc}} \in [0^\circ, 90^\circ)$ and $N_{\text{lyr}} \in \{1, 2, 3, 4, 5, 6, 8, 10, 20, 50\}$, when $h = 1$, $N = 15$, $P = 300$ nm, and $\psi = 0^\circ$

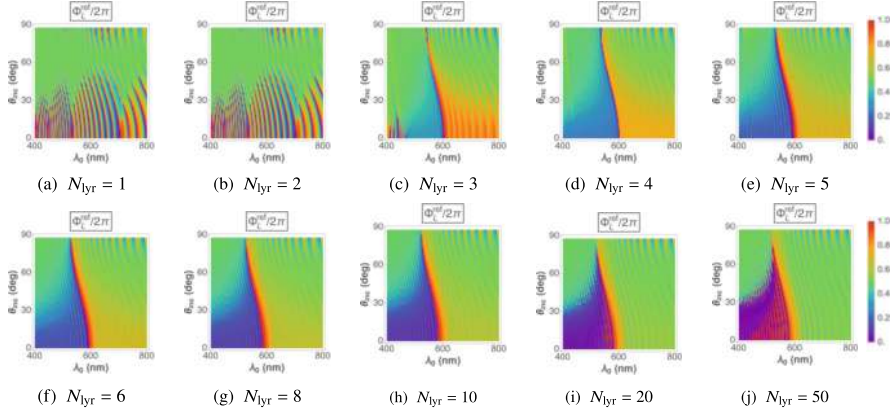


Fig. 21 Spectrums of Φ_L^{ref} for $\theta_{\text{inc}} \in [0^\circ, 90^\circ)$ and $N_{\text{lyr}} \in \{1, 2, 3, 4, 5, 6, 8, 10, 20, 50\}$, when $h = -1$, $N = 15$, $P = 300$ nm, and $\psi = 0^\circ$

Acknowledgments This chapter celebrates curiosity-driven research, as exemplified by Eduard Reusch on periodic multilayers [25] and Pancharatnam on interference [4, 73]. The author thanks the Charles Godfrey Binder Endowment at Penn State for supporting his research from 2006 to 2024.

References

1. M. Born, E. Wolf, *Principles of Optics*, 6th edn. (Cambridge University, Cambridge, 1980). Sec. 1.4.2

2. J.D. Jackson, *Classical Electrodynamics*, 3rd edn. (Wiley, New York, 1999). Sec. 7.2
3. J.C. Gutiérrez-Vega, G. Rendon, Pancharatnam–Berry phase algorithm to calculate the area of arbitrary polygons on the Poincaré sphere. *J. Opt. Soc. Am. A* **37**, 925–929 (2020)
4. S. Pancharatnam, Generalized theory of interference, and its applications. Part I. Coherent pencils. *Proc. Indian Acad. Sci.* **44**, 247–262 (1956)
5. A. Shapere, F. Wilczek (eds.), *Geometric Phases in Physics* (World Scientific, Singapore, 1989)
6. E. Cohen, H. Larocque, F. Bouchard, F. Nejdassattari, Y. Gefen, E. Karimi, Geometric phase from Aharonov–Bohm to Pancharatnam–Berry and beyond. *Nat. Rev. Phys.* **1**, 437–449 (2019)
7. R. Citro, O. Durante, The geometric phase: consequences in classical and quantum physics, in *Sketches of Physics: The Celebration Collection*, ed. by R. Citro, M. Lewenstein, A. Rubio, W.P. Schleich, J.D. Well, G.P. Zank (Springer, Cham, 2023), pp. 63–84
8. M. Rafayelyan, G. Agez, E. Brasselet, Ultrabroadband gradient-pitch Bragg–Berry mirrors. *Phys. Rev. A* **96**, 043862 (2017)
9. J. Kobashi, H. Yoshida, M. Ozaki, Planar optics with patterned chiral liquid crystals. *Nat. Photonics* **11**, 389–392 (2016)
10. J.P. Balthasar Mueller, N.A. Rubin, R.C. Devlin, B. Groever, F. Capasso, Metasurface polarization optics: independent phase control of arbitrary orthogonal states of polarization. *Phys. Rev. Lett.* **118**, 113901 (2017)
11. C.P. Jisha, S. Nolte, A. Alberucci, Geometric phase in optics: from wavefront manipulation to waveguiding. *Laser Photonics Rev.* **15**, 2100003 (2021)
12. I.J. Hodgkinson, Q.h. Wu, *Birefringent Thin Films and Polarizing Elements* (World Scientific, Singapore, 1997)
13. M. Pelayo Garcia, D. Gibson, K.L. McAughey, D.A. Hughes, C. García Núñez, Ultra-inclined nanocolumnar ZnO films sputtered using a novel masking configuration providing controlled and restricted oblique angle deposition for enhanced sensing platforms. *Adv. Phys. Res.* **3**, 2400020 (2024)
14. A. Lakhtakia, R. Messier, *Sculptured Thin Films: Nanoengineered Morphology and Optics* (SPIE, Bellingham, 2005)
15. A. Das, S. Mandal, R.A. Fiallo, M.W. Horn, A. Lakhtakia, M. Pradhan, Geometric phase and photonic spin Hall effect in thin films with architected columnar morphology. *J. Opt. Soc. Am. B* **40**, 2418–2428 (2023). Replace “tan” by “sin” in Eq. (5b)
16. P.M. Martin, *Handbook of Deposition Technologies for Films and Coatings*, 3rd edn. (Elsevier, Oxford, 2010)
17. S. Juodkazis, V. Mizeikis, H. Misawa, Three-dimensional microfabrication of materials by femtosecond lasers for photonics applications. *J. Appl. Phys.* **106**, 051101 (2009)
18. M. Thiel, H. Fischer, G. von Freymann, M. Wegener, Three-dimensional chiral photonic superlattices. *Opt. Lett.* **35**, 166–168 (2010)
19. H.S. Kim, S.O. Hwang, Y. Myung, J. Park, Three-dimensional structure of helical and zigzagged nanowires using electron tomography. *Nano Lett.* **8**, 551–557 (2005)
20. K. Ding, J. Ai, Q. Deng, B. Huang, C. Zhou, T. Duan, Y. Duan, L. Han, J. Jiang, S. Che, Chiral mesostructured BiOBr films with circularly polarized colour response. *Angew. Chem. Int. Ed.* **60**, 19024–19029 (2021)
21. J.A. Kelly, M. Giese, K.E. Shopsowitz, W.Y. Hamad, M.J. MacLachlan, The development of chiral nematic mesoporous materials. *Acc. Chem. Res.* **47**, 1088–1096 (2014)
22. J. Yeom, B. Yeom, H. Chan, K.W. Smith, S. Dominguez-Medina, J.H. Bahng, G. Zhao, W.-S. Chang, S.-J. Chang, A. Chuvilin, D. Melnikau, A.L. Rogach, P. Zhang, S. Link, P. Král, N.A. Kotov, Chiral templating of self-assembling nanostructures by circularly polarized light. *Nat. Mat.* **14**, 66–72 (2015)
23. I.J. Hodgkinson, A. Lakhtakia, Q.h. Wu, L. De Silva, M.W. McCall, Ambichiral, equichiral and finely chiral layered structures. *Opt. Commun.* **239**, 353–358 (2004)

24. E. Reusch, Untersuchung über Glimmercombinationen. *Ann. Phys. Chem.* **138**, 628–638 (1869)
25. E. Reusch, Optical investigations on periodic multilayers of mica, in *More Adventures in Contemporary Electromagnetic Theory*, ed. by F. Chiadini, V. Fiumara (Springer, Cham, 2024). This is an English translation of Ref. [24].
26. Q. Zaidi, Last but not the least. *Perception* **34**, 121–123 (2005). <https://doi.org/10.1068/p5359>
27. Y. Bouligand, Sur une architecture torsadée répandue dans de nombreuses cuticules d'Arthropodes. *C. R. Acad. Sci. Phys.* **261**, 3665–3668 (1965)
28. Y. Bouligand, Liquid crystals and biological morphogenesis: ancient and new questions. *C. R. Acad. Sci. Chimie* **11** 281–296 (2008)
29. I. Šolc, A new kind of double refracting filter. *Czech. J. Phys.* **4**, 65–66 (1954)
30. A. Lakhtakia, Dielectric sculptured thin films as Šolc filters. *Opt. Eng.* **37**, 1870–1875 (1998)
31. E. Ertekin, A. Lakhtakia, Sculptured thin film Šolc filters for optical sensing of gas concentration. *Eur. Phys. J. Appl. Phys.* **5**, 45–50 (1999)
32. L. Dettwiller, Polarizing Šolc filters: a pedagogical derivation in the complex plane. *Comptes Rendus Physique* **22**, 89–97 (2021)
33. G. Joly, J. Billard, Quelques champs électromagnétiques dans les piles de Reusch II. Piles éclairées sous l'incidence normale par des ondes monochromatiques planes et uniformes. *J. Opt.* **13**, 227–238 (1982)
34. M. Dixit, A. Lakhtakia, Electrically controlled Bragg resonances of an ambichiral electro-optic structure: oblique incidence. *Asian J. Phys.* **17**, 213–223 (2008)
35. G. Joly, J. Billard, Quelques champs électromagnétiques dans les piles de Reusch IV. Domaines multiples de réflexion sélective. *J. Opt.* **17**, 211–221 (1986)
36. M. Faryad, A. Lakhtakia, The circular Bragg phenomenon. *Adv. Opt. Photonics* **6**, 225–292 (2014)
37. P. Kinsler, How to be causal: time, spacetime and spectra. *Euro. J. Phys.* **32**, 1687–1700 (2011)
38. J. Wang, A. Lakhtakia, J.B. Geddes III, Multiple Bragg regimes exhibited by a chiral sculptured thin film half-space on axial excitation. *Optik* **113**, 213–221 (2002)
39. A. Lakhtakia, J.T. Moyer, Post- versus pre-resonance characteristics of axially excited chiral sculptured thin films. *Optik* **113**, 97–99 (2002)
40. M. Dixit, A. Lakhtakia, Selection strategy for circular-polarization-sensitive rejection characteristics of electro-optic ambichiral Reusch piles. *Opt. Commun.* **281** 4812–4823 (2008)
41. R. Nityananda, On the theory of light propagation in cholesteric liquid crystals. *Mol. Cryst. Liq. Cryst.* **21**, 315–331 (1973)
42. S. Garoff, R.B. Meyer, R. Barakat, Kinematic and dynamic light scattering from the periodic structure of a chiral smectic C liquid crystal. *J. Opt. Soc. Am.* **68**, 1217–1225 (1978)
43. C. Oldano, P. Allia, L. Trossi, Optical properties of anisotropic periodic helical structures. *J. Phys.* **46**, 573–582 (1985)
44. I. Abdulhalim, L. Benguigui, R. Weil, Selective reflection by helicoidal liquid crystals. Results of an exact calculation using the 4×4 characteristic matrix method. *J. Phys.* **46**, 815–825 (1985)
45. S. Erten, A. Lakhtakia, G.D. Barber, Experimental investigation of circular Bragg phenomenon for oblique incidence. *J. Opt. Soc. Am. A* **32**, 764–770 (2015)
46. P.D. McAtee, A. Lakhtakia, Experimental and theoretical investigation of the co-occurrence of linear and circular dichroisms for oblique incidence of light on chiral sculptured thin films. *J. Opt. Soc. Am. A* **35**, 1131–1139 (2018). Replace “ $-(z-L)$ ” by “ $+(z-L)$ ” in Eq. (8b)
47. H.J. Gerritsen, R.T. Yamaguchi, A microwave analog of optical rotation in cholesteric liquid crystals. *Am. J. Phys.* **39**, 920–923 (1971)
48. N.V. Rudakova, I.V. Timofeev, S.Y. Vetrov, W. Lee, All-dielectric polarization-preserving anisotropic mirror. *OSA Continuum* **1**, 682–689 (2018)
49. R.A. Fiallo, A. Lakhtakia, M.W. Horn, Polarization-universal bandgaps realized with columnar thin films. *J. Nanophotonics* **16**, 046004 (2022)

50. A.C. van Popta, M.J. Brett, J.C. Sit, Double-handed circular Bragg phenomena in polygonal helix thin films. *J. Appl. Phys.* **98**, 083517 (2005)
51. G. Joly, J. Billard, Quelques champs électromagnétiques dans les piles de Reusch III. Biréfringence elliptique des vibrations itératives; activité optique de piles hélicoïdales d'extension finie. *J. Opt.* **16**, 203–213 (1985)
52. F. Babaei, On optical rotation and selective transmission in ambichiral sculptured thin films. *J. Mod. Opt.* **60**, 1370–1375 (2013)
53. I. Abdulhalim, Effect of the number of sublayers on axial optics of anisotropic helical structures. *Appl. Opt.* **47**, 3002–3008 (2008)
54. F. Babaei, On circular Bragg regimes in ellipsometry spectra of ambichiral sculptured thin films. *J. Mod. Opt.* **60**, 886–890 (2013)
55. M. Faryad, A. Lakhtakia, Evolution of surface-plasmon-polariton and Dyakonov–Tamm waves with the ambichirality of a partnering dielectric material. *J. Nanophotonics* **8**, 083082 (2014)
56. V. Vepachedu, P.D. McAtee, A. Lakhtakia, Nonexhibition of Bragg phenomenon by chevronic sculptured thin films: experiment and theory. *J. Nanophotonics* **11**, 036018 (2017)
57. A. Lakhtakia, V.C. Venugopal, On Bragg reflection by helicoidal bianisotropic mediums. *Arch. Elektronik Übertragungstechnik* **53**, 287–290 (1999)
58. T.G. Mackay, A. Lakhtakia, *The Transfer-Matrix Method in Electromagnetics and Optics* (Morgan & Claypool, San Ramon, 2020)
59. M. Frisch, ‘The most sacred tenet’? Causal reasoning in physics. *Br. J. Philos. Sci.* **60**, 459–474 (2009)
60. H. Silva, B. Gross, Some measurements on the validity of the principle of superposition in solid dielectrics. *Phys. Rev.* **60**, 684–687 (1941)
61. W.S. Weighofer, A. Lakhtakia, On causality requirements for material media. *Archiv für Elektronik und Übertragungstechnik* **50**, 389–391 (1996)
62. F. Wooten, *Optical Properties of Solids* (Academic, New York, 1972). Sec. 3.1
63. A. Lakhtakia, Transmission-mode geometric-phase signatures of circular Bragg phenomenon. *J. Opt. Soc. Am. B* **41**, 500–507 (2024)
64. A. Lakhtakia, Geometric phase in plane-wave transmission by a dielectric structurally chiral slab with a central phase defect. *Phys. Rev. A* **109**, 053517 (2024)
65. T.G. Mackay, A. Lakhtakia, Modeling columnar thin films as platforms for surface-plasmonic-polaritonic optical sensing. *Photonics Nanostruct. Fundam. Appl.* **8**, 140–149 (2010)
66. A. Perot, C. Fabry, On the application of interference phenomena to the solution of various problems of spectroscopy and metrology. *Astrophys. J.* **9**, 87–115 (1899)
67. A. Lakhtakia, R. Messier, Reflection at the Motohiro–Taga interface of two anisotropic materials with columnar microstructures. *Opt. Eng.* **33**, 2529–2534 (1994)
68. G.Y. Slepyan, A.S. Maksimenko, Motohiro–Taga interface in sculptured thin films—absence of Bragg phenomena. *Opt. Eng.* **37**, 2843–2847 (1998)
69. I. Hodgkinson, Q.h. Wu, B. Knight, A. Lakhtakia, K. Robbie, Vacuum deposition of chiral sculptured thin films with high optical activity. *Appl. Opt.* **39**, 642–649 (2000)
70. S.M. Pursel, M.W. Horn, Prospects for nanowire sculptured thin-film devices. *J. Vac. Sci. Technol. B* **25**, 2611–2615 (2007)
71. P.D. McAtee, A. Lakhtakia, Reflection and transmission of obliquely incident light by chiral sculptured thin films fabricated using asymmetric serial-bideposition technique. *J. Nanophotonics* **11**, 043502 (2017)
72. A. Lakhtakia, The circular Bragg phenomenon updated, in *More Adventures in Contemporary Electromagnetic Theory*, ed. by F. Chiadini, V. Fiumara (Springer, Cham, 2024)
73. L. Garza-Soto, N. Hagen, D. Lopez-Mago, Y. Otani, Wave description of geometric phase. *J. Opt. Soc. Am. A* **40**, 388–396 (2023)



Akhlesh Lakhtakia received his B.Tech. (1979) and D.Sc. (2006) degrees from the Banaras Hindu University and his M.S. (1981) and Ph.D. (1983) degrees from the University of Utah. He joined the Department of Engineering Science and Mechanics at The Pennsylvania State University in 1983, where now he is Evan Pugh University Professor of Engineering Science and Mechanics. He is also a Visiting Professor of Mathematics at the University of Edinburgh.

Dr. Lakhtakia has been elected a fellow of Optical Society of America, SPIE, Institute of Physics (UK), American Association for the Advancement of Science, American Physical Society, Institute of Electrical and Electronics Engineers, Royal Society of Chemistry, Royal Society of Arts, and Sigma Xi. He has been designated a Distinguished Alumnus of both of his *almae matres* at the highest level. Awards at Penn State include: Outstanding Research Award, Outstanding Advising Award, Premier Research Award, Outstanding Teaching Award, and the Faculty Scholar Medal in Engineering. He received the 2010 SPIE Technical Achievement Award, the 2016 Walston Chubb Award for Innovation, the 2022 Smart Structures and Materials Lifetime Achievement Award, the 2022 IEEE Antennas and Propagation Society Distinguished Achievement Award, the 2022 Radio Club of America Lifetime Achievement Award, and the 2024 SPIE Gold Medal. He has served as a Sigma Xi Distinguished Lecturer (2022–24) and a Jefferson Science Fellow at the US State Department (2022–23). His current research interests include electromagnetic scattering, surface multiplasmonics, photovoltaic solar cells, sculptured thin films, mimics, engineered biomimicry, and forensic science.

UWVF: A Trefftz Numerical Method for Maxwell's Equations



Timo Lähivaara , William F. Hall, Matti Malinen, Dale Ota, Vijaya Shankar, and Peter Monk 

1 Introduction

In 1926, Erich Trefftz [1] proposed to use a superposition of known solutions to a linear partial differential equation to approximate the true solution. In recent years, the term “Trefftz method” now indicates that an approximation scheme (which might be very different from Trefftz’s original proposal) uses exact solutions as part of the solution procedure [2]. This chapter will present a discussion of a particular Trefftz-based solution method for approximating the time harmonic Maxwell’s equations on a finite element mesh. We will use our Trefftz code *ParMax* to provide numerical results, illustrate some of the features of mesh-based Trefftz methods for Maxwell’s equations, and comment on possible improvements and extensions.

In the context of computational electromagnetism, Trefftz methods have made significant contributions. An example is the T-matrix method of Waterman [3–5] for solving a scattering problem in the exterior of a smooth bounded scatterer. This uses a superposition of solutions of the exterior problem in terms of Hankel functions to approximate the scattered wave. A variational technique is used

T. Lähivaara

Department of Technical Physics, University of Eastern Finland, Kuopio, Finland

e-mail: timo.lahivaara@uef.fi

W. F. Hall · D. Ota · V. Shankar

HyperComp Inc., Westlake Village, CA, USA

e-mail: wfhall@hypercomp.net; dkota@hypercomp.net; vshankar@hypercomp.net

M. Malinen

Kuava Inc., Kuopio, Finland

e-mail: matti.malinen@kuava.fi

P. Monk (✉)

Department of Mathematical Sciences, University of Delaware, Newark, DE, USA

e-mail: monk@udel.edu

to impose the perfect electrically conducting (PEC) boundary condition on the scatter and determine the coefficients in this expansion. The T-matrix method is a highly efficient numerical scheme provided the solution can be continued into the interior of the scatter such that the special function expansion can converge rapidly. However, the method cannot easily be modified to provide an efficient approximation of the solution when corner and edge effects introduce singularities.

One way to take into account corner and edge effects (and inhomogeneous media) is to couple a Trefftz method for the exterior domain to the finite element method in a suitable region containing the scatterer. For example, Casati et al. [6] use the Method of Auxiliary Sources to approximate the field scattered by a bounded scatterer outside a smooth artificial boundary containing the scatterer. The field in the exterior domain is approximated as a weighted sum of the fields due to finitely many point sources located inside the artificial boundary. This exterior field is coupled to a finite element method solution that is used in the interior of the artificial boundary. Extensive numerical experiments in [6] show the good performance of the method. Issues arise concerning the placement of the auxiliary sources if the artificial boundary has regions of high curvature (see for example [7] in 2D), and this is perhaps the main drawback of the method. In addition, as currently reported, the method uses a direct solver for the linear system resulting from the finite element and Trefftz discretization with the attendant need for large requirements for computer memory. This is due to the fact that the Method of Auxiliary Sources couples all finite element unknowns on the artificial boundary (in the same way as would a Dirichlet-to-Neumann approach).

Another way to ameliorate the slow convergence of Trefftz methods near singularities, while retaining their advantages in approximating fields in free space and near smooth boundaries, is to use local Trefftz methods on geometric elements in a finite element style grid. The Trefftz functions on each element are then coupled using a variational formulation to enforce approximate transmission conditions. One obvious way to couple the fields is to use a least squares method to minimize the jump in the tangential electric and magnetic fields on each face in the mesh [8]. The resulting matrix problem is symmetric positive definite, a preconditioner is developed, and the method is also proved to converge [8].

An alternative approach that we have followed is the Ultra Weak Variational Formulation (UWVF) of Maxwell's equations due to Cessenat and Déspres [9, 10]. In this chapter, we shall give an introduction to the UWVF (see Sect. 2). The classical UWVF uses a tetrahedral finite element grid. On each element in the grid, the solution of the adjoint Maxwell system is approximated by a superposition of plane waves propagating in various directions. The amplitude of the plane wave solutions is found by solving a global sparse matrix problem resulting from a natural variational formulation. An advantage is that the resulting linear system can be solved simply by using the bi-conjugate gradient method (BiCG). We have found that the UWVF is efficient for approximating solutions of Maxwell's equations for a wide range of test problems. As the frequency of the electromagnetic field increases, the UWVF becomes more efficient than edge finite element methods [11].

It was realized, first for the Helmholtz equation [12, 13] and later for Maxwell's equations, that the UWVF is a special case of a Trefftz-discontinuous Galerkin (Trefftz-DG) method provided the scattering medium is lossless. In this special case, it is then possible to use techniques from the theory of discontinuous Galerkin methods, together with approximation error estimates for plane wave expansions to derive convergence results for the Trefftz-DG method and hence for the UWVF [14]. That analysis proves that Trefftz methods of this type converge, even if the solution is not analytic, as the mesh size decreases. In terms of the mesh size, the order of the approximation increases as the number of plane waves per element increases (with an upper limit depending on the smoothness of the solution). For an overview of the techniques used in that analysis, and for more details of the history of Trefftz-DG methods for the related Helmholtz problem, see [15].

The Trefftz-DG approach to solving Maxwell's equations has the advantage compared to UWVF of introducing extra parameters that can be tuned to improve the performance of the algorithm. In [16], Hiptmair et al. suggest using mesh-dependent coefficients to handle grid refinement near singularities. However, in their interesting paper on adaptivity for Trefftz-DG schemes for the Helmholtz equation (including directional adaptivity), Congreve et al. [17] use a constant choice of the Trefftz-DG parameters giving a scheme equivalent to the UWVF, and state that they do not observe quantitative differences using mesh-dependent parameters. Examples in that paper show how the Trefftz-DG scheme can approximate singular solutions.

We have developed an MPI-parallel implementation of the UWVF for Maxwell's equations called *ParMax* with the goal of providing a flexible solver for electrically large problems compared to those usually solved using the finite element method [11, 15]. Extensions to the original UWVF include: support for the Perfectly Matched Layer (PML) absorbing medium [15], elements with curved boundaries, more general element types, a reduced memory version, and the inclusion of a model for resistive sheets [11]. Besides outlining the general UWVF approach, this chapter describes the continued development of *ParMax* by discussing support for a new element type: pyramids. These elements are useful for joining regions covered by tetrahedral elements to those covered with prismatic or hexahedral elements. We also examine further the use of polynomial mappings to approximate smooth boundaries and in particular the use of quartic fits to smooth boundaries.

In our recent paper [11], the majority of the examples are for scattering by a spherical scatterer (penetrable or PEC) because this case has an exact series solution for comparison. However, the sphere is a very special case having a smooth boundary with constant curvature, which allows the full approximation properties of the Trefftz functions and a simple mesh density criterion. Another example in that paper, scattering from aircraft, did not have an analytic solution for comparison. To continue our study, in this chapter, we consider the approximation of the far-field pattern for an almond-shaped scatterer. This scatterer has regions of high curvature and a sharp tip that can create a singularity in the electromagnetic field as the tip is approached. We demonstrate that the UWVF can be used for this test problem and compare the results to published measured data [18].

The remainder of this chapter is as follows. In Sect. 2, we briefly recall the classical UWVF for Maxwell's equations, discuss the discrete UWVF using plane wave bases, comment on the conditioning of the resulting matrix problem, and revisit the implementation of the PML. In Sect. 3, we show how we integrated pyramidal elements into the code and provide a numerical example of their use. In Sect. 4, we discuss how *ParMax* can approximate smooth surfaces, and in Sect. 4.1, we first study surface approximation for a PEC sphere. Then we in Sect. 4.2 give results for a dielectric (penetrable) sphere. In Sect. 5, we move on to provide results for a perfectly conducting almond having the same shape as the NASA almond [19], but comparing to published data from [18]. We end with some comments and a conclusion.

All the finite element meshes in this chapter were generated by COMSOL Multiphysics. Computations are run on the parallel cluster computer Puhti at the CSC—IT Center for Science Ltd, Finland. A detailed description of this supercomputer can be found on the CSC's website [20].

Concerning notation, $i = \sqrt{-1}$ and bold face quantities represent vectors. We assume $\exp(-i\omega t)$ dependence on time t , where ω is the angular frequency of the radiation. For a suitable surface $S \subset \mathbb{R}^3$ with normal \mathbf{v} , we recall the definition of the space of square integrable tangential vector fields

$$\mathbf{L}_T^2(S) = \{\mathbf{u} \in (L^2(S))^3 \mid \mathbf{u} \cdot \mathbf{v} = 0\}$$

having norm denoted by $\|\cdot\|_{2,S}$.

2 The UWVF for Maxwell's Equations

We are concerned with solving the linear, time-harmonic Maxwell system for scattering applications. To truncate the unbounded computational domain typical for such problems, we usually use a PML. However, to simplify the presentation of the UWVF, we first describe the UWVF for a boundary value problem on a bounded domain (see Sect. 2.1). Later in Sect. 2.4, we show how a PML can be implemented.

To describe the main features of the UWVF, we assume that we have a bounded source free domain $\Omega \subset \mathbb{R}^3$, which is Lipschitz and piecewise smooth (it can have disconnected boundary components) and hence has unit outward normal \mathbf{v} almost everywhere. In Ω , the complex time harmonic electric field phasor \mathbf{E} satisfies the following time harmonic Maxwell equation:

$$\nabla \times \mu^{-1} \nabla \times \mathbf{E} - \kappa^2 \epsilon \mathbf{E} = 0 \text{ in } \Omega. \quad (1)$$

Here ϵ is the complex-valued relative electric permittivity, and μ is the complex-valued relative magnetic permeability. The wave number is denoted $\kappa = \omega \sqrt{\epsilon_0 \mu_0}$ where ω is the angular frequency of the radiation, and (ϵ_0, μ_0) are the electric permittivity and magnetic permeability of free space, respectively. Because of the

later use of a plane wave Trefftz approximation, ϵ and μ must be piecewise constant in Ω .

It is convenient for the development of the UWVF to assume the following generalized impedance boundary condition on the boundary of Ω denoted $\partial\Omega$:

$$\mathbf{v} \times \mu^{-1} \nabla \times \mathbf{E} - i\kappa Z \mathbf{E}_T = Q(\mathbf{v} \times \mu^{-1} \nabla \times \mathbf{E} + i\kappa Z \mathbf{E}_T) + \mathbf{g} \text{ on } \partial\Omega. \quad (2)$$

Here $\mathbf{E}_T = \mathbf{v} \times (\mathbf{E} \times \mathbf{v})$ is the tangential component of the electric field on $\partial\Omega$. In addition, Q is a complex scalar valued function on the boundary with $|Q| \leq 1$, and $\mathbf{g} \in \mathbf{L}_T^2(\partial\Omega)$ is a given source function. The positive parameter Z is defined on the boundary $\partial\Omega$, and we take it to be $Z = \sqrt{|\mu|}/\sqrt{|\epsilon|}$. Note that the choice $Q = 1$ corresponds to a PEC-type boundary condition

$$\mathbf{E}_T = -\frac{1}{2i\kappa Z} \mathbf{g}.$$

More generally, if $Q \neq 1$, the boundary condition can be rewritten as

$$\mathbf{v} \times \mu^{-1} \nabla \times \mathbf{E} - i\kappa Z \left(\frac{1+Q}{1-Q} \right) \mathbf{E}_T = \frac{1}{1-Q} \mathbf{g} \text{ on } \partial\Omega.$$

Once Z is chosen, the choice of Q can then be used to implement a standard impedance boundary condition ($Q = 0$ and $Z = 1$ correspond to a low-order absorbing boundary condition). The wavenumber κ is assumed not to be a resonance frequency for the problem of solving (1) with boundary conditions (2) so that an exact solution exists for the problem provided $\mathbf{g} \in \mathbf{L}_T^2(\partial\Omega)$.

As usual for a discontinuous Galerkin method, the definition of the method starts by choosing a finite element mesh denoted \mathcal{T}_h of non-intersecting and non-degenerate geometric elements that cover Ω and have maximum element diameter $h > 0$. The mesh elements must satisfy the geometric constraints from [15], and in our work so far, these elements are curvilinear tetrahedra, prisms, or hexahedra (i.e., generalizations of the standard elements allowing for curved faces and edges). In the remainder of the chapter, K will denote an element in the mesh having boundary ∂K and outward normal \mathbf{v}^K .

It is important that the functions ϵ and μ be constant on each element in the mesh but they can vary between different elements. We extend Z to a piecewise constant function that is constant on each face in the mesh as follows: if F denotes a face shared by elements K and K' then we set

$$\hat{\epsilon} = \begin{cases} |\sqrt{\epsilon|_K \epsilon|_{K'}}| & \text{on } F = K \cap K' \text{ for } K, K' \in \mathcal{T}_h \\ |\epsilon| & \text{on boundary faces,} \end{cases}$$

where $|_K$ denotes the restriction to K . The edge function $\hat{\mu}$ is defined in the same way. Then $Z = \sqrt{\hat{\mu}}/\sqrt{\hat{\epsilon}}$ on F .

2.1 Derivation of the UWVF

We are now in a position to derive the UWVF for Maxwell's equations (before discretization) following [9, 11]. Consider an element $K \in \mathcal{T}_h$. Taking the dot product of Maxwell's equations (1) with the complex conjugate of a smooth test vector function ξ^K and integrating by parts twice gives

$$\begin{aligned}
 0 &= \int_K (\nabla \times \mu^{-1} \nabla \times \mathbf{E} - \kappa^2 \epsilon \mathbf{E}) \cdot \overline{\xi^K} dV \\
 &= \int_K \left[(\mu^{-1} \nabla \times \mathbf{E}) \cdot \nabla \times \overline{\xi^K} - \kappa^2 \epsilon \mathbf{E} \cdot \overline{\xi^K} \right] dV \\
 &\quad + \int_{\partial K} (\mathbf{v}^K \times \mu^{-1} \nabla \times \mathbf{E}) \cdot \overline{\xi^K}_T dA \\
 &= \int_K \mathbf{E} \cdot \left(\nabla \times \overline{\mu^{-1} \nabla \times \xi^K} - \kappa^2 \overline{\epsilon} \xi^K \right) dV \\
 &\quad + \int_{\partial K} \left[(\mathbf{v}^K \times \mu^{-1} \nabla \times \mathbf{E}) \cdot \overline{\xi^K}_T + \mathbf{v}^K \times \mathbf{E} \cdot (\overline{\mu^{-1} \nabla \times \xi^K})_T \right] dA = 0,
 \end{aligned}$$

where $\mathbf{w}_T = (\mathbf{v}^K \times \mathbf{w}) \times \mathbf{v}^K$ on ∂K for any sufficiently smooth vector function \mathbf{w} . The overline in the above formula denotes complex conjugation.

If ξ^K solves the following adjoint Maxwell system in K given by

$$\nabla \times \overline{\mu}^{-1} \nabla \times \xi^K - \kappa^2 \overline{\epsilon} \xi^K = 0 \text{ in } K, \quad (3)$$

then we obtain the fundamental identity

$$\int_{\partial K} \left[(\mathbf{v}^K \times \mu^{-1} \nabla \times \mathbf{E}) \cdot \overline{\xi^K}_T + \mathbf{v}^K \times \mathbf{E} \cdot (\overline{\mu^{-1} \nabla \times \xi^K})_T \right] dA = 0.$$

Using this identity, we can derive the formula that underlies the UWVF.

Expanding both integral terms on the left hand side, and using the fundamental equality shows that

$$\begin{aligned}
 &\int_{\partial K} \frac{1}{Z} \left(\mathbf{v}^K \times \mu^{-1} \nabla \times \mathbf{E} + i\kappa Z \mathbf{E}_T \right) \cdot \left(\overline{\mathbf{v}^K \times \mu^{-1} \nabla \times \xi^K + i\kappa Z \xi^K_T} \right) dA \\
 &\quad - \int_{\partial K} \frac{1}{Z} \left(\mathbf{v}^K \times \mu^{-1} \nabla \times \mathbf{E} - i\kappa Z \mathbf{E}_T \right) \cdot \left(\overline{\mathbf{v}^K \times \mu^{-1} \nabla \times \xi^K - i\kappa Z \xi^K_T} \right) dA \\
 &= -2i\kappa \int_{\partial K} \left[(\mathbf{v}^K \times \mu^{-1} \nabla \times \mathbf{E}) \cdot \overline{\xi^K}_T + \mathbf{v}^K \times \mathbf{E} \cdot (\overline{\mu^{-1} \nabla \times \xi^K})_T \right] dA = 0.
 \end{aligned}$$

We have thus proved next equality (see [9, Theorem 13, page 97]) that underlies the UWVF:

$$\begin{aligned}
& \int_{\partial K} \frac{1}{Z} \left(\mathbf{v}^K \times \mu^{-1} \nabla \times \mathbf{E} + i\kappa Z \mathbf{E}_T \right) \cdot \left(\overline{\mathbf{v}^K \times \mu^{-1} \nabla \times \boldsymbol{\xi}^K + i\kappa Z \boldsymbol{\xi}_T^K} \right) dA \\
& = \int_{\partial K} \frac{1}{Z} \left(\mathbf{v}^K \times \mu^{-1} \nabla \times \mathbf{E} - i\kappa Z \mathbf{E}_T \right) \cdot \left(\overline{\mathbf{v}^K \times \mu^{-1} \nabla \times \boldsymbol{\xi}^K - i\kappa Z \boldsymbol{\xi}_T^K} \right) dA.
\end{aligned} \tag{4}$$

The faces of an element K in the mesh will either be shared with a neighboring element or be on the boundary $\partial\Omega$. For a face shared with an element K' having field $\mathbf{E}' = \mathbf{E}|_{K'}$ we have, by the transmission conditions for Maxwell's equations across a surface,

$$\mathbf{E}_T = \mathbf{E}'_T \text{ and } \mathbf{v}^K \times \mu^{-1} \nabla \times \mathbf{E} = -\mathbf{v}^{K'} \times \mu^{-1} \nabla \times \mathbf{E}',$$

where we used $\mathbf{v}^K = -\mathbf{v}^{K'}$. Thus

$$\mathbf{v}^K \times \mu^{-1} \nabla \times \mathbf{E} - i\kappa Z \mathbf{E}_T = - \left(\mathbf{v}^{K'} \times \mu^{-1} \nabla \times \mathbf{E}' + i\kappa Z \mathbf{E}'_T \right) \text{ on } K \cap K'.$$

This equality is used to couple fields on adjacent elements via the right-hand side of (4). For faces on $\partial\Omega$, the boundary condition (2) can be used to replace the same term for faces on $\partial\Omega$.

We obtain

$$\begin{aligned}
& \int_{\partial K} \frac{1}{Z} \left(\mathbf{v}^K \times \mu^{-1} \nabla \times \mathbf{E} + i\kappa Z \mathbf{E}_T \right) \cdot \left(\overline{\mathbf{v}^K \times \mu^{-1} \nabla \times \boldsymbol{\xi} + i\kappa Z \boldsymbol{\xi}_T} \right) dA \\
& = \sum_{K' \neq K} \int_{\partial K \cap \partial K'} \frac{-1}{Z} \left(\mathbf{v}^{K'} \times \mu^{-1} \nabla \times \mathbf{E}' + i\kappa Z \mathbf{E}'_T \right) \\
& \quad \cdot \left(\overline{\mathbf{v}^K \times \mu^{-1} \nabla \times \boldsymbol{\xi} - i\kappa Z \boldsymbol{\xi}_T} \right) dA \\
& \quad + \int_{\partial K \cap \Gamma} \frac{1}{Z} \left[Q \left(\mathbf{v}^K \times \mu^{-1} \nabla \times \mathbf{E} + i\kappa Z \mathbf{E}_T \right) + \mathbf{g} \right] \\
& \quad \cdot \left(\overline{\mathbf{v}^K \times \mu^{-1} \nabla \times \boldsymbol{\xi} - i\kappa Z \boldsymbol{\xi}_T} \right) dA.
\end{aligned} \tag{5}$$

This can be simplified by defining the boundary quantities

$$\begin{aligned}
\mathcal{X}_K &= \mathbf{v}^K \times \mu^{-1} \nabla \times \mathbf{E}|_K + i\kappa Z (\mathbf{E}|_K)_T \text{ on } \partial K, \\
\mathcal{Y}_K &= \mathbf{v}^K \times \mu^{-1} \nabla \times \boldsymbol{\xi}^K + i\kappa Z \boldsymbol{\xi}_T^K \text{ on } \partial K,
\end{aligned}$$

for each element K in the mesh.

One more component is needed to complete a more concise statement of the UWVF. Cessenat [9] defines the operator $\mathbf{F}_K : \mathbf{L}_T^2(\partial K) \rightarrow \mathbf{L}_T^2(\partial K)$ by setting

$$\mathbf{F}_K \mathcal{Y}_K = \mathbf{v}^K \times \mu^{-1} \nabla \times \boldsymbol{\xi}^K - i\kappa Z \boldsymbol{\xi}_T^K.$$

Now we can now use the aforementioned notation to rewrite equation (5). For each element K in the mesh, the unknown boundary flux $\mathcal{X}_K \in \mathbf{L}_T^2(\partial K)$ satisfies

$$\begin{aligned} \int_{\partial K} \frac{1}{Z} \mathcal{X}_K \cdot \mathcal{Y}_K dA &= \sum_{K' \neq K} \int_{\partial K \cap \partial K'} \frac{1}{Z} \mathcal{X}_{K'} \cdot \mathbf{F}_K \mathcal{Y}_K dA \\ &+ \int_{\partial K \cap \Gamma} \frac{1}{Z} [Q\mathcal{X}_K + \mathbf{g}] \cdot \mathbf{F}_K \mathcal{Y}_K dA, \end{aligned} \quad (6)$$

for all test functions $\mathcal{Y}_K \in \mathbf{L}_T^2(\partial K)$. This is the UWVF before discretization. Note that equation (6) holds element by element in the mesh.

If ϵ and μ are real, $\boldsymbol{\xi}^K$ and \mathbf{E} both satisfy Maxwell's equations (1) element by element. In that case, we can take $\boldsymbol{\xi}^K = \mathbf{E}$ in (4) to obtain the following

$$\|\mathcal{X}_K\|_{2,\partial K} = \|\mathbf{F}_K \mathcal{X}_K\|_{2,\partial K} \text{ for all } \mathcal{X}_K \in \mathbf{L}_T^2(\partial K).$$

This shows that \mathbf{F}_K is an isometry. Using this fact, Cessenat [9] proves that, provided the non-resonance condition holds, the UWVF system (6) has a unique solution. This fact can also be proved using the equivalent Trefftz-DG scheme.

2.2 The Plane Wave Basis

To obtain a computable scheme, it is necessary to discretize the fields \mathcal{X}_K and \mathcal{Y}_K on the boundary of each element $K \in \mathcal{T}_h$. The key issue is that, given a discrete boundary field \mathcal{Y}_K , we need to be able to compute $\mathbf{F}_K \mathcal{Y}_K$. To do this, we have used the method proposed by Cessenat [9]: an indirect discretization of $\mathbf{L}_T(\partial K)$ using the traces of plane waves defined on the interior of K .

To be more precise, we enumerate the elements in \mathcal{T}_h as K_1, K_2, \dots, K_N . Then for the k th element in the mesh K_k let p_k denote the number of plane wave directions on this element. Let $\mathbf{d}_{k,\ell}$, $\ell = 1, \dots, p_k$ denote linearly independent unit vectors giving the directions of the plane wave in K_k . Since $\boldsymbol{\xi}^K$ needs to satisfy the adjoint Maxwell system, the plane wave functions can be chosen as

$$\boldsymbol{\xi}_{k,\ell,m} = \mathbf{A}_{k,\ell,m} e^{i\kappa \sqrt{\epsilon_k \mu_k} \mathbf{d}_{k,\ell} \cdot (\mathbf{x} - \mathbf{x}_{k,0})}$$

for $m = 1, 2$, $\ell = 1, \dots, p_k$. Here $\mathbf{x}_{k,0}$ is the centroid of the element K_k , the polarization vectors $\mathbf{A}_{k,\ell,m}$ are such that $\mathbf{A}_{k,\ell,1} \neq 0$, $\mathbf{A}_{k,\ell,1} \cdot \mathbf{d}_{k,\ell} = 0$ and $\mathbf{A}_{k,\ell,2} = \mathbf{d}_{k,\ell} \times \mathbf{A}_{k,\ell,1}$. Using the definition of \mathcal{Y}_K , we then define test functions on ∂K_k by

$$\mathcal{Y}_{k,\ell,m} = \mathbf{v}^K \times \mu^{-1} \nabla \times \boldsymbol{\xi}_{k,\ell,m} + i\kappa Z \boldsymbol{\xi}_{k,\ell,m,T}.$$

We can now create a discrete space of functions on ∂K :

$$\mathbf{W}_{k,p_k} = \text{span}\{\mathcal{Y}_{k,\ell,m} \mid m = 1, 2 \text{ and } \ell = 1, \dots, p_k\}. \quad (7)$$

Thus, element by element, \mathcal{X}_{K_k} is approximated by

$$\mathcal{X}_{k,h} = \sum_{m=1}^2 \sum_{\ell=1}^{p_k} x_{k,\ell,m} \mathcal{Y}_{k,\ell,m}, \quad (8)$$

where $\{x_{k,\ell,m}\}$ for $m = 1, 2$ and $\ell = 1, \dots, p_k$ are the unknown degrees of freedom (DoF) to be computed. Each geometric element is associated with $2p_k$ DoF, and the total number of unknowns for the problem is then $N_{tot} = 2 \sum_{k=1}^N p_k$.

In our code, for each p_k , the directions $\mathbf{d}_{k,\ell}$, $\ell = 1, \dots, p_k$ are chosen to be the Hammersley points on the unit sphere (with p_k from 4 to 1,200) [21]. We shall discuss more the choice of p_k in Sect. 3.1

The DoFs are computed by substituting the expression (8) for $\mathcal{X}_{k,h}$ in Eq. (6) and testing with functions \mathcal{Y}_K from the spanning set for \mathbf{W}_{k,p_k} defined in (7). Then the resulting sparse linear system is solved by BiCG.

Other choices of Trefftz functions are possible. For example, we could choose the spherical vector wave functions (see [22, Theorem 6.26]) or the Method of Auxiliary Sources element by element. Both these choices would require the use of numerical quadrature on all faces in the mesh, whereas for plane waves, the integrals can be computed exactly in closed form for flat facets.

2.3 The Discrete UWVF, Conditioning and Accuracy

To obtain a matrix problem, we can list all the N_{tot} DoF in a vector denoted $\vec{\mathcal{X}} \in \mathbb{C}^{N_{tot}}$ as follows. On each element K_k , we enumerate the local basis functions on ∂K_k , $k = 1, \dots, N$ so that $\mathcal{Y}_{k,\ell,m}$ is the $(2(\ell-1)+m)$ th local basis function. These local basis functions can then be ordered element by element. Using the global DoF vector, we then write the discrete equations based on (6) as

$$(D + C)\vec{\mathcal{X}} = \vec{g}, \quad (9)$$

where D is the $N_{tot} \times N_{tot}$ matrix corresponding to the left-hand side of Eq. (6). In particular, because of the ordering of the DoF, D is block diagonal, with each diagonal block being a $2p_k \times 2p_k$ matrix for $k = 1, \dots, N$. The k th diagonal block denoted D^k is given by

$$D_{2(\ell-1)+m, 2(r-1)+s}^k = \int_{\partial K_k} \frac{1}{Z} \mathcal{Y}_{k,\ell,m} \cdot \overline{\mathcal{Y}_{k,r,s}} dA, \quad (10)$$

for $m, r = 1, 2$ and $\ell, s = 1, \dots, p_k$. This matrix is Hermitian and positive definite. The matrix C encodes the remaining sesquilinear forms in (6), while the vector $\vec{g} \in \mathbb{C}^{N_{tot}}$ is given by the data term in (6) in the obvious way.

Since D is block diagonal, we can easily invert D and rewrite (9) as

$$(I + D^{-1}C)\vec{\chi} = D^{-1}\vec{g}. \quad (11)$$

This is the matrix system solved in *ParMax*. Note that in assembling D and C , only integrals on faces in the mesh need to be performed. Furthermore, on flat triangular facets, the integrals can be computed analytically [9], which speeds up assembly. On curved elements, numerical quadrature must be used.

Matrices from the UWVF are sparse but can be very ill-conditioned if p_k is too large or if elements have a large aspect ratio [23]. Thus, in *ParMax*, it is important that the number of basis plane wave directions p_k can vary from element to element in order to control ill-conditioning.

A particularly attractive feature of the discrete UWVF is that the simple BiConjugate-Gradient (BiCG) method can be used to solve the system (11) provided the condition number of the overall system is not too large. We control the global condition number by controlling the local condition number of the diagonal blocks of D by the choice of p_k [15]. As we shall see in the next section, this is accomplished by using a heuristic expression for p_k in terms of the size of K_k (other techniques are discussed in [15]). The MPI-parallel implementation of BiCG is relatively straightforward since it requires just parallel matrix multiplication, and the fact that elements only communicate via faces also improves parallel efficiency.

Of course, our strategy is not the only way to control conditioning. In [23] and [24], it is suggested to use a local SVD of D_k to construct basis vectors as sums of plane waves by controlling the local condition number. An interesting alternative is to use evanescent plane waves to control both conditioning and accuracy [25]. This certainly requires study in the context of Maxwell's equations.

2.4 Scattering Calculations: Inclusion of the PML

The examples in Sects. 4 and 5 are for scattering calculations. In this section, we describe how we perform these simulations and in particular describe how we implement the PML in the current version of *ParMax*. We assume that we have a bounded scatterer, which can be impenetrable (for example, with an impedance or PEC boundary condition) or penetrable (for example, a dielectric) occupying a domain $S \subset \mathbb{R}^3$. A known incident field \mathbf{E}^i impinges on the scatterer and creates an outgoing scattered field \mathbf{E}^s (see for example [22]). Then the total field $\mathbf{E} = \mathbf{E}^i + \mathbf{E}^s$ satisfies the homogeneous Maxwell system (1). The incident field \mathbf{E}^i is assumed to satisfy the background Maxwell's equations in the neighborhood of S :

$$\nabla \times \nabla \times \mathbf{E}^i - \kappa^2 \mathbf{E}^i = 0.$$

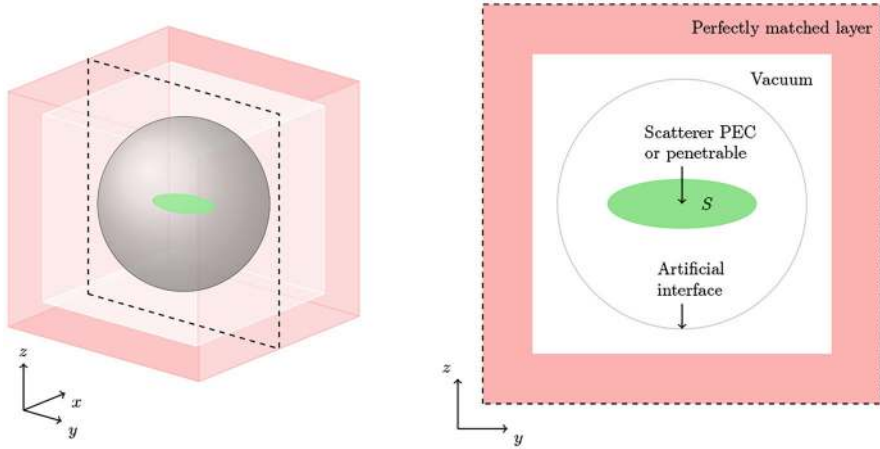


Fig. 1 A cartoon of a cross section of the geometric domains used when simulating electromagnetic scattering. The bounded scatterer S (green) is in the interior of an artificial boundary (shown in gray) separating zones in which the scattered field or total field is used. The PML occupies the outer rectilinear annular region (red)

An important example is the incident plane wave $\mathbf{E}^i = \mathbf{E}_0^i \exp(i\kappa \mathbf{d} \cdot \mathbf{x})$ where the real direction vector \mathbf{d} satisfies $\|\mathbf{d}\| = 1$ and the real polarization $\mathbf{E}_0^i \neq 0$ is such that $\mathbf{E}_0^i \cdot \mathbf{d} = 0$. The polarization and direction of propagation of this plane wave are independent from the directions and polarizations used in the discrete UWVF.

We then select a bounded computational domain Ω containing the scatterer S in its interior. We can use a simple absorbing boundary condition ($Q = 0$ in (2)) on the outer boundary, but this requires a large computational domain to achieve accuracy. Often a better approach is to use a PML. In this case, for *ParMax*, the outer boundary of Ω must be a box with sides parallel to the coordinate axes. We can then choose a rectilinear annulus in Ω of thickness $\delta_{\text{PML}} > 0$ where we impose the PML to absorb the scattered field. A cartoon of this geometry is shown in Fig. 1.

Since the UWVF does not easily handle distributed current sources, one more surface needs to be defined in the grid. We choose an artificial surface in Ω but not in the PML that contains the scatterer in its interior (see the gray sphere in Fig. 1 (left)). This surface need not be a sphere and is just required to contain the scatterers in its interior (the surface can be multiply connected if the scatterer is multiply connected). Outside this artificial interface, we compute with the scattered field \mathbf{E}^s as needed by the PML. Inside the surface we compute with the total field \mathbf{E} . The incident wave is imposed via transmission data on the artificial interface surface (see [11] for the definition of \mathbf{g} on the interface).

Next we describe how the PML is included in the current version of *ParMax*. Previous versions used the implementation describe in [15]. The slightly modified version here provides better absorption. We use the complex stretching approach to

the PML of Chew and Wheedon [26]. We note that in *ParMax* we assume $\epsilon = \mu = 1$ in the PML.

For simplicity, we only give details of the construction of the PML in the positive orthant. Suppose the PML starts at $x = a_1 > 0$ in the direction $x > 0$, at $a_2 > 0$ in the y direction and $a_3 > 0$ in the z direction. We then consider the complex stretched coordinate

$$\hat{x}_j = x_j + \int_{a_j}^{x_j} \frac{i\sigma_j^{\text{PML}}(s)}{\kappa} ds \text{ for } j = 1, 2, 3.$$

The real absorption parameters satisfies $\sigma_j^{\text{PML}}(s) > 0$ in the PML. Often $\sigma_j^{\text{PML}}(s)$ is chosen to be an increasing function of s , but because we need plane waves to incorporate into the UWVF, we assume

$$\sigma_j^{\text{PML}}(s) = \begin{cases} \sigma_j & \text{if } s > a_j \\ 0 & \text{otherwise} \end{cases}.$$

where σ_j is a positive constant. Assuming $x_j \geq 0$ for $j = 1, 2, 3$

$$\frac{d\hat{x}_j}{dx_j} = 1 + \frac{i\sigma_j^{\text{PML}}(s)}{\kappa} := \gamma_j. \quad (12)$$

Note that γ_j is piecewise constant in the PML.

Formally, we assume that the Maxwell system is satisfied in the stretched coordinates $\hat{\mathbf{x}}$ so that

$$\hat{\nabla} \times \hat{\nabla} \times \hat{\mathbf{E}} - \kappa^2 \hat{\mathbf{E}} = 0 \text{ in the PML.}$$

Then we define $\mathbf{E}_{\text{PML}} = \mathcal{D}\hat{\mathbf{E}}$ where the matrix \mathcal{D} is given by

$$\mathcal{D} = \begin{pmatrix} \gamma_1 & 0 & 0 \\ 0 & \gamma_2 & 0 \\ 0 & 0 & \gamma_3 \end{pmatrix}.$$

Transforming back to real spatial coordinates using (12), we obtain a standard Maxwell system (but with anisotropic coefficients) for \mathbf{w} :

$$\nabla \times \left(\mu_{\text{PML}}^{-1} \nabla \times \mathbf{E}_{\text{PML}} \right) - \kappa^2 \epsilon_{\text{PML}} \mathbf{E}_{\text{PML}} = 0, \quad (13)$$

where $\epsilon_{\text{PML}} = \mu_{\text{PML}}$ and

$$\epsilon_{\text{PML}} = \begin{pmatrix} \frac{\gamma_2 \gamma_3}{\gamma_1} & 0 & 0 \\ 0 & \frac{\gamma_1 \gamma_3}{\gamma_2} & 0 \\ 0 & 0 & \frac{\gamma_1 \gamma_2}{\gamma_3} \end{pmatrix}.$$

We need to find plane wave solutions of (13), and this is where we use the assumption that γ_j is constant on each element.

On an element K in the PML, we consider plane waves \mathbf{w}_{PW} of the form

$$\mathbf{w}_{PW}(\mathbf{x}) = \mathbf{E}_0^{\text{PML}} \exp(i\kappa \mathbf{d}_{\text{PML}} \cdot \mathcal{D}(\mathbf{x} - \mathbf{x}_0)),$$

where \mathbf{x}_0 is the centroid in the element K , $\mathbf{E}_0^{\text{PML}}$ is a constant polarization, and \mathbf{d}_{PML} is a unit direction vector (to be chosen as in Sect. 2.2). Then:

$$\begin{aligned} & \nabla \times \mu^{-1} \nabla \times \mathbf{w}_{PW} \\ &= -\kappa^2 (\mathcal{D} \mathbf{d}_{\text{PML}}) \times \mu^{-1} ((\mathcal{D} \mathbf{d}_{\text{PML}}) \times \mathbf{E}_0^{\text{PML}}) \exp(i\kappa \mathbf{d}_{\text{PML}} \cdot \mathcal{D}(\mathbf{x} - \mathbf{c})). \end{aligned}$$

So, for \mathbf{w}_{PW} to satisfy (13) we need to find eigenpairs $(\eta, \mathbf{E}_0^{\text{PML}})$ such that

$$(\mathcal{D} \mathbf{d}_{\text{PML}}) \times \mu_{\text{PML}}^{-1} (\mathcal{D} \mathbf{d}_{\text{PML}} \times \mathbf{E}_0^{\text{PML}}) = -\eta \epsilon_{\text{PML}} \mathbf{E}_0^{\text{PML}}. \quad (14)$$

and, to be successful, we must have $\eta = 1$ as the eigenvalue.

If we define

$$C = \begin{pmatrix} 0 & -\gamma_3 d_{\text{PML},3} & \gamma_2 d_{\text{PML},2} \\ \gamma_3 d_{\text{PML},3} & 0 & -\gamma_1 d_{\text{PML},1} \\ -\gamma_2 d_{\text{PML},2} & \gamma_1 d_{\text{PML},1} & 0 \end{pmatrix}.$$

Then $(\mathcal{D} \mathbf{d}_{\text{PML}}) \times \mathbf{E}_0^{\text{PML}} = C \mathbf{E}_0^{\text{PML}}$ and the eigenvalue problem is

$$C \mu_{\text{PML}}^{-1} C \mathbf{E}_0^{\text{PML}} = -\eta \epsilon_{\text{PML}} \mathbf{E}_0^{\text{PML}}.$$

Choosing

$$\mathbf{d}_{\text{PML}} = \begin{pmatrix} \sin(\phi) \cos(\theta) \\ \sin(\phi) \sin(\theta) \\ \cos(\phi) \end{pmatrix},$$

where (θ, ϕ) are polar angles, we obtain the following eigenvalues and eigenfunctions thanks to the computer algebra system Maple

$$\eta = 0, \quad \mathbf{E}_{0,1}^{\text{PML}} = C \mathbf{d}_{\text{PML}},$$

$$\eta = 1, \mathbf{E}_{0,2}^{\text{PML}} = \begin{pmatrix} \gamma_1 \cos(\phi) \\ 0 \\ -\gamma_3 \cos(\theta) \sin(\phi) \end{pmatrix},$$

$$\eta = 1, \mathbf{E}_{0,3}^{\text{PML}} = \begin{pmatrix} \gamma_1 \sin(\theta) \sin(\phi) \\ -\gamma_2 \cos(\theta) \sin(\phi) \\ 0 \end{pmatrix} = \sin(\phi) \begin{pmatrix} \gamma_1 \sin(\theta) \\ -\gamma_2 \cos(\theta) \\ 0 \end{pmatrix}.$$

We reject the $\eta = 0$ eigenvalue/eigenvector pair and use the remaining two polarizations. We see that

$$\mathbf{w}_{PW}(\mathbf{x}) = \mathcal{D}\hat{\mathbf{E}}_0 \exp(i\kappa \mathbf{d}_{\text{PML}} \cdot \mathcal{D}(\mathbf{x} - \mathbf{c})),$$

where $\hat{\mathbf{E}}_0$ is a standard polarization orthogonal to \mathbf{d}_{PML} .

Note the new polarizations $\mathbf{E}_0^{\text{PML}}$ are not mutually orthogonal, but they are linearly independent.

We can also check the divergence-free condition

$$\nabla \cdot (\epsilon_{\text{PML}} \mathbf{w}_{PW}) = i\kappa (\mathcal{D}\mathbf{d}_{\text{PML}}) \cdot (\epsilon_{\text{PML}} \mathbf{E}_0^{\text{PML}}) \exp(i\kappa \mathbf{d}_{\text{PML}} \cdot \mathcal{D}(\mathbf{x} - \mathbf{c}))$$

and, using the definitions of \mathcal{D} and ϵ_{PML} together with the fact that $\hat{\mathbf{E}}_0$ is orthogonal to \mathbf{d}_{PML} , we have:

$$(\mathcal{D}\mathbf{d}_{\text{PML}}) \cdot \epsilon_{\text{PML}} \mathbf{E}_0^{\text{PML}} = \mathbf{d}_{\text{PML}} \cdot (\mathcal{D}\epsilon_{\text{PML}}\mathcal{D})\hat{\mathbf{E}}_0 = 0.$$

In the UWVF, we actually need plane wave solutions of the adjoint Maxwell problem (see (3)) for the UWVF. That is, plane wave functions ξ_{PML} that satisfy

$$\nabla \times (\bar{\mu}_{\text{PML}}^{-1} \nabla \times \xi_{\text{PML}}) - \kappa^2 \bar{\epsilon}_{\text{PML}} \xi_{\text{PML}} = 0.$$

So we use the solution obtained earlier but with conjugated coefficients:

$$\xi_{PW} = \overline{\mathcal{D}\hat{\mathbf{E}}_0} \exp(i\kappa \mathbf{d}_{\text{PML}} \cdot \overline{\mathcal{D}}(\mathbf{x} - \mathbf{c})).$$

The PML is not the only way to improve on the lower-order absorbing boundary condition inherent in the UWVF. In [27], the authors use an overlapping strategy whereby the scattered field is approximated using a boundary integral representation on the surface of the scatterer, and this is matched to the UWVF solution on the exterior of Ω away from the surface of the scatterer. The problem can be solved iteratively using successive UWVF solutions and multipole evaluations of the integral operator. Since the integral operator is evaluated away from the surface where it is defined, near interactions are avoided and the fast multipole method is much simpler. The method is efficient for impenetrable scatterers since the outer

boundary of Ω needs only be a few elements from the scatterer. The method can be used for penetrable scatterers, but there the memory advantage is less since the interior of the scatterer needs to be meshed. For this reason, we use the PML here.

3 A New Element Type: Pyramids

In [11], we demonstrated that multiple mesh element types including tetrahedral, hexahedral, and prismoidal elements are useful when discretizing a scattering problem. One element type was missing in that report: pyramidal elements (see Fig. 2 right panel). These are useful when transitioning between regions filled with hexahedra and regions filled with tetrahedra. We now indicate how this element can be added to *ParMax*. First, by dividing the base of the pyramid into two subtriangles, we can accomplish all necessary integrals during matrix assembly by using the existing methods in *ParMax* for evaluating integrals on triangles. In fact, this is how all integrals on faces of geometric elements are implemented.

3.1 Plane Wave Selection for Pyramidal Elements

A key issue is the choice of the number of directions p for a pyramid element. In [28], we noted that the conditioning of the overall matrix $(D + C)$ can be estimated using the diagonal block of D , and this allowed us to suggest a heuristic for choosing the number of directions per element as follows. Because the blocks are independent, the problem then reduces to choosing p on each element to control the local condition number, which we do as follows.

We choose a reference element (in this case the pyramid with four base vertices $(\pm 1, \pm 1, 0)$ and the vertex $(0, 0, 1)$). Then for different target choices of the maximum condition number of D_k for that element, we can find the choice of p that gives a condition number just below this target condition number. This can be done for a range of scaled wave numbers $\kappa_{el}h$ where h is defined as the mean distance of the element's vertices from its centroid, and κ_{el} is defined locally on the element by $\kappa_{el} = \omega\sqrt{|\epsilon\mu|}$. We are particularly interested when $\kappa_{el}h$ is large, which corresponds to elements that are a multiple of the local wavelength in diameter. Following [11], in Fig. 2, the number of plane waves p found for given choices of the desired condition number is plotted as a function of $\kappa_{el}h$. In particular, we choose the maximum condition number of the matrix blocks of D_k to be limited by the tolerances 10^5 , 10^7 , or 10^9 .

For use in *ParMax*, this data are fitted by a quadratic polynomial in $\kappa_{el}h$ together with the constraint that the polynomial gives at least four directions even on the finest grid so we choose the coefficients a , b , and c in

$$p = \left\lceil a (\kappa_{el}h)^2 + b (\kappa_{el}h) + c \right\rceil \quad (15)$$

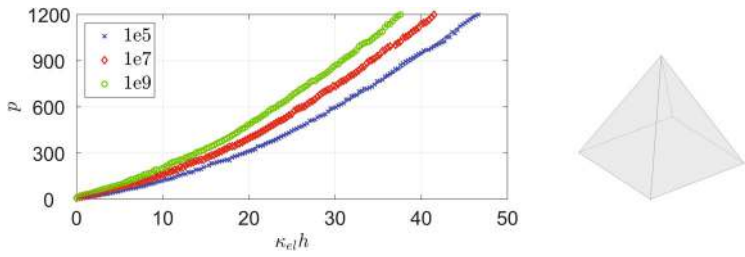


Fig. 2 Left: The number of directions p as a function of $\kappa_{el}h$ where the basis dimension is chosen by constraining the maximum condition number of D on the reference element to be respectively 10^5 , 10^7 or 10^9 . Right: the pyramidal reference element

Table 1 Parameters for the polynomial (15) predicting the number of directions for the pyramidal reference element

$\max(\text{cond}(D_k))$	a	b	c
1e5	0.3854	8.0358	4.0000
1e7	0.4237	11.4219	5.5439
1e9	0.4526	14.7671	11.4419

to fit the data. Results of this fitting are shown in Table 1. This polynomial is used in *ParMax* to set the local number of directions p_k on elements K_k , $k = 1, \dots, N$ that are pyramids.

Despite the fact that the number of plane wave directions is computed using just one reference element, we find that the aforementioned formula gives a number of directions that effectively controls the global condition number while providing good accuracy (the accuracy of the plane wave approximation increases with the number of directions). Effectively we are asking for the best accuracy given a specified condition number. A more advanced choice might estimate p by including more geometric information from a range of element shapes, but this would be more costly. No attempt is made to align the directions of the plane waves with features of the scattering solution (cf. [17]).

3.2 Hybrid Elements

The calculation of the entries of D^k on element K_k , $k = 1, \dots, N$ as well as the entries of C are computed by dividing the (possibly curvilinear) faces of K_k into triangular (or curvilinear triangular) patches. For example, in the case of the cube, each face is subdivided into two triangles. Then, if a triangular facet is planar, we compute the entries analytically or else, when the facets are curvilinear, we use quadrature as described in [11].

As an example of the use of multiple element types, we show results for a very simple test problem on the cube $[-1.5, 1.5]^3$ using as exact solution a plane wave not in the direction of any plane wave in the basis. The frequency is 1 GHz and the boundary condition is set using $Q = 0$. Three meshes are considered, one is a

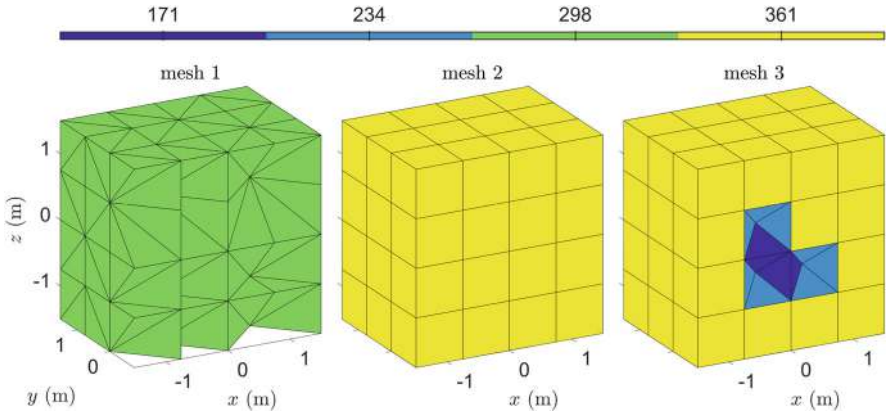


Fig. 3 Cross sections of the computational meshes used in the hybrid mesh numerical experiment: Left: mesh 1 consists solely of tetrahedral elements. Middle: mesh 2 consists solely of hexahedral elements. Right: mesh 3 comprises hexahedral, tetrahedral, and pyramid elements. The colorbar indicates the number of directions for the plane waves in the elements

Table 2 The table summarizes results for the cube test problem using the meshes in Fig. 3. For each mesh we list the number of elements for different element types, number of vertices, and minimum and maximum distance between vertices, and percentage relative L^2 error

mesh	$N_{\text{tetra elements}}$	$N_{\text{pyramid elements}}$	$N_{\text{hexa elements}}$	N_{vertices}	h_{\min} (m)	h_{\max} (m)	Relative L^2 error (%)
1	384	0	0	125	0.75	1.30	0.11
2	0	0	64	125	0.75	1.30	0.15
3	8	14	61	128	0.65	1.30	0.15

pure tetrahedral mesh (mesh 1), the second a pure hexahedral mesh (mesh 2), and the third (mesh 3) has an L-shaped inclusion filled with tetrahedral elements, which are then converted to hexahedral elements using pyramid elements. In all cases, $\epsilon = \mu = 1$. Cross sections of the meshes are shown in Fig. 3.

Results are summarized in Table 2. The results indicate that the numerical accuracy is comparable across all mesh configurations. This suggests that we can use hybrid grids without a large adverse impact on accuracy.

4 Approximation of Smooth Surfaces

A Trefftz method simplifies fitting a curved boundary compared to the finite element method. The approximation theory for plane waves described in [15] holds for curvilinear elements (provided some nonrestrictive geometric conditions hold). It is then a matter of computing the contributions to the matrices D and C (see for example (10)) by computing integrals face by face.

Consider a face F in the mesh, then F is the image of a smooth invertible map $\mathbf{G}_F : \hat{F} \rightarrow F$ from the reference triangle $\hat{F} \subset \mathbb{R}^2$ with vertices $(0,0)$, $(1,0)$, $(0,1)$ to F . If \mathbf{G}_F is known exactly, it can be used, but in general we approximate \mathbf{G}_F using a vector polynomial $\mathbf{G}_{q,F}$ of degree q on the reference element. This polynomial is defined by interpolating \mathbf{G}_F , and for simplicity, we use the standard Lagrange interpolation points on F .

Using $\mathbf{G}_{q,F}$ we have an approximation to F given by $\mathbf{G}_{q,F}(\hat{F})$, and we use this approximate curvilinear facet to compute the necessary integrals on the faces of an element using numerical quadrature. Currently, we do not have a sophisticated way of choosing the order of quadrature on each face, instead opting for a dense set of quadrature points. Optimization of the quadrature scheme in terms of the number of quadrature points to obtain a given accuracy would improve efficiency of matrix assembly.

4.1 Scattering from a PEC Sphere

In [11], we studied the dependence of the Radar Cross Section (RCS) computed from the far field pattern of the wave scattered by a PEC sphere of radius 1m at the frequency 2.0GHz. This was studied for the surface approximation with $q = 1, 2$ (obviously $q = 1$ is the case when the surface of the sphere is approximated by flat facets). In that paper, we observed a marked improvement in accuracy comparing $q = 1$ and $q = 2$, which allowed us to increase the mesh size relative to the wavelength of the incident wave on the surface of the scatterer when $q = 2$. Hence, we can compute the solution more rapidly for a given desired accuracy.

Interestingly, as we shall see, the case $q = 3$ does not produce an improved RCS compared to $q = 2$. In order to investigate this further, we also implemented a quartic ($q = 4$) approximation of the curvilinear facets, and tested the accuracy of *ParMax* using different surface grids and $q = 1, 2, 3, 4$.

For these tests, the incident electric field is a plane wave propagating in the direction of the positive x -axis, and the field is polarized in the y -direction. The frequency of the incident field is $f = 2.0$ GHz. The propagation medium is assumed to be a vacuum, and the PML (thickness δ_{PML} of $5\lambda_0$) is set to a minimum distance of $3\lambda_0$ from the PEC sphere. In the PML, we use hexahedral elements, while the vacuum is filled with tetrahedral and pyramid elements.

We tested eight configurations for the computational grids. Figure 4 shows the surface triangulations for the PEC sphere, ranging from a very sparse to a highly dense grid, see Table 3 for details. For each surface triangulation, we request COMSOL Multiphysics to build a grid of Ω with a suggested grid size of $5\lambda_0$ where λ_0 is the wavelength of the radiation in the air away from the sphere. We use the same PML and outer boundary condition for each test case. We then compute the scattered field using surface approximations with degree $q = 1, 2, 3, 4$. From the scattered field, the RCS is computed for directions that are defined by the the

Table 3 This table provides details of the computational grids used for the scattering from the PEC sphere case

Mesh	$N_{\text{tetra elements}}$	$N_{\text{pyramid elements}}$	$N_{\text{hexa elements}}$	N_{vertices}	h_{min} (cm)	h_{max} (m)
1	357	96	152	374	32.51	1.30
2	383	96	152	385	35.13	1.30
3	571	96	152	430	22.59	1.30
4	870	96	152	505	9.90	1.30
5	827	96	152	499	16.44	1.30
6	1474	96	152	638	7.09	1.30
7	1670	96	152	702	8.46	1.30
8	24,868	96	152	8023	0.94	1.30

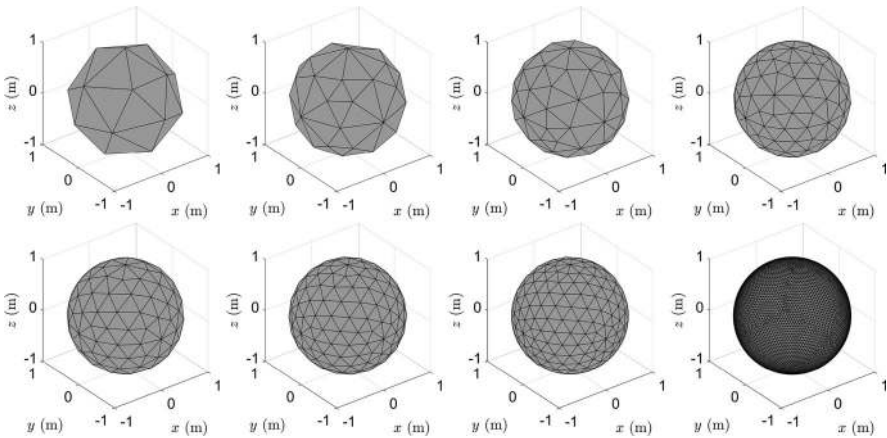


Fig. 4 Surface triangulations used for testing the effects of different surface approximations for the PEC sphere

azimuth angle ϕ ($^{\circ}$) as $(\cos(\phi\pi/180), \sin(\phi\pi/180), 0)$. The Mie series is used to compute a reference exact value (c.f. [29]).

Figure 5 shows the relative L^2 error in the bistatic RCS as a function of surface grid density (for the surface grids in Fig. 4) for different curved elements (using $q = 1, 2, 3, 4$). Several observations can be made from the results:

- As expected from our results in [11], when using flat elements good numerical accuracy is obtained only for the densest surface grid in which the flat facets approximate the curved surface sufficiently well. Of course, this dense surface grid causes a denser volume grid near the PEC surface and hence more DoF for the problem.
- Quadratic and cubic surface approximations lead to comparable numerical accuracy except on the coarsest grid, and hence, the motivation of using cubic surfaces is limited in this case.

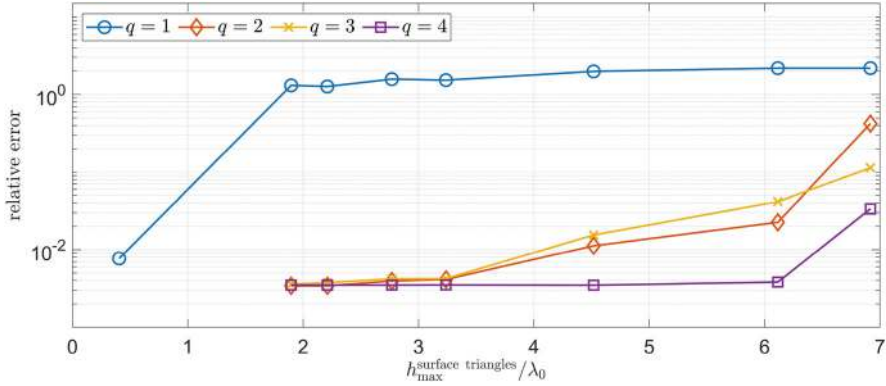


Fig. 5 Relative error in the bistatic RCS as a function of element size normalized against wavelength λ_0 in vacuum for different surface meshes (see Fig. 4) and order q of the curved surface elements

- Interestingly, the quartic ($q = 4$) surface approximation leads to good numerical accuracy for more sparse surface representations (except on the coarsest surface grid). Hence, the use of quartic surfaces is justified and provides a useful add-on to the software.

We conjecture that the small difference between the relative error when using quadratic $q = 2$ and cubic $q = 3$ surface representations is due to the symmetry of the spherical scatterer. Suppose a surface element has its centroid at $x = 0, y = 0$ and let $z = \sqrt{1 - x^2 - y^2}$ (by rotating the coordinate system, this is possible for any surface face). Then for small x and y , the Maclaurin series of z in (x, y) is

$$z = 1 - \frac{x^2}{2} - \frac{x^4}{8} + \left(-\frac{1}{2} - \frac{1}{4}x^2 - \frac{3}{16}x^4\right)y^2 + \left(-\frac{1}{8} - \frac{3}{16}x^2 - \frac{15}{64}x^4\right)y^4 + O(x^6 + y^6).$$

Notice that cubic terms are not present in this series. Thus, for a small facet with centroid at $x = y = 0$, we expect the cubic terms in the interpolating function $\mathbf{G}_{q,F}$ to be small for $q = 3$. As a result, the $q = 3$ fit should not give markedly different results compared to the $q = 2$ case until the surface elements get large. This is seen in Fig. 5, where the accuracy for $q = 2$ and $q = 3$ is comparable until the largest surface element size. However, the quartic ($q = 4$) surface approximation is expected to improve the surface fit (quartic terms do not vanish in the above series), and this explains why the quartic approximation improves over the quadratic or cubic cases for larger surface element size.

A further remark is that for small surface element size, the use of $q = 2, 3, 4$ gives similar error. Most likely this reflects the limits on accuracy imposed by the discretization errors due to the volume plane wave discretization away from the sphere and the choice of PML (both of which are unchanged as we vary q).

4.2 Penetrable Dielectric Sphere

In [11], we also considered scattering from a dielectric sphere. In this case, the electromagnetic wave enters the sphere, which is now termed penetrable. In this numerical experiment, a penetrable sphere with a radius of 1 meter is centered at the origin inside a cube defined by $[-1-10\lambda_0, 1+10\lambda_0]^3$, where λ_0 is the wavelength in vacuum. For the sphere, we assume a relative permittivity of $\epsilon = 2.5$ and a relative permeability of $\mu = 1$. The surrounding medium is vacuum. The incident field has a frequency of $f = 2$ GHz, and a PML with a thickness of $5\lambda_0$ is applied on each side of the cube.

An artificial spherical boundary with a radius of $1 + \lambda_0$ is employed to distinguish the scattered field region outside the artificial boundary from the region inside the artificial boundary where the total field is used instead. The scattered-total field formulation described in [11] is utilized to introduce a source on this artificial boundary. This artificial boundary was also used to compute the far-field pattern using surface integrals [22].

We utilised quartic curved elements ($q = 4$) and a mesh size parameter of $5\lambda_s$ in the volume, where λ_s is the local wavelength. Figure 6 shows cross section of the computational grid, which uses the tetrahedral, hexahedral, and pyramidal element types available in *ParMax*. In the PML layer, only hexahedral elements are used, whereas in and around the scatterer, tetrahedra are used. To connect the two mesh regions, pyramid elements are employed. The colorbar on the figure (Fig. 6) indicates that $88 \leq p_K \leq 934$ with the maximum number of plane waves used in the large hexahedral element in the PML. The grid comprises 150 pyramid elements and 2,116 tetrahedral elements. Furthermore, the PML layer is discretized using 218 hexahedral elements. The entire grid is composed of 791 vertices, with $h_{\min} = 0.15$ m and $h_{\max} = 1.30$ m.

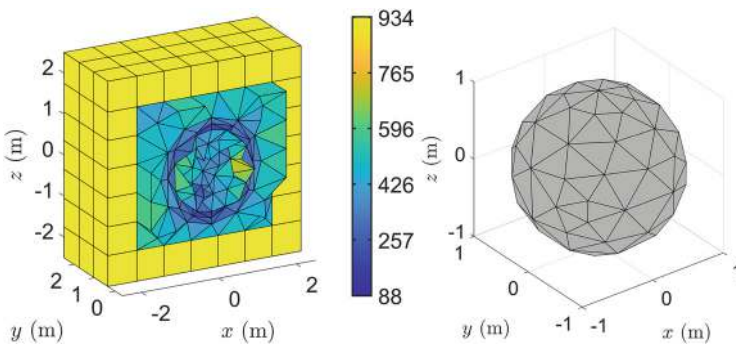


Fig. 6 Left: Cross section of the computational grid for the penetrable dielectric sphere. The colorbar shows the number of directions p_K used in the elements in the mesh. Right: Surface triangulation on the interface between the vacuum and penetrable sphere

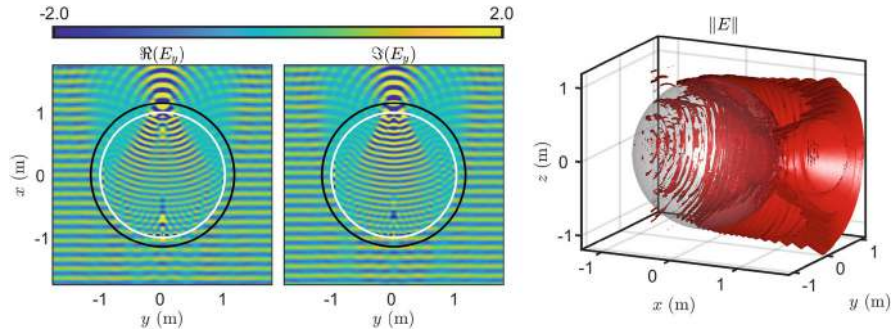


Fig. 7 The left and center panels show snapshots of the electric field $\Re(E_y)$, and $\Im(E_y)$ on the $z = 0$ plane for the penetrable dielectric sphere. The solid white line shows the material interface, and the solid black line marks the artificial interface used to introduce the incident wave. The right panel shows an isosurface of $\|E\|$ at value 0.5

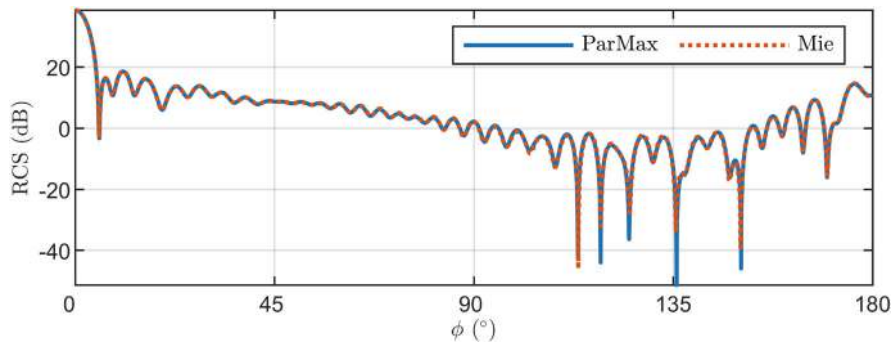


Fig. 8 Bistatic RCS for the penetrable dielectric sphere as a function of the azimuthal angle ϕ at 2 GHz

Rather than repeat the investigation of the effects of surface triangulation and surface approximation degree, we perform a single experiment with the quartic approximation of the curved surface of the sphere. In Fig. 7 left and center panels, we show the total field components $\Re(E_y)$ and $\Im(E_y)$ on the $z = 0$ -plane and in the right panel the isosurface $\|E\|$ at value 0.5.

Having computed the near field, we can compute the far field pattern and hence the RCS. This is shown in Fig. 8 together with the Mie series result. There is good agreement with the Mie series over the entire range of angles.

5 Numerical Results for a PEC Almond

In this section, we study scattering from a PEC metallic almond target. The target has the same shape as the well-known NASA almond [19], but we compare it to published experimental data from [18]. We compare the monostatic RCS, for which

Table 4 This table provides details of the computational grids used for the almond scatterer

f (GHz)	N_{tetra} elements	N_{pyramid} elements	N_{hexa} elements	N_{vertices}	h_{min} (cm)	h_{max} (m)
3.5	3326	96	152	950	0.30	0.56
5.125	4023	96	152	1120	0.27	0.41
7.0	5231	112	172	1434	0.13	0.30
10.25	6054	94	150	1617	0.13	0.23

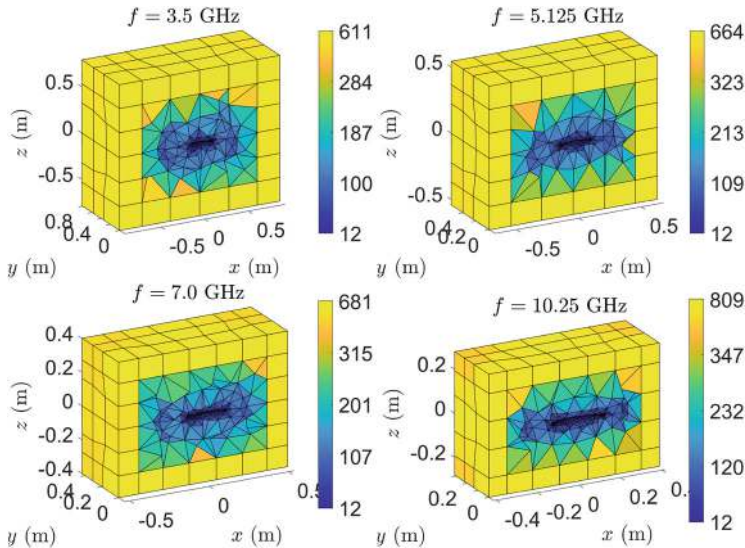


Fig. 9 Cross sections of the computational grids for the almond shown in Fig. 10. The colorbar shows the number of plane wave directions per element

the radar transmitter and receiver are collocated, to measured data obtained from [30]. The RCS is computed from the far-field pattern of the electric field and is measured at polar angles $\phi \in [0, 180]^\circ$. The geometry of the almond can be seen from the surface triangulation plots in Fig. 10. We use $q = 4$.

The propagation medium is vacuum, and the incoming plane wave is studied for frequencies $f \in [3.5, 5.215, 7.0, 10.25]$ GHz. The geometry is modeled by assuming a minimum distance of $6\lambda_0$ from the almond to the PML. In addition, the PML thickness is set to $3\lambda_0$.

Grid generation details are given in Table 4, and cross sections of the meshes are visualized in Fig. 9 showing the number of plane wave directions on each element. We have used hexahedral elements in the PML and curvilinear tetrahedra with $q = 4$ to fit the almond surface. The surface triangulations are shown in Fig. 10 where we note that the surface grids have been refined in regions of high curvature.

The monostatic numerical and experimental values of the RCS for different frequencies and polarizations are shown in Fig. 11. The results illustrate that the RCS predicted by the UWVF aligns well with the measured data at each of

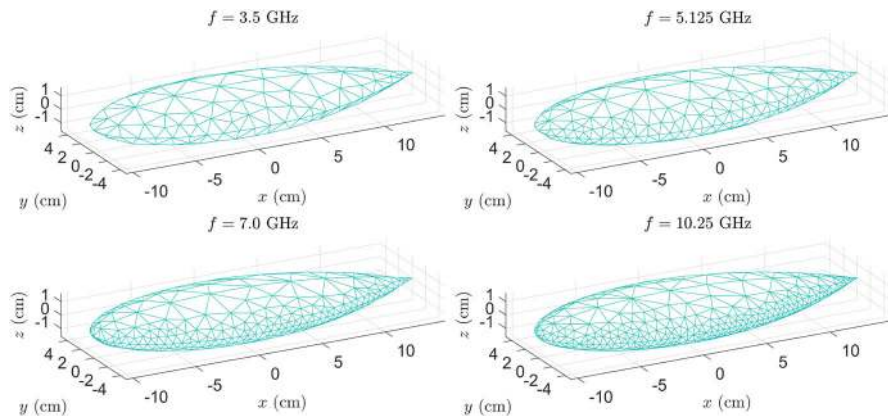


Fig. 10 Surface triangulation of the almond geometry at different frequencies

the frequencies over the whole angle range. This indicates the accuracy of the simulation model in capturing the frequency-dependent behavior of the almond case. The simulations were conducted for horizontal and vertical polarizations, and the results demonstrate a high level of agreement with the measurements in each case. This consistency across polarizations further validates the robustness of *ParMax*.

6 Conclusion

We have described our efforts to implement a general purpose scattering code using Trefftz basis functions via the UWVF. We showed two recent improvements: pyramidal elements and quartic boundary surface approximation. The latter was shown to allow larger surface mesh sizes on a smooth curved scatterer, and hence, good convergence was demonstrated for PEC and dielectric balls. Since spherical scatters have constant curvature, they do not offer a challenging test of surface approximation. To probe this more, we showed results for an almond-shaped scatterer that also has a sharp tip that causes the electromagnetic field to have a singularity at the tip. Compared to published measurements of real data, our predictions are a good fit.

The main challenge of this Trefftz method is the rapid rise in the condition number of the system as the mesh size h or wave number κ decreases. We have discussed a few ways to help with this problem, but currently make use of a simple a priori strategy to choose the number of directions per element. Our next effort will be to improve the choice of the element basis based on geometric properties of the element.

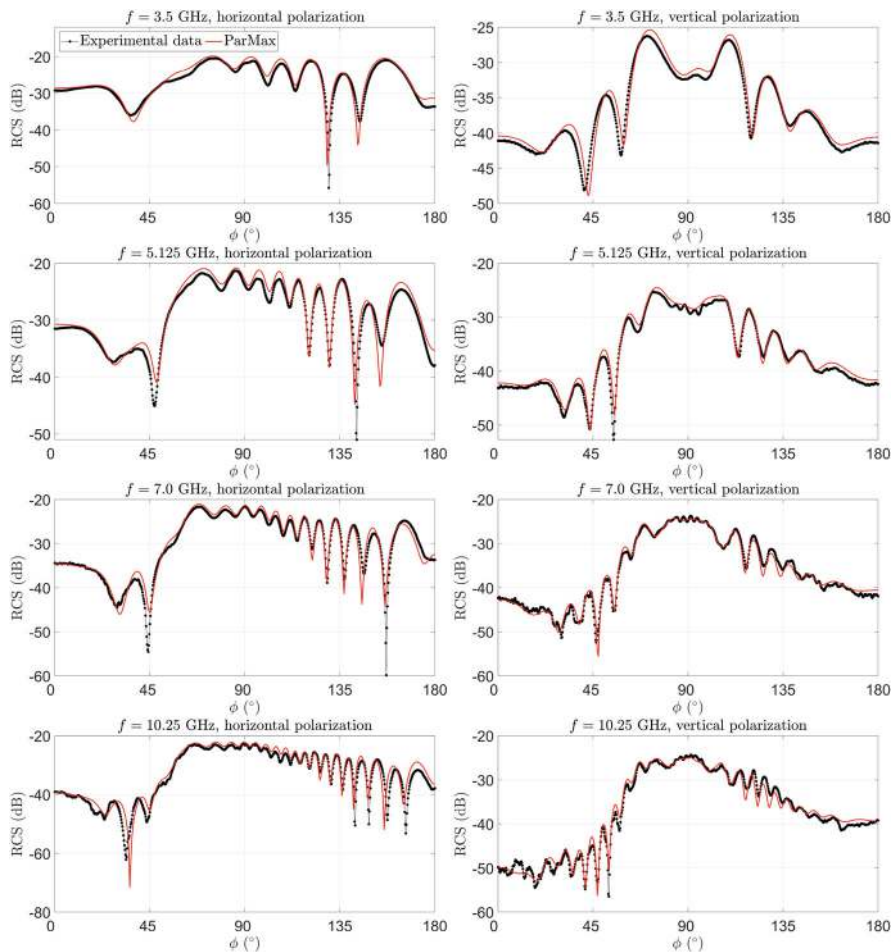


Fig. 11 Monostatic RCS for horizontal (left) and vertical (right) polarization for the almond from [18] for frequencies $f \in [3.5, 5.125, 7.0, 10.25]$ GHz (from top to bottom row). Measured data are from [30]. The fidelity of the computational results is similar to published results from other software (see for example [31])

Acknowledgments The research of P. M. is partially supported by the US AFOSR under grant number FA9550-23-1-0256. The research of T. L. is partially supported by the Research Council of Finland via the Finnish Center of Excellence of Inverse Modeling and Imaging, Flagship of Advanced Mathematics for Sensing Imaging and Modelling (grant no. 358944), and research project (grant no. 321761). The authors also wish to acknowledge the CSC—IT Center for Science, Finland, for generously sharing their computational resources.

References

1. E. Trefftz, Ein gegenstück zum Ritzschen verfahren, in *Proceedings of the 2nd International Congress of Applied Mechanics*, Zurich (1926), pp. 131–137
2. J.A. Kolodziej, J.K. Grabski, Many names of the Trefftz method. *Eng. Anal. Boundary Elements* **96**, 169–178 (2018)
3. P. Waterman, Matrix formulation of electromagnetic scattering. *Proc. IEEE* **53**, 805–812 (1965)
4. L. Bi, P. Yang, G.W. Kattawar, M.I. Mishchenko, Efficient implementation of the invariant imbedding T-matrix method and the separation of variables method applied to large nonspherical inhomogeneous particles. *J. Quant. Spectros. Radiat. Trans.* **116**, 169–183 (2013)
5. A. Lakhtakia, The Ewald–Oseen extinction theorem and the extended boundary condition method, in *The World of Applied Electromagnetics* (Springer, Cham, 2018)
6. D. Casati, R. Hiptmair, J. Smajic, Coupling finite elements and auxiliary sources for electromagnetic wave propagation. *Int. J. Numer. Modell. Electro. Netw. Devices Fields* **33**(6), e2752 (2020)
7. A. Barnett, T. Betcke, Stability and convergence of the method of fundamental solutions for Helmholtz problems on analytic domains. *J. Comput. Phys.* **227**, 7003–7026 (2008)
8. Q. Hu, L. Yuan, A plane-wave least-squares method for time-harmonic Maxwell’s equations in absorbing media. *SIAM J. Sci. Comput.* **36**, A1937–A1959 (2014)
9. O. Cessenat, Application d’une nouvelle formulation variationnelle aux équations d’ondes harmoniques. Problèmes de Helmholtz 2D et de Maxwell 3D. Ph.D. Dissertation, Université Paris IX Dauphine, 1996
10. O. Cessenat, B. Després, Using plane waves as base functions for solving time harmonic equations with the Ultra Weak Variational Formulation. *J. Comput. Acoust.* **11**, 227–38 (2003)
11. T. Lähivaara, W.F. Hall, M. Malinen, D. Ota, V. Shankar, P. Monk, A high-order ultraweak variational formulation for electromagnetic waves utilizing curved elements. *IEEE Trans. Antennas Propag.* **72**, 4440–4453 (2024)
12. A. Buffa, P. Monk, Error estimates for the ultra weak variational formulation of the Helmholtz equation. *ESAIM Math. Model. Numer. Anal.* **42**, 925–940 (2008)
13. C. Gittelsohn, R. Hiptmair, I. Perugia, Plane wave discontinuous Galerkin methods. *ESAIM Math. Model. Numer. Anal.* **43**, 297–331 (2009)
14. R. Hiptmair, A. Moiola, I. Perugia, Error analysis of Trefftz-discontinuous Galerkin methods for the time-harmonic Maxwell equations. *Math. Comput.* **82**, 247–268 (2011)
15. R. Hiptmair, A. Moiola, I. Perugia, A survey of Trefftz methods for the Helmholtz equation, in *Building Bridges: Connections and Challenges in Modern Approaches to Numerical Partial Differential Equations*. ser. Lecture Notes in Computational Science and Engineering (LNCSE), ed. by G.R. Barrenechea, A. Cangiani, E.H. Georgoulis, vol. 114 (Springer, Berlin, 2016), pp. 237–278
16. R. Hiptmair, A. Moiola, I. Perugia, Trefftz discontinuous Galerkin methods for acoustic scattering on locally refined meshes. *Appl. Numer. Math.* **79**, 79–91 (2014)
17. S. Congreve, P. Houston, I. Perugia, Adaptive refinement for hp-version Trefftz discontinuous Galerkin methods for the homogeneous Helmholtz problem. *Adv. Comput. Math.* **45**, 361–393 (2019)
18. T. Kelley, D.A. Chamulak, C.C. Courtney, A.E. Yilmaz, Rye canyon radar cross-section measurements of benchmark almond targets. *IEEE Antennas Propagat. Mag.* **62**, 120–135 (2020)
19. A.C. Woo, H.T.G. Wang, M.J. Schuh, M.L. Sanders, Benchmark radar targets for the validation of computational electromagnetics programs. *IEEE AP Mag.* **35**, 84–89 (1993)
20. CSC – IT Center for Science Ltd, Computing environments. <https://docs.csc.fi/computing/available-systems/>, Accessed: 26 Jun 2024
21. D. Hardin, T. Michaels, E. Saff, A comparison of popular point configurations on S^2 . *Dolomites Res. Notes Approx.* **9**, 16–19 (2016)

22. D. Colton, R. Kress, *Inverse Acoustic and Electromagnetic Scattering Theory*, 4th edn. (Springer, New York, 2019)
23. S. Congreve, J. Gedicke, I. Perugia, Numerical investigation of the conditioning for plane wave discontinuous Galerkin methods, in *Numerical Mathematics and Advanced Applications ENUMATH 2017*, ser. Lecture Notes in Computational Science and Engineering, ed. by F. Radu, K. Kumar, I. Berre, J. Nordbotten, I. Pop, vol. 126 (Springer, Cham, 2019)
24. H. Barucq, A. Bendali, J. Diaz, S. Tordeux, Local strategies for improving the conditioning of the plane-wave Ultra-Weak variational formulation. *J. Comput. Phys.* **441**, 110449 (2021)
25. E. Parolin, D. Huybrechs, A. Moiola, Stable approximation of Helmholtz solutions in the disk by evanescent plane waves. *ESAIM: Math. Modell. Numer. Anal.* **57**, 3499–3536 (2023)
26. W.C. Chew, W.H. Weedon, A 3D perfectly matched medium from modified Maxwell's equations with stretched coordinates. *Microwave Opt. Technol. Lett.* **7**(13), 599–604 (1994)
27. E. Darrigrand, P. Monk, Combining the ultra-weak variational formulation and the multilevel fast multipole method. *Appl. Numer. Math.* **62**(6), 709–719 (2012). *Advances in Boundary Integral Equations and Related Topics: On the Occasion of Professor George C. Hsiao's 75th Birthday*
28. T. Huttunen, M. Malinen, P. Monk, Solving Maxwell's equations using the ultra weak variational formulation. *J. Comput. Phys.* **223**, 731–758 (2007)
29. P. Monk, *Finite Element Methods for Maxwell's Equations* (Oxford University Press, Oxford, 2003)
30. Austin CEM Benchmarks. <https://github.com/UTAustinCEMGroup/AustinCEMBenchmarks>. Accessed: 26 Jun 2024
31. Lucernhammer Website. https://lucernhammer.tripointindustries.com/benchmark_data/AustinCEMBenchmarks/almonds/almonds.html. Accessed: 26 Jun 2024

Weiglhofer Symposium Panel Discussion: Future Developments



**Ibrahim Abdulhalim, Gérard Gouesbet, Gerhard Kristensson ,
Guy Vandenbosch, and Theo Rasing**

The second Weiglhofer Symposium on Electromagnetic Theory concluded with a round table discussion on “Future Developments.” The panel featured Ibrahim Abdulhalim from the ECE School at Ben Gurion University, Gérard Gouesbet from the Institut National des Sciences Appliquées de Rouen, Gerhard Kristensson from Lund University, Guy Vandenbosch from Katholieke Universiteit Leuven, and Theo Rasing from Radboud University Nijmegen, who also served as the chair. All participants in the symposium actively engaged in the discussion. In their opening statements, the panelists highlighted the critical role of Electromagnetism—particularly in the fields of Optics and Photonics—in addressing some of today’s most pressing societal challenges, including Energy, Climate, and Health. The ability to process vast amounts of data rapidly and with significantly improved energy efficiency is vital in these areas, and optics is poised to play a central role. The exponential rise in energy consumption due to Artificial Intelligence (AI) and

I. Abdulhalim

Ben Gurion University, Beër Sjeva, Israel

e-mail: abdulhim@bgu.ac.il

G. Gouesbet

Institut National des Sciences Appliquées de Rouen, Rouen, France

e-mail: gouesbet@coria.fret

G. Kristensson

Lund University, Lund, Sweden

e-mail: gerhard.kristensson@telia.com

G. Vandenbosch

Katholieke Universiteit Leuven, Leuven, Belgium

e-mail: guy.vandenbosch@ku.leuven.be

T. Rasing (✉)

Radboud Universiteit, Nijmegen, The Netherlands

e-mail: theo.rasing@ru.nl

the Internet of Things (IoT) demands more energy-efficient Information Technology (IT). Light is expected to be crucial not only for the fast and energy-efficient transport of data but also for computation itself. Emerging technologies such as wave-based and neuromorphic computing with light are promising but require much more research. Edge computing, which involves the direct analysis of data from numerous sensors, is another area of interest that necessitates the development of real-time solutions for inverse problems—a challenge that is not yet fully met and requires further research.

In the context of energy, the development of photon-harvesting technologies, whether for direct use or conversion to electricity, will benefit from advances in antenna design, particularly in the microwave domain. The expanding use of THz sources will also drive research in this area. Light scattering, which enables real-time data analysis, is a powerful tool for characterizing small particles, which play a crucial role in pollution and, consequently, health.

Beyond these societal issues, the discussion also touched on broader concerns closely tied to the future of the field. One key observation was the tendency for redundant research efforts—essentially “reinventing the wheel”—due to a lack of information sharing. Addressing this issue will require standardized formats for data sharing, a challenge that, while complex, should not be an excuse to avoid pursuing a solution. Collaboration with industrial partners will also be crucial for addressing many of the challenges discussed. However, it was noted that such collaborations are often more successful with large industries, which typically have their research labs than with small and medium-sized enterprises, which may have the need but lack the resources and connections to engage in application-oriented academic research. Additionally, fostering better relationships with industry for future developments will require an understanding of cultural differences: while industry seeks solutions, academia is often focused on exploring problems. Although this seems like an ideal match, in practice, it can create significant challenges.

Index

A

Ambichiral Reusch pile, 364, 365, 373–378, 380–383
Anisotropy, 48, 52, 64, 71, 73, 77, 82, 94, 96, 98, 100

B

Biosensors, 108, 118
Boundary integral equations, 195–218

C

Chevronic thin film, 364, 365, 371–373
Chiral material, 238, 367
Chiral sculptured thin films (CSTFs), 173, 175, 188, 281–284, 289, 290, 299, 302, 362, 364, 374, 383
Circular Bragg phenomenon, 173–192, 330, 337–343, 345, 364, 374, 375
Circular dichroism, 181–184, 337
Circular polarization, 12, 13, 182, 184, 330, 346, 347, 363
Circular polarization state, 173, 178, 182, 184, 347, 363
Circular reflectance, 177–180, 188, 379
Circular transmittance, 177, 178, 180, 189, 379
Columnar thin film (CTF), 144, 281, 282, 295, 362, 364, 365, 370–371
Computational electromagnetism, 393
Cylindrical arrays, 307–327

D

Dichroism, 181–184
Dispersion relations, 32, 38, 91, 133–141, 145, 335, 351

E

Electromagnetic potentials, 236
Electromagnetic shielding, 307–327
Ellipticity, 184–187
Energy saving, 87–121
Equichiral, 363–365, 378

F

Finely chiral Reusch pile, 362, 364, 380–383

G

Generalized Lorenz-Mie theories, 223–242
Geometric phase, 185–192, 361–388
Gradient media, 151, 154–157, 170

H

Holography, 133
Hydrodynamic Drude Model (HDM), 198, 208–210, 213, 218

L

Lakhtakia, A., 1–15, 63–82, 173–192, 281–303, 361–388
 Light modulation, 87–121
 Light scattering, 98, 239, 242, 422
 Linear, 17, 18, 22, 31, 34, 36, 37, 92, 158, 159, 173, 176, 178–184, 197, 205, 207, 237, 282, 307, 311, 312, 315, 316, 318, 330, 333–335, 339, 340, 342, 345, 346, 348, 349, 353, 356, 370, 375, 379, 396, 401
 Linear reflectance, 178, 180, 181, 190
 Linear transmittance, 178–180, 182, 191, 379
 Line waves, 43–59

M

Maxwell Garnett formalism, 63, 64, 67–70, 82
 Metasurfaces, 43–46, 48, 51, 53, 54, 56–58, 89–94, 100, 108, 111–121, 307, 308, 326
 Mica, 1–17
 Multiple scattering, 240, 307–327

N

Nanophotonics, 108, 151–170

O

Optical rotation, 11, 184–187, 330, 331, 339, 342, 353–357

P

Particulate slab, 253–279
 Photonic metamaterials, 87–121
 Physical bounds, 253–279
 Plasmonic waveguide, 17–41
 Poincaré spinor, 186, 187, 190–192, 361–362, 368–369, 376

R

Reflectance, 118, 134, 135, 173, 177–181, 188–190, 295, 299, 302, 334, 342, 346, 347, 352, 362, 364, 368, 369, 379
 Reusch pile, 361–388
 Reverse circular Bragg Phenomenon, 340

S

Scattering, 47, 63, 93, 144, 196, 225, 307, 331, 393, 422
 Sculptured, 116, 337, 363
 State, 10, 14, 45, 87, 90, 95, 96, 105, 110, 155–157, 163–169, 174, 184, 187, 195, 229, 237, 330, 337, 341, 342, 344–347, 349, 351, 355, 356, 363, 369, 370, 395
 Structural handedness, 174, 175, 177, 188, 281, 282, 284, 337, 341, 363, 366, 367, 371, 373, 376, 378, 380
 Structurally chiral materials (SCMs), 173–175, 178, 179, 182, 184
 Sum rules, 253, 260–264, 266, 268–270
 Surface electromagnetic waves, 151–170
 Surface plasmon polariton (SPP), 17, 21, 31–34, 36–40, 43, 56, 105, 151, 155, 162, 169, 282, 284–293, 302

T

Temporal Bragg gratings, 354
 Thin film, 100, 103, 112, 118, 362, 365, 370–374, 384
 T-matrix, 223–242, 393, 394
 Transmission, 91, 93, 94, 103, 104, 108, 113, 120, 133–135, 151, 158–163, 165, 167–170, 174, 176–178, 182, 187, 189, 191, 225, 253, 254, 257–270, 275, 293, 295, 308, 331, 357, 362, 364, 367–369, 394, 399, 403
 Transmittance, 90, 135, 137, 139–141, 177–182, 189, 191, 295, 299, 302, 334, 340, 341, 346, 347, 362, 364, 368, 369, 379
 Trefftz method, 393–417
 Truncated ellipsoids, 64, 70, 78–81

U

Unidirectional wave, 17–41
 Uniform Bragg reflector, 349
 Universal bandgap, 282, 293–302, 380

W

Wave propagation, 159, 282, 284–293, 302, 308, 330, 349, 364